



FACULTY OF ENGINEERING AND THE ENVIRONMENT

Research group: National Centre Of Advanced Tribology (nCATS)

# **Cavitation erosion-corrosion in marine propeller materials**

By

**Jahnabi Basumatary (B.E., MSc)**

**Supervised by:**

Prof. R. J. K. Wood,  
National Centre of Advanced Tribology

Prof. S. R. Turnock,  
Fluid Structure Interaction

**Industrial sponsor:**

Lloyd's Register

Thesis for the degree of Doctor of Philosophy

June 2017

## Abstract

Cavitation erosion process is a very complex phenomenon depending not only on the type and unsteadiness of cavitation, but also the response of the propeller and rudder materials to the cavitation energy imparted upon. It is highly destructive in nature and can cause severe loss in the performance of the ships that may eventually lead to frequent dry dockings, inspections and preventive maintenance or replacement of the damaged parts, resulting in a rather expensive maintenance.

The aim of this PhD project is to look at different aspects in characterising the materials generally used for manufacturing the ship propellers and rudders based on their resistance to cavitation erosion. It aims to understand the cavitation phenomena simulated by the ultrasonic vibratory probe device on various ship propeller material samples. Several ultrasonic vibratory cavitation tests were conducted for cavitation erosion, pure corrosion and combined cavitation erosion-corrosion on the two most common metallic propeller materials, Duplex Stainless Steel (DSS) and Nickel Aluminium Bronze (NAB), especially comprising of well-formed oxide films in different conditions. The investigation of the synergistic effect existing between the cavitation erosion and corrosion was carried out with the help of steady mass loss over a period of time and in-situ electrochemical measurements of corrosion. Alicona was employed for surface analyses, and comparisons between gravimetric and volumetric/optical loss measurements were obtained using precision weighing machine and Alicona respectively. Ag/AgCl reference electrode was used for in-situ electrochemical experiments done on both the sample materials kept at open circuit potential, and electrochemical impedance spectroscopy to study the corrosion behaviour during the experimental tests.

In order to understand the combined synergistic effects of cavitation erosion and corrosion in seawater five different methods were employed to measure and quantify synergism. The experiments were conducted using an ultrasonic vibratory horn functioning at 19.5 kHz frequency and  $80\text{ }\mu\text{m} \pm 0.2\text{ }\mu\text{m}$  peak-to-

peak amplitude. The test methods used to obtain the synergy included gravimetric mass loss technique, volumetric mass loss and mean depth of penetration rate methods, and polarization technique. Scanning electron microscopy was used to analyse microstructural characteristics of the cavitated sample surfaces, as well as the transverse-sections of the surface features. The materials were subjected to pure erosion, pure corrosion and the combined effect of erosion-corrosion in order to understand and measure the individual contributions of each aspect.

The extensive experimental results obtained and the conclusions drawn have attempted to address the aim of the research, and meet all the objectives to the best effect. Synergism was found to have measurable impact on the cavitation erosion-corrosion of both NAB and DSS. NAB underwent selective phase attack, resulting in increased material removal especially in the presence of corrosive environment. Whereas, DSS was observed to undergo ductile failure in the cavitated zone in the form of extrusion of the austenite at the cavity boundary along with microcracks and cleavage facets that could be attributed to the austenite to martensite transformation by either high strain or high temperature generated during cavitation. The implications of immersing as-cast NAB in 3.5% NaCl solution for few months seemed to drastically change the synergy behaviour of the material. Whereas, DSS, having higher mechanical and corrosion property as compared to NAB seemed to give best outcome for cavitation erosion-corrosion.

## Table of Contents

<b>Abstract.....</b>	<b>i</b>
<b>Table of Contents .....</b>	<b>iii</b>
<b>Table of Figures.....</b>	<b>vii</b>
<b>Table of Tables .....</b>	<b>xv</b>
<b>Nomenclature .....</b>	<b>xvii</b>
<b>Declaration of Authorship .....</b>	<b>xix</b>
<b>Acknowledgment.....</b>	<b>xxi</b>
<b>Chapter 1: Introduction.....</b>	<b>1</b>
<b>1.1. Cavitation – Background and Theory.....</b>	<b>1</b>
<b>1.2. Boat and marine propellers .....</b>	<b>5</b>
1.2.1 <i>Boat and marine propulsion System .....</i>	<i>5</i>
1.2.2 <i>Propeller materials.....</i>	<i>7</i>
1.2.3 <i>Propeller issues.....</i>	<i>9</i>
<b>1.3. Aims and Objectives .....</b>	<b>12</b>
<b>1.4. Scope of the Research .....</b>	<b>13</b>
<b>1.5. List of Publications and work presented .....</b>	<b>14</b>
<b>Chapter 2: Cavitation process .....</b>	<b>17</b>
<b>2.1. Mechanism of Cavitation .....</b>	<b>18</b>
2.1.1. <i>Nucleation.....</i>	<i>18</i>
2.1.2. <i>Bubble formation, shape distortion and collapse.....</i>	<i>20</i>
<b>2.2. Cavitation Impact.....</b>	<b>22</b>
2.2.1. <i>Microjet impingement.....</i>	<i>22</i>
2.2.2. <i>Shock waves.....</i>	<i>26</i>
2.2.3. <i>Cavitation wear.....</i>	<i>28</i>
<b>2.3. Cavity properties .....</b>	<b>31</b>
<b>2.4. Cavitation Detection.....</b>	<b>33</b>
<b>2.5. Propeller Cavitation .....</b>	<b>35</b>
2.5.1. <i>Effects of cavitation on ship propellers.....</i>	<i>35</i>
2.5.2. <i>Types of propeller cavitation .....</i>	<i>38</i>
<b>2.6. Effect of corrosion environment on propeller cavitation .....</b>	<b>42</b>
2.6.1. <i>Effect of temperature .....</i>	<i>42</i>
2.6.2. <i>Effect of chemical activity and corrosion.....</i>	<i>43</i>
2.6.3. <i>Effect of liquid properties.....</i>	<i>44</i>



<b>2.7. Summary .....</b>	<b>44</b>
<b>Chapter 3: Literature Review .....</b>	<b>47</b>
<b>3.1. Cavitation test methods .....</b>	<b>48</b>
<b>3.2. Ultrasonic vibratory cavitation method.....</b>	<b>60</b>
<b>3.3. Cavitation wear vs. fatigue failure.....</b>	<b>68</b>
<b>3.4. Cavitation erosion-corrosion .....</b>	<b>71</b>
<b>3.5. Synergy between cavitation erosion and corrosion .....</b>	<b>77</b>
<b>3.6. Summary .....</b>	<b>82</b>
<b>Chapter 4: Methodology .....</b>	<b>85</b>
<b>4.1. Experimental set-up.....</b>	<b>86</b>
4.1.1. <i>Ultrasonic sonotrode .....</i>	<i>86</i>
4.1.2. <i>Ultrasonic cavitation rig arrangement.....</i>	<i>89</i>
<b>4.2. Propeller Materials.....</b>	<b>94</b>
4.2.1. <i>Duplex stainless steel.....</i>	<i>94</i>
4.2.2. <i>Nickel Aluminium Bronze.....</i>	<i>100</i>
4.2.3. <i>Galvanic corrosion properties in Seawater.....</i>	<i>109</i>
<b>4.3. Experimental methods .....</b>	<b>112</b>
4.3.1 <i>Sonotrode preparation .....</i>	<i>113</i>
4.3.2 <i>Sample preparation .....</i>	<i>115</i>
4.3.3 <i>Experimental techniques used.....</i>	<i>119</i>
4.3.4. <i>Synergy experimental measurements.....</i>	<i>124</i>
<b>4.4. Summary .....</b>	<b>127</b>
<b>Chapter 5: .....</b>	<b>129</b>
<b>Cavitation erosion-corrosion results and material characterization .....</b>	<b>129</b>
<b>5.1. Cavitation erosion rate.....</b>	<b>132</b>
5.1.1. <i>Nickel aluminium bronze.....</i>	<i>135</i>
5.1.2. <i>Duplex stainless steel.....</i>	<i>139</i>
<b>5.2 Surface profilometry .....</b>	<b>140</b>
5.1.1 <i>Talysurf surface profilometry.....</i>	<i>140</i>
5.1.2 <i>Alicona surface profilometry.....</i>	<i>142</i>
<b>5.3 Microstructural analysis.....</b>	<b>145</b>
5.3.1. <i>Cavitation results .....</i>	<i>145</i>
<b>5.4 Discussion .....</b>	<b>161</b>
<b>5.5. Summary .....</b>	<b>164</b>

<b>Chapter 6:</b>	<b>167</b>
<b>Electrochemical analysis</b>	<b>167</b>
<b>6.1. Open circuit potential analysis</b>	<b>168</b>
6.1.1. <i>Open circuit trends</i>	168
6.1.2. <i>Water-formed oxide filmed NAB</i>	172
<b>6.2. Electrochemical impedance spectroscopy analysis</b>	<b>178</b>
<b>6.3. Potentiodynamic polarization</b>	<b>187</b>
<b>6.4. Discussion</b>	<b>190</b>
<b>6.5. Summary</b>	<b>191</b>
<b>Chapter 7: Synergy quantification</b>	<b>195</b>
<b>7.1. Introduction</b>	<b>195</b>
<b>7.2. Synergy evaluation</b>	<b>199</b>
7.2.1. <i>Gravimetric method</i>	199
7.1.2. <i>Polarization method</i>	200
7.2.2. <i>Volumetric method</i>	204
7.2.3. <i>Cathodic protection method for pure erosion test</i>	206
7.2.4. <i>Mean depth of penetration method</i>	209
<b>7.3. Comparison of the synergy values and discussion</b>	<b>211</b>
7.3.1. <i>Discussion</i>	213
7.3.2. <i>Limitations of the techniques used</i>	221
<b>7.4 Summary</b>	<b>222</b>
<b>Chapter 8: Conclusion and</b>	<b>225</b>
<b>Future Work</b>	<b>225</b>
<b>8.1. Conclusion</b>	<b>226</b>
<b>8.2. Future Work</b>	<b>228</b>
8.2.1 <i>Modern composite propeller materials</i>	230
8.2.2. <i>Computational modelling simulation</i>	235
<b>Reference:</b>	<b>239</b>
<b>Appendix A</b>	<b>261</b>
<b>Appendix B</b>	<b>275</b>
<b>Appendix C</b>	<b>307</b>
<b>Appendix D</b>	<b>321</b>
<b>Appendix E</b>	<b>351</b>



## Table of Figures

<b>Fig. 1.1:</b> (a) Sheet and cloud cavitation damage together with a tip vortex on a propeller blade [9]; (b) Cavitation damage on the blades at the discharge from a Francis turbine; (c) Cavitation damage to the concrete wall of the 15.2m diameter Arizona spillway at the Hoover Dam; (d) Axial views from the inlet of the cavitation and cavitation damage on the hub or base plate of a centrifugal pump impeller [8].....	3
<b>Fig. 1.2:</b> Marine propeller thrusting water through its blades [22]. .....	6
<b>Fig. 1.3:</b> Cavitation formation on the suction side of the propeller [14]. .....	11
<b>Fig. 2.1:</b> Nucleation model for a crevice in an entrained micro-particle in a liquid [1].....	19
<b>Fig. 2.2:</b> Equilibrium water vapour pressure of water vs. temperature plot, adapted from Ref. [46]. .....	20
<b>Fig. 2.3:</b> Vapour Bubble Collapse near a solid boundary in a quiescent liquid comparing the theoretical observations of Plesset and Chapman (solid lines), with the experimental observations of Lauterborn and Bolle (dotted lines) [1], [45], [60], [61].....	22
<b>Fig. 2.4:</b> Growth of cavity into a hemispherical bubble and undergoing the “pancaking” mode of collapse against a solid wall. Timing A and B at 0 and 0.4 ms; C and D at 5.8 and 11.4 ms; E, F and G at 16.8, 17.4 and 17.8 ms respectively [64]. .....	23
<b>Fig 2.5:</b> Series of photographs showing the development of the microjet in a bubble collapsing (a) very close to a solid wall; and (b) away from the solid wall at the top of the frame . The interval between the numbered frames is 2 $\mu$ s and the frame width is 1.4mm [69].....	25
<b>Fig. 2.6:</b> A spherically symmetric shock wave emitted by a laser-generated bubble upon first collapse taken at 20.8 million frames per s with the arrangement depicted in frame 1. The frame size is 1.5 x 1.8 mm <sup>2</sup> and the exposure time is ca. 5 ns [62]. .....	27
<b>Fig. 2.7:</b> Typical classification of erosion periods [75]. .....	30
<b>Fig. 2.8:</b> Positive angle of attack on the propeller blade with pressure distribution	

at different areas of the propeller blade [83].....	36
<b>Fig. 2.9:</b> Negative angle of attack on the propeller blade with the pressure distribution depicting the cavitation zone on the propeller blade [83]......	37
<b>Fig. 2.10:</b> Different locations of cavitation attack causing different types of cavitation [83]......	38
<b>Fig. 2.11:</b> Bubble cavitation occurring on the model of a ship propeller [89]. ....	39
<b>Fig. 2.12:</b> (a) Sheet cavitation on a propeller blade [90]; (b) Vortex cavitation of the blade tip [91].....	40
<b>Fig. 3.1:</b> Parsons' cavitation tunnel 1895 [1].....	48
<b>Fig. 3.2:</b> Vibratory system in the University of Michigan used by Hammit and He [105].....	55
<b>Fig. 3.3:</b> The direct and indirect test configurations used for the ultrasonic vibratory cavitation test method under ASTM G-32 standards [124]. ....	61
<b>Fig. 3.4:</b> SEM micrographs obtained from cavitation erosion test performed on AISI-SAE 1018 carbon steel at a test duration of 150 min: (a) central damage region; and (b) transition region in Ann Arbour tap water; (c) central and transition region in 0.1 M $\text{CaCO}_3$ ; (d) central and transition region in 0.1M $\text{CaO}$ ; (e) central and transition region in 0.1M $\text{NaHCO}_3$ ; (f) central and transition region in 0.1 M $\text{NaOH}$ [107]. ....	64
<b>Fig. 3.5:</b> Cone-like bubble structure for different acoustic intensities I. Sonotrode C: (a) $1.8 \text{ W cm}^{-2}$ , (b) $3.5 \text{ W cm}^{-2}$ , (c) $5.3 \text{ W cm}^{-2}$ , and (d) $8.2 \text{ W cm}^{-2}$ [134]......	67
<b>Fig. 3.6:</b> Development of plastic deformation near the centre for various t:.....	69
(a) 0 min; (b) 5 min; (c) 15 min; (d) 20 min [137]. ....	69
<b>Fig. 3.7:</b> (a) Crack nucleated from the voids growth and coalescence at 40 min; and (b) Initiation and progress of the fatigue crack at 45 min [138]. ....	70
<b>Fig. 4.1:</b> Longitudinal vibration modes [33]......	89
<b>Fig. 4.2:</b> Schematics of an indirect cavitation method. ....	90
<b>Fig. 4.3:</b> (a) Effect of probe length on its vibration amplitude; (b) Effect of probe length on its vibration frequency [33]......	92
<b>Fig. 4.4:</b> Mass loss on LRAH32 material as a function of probe power setting and probe-specimen gap [33]......	93
<b>Fig. 4.5:</b> Two-phase (duplex) microstructure of austenite and ferrite grains of 2205 duplex stainless steel, as obtained under SEM at a magnification of 100x.	95

<b>Fig. 4.6:</b> The change in crystallographic structure of ferritic BCC structure to austenitic FCC structure by addition of (at least 6%) nickel [185].	97
<b>Fig. 4.7:</b> Phase diagrams of (a) A binary Cu-Al system; (b) a vertical section of the Cu-Al-Ni-Fe system with 5% Ni, 5% Fe [197].	102
<b>Fig. 4.8:</b> NAB microstructure heat-treated at (a) 860 °C for 72 h (at 480x); and (b) 675 °C for 6 h (at 600x) [197].	103
<b>Fig. 4.9:</b> Crystals structures of (a) $\kappa_I$ , $\kappa_{II}$ and $\kappa_{IV}$ phases having a $Fe_3Al DO_3$ structure, and (b) $\kappa_{III}$ phase with a $NiAl B_2$ structure [198], [199].	104
<b>Fig. 4.10:</b> Microstructural morphology of UNS C95800 cast NAB at a magnification of 1000x and 4000x. $\kappa_I$ is the globular dendritic structure, $\kappa_{III}$ is the lamellar “finger-like” structure, and $\kappa_{IV}$ is the very fine particulate imbedded within the $\alpha$ matrix [18], [202]–[204].	106
<b>Fig. 4.11:</b> The sonotrode amplitude calibration set up showing (a) the amplitude reader-sonotrode arrangement; and (b) the signal express software used in order to calibrate the sonotrode.	114
<b>Fig. 4.12:</b> Optical image of general oxide film (a) after 1 week in air; (b) after 3 months of immersion in 3.5% NaCl solution [202], [204].	116
<b>Fig. 4.13:</b> Schematics of the cavitation rig with specimen connected to the potentiostat for cavitation erosion-corrosion measurements [18], [202]–[204].	117
<b>Fig. 4.14:</b> Perspex sample holder with adjustable fixtures securing the sample of size 25 mm x 25 mm x 5 mm with perspex screws.	118
<b>Fig. 4.15:</b> Three ways of scanning the sample surface by selecting (a) the entire surface at once, (b) one strip at a time across the entire sample surface, or (c) a quarter of the eroded surface at a time.	122
<b>Fig. 4.16:</b> Schematics of a section of projected area under the datum line considered for volume loss.	123
<b>Fig 5.1:</b> Sonotrode tip (a) Before the test; (b) After 5 h test.	130
<b>Fig. 5.2:</b> Cavitated surface of DSS in 3.5% NaCl solution after 1 h of test.	131
<b>Fig. 5.3:</b> Cumulative mass loss vs. time erosion wear rate for NAB and DSS in 3.5% NaCl solution under cavitation.	133
<b>Fig. 5.4:</b> Cumulative mass loss vs. time erosion wear rate during incubation period for NAB and DSS in 3.5% NaCl solution under cavitation.	133

<b>Fig. 5.5:</b> Cumulative mass loss rate vs. time for NAB and DSS in 3.5% NaCl solution under cavitation. ....	134
<b>Fig. 5.6:</b> Cumulative mass loss rate vs. time during incubation period for NAB and DSS in 3.5% NaCl solution under cavitation.....	135
<b>Fig. 5.7:</b> Microstructure of air-formed oxide filmed NAB before cavitation as seen under the optical microscope.....	136
<b>Fig 5.8:</b> Optical images of the progression of cavities on the central region of the air-formed oxide filmed NAB after cavitation erosion for (a) 30 min, (b) 1 h, (c) 2 h, (d) 3 h, (e) 4 h, and (f) 5 h in 3.5% NaCl solution, showing the increasing roughness of the surface, and growth in cavity sizes with time.....	137
<b>Fig 5.9:</b> Optical images of the central region of NAB with water-formed oxide layer subjected to cavitation erosion for (a) 30 min, (b) 1 h, (c) 2 h, (d) 3 h, (e) 4 h, and ..... (f) 5 h in 3.5% NaCl solution, showing the periodic removal of oxide film, increasing roughness of the surface, and growth in cavity sizes with time.....	138
<b>Fig. 5.10:</b> Microstructure of 2205 duplex stainless steel.....	139
<b>Fig 5.11:</b> Optical images of the central region of a DSS sample subjected to cavitation erosion for (a) 30 min, (b) 1 h, (c) 2 h, (d) 3 h, (e) 4 h, and (f) 5 h in 3.5% NaCl solution, showing the increasing roughness of the surface, and growth in cavity sizes over time. ....	139
<b>Fig. 5.12:</b> Talysurf surface roughness profilometry at the centre of the cavitated surface of DSS in distilled water after 1 h of test [18]. ....	141
<b>Fig. 5.13:</b> Wear scar profile of DSS after cavitation in (a) distilled water, and (b) in 3.5% NaCl solution for 1 h obtained using Alicona 3D profilometer.....	143
<b>Fig. 5.14:</b> Wear scar profile of air-formed oxide filmed NAB after cavitation in (a) distilled water, and (b) in 3.5% NaCl solution for 1 h obtained using Alicona 3D profilometer.....	144
<b>Fig. 5.15:</b> Cavitated region of DSS obtained under an optical microscope (a) in distilled water; (b) cavity of 10- $\mu$ m size under distilled water after 1 h; (c) in 3.5% NaCl solution; and (d) 20 $\mu$ m – 50 $\mu$ m cavities obtained in 3.5% NaCl solution after 1 h.....	146
<b>Fig. 5.16:</b> The SEM image of DSS surface after 1 h of cavitation in 3.5% NaCl solution with pitting and cavities of sizes 5 $\mu$ m – 10 $\mu$ m.....	147

<b>Fig. 5.17:</b> Striation marks within the cavity of the size 100 $\mu\text{m}$ obtained by after 1 h cavitation in 3.5% NaCl solution. ....	148
<b>Fig. 5.18:</b> SEM image of (a) plastic deformation at cavitation damaged edge for DSS in 3.5% NaCl solution, (b) detailed magnified image of plastic deformation at the cavity edges in (a) [18].....	148
<b>Fig. 5.19:</b> Transverse of the DSS cavitated in 3.5% NaCl solution for 1 h.....	149
<b>Fig. 5.20:</b> SEM images of (a) small boundary erosion on air-formed filmed NAB at a magnification of 1500x in distilled water; (b) shows the magnified image of the cavities of size 10- $\mu\text{m}$ at the selected area in (a); (c) SEM image of a 50- $\mu\text{m}$ large cavity on the sample surface undergone cavitation erosion-corrosion in 3.5% NaCl solution; and (d) the magnified image of a cavity in (c) showing selective phase attack at the $\alpha$ - $\kappa$ phase boundaries leaving $\kappa_I$ globules and $\kappa_{III}$ lamellar phases exposed [202], [203]. ....	151
<b>Fig. 5.21:</b> SEM images of NAB sample cavitated for 1 h in distilled water: (a) transverse-sections of a cavity; (b) detailed magnified image of cavities in (a) exhibiting crack growth and propagation along the $\alpha$ - $\kappa_{III}$ phase boundaries [202]. ....	152
<b>Fig. 5.22:</b> SEM images of transverse sections of NAB after 1 h of cavitation erosion-corrosion test in 3.5% NaCl solution with air-formed film showing crack propagation along the $\alpha$ - $\kappa_{III}$ phase boundaries and plastic deformation [203].	153
<b>Fig. 5.23:</b> Optical images of: (a) dendritic surface and potential subsurface cracks; and (b) detail of the selected area in (a) of surface cracks forming along the grain boundaries, linking $\kappa_I$ and $\kappa_{II}$ , after 1 h of cavitation erosion-corrosion test in 3.5% NaCl solution [203]. ....	154
<b>Fig. 5.24:</b> SEM images the oxide film cross-section on the as-cast NAB substrate used for the research after 3 months of immersion in 3.5% NaCl solution: (a) selective phase corrosion attack reaching up to 40 $\mu\text{m}$ in depth; (b) the area selected in (a) showing selective corrosion of the $\kappa_{III}$ phase under the surface [203].....	156
<b>Fig. 5.25:</b> SEM images of water-formed oxide filmed NAB sample under pure cavitation erosion conditions: (a) showing cavities formed on the sample surface; (b) magnified image of a cavity on the surface; (c) transverse-sections of a cavity; (b) detailed magnified image of a cavity in (d) exhibiting crack growth and	



propagation along the $\alpha$ - $\kappa_{III}$ phase boundaries [203].....	157
<b>Fig. 5.26:</b> SEM images of the distinguished phase erosion of the oxide filmed sample in 3.5% NaCl solution after 1 h of cavitation [203].....	159
<b>Fig. 5.27:</b> SEM image of the eroded surface of NAB sample with water-formed oxide film after combined cavitation erosion-corrosion test conducted in 3.5% NaCl solution for 1 h [203]. ....	160
<b>Fig. 5.28:</b> SEM image of transverse section of NAB after 1 h of cavitation erosion-corrosion test in 3.5% NaCl solution with water-formed film showing crack propagating along the lamellar eutectoid grain boundaries [203]. ....	161
<b>Fig. 6.1:</b> OCP for DSS, air-formed filmed NAB and water-formed filmed NAB in 3.5% NaCl solution for 1 h with and without cavitation as adapted from references [18], [202], [203].....	169
<b>Fig. 6.2:</b> Optical images of the cavitated region from the central region of the air-formed oxide filmed NAB samples (a) before OCP and cavitation; (b) after 1 h of OCP; and (c) after 1 h of cavitation while kept at OCP in 3.5% NaCl solution. Water-formed oxide filmed NAB (d) before OCP and cavitation, and (e) after 1 h of cavitation while kept at OCP in 3.5% NaCl solution. And DSS (f) before OCP and cavitation, and (g) after 1 h of cavitation while kept at OCP in 3.5% NaCl solution. ....	171
<b>Fig. 6.3:</b> OCP for NAB with air- and water-formed film in distilled water and 3.5% NaCl solution for 1 h each.....	173
<b>Fig. 6.4:</b> Mass change data plotted against the OCP for air- and water-formed oxides on NAB after pure static corrosion tests in 3.5% NaCl solution tested for 1 h each [204]. ....	175
<b>Fig. 6.5:</b> (a) OCP trends for water-formed oxide-filmed NAB samples in 3.5% NaCl solution for 1 h; (b) magnified section of the OCP during incubation period when under cavitation. ....	176
<b>Fig. 6.6:</b> The OCP trend for NAB with air and water-formed oxide film in 3.5% NaCl solution at the incubation period. ....	177
<b>Fig. 6.7:</b> Bode plot for DSS and air-formed oxide filmed NAB in 3.5% NaCl solution under pure corrosion and during cavitation [18], [202].....	178
<b>Fig. 6.8:</b> Blod plot of DSS and air-formed filmed NAB obtained after 1-h cavitation in 3.5% NaCl solution. ....	179

<b>Fig. 6.9:</b> Bode plot for air-formed filmed NAB after 1 h of cavitation, and NAB with water-formed film while under the cavitation erosion-corrosion conditions....	180
<b>Fig. 6.10:</b> Nyquist plots for (a) air-formed filmed NAB, and (b) DSS samples in 3.5% NaCl solution with and without cavitation.....	181
<b>Fig. 6.11:</b> Nyquist plots for three water-formed filmed NAB samples in 3.5% NaCl solution under (a) pure corrosion, and (b) the combined erosion-corrosion conditions. ....	183
<b>Fig. 6.12:</b> A porous passive layer with the resulting equivalent circuit [202]. ..	184
<b>Fig. 6.13:</b> EIS plots for DSS and air-formed as well as water-formed oxide filmed NABs under C and T test conditions, obtained using fit models.....	186
<b>Fig. 6.14:</b> Polarization curves for DSS in 3.5% NaCl solution, showing the location of the current density derived from Tafel extrapolation.....	188
<b>Fig. 6.15:</b> Polarization curves for NAB samples with air-formed and water-formed oxide films in 3.5% NaCl solution [203]. ....	189
<b>Fig. 7.1:</b> Flow chart for different methods used for synergy evaluation. ....	198
<b>Fig 7.2:</b> $R_T$ and $R_E$ graph for DSS, and NAB with air-formed oxide films obtained from the volumetric mass loss analysis for T and E.....	205
<b>Fig. 7.3:</b> $R_T$ and $R_E$ graph for DSS, and NAB with air- and water-formed oxide films obtained from Table 7.3 and 7.5. ....	208
<b>Fig. 7.4:</b> $R_T$ and $R_E$ plots for air-formed filmed NAB and DSS from the MDPR values. ....	210
<b>Fig. 7.5:</b> Extended S/C vs. E/C plot showing the locations of DSS, air-formed filmed and water-formed filmed NAB on the graph plotted using data from Table 7.8, adapted from Ref. [203], [204].....	217
<b>Fig 8.1:</b> FRP propeller of diameter 305 mm painted in preparation for open water testing [248].....	231
<b>Fig. 8.2:</b> Mass loss vs. cumulative exposure time plots for E-glass and carbon fibre composites for two different standoff distances [204], [252].....	233
<b>Fig. 8.3:</b> Optical images of (a) E-glass sample [204], [252]; and (b) carbon fibre composite, cavitated for 10 minutes at 1 mm. The resin layers are clearly removed from the top of the weaves [252]. ....	234
<b>Fig. 8.4:</b> Contour plots showing cavitation phenomena beneath the probe occurring within 1ms (where, blue signifies vapour, and red signifies liquid)..	236



## Table of Tables

<b>Table 1.1:</b> Standard propeller materials, their mechanical properties, and their advantages and disadvantages [28].	8
<b>Table 2.1:</b> Review of impact loadings for different cavity phenomena [78].	32
<b>Table 3.1:</b> List of different methods of cavitation tests [21], [103], [105], [120]–[123].	52
<b>Table 4.1:</b> Geometrical parameters of sonotrode shapes, adapted from ref. [184].	87
<b>Table 4.2:</b> Specifications of the experiment.	90
<b>Table 4.3:</b> Chemical compositions of the materials used for the research as found under EDS.	98
<b>Table 4.4:</b> The crystal structure, morphology and the typical chemical composition of the individual phases in the NAB samples as tested under EDS; $\kappa_{IV}$ in as-cast NAB adapted from Ref [198].	105
<b>Table 4.5:</b> DSS and NAB highlighted in the simplified galvanic series for metallic materials in flowing seawater of velocity between $2.5 \text{ m s}^{-1}$ to $4 \text{ m s}^{-1}$ and temperature range of $10 \text{ }^{\circ}\text{C}$ – $27 \text{ }^{\circ}\text{C}$ , referenced to saturated calomel half-cell [218].	110
<b>Table 4.6:</b> Galvanic series of metals in flowing seawater with reference to saturated calomel half-cell [218].	111
<b>Table 4.7:</b> Parameters defined for the electrochemical experiments.	125
<b>Table 5.1:</b> $R_a$ and $R_q$ for NAB and DSS measured after 1 h of cavitation using Talysurf.	142
<b>Table 5.2:</b> Average roughness, mean depth of penetration and volume loss measured after 1 h of cavitation using Alicona.	145
<b>Table 6.1:</b> OCP and mass changes for the water-formed oxide-filmed NAB samples as tested in 3.5% NaCl solution for 1 h each [204].	174
<b>Table 6.2:</b> Parameters for the fit models used for air-formed filmed NAB, water-formed filmed NAB and DSS under C and T conditions.	185
<b>Table 6.3:</b> free corrosion potentials for the cathodic protection tests for the test samples.	190

<b>Table 7.1:</b> Synergism summary for the samples using mass loss measurements. DSS and air-formed filmed NAB results taken from [18].	199
<b>Table 7.2:</b> Current density and mass loss obtained for NAB with air-formed oxide film and water-formed oxide film from polarization scanning in 3.5% NaCl solution.	202
<b>Table 7.3:</b> Synergism summary obtained for DSS, NAB with air- and water-formed oxide films obtained from gravimetric analysis for T and E, and polarization scanning for C in 3.5% NaCl solution.	203
<b>Table 7.4:</b> Synergism summary for the samples using volumetric mass loss method.	205
<b>Table 7.5:</b> Mass loss measurements and synergy quantification for the test samples using cathodic protection for the pure erosion test after 1 h in 3.5% NaCl solution.	207
<b>Table 7.6:</b> Synergy quantification for the samples using the MDPR method.	209
<b>Table 7.7:</b> $R_T$ and $R_E$ values for air-formed filmed NAB and DSS from the MDPR values.	210
<b>Table 7.7:</b> Synergism summary for NAB and DSS using distilled water, cathodic protection, mean depth of penetration rate, volumetric mass loss, and Faradaic conversion methods.	211
<b>Table 7.8:</b> Data used for S/C vs. E/C map (as plotted in Figure 7.4) and their corresponding references [204], [229].	215
<b>Table 7.9:</b> S/C and E/C values calculated for DSS and the two types of oxide-filmed NAB samples using gravimetric method for E measurement, and polarization and Faradaic conversion for C measurement.	216

## Nomenclature

### Abbreviations:

AC – Alternating current	EN – European Standards
AD – After Death	FCC – Face centred cuboid
A.E – Acoustic Emission	FIB – Focused Ion Beam
AISI – American Iron and Steel Institute	FOH – Fibre-optic hydrophone
ASTM – American Society for Testing and Materials	FP – Fixed pitch
BCC – Body centred cuboid	FRP – Fibre reinforced plastic
BS – British Standards	HN – Hsu-Nielson
BSI – British Standards Institution	IP – Incubation Period
C – Pure corrosion rate	ISO – International Organization for Standardization
CBS – Cone-like Bubble Structure	MDP – Mean depth of penetration
CDF – Cumulative distribution function	MDPR <sub>max</sub> – Maximum Mean Depth of Penetration Rate
CEN – European committee for Standardization	MIG – Metal Inert Gas
CER – Cavitation Erosion Resistance	NAB – Nickel-Aluminium Bronze
CFD – Computational Fluid Dynamics	NPL – National Physics Laboratory
CLE – Circular Leading Edge	OCP – Open circuit potential
CP – Cathodic Protection	SAE – Society of Automotive Engineers
DAS – Data Acquisition System	SEM – Scanning Electron Microscopy
DIN – Deutsches Institut für Normung	SS – Stainless Steel
DSS – Duplex Stainless Steel	T – Total or combined erosion- corrosion rate
E – Pure Erosion rate	TEM – Transmission Electron Microscopy
EDS – Energy Dispersive X-ray Spectroscopy	TIG – Tungsten Inert Gas
EIS – Electrochemical Impedance Spectroscopy	UR – Ultimate Resilience
	UTS – Ultimate Tensile Strength
	VCE – Vibratory Cavitation Erosion
	VLR – volume loss rate
	XRD – X-Ray Diffraction

**Symbols:**

$\alpha$  – Angle of inclination,  
 $\alpha$  – copper rich alpha phase  
 $\beta'$  – Martensitic phases  
 $\beta$  – Beta Phases  
 $^{\circ}\text{C}$  – Degree Celsius  
 $\varepsilon$  – Martensite  
 $^{\circ}\text{F}$  – Degree Fahrenheit  
 $\gamma$  – Metastable austenite  
 $\kappa$  – kappa phase  
 $\rho$  – Density of water  
 $\sigma$  – Cavitation number  
 $\sigma_{\text{crit}}$  – Cavitation inception number  
 $u$  – Amplification factor  
2D – Two dimensional  
3D – Three dimensional

**A:**  $A_0$  – Amplitude at the  
sonotrode input end

$A_1$  – Amplitude at the  
sonotrode output end

Ag – Silver

AgCl – Silver chloride

Al – Aluminium

$\text{Al}_2\text{O}_3$  – Aluminium oxide

At% – Atomic weight  
percentage

**C:** C – Carbon

$C$  – Pure corrosion  
contribution

$\Delta C$  – Erosion enhanced

**corrosion**

$\text{CaCO}_3$  – Calcium Carbonate

CaO – Calcium Oxide

Cl – Chlorine

$C_p$  – Pressure coefficient

$C_{\text{pore}}$  – Capacitance of porous  
layer

CP-Ti – Commercially Pure  
Titanium

Cr – Chromium

$\text{Cr}_2\text{O}_3$  – Chromium oxide

Cu – Copper

$\text{Cu}_2\text{O}$  – Copper (I) oxide

CuNiAl – Copper-Nickel  
Aluminium

**D:**  $D^*$  – characteristic pit  
equivalent diameter

$D/d$  – Diameter

**E:**  $e^-$  – Electron

$E$  – Elastic modulus

$E$  – Pure erosion contribution

$E_{\text{corr}}$  – Corrosion potential

$\Delta E$  – Corrosion enhanced  
erosion

**F:** F – towing resistance

Fe – Iron

$\text{Fe}_3\text{O}_4$  – Iron (II/III) oxide

**H:**  $\bar{h}$  – characteristic mean  
erosion depth

$\text{H}_2$  – Hydrogen

$\text{H}_2\text{O}$  – Hydrogen oxide  
(water)

HCl – Hydrochloric Acid

	Hg – Mercury		$\Delta P$ – Change in pressure
	Hg <sub>2</sub> Cl <sub>2</sub> – Mercury Chloride	<b>Q:</b>	q – Stagnation pressure
	H <sub>2</sub> SO <sub>4</sub> – Sulphuric Acid	<b>R:</b>	r – Radius
	Hv – Brinell Hardness		R – Nuclei size
<b>I:</b>	i <sub>0</sub> – Exchange Current Density		R <sub>a</sub> – Average roughness
	$\Delta i$ – Change in current		R <sub>q</sub> – Quadratic mean square roughness
	I – Current		R <sub>s</sub> – Resistance of solution
<b>J:</b>	J – Ultrasound Intensity		R <sub>inner</sub> – Inner layer resistance
<b>K:</b>	k – Shape factor		R <sub>pore</sub> – Porous layer resistance
<b>L:</b>	L – lift force		R <sup>2</sup> – Coefficient of Determination
	l – Length		Ref – reference electrode
<b>M:</b>	Mn – Manganese	<b>S:</b>	S – combined contribution due to synergistic effect
	Mo – Molybdenum		Si – Silicon
<b>N:</b>	N* - Characteristic pitting rate or number of pits per unit area per unit time		SiC – Silicon Carbide
	N – Number of pits per unit surface area and unit time,		SiO <sub>2</sub> – Silicon oxide
	N <sub>2</sub> – Nitrogen	<b>T:</b>	t – Characteristic time
	NaCl – Sodium Chloride		T – total mass loss or overall cavitation erosion- corrosion rate
	NaHCO <sub>3</sub> – Sodium hydro-carbonate		T – thrust
	NaOH – Sodium hydroxide		Ti – Titanium
	Ni – Nickel	<b>V:</b>	V – speed
<b>P:</b>	P <sub>0</sub> - undisturbed fluid pressure		V – Potential/voltage
	P <sub>r</sub> – Reference pressure		V <sub>f</sub> – Potential vs. reference
	P <sub>v</sub> – Vapour pressure	<b>W:</b>	Wt% - weight percentage
	P <sub>d</sub> – Water pressure at propeller hub	<b>Z:</b>	Z – Impedance
	P <sub>a</sub> – Atmospheric pressure		



**Units:**

$\mu\text{m}$  – Micrometre

$\mu\text{s}$  – Microsecond

A – Ampere

C - coulomb

cm – Centimetre

g - Gram

GPa – Giga Pascal

Hz – Hertz

kN – Kilo newton

kHz – Kilohertz

Kmph – Kilometre per h

L - Litre

m – Metre

M – Mole

min – Minute

mm – Millimetre

mg – Milligram

MPa – Mega Pascal

$\text{m s}^{-1}$  – Metre per second

nm – Nanometre

Pa – Pascal

s – Second

V – Volt

W – Watt

## Declaration of Authorship

I, Jahnabi Basumatary,

Hereby declare that the thesis entitled

### **CAVITATION EROSION-CORROSION IN MARINE PROPELLER MATERIALS**

and the work presented in the thesis are generated on my own as a result of original research. I confirm that:

- This work is done wholly or mainly while in the candidature for a doctorate degree at the University of Southampton;
- Where any part of the thesis that has been previously submitted and/or published at this University or any other institution, this has been clearly stated;
- Where I have consulted the published work of others, this is clearly attributed;
- I have acknowledged all main sources of help;
- Where the thesis is based on work done by myself jointly with others, I have made clear exactly what was done by others and what I have contributed myself;
- Parts of this work has been submitted and/or published as journal papers listed in chapter 1. The papers are also attached as appendices.

Signed.....

Date.....



## Acknowledgment

I would like to take this opportunity to thank and acknowledge, first and foremost, my supervisor, Prof. Robert J. K. Wood, for his exemplary supervision, meticulous scrutiny, insightful guidance, and undivided support all throughout the course of my PhD.

I would also extend this gratitude towards Prof. Stephen Turnock, who is a part of the supervisory team, and my industrial sponsors and advisors, Lloyds Register, with special thanks to Crispin Fetherstonhaugh, Roy Dark, Richard Marchant and D. Reddy for their generous help with troubleshoot, equipment handling, and valuable advices during my research. A big thanks to Dr. Mengyan Nie for his training, assistance and labour with my electrochemical analyses, Dr. Pawee Kucita for his altruistic help especially with the SEM, and Dr. Liam Goodes and Dr. Nicola Symonds for providing the required trainings for the Alicona and talysurf.

I would also thank my parents, Wing Cmdr. Nileswar Basumatary and Maya Basumatary, without whose undying love, encouragement, and financial and moral support this research would not have been a success. My colleagues and friends Vanesa, Stefania, Viktorija, Jim, Kasia, Natalia, and Kiki, who were constantly available for motivation, support, brainstorming, and technical helps whenever required; My mentors Tim and Eric for their invaluable guidance with management of my PhD, and for always finding time for me despite their busy schedules. And a heartfelt thanks to my partner, Benjamin, who stuck by me through thick and thin, pushed me to meet my goals, and graciously helped me review my thesis from time to time, giving me the much-needed feedbacks.

Lastly, a sincere thanks to my friends Karoline, Chris, Rachel, Max, and Kingsley for making me feel welcomed in the country, and being there for me with constant moral support for the times when I needed them the most.



# Chapter 1:

# Introduction

---

## 1.1. Cavitation – Background and Theory

The cavitation phenomenon has been known especially to ship builders and engineers since the 18<sup>th</sup> century. In 1754, it was first reported by the famous Swiss mathematician Euler, on a particular design of water wheel and the influence it might have had on the wheel's performance [1]. Such a process is destructive in nature and causes severe loss especially in performance of the ships. The resultant destruction and losses could lead to expensive maintenance in the form of frequent dry dockings, inspections and prevention or replacement of the damaged part itself [2].

The word cavity is derived from the Latin word 'cavus', which means hollow [3]. Cavitation is a fluid mechanics phenomenon, which occurs whenever there is fluctuation in the pressure field and/or the velocity of the fluid. Hence, regions where the flow conditions cause the absolute pressures in the fluid to fall below its vapour pressure, causing the fluid to boil even at ambient temperature undergo cavitation. This causes small vapour bubbles called "cavities" to form within the fluid. These cavities implode when the surrounding pressure rises again. These collapsing create a very high localized and instantaneous pressure, where the vapour pressure of water can go from  $1.704 \text{ kN m}^{-2}$  at  $15^\circ\text{C}$  up to  $101.325 \text{ kN m}^{-2}$  at  $100^\circ\text{C}$  [4], resulting in high intensity shock waves and jet impacts, which can significantly erode any material surface in contact. And this phenomenon of bubbles collapsing on the material surface, causing erosion, is termed as cavitation [5].

It is often deemed detrimental to anything it comes in contact with, causing erosion of materials. Cavitation damage is a serious issue, especially in restricted waterways with high flow-rates, pumps, impellers, turbines, and boat and marine propellers. It can also occur during a traumatic brain injury causing pressure change in the brain agar phantom, and even during pressure changes in the fluid in the heart and knee joints [2], [6]–[9]. Figure 1.1 shows severe cavitation damage that has incurred in various different machine parts such as propeller blades, tunnels, turbines and pump impellers [8], [9].

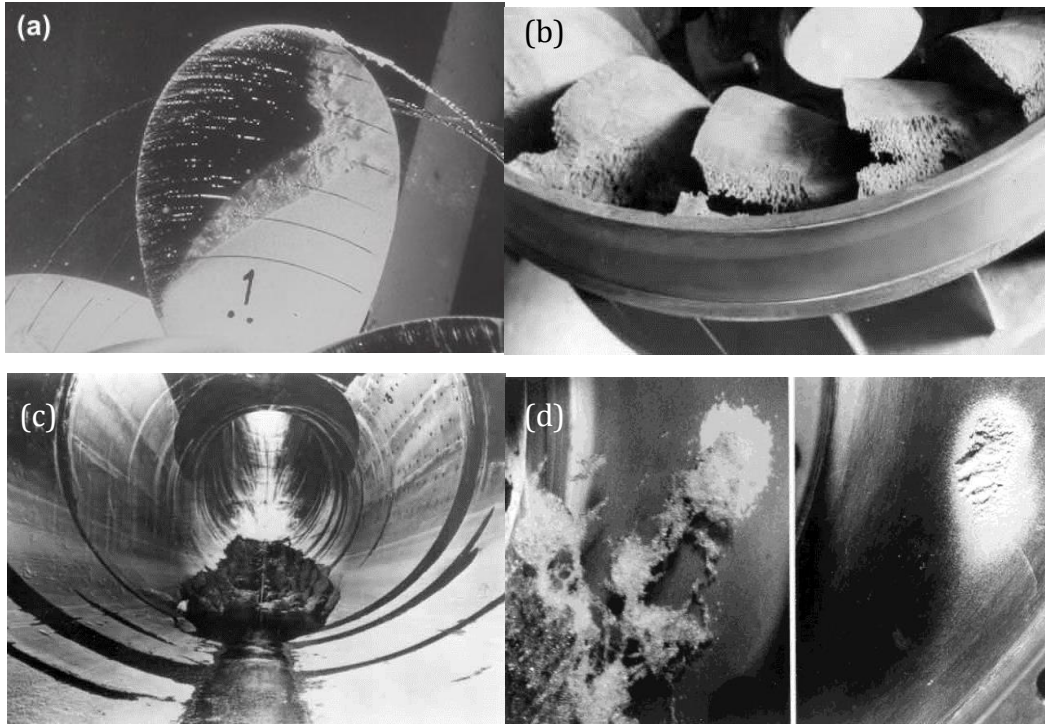


**Fig. 1.1:** (a) Sheet and cloud cavitation damage together with a tip vortex on a propeller blade [9]; (b) Cavitation damage on the blades at the discharge from a Francis turbine; (c) Cavitation damage to the concrete wall of the 15.2m diameter Arizona spillway at the Hoover Dam; (d) Axial views from the inlet of the cavitation and cavitation damage on the hub or base plate of a centrifugal pump impeller [8].

Marine vessels in particular suffer severely from cavitation in the harsh marine environment. Many counter measures are adapted in order to avoid or reduce cavitation, such as, ships and boats can lower the rotational speed (rpm) of the propellers, and hence, the speed of the vessel. Submarines can make further adjustments by lowering their propulsion system or diving to a higher-pressure region, to lift the end pressure of the propeller above the vapour pressure of the liquid.

However, cavitation erosion has been desirable in some special situations as well, such as subsurface drilling, welding and process mixing applications where the associated turbulence caused by cavitation is advantageous. A recent development in mixing micro-technology called cavitation micro-streaming, whereby a gas bubble inside a liquid is made to oscillate at various frequencies, which greatly enhances the mixing of blood samples with reagents [3].



Ultrasonic waves have also been used to induce complex high-frequency alternating compression and rarefaction phases in liquids, causing cavitation. This has helped for the cavitation effects to be usefully applied for cleaning surfaces, for non-invasive operations in the field of medicine, such as in the wear of knee joints, and in a variety of cardiovascular applications of lasers and ultrasound, for breaking down agglomerates in the textile finishing industry, and in sewage treatment plants, where cavitation can help break down the molecules and bacteria cell walls, as well as pollutants and dissolve out minerals from organic material [10], [11]. However, cavitation in marine propulsion system is inevitable and can cause severe damage in the form of cavitation erosion and corrosion [2], [12].

The study on the correlation between erosion and corrosion is also an important subject to understand the interaction between them. The simultaneous existence of mechanical erosion and electrochemical corrosion is a common scenario for engineering alloys used in marine environments. However, the effects of erosion and corrosion in general are not always additive owing to the interactions between them, which makes understanding this interaction even more complicated. The overall damage arising from cavitation erosion and corrosion including the interaction between them is termed as cavitation erosion–corrosion. Hence, it is a tribo-corrosion process which involves mechanical as well as electrochemical factors, formation and removal of the passive and tribo films, and either synergism or antagonism of wear and corrosion [13]. The relative significance of corrosion, erosion, and the interaction between them depends especially on the material and the environmental system [14]. The nature of the interaction depends on a number of factors such as the passivity of the metal surface, the adherence of the corrosion product, the metallurgy of the metal, the amount of dissolved oxygen, the presence of aggressive radical ions, and the intensity of the cavitation. These factors also help determine the mode of corrosion and the rate of erosion–corrosion loss. Several studies on synergy have been conducted in the past but these were usually carried out under various different conditions by different authors, making results difficult to correlate [15]–[18].

In many cases, the service life of equipment and hydraulic structures subjected to cavitation erosion-corrosion can range from months to years. Because of these relatively lengthy periods required to observe measurable erosion in the field, many different techniques have been developed to achieve the significant time compression. The time compression factor currently achievable in accelerated erosion tests is as high as  $10^5$  [19].

At present, the industry has to rely on several factors such as laboratory testing, use of accelerated erosion testing methods, and comparative tests between the new material and previously used materials. However, despite the numerous investigations into the subject of cavitation many of the accompanying effects are still unexplained. Prediction of the occurrence of cavitation as well as the material performance is very important since it leads to a loss of mechanical efficiency. It is very difficult to predict the cavitation location and its intensity under hydrodynamic conditions considering the complexity of the process that involves the areas of acoustics, thermodynamics, optics, plasma physics and chemistry. It involves good knowledge of both the material and the cavitation environment. Numerical analysis is especially a challenge since highly localized variations in density exist between the gas and liquid interface whereas, remainder of the flow generally remains incompressible [13], [20], [21].

## **1.2. Boat and marine propellers**

### ***1.2.1 Boat and marine propulsion System***

The propeller is a vital part of a ship/boat. Marine vessels as well as boats move forward when the water is thrust through the propeller blades as they rotate. The ship propulsion system mainly comprises of either one, two or, in very rare cases, more than two propellers, propeller shaft bearings, power turbine, clutch and gearbox, and propulsion motor. The propeller is generally the only component that is positioned externally on the boat or marine vessels. It is a rotating blade system that propels to exert enough thrust for the ship to move forward by using

the power generated and transmitted by the main engine of the ship. Figure 1.2 illustrates a marine propeller thrusting water through its blades [22], [23].

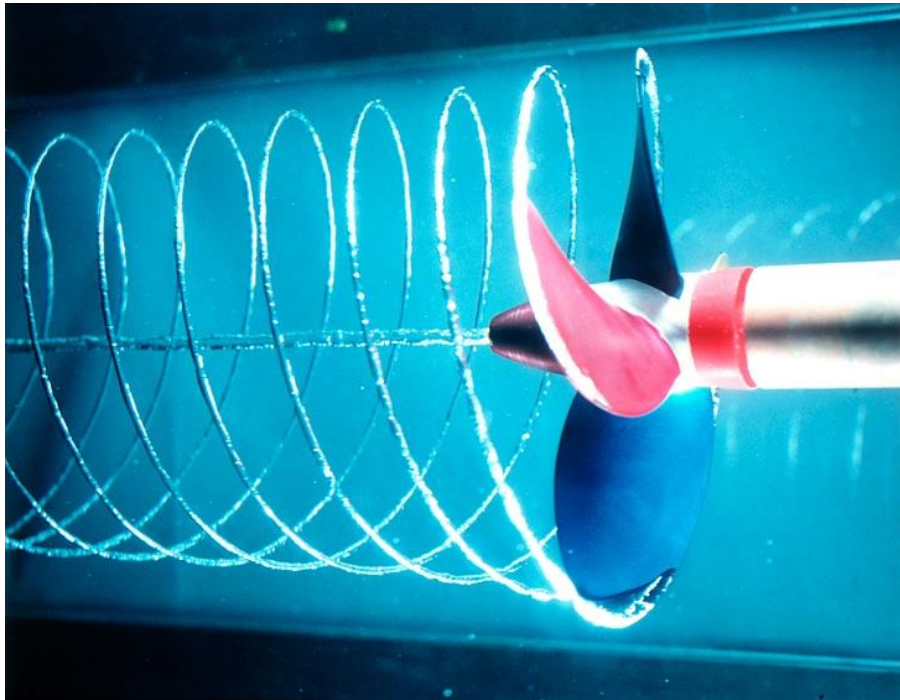


**Fig. 1.2:** Marine propeller thrusting water through its blades [22].

A propeller may consist of any number of blades more than 1 and based on the number of blades the propellers can be classified in to different types of propellers [23]. Propellers can also be classified depending on the pitch of the blade: fixed pitch (FP) type, where the position of the blades are fixed permanently to the hub, thereby giving the propeller a constant pitch, and the controllable pitch (CP) type, where the blades can be rotated about its vertical axis to adjust the pitch. Fixed pitch propellers are cast in one single block. Due to a constant pitch, the ship maneuverability becomes extremely difficult especially when operating in heavy weather conditions. Most ships with low requirement for good maneuverability are generally equipped with a fixed pitch propeller. Whereas, the propellers with controllable pitch have a relatively large hub compared to the fixed pitch propellers. This is because the hubs require large space for hydraulically activated mechanisms that control the pitch (angle) of the blades. And hence, due to the relatively larger hub, the propeller efficiency of the controllable pitch propeller is slightly lower than that of a fixed pitch propeller. Also, it is up to 2-3 times more

expensive, than a corresponding fixed pitch propeller [23], [24].

Since propellers are subjected to heavy loads, to maintain the strength of the propellers, they cannot be manufactured with less than four blades [23], [25], [26]. A propeller produces a thrust through the production of lift by their rotating blades, which create a difference between the pressure on the face and the back of the propeller blades [27]. It is during this pressure difference created that a propeller undergoes the risk of encountering cavitation at the low-pressure end/side of the propeller blade, leading to loss in propeller efficiency.

### ***1.2.2 Propeller materials***

A propeller material has certain factors that it must suffice before it can be chosen for boat and ship propeller building. These factors include the material properties, physical as well as chemical, propeller efficiency, the design benefits, manufacturing and maintenance cost, durability, the ideal usage, ease of reparability, the working environment, etc. The most desirable mechanical properties of a propeller material have to be its high strength, toughness, ductility, and fatigue strength. This way the blade dimensions and thickness can be controlled without compromising the efficiency. Another very important property desirable for a propeller material is resistance to corrosion, especially in corrosive environments such as seawater.

<b>General Propeller Materials</b>	<b>Ultimate Tensile Strength [MPa]</b>	<b>Yield strength [MPa]</b>	<b>Brinell Hardness [HB10]</b>	<b>Advantages</b>	<b>Disadvantages</b>
Low Carbon Steel	504	330	137	Inexpensive	Poor corrosion resistance
13/4 Martensitic Stainless Steel	661	498	210	Ductile, higher corrosion resistance than austenitic SS	Expensive
2205 Duplex Stainless Steel	774	542	233	High strength, high corrosion resistance, high durability and easily reparable	Hydrogen embrittlement and pitting
Low alloy steel	803	493	236	High hardenability, high temperature strength, and stress relief	Prone to austenite retention and corrosion
Manganese Bronze	496	227	130	High corrosion resistance, easily reparable	Possible dezincification
Nickel Aluminium Bronze	650	273	161	High corrosion resistance, easily reparable, high resistance to notch sensitivity	High density and expensive
Composite/ Polymer	-	-	-	Light weight and corrosion resistant	Delamination, difficult to repair

**Table 1.1:** Standard propeller materials, their mechanical properties, and their advantages and disadvantages [28].

Table 1.1 tabulates the standard materials used for propeller fabrication, their mechanical properties such as tensile strength, yield strength and Brinell hardness, and also the advantages and disadvantages of each material with respect to fresh and marine water usage [28]. The conventional materials used for boat and ship propellers include composite/plastics, aluminium bronze alloys, various different grades of steel and stainless steel (SS) [29]. The first materials widely used for ship propellers were cast iron, however, their low strength, low ductility, high risk of corrosion and erosion, and reduced fatigue strength in seawater rendered them non-ideal for robust propeller engineering. Nowadays, the most widely used materials for the boat and marine propellers are stainless steel grades, and copper alloys such as nickel aluminium bronze and manganese bronze. Although, stainless steels are difficult to cast, they exhibit excellent mechanical properties and resistance to corrosion, which make them ideal for propellers [4].

### ***1.2.3 Propeller issues***

There are several propeller related problems that a ship may encounter during its lifetime. This may include propeller induced vibrations caused by inaccuracies in pitch, camber and section shape, blade tip erosion due to abrasives in the surroundings, propeller induced engine overload, unsynchronized propellers, corrosion and propeller cavitation [30].

During the ship movement, the friction of the hull creates a boundary layer of water, called friction belt, around the hull. The velocity of the water on the surface of the hull in this friction belt is equal to that of the ship, and reduces with increasing distance from the hull surface. The thickness of this friction belt increases with its distance from the hull fore-end and hence, it is thickest at the aft-end of the hull. This causes a certain wake velocity to manifest due to the friction along the sides of the hull, which is further augmented by the ship's displacement of water. This, in turn, also causes wake waves at both fore and aft. The combined effect results in the propeller behind the hull to work in a wake field. Therefore, the water at the propeller will have an effective wake velocity in the same

direction as the ship's velocity, expressed by a dimensionless form called the wake fraction coefficient. The value of the wake fraction coefficient depends on the shape of the hull, the location of the propeller, and its size, and has a great influence on a propeller's efficiency. A larger wake fraction coefficient increases the risk of propeller cavitation, due to an inhomogeneous distribution of the water velocity around the propeller.

The effects of cavitation, including loss of speed and damage to the propeller blades, could be minimised by ensuring that the propeller has sufficient blade area relative to the area described by the propeller blade tips [23].

The cavitation erosion on propellers may occur behind the blade of a rapidly rotating propeller or an overloaded propeller, i.e. when the surface area of the propeller is insufficient for the size or weight of the vessel. It may also occur when air is sucked into a propeller while a boat makes a sharp turn, or when wave action brings the propeller out of the water, or when too much power causes bubbles of partial vacuum. These bubbles can have varying degrees of effects, such as reduction in thrust, noise at a high propeller rpm, and visible damages seen on the propellers even after short amounts of run time.

In order for cavitation to occur, the bubbles generally need a surface on which they can nucleate, which is where the propeller surface comes into play. Depending on the either side of the propeller, the pressure can be higher or lower. Cavitation bubbles form on either the low-pressure side (suction side) at as low as 80°C or on the high-pressure side (discharge side) at as high as 150°C. Figure 1.3 shows cavitation formation on the suction side of the propeller [14]. As water rushes in to fill the vacuum, it is vaporized due to the lowered pressure. It implodes against the propeller blades with enough force to cause pitting, which in turn leads to poor balance, vibration, and further pitting, so that the metal of the blades is greatly weakened [31], [32].

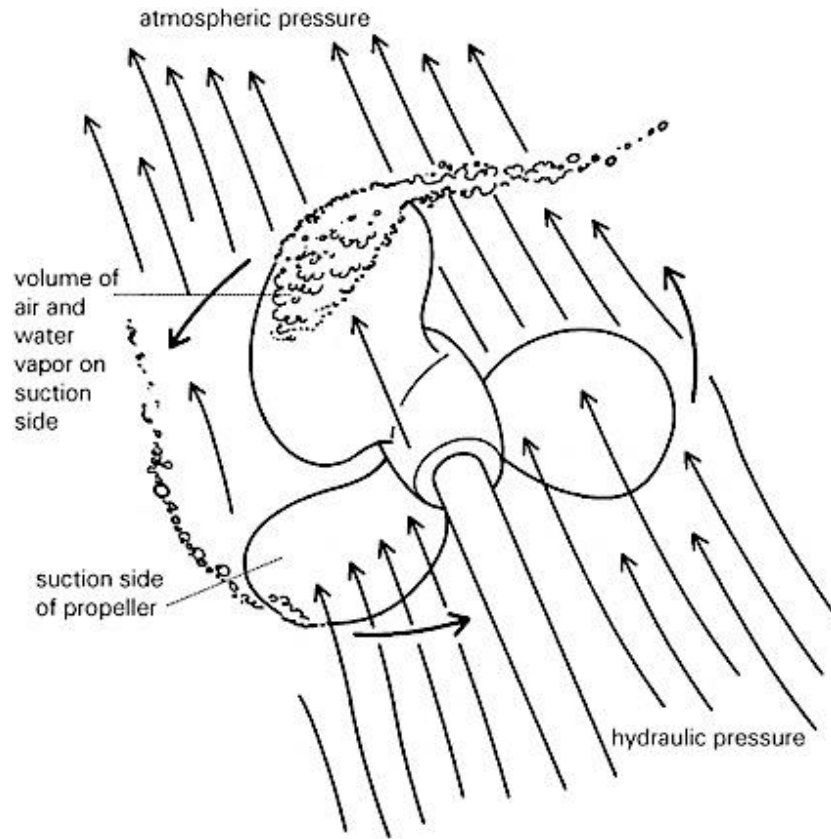


**Fig. 1.3:** Cavitation formation on the suction side of the propeller [14].

When cavitation occurs, depending upon its extend and severity, the propeller may suffer from performance breakdown, noise, vibration and erosion. Partial cavitation on a propeller blade does not affect its thrust. In fact a small amount of cavitation may even increase the camber of the blade section, and hence, increase the thrust. But when cavitation covers about 20 – 25% of blade section, both thrust and torque are reduced. As thrust decreases more rapidly than torque, it reduces the propeller efficiency. On commercial propellers, this rarely happens since the propeller loading and the rate of rotation is low. However, on highly loaded propellers and particularly propellers with high rotational speeds, such as the fast naval ships at full speeds, tugs in towing condition, fast ferries, container ships, etc., the effect of cavitation influence the performance characteristics. Hence, detection of this detrimental phenomenon can be vital for the longevity of the propeller. Chapter 2 further elucidates on the mechanism of propeller cavitation and the various types of propeller cavitation.



### 1.3. Aims and Objectives

This research stems from the studies conducted by Lloyds Register to characterize several propeller materials according to their response to cavitation erosion in laboratory prepared ASTM standard seawater [33]. The materials tested were 2205 duplex stainless steel (DSS), as-cast nickel aluminium bronze (NAB), 13/4 martensitic stainless steel, 42CrMo4 low alloy steel, carbon fibre reinforced composites, and LRAH32 low carbon steel. During their tests, they obtained periodic measurements of mass loss and acoustic emission signatures on the specimen. From their experiments they established that DSS and NAB produced the best results. Hence, only the two materials have been used for the current research.

The main aim of this PhD project was to investigate the relation between cavitation erosion and corrosion of the two chosen propeller materials, DSS and NAB, and the interaction between them. The main objectives of the research involved:

- Use of ultrasonic cavitation rig under ASTM G-32 standards. Steady state mass loss of material was conducted using the ultrasonic vibratory sonotrode with in-situ electrochemistry to understand cavitation erosion-corrosion behaviour of the materials.
- Study of the detailed mechanisms involved within cavitation erosion and corrosion. Comparisons were made before and after each experiment between mass losses using both gravimetric as well as volumetric measurements obtained using precision weighing machine and Alicona respectively, and also the surface profilometry using Alicona.
- Understanding the electrochemical aspects of cavitation erosion-corrosion, and the corrosion behaviour of the material samples used during the experiments. This would further help establish the existence of synergy and the interaction between the cavitation wear and corrosion.

- Study the air- and water-formed protective films on NAB samples. The novelty of the research included investigating the effects of cavitation on the well-developed films on NAB using SEM of the cavitated surfaces and their transverse sections. Attempts were also made to understand the corrosion behaviour of NAB with water-formed oxide films.
- Understanding and attempting to quantify synergy to the best effect from the results obtained, using various methods.

#### **1.4. Scope of the Research**

The scope of the research is as follows:

- Chapter 1 briefly outlines the concept of cavitation, ship propellers, their functions and problems faced, and lays out the aim and objective of the research project.
- Chapter 2 elucidates the cavitation processes involved, the stages of cavitation wear process and occurrences, the wear incurred by propeller materials due to cavitation, and the different types of propeller cavitation.
- Chapter 3 gives the literature review on cavitation erosion test methods, cavitation erosion-corrosion test methods, and synergistic effects between cavitation wear and corrosion.
- Chapter 4 details the different propeller materials used, NAB and DSS, and their material properties. It also discusses the methodology employed in conducting the experiments in order to understand the cavitation erosion-corrosion behaviour of the ship propeller materials used.
- Chapter 5 gives the erosion rate, topographical and microstructural analyses for the cavitation erosion-corrosion experiments conducted on the test materials.

- Chapter 6 gives the electrochemical and corrosion analyses for the results obtained using electrochemistry for the sample materials.
- Chapter 7 focuses on the various synergy results obtained from the experimental tests conducted in chapter 4, 5 and 6, and discussion on the results obtained.
- Chapter 8 reviews the conclusion of the research done so far, the prospect future plan for the research for the next one-year, and the corresponding Gantt chart.

## 1.5. List of Publications and work presented

Following are the list of publications, posters and oral presentations presented as a part of the research:

### List of Publications:

- Basumatary, J., Wood, R. J. K. (2017) "Synergistic effects of cavitation erosion and corrosion for nickel aluminium bronze with oxide film in 3.5% NaCl solution," *Wear, Volumes 376–377, Part B, 1286–1297*. (See Appendix I)
- Basumatary, J., Wood, R. J. K. (2017) "Different methods of measuring synergy between cavitation erosion and corrosion for nickel aluminium bronze in 3.5% NaCl solution," submitted to *Tribology International*. (See Appendix II)
- Basumatary, J., Nie, M. and Wood, R.J.K. (2015) "The synergistic effects of cavitation erosion-corrosion in ship propeller materials." *Journal of Bio-and Tribo-Corrosion*, 1, (12), 1-12. ([doi:10.1007/s40735-015-0012-1](https://doi.org/10.1007/s40735-015-0012-1)) –

(See Appendix III)

- Wood, R.J.K., Basumatary, J. and Evans, M.-H. (2013) “Energy-related tribo-corrosion research at the National Centre for Advanced Tribology at Southampton.” In, *Tribo-Corrosion: Research, Testing, and Applications.* , ASTM International, 169-202. (Selected Technical Papers 1563). ([doi:10.1520/STP156320120148](https://doi.org/10.1520/STP156320120148)). (See Appendix IV)

#### **Poster presentations:**

- “Cavitation Erosion-Corrosion of Ship Propeller Materials,” 10<sup>th</sup> Tribo-UK conference ‘Future of Tribology,’ University of Leeds, Leeds, U.K., 25-26 March 2013.
- “Investigation of cavitation erosion-corrosion in ship propeller materials,” 2<sup>nd</sup> International Conference on Abrasive Processes (ICAP), Institute of Manufacturing, Cambridge, U.K., 8-10 September 2014.
- “The synergistic effect of cavitation erosion-corrosion on nickel aluminium bronze and duplex stainless steel,” 20<sup>th</sup> International Conference on Wear Of Materials, Toronto, Canada, 12-16 April 2015.

#### **Oral presentations:**

- European Corrosion Congress organized EUROCORR 2016, Montpellier, France, from 11-15 September 2016.
- 71<sup>st</sup> STLE annual meeting and exhibition, Las Vegas, Nevada, U.S.A., 15-19 May 2016.
- 20<sup>th</sup> International Conference on Wear Of Materials, Toronto, Canada, 12-16 April 2015.

- “Investigation of the synergistic effects of cavitation erosion-corrosion in marine propeller materials” 7<sup>th</sup> UK-China Symposium on Tribology, Wuhan, China, 6-8 April 2015.
- 2<sup>nd</sup> International Conference on Abrasive Processes (ICAP), Institute of Manufacturing, Cambridge, U.K., 8-10 September 2014.
- “Cavitation Erosion-Corrosion of Ship propeller materials”, 69<sup>th</sup> STLE annual meeting and exhibition, Lake Buena Vista, Orlando, Florida, U.S.A., 18-22 May 2014.
- “Investigation of the synergistic effects of erosion-corrosion using ultrasonic cavitation method” 4<sup>th</sup> Tribocorrosion Symposium, Glasgow, U.K., 9-11 April 2014.

#### **Prizes:**

- Thomas Andrew travel grant awarded by Institute of Mechanical Engineers (IMEchE) to attend the 71<sup>st</sup> STLE annual meeting and exhibition at Las Vegas, Nevada, U.S.A. 2016.
- Thomas Andrew travel grant awarded by Institute of Mechanical Engineers (IMEchE) to attend the 69<sup>th</sup> STLE annual meeting and exhibition at Orlando, Florida, U.S.A. 2014.
- Poster prize, 10<sup>th</sup> Tribo-UK conference ‘Future of Tribology,’ University of Leeds, Leeds, UK, 25-26 March 2013.

# Chapter 2:

## Cavitation process

---

Cavitation can occur in all types of liquids. Different liquids will generally have different degrees of resistance to cavitation as they depend upon their tensile strength as well as concentration of gas and foreign particles in the liquid to a considerable degree. But for the cavitation to occur, several factors such as the vapour pressure, the liquid temperature, the amount of dissolved gas, the nucleation of the bubbles, their growth and the imminent collapse are requisite [34], [35]. The following section discusses the mechanism of the cavitation phenomenon, the erosion incurred and its effects on propellers.

## 2.1. Mechanism of Cavitation

### 2.1.1. Nucleation

One of the most important factors for cavitation to occur is the existence of nuclei and nucleation sites. The prediction and control of nucleation sites is, however, very uncertain even for water. Any liquid most certainly contains dissolved air in the form of miniscule gaseous and/or vaporous bubbles whose diameters may vary from a few microns to the visible bubbles of the order of 1mm, which serve as the cavitation nuclei [5], [34]. When these nuclei enter a low-pressure region where the equilibrium between the various forces acting on the nuclei surface is un-established, cavitation begins to occur. As a result, bubbles appear at discrete spots in low-pressure regions [36]. Nucleation of vapour bubbles in a metastable liquid is an important yet not well-understood phenomenon. In most liquids, the reduction in volumetric stability is facilitated by the presence of external surfaces, which usually take the form of various admixtures such as dissolved or suspended impurities, particularly those on a sub-microscopic level, or even the walls containing the liquid, and serve as cavitation nucleation sites [5], [37].

There are mainly two types of nucleation modes: homogeneous and heterogeneous. Homogeneous nucleation takes place when there is no prior presence of additional gaseous phases in a liquid phase [38], [39]. It takes place due to the distribution of thermal energy among the molecules in the liquid volume. But due to the difference in the level of excitation in each molecule, the cavitation nuclei are rather unstable. A gas bubble will easily dissolve in an under-saturated solution, while the effect of surface tension will cause it to dissolve in a saturated solution. However, it will not dissolve in a super-saturated liquid due to the conflict between the bubble surface tension and the growth of the bubbles by diffusion [36]. A heterogeneous nucleation, on the other hand, comprises of small pockets of gas that are stabilized at the bottom of the cracks or crevices, found on hydrophobic solid impurities in the liquid, that may exist without dissolving into the liquid [1], [40]–[42]. Figure 2.1 shows a heterogeneous nucleation process in a crevice of a suspended micro-particle in a liquid [1].

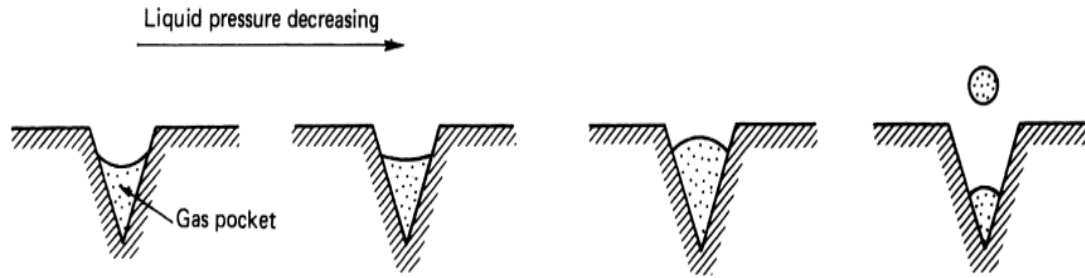


**Fig. 2.1:** Nucleation model for a crevice in an entrained micro-particle in a liquid [1].

The beginning of cavitation phenomenon is termed as the cavitation inception. This stage is crucial as nuclei play the main part in the initial formation of cavitation, and once the cavitation occurs these nuclei lose their importance [34]. The initial formation of vapour is however much more complicated, because pure water has been observed to withstand much lower pressures than the equilibrium vapour pressure without vaporization. This is mostly due to the cohesion of the water molecules, which gives water high tensions [34], [37], [43]–[45]. The cohesiveness of liquid molecules is generally stronger than the adhesion between the liquid molecules and the container surface it is in contact with. So, when a low pressure occurs on a surface, cavitation starts. The vaporization pressure of a fluid is dependent on its temperature, as shown in Figure 2.2. The vapour pressure of water drastically increases with the rise in temperature hence, increasing the chances of cavitation in water [46].



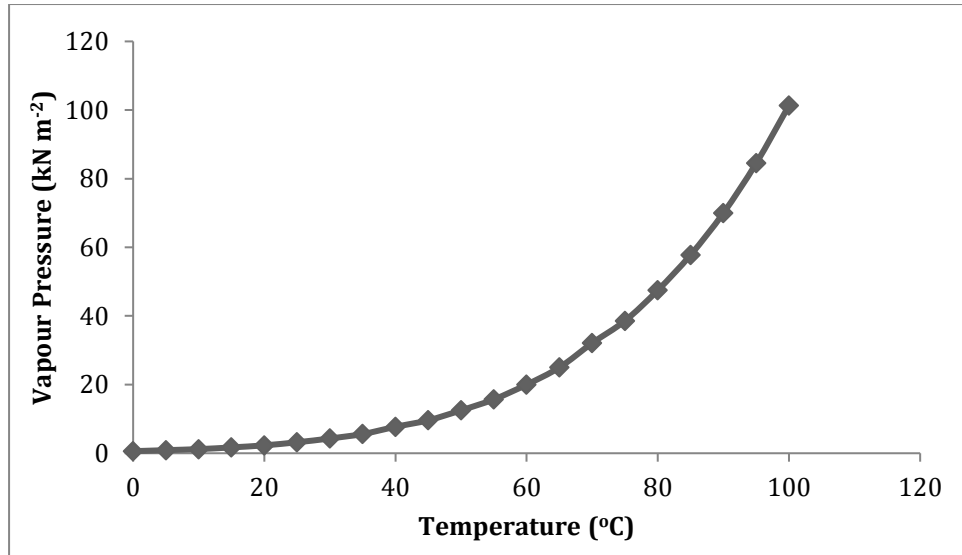


**Fig. 2.2:** *Equilibrium water vapour pressure of water vs. temperature plot, adapted from Ref. [46].*

However, cavitation is not always a consequence of the reduction of pressure to the liquid's vapour pressure at a specified temperature. Cavity formation in a homogeneous liquid requires a sufficiently large amount of stress to rupture the liquid. This stress represents the tensile strength of the liquid at a given temperature[45]. The temperature of the liquid as well as any contamination in the liquid, which is unavoidable in practice, determine the tensile strength of water [43], [44], [46]. However, the tensile strength, due to the adhesive forces between a surface and the liquid, is still in orders of magnitude higher than the equilibrium vapour pressure [34].

### **2.1.2. Bubble formation, shape distortion and collapse**

Once the pressure in the liquid is reduced to a certain level, cavities become the repository of vapour or dissolved gases. This change in the hydrodynamic pressure causes phase transition in the liquid, forming a two-phase flow mainly composed of the liquid and its vapour. The immediate result of this condition is the rapid increase in the cavity size. When this larger cavity enters a zone of higher pressure, there is a reduction in its size as a result of condensation of the vapours in the liquid causing collapse of the bubble [47]–[51]. During the collapse, particles of liquid surrounding the bubble quickly move to its centre. Kinetic

energy from these particles create local water hammers of high intensity (shock), which grow as the particles progress towards the centre of the bubble [5]. However, due to the rise in the pressure inside the bubble, the contraction of the bubble eventually slows down and stops. After the collapse, the bubble reappears in the form of a rebound bubble of smaller size. The rebound happens due to gas trapped in the bubble at the collapse. The cavitation bubbles are filled with a mixture of vapour and non-condensable gas, the origin of which is still unclear, but is thought to come from a combination of gas dissolved in the water, and gas created at the energy deposition due to the generation of the bubbles. The quantity of these non-condensable gas in the bubble influences the maximum radius of the rebound bubble [52]–[55].

During a bubble collapse the shape of the bubble is distorted, depending on its location from a solid or a free surface in the liquid, due to the Rayleigh-Taylor instability theorem of the existence of instability at the interface between fluids of two different densities that occurs when the fluid of lower density tries to accelerate through the fluid of higher density [56]. The two major ways a bubble generally distorts are either spherical or asymmetrical, and the shape of the rebound bubble is determined by the symmetry or asymmetry of the dynamics of the collapse. A perfectly spherical collapse produces a spherical rebound bubble, however, an asymmetry leads to the deformation of the bubble and in some cases the apparition of a ‘re-entrant’ jet emerges from the rebound bubble. This re-entrant jet, also known as microjet, is caused due to the Rayleigh-Taylor instability theorem. The spherical bubble starts to deform because of the pressure variations, obtaining a toroidal shape [57]–[59]. Figure 2.3 represents the theoretical shapes of Plesset and Chapman (solid lines) compared with the experimental observations of Lauterborn and Bolle (dotted lines) [1], [45], [60], [61].

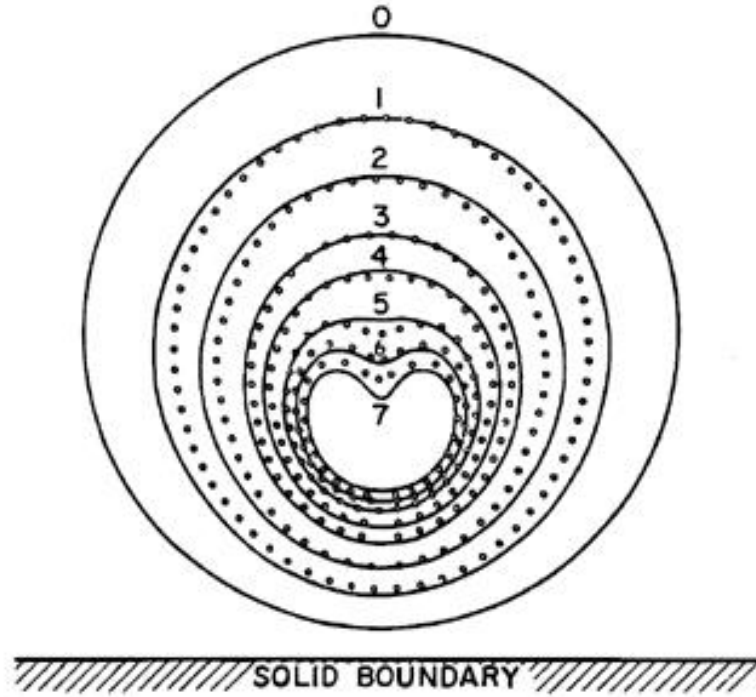


**Fig. 2.3:** Vapour Bubble Collapse near a solid boundary in a quiescent liquid comparing the theoretical observations of Plesset and Chapman (solid lines), with the experimental observations of Lauterborn and Bolle (dotted lines) [1], [45], [60], [61].

## 2.2. Cavitation Impact

### 2.2.1. Microjet impingement

As depicted in Figure 2.3, the bubble placed close to the wall initially collapses spherically (shown by sphere number 0), and the re-entrant jet penetrates the fluid between the bubble and the wall as the bubble is rebounding from the first collapse (most prominent in sphere number 7) [45]. When the pressure within the bubble rises steeply, with the gas content acting as a hard spring, abruptly stopping the inward motion and driving the bubble back into expansion, this is known as rebounding of the bubble [62]. This rebound bubble then collapses releasing a high velocity destructive impact to the boundary wall while a microjet is obtained and a powerful shock wave is emitted. The impact of this microjet occurs before the bubble reaches minimum size, and the microjet flow vanishes as

the bubble re-expands. The pressure within the bubble rises steeply, with the gas content acting as a hard spring, abruptly stopping the inward motion and driving the bubble back into expansion [62].

When the bubble surroundings are strongly asymmetrical such as near a solid wall or a free surface, a re-entrant microjet emerges. In case of a solid boundary near the bubble, the furthest side of the bubble wall accelerates inward through the centre more rapidly than the side close to the wall, typically resulting in a re-entrant microjet that penetrates the bubble at a very high speed [45], [63], [64]. But it is not necessarily always the case. As observed by Benjamin and Ellis, when a spherical bubble much closer to a solid wall collapses, it collapses in what is called a “pancake” mode where the hemispherical bubble flattens down on the wall before dissipating with no recognizable microjets, see Figure 2.4 [64].

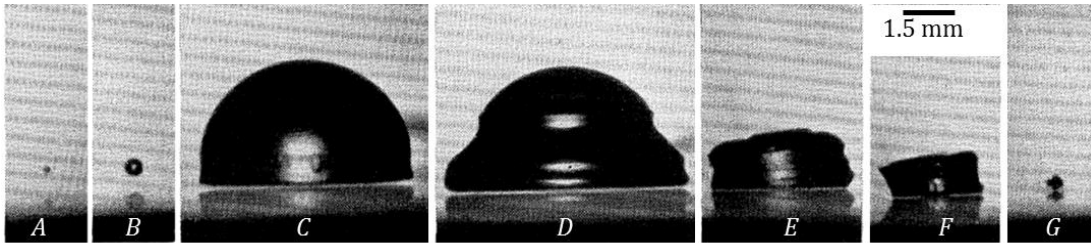


**Fig. 2.4:** Growth of cavity into a hemispherical bubble and undergoing the “pancaking” mode of collapse against a solid wall. Timing A and B at 0 and 0.4 ms; C and D at 5.8 and 11.4 ms; E, F and G at 16.8, 17.4 and 17.8 ms respectively [64].

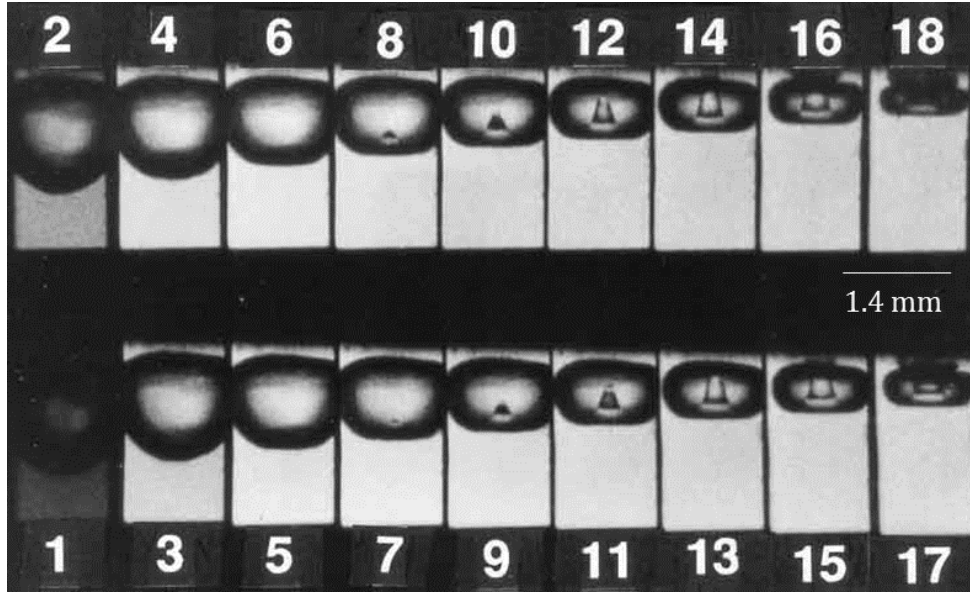
Other strong asymmetries may also cause the formation of a re-entrant jet such as a solid surface. Bubbles collapsing near a free surface have been observed to produce a re-entrant jet directed away from the free surface as observed by Chahine [65]. This is due to the critical flexibility of the free surface that separates the circumstances in which the re-entrant jet is directed away from rather than toward the surface. Hence, flexible coatings or liners may be a mean to avoiding cavitation damage on ship propellers as demonstrated experimentally and analytically by Gibson and Blake [66]. Another possible asymmetry may arise at the close proximity of other bubbles within a small cavitation cloud as observed by Chahine and Duraiswami in their experiment that the bubbles on the outer

edge of such clouds tend to develop jets toward the center of the cloud [67].

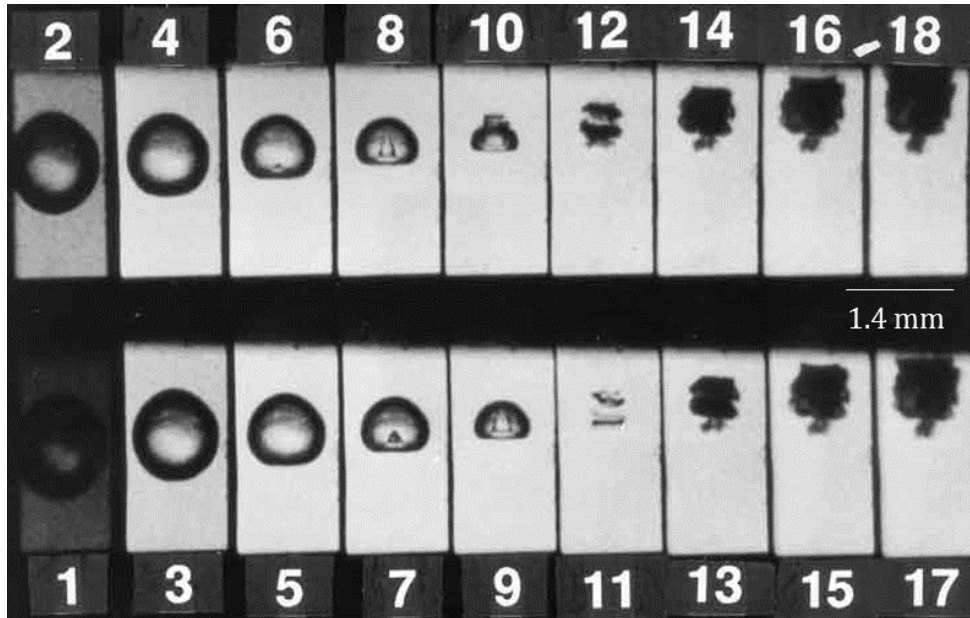
The rebound bubble can also sometimes break into several bubbles. This phenomenon is called fission of the bubble. It is thought to be caused by either Rayleigh-Taylor instabilities on the bubble interface or by the re-entrant jet at the collapse of the bubble [56]. It has also been shown that when bubble fission occurs, the resulting rebound bubble is smaller than expected because the process dissipates energy [68].

Ebullition can occur the instant pressure drops. Due to this, vapour bubbles form and collapse frequently and quickly (within ms), often accompanied by the devastating impact on the adjacent metal surface. Many other experimentalists have subsequently observed re-entrant jets forming in cavitation bubbles during their collapse near solid walls. The way cavities collapse seems to differ from one cavity to another depending on the initial distance of the cavity centre from the wall [45].

The difference in the development of the microjets can be compared using the two different series of pictures taken of two individual bubbles by Tomita and Shima. In their experiment of laser-induced cavitation bubbles in water, they observed and recorded the process of microjet evolution using an Imacon high-speed camera with a Xenon micro-flash as a light source. They used a lens with a focal length of 150 mm, and later magnified about 3 times the original size on the polaroid film. The interval between the numbered frames was 2  $\mu\text{s}$ , and the frame width set at 1.4 mm. The maximum bubble radius reached was approx. 1.3 mm. As seen in Figure 2.5 (a), the 1<sup>st</sup> bubble is initially spherical, situated close to the solid wall. The typical development of the microjet is as illustrated in Figure 2.5 (a), where an asymmetrical implosion was observed to take place, and a liquid jet was seen to penetrate the bubble surface at a recorded velocity of 98  $\text{m s}^{-1}$ . After the impingement of the liquid jet, it rapidly flowed outwards with a maximum speed of 134  $\text{m s}^{-1}$ . As can notably be observed, the size of the liquid jet became wider as time lapsed [69].



(a)



(b)

**Fig 2.5:** Series of photographs showing the development of the microjet in a bubble collapsing (a) very close to a solid wall; and (b) away from the solid wall at the top of the frame. The interval between the numbered frames is  $2\mu\text{s}$  and the frame width is  $1.4\text{mm}$  [69].

When the bubble is further away from the wall (as in Figure 2.5(b)), the events are comparatively different. Figure 2.5(b) illustrates the series of the formation of two toroidal vortex bubbles in frame 10 and 11, after the microjet has completed its

penetration of the original bubble (similar to Figure 2.3) at a velocity of  $98 \text{ m s}^{-1}$  [45], [60], [69].

The cavitation process can be divided into two principal types: vaporous and gaseous. Vaporous cavitation takes place if the bubble grows explosively in an unbounded manner as liquid changes into vapour. This situation occurs when the pressure level goes below the vapour pressure of the liquid. Whereas, gaseous cavitation is a diffusion process that occurs whenever the pressure falls below the saturation pressure of the non-condensable gas dissolved in the liquid. While vaporous cavitation is extremely rapid, occurring in ms, gaseous cavitation is much slower; the time it takes depends upon the degree of convection (fluid circulation) present. It is only under the vaporous cavitation conditions that cavitation wear occurs. Gaseous cavitation mostly creates noise, generates high temperatures and degrades the chemical composition of the fluid through oxidation [5].

### ***2.2.2. Shock waves***

When the cavitation bubbles collapse, they force energetic liquid of very small volumes, thereby, creating spots of high temperature and emitting destructive shock waves. These shock waves produce a crackling noise during cavitation [70], [62]. Figure 2.6 gives an example of a high-speed photographic sequence, which probes the final collapse stages. This series was taken at 20.8 million frames per s with an image converter camera. The maximum number of frames per shot is limited to eight. Therefore, four different shots corresponding to nearly identical bubbles have been combined together [62]. The picture shows a series of bubble growth, followed by collapse and finally, radial expansion of shock waves from the bubble.

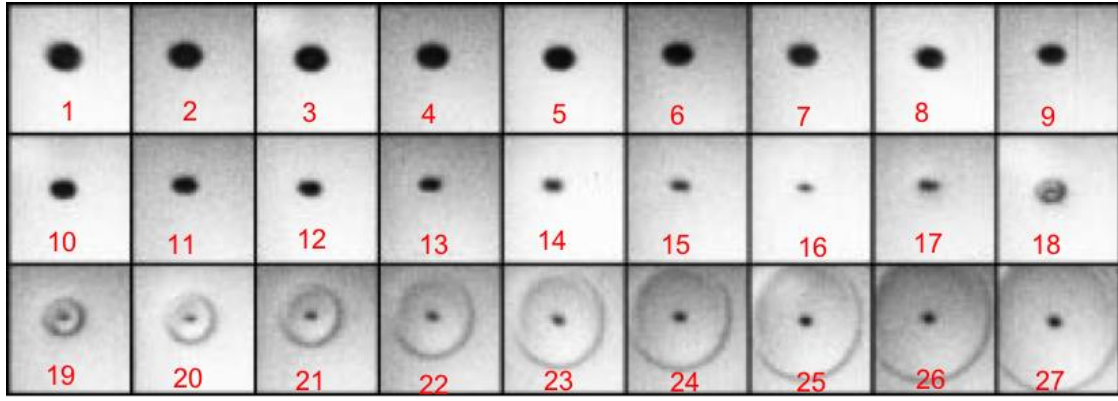


**Fig. 2.6:** A spherically symmetric shock wave emitted by a laser-generated bubble upon first collapse taken at 20.8 million frames per s with the arrangement depicted in frame 1. The frame size is  $1.5 \times 1.8 \text{ mm}^2$  and the exposure time is ca. 5 ns [62].

In Figure 2.6, a free spherical bubble (frame 1) produced in water is shown to undergo a rapid first collapse from frame 17 onwards and, in this process, radiate a spherically symmetric shock wave. The series starts after the bubble has reached maximum radius at frame 4 and 5. The bubble is seen as a dark disc as the illuminating backlight is deflected of the bubble wall. From the point of maximum expansion (frame 5), the bubble starts to shrink, gaining speed at an ever increasing rate, driven by the ambient pressure and leading to a collapse with strong compression of the bubble content in the final phase. In the stage of maximum compression (frame 16), an outward going shock wave is emitted (the circular ring seen around the black dot). The shock wave propagates at about the velocity of sound, i.e. at about  $1500 \text{ m s}^{-1}$  in water [62].

Another important feature of cavitation phenomenon is the amount of energy dissipated during the collapse. When the cavitation bubbles collapse, they force energetic liquid of very small volumes, thereby, creating spots of high temperature and emitting destructive shock waves. A major part of the shock wave energy is dissipated within the first  $100 \text{ }\mu\text{m}$  from the bubble wall [71]. These shock waves produce a crackling noise during cavitation [62], [70]. The energy emitted during collapsing of a cavity is generally of low order and does not cause the actual damage. However, when highly localized, these repetitive collapses are known to



erode almost anything over time. These bubble collapses also produce high impact forces, causing work hardening, fatigue and cavitation pits resulting in cracks, wear and erosion of the material. Surface damage similar to surface fatigue takes place and particles smaller than those generated by surface fatigue are removed [62].

The impulses that result when vapour bubbles form and collapse cause individual symmetrical craters and permanent material deformations on the surface [5]. The pittings due to fatigue and plastic deformation caused by the collapses on the metal surface produce great wear on the components, and dramatically shorten a propeller or pump's lifetime since, after a surface is initially affected by cavitation, it tends to erode at an accelerating pace, and also undergoes oxidation especially under corrosive environment. The cavitation pits increase the turbulence of the fluid flow and create crevices, which act as nucleation sites for additional cavitation bubbles. The pits also increase the components' surface area and leave behind residual stresses. This makes the surface more prone to stress corrosion cracking (crack occurring in and propagated by corrosive environment) [72].

### ***2.2.3. Cavitation wear***

Cavitation wear is mechanical in nature and cannot occur without the application of the tensile and compressive stresses. Cavitation wear damage undergoes several periods of activity. Depending on the surface structure, the material surface is deformed, loosened and eventually eroded in various ways due to the frequent strain from the shock waves [5], [73], [74], [10]. The rate of erosion is a function of the exposure period and it increases from negligible values, reaching a maximum before decreasing again and finally levelling off to a steady value. Figure 2.7 classifies the typical cavitation erosion process into four periods, indicating the incubation period, the maximum rate period, deceleration period and the steady-state period, also indicating the different physical changes undergoing during each stage [5], [10], [75].

- **Incubation period** – This is the “zero loss” period depicted by zone I in

Figure 2.7, where the mass loss is almost zero or negligible [5], [10], [75]. The micro-cracks nucleate around grain boundaries and inclusions due to both elastic and plastic deformation of the surface [5]. The surface of a ductile metal first undergoes elastic deformation and then plastic deformation causing dents and bulges to arise with time. After the deformability of the material is exceeded, fractures occur and individual particles break off [10].

- **Acceleration period** – The steep linear rise in zone II corresponds to the maximum rate period when the crack growth proceeds in relation to the degree of splitting, shearing and tearing action on the material [5]. This is due to internal tensions forming at the end of the incubation phase that exceed the material strength [10].
- **Deceleration Period** – Shown in zone III, the mass loss rate decreases after a certain amount of time till it reaches a steady period. For certain materials, this period sometimes consists of oscillating rate period [5], [10], [75].
- **Steady-state period** – Most of the time the material erosion rate reaches a steady period, zone IV, where the rate of crack nucleation and propagation becomes constant for the remainder of the exposure time [5]. This is because the surface, that is already strongly fractured, reduces the probability for an implosion close to the surface. The fractured surface acts as a kind of protective cushion. As a result, the material erodes at a lower steady rate [10].

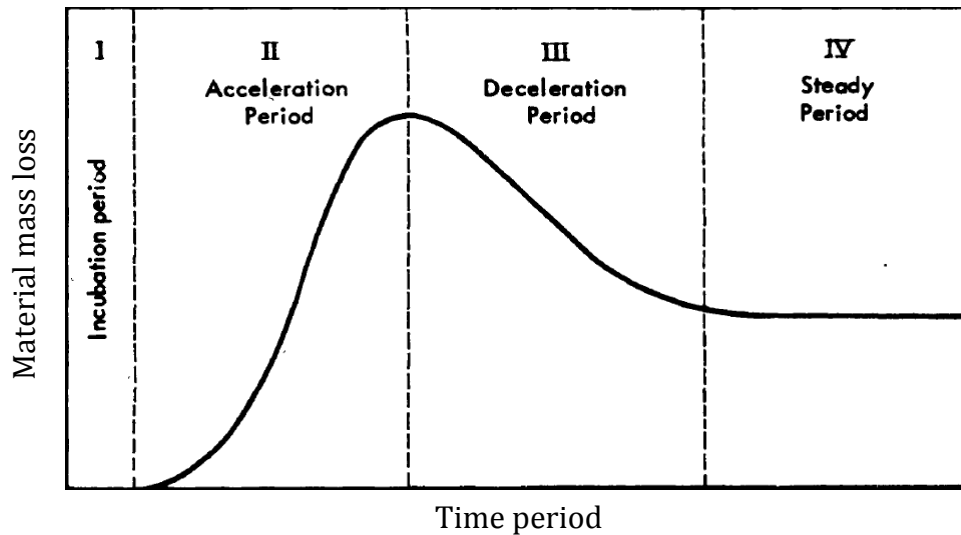


**Fig. 2.7:** Typical classification of erosion periods [75].

Figure 2.7 depicts the material mass loss rate curve where, the incubation period is generally extremely difficult to observe in some accelerated tests. But, its duration is actually very important to determine the life of the cavitating device [75].

Cavitation erosion process is a result of both mechanical as well as electrochemical action and is known to be a very complex phenomenon depending not only on the type and unsteadiness of cavitation, but also the response of the material to the cavitation energy [17], [76]. The shock wave generated impinges on the adjacent metal surfaces and destroys the material bonds. It first produces a compressive stress on the solid surface, and then when it is reflected, produces a tensile stress that is normal to the surface. Any system that can repeat this tensile and compressive stress pattern is subject to cavitation wear. Cavitation wear is similar to surface fatigue wear, hence, hard ductile materials that resist surface fatigue also resist cavitation damage [5].

In cavitation wear, micro-cracks propagate to the point where the material can no longer withstand the impulse load that the imploding vapour bubbles impose, causing the particles to finally break off. As with any fatigue failure, micro-cracks first form at stress risers (notches, tears, undercuts, welding defects, etc.) or at

heterogeneous areas of the material such as at the directionality of metal flow, inclusions, and decarburized sections. Therefore, a rough surface is prone to cavitation wear. And because pits and a rough profile characterize the cavitation damage, the damage increases as the surface becomes rougher [5].

A critical aspect of the cavitation wear process is surface destruction and material displacement caused by high relative motions between a surface and the exposed fluid. The amount of damage that cavitation causes depends on how much fluid pressure and velocity the collapsed bubbles create. As a result of this pressure and velocity, the exposed surface undergoes widely varying intensities. Each imposition lasts only a short time. For example, in a study conducted by Akhatov, et al. on collapse and rebound of laser induced cavitation bubbles, a bubble of maximum radius between 0.5 and 3mm seemed to collapse in about  $100\ \mu\text{s}$  [5], [52]. The impulse magnitudes and collapse times are greater for larger bubbles at given collapsing pressure differentials. Thus, the greater the tensile stress on the fluid (the lower the static pressure), the larger the bubbles, the more intense the cavitation would occur causing more damages [5].

### 2.3. Cavity properties

As mentioned earlier, the bubbles that collapse away from a surface have high pressure of up to 8 GPa forming inside them and collapse in a symmetrical (spherical) way, whereas the bubbles that collapse closer to a solid surface generate high stress with a re-entrant jet. For example, at  $68\ \mu\text{m}$  distance away from the surface, the shock pressure generated by the bubble was measured up to  $1.3 \pm 0.3\ \text{GPa}$  [71].

Franc and Michel estimated in their study the impact pressures and the duration of the impact on four different phenomena associated with the various forms of cavity collapse, namely: the micro bubble collapse, an impinging microjet, the collective micro-bubble cloud collapse, and the impacting cavitating vortices. Table 2.1 gives the mechanisms of the bubble collapse along with their type of

loading, amplitude and the time period of the collapse [77], [78].

The pressure amplitude and pulse period of a cavitating bubble jet can be estimated from the pressures found in the water hammer. As shown in Table 2.1, a cavity bubble of 1 mm diameter is estimated to produce a jet diameter of 0.1 mm with a pressure pulse for duration of about 0.03  $\mu$ s. The duration of the pressure pulse is generally fixed by the diameter of the jet. However, in case of a collective collapse, the pressure wave emitted by the collapse and rebound of a particular bubble tends to enhance the collapse velocities of the neighbouring bubbles, thus increasing the amplitude of their respective pressure waves. Franc and Michel concluded that the most aggressive acoustic power was emitted from the collective micro-bubble collapse. They also established that the cavitating vortices were an effective mean to focus the release of acoustic power, thereby increasing the aggressiveness [77], [78].

<b>Mechanism</b>	<b>Type of loading</b>	<b>Amplitude [MPa]</b>	<b>Duration [<math>\mu</math>s]</b>
Micro-bubble collapse	Pressure wave	100	1
Microjet (from a 1 mm bubble)	Impacting jet	150	0.03
Collective micro-bubble collapse	Pressure waves	>100	>1
Cavitating vortices	Impacting jet	>100	> 10

**Table 2.1:** Review of impact loadings for different cavity phenomena [78].

In 1977, Tomita and Shima [79] conducted the adiabatic calculations for handling liquid compressibility, where they obtained that the maximum gas temperatures in the bubble centre was as high as 8527°C. However, despite the small elapsed times, Hickling [80] demonstrated that heat transfer between the liquid and the gas was equally important due to the extremely high temperature gradients and the short distances involved. In later calculations, Fujikawa and Akamatsu [81] included the heat transfer and, for a case similar to that of Tomita and Shima [79],

found lower maximum temperatures and pressures of the order of 6427°C and 84.8 MPa, respectively, at the bubble centre, which seemed to exist for a fraction of a microsecond. For example, within 2  $\mu$ s, the interface temperature dropped from maximum interface temperature of about 3127°C to 27°C [81]. It was also found that a bubble having a maximum radius of 1.45 mm could give a maximum implosion depth of 7  $\mu$ m on softer materials such as aluminium [82].

## 2.4. Cavitation Detection

On ship propellers, noise can be created due to the individual or combined effects of sudden collapse of a cavity bubble, or the periodic fluctuations of the cavity volumes. On the other hand, the inception stage of cavitation may affect the noise level [83]. Cavitation implosion usually produces loud crackling noise that can be easily detected by acoustical emission (AE) instrumentation, by machine vibration sensors, through sonoluminescence measurement, hydrophones, vibration analysis or change in performance from that produced under single-phase flow conditions (for example, loss of flow, rigidity and response) [84]. Detecting acoustic signals from cavitation has proven to be a powerful technique for understanding the cavitation process [85]. AE transducers detect the high frequency noise created by the cavitation bubble implosion as well as the high-frequency acoustic energy released by the development of crack in a solid material surface due to cavitation. AE sensors are generally either directly mounted on the flow boundaries, or attached to the sample materials [84]. It has been found by Alfayez, Mba and Dyson, who conducted AE analysis to measure cavitation, that AE technique was suited for detecting incipient, and not developed, cavitation [86].

Hydrophones are another means for acoustic cavitation detection. Time domain signals or output signals from the hydrophone can be recorded using an oscilloscope or a dynamic signal analyser like the Hewlett Packard 3561A [84]. Piezo-electric and Fibre-optic hydrophone (FOH) sensors are the two types of hydrophone sensors that are used as acoustic cavitation detectors. As observed by

Bull, Civale, Rivens and Haar, Piezo-electric hydrophones have higher sensitivity than FOH sensors, but FOH sensors are useful for applications involving limited space or magnetic resonance-guided studies [87].

National Physics Laboratory (NPL) has developed cavitation sensors that detect broadband acoustic signals emitted by oscillating and collapsing bubbles. The sensor spatially resolves cavitation activity in cleaning vessels and sonochemical reactors. NPL has also developed a signal processing electronics unit, called Cavimeter, designed to be used with the cavitation sensor. It provides a near real-time indication of the acoustic signals emitted by oscillating and collapsing bubbles detected by the cavitation sensor [85].

Detection of erosion at an early stage through acoustic measurements can be valuable in modifying the operating profile of the vessel apart from taking preventive maintenance. In a fluid flow system (unlike an ultrasonic tank), vapour bubbles form where, fluid tensile stresses (low pressures) occur, and vapour bubbles collapse in higher-pressure regions. Compressive stresses can be imposed on the fluid. So the region, where damage occurs, is often separate from the region in which cavities are created, leading to an incorrect diagnosis of the problem [5].

The detection and quantification of cavitation can also be done using optical techniques such as sonochemistry and sonoluminescence. Both help detect the location and intensity of the cavitation, mainly by monitoring the light emission during cavitation due to its reaction with radicals. As observed by Price in his study for detection of cavitation by sonochemistry, he quantified that the radical production as well as other physical (e.g. acoustic emission) and chemical (product analysis) techniques allowed the amount of cavitation to be measured [88].

## 2.5. Propeller Cavitation

### 2.5.1. *Effects of cavitation on ship propellers*

When the propeller rotates, it absorbs the torque developed by the engine at given revolutions and converts that to the thrust which, in turn, pushes the vessel through the water. As the hydrofoil passes through the water, it induces a positive pressure on the face of the blade, while a negative pressure acts on its back. The ratio of the absorbed power and the delivered thrust to the total blade area of the propeller is called, respectively, the power and the thrust loading. If either of these exceed a certain value, depending on the propeller type, the flow around it, the mean depth below the water relative to its diameter, and the relation between them, then the flow pattern of the water over the propeller blades breaks down causing cavitation which may lead to severe loss of thrust along with physical damage to the surface of the propeller blades and, also, the rudder and local steel-work of the vessel's hull. Cavitation is a highly complex phenomenon and the pitting damage it causes usually appears by an increase in the propeller rpm without a commensurate increase in the speed of the ship [4].

As mentioned in chapter 1, section 1.2.3, cavitation erosion may occur either behind the blade of a rapidly rotating propeller or on the face of propeller blades when the propeller is overloaded. Cavitation can attack several different parts of ships. The propeller itself is the greater zone of cavitation due to induced high local velocities (or low pressures) around the blades and vortexes [83]. Based on the angle of inclination,  $\alpha$ , of the ship propeller the location of the cavitation attack can vary greatly.

#### 2.5.1.1. *Positive angle of attack*

As seen in Figure 2.8, a positive angle of attack,  $\alpha > 0$ , can be seen to cause cavitation at the back of the profile and towards the trailing edge. Figure 2.8 shows the angle of inclination and attack of the propeller blade with two points of stagnation, at the leading edge and at the trailing edge. Stagnation point refers to the region where the pressure distribution is either zero or negligible. Figure 2.8



shows that when the pressure distribution exceeds the cavitation number ( $-1$ ), it enters the cavitation zone where the propeller blade starts to cavitate at the back-end [83].

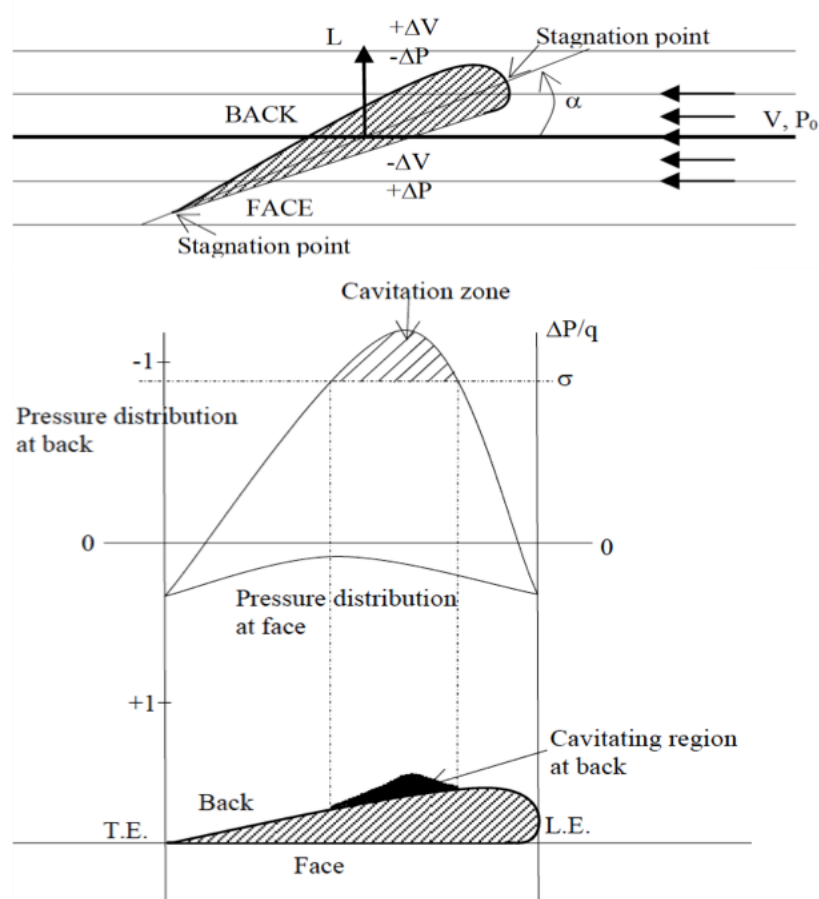


**Fig. 2.8:** Positive angle of attack on the propeller blade with pressure distribution at different areas of the propeller blade [83].

Where,  $L$  is lift force,  $V$  is the undisturbed flow velocity,  $P_0$  is the undisturbed fluid pressure,  $\Delta V$  and  $\Delta P$  is the integration of the velocity and the pressures, respectively. T.E is the tail end and L.E. is the leading end of the of the propeller blade,  $\Delta P/q$  is the pressure distribution around the blade, and  $\sigma$  is the cavitation number.

#### 2.5.1.2. Zero angle of attack

This is when the angle of attack,  $\alpha \cong 0$ . This results in the cavitation zone formation behind the maximum thickness region of the profile at the back (i.e. towards trailing edge) [83].

### 2.5.1.3. Negative angle of attack

When  $\alpha < 0$  cavitation will likely occur at the face of the profile rather than back as in the positive angle of attack case as seen in Figure 2.9 and the pressure distribution graph across the propeller blade with negative angle of cavitation attack in Figure 2.9. As seen from figure, when the pressure distribution exceeds the maximum negative value of cavitation number, it reaches the cavitation zone where the blade starts to cavitate [83].

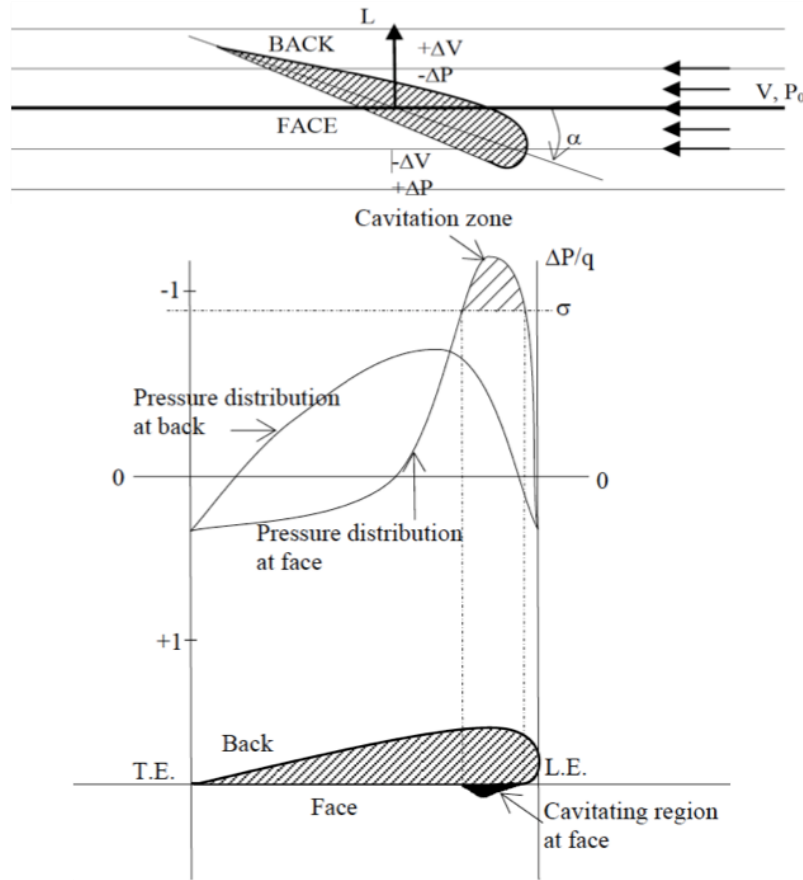


**Fig. 2.9:** Negative angle of attack on the propeller blade with the pressure distribution depicting the cavitation zone on the propeller blade [83].

Changing the angle of attack on a propeller blade influences the extent and position of cavitation. The angle of attack can be increased by keeping local velocity constant and by increasing rate of propeller rotation. Different rotational speeds affect results in different cavitation patterns. Generally, it is the peak values of the negative pressure distribution that, when exceeding the cavitation number, cause cavitation to occur [83].

### 2.5.2. Types of propeller cavitation

The type of propeller cavitation can be classified depending on the physical appearance of the cavitation, such as:

- Bubble cavitation,
- Sheet cavitation,
- Vortex cavitation,
- Root cavitation.

Figure 2.10 shows the schematic figure of all the possible locations of cavitation attack on a propeller [83].

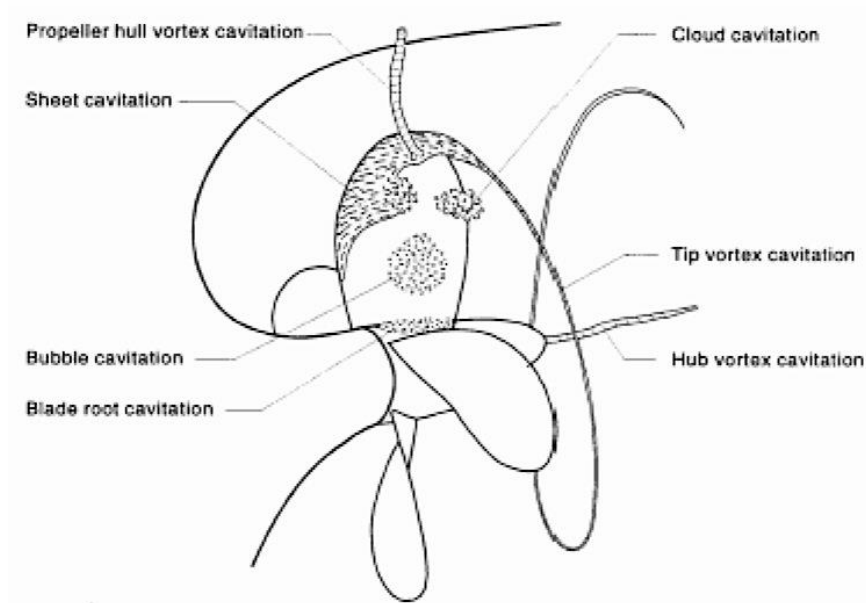


**Fig. 2.10:** Different locations of cavitation attack causing different types of cavitation [83].

#### 2.5.2.1. Bubble Cavitation

The natural type of cavitation following from expanding nuclei is the bubble cavitation. It is the vaporous type of cavitation that has destructive consequences on the contact materials. Cavitation erosion due to bubble cavitation is a serious problem especially in heavily loaded propellers. When the nuclei grow to visible sizes and larger, due to a low external pressure, the gas content inside the bubble

as well as the surface pressure on the bubble wall become insignificant and the pressure inside the bubble will be close to the vapour pressure, causing cavitation erosion. Figure 2.11 shows bubble cavitation on the model of a ship propeller [89].

Bubble cavitation is primarily affected by the pressure distribution, which causes high suction pressure in the mid- chord region of the blade section. Thus the combination of camber line and section thickness plays an important role on the susceptibility of a propeller towards bubble cavitation [83].

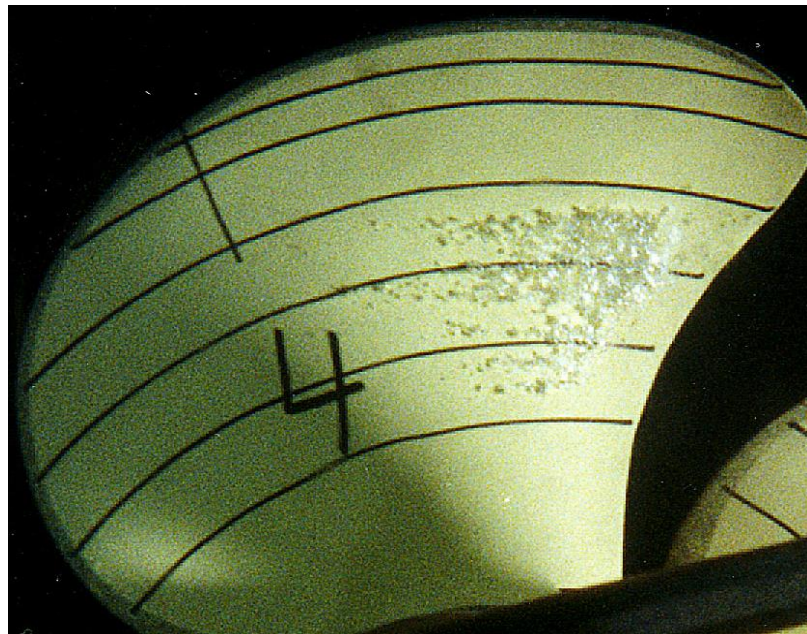


**Fig. 2.11:** Bubble cavitation occurring on the model of a ship propeller [89].

The origin of each bubble in Figure 2.11 is a nucleus, which grows with decreasing pressure. The essential element of the formation of bubble cavitation is that the bubbles have time to grow without causing flow separation. The result is that the cavitation bubbles move with the flow. Therefore, this type of cavitation is also called traveling bubble cavitation [89].

#### *2.5.2.2 Sheet Cavitation*

This is a type of fixed cavitation where the cavities form on a solid boundary and remain attached as long as the conditions that caused their formation remain unchanged. Also known as steady-state cavitation, sheet cavitation is a region of

vapour that remains approximately at the same position relative to the profile or propeller blade [90]. Sheet cavitation occurs when the pressure distribution has a strong adverse pressure gradient and the flow separates from the blade surface. Sheet cavitation initially becomes apparent at the leading edges of the propeller blades, when the blade sections are working at large positive angle of attack, or on the face side if the attack has a large negative value [83]. The surface of sheet cavitation can be very glossy, at least at model scale, but at full scale, the surface is often not as transparent. An example of sheet cavitation on a ship propeller is given in Figure 2.12 (a) [90].

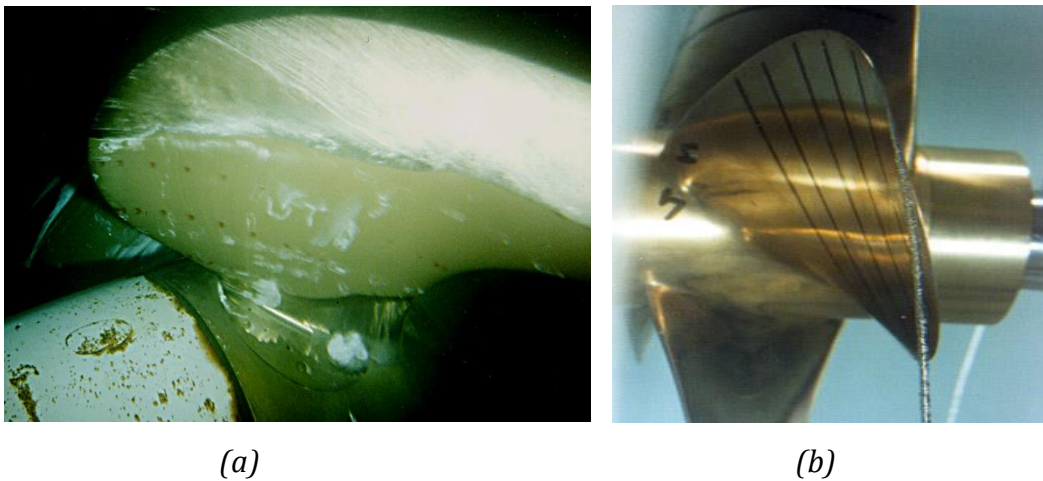


**Fig. 2.12:**(a) Sheet cavitation on a propeller blade [90]; (b) Vortex cavitation of the blade tip [91].

Sheet cavitation can have considerable volume of cavitation bubbles on the propeller blade whose dynamic behaviour may generate strong pressure fluctuations at frequencies lower than the noise frequencies. Which is why, these pressure fluctuations tend to have very large wavelength and, hence, are independent of the compressibility of the flow. Therefore, the pressure around the propeller and aft end varies in phase with the compressibility of the fluid. Which distinguishes the “Cavitation Induced Pressure Fluctuations” from cavitation induced noise. The constant phase of the cavitation induced pressure causes hull vibrations. This is different from the pressure field from the passage of a blade without cavitation, which is felt at different times at different places along the hull [83]. Without diffusion the pressure in the sheet cavity will be close to the

equilibrium vapour pressure and the surface of the cavity can be considered as a free surface [90].

#### *2.5.2.3. Vortex Cavitation*

The propeller blade producing thrust sheds vortices from its trailing edge. These vortices are generally strong at the tip and the root. The strength of the vortex shed from the blade tip increases downstream as the induced velocities increase. The pressure at the core of a vortex tends to be lower than that in the outer layers, and if the pressure at the vortex core falls to the vapour pressure then it results in tip vortex cavitation. Vortices are important for ship propellers because the pressure in the core is low and thus cavitation may occur. Vortex cavitation takes place in three places, the propeller hull, the blade tips, and the hub, forming in zones of high shear. Cavitation in the vortices shed by the blade roots appears as this rope with several strands. When the vortex cavity extends from the propeller to the hull of the ship, it is referred to as propeller hull vortex cavitation. It is not generally erosive if not very aggressive or in excessive amount. However, it is a major source of noise during cavitation. As noise is used to detect ships, it is important to keep cavitation minimum within navy ships and submarines. They are easily observed and detectable due to noise as well as due to the occurrence of the cavitation on the blade tips of the propellers. Figure 2.12 (b) shows a trail of water cavitating the propeller blade around the blade tip [1], [91].

#### *2.5.2.4. Root Cavitation*

Propeller root cavitation can be among the most complex of the cavitation damages. Root cavitation is known to originate in the high angle of attack caused by the variations at the blade roots due to the propeller shaft's inclination. Root cavitation erosion cannot be easily reconciled. It may appear at different times in the propeller rotation if the circulation around the root is sufficiently strong and can be sufficiently aggressive to cause erosion damage. The top of the wedge can be at the leading edge, but it can also start on the blade itself. Root cavitation is related to the horseshoe vortex developed at the root as well as inclined shaft and wake shadow effect created by the shaft brackets, bossings, etc. It is commonly observed on controllable pitch propellers (CPP) [2], [83].

## **2.6. Effect of corrosion environment on propeller cavitation**

Cavitation is complex phenomenon that involves not only the erosional aspect but also the corrosion aspect especially in the marine environment. In most cases, the damage to materials in a cavitated region occurs almost entirely due to mechanical processes, there is also evidence that electrochemical corrosion is often a very important factor. There are several factors influencing cavitation damage in an aggressive environment such as the sea, which includes the chemical activity/corrosion reaction occurring, as well as the dissolved or entrained gas content in the water, the temperature, the vapour pressure, and other such properties of the water, etc. [92].

### ***2.6.1. Effect of temperature***

In the marine environment, the seawater has many particles (organic and inorganic) dissolved or suspended in the water. These can react chemically with the propeller materials, depending on their chemical inertness. In the presence of cavitation, these reactions can sometimes be affected, due to the aggressive nature of the process. Cavitation is known to generate or produce temperature, even though it does not increase the temperature of the surrounding drastically. However, the temperature of the micro - environment around the cavity is certainly affected for fraction of a s. Which may induce corrosion or enhance the reaction, as observed by Okada [93].

The effects of temperature of the liquid on the damage process have been studied extensively [94]–[97]. From these studies it was observed that at lower temperatures, the vapour pressure of the liquid was relatively low, however, the amount of dissolved or entrained gasses were found to be relatively high. Which, in turn, provided cushioning effect for bubble collapse, causing relatively low damage. On raising the liquid temperature just enough to make some of the dissolved gas to be liberated, but without increasing the liquid vapour pressure too high to stop cavitation, it was seen that this increment in the vapour pressure provided additional unstable nuclei. This, in turn, led to the inception of more

cavitation bubbles, and hence, an increase in the cavitation damage. And on further increment of the temperature, the pressure also rose above the liquid vapour pressure to provide the considerable cushioning for the collapsing bubbles and reduce further damage [92].

### ***2.6.2. Effect of chemical activity and corrosion***

As already mentioned, the marine environment comprises of an amalgamation of gases, chemicals, organic and inorganic particles, corrosive solutes, abrasives, etc. dissolved or suspended in the liquid medium. These substances may induce a chemical reaction with the propeller materials under the right conditions. It has been observed that there have been electrochemical and chemical reactions occurring during the cavitation damages. This has been attributed to the production of very high temperatures, ranging up to of thousands of degrees, in the gases within the cavities themselves (as mentioned in section 2.3) [92].

Also, materials comprising of protective oxide or passive films may also suffer corrosion due to the rigorous erosion of the protective layers, causing pits, pores and cavities that act as the sites for pitting corrosions, crevice corrosion, and other chemical reactions. From the observations made on the chemical corrosion occurring during cavitation attack it has been established that the materials may undergo corrosion whilst exposed to cavitation. As reported by Nowotny [97], for the cavitation tests conducted in tap water in a venturi tunnel, several brass specimens as well as various steel samples were seen to exhibit pronounced tarnishing. He reported that after long exposures to cavitation, thick oxide films seemed to form and attach themselves to the substrate metal. These films were then seen to get subsequently removed by cavitation erosion, which further facilitated a secondary chemical effect within the localized micro-pores created by the mechanical attack [92].

However, use of corrosion inhibitors has been seen to reduce the influence of corrosion during cavitation erosion damage. Tests conducted by Rheingans [98] on steels and various non-ferrous metals in sulphuric acid and hydrochloric acid



for 2 h showed lower effect of the corrosive medium on the samples when compared to those cavitated in distilled water. Hence, corrosion inhibitors have been tried and used with increasing frequency as prevention to corrosion induced damage [92].

### ***2.6.3. Effect of liquid properties***

Many studies have also been conducted in order to understand the effect of water properties, such as surface tension, viscosity, liquid compressibility, etc. on the cavitation-induced damage. As reported by Nowotny, while keeping other factors constant, the damage of the test material is expected to increase with an increase in the surface tension. This is due to the dynamics of transient cavities, where the increment in the collapse pressures causes an increment in the surface tension, leading to higher cavitation damage [92], [97].

Another important liquid property is its viscosity. It has been found that higher viscosity of liquid tends to reduce the pressures in liquids, resulting in reduction of cavitation damage. This was because the viscosity in the liquid was seen to help dampen the cavitation bubble collapse. Also, the effects of other liquid properties like compressibility and density also showed that cavitation damage increased with increase in density and decrease in compressibility (based on the Rayleigh theory of bubble collapse) [92].

## **2.7. Summary**

In this chapter the main mechanisms of cavitation process were explained in detail. The details looked at the nucleation of the cavity bubble, the growth of the nuclei into bubbles, the collapse of the bubble, and the subsequent rebound of the bubbles. The most important factor for cavitation to occur comprises of the existence of nuclei and nucleation sites, which is due to the inevitable existence of dissolved air in the liquid. These nuclei, when pass through a low-pressure zone, grow in size reaching a critical size as they enter a high-pressure flow region.

Beyond this critical size, the bubbles collapse, imploding at a very high intensity, producing a very high pressure of up to 8-GPa and temperatures over 8500°C in the centre of the bubble.

The bubbles collapse in two ways namely, symmetrical and asymmetrical depending on the distance of the cavity bubble from a solid surface. The bubbles collapsing asymmetrically tend to have a rebound, called fission of the bubble, that result in to a re-entrant jet responsible for a high intensity shock wave and jet impingement that causes, combined with the high temperature emitted from the bubble, severe damage to the surface and material in the form of erosion and corrosion.

The erosion of material itself happens rapidly with repeated implosion of the bubbles on the material surface, the rate of which can be described using a typical cavitation erosion mass loss rate S-plot that includes an incubation period, the acceleration period, and finally a steady-state period. This phenomenon is a serious issue for marine and boat propellers. Cavitation may also be detected using audio as well as visual means such as acoustic emission instrumentation machine vibration sensors, sonoluminescence measurement, and hydrophones.

Propeller cavitation effects propellers depending on the angle of attack, positive, negative or zero, and occurred in four major ways which are bubble cavitation at the propeller blades, sheet cavitation that attacks the tip of the propeller blades, vortex cavitation that effects the hull, the propeller hub as well as the blade tip, and root cavitation forming at the roots of the propeller blades.

Hence, understanding the cavitation phenomenon, the various mechanisms involved, the different angles of attacks on the propeller blade and the different ways of propeller cavitation, and the working conditions themselves may aid in understanding propeller cavitation mechanism altogether. This could provide insightful knowledge on the ways to combat, prevent or reduce cavitation of boat and marine propellers.



# Chapter 3:

## Literature Review

---

Marine propellers undergo cavitation inevitably throughout their lifetime, one of the consequences of cavitation on these marine propellers is the damage that occurs to the propellers due to the detrimental effects of cavitation in the form of cavitation erosion, corrosion and bent trailing edges along large amplifications of vibration-exciting hull forces and the noise. Many research studies have been employed to understand these detrimental effects of cavitation in the form of individual cavitation tests under different techniques and on different materials for their behaviour towards cavitation. This chapter gives an overview on the current knowledge and relevant studies conducted to understand the cavitation phenomenon.

### 3.1. Cavitation test methods

In 1893 Barnaby reported the performance of a ship to be well below her designed speed of 27 knots (50 kmph), in the trials of the Torpedo boat destroyer HMS 'Daring'. Barnaby and Parsons traced this characteristic to poor propeller performance due to formation of vapour bubbles on the blades. The term "cavitation" was termed for the first time following a proposal by E. R. Froude [99]–[102]. Shortly afterwards Parsons built the world's first cavitation tunnel to observe the phenomena in model scale and tested the propellers of his famous world's first steam turbine boat "Turbinia" shown in Figure 3.1. He also constructed a larger tunnel 15 years later in which he could test 12" diameter propeller models [1], [100], [102].

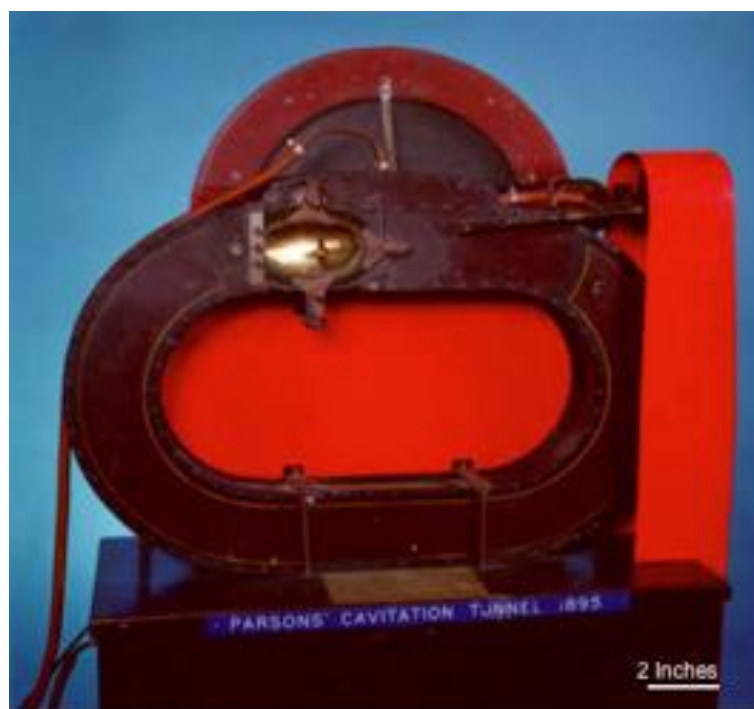


**Fig. 3.1:** *Parsons' cavitation tunnel 1895 [1].*

Between 1908-1924 detailed knowledge on the cavitation onset was collected, in 1917 British physicist, Lord Rayleigh, investigated the cause of quick erosion in the fast rotating ship propellers where he discovered that the effect of cavitation was the source of the problem, also tests with Venturi nozzles conducted by Föttinger in 1932, and pressure measurements on circular arc and aerofoils

performed by Ackeret in 1930 as well as Walchner in 1932 gave more meaning to the study of the phenomenon [10], [102].

Since, 1960 onward ultrasonic waves have been used to induce complex high-frequency alternating compression and rarefaction phases in liquids, causing cavitation. This has helped for the cavitation effects to be usefully applied for various applications such as cleaning surfaces, non-invasive operations in the field of medicine, in the wear of knee joints and other varieties of cardiovascular applications of lasers and ultrasound. It has also been used for breaking down agglomerates in the textile finishing industry, and in sewage treatment plants, where cavitation can help break down the molecules and bacteria cell walls, as well as pollutants and dissolve out minerals from organic material [10], [11].

Several studies have been conducted in the field of cavitation, multiphase flow, cavitation erosion, as well as cavitation due to vibration. Different methods have been applied to study cavitation behaviour of materials in varying mediums such as distilled water, tap water, artificial as well as natural sea water, mercury, to name a few [73], [103]–[107], and the microstructural changes due to cavitation have also been investigated [21], [108].

A comprehensive set of cavitation damage data was obtained by Hammit and Garcia [103] in a vibratory facility using water, mercury at room temperature, and even liquid lithium and lead-bismuth alloy at a high temperature of 815°C as test fluids to better understand the cavitation damage process and the effects of different fluids and material properties. Materials tested included a wide variety of metals and alloys including 304 SS, 316 SS, cobalt, molybdenum, carbon steel, plexiglas, copper, copper-nickel bronze, copper-zinc alloy, nickel, etc.. As a result it was found that ultimate resilience (UR), which is the ability of the material to absorb energy during elastic deformation, was the most successful of the conventional mechanical properties for predicting cavitation damage and a damage predicting equation was derived using only the ultimate resilience which is given by equation 3.1:

$$UR = UTS^2 / 2E \quad \dots(3.1)$$

Where, UTS is the ultimate tensile strength and E is the elastic modulus.

However, corrections for cavitation “thermodynamic effects” and net positive suction head were also conducted. They also conducted a comparison between venturi and vibratory cavitation damage which showed that the relative rankings of materials remained about the same for mercury, and a good correlation was obtained between the data for mercury medium from the venturi and ultimate resilience. However, due to the greater effects of corrosion in the low intensity cavitation field the same correlation could not be applied for the water venturi data [103].

There have been several test methods employed to re-create cavitation in the laboratories since 1940 [109]. The three most prominent methods are ultrasonic or vibrating horn test method, cavitating tunnel test method, and cavitating liquid jet erosion test method. The most widely used standard is the international standards organization called the American Society for Testing and Materials (ASTM) International. The ASTM standards used for the cavitation testing methods are:

**ASTM G32-16:** Standard test method for cavitation erosion using vibratory apparatus, where G is for corrosion, deterioration, and degradation of materials, 32 is the assigned sequential number, and 10 signifies the latest year of update - 2010. This test method may be used to estimate the relative resistance of materials to cavitation erosion as may be encountered, for instance, in pumps, hydraulic turbines, hydraulic dynamometers, valves, bearings, diesel engine cylinder liners, ship propellers, hydrofoils, and in internal flow passages with obstructions[110].

**ASTM G134 - 95(2016):** Standard test method for cavitation erosion via liquid jet impingement [111].

**ASTM D2809 – 09(2016)**: standard test method for cavitation corrosion and erosion-corrosion characteristics of aluminium pumps with engine coolants [112].

Other standards used are the British Standards (BS) under British Standards Institution (BSI) such as BS EN 60609-2:1999 – Cavitation pitting evaluation in hydraulic turbines, storage pumps and pump turbines – Evaluation in Pelton turbines, and BS ISO 7146-2:2008 – Plain bearings – Appearance and characterization of damage to metallic hydrodynamic bearings – Part 2: Cavitation erosion and its counter-measures [113]–[115]; and DYNAJETS® under DYNAFLOW, Inc. for cavitating Jet erosion testing and droplet impact erosion testing [116]. Many of the devices used have little relationship to actual field conditions. For this reason they have been typically used for screening tests of different types of materials. Recent research at St. Anthony Falls Laboratory (SAFL) aimed at relating screening tests to predictions of service life in various applications [117]. The most commonly used device is the ASTM vibratory apparatus. An oscillating horn produces a periodic pressure field that induces the periodic growth and collapse of a cloud of cavitation bubbles. A sample placed at the tip of the horn or immediately below it is easily eroded. The standard frequency of operation is 20 kHz, which produces a very high erosion rate due to the rapid recycling of the cavitation process. This is the technique used at SAFL [118].

Several comparisons have also been made between different types of cavitation test methods such as venturi apparatus, vibratory apparatus, single hydrofoils, radial pumps, etc. Among the various laboratory techniques used in the literature to study cavitation, three have been most commonly used for erosion measurements namely rotating disk, the hydrodynamic tunnel and a vibratory device. The characteristics of these facilities and their applications have been described by Preece [119] and Hammitt [74]. Stettler et al. [4] tested specimens of Armco iron, brass and cast steel on a magnetostrictive vibratory device, on a rotating disk and in the impeller chamber of a water turbine. They observed a statistical distribution of the pits in flow cavitation, but compact damage in



vibratory tests. Using a micro-hardness measurement technique, they evaluated the depth of the hardened layer in iron alloys as 30 - 60  $\mu\text{m}$  for vibratory cases and 250 - 500  $\mu\text{m}$  for the other cases. Hoss et al. [5] investigated the erosion of pure aluminium in different cavitation devices. They assert that there are many similarities in the kinetics of material loss and in the evolution of microstructure. Table 3.1 gives a brief comparison among the various methods used for cavitation [21], [103], [105], [120], [121].

<b>Techniques</b>	<b>Principle</b>	<b>Time taken to achieve measurable loss</b>
Cavitating Jets	High speed and pressure jet discharge cause cavitation	A few days
Cavitation tunnel	Radial divergent introduced in the flow to create unsteady cavity	Minimum 10 h
Vibratory cavitation	Ultrasonic vibratory horn is used to create cavitation	30 minutes
Venturi flow test	Cavitation is introduced by using a venturi throat	16 h
Rotating disk	A disk with cavitation inducers and specimens fixed on it rotates in water to provide cavitating flow)	24 h
Radial pump	Samples are mounted on an impeller blade rotating in a closed loop of cavitation flow	A few days
Circular Leading Edge (CLE) Single hydrofoil	Closed loop with an air dome and vacuum pump to enable variation of the static pressure.	A few days

**Table 3.1:** List of different methods of cavitation tests [21], [103], [105], [120]–[123].

In comparison to the other methods of cavitation techniques, tests conducted using an ultrasonic vibratory rig has been known to give the most reproducible

cavitation results within a controlled laboratory environment. However, the cavitation generated is generally under more hydrostatic conditions, and hence, differs significantly from that on a propeller or a rudder. The cavitation bubbles produced are of nearly uniform sizes, forming at the same locations, and excited at a fixed frequency. Whereas, the actual cavitation fields have varying bubble nuclei sizes and cavitation forms, at forming at varying exciting frequencies at various locations of the propeller, among many other variables [124].

Hansson and Morch [122] compared the initial erosion stage of aluminium and austenitic stainless steel exposed to vibratory-induced and flow cavitation comprising of a channel with a Venturi test chamber. They observed that, in flow cavitation, erosion starts immediately at the onset of cavitation and appears as an isolated, hollow and plastically deformed area of diameter up to about 300  $\mu\text{m}$  for aluminium and 80  $\mu\text{m}$  for stainless steel. Whereas, cavitation generated with a magnetostrictive oscillator produces a few visible indentations in soft materials, it does not show any visual surface changes in stronger materials but induces significant work hardening.

Karimi and Avellan [123] tested specimens of indium and  $\alpha + \beta$  brass in various different cavitation equipments such as Francis turbine model, a cavitation water tunnel, a vibratory cavitation device, and our vortex cavitation generator. Scanning electron microscopy was employed to examine the surface deformation and the development of damage in exposed specimens. It was observed that for all the techniques except for the vibratory cavitation device the damage initiated with the formation of isolated pits and craters of similar morphologies and sizes, that were believed to be produced by collapse impingements. As for the vibratory cavitation, the damage was found to initially scatter uniformly over the specimen surface and develop progressively. The wear scar topographies of severely eroded surfaces in all the types of cavitation methods did not exhibit any noticeable differences. On further examination under transmission electron microscopy, it was seen that the subsurface microstructures in eroded specimens indicated dislocations and the appearance of large-scale deformation twins. Additionally, there were hardened superficial layers in the specimens formed in flow cavitation

that were thicker than those in vibratory cavitation. This was considered responsible for higher erosion rates.

In general, the erosion process in the vortex cavitation generator device is similar to that which occurs in the Francis turbine model and in the cavitation water tunnel. Therefore, it could be considered as a credible laboratory cavitation device for studying vortex cavitation phenomena and for use in predicting the erosion behaviour of hydraulic machinery. The differences between the erosion mechanisms in flow and vibratory cavitation are attributed to the differences in the spatial distributions of the cavities and in the intensities of collapse impingements.

In contrast with flow cavitation, in vibratory cavitation there is no singular character of the collapse impacts. Damage is distributed uniformly over the exposed area and develops with exposure time. For brass specimens exposed to flow cavitation attack, both the  $\alpha$ -phase and the  $\beta$ -phase are simultaneously affected. However, in vibratory tests, erosion begins from grain boundaries and progresses in the  $\beta$ -phase before developing in the  $\alpha$  phase. The thickness of subsurface hardened layers in flow-cavitation-eroded specimens is higher than in vibratory cavitation tests. This results in a higher destructive power for flow cavitation attack.

A detailed comparison of cavitation erosion was performed by Hammit and He [105] in tap water for five alloys in a vibratory (no-flow) system and a venturi (flow) system using the vibratory system in the University of Michigan, at a frequency of 20 kHz and the specimen diameter of 13.92 mm, which Hammit also used in several other cavitation experiments conducted, shown in Figure 3.2. The effects of temperature variation (28 – 93°C), venturi throat velocity (34 – 49 m s<sup>-1</sup>) and vibratory horn double amplitude were studied. Correlations between maximum erosion rate, incubation period (IP), the material mechanical properties, Brinell hardness and ultimate resilience were made. And as a result it was found that only moderate correlations between maximum erosion rate, IP and the material mechanical properties were found. They established one way of

measuring the cavitation intensity using the cavitation erosion rate that can be expressed in terms of the ratio of volume loss rate over exposed area. This ratio is termed as the mean depth of penetration rate (MDPR).

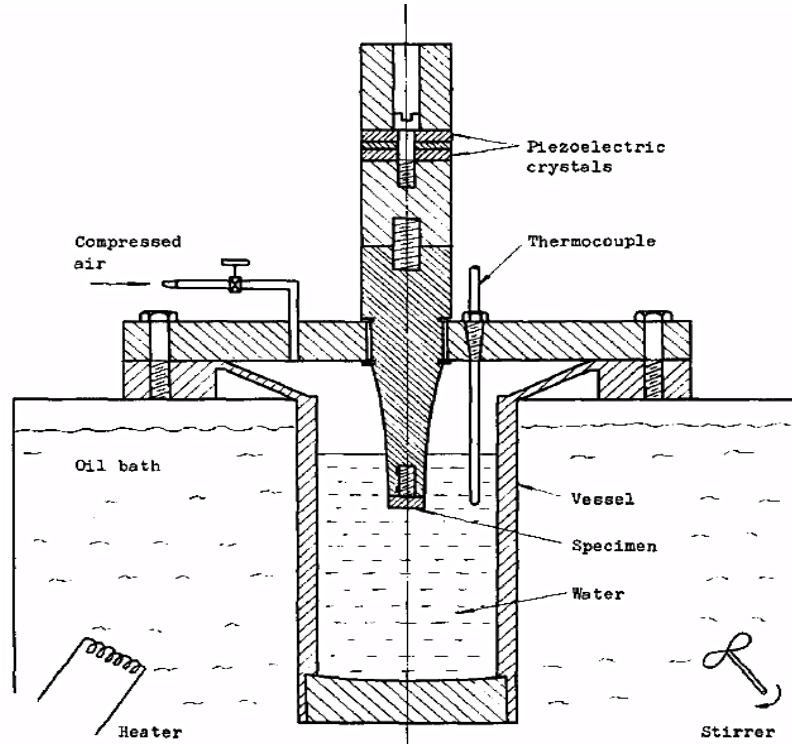


**Fig. 3.2:** Vibratory system in the University of Michigan used by Hammit and He [105].

It was found that IP data could be used to predict eventual maximum mean depth of penetration (MDPR<sub>max</sub>) values according to the relation:

$$\text{MDPR}_{\text{max}}^{-1} \propto (\text{IP})^n \quad \dots(3.2)$$

Where,  $n \approx 0.93$  for the vibratory data, and  
 $n \approx 0.95$  for venturi data.

The cavitation intensity measured using MDPR<sub>max</sub> was found to be 10–20 times greater in the vibratory system as compared to the venturi system, depending on horn amplitude and material. This ratio varied between 5 and 30 if individual materials were considered separately, with the ratio being the greatest for 1018 carbon steel and the least for 316L SS [105].

Hammit conducted a series of tests with Zhou in 1983 using the same vibration facility in the University of Michigan as shown in Figure 3.2, where they compared the tests results obtained from both vibration system and a Venturi system, changed the parameters of the experiment such as temperature, pressure, vibration amplitude and materials, and also conducted tests in different mediums of salt and alkali solutions [73], [106], [107]. From these studies it was concluded that a good correlation could be found between  $MDPR_{max}$  and IP for both the vibratory as well as venturi facilities, of the form  $MDPR_{max}^{-1} = aIP^n$ . A maximum damage rate temperature of 160 °F was found for vibratory cavitation erosion tests for all the materials tested. The cavitation intensity in the vibratory system was found to be 10 - 20 times greater than the venturi system, depending on horn amplitude and the test material. The  $MDPR_{max}$  ratio varied between 5 and 30 if individual materials are considered separately, being greatest for 1018 carbon steel and least for 316 SS. It was also concluded that general mechanical property correlations between  $MDPR_{max}^{-1}$  and either UR or Hardness (HB) for all materials tested was not found to exist for either facility [105].

Bachert, Dular, Baumgarten, Ludwig and Stoffel [125] conducted an experimental investigation of the erosive aggressiveness of cavitation in the initial and developed stage involving three different cavitation test configurations. These test methods involved a radial pump system with two-dimensionally curved impeller blades, a single hydrofoil system and a rotating disk unit. The tests were conducted for copper, due to its low hardness and mechanical properties, for 1 h under three different methods of cavitation investigations. The first cavitation investigation method was based on “pit-count” method, where only plastic deformation was responsible for erosion and the erosion aggressiveness was measured based on the number and size of pits in relation to time of exposure to the cavitation. The second technique applied acoustic measurements involving structure-borne noise sensors and signal processing systems, this method applied the principle of pressure waves emitted by imploding bubbles that are held responsible for the pitting. The third technique employed the mass loss measurement. While the pit-count method and acoustics were carried out for all

three of the configurations, the mass loss investigation was however only applicable for the rotating disc test rig since it was the only configuration to produce sufficient mass loss at the given test duration time. The results from pit-count and mass loss methods were comparable using digitally recorded images. The experimental results demonstrated the significant influence of the flow velocity and the rotation speed on the erosive aggressiveness of the cavitating flows.

The effects of cavitation on microstructure were also studied. Li, Zou, Zheng and Yong [108] investigated the changes of surface layer mechanical properties for DSS and austenitic SS after cavitation corrosion using nano-indentation. They also investigated the relationship of surface layer mechanical properties with cumulative mass loss and microscopic corrosion morphologies using weight loss method and SEM. The results showed that although SS with different microstructures exhibited different corrosion morphologies after cavitation corrosion, there was a common threshold for the degradation of surface layer mechanical properties. This threshold was not related with the microstructures of SS; however, below this threshold the SS were heavily subjected to cavitation corrosion and the microscopic morphologies of their corroded surfaces changed significantly. Hence, it was concluded that the microstructures had significant effects on the changes of surface layer mechanical properties with displacement.

Choi, Jayaprakash and Chahine [120] conducted another test involving the two accelerated erosion testing methods namely ASTM G32 Ultrasonic Cavitation Erosion tests and the DynaJets® cavitating jets to study the cavitation pitting. They examined pitting rates during the incubation period where the test samples were presumed to undergo localized permanent deformations shaped as individual pits. In this study, samples from three metallic materials made of aluminium alloy (Al7075), NAB and DSS (A2205) were subjected to a vast range of cavitation intensities generated by two different cavitating methods, by cavitating jets at different driving pressures and an ultrasonic horn. The cavitated sample surfaces were then examined and characterized with a non-contact 3D optical scanner for a statistical analysis of the pit population and its characteristics. They established

that the various cavitation field strengths could be correlated to the measured pit distributions. Statistical analysis of pitting data revealed that the distribution of pits with diameter may be approximated using a Weibull three-parameter function,

$$N = N^* e^{-\left(\frac{D}{D^*}\right)^k} \quad \dots(3.3)$$

Where,  $N$  is the Weibull three-parameter function,  $D^*$  is characteristic pit equivalent diameter,  $N^*$  is characteristic pitting rate or number of pits per unit area per unit time,  $D$  is the pit diameter, and  $k$  is the shape factor. They found that both  $D^*$  and  $N^*$  could be attributed to and depended upon the material and the given level of cavitation intensity, whereas  $k$  was found to be both material and cavitation field strength independent. They observed that during the short exposure to cavitation field the sample underwent plastic deformation resulting in pit formation. Using a value of  $k = 0.7$  for the optically scanned and counted pits could be the overall pit number versus diameter distribution could be calculated. The geometric characteristics of the pits were also studied. On average, the pit shapes were similar in terms of pit depth to diameter ratio and pit volume to diameter ratio. These geometric ratios were more or less independent of the materials and the cavitation intensities, and always corresponded to very shallow pits with aspect ratio (depth to diameter) of less than 10% [120].

They also conducted systematic long term erosion tests on several materials using the same accelerated erosion testing methods: the modified ASTM G32 Ultrasonic Cavitation Erosion tests and the DynaJets® cavitating jets with a varying jet pressures between 1000 to 7000 psi to understand the intensity of the cavitation of a given cavitating flow field and the resistance of the material to cavitation erosion. The combination of accelerated erosion testing and analysis helped establish a comparative evaluation and energy ranking of the materials and the erosion testing methods. Comparisons of the erosion rates from the two accelerated erosion methods using various different cavitation intensity levels showed that while ranking of several materials conformed with different erosion intensities and test methods, some materials responded to erosion depending on

the cavitation intensity applied. To prove this, they employed a simple mathematical equation to express the erosion progression with characteristic parameters such as time,  $t$ , which occurs at 75% of the time of maximum rate of erosion, and a corresponding material characteristic mean erosion depth,  $\bar{h}$ , used to normalize the mean depth erosion and time, the simple erosion depth time evolution expression found is:

$$\bar{h} = 1 - e^{-\bar{t}^2} + e^{-1}\bar{t}^{1.2} \quad \dots(3.4)$$

Through this mathematical representation of the erosion time evolution it was possible to compare various materials tested under cavitation fields of different intensities and rank them based on their cavitation resistance, following the determination of the two main characteristic parameters: characteristic mean depth of erosion and characteristic erosion time [121].

Xiaojun [126] attempted to understand the effects of surface modification processes on cavitation erosion resistance. For his PhD thesis he tried to evaluate the influence of the surface finishing procedure on the surface features for which two procedures were tested namely grinding and tungsten inert gas (TIG) remelting. The experiments were conducted in two stages, the first stage included metallurgical features characterized by optical and scanning electronic microscopy to evaluate microstructures, the phases were identified using X-ray diffraction, they also employed EDS to determine the dilution, and Vickers indenter for micro-hardness profiles. Four different materials were deposited with metal inert gas (MIG) welding, namely the AISI 309 SS, two cobalt SS (Hidrology 914 and Cavitec), and a low carbon cobalt alloy (Stellite 21) whose surfaces then prepared using grinding and TIG remelting. The second stage involved the evaluation of the cavitation erosion behaviour using the ASTM 63292 ultrasonic vibratory tests on two materials, Hidroloy and Stellite 21. As a result, it was observed that TIG remelting of the MIG deposited multilayer surface resulted in the structure refinement that the remelted surfaces had superior cavitation resistance as compared to ground surfaces due to prolonged incubation period of the samples under cavitation caused by remelting of the surface, they also



concluded that austenite to martensite phase transformation in SS was responsible for up to 25% of the erosion stage since the  $\epsilon$ -martensite plate fracture absorbed most of the impact energy.

### **3.2. Ultrasonic vibratory cavitation method**

In ultrasonic cavitation tests, an ultrasonic vibratory transducer that employs a magnetostrictive ultrasonic horn, most commonly oscillating at a high frequency of 20 kHz, generates the cavitation cloud. This oscillation of the horn induces cyclic formation of very high and very low pressures, which generates the high negative tension in the liquid, causing growth and implosion of the cavitation bubbles [124].

According to ASTM G-32 standard [110], the samples are made into “buttons” of the material to be tested with threaded appendage that is affixed to the end of the horn, subjected to cavitation resulting from the vibrations of the horn. The cavitation cloud forms and collapse at the tip of the specimen. An alternative G-32 test configuration, also called indirect or stationary specimen method, consists of separate specimen sample placed at a small distance from the horn. A conical cavitation cloud is generated in between the sample and the tip of the horn [124]. The test procedure comprises of exposing the sample to cavitation for a certain period of time, with periodic recording of the sample weight for weight loss calculation as a function of time. Several researches have been done in order to understand the material behaviour and the cavitation phenomenon under the ultrasonic vibratory cavitation. Figure 3.3 shows the two different types of test configurations used widely, the direct and the indirect methods [124].

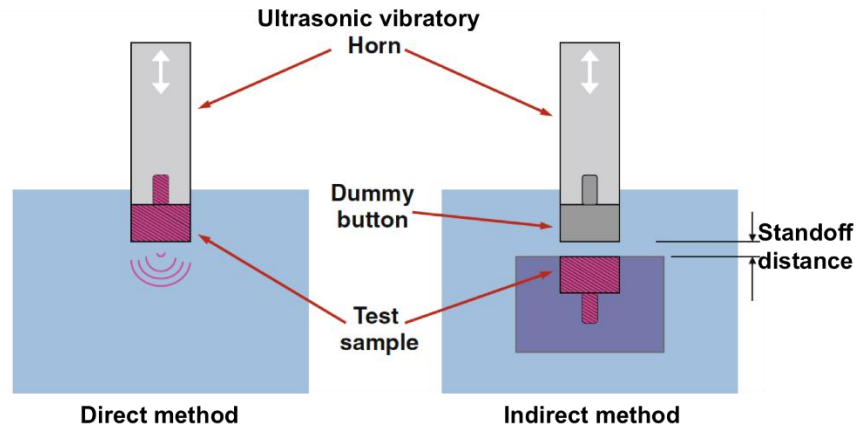


**Fig. 3.3:** The direct and indirect test configurations used for the ultrasonic vibratory cavitation test method under ASTM G-32 standards [124].

Other erosion characteristics such as volume loss and maximum depth incurred have also been recorded, along with photographic accounts of the evolution of the eroded region as a function of time [124].

Barber [127] attempted to develop a correlation between the product of ultimate resilience and the cavitation damage volume loss rate (VLR) of a material to the acoustic energy present in a cavitation field for this Masters thesis in University of Michigan. The product of this correlation (i.e.  $UR \times VLR$ ) was termed as “erosion power”. Also, to quantify cavitation noise (i.e. acoustics), another quantity called “spectral area power” was used, which was the energy/time imparted to the specimen surface by the cavitation cloud. And the ratio of erosion power to the spectral area power was considered to be the “cavitation erosion efficiency” which represented the actual amount of energy/time imparted from the cavitation cloud to the material. This cavitation erosion efficiency was calculated using a vibratory cavitation rig, which employed acoustic “wave guide” probes that comprised of a barium titanate piezoelectric crystal assembly and conducting epoxy instead of conventional pressure probes due to the high temperatures involved, between  $250^{\circ}\text{C}$  -  $550^{\circ}\text{C}$ . The test material and test liquid used were 304 SS and liquid sodium respectively. As a result of the experiment it was determined that maximum damage occurred at an intermediate temperature ( $350^{\circ}\text{C}$  -  $400^{\circ}\text{C}$ ) and the effect of temperature in cavitating the material over volume loss rate could be predicted in terms of the erosion power.

In the vibration cavitation experiment conducted by Hammit and Zhou [128] for elevated temperatures, the vibratory cavitation erosion (VCE) curves in tap water from Ann Arbor without deaeration were presented for different material samples of cast iron (3% C), 1018 carbon steel, and 316 SS using the same vibratory facility as shown in Figure 3.2, at suppression pressures of 1-2 bar, with a frequency of 20 kHz and horn amplitudes of 25.4, 35.1 and 45.2  $\mu\text{m}$  and at varying temperatures of 27°C - 110°C [106]. Similar study was also conducted by Hammit, Iwai and Okada using the same facility to study the effects of temperature on the cavitation erosion of cast iron at various water temperatures and horn amplitudes under a constant pressure of 1 bar.

As a result it was found that the erosion processes for cast iron under the highest temperatures used (90 and 110°C) were similar to those at room temperature [128]. It was also found that the maximum mass loss rate first increased with temperature, where the erosion was most substantial at the highest damage temperature (110°C), forming a peak and then gradually decreased with further increase in the temperature. This behaviour was mostly attributed to the increased chemical action under high temperatures, especially for cast iron. It was also found that amplitude played an important role in the maximum damage temperature, especially for cast iron. The occurrence of black oxide rim were also observed to be formed on each of the 1018 carbon steel specimens but only at the highest temperature, which was assumed to be due to corrosion effects at the higher temperature [106], [128].

Another test conducted by Hammit and Zhou [73] evaluated the “incubation period” (IP) stage of cavitation erosion for which short-duration vibratory horn tests were conducted on 1100-O aluminium alloy and 316 SS in tap water to obtain wide range of mechanical properties. The test was also conducted at a frequency of 20 kHz with horn amplitudes of 25.4, 35.1 and 45.2  $\mu\text{m}$  and at the water temperatures of 27, 71 and 93°C. The effects of horn amplitude and temperature were investigated. Keeping the temperature and probe amplitude constant it was observed that the IP for 316 SS was about 500 times that for aluminium alloy 1100-O. This ratio could also be predicted by applying the relation,

$$\text{MDPR}_{\text{max}}^{-1} = k(\text{IP})^n \quad \dots(3.5)$$

Furthermore, fatigue cracks and individual-impact craters were found for 316 SS whereas, only individual craters were found for aluminium alloy 1100-O, although the two ductilities were approximately equal. It was concurred that if IP was based on the attainment of a given mean depth of erosion MDP, then the incubation period based on the eroded area only was much less than the conventional incubation period, which was based on the total specimen area. It was also verified that only bubble collapse stresses were to be considered important in the vibratory horn test even though specimens were vibrated under very high accelerations [73].

Hammit and Zhou [106] also conducted VCE tests at a frequency of 20 kHz and amplitude of 35.1  $\mu\text{m}$ , on AISI-SAE 1018 carbon steel in Ann Arbour tap water and in mild (0.1 M) aqueous solutions of  $\text{CaCO}_3$ ,  $\text{CaO}$ ,  $\text{NaHCO}_3$  and  $\text{NaOH}$  at a temperature of 27°C, a double amplitude of 35.1  $\mu\text{m}$  and a pressure of 1 bar. Tests were conducted for a maximum of 150 min test duration and it was observed that at the maximum duration the mass loss in tap water with no additive was the least. However, it was reversed in the case for shorter test times. The results showed that the damage around the central damage portion was greater for solutions than tap water [106], [107]. The SEM image of the eroded regions, both central and transition, under Ann Arbour tap water can be seen in Figure 3.4 (a) and (b). There were formations of cracks in the transition region for  $\text{CaCO}_3$  solution (Figure 3.4(c)), and for  $\text{CaO}$  solution a small, undamaged area near a heavily central damaged area was observed as can be seen from Figure 3.4(d). Cavitation under  $\text{NaHCO}_3$  solution showed a narrow boundary between the central portion and the transition region and also a much more complex damage pattern in the central damage region as shown in Figure 3.4(e). Finally, the highest amount of weight loss was observed for  $\text{NaOH}$  solution (Figure 3.4(f)). The biggest difference between mass loss among the various solutions was found to be about 10% – 30%, this was considered beyond natural data scatter for such vibratory tests, which lead them to also consider the effects of released gases and other particles in the

solution since it was established in 1979 by Singer and Harvey that reduction of the gas content in the medium resulted in a decrease in the maximum erosion rate with a corresponding increase in the characteristic time [104], [107].

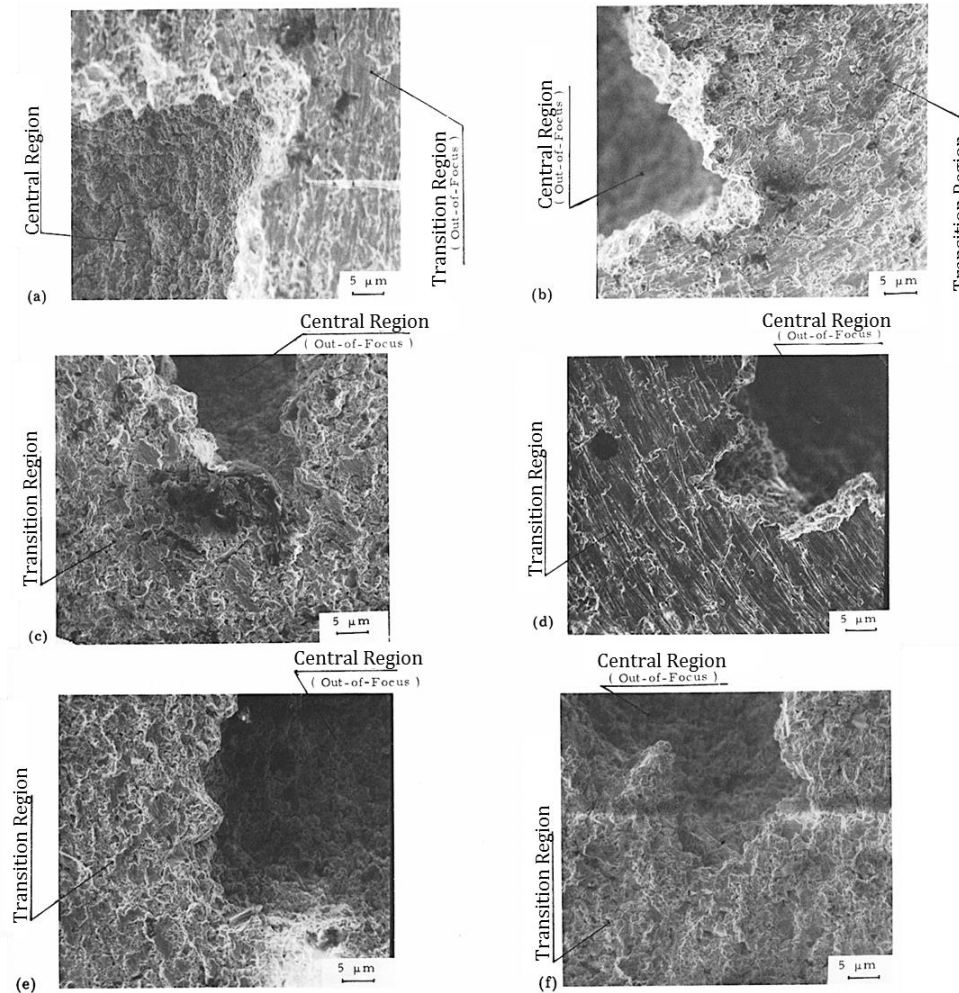


**Fig. 3.4:** SEM micrographs obtained from cavitation erosion test performed on AISI-SAE 1018 carbon steel at a test duration of 150 min: (a) central damage region; and (b) transition region in Ann Arbor tap water; (c) central and transition region in 0.1 M  $\text{CaCO}_3$ ; (d) central and transition region in 0.1 M  $\text{CaO}$ ; (e) central and transition region in 0.1 M  $\text{NaHCO}_3$ ; (f) central and transition region in 0.1 M  $\text{NaOH}$  [107].

In their experiments, Hammit and Zhou [107] also established that for most vibratory tests there are three easily distinguishable damage regions for all cavitated surfaces, the generally undamaged rim, central heavily damaged region, and transition region. The relative areas of the three regions for the conducted test for AISI-SAE 1018 carbon steel in various aqueous solutions were about 53.5%,

0.13% and 46.4%, respectively. The results showed that the solutes used did not necessarily affect the erosion rate and extent of the damaged regions. The increase in damage rate with respect to tap water was about 50% for the maximum test duration. Cracks, inter-crystalline fractures and single-blow craters were found to be most concentrated in the central region, as observed under optical micrographs and SEM photomicrographs of the surface (for a test duration of 150 min).

Feller and Kharrazi [129] investigated the cavitation behaviour and cavitation erosion resistance (CER) i.e. the ability of the material to withstand and resist cavitation, for 10 pure metals namely aluminium, cobalt, chromium, copper, iron, magnesium, molybdenum, nickel, tungsten, zinc, and several commercially available alloys such as copper-, iron-, nickel- and cobalt-based alloys using mass loss measurements and surface analysis with SEM and X-ray photoelectron spectroscopy (XPS). They used laboratory vibratory apparatus for the cavitation tests with a frequency of 21.5 kHz at 20°C and amplitude of 35  $\mu\text{m}$  for pure metals and about 40°C and amplitude of 60  $\mu\text{m}$  for alloys, the specimens being mounted opposite to the horn to investigate the role of the covalent bonding of these metals and hence the binding energy and the crystal structure of the base metal. In their conclusion they found that the binding energy, the crystal structure of the base metal, and the allotropic deformation and transformation abilities of the alloys had the predominant influence on CER. They also found that the second-phase particles were preferentially removed as a result of the initial deformation and cracks at the particle-matrix interface. Single-phase alloys belonging to the d-band metals such as Co, Cr, W with high covalent bonding, low stacking fault energy and high corrosion resistance exhibited highest CER.

Another important factor in cavitation erosion is the impact load acting on the material surface due to cavitation bubble collapse. The impact load measurement and its relation to cavitation flow have been studied extensively by Okada, et al. in 1995 and by Franc et al. in 2011 [130], [131]. Okada et al. established the relation between impact load and erosion damage in their experiment comparing venturi test system with vibratory test systems. They also developed a pressure detector consisting of a test specimen with a diameter of 3 mm and a piezoelectric ceramic

disk that could measure impact loads and erosion damage simultaneously for both venturi tests and vibratory tests. Impact loads by collapsing bubbles were observed directly in a venturi tunnel however, they were observed as piled-up pulses on an alternate wave of hydrodynamic pressure produced by a vibrating disk in a vibratory device. They also compared the impact load occurring in an early stage in the venturi facility and vibratory device with indent size observed with a microscope on the surfaces of pure aluminium, pure copper and austenitic 304 SS. The static load and the area of indents were measured with a 600 micro diameter hardness tester with a spherical indenter. As a result, a linear relation was obtained between the impact load and the area of indents for Cu, Al and 304 SS in both the venturi as well as the vibratory tests, and the resultant slope provided the dynamic hardness under impact load due to cavitation bubble collapse. It was also observed that a linear relation existed between the critical impact loads of face centred cubic (fcc) metal and the dynamic hardness under impact loads due to cavitation bubble collapse irrespective of the type of test methods and test conditions such as type of apparatus, flow velocity for venturi test and the distance between a vibrating disc and specimen for vibratory test. However, Franc, Riondet, Karimi and Chahine [131] established in their experiment that there was an uncertainty on the measured values of impact loads. They measured the impact load in a high-speed cavitation loop by means of conventional pressure sensor flush-mounted in the region of maximum damage near the cavity. Hence, special effort needed to be made to compare quantitatively pitting test results and impact load measurements.

In a study by Laguna-Camacho et al. [130] on cavitation erosion of engineering materials, tests were conducted on different materials such as pure aluminium (99% aluminium) and 1045 steel which were used as vibratory specimens, whereas untreated 6082 aluminium alloy, 304 SS and 4340 steel were used as “stationary” specimens under a sonotrode of diameter 12 mm at the operating frequency of 20.7 kHz with a 1 mm gap between the specimens and the vibratory horn. Tests were conducted using tap water and tap water with silicon carbide (SiC) particles to act as abrasives during the cavitation erosion process. While in

the first case low erosion rate was observed, for the latter case there was an increase in the erosion wear rate, which in turn helped to evaluate the performance of all the tested materials at different testing conditions. A high-speed camera was also used to analyse the bubble formation in the radiating surface of the horn made of 2024 aluminium alloy. In the video captured it was possible to observe the bubble formation, which is a significant parameter since it determines the amount of physical damage occurring on the material surface [132]–[134].

The observed bubble formation was found to be similar to the process of cone-like bubble structure observed in other cavitation studies (see Figure 3.5) [133], [134]. Additionally, high-speed videos were obtained as abrasive particles were used to conduct the tests. In these, it was possible to observe how abrasive particles were moving along the two surfaces, staying in the clearance to cause higher wear damage on both surfaces. The “stationary” specimen was located at a 1 mm distance with respect to the position of the “vibratory” specimen, which was attached to the radiating surface. Optical microscopy was used to identify the wear mechanisms which were characterized by a pitting action when only tap water was used whereas some scratches and irregular indentations similar to those observed in abrasive wear were seen on the surfaces with abrasive particles [135].

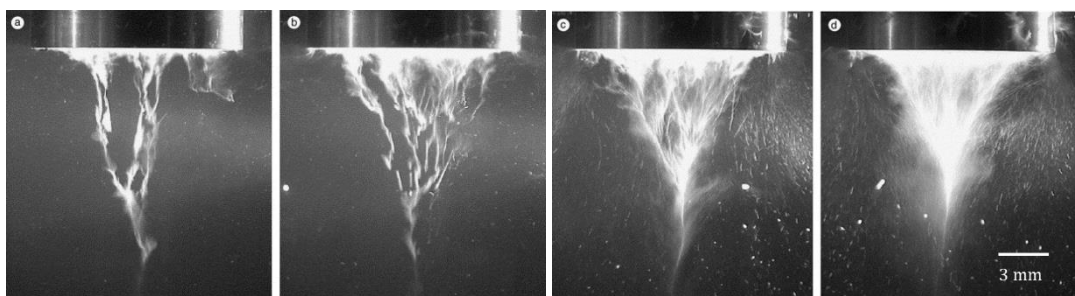


**Fig. 3.5:** Cone-like bubble structure for different acoustic intensities I. Sonotrode C: (a)  $1.8 \text{ W cm}^{-2}$ , (b)  $3.5 \text{ W cm}^{-2}$ , (c)  $5.3 \text{ W cm}^{-2}$ , and (d)  $8.2 \text{ W cm}^{-2}$  [134].

Cavitation erosion tests were also carried out for plastic samples by Hattori and Itoh [136]. They conducted the tests for epoxy resin, polypropylene, high-density polyethylene and polyamide 66, and the relation between cavitation erosion



resistance and the mechanical properties were examined. The changes in the mechanical properties were mostly attributed to temperature due to low thermal conductivity of plastic under cavitation erosion condition. They found that cavitation erosion resistance of plastics ranged between 0.5 (for epoxy) to 30 (for polyamide 66) times that of carbon steel of SS400. This was due to the relatively small acoustic impedance of the plastics causing the impact loads applied by bubble collapse to become very small. It was also revealed that the cavitation erosion of plastics was caused by fatigue fracture similar to metals..

As results, it was observed that specimens abraded with SiC particles had higher mass loss than the tests using only tap water. Also, specimens attacked with SiC particles had less roughened surface compared to the tap water test. Optical microscopy was used to identify the wear mechanisms, which were characterized by a pitting action when only tap water was used whereas the damage on the surfaces caused by abrasives was characterized by a combination of small pits and irregular scratches and grooves generally observed in abrasive wear. With the help of the high speed camera it was possible to observe how abrasive particles were moving along the two surfaces, staying in the clearance to cause higher wear damage on both surfaces [135].

### **3.3. Cavitation wear vs. fatigue failure**

Several tests have also verified the relation between cavitation erosion and fatigue failure of the materials. It has been observed that for many erosion resistant materials such as 304 SS fatigue is the predominant failure mode [136]–[139]. It has been established that due to the cavitation bubbles imploding on the specimen surface random field of pressure changes form leading to local plastic deformation. As a consequence this plastic deformation cause initiation and propagation of fatigue microcracks, which finally causes the fatigue failure and material erosion.

Experiments conducted by Ahmed, Hokkirigawa and Oba [137] to observe the

cavitation erosion mechanism and the IP of VCE showed this relation between cavitation erosion failure and fatigue failure. Vibratory erosion experiment under ASTM standard was carried out with SEM and profilometer observation on the IP of VCE for an erosion resistant material 304 SS. The tests conducted under uniform cavitation nuclei size distribution resulted in polishing lines on the surface that acted as the initializing point for the formation of pits whose diameters and the shapes were independent of the test time ( $t < 20$  min). As a result, it was observed the any roughness on the surface acted as weak points for pit formation along the polished lines and the rate of formation of pits initially increased with test time but gradually decreased after 15 min. Also most of the test surface was locally plastically deformed from the beginning of the vibration resulting in characteristically wavy surface undulation directions of the grain boundaries, slip bands and twin lines as shown in Figure 3.6 ((a) – (d)). These undulations greatly affected the roughness on the eroded surface and remained unchanged in shape and number but their width and height altered with time.

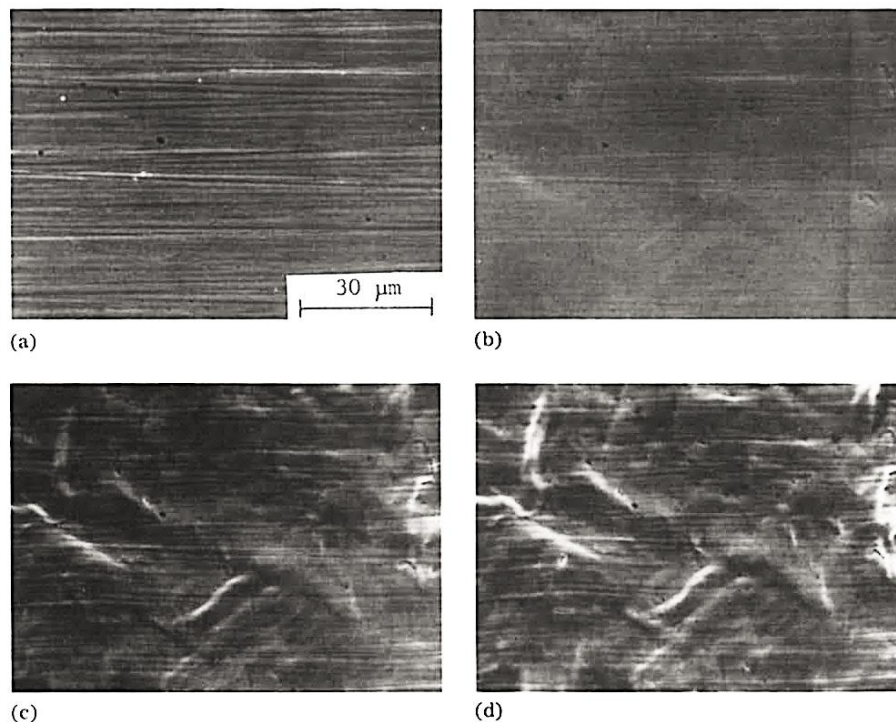


**Fig. 3.6:** Development of plastic deformation near the centre for various  $t$ :  
 (a) 0 min; (b) 5 min; (c) 15 min; (d) 20 min [137].

Again, Ahmed, Hokkirigawa and Oba [138] investigated the failure mechanism of

VCE in details for 304 SS. It was deduced that in the highly accelerated erosion process of ultrasonic cavitation the collapsing of massive voids accompanied by shock pressures caused the most amount of erosion. It was also confirmed from systematic observations of eroded surfaces and dislodged particles that the predominant failure mechanism in cavitation erosion was fatigue. At the beginning of vibration, the eroded surfaces were seen to plastically deform locally and there was a growth in slip bands with time. At this stage the successive growth of the slip bands were in the transverse direction and were found to be below the fatigue limit. As can be seen in Figure 3.7 (a) it was observed that the sites of high stress concentration such as pits, burrs, polishing line traces and discontinuities on the slip bands formed plastically caused nucleation of cracks. The fatigue cracks initiated and propagated first at an inclination to the surface before propagating parallel to the surface (see Figure 3.7 (b)). And finally, as an important feature of fatigue failure process, fatigue striations and 'tire tracks' on the rupture surfaces seemed to appear.

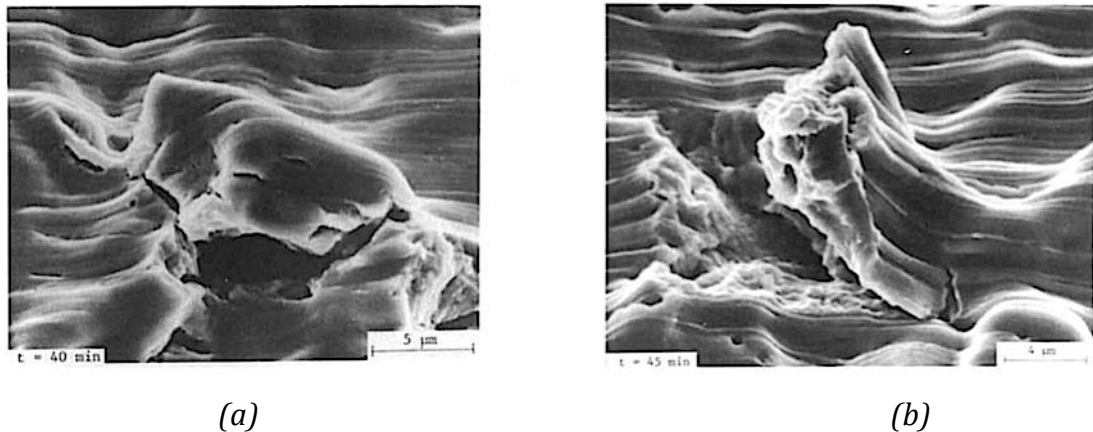


**Fig. 3.7:** (a) Crack nucleated from the voids growth and coalescence at 40 min; and (b) Initiation and progress of the fatigue crack at 45 min [138].

Osman and Ahmed [139] investigated the cavitation damage progress in the incubation period using stepwise erosion and image process techniques. Experiments were conducted using ultrasonic vibratory tests where cavitation damage process of SS during the incubation period was detected and evaluated. For image processing SEM imaging was undertaken to record the eroded surface for several different locations. They also measured the surface roughness the

testing time. In addition to that, image processing based on discrete wavelet transforms and fractal analysis had been adopted in the experiment to characterize the damage images. As expected they found that the surface topography seemed to plastically deform that lead to the fatigue failure, which was the predominant mechanism. It was also found that the feature parameters showed a linear increase with the testing time and showed good correlations with the roughness parameters. The extracted feature parameters included Shannon entropy, energy loss, fractal dimension and fractal intercept. Osman and Ahmed also established the relationships between feature parameters and roughness parameters as linear and it was established that the best correlation was for the Shannon entropy.

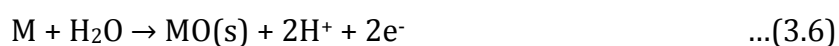
Cavitation erosion tests were also carried out for plastic samples by Hattori and Itoh [136] where they conducted the tests for epoxy resin, polypropylene, high-density polyethylene and polyamide 66, and the relation between cavitation erosion resistance and the mechanical properties were examined. It was revealed that although the impact loads acting on the surface of plastics were lower than metals the cavitation erosion of plastics was caused by fatigue fracture similar to metals. Therefore, the resistance and the incubation period of cavitation erosion of plastics could be evaluated in terms of bubble collapse impact energy and the strain energy obtained from the fatigue strength for unit volume removal in the maximum erosion rate stage. The changes in the mechanical properties were mostly attributed to temperature due to low thermal conductivity of plastic under cavitation erosion condition. They found that cavitation erosion resistance of plastics ranged between 0.5 (for epoxy) to 30 (for polyamide 66) times that of carbon steel SS 400. This was due to the relatively small acoustic impedance of the plastics causing the impact loads applied by bubble collapse to become very small.

### **3.4. Cavitation erosion-corrosion**

Along with the wear analysis, another method employed to investigate cavitation bubble dynamics used in many cavitation studies is electrochemistry. It has been

applied to understand overall cavitation damage, tribocorrosion, synergy between cavitation wear and corrosion processes as well as the electrochemical protection provided by it to the cavitating material against cavitation damage [140]–[145]. Data from combined wear–corrosion testing enables important information relating to the relative influence of the mechanical and electrochemical factors in affecting the mass loss rate under cavitation and liquid–solid erosion to be obtained. It is possible to identify how much of the total mass loss due to wear–corrosion is due to cavitation erosion and electrochemical corrosion [146]. Generally, the passivation film behaviour is considered as the most important reason affecting the cavitation corrosion rate, and the studies on the rupture of the passivation film in different corrosive environments are of the main concern.

It has been already established that high intensity ultrasound causes the formation of cavitation bubbles, which collapse in a manner that in the presence of a solid surface form high velocity fluid microjets directed toward the surface. These microjets cause intense fluid agitation at the surface, which in turn enhances transportation of momentum, heat, and mass, influencing the behaviour and integrity of surface films with respect to the metal electrodes [147]. It has been found that for most metals, passivation dominates the cavitation corrosion rate especially if in a corrosive medium [148]. It has also been found that active radicals are released during bubble collapse that cause chemical reactions to take place even in a neutral medium such as de-ionized water [149]–[153]. The behaviour of the passive film under cavitation involves a complex and interrelated set of processes. Hoar attempted to review and quantify the features of passivation [154]. Primarily, passivation is a metal chemical reaction that results in the creation of an oxide monolayer firmly attached to the metal. This oxide monolayer is called passive layer that forms a compact barrier between the metal and solution. The oxide reaction can be expressed as:



Where, M refers to metal ion, and e is electron. A mathematical model was proposed by Perusich and Alkire [141] to determine the reaction and transport between liquid microjets and a reactive solid surface. The conditions were estimated under which oxide de-passivation (breaking down of metal oxide film in an acidic environment) and re-passivation (addition of layer of oxide after de-passivation) occurred as a function of ultrasonic intensity, surface film thickness, and fluid microjet surface coverage. The model was based on the concept that cavitation induces sufficient momentum and mass transfer rates (water hammer pressures) at a surface to create oxide film stresses leading to de-passivation.

Ogino, Hida and Kishima [155] investigated susceptibility of materials to cavitation erosion-corrosion in 1987 for martensitic type 431 SS with a variety of strengths and corrosion resistance introduced by tempering at high temperatures of 200 - 750°C and quenching from 1060°C by vibratory corrosion in corrosive media of 3% NaCl solution, 0.1 N HCl and 0.1 N H<sub>2</sub>SO<sub>4</sub>. The tests were conducted at either a low frequency of 6.5 kHz with a double amplitude of 75µm or at 20 kHz with 50 µm amplitude at 22°C. The susceptibility of 431 SS to erosion-corrosion was investigated as a function of tempering temperature. The results indicated that the maximum erosion rate as well as minimum corrosion resistance occurred for samples tempered at 550°C irrespective of the vibratory conditions. Also observed was the drop in hardness and strength corresponding with the fall in the corrosion resistance of the material samples. Hence, it was concluded that the susceptibility to erosion-corrosion depended predominantly upon the mechanical strength.

Several investigations on effect of microstructure of the material on the cavitation morphology lead to a correlation between the cavitation erosion behaviour and its resulting mechanical properties as well as microstructural changes. In a paper by Dongliang, Zou and Yong [108] the changes of surface layer mechanical properties for 2205 duplex SS and austenitic SS after cavitation corrosion were investigated by nanoindentation, and the relationship of surface layer mechanical properties with cumulative mass loss and microscopic corrosion morphologies was further investigated by mass loss and SEM. The results showed obvious

effects of the microstructures on the changes of surface layer mechanical properties with indentation depth. Although SS with different microstructures have different corrosion morphologies after cavitation corrosion, the threshold for the degradation of surface layer mechanical properties remained constant for all of them, below which the SS were heavily subjected to cavitation corrosion and the microscopic morphologies of their corroded surfaces changed markedly. This threshold however is not related with the microstructures of the SS.

As per the behaviour of the microstructure of the sample materials during cavitation erosion, it has been observed by Wantang [156] that the characteristics of microstructure does in fact change during cavitation erosion as investigated using X-Ray Diffraction (XRD) and Transmission Electron Microscopy (TEM) analyses for steel (ZG0Cr13Mn8N) with metastable austenite. The results showed that the microstructure of the surface layer of the steel specimens that consists of  $\alpha'$ -martensite, metastable austenite,  $\gamma$ , and a few  $\varepsilon$ -martensite had increased dislocation density and straight or planar dislocations on the surface. It also induced  $\gamma \rightarrow \varepsilon$ ,  $\varepsilon \rightarrow \alpha'$  and  $\gamma \rightarrow \alpha'$ - martensitic transformation.

Li, Han, Lu and Chen [157] from Lanzhou Institute of Chemical Physics most recently investigated the cavitation erosion behaviour of Hastelloy C-276 alloy using an ultrasonic vibratory apparatus in pure water under 1Cr18Ni9Ti stainless specimen as the probe tip and compared it with that of 316 SS, at a vibratory frequency of 20 kHz and 50  $\mu\text{m}$  amplitude. The temperature was kept constant at 25°C and a gap of 0.5 mm between the probe and the specimen was maintained. Hastelloy C-276 is a nickel-molybdenum-chromium alloy widely used as a critical component in aerospace, chemical and nuclear industries because of its good corrosion resistance and high temperature strength [157]–[160]. SEM and field emission scanning electron microscopy (FESEM) were employed to observe the surface morphology and microstructural evolution of the eroded surface. In their investigation, they attained the mean depth of erosion (MDE) and erosion rate curves vs. test time for Hastelloy C-276 alloy [157].

The test was conducted for 9 h and the results showed that the MDE for Hastelloy

C-276 alloy was about 1/6 times lower than that of SS. And the incubation period of Hastelloy C-276 alloy was observed to be about 3 times longer than that of 316 SS. The predominant cavitation erosion mechanism was analysed and it was found that the initial cavitation damage occurred mainly from the twin grain boundaries. Cavitation-induced nanometre-scaled precipitates rich in molybdenum (Mo) and tungsten (W) were formed in the eroded surface because of the strong mechanical action and thermal effect produced by bubble collapsing near the surface during the cavitation erosion process that is expected to play a significant role in the cavitation erosion resistance of Hastelloy C-276. Another peculiar feature observed was the selective cavitation erosion of material surface regions that were rich in Mo. This selective cavitation erosion was considered as the predominant erosion mechanism in Hastelloy C-276 alloy surface [157].

In a paper by Neville and McDougall [146], they studied the characteristics of a commercially pure titanium (CP-Ti) and three alloys in two wear-corrosion situations which were: (a) erosion-corrosion, where the wear was due to solid abrasives in a liquid medium and (b) cavitation-corrosion, where the wear was generally due to cavitation. The erosion-corrosion characteristics of each material was assessed using an impinging-jet apparatus. The tests were performed at an angle of impingement of 90°C at a particle velocity of 17 m s<sup>-1</sup> and in a saline solution of 3.5% NaCl at 18°C. A series of experiments was conducted to determine the mass loss by combined erosion-corrosion before independently determining the electrochemical corrosion contribution to mass loss. It was seen that exposure to liquid-solid erosion caused disruption of the passive film on Ti, which lead to active corrosion of the Ti layer. In contrast, the materials exhibited passive behaviour in static conditions and when exposed to a cavitating liquid only CP-Ti became active.

Dezhkunov, Kulak and Francescutto [142] studied the effect of ultrasound cavitation of the model reversible electrochemical reaction involving the redox species. The impact of the pressure pulses, generated by asymmetrically collapsing cavitation bubbles, on the rate of the electrochemical reaction was analysed within the framework of "Marcus theory," which explains the rate of



electron transfer reactions of electron jumping from one chemical species called electron donor to another species called electron acceptor [161]. The linear growth of the exchange current density ( $i_0$ ) with the ultrasound intensity ( $J$ ) in the  $\ln i_0$  versus  $J^{1/2}$  plot was demonstrated, and it was observed that there was a decrease in  $\Delta i$  at high intensities of ultrasound due to the shielding of the electrode from the acoustic field by the cloud of cavitation bubbles. The results obtained showed that the electrochemical response at certain potentials appeared to be essentially dependent on the intensity of cavitation, and sonoelectrochemical measurements could thus provide important information about the development of the cavitation process. The sensitivity of the electrochemical systems to the ultrasound was also useful for realizing an effective cavitation 'solion', i.e. a cavitation sensor of "chemotronic" type i.e. electrochemistry and electronics [142].

A set of experiments designed to characterize an ultrasonic reactor were presented at the University of Southampton by Birkin et al. [143]. These include electrochemical, acoustic and imaging of the reactor deployed. In particular an electrochemical technique that could detect the erosion caused by single inertial cavitation events within an ultrasonic reactor was reported. The technique relied on the erosion/corrosion of an electrode surface. In order to operate this system an opto-isolation approach was discussed which enabled the electrochemical measurements to be undertaken within an earthed metallic ultrasonic bath. They combined the mapping of the reactor with luminescent imaging.

The cavitation erosion and corrosion characteristics of various engineering alloys including grey cast iron, steels, copper-based alloys and SS were studied by means of a 20 kHz ultrasonic vibrator at a peak-to-peak amplitude of 30  $\mu\text{m}$  in distilled water as well as in 3.5% NaCl solution at 23°C by Kwok, Cheng and Man [162]. The contributions of pure mechanical erosion, electrochemical corrosion, and the synergism between erosion and corrosion to the overall cavitation erosion-corrosion in 3.5% NaCl solution were determined. It was found that in 3.5% NaCl solution, the effect of corrosion on the overall cavitation erosion-corrosion was most pronounced (how much – show percentage) in mild steel and grey cast iron,

whereas the SS only suffered pure mechanical erosion in 3.5% NaCl solution in the presence of cavitation owing to the unfavourable local environment for pit growth.

However, in-situ electrochemical analysis of samples under ultrasonic vibration cavitation has yet to be fully explored and hence, a detailed research study needs to be carried out in order to analyse the corrosion reaction and chemical changes taking place during cavitation erosion which would, in turn, help in understanding the synergy between the cavitation wear and corrosion.

### **3.5. Synergy between cavitation erosion and corrosion**

Several studies have been conducted and proven the existence of synergy between cavitation erosion and corrosion, and that this synergy can have significant effect on the cavitation behaviour of the test materials [17], [149], [162]–[169]. Zheng, Luo and Ke [149] tested the effect of cavitation on electrochemical corrosion of 20SiMn low alloy steel, 0Cr13No5Mo stainless steel and CrMnN DSS in various aqueous mediums such as 0.1 mol L<sup>-1</sup> HCl, 0.5 mol L<sup>-1</sup> NaCl, and 0.5 mol L<sup>-1</sup> NaCl + 0.15 mol L<sup>-1</sup> Na<sub>2</sub>NO<sub>2</sub> solutions, using magnetostrictive-induced cavitation rig and potentiodynamic polarization curves. They used a three-electrode electrochemical cell with saturated calomel reference electrode and a platinum counter electrode for the in-situ electrochemical measurements. They observed that cavitation affected the cathodic corrosion behaviour and the anodic corrosion behaviour differently in the test media. While cavitation seemed to accelerate the cathodic reaction and shift the free corrosion potential in noble direction for non-passivating system, such as 20SiMn low alloy steel in NaCl solution, it affected the anodic reaction more by 2 orders of magnitude, strongly shifting the free corrosion potential in cathodic direction due to erosion of passive film for self-passivating systems like 0Cr13No5Mo SS and CrMnN DSS in 0.5 mol L<sup>-1</sup> NaCl solution, and 20SiMn low alloy steel in 0.5 mol L<sup>-1</sup> NaCl + 0.15 mol L<sup>-1</sup> Na<sub>2</sub>NO<sub>2</sub> solutions.

They also conducted cavitation erosion-corrosion tests on 20SiMn low alloy steel in distilled water and 3% NaCl solution to understand the corrosion behaviour under cavitation. The role of corrosion was analysed using polarization curves, electrochemical impedance spectroscopy, linear polarization resistance, and the corrosion potential with and without cavitation. They also compared the effect of cavitation on corrosion behaviour of 20SiMn steel to that of oxygen bubbling. The subsequent results showed that very small fraction (0.05) of the damage arose from electrochemical corrosion and a fraction (0.59) arose from corrosion-induced erosion, establishing the existence of synergy between cavitation erosion and corrosion. They observed that cavitation not only reduced the magnitude of impedance but it also shifted the corrosion potential in the positive direction and strongly enhanced the cathodic current density in the polarization curves. The morphological examination under SEM revealed that steel underwent selective phase attack at the ferrite area and grain and the ferrite-pearlite boundaries as a result of the low hardness of ferrite [163].

Vyas and Hansson [14] conducted the ultrasonic vibrating cavitation on SS in 3.5% NaCl solution and they found that the degree of intergranular corrosion of the sensitized SS increased with increasing cavitation density. They confirmed that for SS, due to the existence of the passive film, cavitation could either accelerate or decelerate corrosion depending on the intensity of cavitation and the metallurgical state of the SS specimens. Tomlinson and Talks [16] studied the cavitation erosion-corrosion of various types of cast iron in 3% sodium chloride solution, and found that the fractional weight loss due to pure corrosion ranged from 1 to 10% while that due to corrosion-induced erosion ranged from 16 to 90% [16]. Between 1998-2006, Kwok performed several experiments on laser treated metals such as austenitic steel alloy and NiCrSiB alloy in 3.5% NaCl solution. It was found that the synergism was responsible for 50-70% of total loss for laser alloyed 1050 steel specimen and 20% for laser surface alloyed 316 SS specimen, the cavitation erosion-corrosion resistance was noticed improved for 1050 and 316 SS, respectively [168], [170]–[174].

Kwok, Chen and Man [175] conducted another ultrasonic vibrating cavitation at

20 kHz on 9 different kinds of metals including cast irons and SS under 3.5% NaCl solution. From the experimental results it was found that synergism had a significant effect on mass loss with up to 85% total damage. This synergy effect was found to be due to several factors such as impact of corrosive solution, the material property, and also the type of materials itself. The most significant impact was found at a mild corrosive environment [17], [167], [176], [177].

Few studies have also been conducted on ship propeller materials such as SS, copper alloys, manganese bronze, and nickel aluminium bronze among others. A synergy experiment conducted by Kwok, Cheng and Man ranked austenitic (304) SS to have very high cavitation erosion resistance than austenitic 316 SS owing to its higher martensitic transformability and work hardenability, and lower stacking fault energy of  $25 \text{ mJ m}^{-2}$  [178]. They also concluded that materials with high corrosion resistance such as copper alloys also displayed higher resistance to the erosion-corrosion synergy. They established that the effect of cavitation on corrosion behaviour particularly depended on two main effects of cavitation, corrosion film detachment and increase of mass transport [162].

Several cavitation corrosion tests were conducted by Al-Hashem, et. al. on propeller materials like cast-NAB and DSS in seawater using 20-KHz ultrasonic vibrator under free corrosion and cathodic protection conditions, and they found that for DSS, the rate of mass loss was reduced by 19% under cathodic protection, slightly reducing the subsequent number of cavities as a result. The attack was seen to be concentrated in the austenite phase but was eventually seen to spread to the ferrite phase. This was associated with ductile tearing, cleavage-like facets, river patterns, and crystallographic steps at later stages. Specimen cross-sections revealed microcracks at the bottom of the cavities initiating from the ferrite matrix with crack propagation impeded by the austenite islands, branching along the parallel slip systems. They also observed an active shift in the free corrosion potential by 140 mV when cavitation was applied, with a slight increase in the cathodic and anodic currents, shifting the corrosion potential in the noble direction by 75 mV [179]–[181].

Whereas, their cavitation corrosion test of NAB showed a decrease of rate of mass loss by 47% under cathodic protection, and a shift in corrosion potential in the active direction by 70 mV. This could be attributed to the cushioning of bubble collapse by cathodic gas and elimination of electrochemical dissolution. They also observed under the optical and scanning electron microscopy that NAB seemed to suffer from selective corrosion of the copper-rich  $\alpha$ -phase at its boundaries with intermetallic  $\kappa$  precipitates, while the  $\kappa$  precipitates and precipitate-free areas did not suffer corrosion. Also, it was found that selective corrosion was enhanced by cavitation erosion. Under only cavitation, large cavities were found with  $\alpha$ - $\kappa$  grain-boundary corrosion around the pit edge whereas, in the presence of cathodic protection, the number of cavities was found to increase but the grain-boundary attack was seen to be absent. They also found microcracks of 5 – 10  $\mu\text{m}$  long were observed in the  $\alpha$  phase adjacent to  $\kappa$ -precipitates along the cross section of the material. Selective phase corrosion and cavitation stresses were implicated as the causes of cracking [180], [181].

Wood and Fry [17] investigated the fundamental mechanisms of the synergistic effect of cavitation erosion and corrosion. They employed an all-plastic cavitation tunnel comprising of a 60° symmetrical wedge cavitation source and specimens held under potentiostatic control in a flowing seawater system. The experiments were conducted in a 10 × 20 mm working section at an upstream flow velocity of 14.7 m s<sup>-1</sup>. Three separate tests were conducted namely pure erosion, pure corrosion and combined erosion and corrosion, each at two different cavitation intensities in order to investigate the erosion/corrosion performance of copper in seawater. Preliminary results using cupro-nickel were also reported. It was found that depth of penetration measurements gave clearer indication of the level of synergistic effect than mass loss measurements with majority of the depth of penetration being caused by synergistic mechanisms.

Gadag and Srinivasan [182] performed several tests on ductile iron. Ductile iron has been extensively used as components in marine applications such as diesel-engine cylinder liners, valves and pumps. They specifically studied the influence of laser processing on ductile iron undergoing cavitation erosion process in series

of mediums such as SiC slurry water, artificial seawater and mild sulphuric acid water. It was found that pearlitic ductile iron showed modest resistance to cavitation erosion whereas Ferritic ductile iron consistently displayed better resistance to erosion, particularly in corrosive media. The synergistic effect of corrosion and cavitation erosion was found to be more pronounced in the dilute  $\text{H}_2\text{SO}_4$  acid than in the salt water.

As a result, a few observations were made, first of all the cumulative of mean depth of penetration (MDP) or mass loss showed a linear relationship with the time of cavitation erosion whilst the rate of cavitation erosion decreased exponentially to a nearly steady state. Laser treatment effectively brought about a nearly seven-fold enhancement of the erosion resistance of ductile iron in mild corrosive media, four-fold increase in double displacement amplitude nearly doubling the cumulative mean depth penetration of cavitation erosion in ductile iron. This in turn had enabled the delineation of the mechanism of cavitation erosion of ductile iron before and after laser processing, particularly in corrosive baths. Laser melt treatment also seemed to effectively reduce the cavitation rates of ductile iron in all the corrosive water media used. This effectiveness could be theoretically attributed to: (a) ultrafiness, high homogeneity, high hardness and high work-hardenability of the laser-melted ledeburite eutectic structure; (b) the high fatigue strength, crack-blunting nature, resistance to plastic deformation and effective mean free path reduction for dislocation motion through the eutectic [182].

In 2000 Kwok, Cheng and Man [162] investigated the synergistic effect of cavitation erosion and corrosion of various engineering alloys in 3.5% NaCl solution. They investigated the cavitation erosion and corrosion characteristics of grey cast iron, steels, copper-based alloys, brass, bronze, Zeron 100 and SS with the help of a 20 kHz ultrasonic vibrator at an amplitude of 30  $\mu\text{m}$  in distilled water and in 3.5% NaCl solution at a temperature of 23°C. The alloys studied in 3.5% NaCl solution at 23°C were ranked as follows: Zeron 100\ 304\ 316 SS\ 1050\ W1\ bronze\ brass\ grey cast iron\ Cu based on their resistance to cavitation erosion-corrosion, which was analyzed based on their microstructure, mechanical strength, work hardenability, martensitic transformability, stacking

fault energy and also corrosion resistance. As a result, it was found that corrosion only played a minor role of about 0.1–1.8% in the overall cavitation erosion–corrosion for copper-based alloys whereas for the steels and cast iron, corrosion on erosion synergism seemed very significant, amounting to 78% of the overall cavitation erosion-corrosion loss in mild steel. However, both corrosion and corrosion on erosion synergism played an almost negligible role for SS, it only seemed to suffer pure mechanical erosion in 3.5% NaCl solution in the presence of cavitation.

Wang, Bai, and Liu [165] conducted an ultrasonic cavitation experiment in order to understand the real condition of a ship sailing in seawater. They set up a cavitation apparatus of ultrasonic excitation with variable temperature field and self-vibration of a Q235 steel sample. The erosion–corrosion behavior of Q235 steel was studied in a cavitation environment created by ultrasonic excitation. As a result there was the increase in output power. The morphology of the sample surface was observed to evolve from quasi-regular to irregular patterns, and the corrosion pit deepened. The maximum depths of erosion–corrosion pits were found to be 39.5, 31.8, and 24.6  $\mu\text{m}$ , corresponding to output powers of 100, 70, and 40 W, respectively. The collapse of cavitation bubbles, sample vibration, as well as electrochemical reaction enhanced by temperature rise were considered to be the main reasons for worse cavitation erosion–corrosion of the sample in an ultrasonic excitation environment. There was a significant increase in cavitation erosion-corrosion with increase in output power of ultrasonic excitation.

### 3.6. Summary

In this chapter the various cavitation test methods were compared and a general overview obtained. Several studies were conducted in the field of cavitation, multiphase flow, cavitation erosion, as well as cavitation due to vibration. From the tests conducted it was concluded that ultrasonic vibration mechanism provided the fastest approach to obtaining cavitation results for a wide range of engineering materials. Hence, the main focus for the literature review was given

to the ultrasonic vibratory test method, and the corresponding results obtained in the past. Under the ASTM G-32 standard the ultrasonic cavitation employs a high frequency transducer-vibratory device, working at 20 kHz, using a magnetostrictive ultrasonic horn, to generate the cavitation bubbles. Different methods had been applied to study cavitation behaviour of materials in varying mediums such as distilled water, tap water, artificial as well as natural sea water, mercury, to name a few, and the microstructural changes due to cavitation have also been investigated. The test procedures comprised of exposing the sample to cavitation for a certain period of time, with periodic recording of the sample weight for weight loss calculation as a function of time.

Experiments conducted by others to understand the synergistic effects existing between cavitation erosion and corrosion were also reviewed. Data from the combined wear-corrosion testing enabled important information on the relative influence of the mechanical and electrochemical factors in affecting the mass loss rate under cavitation and liquid-solid erosion were obtained. All the studies provided very insightful knowledge on the current state of the art, and the progresses made along the years in the topic of ultrasonic vibratory cavitation, and the vibratory cavitation induced erosion and corrosion. However, much work still needs to be done on understanding the interaction between the cavitation erosion and corrosion. The individual contribution of cavitation wear and corrosion is not quite clear.

Hence, the aim of the research involves delving into understanding the interaction between the cavitation erosion and corrosion and the existing synergy between the two especially for the marine propeller materials. The research study between the cavitation erosion as well as cavitation corrosion will help understand the effect of corrosion on cavitation erosion, and vice versa.





# Chapter 4:

# Methodology

---

It has already been established that the two main detrimental factors that affect a propeller's functionality and longevity in a corrosive environment are cavitation erosion and corrosion. Hence, to understand the material behaviour under cavitation erosion-corrosion, and the synergy existing between the two, the experimental research concentrated on these two aspects of cavitation damage.

This chapter describes the sample materials used, their mechanical and chemical properties, microstructural characteristics, the test mechanisms used, and the

experimental procedures carried out to understand the material behaviour under cavitation erosion and electrochemical corrosion.

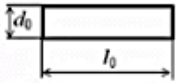
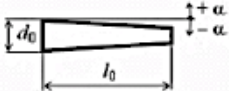
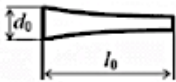
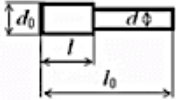
## 4.1. Experimental set-up

### 4.1.1. *Ultrasonic sonotrode*

Ultrasonic probes are single half-wavelength long tools that act as mechanical transformers to increase the amplitude of vibration generated by the converter. The wave-guide focusing device known as ultrasonic horn (also known as sonotrode) is fitted onto the end of the transducer where it transfers the longitudinal ultrasonic waves from the transducer end to the tip end [183], [184]. The principal function of the sonotrode is to amplify the amplitude of tool vibrations to the level required. It also serves as an element transmitting the vibration energy from the transducer into the tool, interacting with work piece by being in resonance with the transducer. The ultrasonic vibrating horn material used is a compromise between the needs of the ultrasonic and the application, and are generally made from high-grade steel or titanium alloy, Ti-6Al-4V, due to their high tensile strength, acoustical properties at ultrasonic frequencies, high resistance to corrosion, low toxicity, and resistance to cavitation erosion [183].

The sonotrode is the only part of the ultrasonic machining system that is unique to each process. They are used in various shapes and sizes, according to the application, while still being resonant at the operating frequency. Table 4.1 gives a list of the most frequently used shapes of ultrasonic horns [184]. The selection of a proper geometric shape and dimensions of the sonotrode is as important as the test parameters applied to it. The design and manufacture of the sonotrode require special attention since, the performance as well as the efficiency of the ultrasonic machining system primarily depends on the specific design of the sonotrode. Incorrectly manufactured sonotrode may impair its machining performance and could lead to considerable damage of the equipment, and the vibration system [184]. The sonotrode geometry affects the stiffness and mass

distribution. It depends on the required function, the value of the resonance frequency, and the amplitude amplification factor on the output side.

SONOTRODE SHAPE		SLENDERNESS RATIO
cylindrical		$\delta = \frac{d_0}{l_0}$
tapered		
exponential		
stepped		

**Table 4.1:** Geometrical parameters of sonotrode shapes, adapted from ref. [184].

Where,  $\delta$  represents the slenderness ratio of the sonotrode,  $l_0$  is the total length of the sonotrode, and  $d_0$  is the diameter of the input end.

From these values, the shape parameters, and the shape function of the sonotrodes can be derived. The sonotrode used for this research was a stepped horn type, which is considered to produce larger amplitude compared to the other types of sonotrodes due to its larger vibration stress (repeated alternating stress) inside the materials.

The most important aspects of sonotrode design are the sonotrode's resonant frequency, and resonant wavelength. The resonant wavelength is generally an integer multiple of the half wavelength of the sonotrode [184]; and the required performance of sonotrode is assessed by an amplification factor given by Equation 4.1:

$$\vartheta = A_1/A_0 \quad \dots(4.1)$$

Where,

$\vartheta$  = amplification factor,

$A_0$  = amplitude at the input end of sonotrode,

$A_1$  = amplitude at the output end of sonotrode.

The basic requirement for the size of the amplification factor is,

$$\vartheta > 1 \quad \dots(4.2)$$

The probe tip dynamic performance and its influence on the cavitation erosion process is a very important and complex aspect of the vibratory cavitation process. The dynamic analysis of the ultrasonically driven probe used for the research has been studied by Reddy, et al. [33], using finite element analysis [33]. The modal analysis of the probe was conducted along with a part of the transducer. The parameters of model comprised of the material properties, and the model was assumed fixed at the transducer end. The probe response frequencies and acceleration levels were measured during the tests, where nineteen natural frequencies were defined within the frequency range of 0 – 30 kHz. The resulting bending natural frequencies and vibration modes were found to occur at 0.9, 3.1, 6.8, 13.9, 18.2 and 26.0 kHz. Additionally, in the analysis frequency range, three longitudinal modes were found to occur at 8.1, 19.6 and 28.4 kHz. Figure 4.1 shows the longitudinal displacements for the three longitudinal modes. It was found that the mode at 19.6 kHz had the highest relative amplitude at the tip, and hence, was used to amplify the device vibrations. The dominant displacements were found to be within the narrow part of the probe.

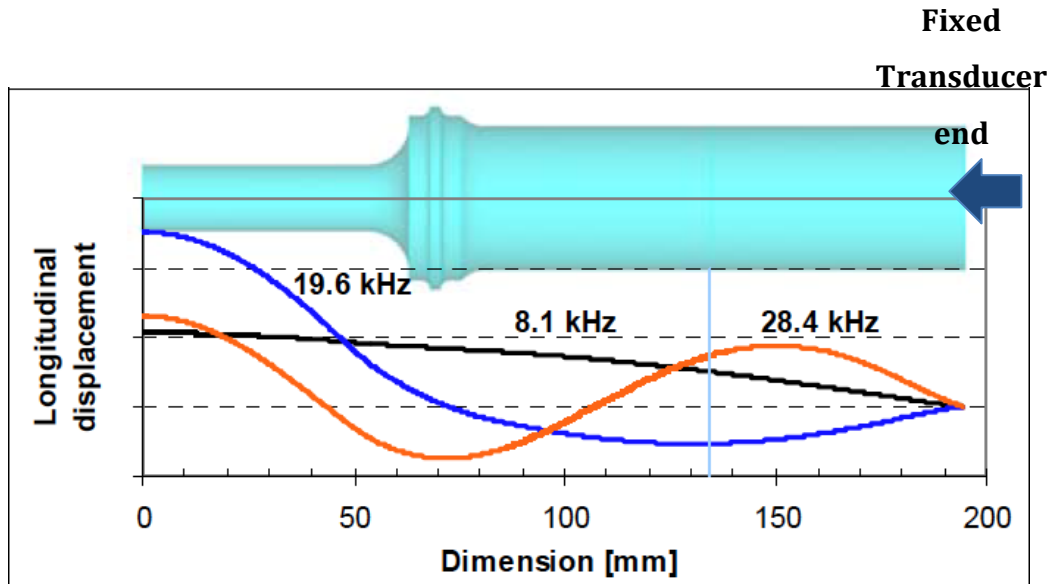


**Fig. 4.1:** Longitudinal vibration modes [33].

#### **4.1.2. Ultrasonic cavitation rig arrangement**

The cavitation experiments were conducted using the ultrasonic cavitation transducer, Hielscher UIP1000hd, consisting of a titanium horn with a tip diameter of 15.9 mm, for the current research. The indirect cavitation method was adapted, where the sample is placed stationary below the sonotrode tip at a set standoff distance. The test samples were placed under the ultrasonic transducer at a constant standoff distance of 2 mm.

Several tests have been conducted in the past using an ASTM G-32 direct cavitation system, where a round sample disk is threaded into the probe tip [124]. However, indirect method was used for the current research because, although the direct method has proven to give higher cumulative mass loss rate, the contact between the sample material and the probe material could render electrochemical analysis difficult. It could also cause possible galvanic corrosion between the sample and the probe itself. This could result in either over or under evaluation of the corrosion-induced loss. And hence, an indirect ultrasonic vibratory cavitation system was adopted for this research instead of the direct system. Figure 4.2 gives the schematics of an indirect cavitation arrangement.

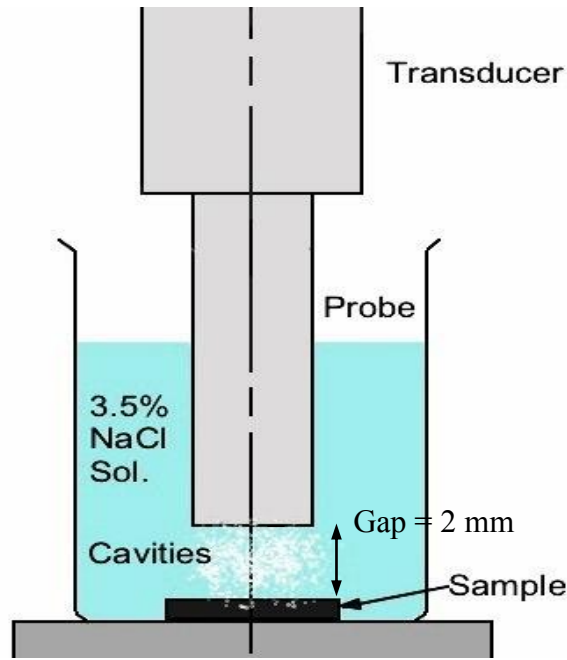


**Fig. 4.2:** Schematics of an indirect cavitation method.

Table 4.2 lists the specifications of the parameters used for the experiments conducted in the current research.

<b>Experimental parameters</b>	
Time period	1 h
Water temperature	17 °C $\pm$ 0.5 °C
Ambient temperature	20 °C – 22 °C
Atmospheric pressure	100.6 kPa $\pm$ 3.0 kPa
pH range	7.5 - 8.5
Oxygen level	3.0 ppm to 4.0 ppm
Frequency	19.5 kHz
Amplitude	80 $\mu$ m $\pm$ 0.2 $\mu$ m
Tip diameter	15.9 mm
Gap between the sample and the sonotrode	2 mm

**Table 4.2:** Specifications of the experiment.

The temperature and pH of the water were monitored before and after the experiment, starting from room temperature at 17 °C  $\pm$  0.5 °C and pH of 7.5 – 8.5. There were no significant changes observed over the course of 1 h of cavitation

test. However, the most important parameter for the experiment was the peak-to-peak amplitude of  $80\text{ }\mu\text{m} \pm 0.2\text{ }\mu\text{m}$ , which was required to be constant for all the experiments. The vibrating frequency of the probe is adjusted by synchronizing excitation to the probe natural frequency, in order to produce a maximum response. Any change in the dimension of the probe would influence the probe's natural frequency and amplitude. In fact, analysis and measurements performed for the probe at various levels of erosion confirmed the changes in the probe natural frequency, as observed by Reddy, et. al. [33].

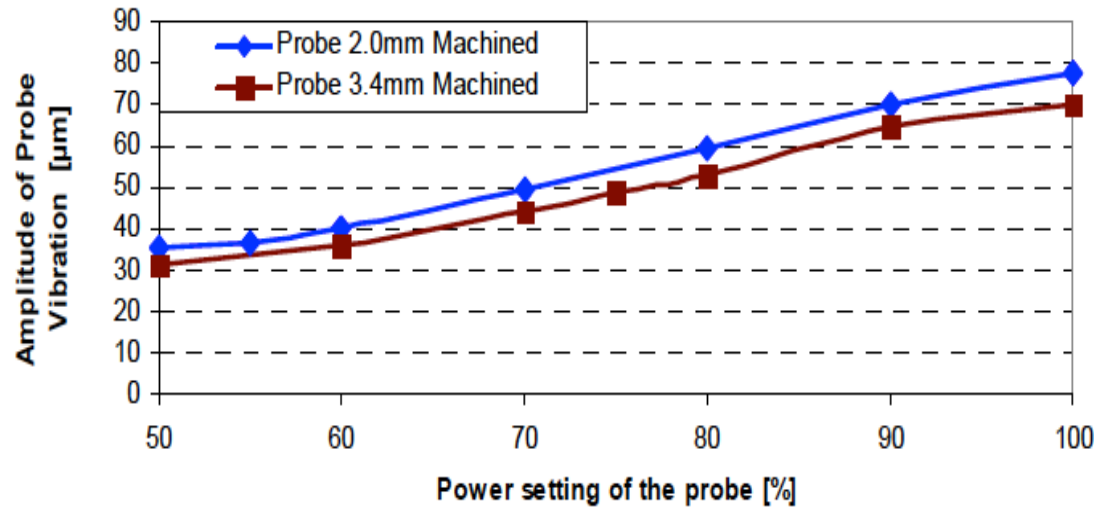
It was also found that the performance of a sonotrode was proportional to the degree of roughness of the tip surface. Both the specimen surface and the probe tip were seen to undergo erosion, requiring the probe tips to be machined after each test. This was because the eroded probe tips were seen to yield lower flow aggression between the probe and the specimen, affecting both the erosion rate, as well as the pattern of erosion on the specimen [33]. This may continue until the level of energy transmitted into the liquid is significantly reduced, beyond which the functionality of the probe is compromised. Machining the tip smooth with lathe to remove cavitation damage may extend the life of a lightly eroded tip. However, machining-off the probe tip will change the probe's dimensions, its mass and natural frequency. This change in the probe's natural frequency is further followed by a change of the excitation frequency within the device. Which, in turn, may enhance the probe tip displacement levels for the same power inputs.

However, it was also observed by Reddy that even though each test was carried out with a freshly machined probe tip, it did not produce repeatability in mass loss measurements. On further investigation it was discovered that shortening of the vibrating probe via machining caused a reduction in amplitude, and an increase in frequency of the probe vibrations [33].

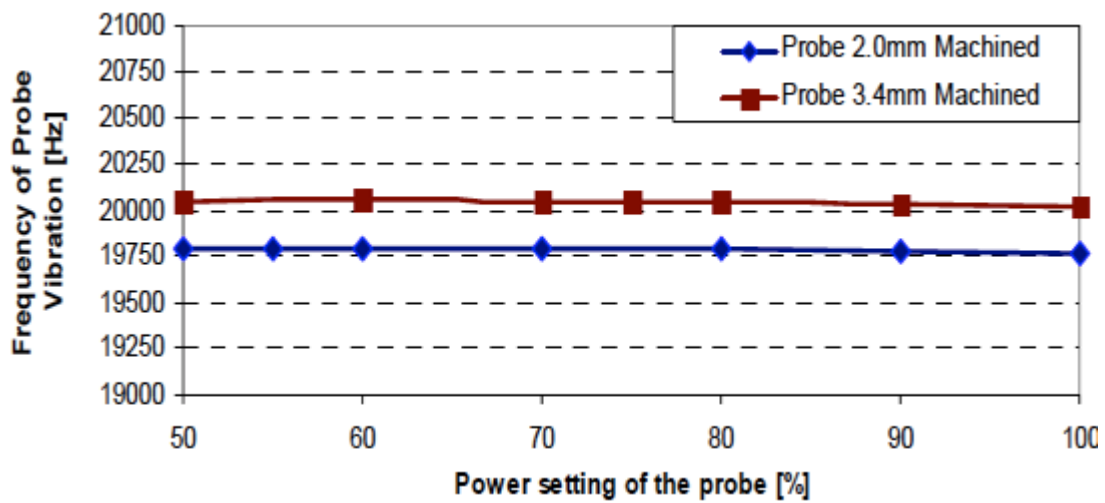
Figure 4.3 (a) and (b) show the effect of probe length on the vibration amplitude and the probe frequency, respectively. It can be seen that the probe machined by 3.4 mm had lower amplitude and higher frequency for each power setting than the longer probe (machined by 2mm). From the results obtained, it can be



concluded that the repeatability of the mass loss measurements due to cavitation erosion depended on the ageing of the vibrating probe tip surface and the vibration amplitude of the probe [33].



(a)



(b)

**Fig. 4.3:** (a) Effect of probe length on its vibration amplitude; (b) Effect of probe length on its vibration frequency [33].

Hence, this indicated the importance of maintaining the vibration amplitude for all the tests for consistency of the results pertaining to the mass loss measurements. However, special attention must be given when removing the severely eroded tip so as to remove only the contaminated area. An ultrasonic probe is a finely tuned tool, and hence, removal of too much material from the

probe tip will shorten its length, changing its resonant frequency and causing the ultrasonic generator to go into an overload condition, or even fail [183]. To achieve optimal performance, it is necessary to take into account all relevant effects and parameters that affect the dynamics of the system [184]. Furthermore, it was observed that the vibrating device did not function when the probe length was machined beyond a certain length [33].

From the modal analysis of the probe tip deformations it was found that the erosion of the probe tip and the standoff distance between the probe tip and specimen influenced the probe vibration amplitude levels. And the erosive behaviour on the specimen also seemed to strongly depend on the gap-power settings of the probe test rig. Additionally, Reddy et. al., also conducted several tests at different values for the standoff distance between the probe tip and the specimen surface. It was concluded that maximum mass loss on the specimen was observed to occur when the gap between the probe tip and specimen surface was 1mm, with other parameters remaining constant. However, this value differed for accelerometer measurements made different parts of the probe. Figure 4.4 shows the relationship between the measured mass loss of LRAH32 low alloy steel as a function of probe power setting and probe-specimen gap [33].

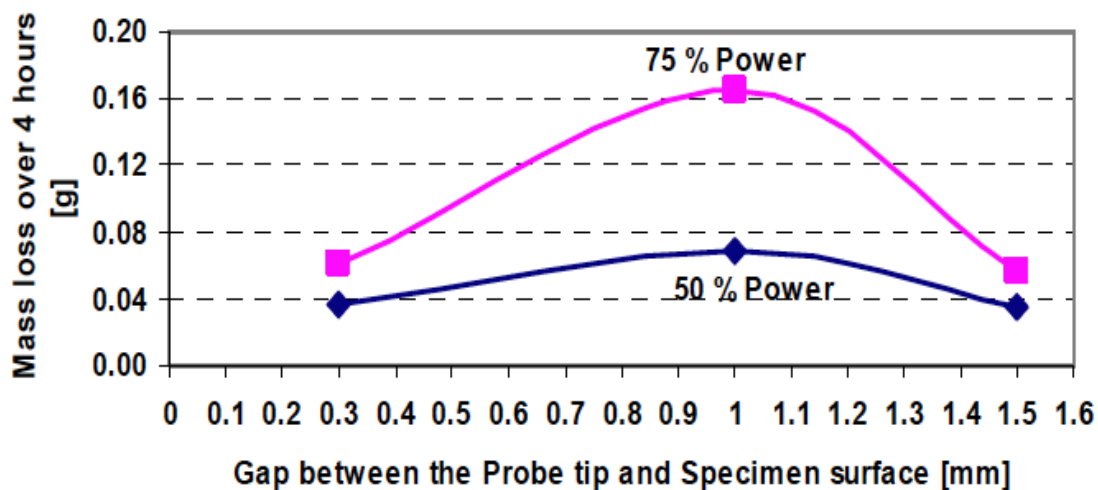


**Fig. 4.4:** Mass loss on LRAH32 material as a function of probe power setting and probe-specimen gap [33].

Hence, for the current research, in order to obtain a consistent result as well as

repeatability, the amplitude as well as the standoff distance for all the test samples was kept constant at  $80\text{ }\mu\text{m} \pm 0.2\text{ }\mu\text{m}$  and 2 mm respectively.

## 4.2. Propeller Materials

Marine propellers work in a very harsh corrosive environment under the sea for the majority of their lifetime. Hence, it is only reasonable for the chosen test materials to be based not only on their high tensile strength and hardness, but also their resistance to corrosion. The properties of the materials depend greatly on their microstructural characteristics. The impact cavitation and corrosion has on the microstructure of a material can vary depending on its chemical composition, alloying elements, the phases formed, the crystallographic structure, the combined microstructural morphology, etc. The following sections will elucidate on the sample materials, their microstructural characteristics, and the importance of each alloying elements in further details.

### 4.2.1. Duplex stainless steel

Duplex stainless steel has been well known for its high resistance to corrosion and work hardenability. Due to this, they may serve as a raw material for building of the marine propellers. DSS used for the experiment was type UNS 31803 (2205) DSS. The general chemical composition of 2205 DSS consists of 22% Cr, 5.5% Ni, 3% Mo, and 0.03% C. The carbon content is required to be low in order to avoid carbide precipitation [185].

#### 4.2.1.1. Composition and microstructural morphology

The most significant feature of DSS that sets it apart from either ferritic or austenitic stainless steels is its combined properties of both ferrite and austenite. This is due to its duplex microstructure, consisting of a ferritic matrix with islands of austenite grains. Figure 4.5 shows the duplex microstructure of the 2205 DSS sample used for the research, as observed under the JSM6500F SEM after

undergoing electrochemical etching. As a result, DSS display properties characteristic of both austenitic and ferritic stainless steels. DSS are in most cases, tougher than ferritic SS, and the mechanical strength of DSS (refer to section 4.2.1.2), in some cases, can be double of that for austenitic SS. DSS are extremely corrosion resistant with high resistance to inter-granular corrosion, especially due to the nitrogen contents in the alloy. Even in chloride and sulphide environments, DSS exhibits very high resistance to stress corrosion cracking, a property they have “inherited” from the ferritic side. Stress corrosion cracking can be a serious problem under certain circumstances such as chlorides, humidity, elevated temperature, etc. for standard austenitic stainless steels such as Types 304 and 316 [186].

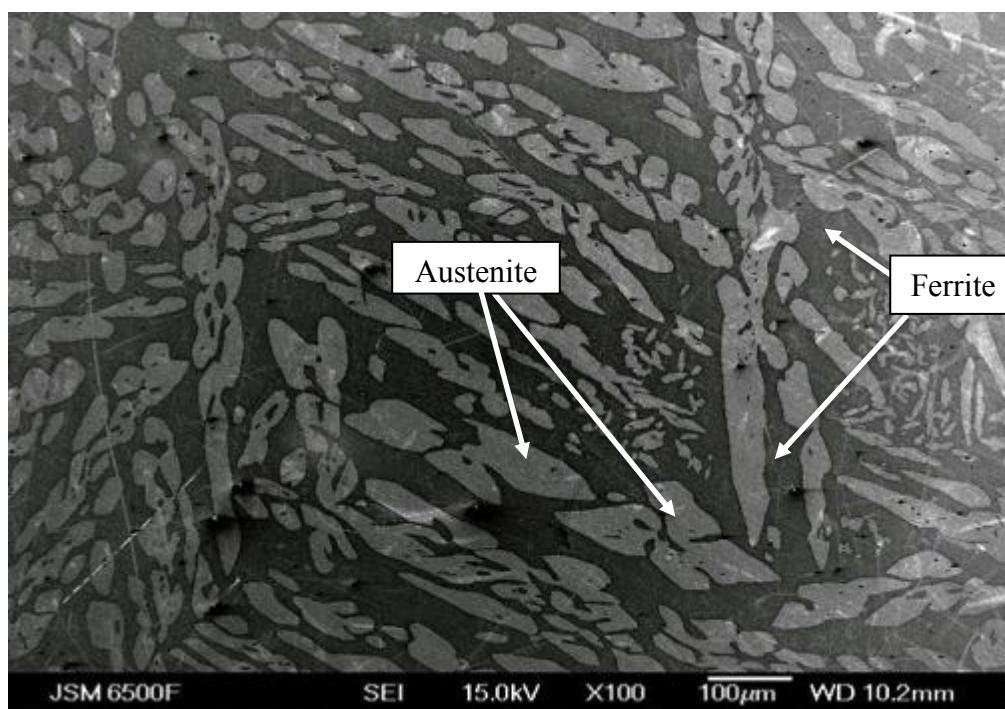


**Fig. 4.5:** Two-phase (duplex) microstructure of austenite and ferrite grains of 2205 duplex stainless steel, as obtained under SEM at a magnification of 100x.

The main alloying elements for 2205 DSS can be classified as ferrite formers (Mo and Cr) and the austenite stabilizers (Ni and N). Analysing the individual role of each element, Cr plays an extremely important role in the corrosion resistance as well as the overall properties of DSS, including mechanical, chemical as well as microstructural. It enhances the formation of ferrite and hence, promotes the

body-centred cubic (BCC) structure of iron. Generally, the Cr content in any DSS is expected to be minimum 20%. At higher Cr contents, such as in the case of superduplex stainless steel ( $\leq 25\%$  Cr), more Ni is necessary to form an austenitic or duplex structure. A minimum of about 10.5% Cr is necessary to form a stable Cr passive film that is sufficient to protect steel against any atmospheric corrosion. However, higher Cr content increases oxidation (and hence, corrosion) resistance at elevated temperatures, but it also promotes the formation of detrimental intermetallic phases [185].

Another important alloying element in DSS is molybdenum. As explained by Abreu et al., Mo was found to stabilise the passivity of the alloy and enhance the pitting corrosion resistance and crevice corrosion resistance of stainless steel in chloride-containing environments [185], [187]. Mo, like Cr, is also a ferrite former, and it increases the tendency of a stainless steel to form intermetallic phases. Therefore, it is usually restricted to a maximum of 4% in DSS.

Nickel and nitrogen, on the other hand, is an austenite stabilizer, which promotes a change of the crystal structure of stainless steel from ferritic BCC to austenitic face centre cubic (FCC) structure. The addition of nickel helps delay the formation of the detrimental intermetallic phases in austenitic stainless steels, but is far less effective in delaying their formation in DSS than nitrogen.

Figure 4.6 shows the change of crystal structure from ferritic BCC to austenitic FCC by the addition of nickel in stainless steel. DSS generally contains an intermediate amount (at least 6%) of nickel content, having a microstructure of both ferritic as well as austenitic grains, ideally in equal amounts [185].

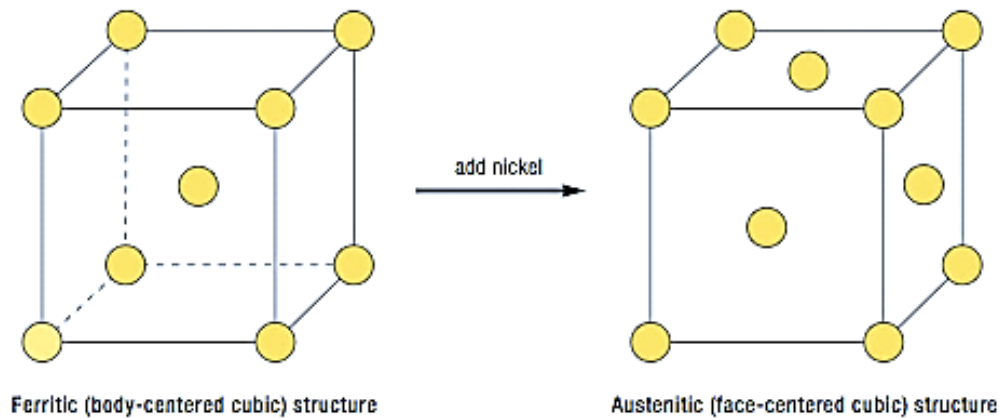


**Fig. 4.6:** *The change in crystallographic structure of ferritic BCC structure to austenitic FCC structure by addition of (at least 6%) nickel [185].*

Nitrogen is also an essential alloying element because it contributes to various factors including structural stability, pitting resistance, crevice corrosion resistance austenite formation, and also helps inhibit the formation of the precipitate phases. Much like Ni, nitrogen is also a strong austenite former and stabilizer that is added to highly corrosion resistant austenitic and duplex stainless steels that contain high chromium and molybdenum contents to offset their tendency to form the detrimental intermetallic phases in austenitic stainless steels. This, in turn, substantially improves the toughness of nitrogen-bearing DSS, effectively causing solid solution strengthening. Nitrogen does not, however, prevent the precipitation of intermetallic phases. In DSS, nitrogen is typically added first, and then the amount of nickel is adjusted to achieve the desired phase balance [185].

Tables 4.3 gives the chemical composition of the 2205 duplex stainless steel used for the research as obtained from Energy Dispersive X-ray Spectroscopy (EDS) analysis.

Material alloying elements	Composition in wt.%
C	0.024
Mn	1.83
Ni	5.10
Cr	22.73
Mo	3.40
Fe	63.53

**Table 4.3:** Chemical compositions of the materials used for the research as found under EDS.

However, this combination of austenitic-ferritic properties can also mean some compromise when compared to pure austenitic and pure ferritic grades. Such as, whilst DSS is considered to have high resistance to stress corrosion cracking, it is not as resistant to this form of attack as ferritic stainless steel. Also, DSS is susceptible to crevice corrosion, and not as noble (passive) as super austenitic stainless steel or super DSS [188], [189].

The alloying elements in DSS may form a third phase, called the precipitate phase that may not be to the alloy's advantage. To achieve proper corrosion resistance the alloy requires suitable blending during manufacturing with proper heat-treatment, and also ensuring proper welding procedure during fabrication. Sulphur, if present in the alloy, can be deleterious to the passivity of DSS as it combines with several oxides to form precipitates that eventually act as sites for pitting. Also, having high content of Mo and Cr, especially in the case of poor heat-treatment, would encourage the formation of carbide precipitates, which would render the surrounding matrix deficient of the passivating and re-passivating elements, hence exposing the alloy to corrosion [190].

Furthermore, the high Cr content of DSS can also cause embrittlement at temperatures over 300 °C, but at lower temperatures DSS have better ductility than the ferritic and martensitic grades. Another major issue with DSS is the hydrogen induced stress corrosion that mostly impacts the ferrite phase. Duplex grades can readily be used down to at least -50 °C. In terms of machinability,

although machinable, the high strengths of DSS make machining difficult. DSS cannot be hardened by heat-treatment either, and in turn solution treatment or annealing is done by rapid cooling after heating to around 1100 °C [191].

#### *4.2.1.2. Mechanical properties*

The 2205 DSS samples used for the research had an UTS of 774 MPa, yield strength of 542 MPa, modulus of elasticity of 200 GPa, density of 7.8 g cm<sup>-3</sup>, and a hardness of 233 HB, as provided by the supplier, Lloyd's Register.

Duplex grades, due to their combination of high surface hardness and corrosion resistance, offer excellent resistance to erosion-corrosion. In comparison to 316 SS, DSS has twice the yield strength of 316 and it is also 50% harder, and has higher Young's modulus, so hence, stiffer than 316 SS. DSS are also magnetic, a property that can be used to easily differentiate them from common austenitic grades of stainless [192].

#### *4.2.1.3. Passive film formation*

The passivation and the protective film growth on materials are generally considered to depend on several factors, most importantly the rate of anion diffusion, from the material into the surrounding environment, responsible for film growth, and the rate of reaction that is determined by the emission of anion from the environment into the film at the film/environment interface. The erosion-corrosion resistance of an alloy can also be determined by the rate of generation of the protective oxide or the passive film, along with its repassivation rate. The total amount of material loss by the impact of cavitation and that of corrosive medium can, hence, be measured as a function of the behaviour of the passive film. Generally, an alloy with a fast regenerating passive film remains corrosion resistant even during erosion-corrosion impact. The passivation and repassivation of a damaged film follows the growth pattern where the metal oxidation is assumed to occur on the bare metal/alloy surface, leading to lateral growth of an oxide film. Once the entire area is covered by the new passivating film, it then follows the normal growth pattern where the anodic oxide grows uniformly on the initially formed film [190].



#### *4.2.1.4 Corrosion properties*

DSS inherently has high corrosion fatigue strength and resistance to corrosion due to the passivity of the alloy surface provided by the high chromium (22-23%) and molybdenum (3%) contents in the alloy chemical composition as evident from section 4.2.1.1 and Table 4.3. The general corrosion rate of DSS is less than  $0.001 \text{ mm y}^{-1}$  [185].

For steels, the pitting and crevice corrosion resistance increases with the percentage of chromium, molybdenum and nitrogen contents. While Cr is known to increase the corrosion resistance by forming oxide that contributes to the passive film on the surface, molybdenum is found to increase the stability of the passive film and the ability of the DSS to resist the localised corrosion including pitting and crevice corrosion, especially in chloride solutions and seawater. The passive film on DSS surface contain the oxides mainly of chromium ( $\text{Cr}_2\text{O}_3$ ) and iron ( $\text{Fe}_3\text{O}_4$ ) with the film thickness in the range of 2 nm, that form immediately on exposure to the environment [187], [193], [194].

DSS may be vulnerable to sulphide induced stress corrosion cracking in the presence of hydrogen sulphide and chlorides, especially at low temperatures. However, due to their duplex microstructure and low carbon ( $<0.03\%$ ) content, the 2205 DSS has high resistance to intergranular corrosion. However, due to the existence of two distinct sites, the anodic ferrite islands and the more cathodic austenite sites, the ferrites undergo selective dissolution when compared to the austenitic phase. This may also effect the phase boundaries, especially at high anodic potentials [195]. However, under normal seawater conditions, without the application of anodic potentials, there is no significant selective dissolution of the ferrite generally observed [196].

#### **4.2.2. Nickel Aluminium Bronze**

NAB is a conventional ship propeller alloy used in the research experiment for its high strength mechanical properties. The empirical composition of a cast NAB is Cu-Al-Fe-Ni, with a nominal composition of 80% Copper, 10% aluminium, 5% iron

and 5% nickel. The sample material used for the research was the UNS C95800 (CC333G) NAB. It has been found to have high ability to retain its original smooth machined surface over a long period of time, thereby retaining its high efficiency factor, it also has the ability to resist failure under impact when notched, contributing greatly to its value as a propeller material [181].

#### 4.2.2.1. *Composition and microstructural morphology*

The microstructure of NAB is more complex than DSS with three distinct phases, namely  $\alpha$ ,  $\beta$  and four forms of kappa ( $\kappa_I$ ,  $\kappa_{II}$ ,  $\kappa_{III}$  and  $\kappa_{IV}$ ) phases, present in the as-cast microstructure. The microstructure generally consists of columnar grains of FCC copper-rich solid solution known as  $\alpha$ -phase and a small volume fraction of  $\beta$ -phase or retained martensitic  $\beta'$ -phase, surrounded by a series of intermetallic Fe-rich kappa phases.

Binary alloys, such as aluminium bronze, containing up to 9.4% aluminium form a single-phase  $\alpha$  solid solution at room temperature under equilibrium conditions. Figure 4.7 (a) shows the phase diagram of the binary Cu-Al system for different Wt% of aluminium at different temperatures. The aluminium content in the alloy is generally considered to define the strength of the alloy. As seen from Figure 4.7 (a), further addition of aluminium normally results in an  $\alpha + \beta$  structure in the alloy, cooled at moderate rates. However, decomposition of the  $\beta$ -phase will occur during slow cooling or annealing below 565 °C to form an  $\alpha + \gamma_2$  eutectoid. This  $\gamma_2$  eutectoid may cause decrease in both mechanical properties and corrosion performance of the alloy. And hence, it is necessary to eliminate the  $\gamma_2$  phase or suppresses the  $\beta$  transformation. One such way is to heat-treat the alloy between 600 °C and 800 °C, followed by a rapid air cool or quench. However, the formation of  $\gamma_2$  phase may still occur if the cooling rate is not sufficiently rapid [197].

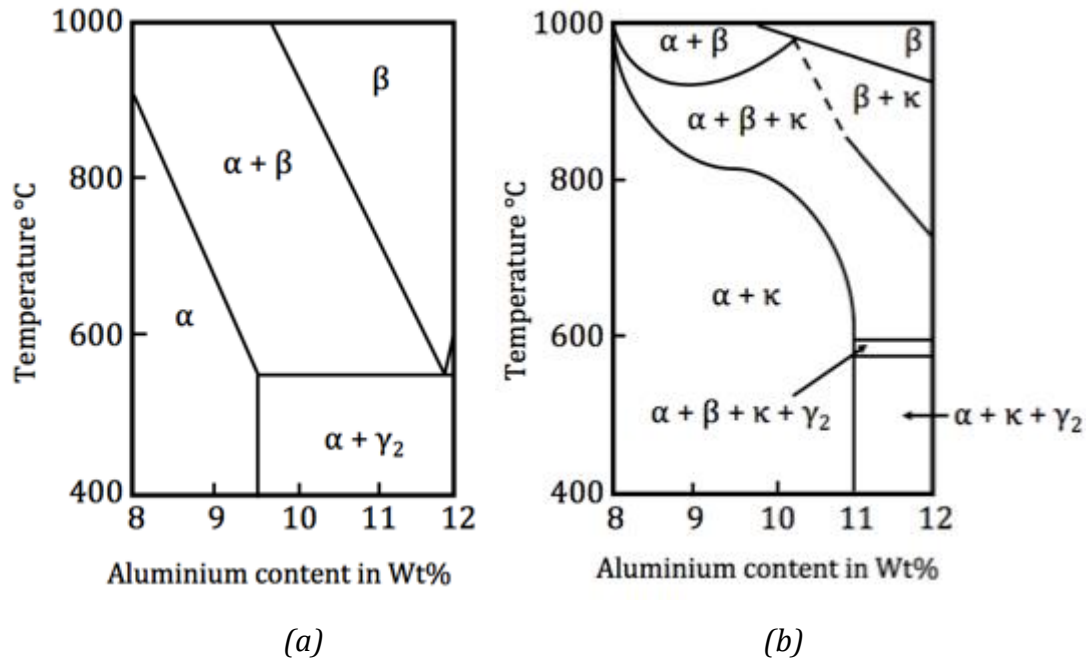


**Fig. 4.7:** Phase diagrams of (a) A binary Cu-Al system; (b) a vertical section of the Cu-Al-Ni-Fe system with 5% Ni, 5% Fe [197].

Another method is to add alloying elements, which retard the formation of  $\gamma_2$ , while maintaining the high strength properties. The principal alloying elements used for this purpose are iron, nickel and manganese. Both nickel and iron combine with aluminium to form a complex  $\kappa$ -phase. The amount and distribution of the phases in NAB and their chemical composition has a significant effect on the properties of the material. Figure 4.7 (b) shows the phase diagram of a NAB alloy with 5% nickel and 5% iron content in the composition. Approximately 1% manganese, which is considered to be equivalent to 0.15% aluminium, is usually present in these alloys, which aid castability, and retard the  $\beta$ -transformation [197].

The morphology, phase transformations and chemical analysis of the complex phases present in cast NAB have been investigated by Culpan and Rose [197] using optical and electron microscopy techniques, and energy dispersive analysis. Their investigation revealed that heat-treatment from 1000 °C and slowly quenching to 900 °C in successive steps of 25 °C for 1 h each via air, before cooling it with cold water (at 20 °C), showed various phase transformations from  $\beta$  to small  $\alpha$ -phases. At temperatures above 850 °C the alloy was seen to comprise of  $\beta + \alpha + \kappa$

depending on its exact chemical composition. Heat-treatment in this region for sufficient time resulted in spheroidization of the  $\kappa$ -phase (Figure 4.8 (a)). On further quenching to 800 °C initiated the nucleation of  $\kappa_I$  precipitate in both  $\alpha$  and  $\beta$  phases, followed by the nucleation of  $\kappa_{II}$  and  $\kappa_{III}$  precipitates at the  $\alpha/\beta$  interface. Heat-treatment of the as-cast NAB at temperatures under 840 °C resulted in the transformation of retained  $\beta'$  to  $\alpha + \kappa$  (Figure 4.7 (b)). A significant increase in the amount of fine precipitate was also observed within the grains. Continued quenching to and below 725 °C initiated the precipitation of  $\kappa_{IV}$  phase in the  $\alpha$ -matrix, see Figure 4.8 (b). Additionally, these phases seemed to exhibit different chemical compositions to those present in as-cast structures [197], [198].

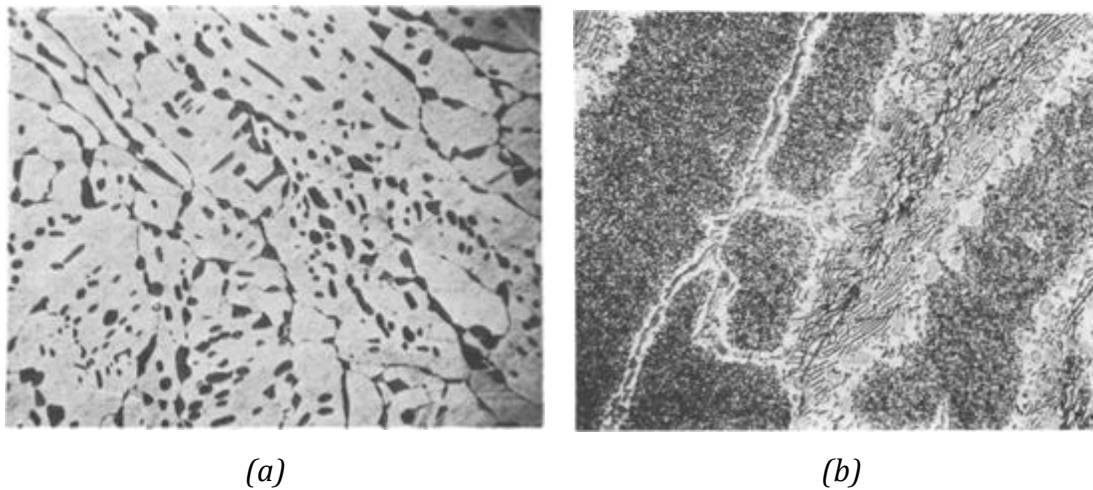


**Fig. 4.8:** NAB microstructure heat-treated at (a) 860 °C for 72 h (at 480x); and (b) 675 °C for 6 h (at 600x) [197].

Figure 4.9 illustrates the crystal structures of  $\kappa_I$ ,  $\kappa_{II}$  and  $\kappa_{IV}$  phases as  $DO_3$   $Fe_3Al$ ,  $\kappa_{III}$  phase as  $B_2$   $NiAl$ . The  $\kappa_I$ ,  $\kappa_{II}$  and  $\kappa_{IV}$  phases are all iron-rich precipitates distributed in the nickel-aluminium structure of  $DO_3$   $Fe_3Al$  crystal structure (Figure 4.9 (a)).  $DO_3$  crystal structure is an ordered FCC crystal unit cell with four body centred cubes and four  $Fe_3Al$  cubes arranged alternatively.  $\kappa_{III}$  phase on the other hand is a Ni-rich  $B_2$  structure, which is a BCC unit with Ni elements at the eight corners but with Al element at the centre of the cube (Figure 4.9 (b)) [198], [199].

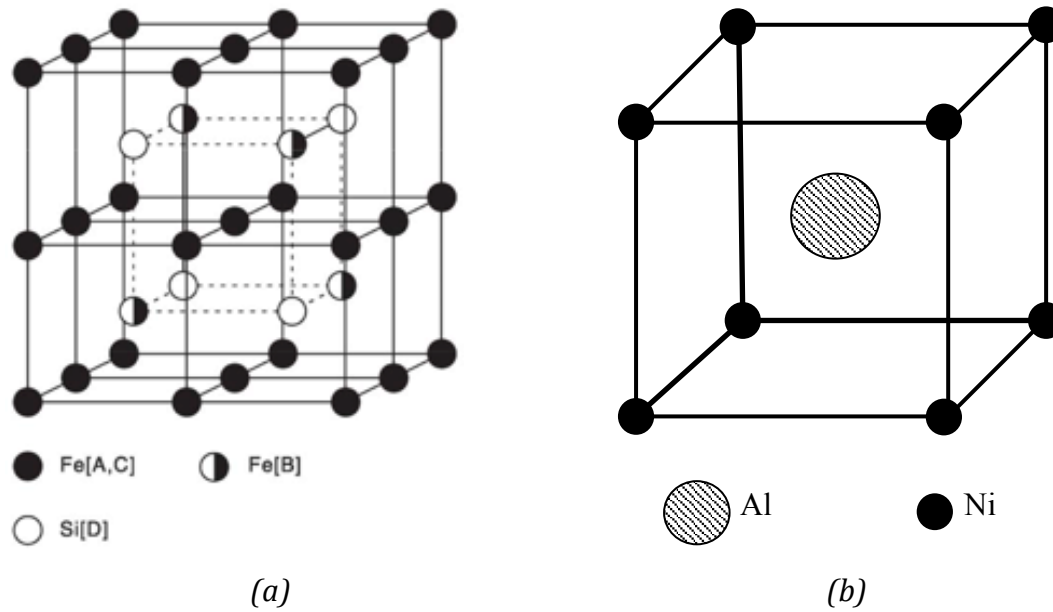


**Fig. 4.9:** Crystals structures of (a)  $\kappa_I$ ,  $\kappa_{II}$  and  $\kappa_{IV}$  phases having a  $Fe_3Al DO_3$  structure, and (b)  $\kappa_{III}$  phase with a  $NiAl B_2$  structure [198], [199].

Among the intermetallic compounds,  $\kappa_I$  phase is rosette shaped precipitate formed at high temperatures in high Fe content alloys and hence, is coarser than the rest,  $\kappa_{II}$  phase is smaller than  $\kappa_I$  phase and form a dendritic rosette shape which is distributed mostly at the  $\alpha/\beta$  boundaries, and  $\kappa_{IV}$  phase is a fine Fe rich precipitation of varying sizes with plate-like morphology that are distributed throughout the  $\alpha$  grains along certain crystallographic directions forming within the  $\alpha$ -matrix, forming at 850 °C.  $\kappa_{III}$  phase is a fine lamellar “finger-like” eutectoid structure and forms at the boundary of  $\kappa_I$  phase [181], [197], [200], [201]. The chemical compositions, in weight %, for the alloy as well as the individual phases obtained under EDS are tabulated in Table 4.4.

Micro- structural Phases	Chemical composition in weight %					Morphology	Structure
	Cu	Al	Mn	Fe	Ni		
Alloy	80.25	8.79	3.56	4.63	5.13	-	-
Alpha	85.39	7.19	0.87	3.35	3.20	FCC solid solution	-
Kappa 1	15.08	13.29	1.72	57.53	12.38	Rosetta globular	Fe <sub>3</sub> Al (DO <sub>3</sub> )
Kappa 2	17.61	15.54	1.50	51.90	13.44	Dendritic	Fe <sub>3</sub> Al (DO <sub>3</sub> )
Kappa 3	45.15	18.76	1.19	10.91	23.99	Lamellar	NiAl (B <sub>2</sub> )
Kappa 4	7	11	2	73	7	Cuboidal	Fe <sub>3</sub> Al (DO <sub>3</sub> )

**Table 4.4:** The crystal structure, morphology and the typical chemical composition of the individual phases in the NAB samples as tested under EDS;  $\kappa_{IV}$  in as-cast NAB adapted from Ref [198].

From Table 4.4, the molecular formula of the NAB alloy used in the research experiment can be written as CuAl10Fe5Ni5. The  $\kappa_{IV}$  participates observed under SEM were less than 0.5  $\mu\text{m}$  and their chemical composition could not be determined due to the limited magnification of SEM allowing interference from the surrounding  $\alpha$ -phase, giving less accurate results. The typical chemical composition of  $\kappa_{IV}$  are tabulated from ref. [198]. No visible retained martensitic  $\beta'$ -phase were observed.

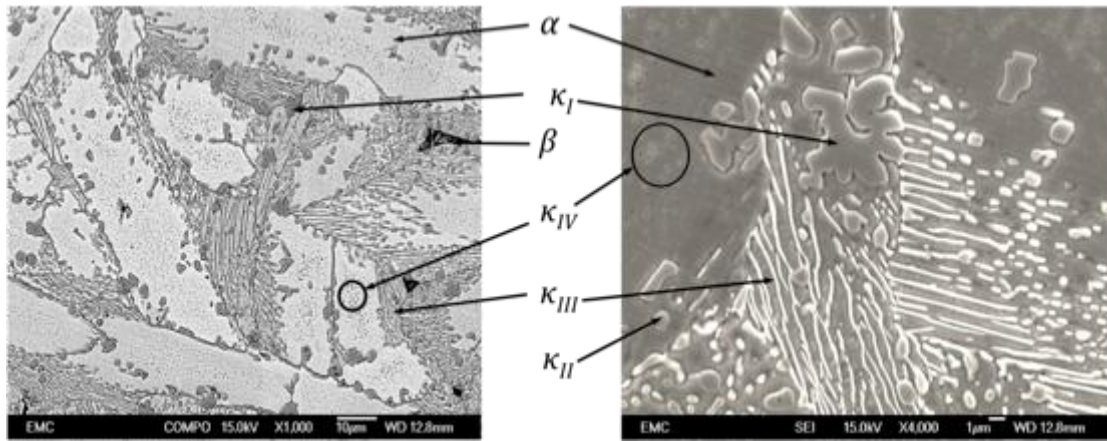


**Fig. 4.10:** Microstructural morphology of UNS C95800 cast NAB at a magnification of 1000x and 4000x.  $\kappa_I$  is the globular dendritic structure,  $\kappa_{III}$  is the lamellar “finger-like” structure, and  $\kappa_{IV}$  is the very fine particulate imbedded within the  $\alpha$  matrix [18], [202]–[204].

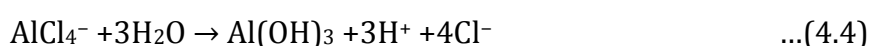
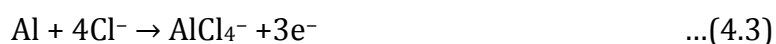
Figure 4.10 shows the general microstructural morphology of the as-cast NAB, UNS C95800, used for the experimental research, taken via SEM at 1000x magnification.

#### 4.2.2.2. Protective oxide film

The corrosion resistance of NAB is attributed to the formation of protective oxide film on NAB. This formation may occur either in air or submerged in corrosive environment like chloride solution. The rate of oxide film growth is much more rapid when fully immersed in corrosive solution than in air. The oxide layer mainly comprises of cuprous oxide ( $\text{Cu}_2\text{O}$ ) and aluminium oxide or alumina ( $\text{Al}_2\text{O}_3$ ) films, with traces of copper salts and hydrochlorides ( $\text{Cu}_2(\text{OH})_3\text{Cl}$  and  $\text{Cu}(\text{OH})\text{Cl}$ ) that form after long exposures to chloride solutions like 3.5% NaCl solutions or seawater. These oxides tend to adhere firmly to the substrate, giving very little permeability to liquid corrodant once formed. The oxide layer formed on the substrate/base metal is mostly aluminium-rich, whereas, the oxide formed in the outer regions is generally richer in copper. The oxide films rich in copper, according to Poggie et al., have mechanical properties similar to those of the parent aluminium bronze and are resistant to mechanical disruption during sliding. They greatly reduce the corrosion rate by decreasing the anodic dissolution reactions of aluminium and copper, hampering not only the ionic

transport across the oxide layers, but also decreasing the rate of the cathodic reaction on these oxide layers. The oxide films are also considered resistant to most chemical attack, provide resistance to flow velocity (up to  $22.9 \text{ m s}^{-1}$ ), and heal rapidly when damaged especially in a corrosive environment like seawater in the presence of oxygen [205]–[208].

These oxide films, especially alumina, are relatively hard and abrasive but brittle, with notch sensitivity, like other ceramics. If the oxide film is breached, the substrate becomes vulnerable to galvanic corrosion [205]. There have been several studies on the corrosion behaviour of NAB alloy and its protective oxide film formation. Schüssler and Exner established that when the oxide-free substrate surface is introduced to a corrosive environment, the aluminium in the alloy would preferentially oxidize first in the presence of oxygen. However, after a certain thickness is achieved, the formed alumina film, prevents further diffusion of aluminium, leaving copper to oxidize on the surface of the corrosion product [205], [206]. The formation of the  $\text{Al}_2\text{O}_3$  oxide layer is done by “complexation” of aluminium by chloride as demonstrated in Equation 4.3, which is then followed by hydrolysis of the chloride product to form  $\text{Al}(\text{OH})_3$  layer (Equation 4.4):

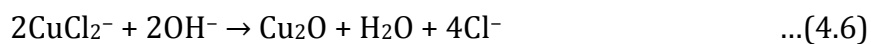


The chloride ions released play an important role in the formation and properties of protective oxide films especially on copper-based alloys. Hence, it has been observed and established by Wharton and Stokes that the most prominent oxide forming in aerated chloride media on a NAB surface is  $\text{Cu}_2\text{O}$  [208]. This is because the main corrosion process in such environment mainly constitutes of the dissolution of copper to form a dichlorocuprous anion complex [208]–[210], given by Equation 4.5:





The Cu<sub>2</sub>O may form via number of processes in Cl<sup>-</sup> containing environments, the extent of which depends on the relative chloride ion concentration and pH. The oxide layers considered are formed by a dissolution process shown in Equation 4.6 [211].



The predominant cathodic reaction in aerated solutions is given by Equation 4.7:



#### 4.2.2.3. *Mechanical properties*

NAB has material properties of 650 MPa UTS, yield strength of 270 MPa, hardness of 160 HB, and high ability to retain its original smooth machined surface over a long period of time, thereby retaining its high efficiency factor. Researchers have also tried to correlate the cavitation erosion resistance of materials with their other mechanical properties. One such major factor for propeller material selection is its ultimate resilience [212]. The UR value for NAB samples used in the experiments was 3.8 MPa.

#### 4.2.2.4. *Corrosion properties*

As mentioned before, due to the lack of  $\gamma$  and  $\gamma_2$  phases in NAB, the corrosion resistance of NAB is generally high. To ensure that the kappa phase itself is corrosion resistant the nickel content of the alloy should exceed the iron content and the manganese content should not exceed 1.3% [213].

However, the corrosion behaviour of cast (as well as wrought) NAB in sea water depends not only on the metallurgical composition, but also the processing history, surface roughness, and the corrosion environment [207]. It is found to be susceptible to selective phase erosion and corrosion attacks [181], [201], [207], [214]–[217]. The general corrosion rate of NAB in seawater is considered to be 0.06 mm y<sup>-1</sup> [213].

#### *4.2.2.5. Selective phase attack*

In multiphase alloys if the phases have different electrochemical potentials then there is a tendency for the most anodic phase to be corroded preferentially. This is called selective phase attack. The extent of corrosion would depend on how great the potential difference is between the anodic phase and the surrounding phases, and upon the distribution and intrinsic corrosion resistance of the anodic phases [213].

In NAB, as mentioned in section 4.2.1.2, there are various phases, mainly  $\alpha$ ,  $\beta$ ,  $\kappa_I$ ,  $\kappa_{II}$ ,  $\kappa_{III}$  and  $\kappa_{IV}$ . The aluminium-rich phases and martensitic  $\beta$ -phase are generally the highly susceptible phases, but in absence of the  $\beta$ -phase also selective phase attack may occur. The  $\alpha$ -phase, being copper-rich, becomes anodic when in galvanic coupling with iron rich  $\kappa$ -phases that act as the cathode due to its higher electronegativity. This causes the  $\alpha$ -phase to undergo galvanic corrosion within NAB. This selective phase attack affects especially the narrow bands of  $\alpha$ -phase adjacent to the lamellar  $\kappa_{III}$  phases, and from there it may spread further into the  $\kappa_{III}$  phase itself [213].

#### *4.2.3. Galvanic corrosion properties in Seawater*

For the longevity of propellers functioning in a harsh environment like seawater it is very important that the materials used for the propellers are highly corrosion resistant. Hence, one of the ways to determine the corrosion properties of a metal or alloy is by locating its position in the galvanic series to understand how it would fair in the seawater environment.

Galvanic series is a series of electrode potential values, generally expressed in volts or millivolts, of various metals and alloys when exposed to corrosive environment like seawater at a given temperature against a reference electrode such as Standard Calomel cell.

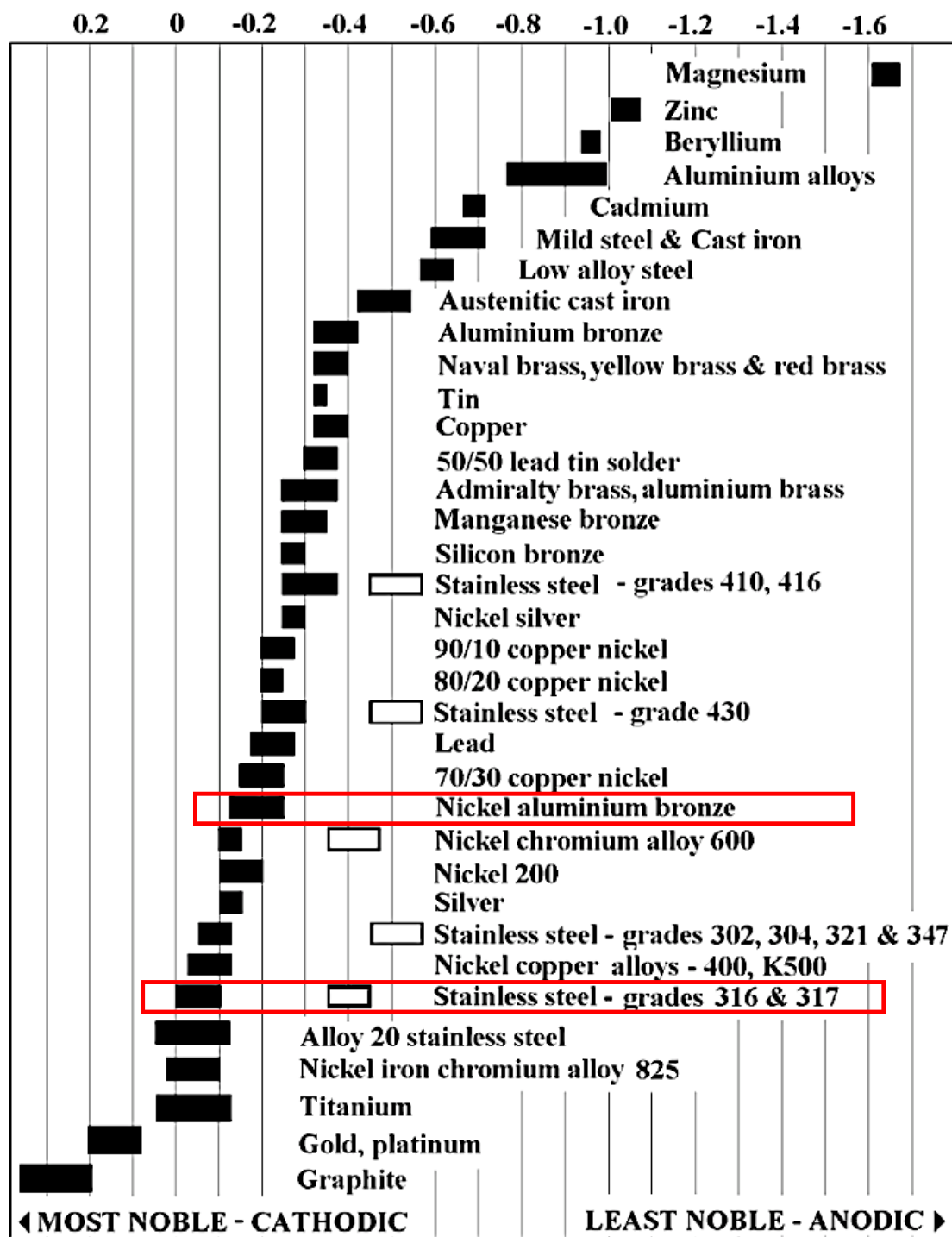


**Table 4.5:** DSS and NAB highlighted in the simplified galvanic series for metallic materials in flowing seawater of velocity between  $2.5 \text{ m s}^{-1}$  to  $4 \text{ m s}^{-1}$  and temperature range of  $10^\circ\text{C}$  –  $27^\circ\text{C}$ , referenced to saturated calomel half-cell [218].

Table 4.5 shows a general galvanic series of various metallic materials, with the positions of NAB and DSS highlighted, in flowing seawater at the velocity of  $2.5 \text{ m}$

$\text{s}^{-1}$  to  $4 \text{ m s}^{-1}$ , at a temperature range of  $10\text{ }^{\circ}\text{C}$  –  $27\text{ }^{\circ}\text{C}$ , relative to a Saturated Calomel half-cell [218]. The value of the potential for any alloy can be changed in a galvanic series by a variety of factors such as water temperature, velocity, pH values, aeration, turbulence, chlorine content, etc. even in seawater. However, the relative ranking of alloys remains largely unchanged by these factors [205], [218].

The empty (un-shaded) rectangles in Table 4.5 show ranges exhibited by stainless steels in acidic water such as may exist in a stagnant, low velocity or poorly aerated water where stainless steel become active, whereas the shaded areas show the potentials of stainless steel in its passive state. As can be seen from Table 4.5, DSS has almost the same galvanic potentials as the grade 300 austenitic stainless steel, and has higher galvanic potentials than NAB. Hence, if the two materials were kept in contact under seawater, NAB would be more susceptible to bimetallic corrosion than DSS [189]. Table 4.6 lists the galvanic potentials of both NAB and DSS in flowing salt water at a velocity of  $2.5 \text{ m s}^{-1}$  to  $4 \text{ m s}^{-1}$  at a temperature range of  $10\text{ }^{\circ}\text{C}$  -  $27\text{ }^{\circ}\text{C}$ , where it can be seen that DSS and NAB both have high corrosion potentials [218]–[220].

Alloy	Galvanic Potential (volts DC)
Nickel aluminium bronze	-0.15 V to -0.22 V
Duplex stainless steel	-0.1 V to -0.2 V

**Table 4.6:** *Galvanic series of metals in flowing seawater with reference to saturated calomel half-cell [218].*

The corrosion resistance on NAB is more complex than DSS. Unlike DSS that has strong corrosion resistance due to its passive layer, NAB gets its corrosion properties from a thick layer of protective oxide film predominantly composed of aluminium oxide ( $\text{Al}_2\text{O}_3$ ) near the substrate with copper oxide ( $\text{Cu}_2\text{O}$ ) formed mostly on the outer layer [205]. These films generally take several days to reach a substantial thickness of  $900 \text{ nm}$  –  $1000 \text{ nm}$ , that may have a visible brown colouration over the alloy surface provide sufficient corrosion resistance [221]. But when disrupted may exhibit different corrosion behaviour for the NAB substrate. However, the protective layer is not susceptible to localised breakdown

and consequent pitting in the presence of chlorides and therefore, making NAB very resistant to corrosion by seawater [213].

### 4.3. Experimental methods

Three different tests were conducted and compared in order to establish the wear-corrosion relation and synergy for the materials. Eighteen different samples of NAB and DSS (six each) were used for the experiments. Both the sonotrode tip and the samples were immersed in the test liquids in the tank. The un-attached or indirect method of cavitation was used in the test and the specimen was held below the vibrating horn at a distance of 2 mm. The prepared samples were cavitared in 5 L of medium for 1 h at a frequency of 20 kHz and peak-to-peak amplitude of  $80\text{ }\mu\text{m} \pm 0.2\text{ }\mu\text{m}$  (all specifications listed in Table 4.2). The mediums used were triple distilled water from department lab and 3.5% NaCl solution prepared in the lab.

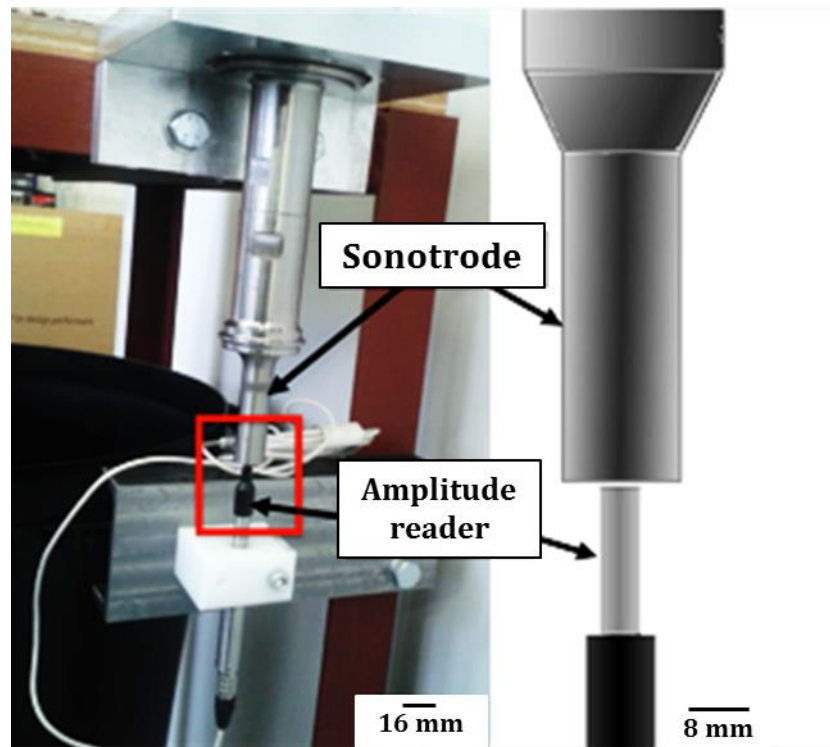
The samples were analysed for microstructural characterization using JOEL (JSM6500F) scanning electron microscope (SEM) employed for microstructural morphology analysis before and after cavitation at an acceleration voltage of 15.0 kV, a probe current at medium (6 nA – 13 nA), and a working distance of 10 mm and above. For clearer microstructural evaluation, backscattered electron imaging was also employed. Samples were also transverse sectioned to observe the subsurface impacts of cavitation on the microstructure. For SEM analysis of the transverse sections, the samples were cut laterally with diamond saw, and then hot-mounted in Bakelite resin mould. The interested surface was then polished using 1200- and 4000- grit SiC abrasive paper before mirror finishing it with 6- and 1-  $\mu\text{m}$  diamond paste.

Alicona measurements were taken using Alicona 3D optical profilometer to measure the volumetric mass loss of the samples along with surface roughness of cavitared regions and compared with each other, as well as surface topography. A form Talysurf 120L was also employed to capture the overall surface roughness.

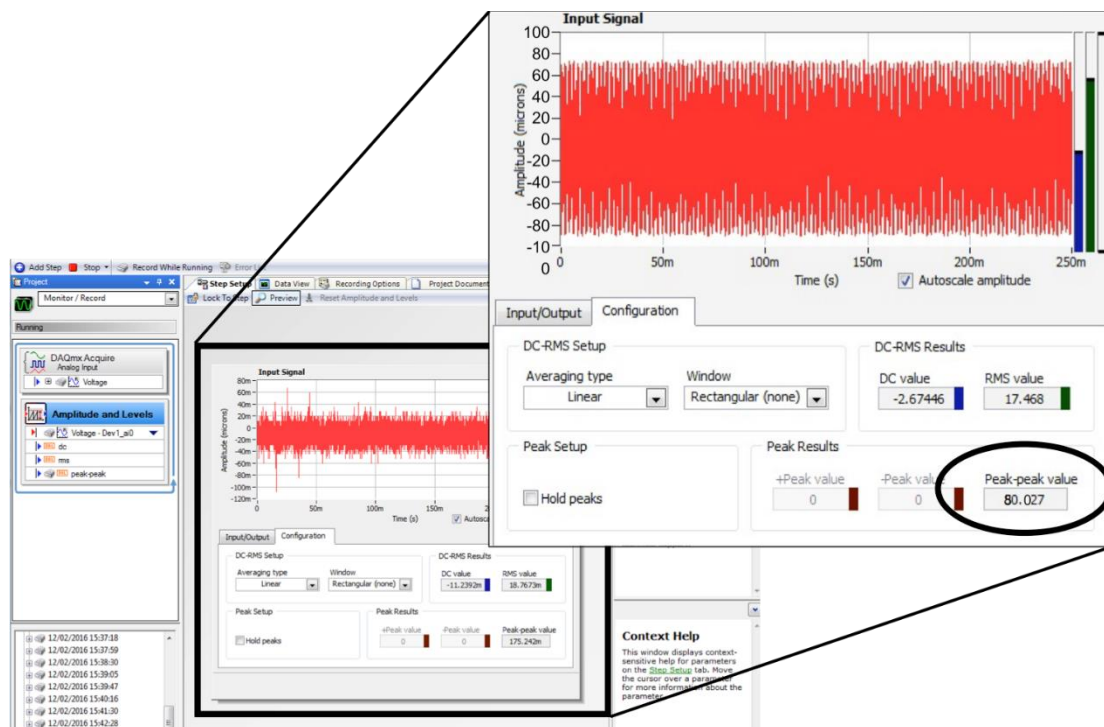
#### ***4.3.1 Sonotrode preparation***

The sonotrode tip was also prepared before each test by grinding the tip surface with lathe, then washed with distilled water and methanol, before blow-drying the probe to be mounted for the test. The amplitude of the probe was calibrated and kept constant before each test using an ADE technologies 6000 series (6810) amplitude sensor. The calibration was done by mounting the amplitude vertically on a 2-axis flexure stage that moved the sensor vertically as well as horizontally to adjust the distance between the tip of the sensor and the probe tip to first set zero. The sensor was then connected to the signal express software that recorded the output voltage and converted it to the peak-to-peak amplitude of the sonotrode tip.

Figure 4.11 (a) shows the amplitude reader for sonotrode amplitude calibration required before each test. Figure 4.11 (b) shows the signal express software used to calibrate the sonotrode for the correct amplitude. The input signal and peak setup give the peak-to-peak value of amplitude, as read by the amplitude reader.



(a)



(b)

**Fig. 4.11:** The sonotrode amplitude calibration set up showing (a) the amplitude reader-sonotrode arrangement; and (b) the signal express software used in order to calibrate the sonotrode.

### **4.3.2 Sample preparation**

#### *4.3.2.1. Sample surface preparation*

Eighteen test samples, six of DSS and twelve of as-cast NAB, were prepared for the experiments. Each sample had a dimension of 25 mm x 25 mm ( $\pm 2$  mm) with a thickness of 5 mm ( $\pm 0.5$  mm). The surface of all the test samples facing the cavitation rig were wet polished using 800-, 1200- and 4000- grit silicon carbide (SiC) abrasive papers, and 6-  $\mu$ m diamond paste. They were then cleaned with methanol in the ultrasonic bath at a regular interval for 2 min between each change of SiC paper, and then washed with distilled water and methanol before air-drying them.

Six samples of DSS and NAB each were then left inside twelve individual, clean and uncontaminated plastic bags for a week to ensure the formation of air-formed oxide films. The preparation procedure was repeated for each sample after each test in order to reuse the samples. The samples were all wired with the help of M3 screws at one side for facilitating electrochemical analyses. The sample surfaces were all coated with lacquer on five of the six sides of the sample, except one, i.e. the test surface.

#### *4.3.2.2 Oxide film preparation*

As one of the main novelties of the research, cavitation erosion-corrosion was also performed for NAB samples with water-formed oxide filmed samples, in order to understand the effect of cavitation on the oxide films themselves and the cavitation as well as corrosion behaviour of NAB with an water-formed oxide layer.

For this, six NAB samples were submerged in 3.5% NaCl solution for three months to form a thick layer of water-formed oxide film on the samples. Figure 4.12 shows the differences in the optical images of the oxide-films formed after 1 week of air exposure, and 3 months of immersion in 3.5% NaCl solution.



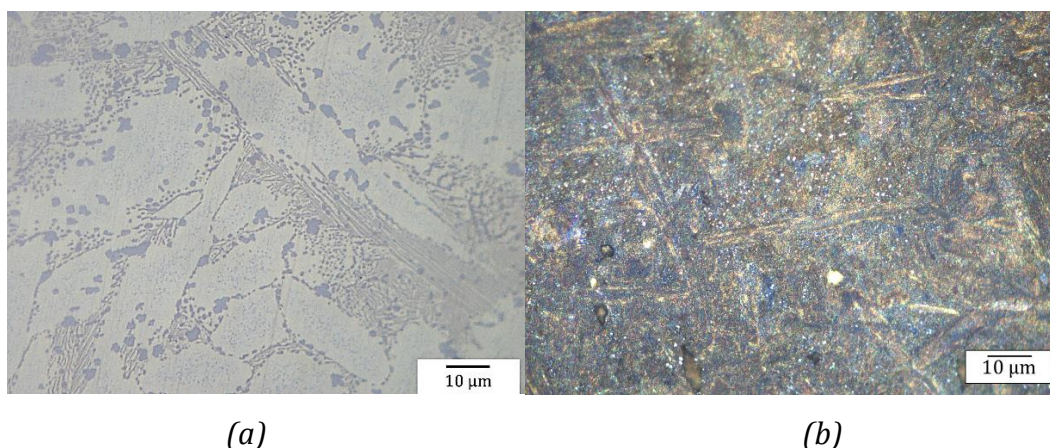


**Fig. 4.12:** Optical image of general oxide film (a) after 1 week in air; (b) after 3 months of immersion in 3.5% NaCl solution [202], [204].

From the image in Figure 4.12 (a) it can be seen that considering the protective oxide film formation is a slow process, especially in the absence of corrosive environment like seawater, there is no visibly significant difference in the microstructure of the substrate after one week of exposure to air, although the  $\kappa_{III}$  phases seemed to appear more prominent, meaning localised etching or selective phase attack at the phase boundaries. Whereas, in Figure 4.12 (b) the sample immersed for three months in 3.5% NaCl solution had a completely different morphology where the microstructural details of the base material were no longer clearly visible.

#### 4.3.2.3 Electrochemical arrangement

For the electrochemical tests, the surfaces other than the one facing the ultrasonic probe were coated with lacquer in order to prevent them from any external chemical attack. Two extra features were also added to the samples for the electrochemical tests that comprised of two adjacent drill holes of length 8 mm and 5 mm, and a diameter of 3 mm each at one corner of each sample, as shown in Drawing 1 (Appendix E). The two blind holes were meant to connect at a right angle inside the sample. The shorter hole (of 5 mm length) was meant for docking the metallic wire that connected the sample with the potentiostat, whereas the longer hole (8 mm) was threaded so that an M3 threaded socket set screw could be inserted, securing the wire within the sample. The holes were then sealed with

waterproof epoxy resin glue, prepared at least 12 h before handling again.

Once the wire was secured, the samples could be easily polished without damaging the wire. The wire from the sample was then connected to the GAMRY Reference 600 potentiostat as the working electrode. The reference electrode used for the electrochemical tests was that of an Ag/AgCl, since it is the most commonly used aqueous reference electrode for applying in measuring the concentration of hydrogen ions present and providing cathodic protection against corrosion in marine environment [222], [223]. The counter electrode used was a graphite rod using cell cables, while the samples underwent electrochemical as well as cavitation erosion-corrosion tests.

Figure 4.13 shows the schematics of the cavitation rig with the titanium probe and the specimen positioned at 2 mm standoff distance from each other for the cavitation erosion-corrosion experiments, and connected to Gamry 600Ref potentiostat for pure corrosion tests, as used for the studies presented in ref. [18], [202]–[204].

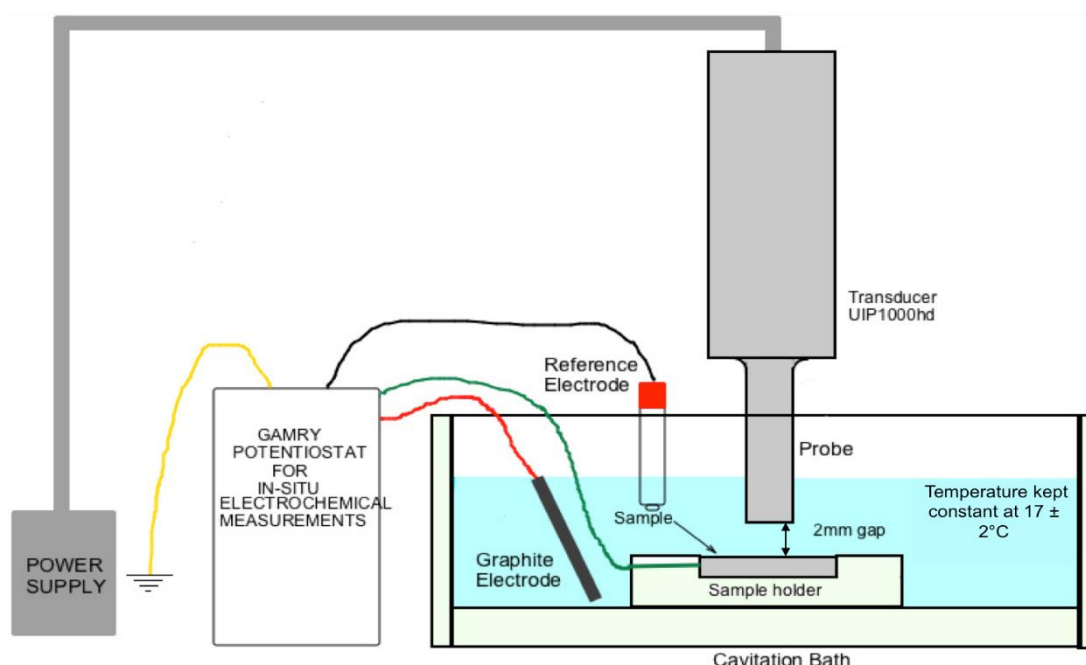


**Fig. 4.13:** Schematics of the cavitation rig with specimen connected to the potentiostat for cavitation erosion-corrosion measurements [18], [202]–[204].

The prepared samples were then mounted on to an acrylic perspex holder comprising of adjustable fixtures that tightened the samples using two nylon screws positioned at 90 degrees from each other. These screws secured two identical rectangular acrylic pieces of size 25 mm x 10 mm x 5 mm that clamped the sample tightly in the holder.

Figure 4.14 shows the sample holder with the sample, along with the groove for the wire connecting the sample to the potentiostat for the electrochemical tests. The holder was then secured on to a perspex tank of length 51.5 cm, breadth 33 cm, and depth of 11.5 cm with nylon screws at all four corners of the holder, ensuring the bath was kept leak proof.

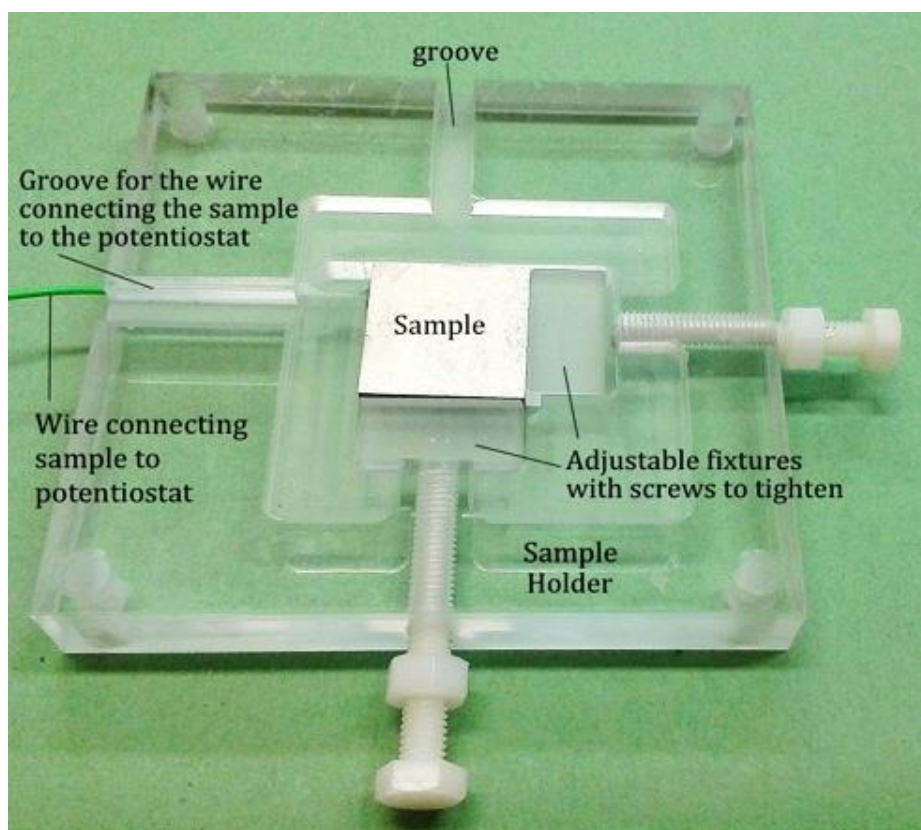


**Fig. 4.14:** Perspex sample holder with adjustable fixtures securing the sample of size 25 mm x 25 mm x 5 mm with perspex screws.

### **4.3.3 Experimental techniques used**

#### *4.3.3.1 Gravimetric measurements*

For the gravimetric measurements, a precision balance, Mettler Toledo XP205 (accurate to  $\pm 0.01$  mg) was used. The samples were first placed in a beaker of methanol and cleaned in an ultrasonic bath for 5-7 minutes. Then distilled water and methanol was used to again rinse the surface, before blow-drying it with compressed air. The samples were then weighed at least 5 times, with the weighing machine recalibrated before each measurement. The average of the 5 measurements were then taken.

After the cavitation erosion and corrosion experiments, each sample was once again cleaned in the ultrasonic bath, before rinsing with distilled water and methanol, and blow-drying with compressed air. The sample was then weighed again 5 times and averaged for mass loss, with the weighing machine calibrated before each measurement.

#### *4.3.3.2 Microstructural characterization*

The nature and properties of the sample materials as well as the corrosion products formed in a corrosive environment, and the effects of cavitation is said to determine the behaviour of the sample alloys as well as help characterize them. Hence, SEM images were required to be obtained after each tests to obtain the microstructural morphologies of each sample. The SEM imaging and microstructural characterisation was performed for one of each sample material that were also wet polished using 1200- and 4000- SiC abrasive papers, before further polishing to mirror finish with 6, 3 and 1  $\mu\text{m}$  diamond paste. The accelerating voltage used for the SEM analysis was 15 kV. Then both material samples were etched using Kalling's no. 2 etchant, which is a liquid solution of 100 mL conc. HCl, 100 mL ethanol and 5 g of cupric chloride, for 10 s in order to reveal the microstructures of the sample materials.

NAB generally does not require to be etched for examining under SEM since back-scattered imaging can reveal the microstructure with ease. However, when

etching the samples, care must be taken for NAB as copper deposition may occur in the etchant from repeated use of the same solution. Also, the etching of the samples need to be rapid as the etchant may destroy the oxide layer on the sample, and also the small phases of NAB may get dissolved if kept in too long. Whereas, the polishing and etching of the DSS samples need to be done quickly due to the high passivity of the material. Once the samples were etched they were taken for SEM imaging for microstructural characterisation. Etching was also done for cavitated samples, however it was found that not etching the cavitated samples was better in order to view SEM imaging of the cavitation features as the etchant tend to remove both the protective film and some of the intricate phases in the samples.

#### *4.3.3.3 Surface profilometry*

For the surface profilometry, Talysurf and Alicona were employed to study the scar profile and the irregularities of the scar. Both Talysurf and Alicona can be used to observe the cavitation erosion depths, the surface roughness of the test samples before and after the erosion experiments to analyse the extent of cavitation erosion, and Alicona especially may also provide useful information regarding mass loss due to cavitation by the means of volumetric analysis.

##### *4.3.3.3.1. Talysurf*

A Taylor Hobson Form Talysurf 120L profilometer was employed with a 10  $\mu\text{m}$  diamond stylus ( $\pm 2\%$  of measured value + 0.004  $\mu\text{m}$ ). The evaluation or transverse length that comprises of the total length of the measurement, taken laterally was set to little over the total length of the diameter to incorporate the uncavitated surface as a datum surface. Hence, an evaluation length of 20 mm was considered. The cut-off value was required to be taken between the range of 0.5-10, depending on the estimated roughness obtained from the initial run, the cut-off value of 0.8 was set as per the industry standards. Various measurements were taken across the diameter of the cavitation scar, both across vertically and then laterally. Samples were measured three times at three different orientations, horizontally, vertically, and across at 45° angle.

#### 4.3.3.3.2 Alicona

The second surface metrology instrument used was the optical 3D profilometer, Alicona InfiniteFocus Mark 4. Alicona is a non-contact optical micro-coordinate system that can generate 3D profiles due to very shallow depth of field, making measurements more detailed and accurate. It is used for form as well as roughness measurement for most kinds of surfaces and textures. Due to its high vertical resolution, complex measurements can be done such as steep flanks (up to 86°), steep angles, small radii and minute details such as within cavities. While, Talysurf generates the average roughness, with maximum valley depth and peak height, Alicona generates the actual 2D or 3D profile of the measured surface, hence the profile obtained using Alicona gives a better visual understanding of the surface texture. For the Alicona measurement, after conducting the cavitation tests on the samples for 1 h each, the two materials were analysed under the lens. Several images were captured at various different locations of the samples one at a time and their surface profiles were generated. The polished un-cavitated surface was considered as the datum (reference surface), and the minimum and maximum z-axis values were set by moving the microscope to and fro vertically within microns, covering all the asperities and valleys of the cavitated surface within the range.

#### 4.3.3.3.3. Methodology

The wear profiles were then compared between the samples tested in 3.5% NaCl solution and distilled water. Alicona was also employed to obtain volume loss to calculate the volumetric mass loss incurred after cavitation and compare that with the gravimetric mass loss measurement obtained using a precision weighing machine. For this, first, the volume of the eroded region was determined. Sample surface containing both the eroded as well as non-eroded regions was scanned, which can be done in three different ways as shown in

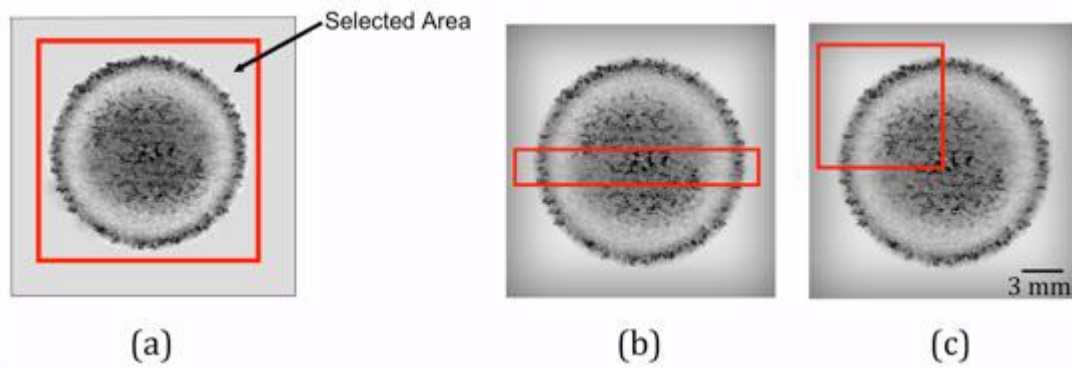


**Fig. 4.15:** Three ways of scanning the sample surface by selecting (a) the entire surface at once, (b) one strip at a time across the entire sample surface, or (c) a quarter of the eroded surface at a time.

Figure 4.15, which are either (a) the entire surface at once, (b) one strip at a time across the entire sample surface including the un-eroded regions, or (c) a quarter of the eroded surface at a time. Due to the high magnification required for the samples used, it was difficult to analyse the entire surface at once, and if lower magnifications were used, the data were compromised often manifesting different roughness values, causing loss of details. Whereas, scanning each strip gave the best results, but it was extremely time consuming and the software was prone to failure. Hence, the most efficient way was found to be the quarter system at a magnification of 50x. And the method of considering the uncavitated surface as the datum and setting the z-values by focusing the microscope up and down the z-axis to obtain the maximum depth of penetration and the highest protrusion above the datum on the material surface was used again. Finally, using the projected area and the depth of the profile, the volume was analysed automatically by Alicona. Figure 4.16 gives a schematic example of a small section of projected area under the datum line considered for volume loss.



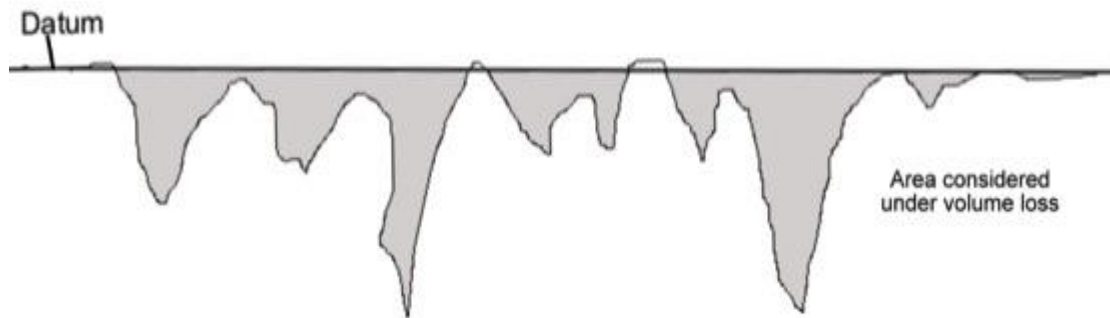


**Fig. 4.16:** *Schematics of a section of projected area under the datum line considered for volume loss.*

While both Talysurf and Alicona act as excellent surface metrology tools, the Talysurf is a stylus-based contact instrument that can be used to measure the average roughness, maximum valley depth and peak height, and maximum height of the profile; however, this may result in damage of any delicate surface film on the sample. If the measurements are performed as per ISO4287/4288/25178, and the instrument is calibrated, then it will be an accurate measurement. However, they both have a spatial resolution limitation, which generally determine their accuracy. For the Talysurf, the limiting factor is the resolution of the tip of the stylus, since deformations or features below a certain size will most certainly be passed over.

The spatial accuracy of Alicona, on the other hand, is limited by its vertical resolution. Alicona has the highest magnification of 1000x, which may sometimes cause loss of data while looking re-entrant topography of the surface. It is also often incapable of picking up the data from smooth surfaces and reflective surfaces since it can only plot the data points as long as it is able to perform a comparison between adjacent areas, and it may also plot false data such as spikes rather than void (black) data holes if illumination is poor, which should be avoided as much as possible. In case there are sediments, corrosion products, micro scratches and burrs existing on the sample surface then Alicona cannot differentiate and do selective volume loss, which again causes deviation from the result. It may also manifest its own roughness and waviness of the surface when



using lower magnification or highly reflective surface, which was applicable for the experiments undertaken. The absolute precision (and not the accuracy) limit for the Alicona is  $\sim 10$  nm, which can be extracted from the repeatability of the measurements on a sample.

#### ***4.3.4. Synergy experimental measurements***

##### *4.3.4.1. Cavitation erosion measurement*

The first test conducted was the pure erosion test using two different methods, first was by using distilled water as the medium, and second, by applying cathodic protection to the samples in 3.5% NaCl solution. Using the first method, the prepared samples were cavitated in 5 L of stagnant distilled water for 1 h.

For the pure erosion tests performed under cathodic protection, the sample materials were connected to the GAMRY Reference 600 potentiostat. Potentiostatic tests were conducted, where current was applied to the samples at constant potentials in order to make them more cathodic, which were attained from the polarisation curves of each material. The erosion test was conducted in 3.5% NaCl solution.

The weight of the sample was recorded both before and after each experiment for gravimetric analysis. The samples were also analysed under Alicona and Talysurf to obtain the surface roughness, mean depth of penetration, volume loss and the subsequent volumetric mass loss incurred. SEM was then finally used to examine the cavities formed.

##### *4.3.4.2. Electrochemical measurements*

For the pure corrosion test the samples of the test materials were prepared the same way as for pure erosion, by wet-polishing with 1200 and 4000 grit SiC paper, and connecting to GAMRY potentiostat, as shown in Figure 4.7, as mentioned in section 4.3.1. For the electrochemical tests, the samples were equipped with a metallic wire that could be connected to the potentiostat using the cell cables. The

electrochemical measurements included measuring the open circuit potentials (OCP), as well as the electrochemical impedance spectroscopy (EIS) with and without cavitation. OCP is the difference in the electrical potentials between the working electrode and the reference electrode when there is no current or potential existing in the cell.

The aqueous solution used for the electrochemical measurements was 5 L of 3.5% NaCl solution. EIS was also gathered for the two samples to understand the corrosion resistance behaviour of the materials. Impedance, like resistance, is a measure of the ability of a circuit to resist the flow of electrical current, but in more complex conditions. Hence, EIS is a method that measures or evaluates the energy dissipation properties of an electrochemical cell. Electrochemical impedance of an electrochemical cell is generally measured using small excitation signals by applying an AC potential to the cell and then measuring the current through it.

The parameters for conducting the OCP and EIS tests were set and the electrochemical experiments were performed in the Gamry Framework software, whereas and the data obtained were analysed in the Gamry Echem Analyst (software). Table 4.7 tabulates the parameters used for the tests. The total test time was set for 1 h and 10 min, 1 h for the OCP test and 10 min for the EIS test.

<b>Experimental parameters</b>	
Initial Frequency	100000 Hz
Final Frequency	0.1 Hz
AC Voltage	10 mV rms
Sample Area	6.25 cm <sup>2</sup>
Estimated impedance range	50 ohms
Total Time	4200 s

**Table 4.7:** *Parameters defined for the electrochemical experiments.*

The input sequence for the electrochemical test was:

Open circuit potential -> 10 s delay -> potentiostat EIS -> 10 s delay

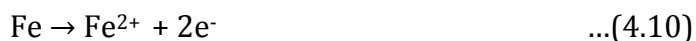
Once the sequence was set and the parameters given, the experiment was conducted. The sample materials were expected to undergo redox reactions during the electrochemical experiments as shown from Equations 4.8 - 4.11 taking place in the electrochemical cell.

Anodic reaction:

For NAB,



For DSS,



And cathodic reaction:

For both DSS and NAB,



In addition to that, potentiodynamic polarization technique was also employed at a scan rate of  $0.167 \text{ mV s}^{-1}$  under static conditions in order to obtain pure corrosion rate in terms of mass loss by applying Faraday's laws of electrolysis (further details in chapter 6 and 7). Electrochemistry, in conjunction with weight-loss analysis, was also conducted to determine the total material loss and also to try and understand the contribution of pure corrosion to the combined erosion-corrosion.

#### 4.3.4.3. Combined measurements

In the past, the electrochemical tests conducted by others used potentiodynamic polarization curves, EIS, linear polarization resistance, and the corrosion potential with and without cavitation. However, these experiments were all conducted

separately, with the samples tested for cavitation and then tested for corrosion. But to understand the corrosion behaviour of the materials while under cavitation, it was important to run the experiments at the same time, i.e. cavitation while being corroded electrochemically. Hence, the samples were tested for cavitation at OCP for the current research along with EIS. For the erosion-corrosion test the samples were cavitated in 5 L of 3.5% NaCl solution while kept under OCP for 1 h as explained in section 4.3.1, with the same electrochemical arrangements as pure corrosion tests (Figure 4.13). The corrosion test preceded cavitation test by 10 min, after which the cavitation was applied.

The samples were then analysed under both Alicona and Talysurf to obtain the surface roughness, maximum depth of penetration, volume loss and the subsequent volumetric mass loss incurred to compare with the pure erosion results. Again, the weights of the samples were recorded both before and after each experiment with a precision weighing machine.

#### 4.4. Summary

The chapter examines the ultrasonic vibratory cavitation experiment conducted to obtain the synergistic effects existing between the cavitation erosion and corrosion for the two sample materials used, DSS and NAB. The material properties of the two sample materials, given by the supplier, Lloyd's Register, were recorded and their chemical properties analysed theoretically.

An indirect ultrasonic cavitation rig, standardized under ASTM G-32, was used as the test rig that consisted of the sonotrode functioning at a frequency of 20 kHz, and peak-to-peak amplitude of  $80\text{ }\mu\text{m} \pm 0.2\text{ }\mu\text{m}$ . The ultrasonic vibratory sonotrode requires special attention for the design geometry and selection of the horn, which greatly affects the performance as well as the efficiency of the ultrasonic machining system depending on the type of function.

18 propeller material samples in total, 12 for NAB and 6 for DSS, were prepared

for pure erosion, pure corrosion and the combined erosion-corrosion tests. The samples surfaces were prepared by wet polishing with 800-, 1200- and 4000-grit SiC papers, then washed with distilled water and methanol before blow-drying. For oxide film formation, 6 NAB samples were left in individual zip-lock bags for a week, and 6 other samples were immersed in 3.5% NaCl solution for 3 months. The samples were then weighed using precision weighing machine before and after each tests for mass loss analysis. For SEM microstructure analysis, the samples were etched with Kalling's no 2 etchant. The samples were characterized before the tests under SEM and EDS to obtain their chemical composition and microstructural characteristics.

The samples were tested for cavitation erosion in 5 L of distilled water. They were then connected to GAMRY Reference 600 potentiostat for pure corrosion under 5 L of 3.5% NaCl aqueous solution using in-situ electrochemistry kept at OCP. And finally for cavitation erosion-corrosion, the test samples were tested in 3.5% NaCl solution with in-situ electrochemistry kept at OCP. The time period of each test was 1 h, and the test liquids used were distilled water for the pure erosion test, while the other two were conducted in 3.5% NaCl solution. The gap between the ultrasonic vibratory horn and the sample materials were kept constant at 2 mm. Several parameters such as temperature, pH, mass loss, surface roughness and volume loss were measured before and after each test. Precision weighing machine, Alicona, Talysurf and Scanning electron microscopy were used to obtain the various measurements required to conduct the experiment.

# **Chapter 5:**

## **Cavitation erosion-**

## **corrosion results and**

## **material characterization**

---

Following the methods described in chapter 4, this chapter aims to explain the results obtained after conducting intensive cavitation erosion and erosion-corrosion studies for the selected marine materials, i.e. 2205 DSS and as-cast NAB, using microstructural and topographical analyses. The cavitated materials were

observed under the optical microscope, analysed for roughness and wear scar profiles using Alicona and talysurf, and characterized microstructurally using SEM. Erosion rates for each material, and their material behaviour to 1 h of erosion and erosion-corrosion were also observed and reported.

It was observed that during the cavitation erosion tests the specimen surfaces as well as the titanium alloy probe tip were prone to erosion resulting in surface roughness and material loss. Figure 5.1 shows the before and after images of the probe tip under cavitation.

After 1 h of test the surface of the sonotrode seemed to erode, and the tip surface appeared to erode further with time. Probe tip erosion can lead to a significant reduction in the aggressiveness of the flow in the gap between the probe and specimen, affecting both the erosion rate and the pattern of erosion on the specimen, as also observed by Reddy [33]. Hence, to obtain consistent repetitive result, the probe tip was machined using lathe to 6  $\mu\text{m}$  surface finish before each test.

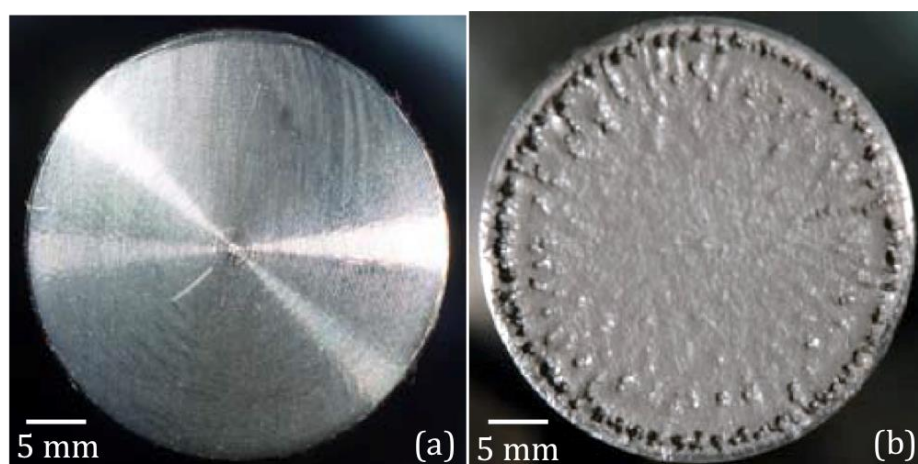


**Fig 5.1:** Sonotrode tip (a) Before the test; (b) After 5 h test.

For the erosion and erosion-corrosion test the test samples had three easily distinguishable damage regions on their cavitated surfaces with concentric rings of cavitated and non-cavitated regions formed around a centrally damaged area (see Figure 5.2).

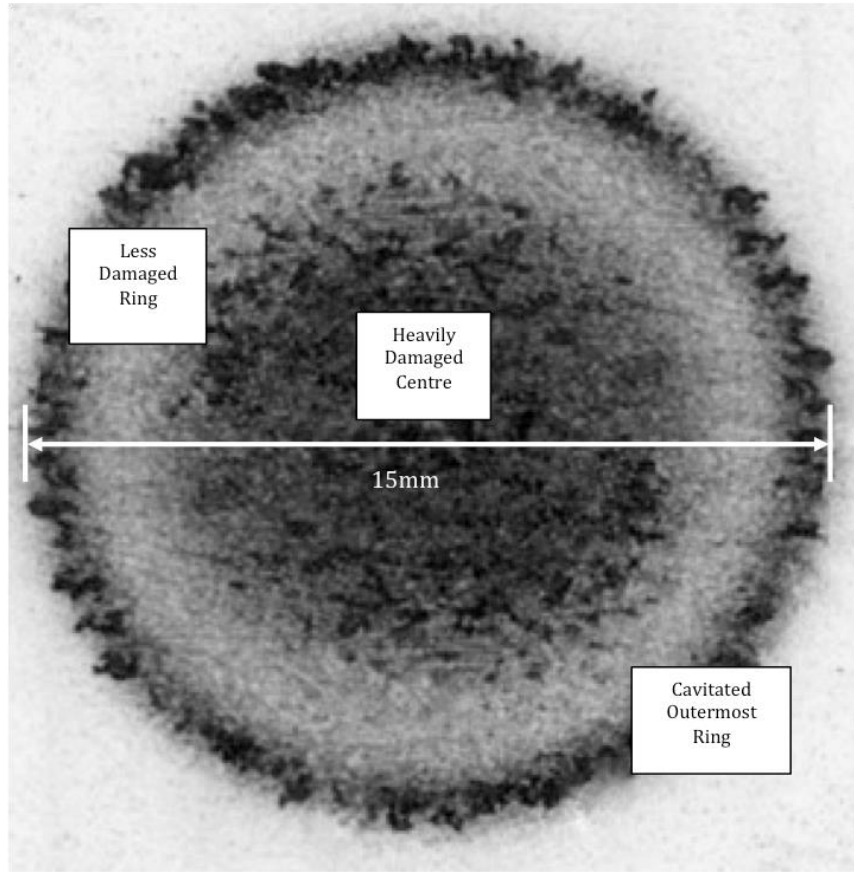


**Fig. 5.2:** *Cavitated surface of DSS in 3.5% NaCl solution after 1 h of test.*

This phenomenon may be attributed to the natural resonant frequency and the dynamic properties of the sonotrode itself [184]. Due to this, as stated by Chahine, Franc and Karimi in their laboratory tests of cavitation erosion, in an indirect cavitation method the cloud would have a cylindrical form between the sample and probe tip, and collapsed quasi-cylindrically [124]. As also observed and noted by Hammitt and Zhou in their study, 3 distinct wear regions were found on the samples; a central damage region, the transition region, and an outer most rim region. They found that the rim region did not have any noticeable damage due to insufficient pressure oscillations (edge effects), and the main concentration of the damage acted towards the centre of the sample because the pressure oscillation being greatest along the specimen's axis. Zhou also observed under SEM that the erosion in the transition region was not uniform [73].

The total cavitated diameter was measured to be 15 mm across for both the materials. The diameter of the ultrasonic probe tip being 15.9 mm, the erosion



area on the specimen was smaller than the cross section area of the probe itself by 0.9 mm. This difference could be attributed to the band of un-eroded area observed around the circumference of the probe. There was a gradual increment in the temperature of the liquid medium from 16 °C – 17 °C up to 22 °C after cavitation for a duration of 1 h for all the tests exhibiting the emission of heat during the cavitation process. This temperature rise could exponentially enhance the electrochemical reaction on the samples. However, the pH value remained constant between the ranges of 7.5 - 8.5, throughout the experiment.

### 5.1. Cavitation erosion rate

Erosion rate tests were conducted for DSS and air-formed filmed NAB samples each using the ultrasonic cavitation rig at 19.5 kHz frequency and  $80\text{ }\mu\text{m} \pm 0.2\text{ }\mu\text{m}$  peak-to-peak amplitude. The standoff distance between the test sample surface and the sonotrode tip was kept at 1 mm, based on the observations made by Reddy showing maximum mass loss at a standoff distance of 1 mm between the sample and the probe tip (see Figure 4.4). The samples were tested for 5 h each, and the trend obtained was compared with the typical trend obtained for cavitation erosion in Figure 2.7. The results were found to be consistent with the observations of Reddy in reference [33].

For both the materials, the overall trend was observed to be similar to the classical cavitation erosion S- curve. Figure 5.3 and 5.4 show the cumulative mass loss trends for DSS and air-formed oxide filmed NAB samples.

In Figure 5.3, it can be seen that initially DSS exhibited low erosion rate. Between 5800 s and 10800 s, NAB exhibited higher mass loss rate over DSS. However, upon reaching 10800 s (3 h), the DSS samples started to erode drastically, entering its accelerated erosion phase (as defined in Figure 2.7). The mass loss rate for DSS increased, surpassing the mass loss rate of NAB. Whereas, the air-formed filmed NAB sample displayed a more gradual erosion rate trend.

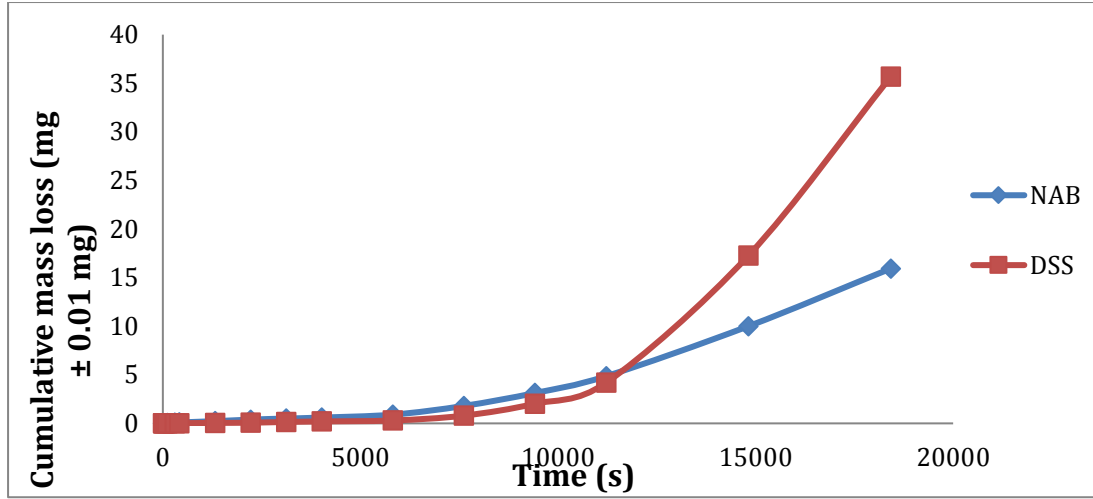


**Fig. 5.3:** Cumulative mass loss vs. time erosion wear rate for NAB and DSS in 3.5% NaCl solution under cavitation.

On closer inspection of the incubation period of the trends obtained (Figure 5.4), it was seen that DSS exhibited longer incubation period, lasting up to 60 s, than the air-formed filmed NAB sample, which had an incubation period of about 30 s. Although, it must be noted that the results obtained for the first 60 s of measurements were within the resolution of the balance ( $\pm 0.01$  mg).

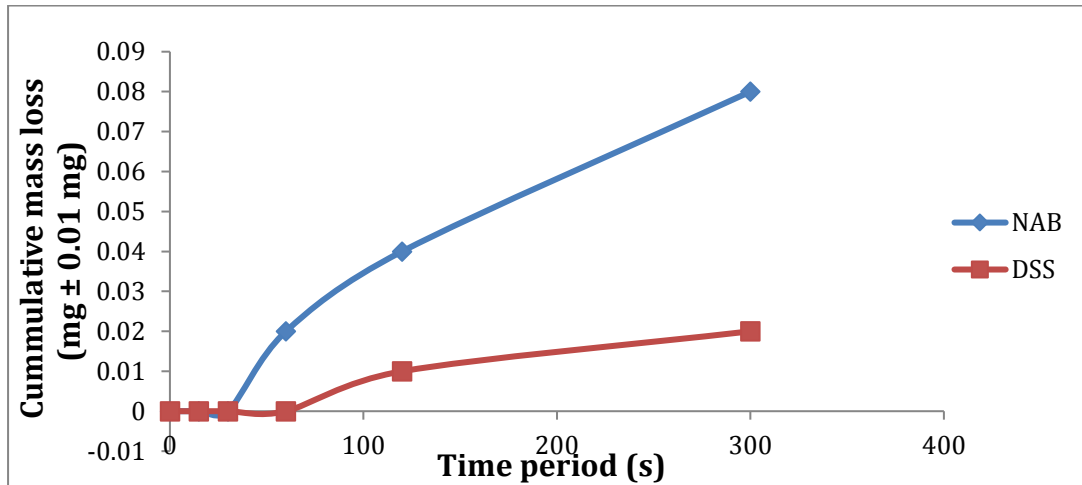


**Fig. 5.4:** Cumulative mass loss vs. time erosion wear rate during incubation period for NAB and DSS in 3.5% NaCl solution under cavitation.

Additionally, cumulative mass loss rate trends for DSS and NAB cavitated in 3.5% NaCl solution for 5 hours were also obtained. Figure 5.5 shows the cumulative

mass loss rate vs. time plot for over 5 h of cavitation in 3.5% NaCl solution. Also Figure 5.6 for the duration of the incubation period for DSS and air-formed oxide filmed NAB samples.

Similar to the cumulative mass loss trend, the cumulative mass loss rate vs. time curves showed that the trend-line for air-formed filmed NAB was more gradual compared to DSS. Whereas, DSS exhibited lower mass loss rate over time, until 3 h, after which the mass loss rate accelerated and surpassed that of NAB.

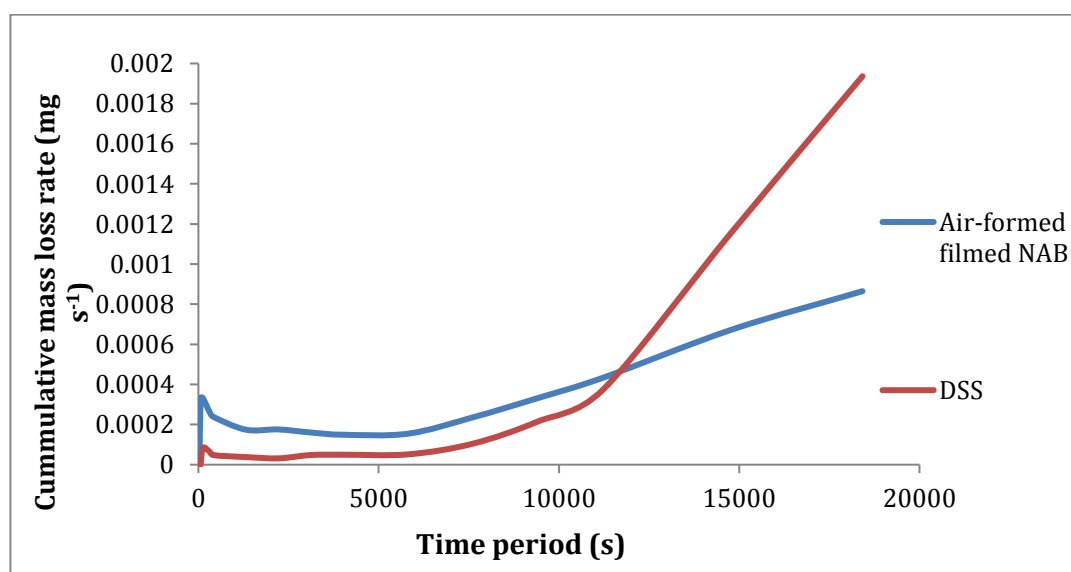


**Fig. 5.5:** Cumulative mass loss rate vs. time for NAB and DSS in 3.5% NaCl solution under cavitation.

Again, a closer analysis of the mass loss rate vs. time plot (Figure 5.6) during the incubation period was done. The cumulative mass loss rate was much lower for DSS, by a factor of 7, as compared to the air-formed filmed NAB sample, which had an incubation period of about 30 s. The mass loss rate for NAB, as seen, shows that the trend declined at a faster rate than the trend line for DSS, whereas DSS showed a more steady state erosion rate for the first 5000 s.

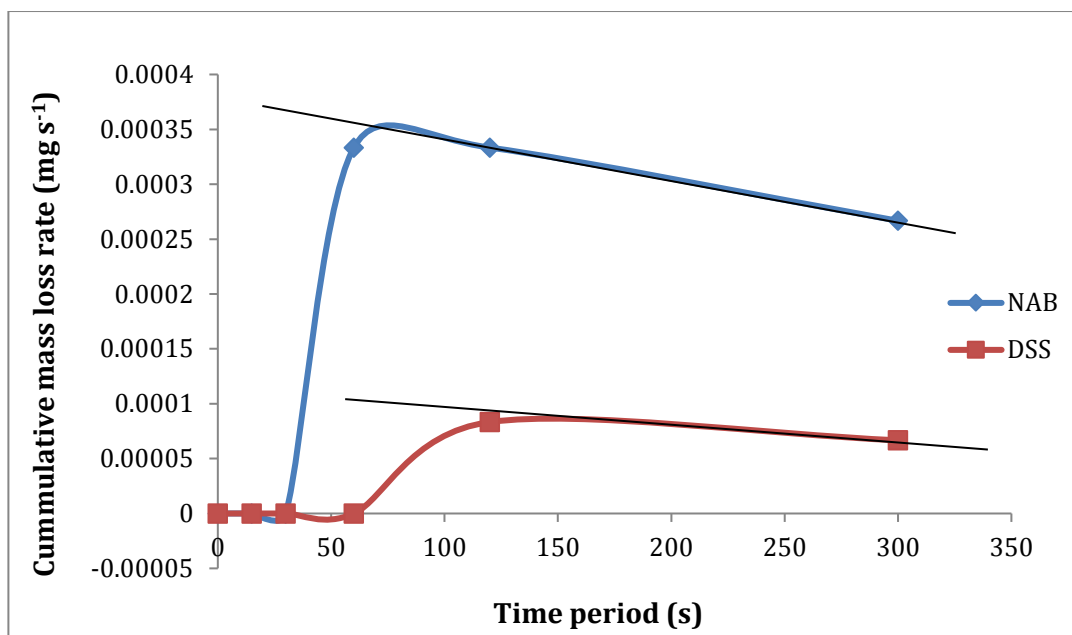


**Fig. 5.6:** Cumulative mass loss rate vs. time during incubation period for NAB and DSS in 3.5% NaCl solution under cavitation.

### 5.1.1. Nickel aluminium bronze

The periodic erosion rates for both air- and water-formed oxide filmed NAB samples were also recorded photographically via optical microscopy. From the pictures obtained, the gradual mass loss was observed in the form of increase in cavities, both in size and number, over the period of 5 h in 3.5% NaCl solution.

#### 5.1.1.1. Air-formed oxide filmed NAB

Figure 5.7 shows the optical image of a NAB sample after 1 week of air-formed oxide film formation, with distinct microstructures, before subjecting to cavitation in 3.5% NaCl solution.

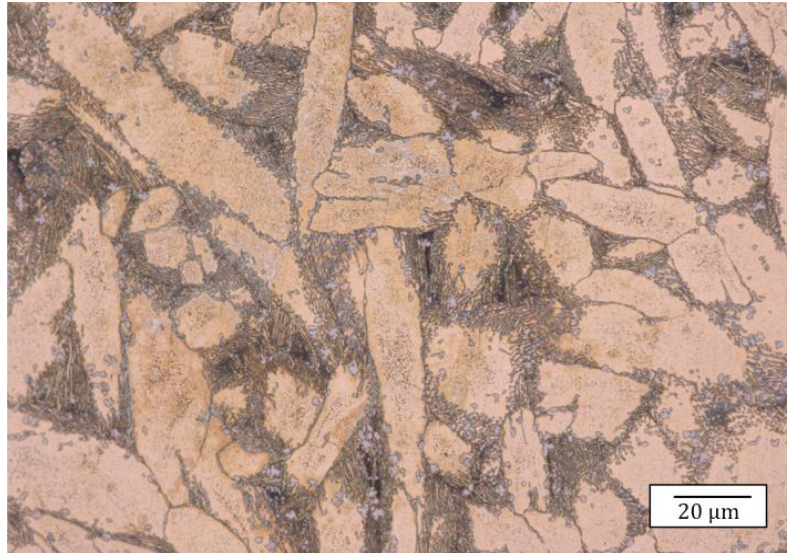


**Fig. 5.7:** *Microstructure of air-formed oxide filmed NAB before cavitation as seen under the optical microscope.*

Figures 5.8 (a)-(f) show the optical images of air-formed oxide filmed NAB surface under cavitation in 3.5% NaCl solution over time, taken from the centre of the erosion scar as this was the region of most aggressive damage, as observed in Figure 5.2. In Figure 5.8 (a) the sample microstructure was seen to have islands of light brown oxide layer, especially in the alpha phase regions, after 30 min of cavitation in 3.5% NaCl solution. This meant the removal of oxide layer from the sample surface especially from around the phase boundaries. After 1 h of cavitation, (as seen from Figure 5.8 (b)), the microstructure seemed to undergo cavitation erosion as well as selective phase attack at the phase boundaries.

On further cavitation, the cavities seemed to grow larger from 10  $\mu\text{m}$  to 80  $\mu\text{m}$  in size as the overall surface seemed to grow rougher over time after 2, 3, 4 and 5 h of cavitation (Figure 5.8 (c)-(f)). Figure 5.8 (e) seemed to have large cavities of about 40  $\mu\text{m}$  – 80  $\mu\text{m}$  in sizes after 4 h of cavitation, and the number of cavities seemed to increase by 5 h of cavitation, as seen in Figure 5.8 (f).

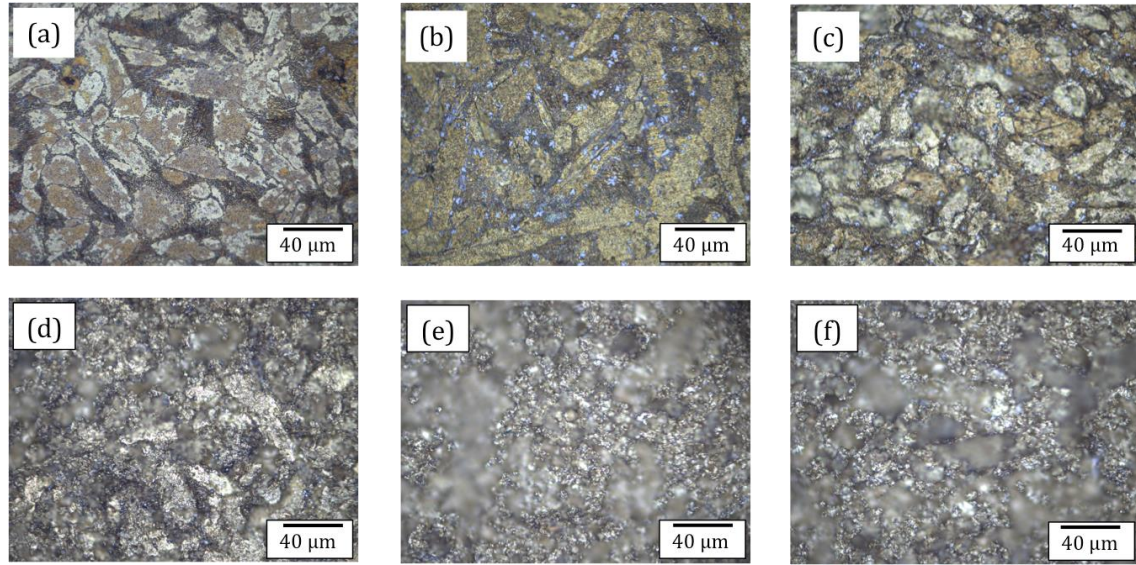


**Fig 5.8:** Optical images of the progression of cavities on the central region of the air-formed oxide filmed NAB after cavitation erosion for (a) 30 min, (b) 1 h, (c) 2 h, (d) 3 h, (e) 4 h, and (f) 5 h in 3.5% NaCl solution, showing the increasing roughness of the surface, and growth in cavity sizes with time.

#### 5.1.1.2. Water-formed oxide filmed NAB

Similarly, Figures 5.9 (a)-(f) show the optical images of water-formed oxide filmed NAB surface under cavitation in 3.5% NaCl solution over the time period of 5 h, again taken from the central region of the wear scar. Comparing to the uncavitated surface of NAB samples with protective water-formed oxide layer seen in Figure 5.7 (b), the sample surface was seen to become perforated after 30 min of exposure to cavitation in 3.5% NaCl solution, as seen in Figure 5.9 (a). This indicated initiation of pits of sizes 5  $\mu\text{m}$  – 10  $\mu\text{m}$ . After 1 h of cavitation, the protective oxide film was partially removed from the sample surface, as seen from Figure 5.9 (b), whence the microstructure of NAB began to appear distinguishable.



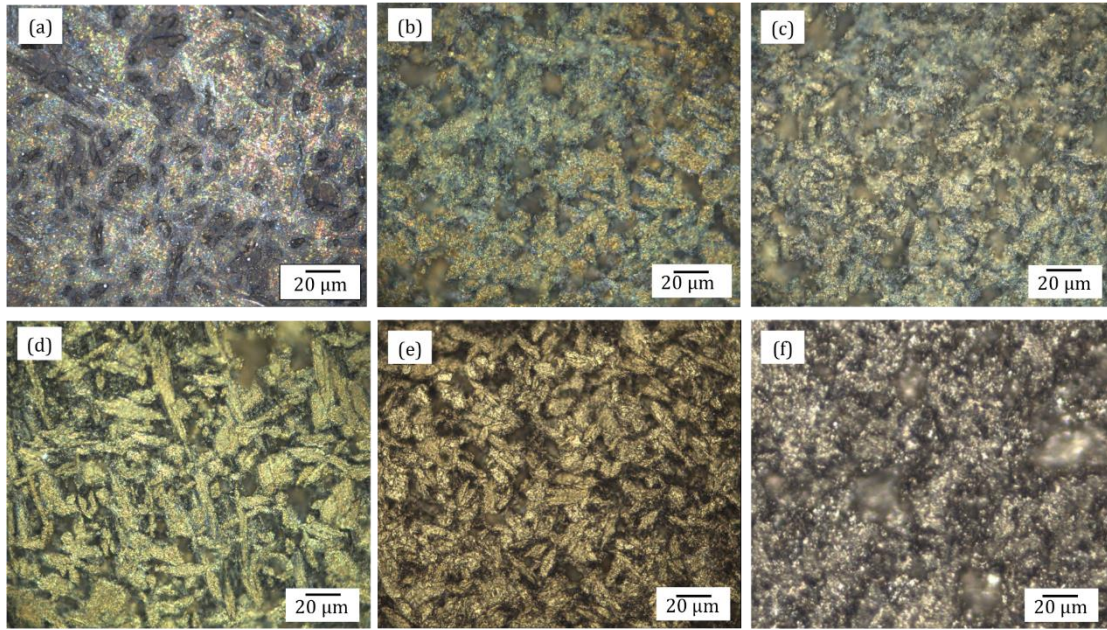


**Fig 5.9:** Optical images of the central region of NAB with water-formed oxide layer subjected to cavitation erosion for (a) 30 min, (b) 1 h, (c) 2 h, (d) 3 h, (e) 4 h, and (f) 5 h in 3.5% NaCl solution, showing the periodic removal of oxide film, increasing roughness of the surface, and growth in cavity sizes with time.

After 2 h of cavitation erosion, the substrate microstructure seemed to become more and more distinguishable, with clear phase boundaries (Figure 5.9 (c) and (d)). The prolonged period of oxide removal is attributed to the mechanical properties of the oxide layer. Aluminium oxide is ceramic-like hard material, generally harder than the NAB substrate, between 1400 HB – 1800 HB, with up to 630 MPa UTS [206]. However, it is also much more brittle than the substrate. Further removal of the protective oxide layer, along with formation of 20 μm – 40 μm large cavities in size occurred after 4 h of cavitation. The number of cavities seemed to increase, and also, there was clear selective phase attack observed at the phase boundaries (Figure 5.9 (e)).

Once the protective oxide layer was completely removed, there was a rapid erosion of the substrate and the sample surface appeared to undergo drastic erosion, and the surface appeared much rougher than at 4 h, with the microstructure no more distinguishable, see Figure 5.9 (f).

### 5.1.2. Duplex stainless steel

The optical images of the DSS microstructure before subjecting to cavitation erosion is shown in Figure 5.10, with distinct ferrite and austenite phases in the duplex microstructure of DSS.

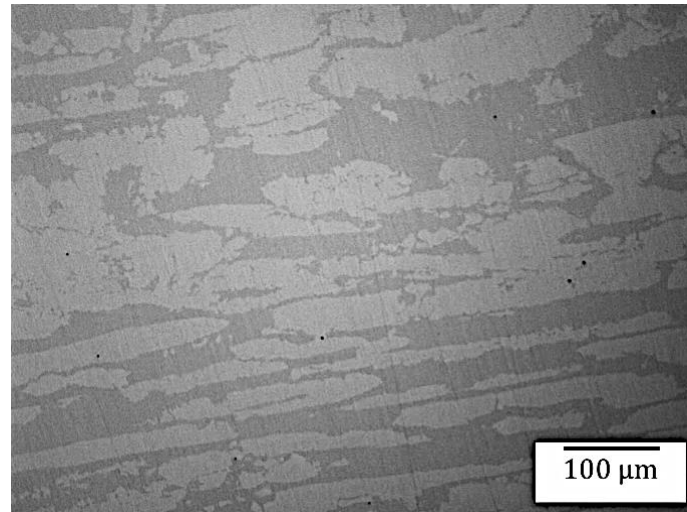


**Fig. 5.10:** Microstructure of 2205 duplex stainless steel.

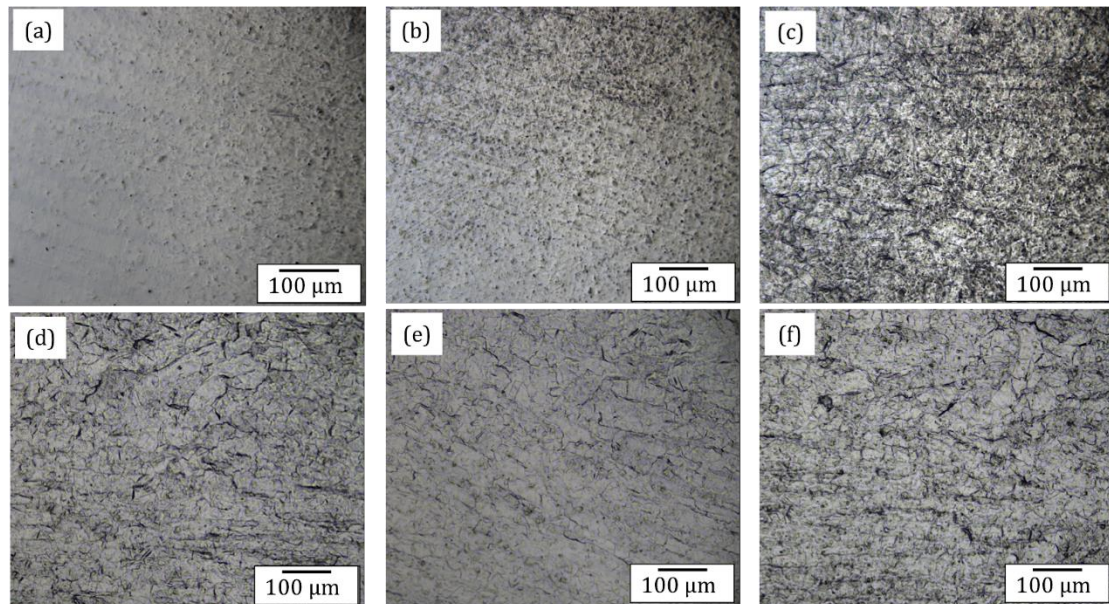


**Fig 5.11:** Optical images of the central region of a DSS sample subjected to cavitation erosion for (a) 30 min, (b) 1 h, (c) 2 h, (d) 3 h, (e) 4 h, and (f) 5 h in 3.5% NaCl solution, showing the increasing roughness of the surface, and growth in cavity sizes over time.



To obtain the erosion mass loss rate for DSS, three samples were prepared for 5 h of erosion with mass loss measurement taken at periodic intervals of 30 min. Photographic records of the evolving surfaces are shown in Figure 5.11 for test conducted for 30 min, 1, 2, 3, 4 and 5 h, consecutively. Figure 5.11 (a)-(f) show the cavitated surfaces of the DSS samples, eroded over a period of 5 h in 3.5% NaCl solution. The images were taken from the central region of the wear scar. As seen from Figure 5.11 (a), after 30 min of cavitation in 3.5% NaCl solution, the sample surface seemed to have light erosion, with the surface roughness increasing from 52 nm before cavitation to 100 nm (as observed under Alicona). In Figure 5.11 (b) and (c) the surface underwent further deformation due to the violent implosion of cavitation bubbles, starting from the phase boundaries with formation of cavities. The surface roughness, measured using Alicona after 1 h of cavitation in 3.5% NaCl solution was found to be 164 nm.

Over the next course of 5 h cavitation in 3.5% NaCl solution, the surface roughness was observed to increase drastically up to about 9  $\mu\text{m}$  as measured after 5 h of cavitation, with increment in the cavity sizes. The cavitation was seen to affect the ferritic-austenitic phase boundaries, with visible deformation of the boundaries (which appeared to be plastic in nature). As seen from the erosion rate graph (Figure 5.3), after 3 h of cavitation, the surface appeared to undergo drastic change, with large cavities, up to 100  $\mu\text{m}$ , and higher surface roughness manifesting on the surface (Figure 5.11 (d)-(f)). This indicated the accelerated material loss of DSS once it reached the accelerated erosion rate period.

## 5.2 Surface profilometry

### 5.1.1 Talysurf surface profilometry

After conducting the cavitation tests on the DSS and air-formed filmed NAB samples, the surface profilometry and average roughness ( $R_a$ ), and mean depth of penetration (MDP) were measured using both Alicona and Talysurf. Data was not taken for water-formed filmed NAB samples in order to avoid damaging the oxide

surface due to the contact nature of the measurement.

For Talysurf measurement, as mentioned in section 4.3.3.1, 6 samples of each material were measured three times at three different orientations, horizontally, vertically, and across at 45° angle. Figure 5.12 shows the surface roughness and individually labelled damage regions of DSS sample after undergoing cavitation in distilled water obtained using Talysurf [18].

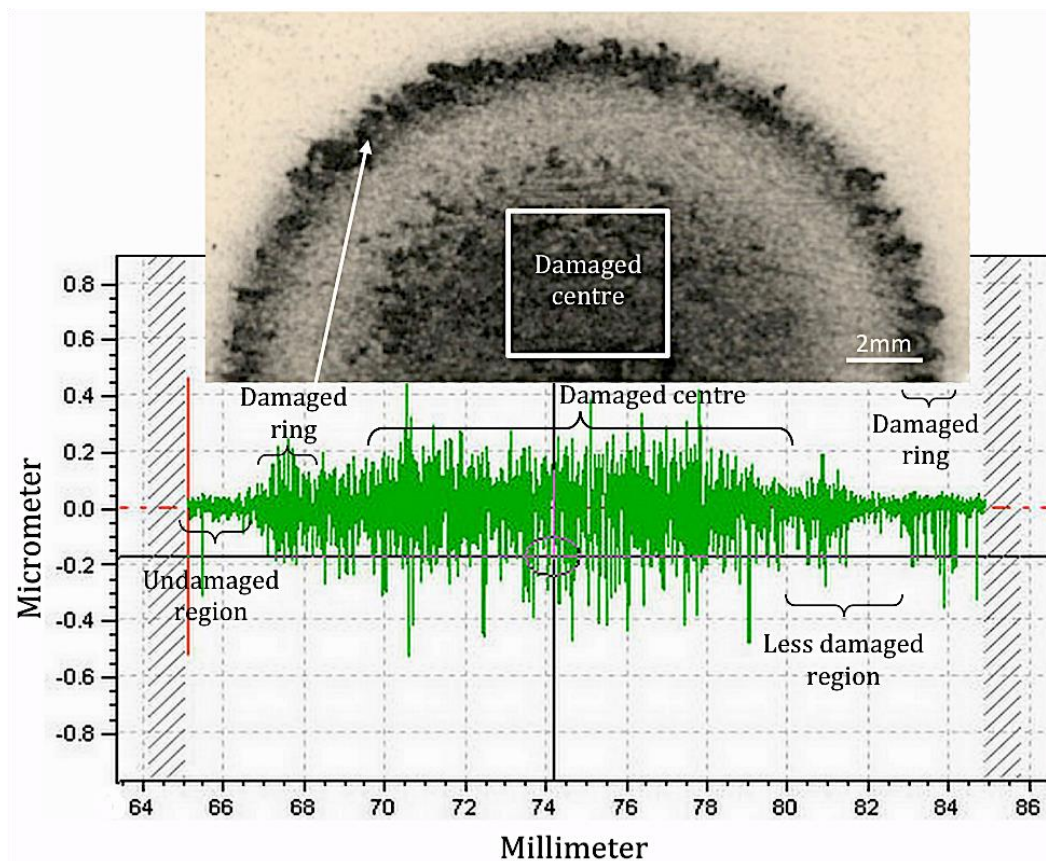


**Fig. 5.12:** Talysurf surface roughness profilometry at the centre of the cavitated surface of DSS in distilled water after 1 h of test [18].

Taking the average from the measurements, the average roughness ( $R_a$ ) and the quadratic mean square ( $R_q$ ) roughness were tabulated in Table 5.1.

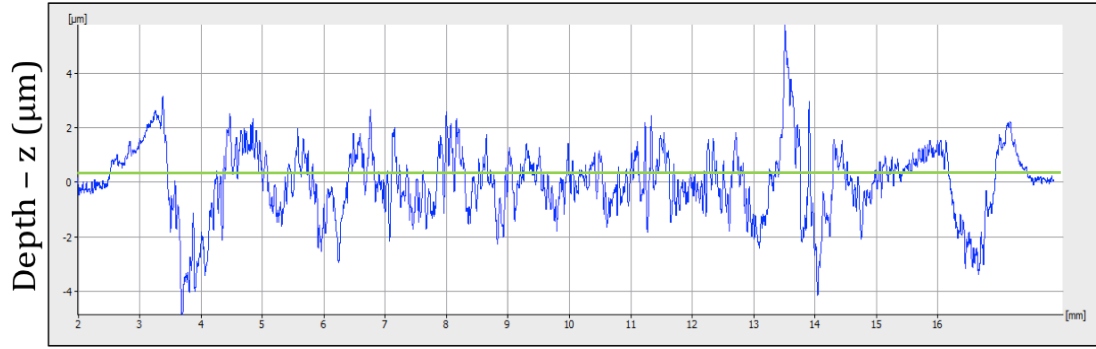
Sample Material	Pre-cavitation $R_a$ (in nm)	$R_a$ , (in $\mu\text{m}$ )		$R_q$ , (in $\mu\text{m}$ )	
		Distilled water	3.5% NaCl sol.	Distilled water	3.5% NaCl sol.
Air-formed oxide-filmed NAB	$49 \pm 5$	0.109 $\pm 0.004$	0.194 $\pm 0.003$	0.243 $\pm 0.003$	0.270 $\pm 0.002$
Duplex Stainless Steel	$52 \pm 5$	0.152 $\pm 0.002$	0.180 $\pm 0.004$	0.183 $\pm 0.002$	0.250 $\pm 0.003$

**Table 5.1:**  $R_a$  and  $R_q$  for NAB and DSS measured after 1 h of cavitation using Talysurf.

### 5.1.2 Alicona surface profilometry

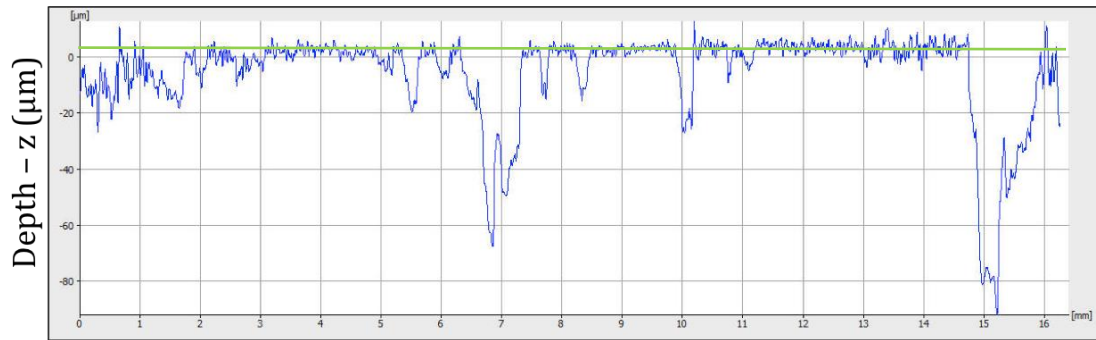
The second surface metrology instrument used was Alicona InfiniteFocus Mark 4. It was found that due to the mirror polish given to the samples before the test and since both the samples showed good resistance to erosion as well as corrosion, the magnification was kept at the highest value of 1000x under polarised light in order to get the best results. As mentioned in section 4.3.3.2, the polished uncavitated surface was considered as the datum, and the z-axis values (min and max) were set by moving the microscope to and fro vertically within microns, covering all the asperities and valleys of the cavitated surface within the range. The surface topography was then obtained by scanning the sample surface laterally across the diameter. The green line denotes the datum for each profile.

Figure 5.13 (a) shows the wear profile of DSS cavitated for 1 h in distilled water. From the profile it can be seen that the DSS cavitated in 3.5% NaCl solution (Figure 5.13 (b)) had comparatively higher erosion profile and hence, higher surface roughness as tabulated in Table 5.2.



Path length (mm)

(a)



Path length (mm)

(b)

**Fig. 5.13:** Wear scar profile of DSS after cavitation in (a) distilled water, and (b) in 3.5% NaCl solution for 1 h obtained using Alicona 3D profilometer.

Figures 5.14 (a) and (b) show the wear profile of air-formed oxide filmed NAB sample cavitated for 1 h in distilled water, and in 3.5% NaCl solution, respectively. Again, as seen for DSS, the wear profile of the air-formed oxide filmed NAB cavitated in 3.5% NaCl solution (Figure 5.14 (b)) exhibited much higher erosion profile (almost double), compared to the profile obtained in distilled water, and hence, higher surface roughness (also tabulated in Table 5.2). From the scar profiles obtained, it was evident that air-formed filmed NABs underwent more erosion as compared to the DSS samples.

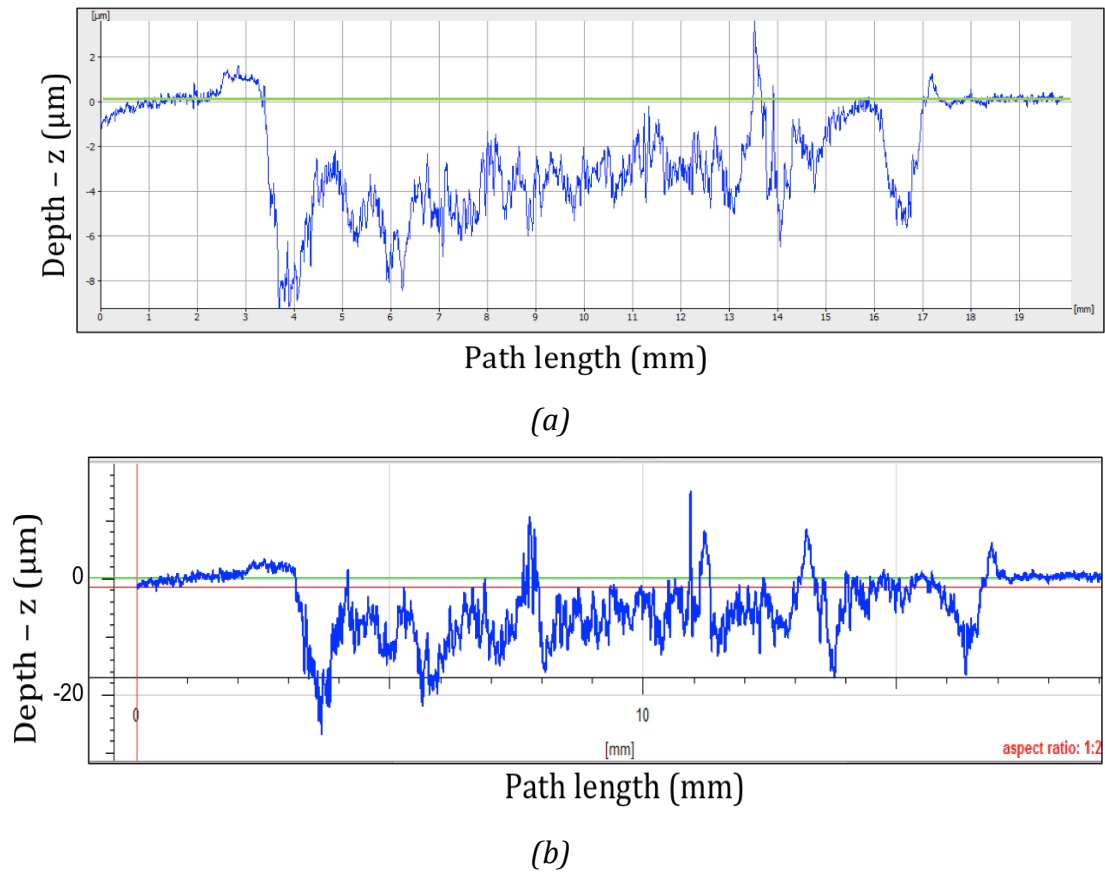


**Fig. 5.14:** Wear scar profile of air-formed oxide filmed NAB after cavitation in (a) distilled water, and (b) in 3.5% NaCl solution for 1 h obtained using Alicona 3D profilometer.

Volume analysis and MDP methods were only used for DSS and air-formed filmed NAB samples since water-formed filmed NAB samples could not be accurately analysed, especially due to the thick layer of porous and fragile oxide film. Table 5.2 tabulates the measured values of  $R_a$ , MDP and volume loss for the air-formed oxide filmed NAB and DSS samples under each condition.

Material used	Average surface roughness $R_a$ (in $\mu\text{m}$ )			Mean depth of penetration (in $\mu\text{m}$ )		Measured volume loss (in $\text{mm}^3$ )	
	Pre-cavitation	Distilled water	3.5% NaCl sol.	Distilled water	3.5% NaCl sol.	Distilled water	3.5% NaCl sol.
Air-formed filmed NAB	0.063 $\pm 0.003$	0.153 $\pm$ 0.003	0.165 $\pm 0.004$	0.645 $\pm 0.005$	0.955 $\pm 0.005$	0.115 $\pm$ 0.005	0.169 $\pm$ 0.003
DSS	0.056 $\pm 0.005$	0.113 $\pm$ 0.003	0.163 $\pm 0.003$	0.460 $\pm 0.002$	0.598 $\pm 0.005$	0.081 $\pm$ 0.005	0.106 $\pm$ 0.004
Water-formed filmed NAB	0.238 $\pm 0.100$	2.000 $\pm 0.500$	5.500 $\pm 1.50$	-		-	

**Table 5.2:** Average roughness, mean depth of penetration and volume loss measured after 1 h of cavitation using Alicona.

The average surface roughness values ( $R_a$ ) of the five water-formed oxide film on NAB samples were measured to range between 140 nm – 240 nm before cavitation. And it was measured to be about  $2.0 \mu\text{m} \pm 0.50 \mu\text{m}$  for samples subjected to cavitation under pure erosion, and about  $5.50 \mu\text{m} \pm 1.50 \mu\text{m}$ .

## 5.3 Microstructural analysis

### 5.3.1 Cavitation results

#### 5.3.1.1 Duplex stainless steel

As observed under optical as well as electron microscopes, the morphologies of DSS under both distilled water and NaCl solution were almost the same with no visible corrosion product (Figure 5.15 (a) and (c)).

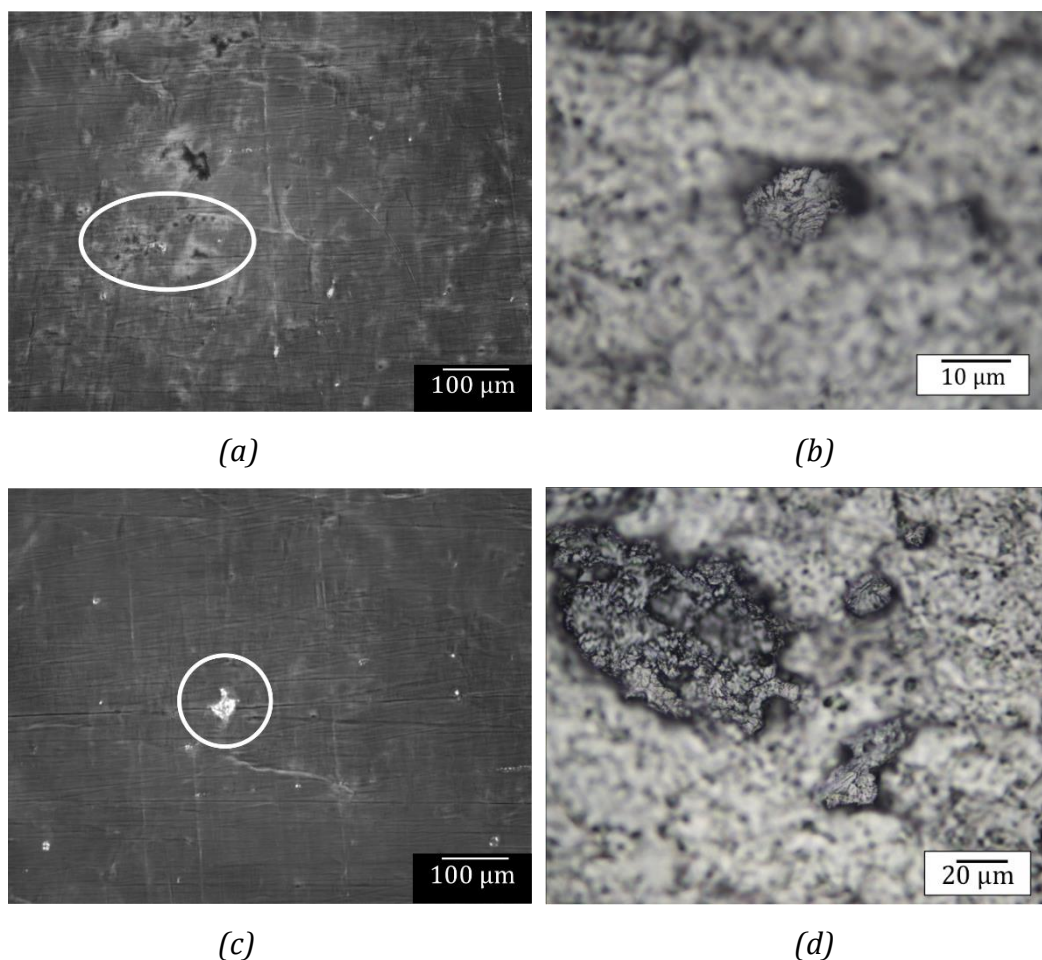


**Fig. 5.15:** Cavitated region of DSS obtained under an optical microscope (a) in distilled water; (b) cavity of 10- $\mu\text{m}$  size under distilled water after 1 h; (c) in 3.5% NaCl solution; and (d) 20  $\mu\text{m}$  – 50  $\mu\text{m}$  cavities obtained in 3.5% NaCl solution after 1 h.

The surface of the sample seemed to undergo plastic deformation due to the rapid and constant hammering of collapsing bubbles, making the surface rough within 1 h. The cavity sizes formed varied from 5  $\mu\text{m}$  – 10  $\mu\text{m}$  in size under distilled water. However, on comparing the cavity sizes with those obtained under 3.5% NaCl solutions, the cavities formed under the combined cavitation erosion-corrosion conditions were increased in size, up to 20  $\mu\text{m}$  – 50  $\mu\text{m}$ , as seen in Figure 5.15 (c) and (d) [18].

The roughness of the cavitation-eroded surface may be attributed to plastic deformation, material extrusion, and possible work hardening of the surface. The SEM analysis of the cavitated surface showed that the combined cavitation erosion-corrosion attack was rather selective, with cavities attacking the ferrite-



austenite grain boundaries, extending into the soft ferritic phases as obtained after cavitation in 3.5% NaCl solution after 1 h, as seen in Figure 5.16. From this, it was confirmed that erosion of DSS was enhanced due to corrosion, as demonstrated via microstructural analysis. On closer analysis of the sample surface, i.e. at a higher magnification, several small pits were seen especially attacking the ferritic matrix, with cavities seen at the grain boundaries and polish lines.

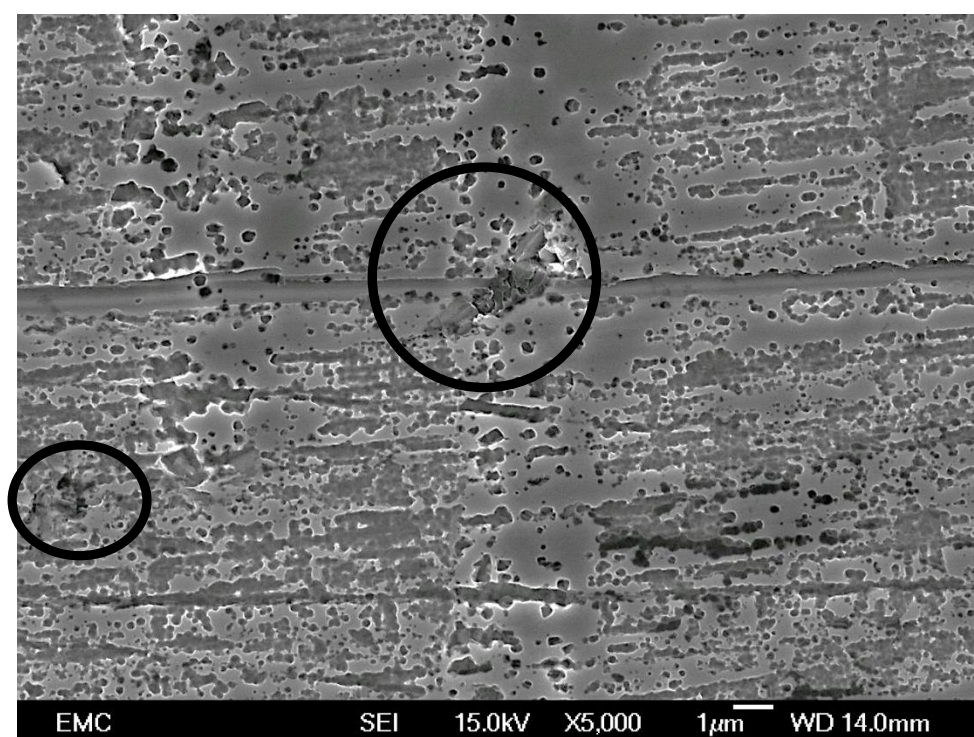


**Fig. 5.16:** The SEM image of DSS surface after 1 h of cavitation in 3.5% NaCl solution with pitting and cavities of sizes  $5\ \mu\text{m}$  –  $10\ \mu\text{m}$ .

Also, Figure 5.17 (a) and (b) show clear ductile striation patterns on the surface of a  $50\text{-}\mu\text{m}$  large cavity, obtained by cavitating the DSS sample for 1 h in 3.5% NaCl solution. This indicated the existence of plastic deformation, especially due to fatigue failure or cyclic mechanism of cavitation erosion, which have also been observed in previous studies by Gould [224].



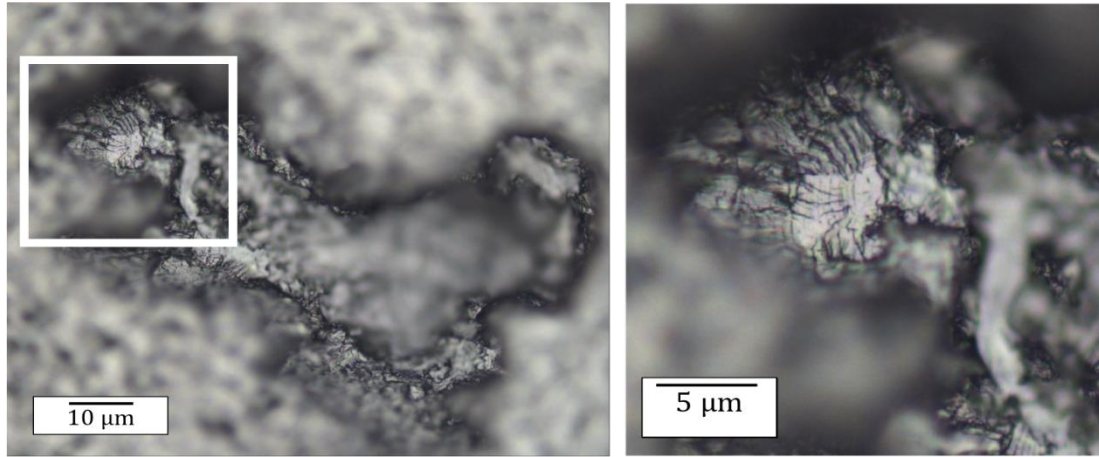


**Fig. 5.17:** Striation marks within the cavity of the size 100  $\mu\text{m}$  obtained by after 1 h cavitation in 3.5% NaCl solution.

Figure 5.18 shows a 40  $\mu\text{m}$  x 70  $\mu\text{m}$  large cavity formed in DSS under the 3.5% NaCl solution, where ductile failure can be seen in the form of extrusion, especially of the austenitic phase, at the cavity boundary. Also visible are tiny microcracks and cleavage-like facets in the magnified image in Figure 5.18 (b).

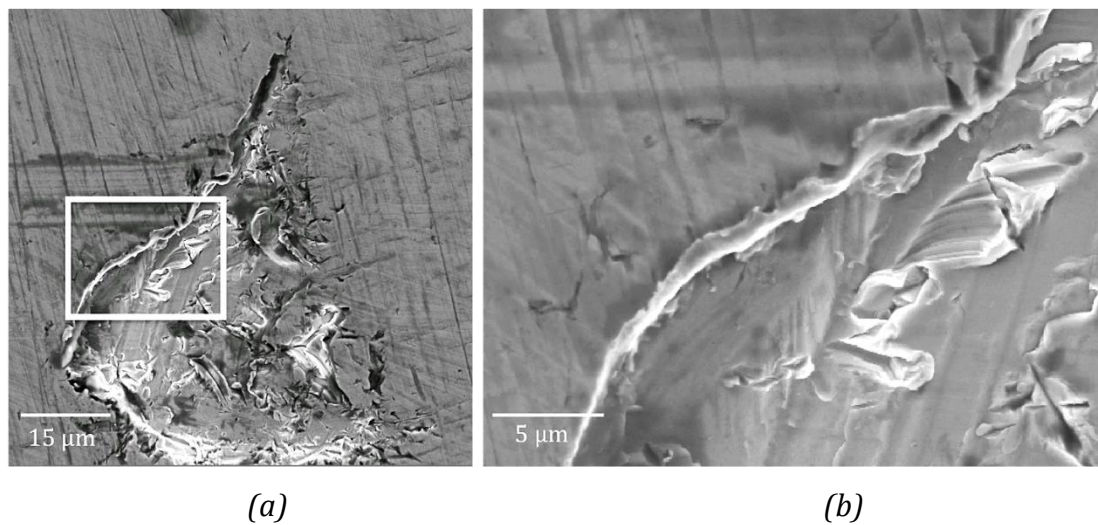


**Fig. 5.18:** SEM image of (a) plastic deformation at cavitation damaged edge for DSS in 3.5% NaCl solution, (b) detailed magnified image of plastic deformation at the cavity edges in (a) [18].

Transverse sectioning of DSS is shown in Figure 5.19, as obtained after cavitation erosion-corrosion for 1 h in 3.5% NaCl solution. The figure shows that most of the ferritic (dark) matrix were eroded away, leaving the (light) austenitic grains onto

the surface. Ferrite is more easily eroded than austenite. The smaller amount of ferrite remaining at the surface of both duplex stainless steels is an indication of the susceptibility of the ferrite to cavitation erosion. This has also been observed for other grades of duplex and super duplex stainless steels by Kwok, Man and Cheng [225], [226].



**Fig. 5.19:** Transverse of the DSS cavitated in 3.5% NaCl solution for 1 h.

#### 5.3.1.2 Air-formed oxide filmed NAB

As seen in the SEM morphology of air-formed filmed NAB, the microstructure exhibited the lighter  $\alpha$ -phase with dark dendritic intermetallic  $\kappa_{III}$  phases distributed in the copper rich  $\alpha$ -matrix, and many visible Fe-rich  $\kappa_I$  and  $\kappa_{II}$  precipitates around the boundaries. Interfaces between the matrix, intermetallic and grain boundaries are generally the weak (softer) regions in the microstructure of metallic materials that are more likely attacked by the cavitation. Also, considering the galvanic corrosion of multiphase alloys, the NAB is seen to undergo selective phase attack at the narrow band of grain boundaries between the  $\alpha$ - $\kappa_{III}$  lamellar phase boundary, from there spreading on to the  $\kappa_{III}$  phase itself [213], [214].

From the cavitation tests conducted for the air-formed oxide filmed NAB in distilled water, as well as 3.5% NaCl solution, microstructural characterisations were obtained via SEM. Figure 5.20 (a) shows the morphology of NAB under cavitation in distilled water. Small cavities of sizes 10  $\mu\text{m}$  – 30  $\mu\text{m}$  were found in the grain boundaries (see Figure 5.20 (b)) as it was established that the soft  $\alpha$ -matrix, especially surrounding the hard iron-rich  $\kappa$  phases, seemed to be most vulnerable to cavitation attack. The  $\kappa$ -precipitates and precipitate-free  $\alpha$ -zones did not suffer any visible cavitation after 1 h of cavitation test in distilled water, as also reported in ref [18].

Comparatively, for the cavitation erosion-corrosion test in 3.5% NaCl solution, the SEM image of cavities were recorded to be much larger ranging between 50  $\mu\text{m}$  – 80  $\mu\text{m}$ , showing selective phase attack at the  $\alpha$ - $\kappa$  phase boundaries leaving  $\kappa_I$  globules and  $\kappa_{III}$  lamellar phases exposed, seen in Figure 5.20 (c).

Figure 5.20 (d) shows the magnified image of one of the cavities on NAB tested in 3.5% NaCl solution. It was also found that the materials underwent selective cavitation erosion-corrosion attack in 3.5% NaCl solution at the  $\alpha$ - $\kappa_{III}$  phase boundaries as seen in Figure 5.20 (c) and (d). Hence, the regions with high lamellar  $\kappa_{III}$  phases were most susceptible. Also seen in Figure 5.20 (d) are  $\kappa$ -phases exposed due to the surrounding soft  $\alpha$ -phase eroded away [202], [203].

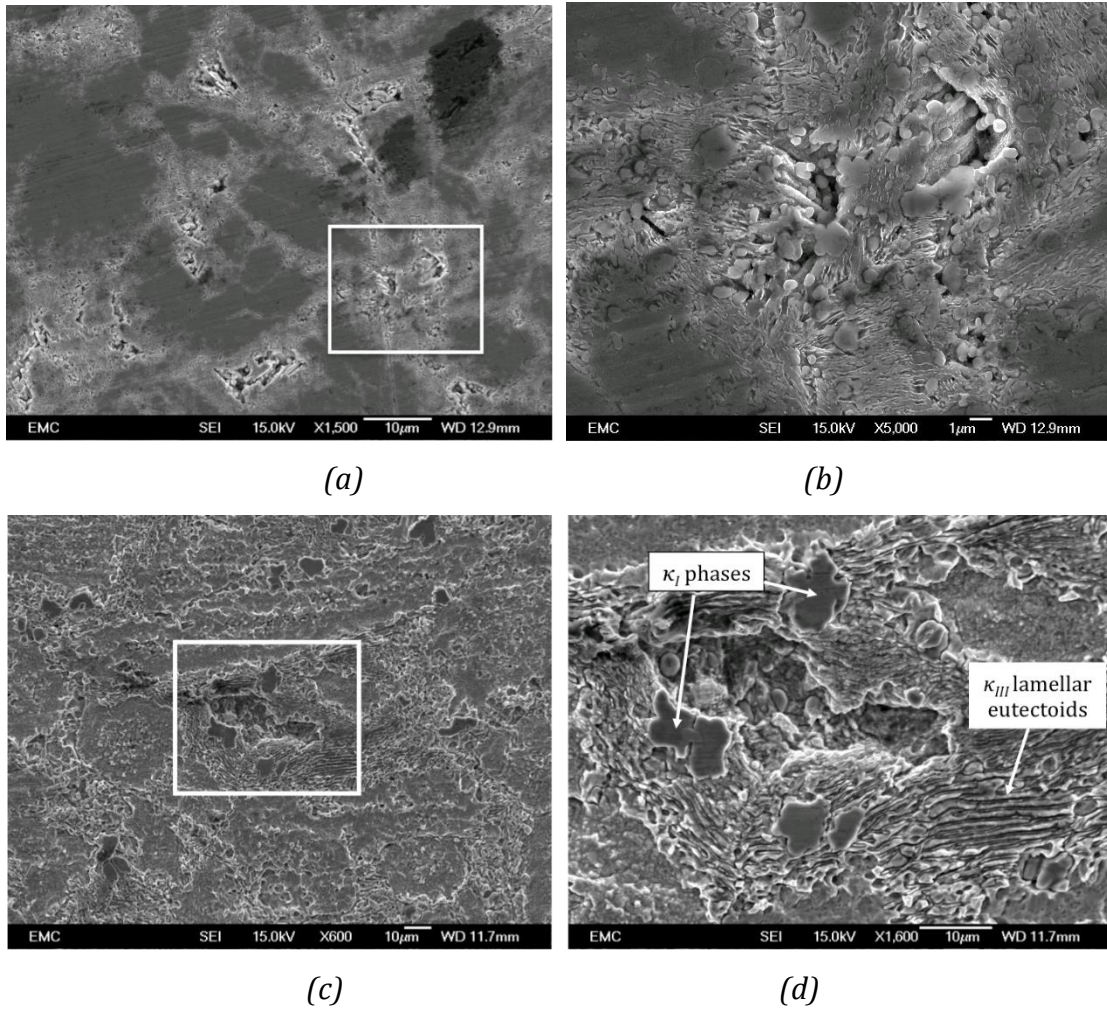


**Fig. 5.20:** SEM images of (a) small boundary erosion on air-formed filmed NAB at a magnification of 1500x in distilled water; (b) shows the magnified image of the cavities of size 10-μm at the selected area in (a); (c) SEM image of a 50-μm large cavity on the sample surface undergone cavitation erosion-corrosion in 3.5% NaCl solution; and (d) the magnified image of a cavity in (c) showing selective phase attack at the  $\alpha$ - $\kappa$  phase boundaries leaving  $\kappa_I$  globules and  $\kappa_{III}$  lamellar phases exposed [202], [203].

Many factors may contribute to the results seen, such as the softer composition of the  $\alpha$ -phase compared to much harder intermetallic precipitates, suggesting the  $\alpha$ -phase to be more susceptible to cavitation erosion. To understand the microstructural behaviour of NAB, the tested samples were etched with Kalling's no. 2 etchant, and then observed under the SEM [202].



Selective phase grain boundary attack was observed, which could indicate that electrochemical dissolution within the structure may contribute in the cavitation damage. Another reason for the selective attack may be due to the cathodic behaviour of Fe-rich phase when compared with the  $\alpha$ -phase which may induce galvanic corrosion. In addition to that, little spherical globules were found to have formed around the cavities that were verified under EDS to comprise of  $\kappa_{IV}$  phase as shown in Figure 5.21 [202].

For further characterization of the cavities, transverse sectioning of the samples were done, and observed under the SEM. Figure 5.21 (a) and (b) show the transverse cavitation erosion pattern on the surface after 1 h of testing in distilled water, detailing a cavity formed due to the erosion of the  $\alpha$ -phase at the  $\alpha$ - $\kappa$  phase boundary [202].

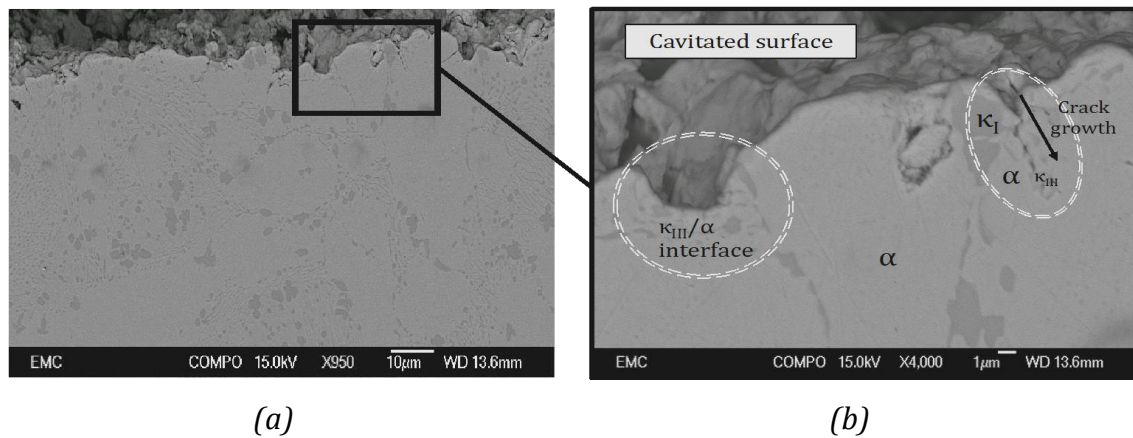
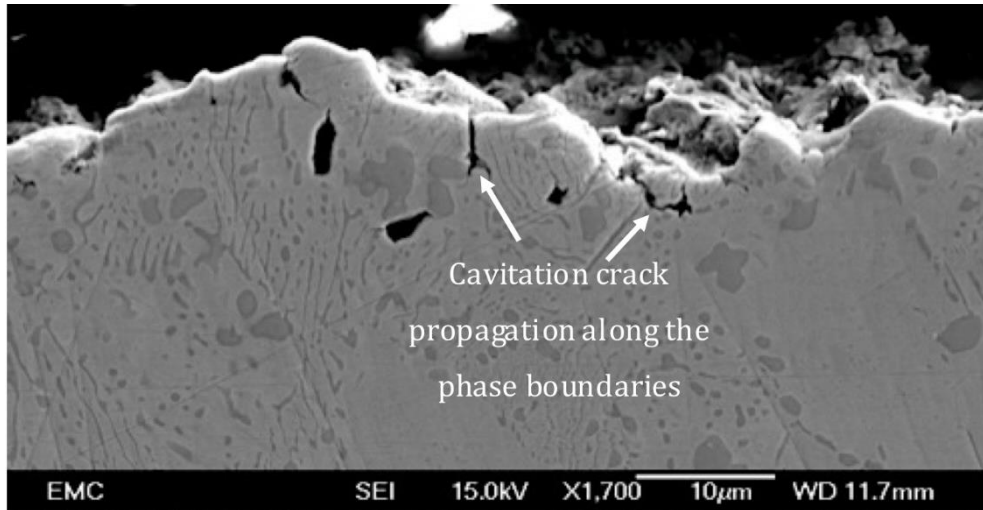


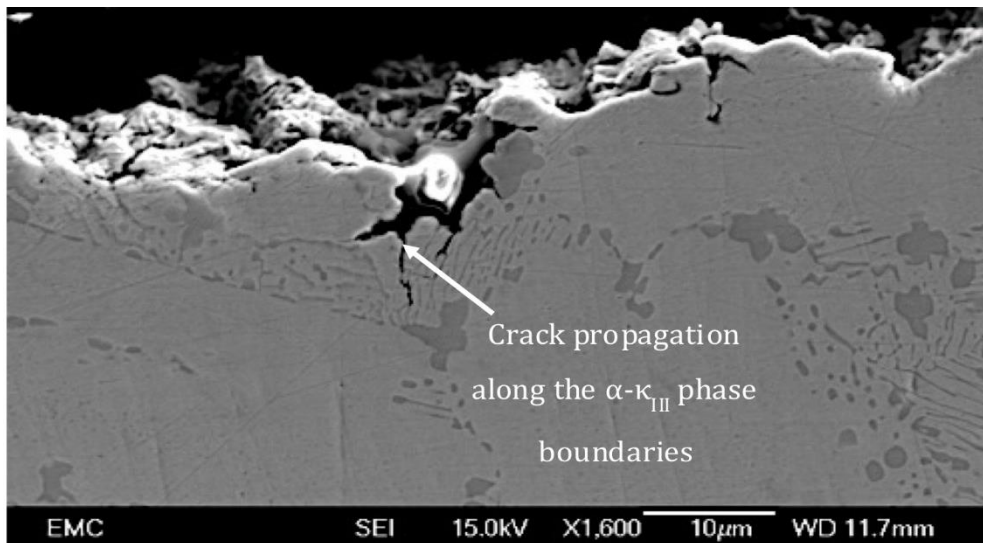
**Fig. 5.21:** SEM images of NAB sample cavitated for 1 h in distilled water: (a) transverse-sections of a cavity; (b) detailed magnified image of cavities in (a) exhibiting crack growth and propagation along the  $\alpha$ - $\kappa_{III}$  phase boundaries [202].

Comparatively, the transverse section of the cavitation erosion pattern in an air-formed oxide filmed NAB sample is shown in Figure 5.22 (a) and (b) obtained in 3.5% NaCl solution. From the figure it was evident that the most vulnerable site of attack was mostly at the  $\alpha$ - $\kappa$  phase boundaries. Once the cavitation erosion took place, several micro-cracks initiated at these erosion sites, and from there on propagated into the microstructure, especially along the  $\alpha$ - $\kappa$  grain boundaries.

Also, several subsurface cracks were observed (Figure 5.22 (a)), however the origin and mechanism of these cracks are not fully determined. Again, the  $\kappa$ -precipitates and precipitate-free  $\alpha$ -phase zones were found to suffer no visible cavitation after 1 h of cavitation test in 3.5% NaCl [18], [202].



(a)



(b)

**Fig. 5.22:** SEM images of transverse sections of NAB after 1 h of cavitation erosion-corrosion test in 3.5% NaCl solution with air-formed film showing crack propagation along the  $\alpha$ - $\kappa_{III}$  phase boundaries and plastic deformation [203].

From these results, it was clear that although the air-formed filmed NAB suffered erosion in pure erosion conditions such as cavitation in distilled water, it suffered further erosion much more adversely under the combined influence of corrosion

in 3.5% NaCl solution. From this, it was confirmed that material underwent corrosion-enhanced erosion, as demonstrated via the microstructural analysis.

Figure 5.23 (a) and (b) show the optical images of the transverse section of an air-formed filmed NAB surface cavitated in 3.5% NaCl solution for 1 h. Figure 5.23 (a) shows a series of cracks formed under the surface up to a depth of 150- $\mu\text{m}$  and interesting crack formation linking the  $\kappa_I$ - $\kappa_{II}$  phase boundaries, especially beneath the largest cavity, about 50- $\mu\text{m}$  in size. Figure 5.23 (b) shows the magnified image of the crack feature, which suggests failure along slip planes. There are a number of stresses acting upon the surface, such as the tensile/compressive shear stress due to the repetitive loading of the cavitation cloud, which may also cause subsurface shear stress build-up, as well as the material property itself that may mitigate cracks along the weakest grain boundaries, and several subsurface cracks, as seen in Figure 5.23 (a) [203].

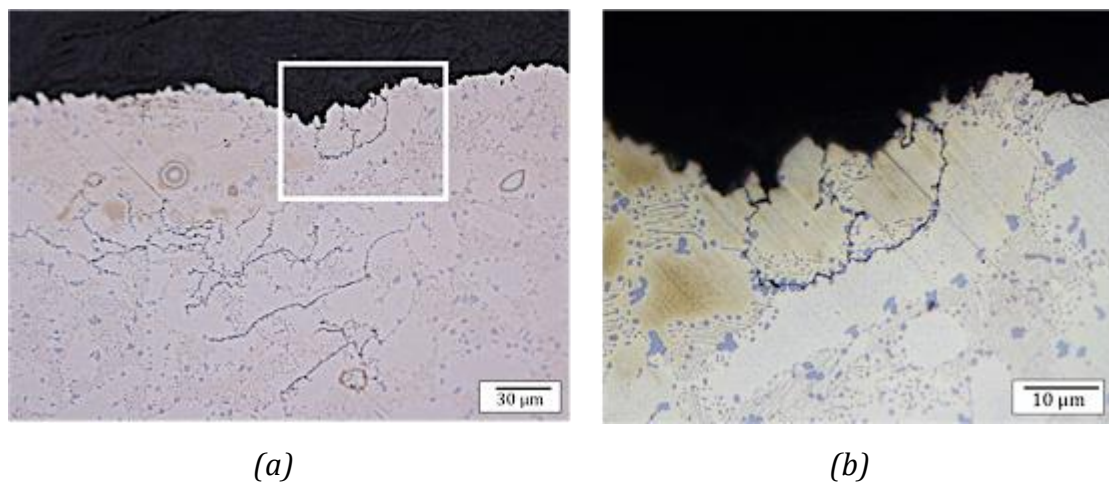


**Fig. 5.23:** Optical images of: (a) dendritic surface and potential subsurface cracks; and (b) detail of the selected area in (a) of surface cracks forming along the grain boundaries, linking  $\kappa_I$  and  $\kappa_{II}$ , after 1 h of cavitation erosion-corrosion test in 3.5% NaCl solution [203].

The formations of the subsurface cracks are speculated to be due to the interaction between the slip lines of the Cu-rich matrix and the hard secondary phases. Due to the multi-phases with differences in the hardness, combined with the accumulate subsurface strain, lower fracture toughness of the softer phase against

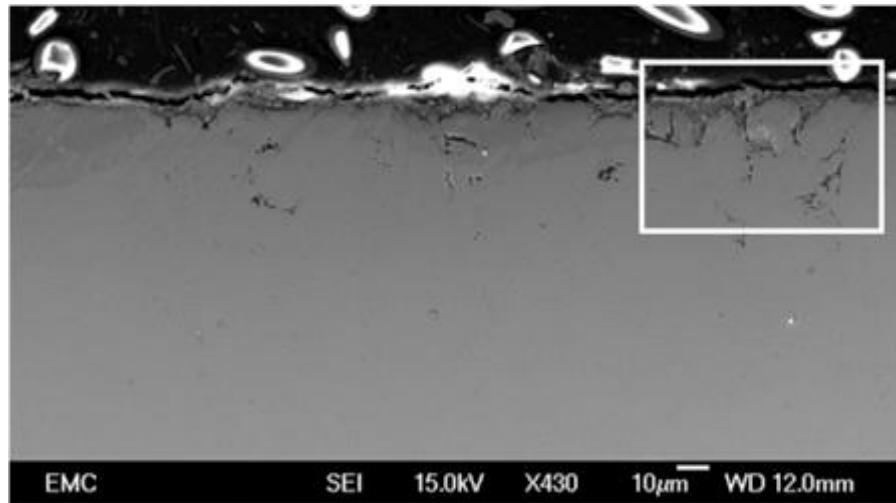
the hard phases with higher mechanical property gives way to stress concentration at the grain boundaries, which then eventually results in the failure under cyclic impact stress generated by the cavitation clouds. And hence, causing the subsurface cracks [203].

However, it should not be disregarded that these cracks may in fact be initiating somewhere on the surface and propagating along the weak grain boundaries with low fracture toughness and into the surrounding microstructure. Further detailed sectioning and characterization of these cracks would be required to explain these cracks, their mechanisms and the crack initiation processes [203].

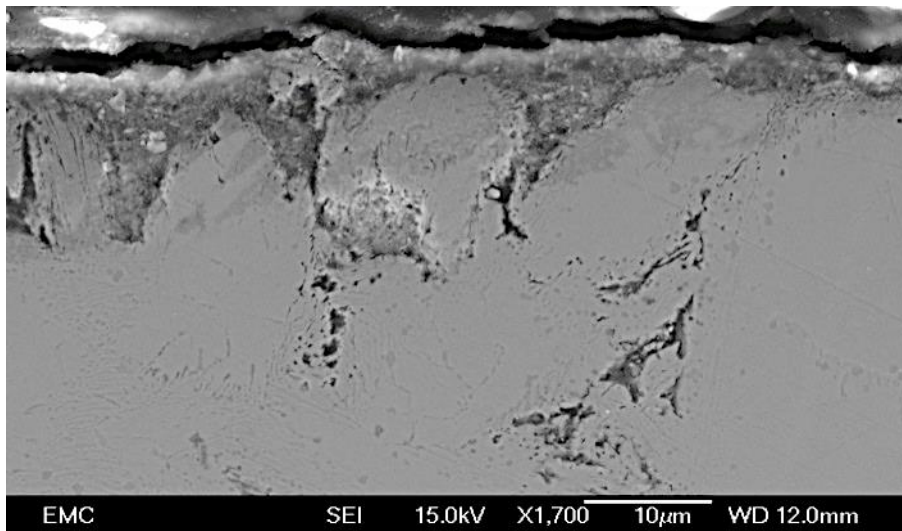
#### *5.3.1.3. Water-formed oxide filmed NAB*

Figures 5.24 (a) and (b) show the transverse section of NAB sample with a thick layer of water-formed oxide layer above the substrate formed after 3 months of immersion in 3.5% NaCl solution showing crevice and selective phase corrosion attack 50- $\mu\text{m}$  deep below the surface. The composition of the layer, obtained in EDS, mostly comprised of Cu, Al and O. Corrosion mainly took place at the  $\alpha$ - $\kappa_{III}$  lamella eutectoid phase boundaries on the surface, and its corroded depth was as deep as 20  $\mu\text{m}$  – 40  $\mu\text{m}$  beneath the exposed surface, propagating deeper into the substrate (as shown in Figure 5.24 (b)). The oxide film formed in air was barely visible to the naked eye but was found to be less than 2 nm. Whereas, the thickness of the oxide layer formed in 3.5% NaCl solution was found to have a thickness of 1000 nm – 1200 nm (Figure 5.24 (b)) [203].





(a)



(b)

**Fig. 5.24:** SEM images the oxide film cross-section on the as-cast NAB substrate used for the research after 3 months of immersion in 3.5% NaCl solution: (a) selective phase corrosion attack reaching up to 40  $\mu\text{m}$  in depth; (b) the area selected in (a) showing selective corrosion of the  $\kappa_{III}$  phase under the surface [203].

It should be noted that the thick oxide layer formed after 3 months of submersion in 3.5% NaCl solution have rough porous surface topography and the thickness of the layer does not form homogenously throughout the surface. This is considered to be due to the inhomogeneous distribution of aluminium and copper, the oxide forming elements in the alloy itself. As reported by Wharton and Stokes, the thickness of the protective oxide films vary with different aluminium content on the phases in aluminium bronzes due to the increased electrical insulation of the

region with thicker aluminium oxide [203], [208]. As found by Wharton and Stokes, the selective corrosion of the  $\kappa_{III}$ -phase can extend up to a depth of 200  $\mu\text{m}$  – 300  $\mu\text{m}$  after 6.5 months of immersion. They also found that under crevice corrosion, the crevice inlet sustained attack at the  $\alpha$ -phase of the eutectoid up to a depth of 20  $\mu\text{m}$  – 40  $\mu\text{m}$ , while the  $\kappa_{III}$ -phase was increasingly more susceptible further below 40- $\mu\text{m}$  [208].

Figure 5.25 (a) – (d) show the SEM images of the water-formed oxide filmed NAB surfaces as well as transverse sections of a cavity obtained under E conditions.

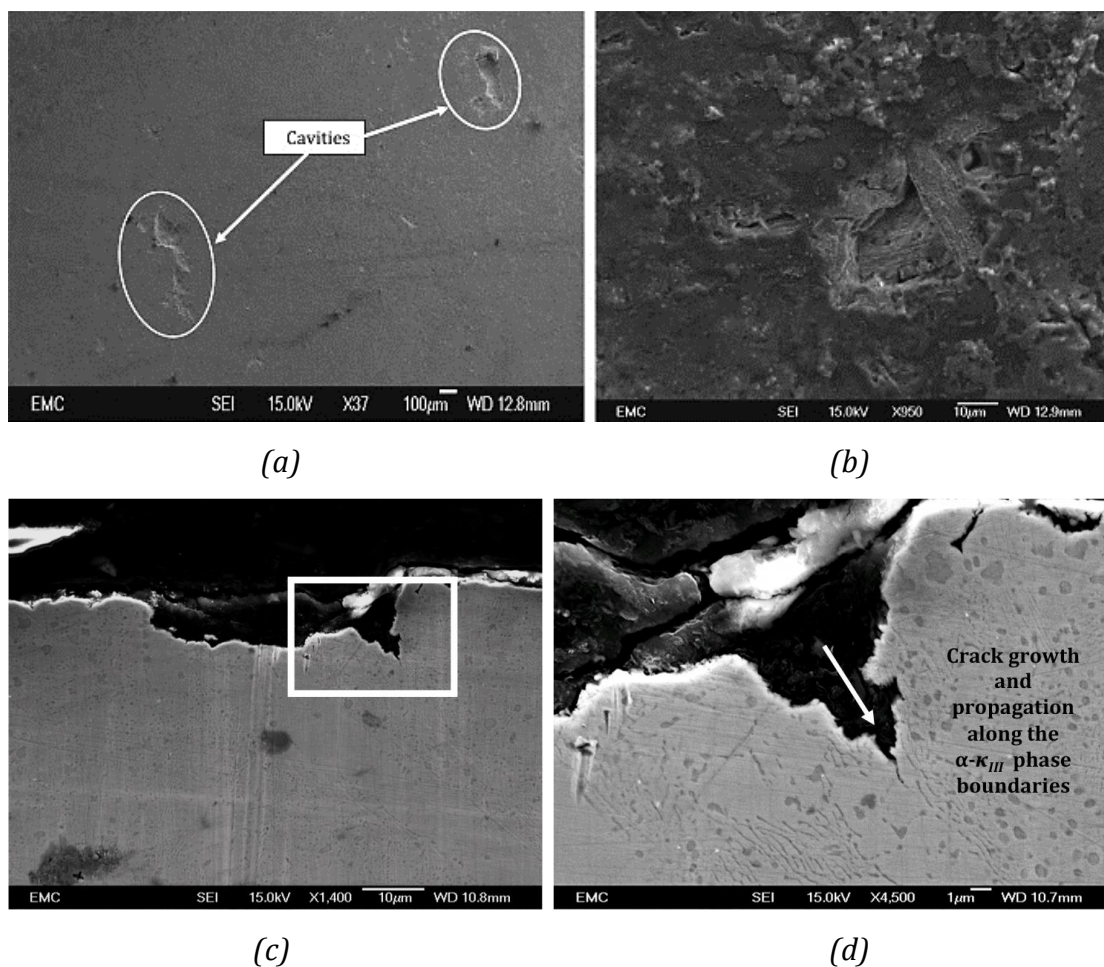


**Fig. 5.25:** SEM images of water-formed oxide filmed NAB sample under pure cavitation erosion conditions: (a) showing cavities formed on the sample surface; (b) magnified image of a cavity on the surface; (c) transverse-sections of a cavity; (d) detailed magnified image of a cavity in (c) exhibiting crack growth and propagation along the  $\alpha$ - $\kappa_{III}$  phase boundaries [203].

As seen from Figure 5.25, the wear mechanism for the water-formed oxide filmed NAB surface was found to be same as the air-formed filmed sample. However, the oxide film formation, the film thickness and the impact of corrosion in chloride solution played a significant role in the cavitation erosion-corrosion behaviour of NAB immersed in 3.5% NaCl solution for 3 months. The cavities were larger under both E and T conditions for water-formed filmed samples than for the air-formed filmed samples.

This is expected since the phase boundaries are considered to already weaken due to crevice corrosion and selective phase attack. And hence, it is the first site of attack for cavitation as well. Figure 5.25 (a) shows the cavitation erosion pattern on the roughened oxide surface, detailing a cavity formed due to the erosion for 1 h in distilled water. On closer analysis under the SEM, the erosion was seen to expose the  $\alpha$ - $\kappa_{III}$  phase boundaries under the oxide film, shown in Figure 5.25 (b) [203].

The samples were transversely sectioned, as shown in Figure 5.25 (c) and (d). Figure 5.25 (c) shows the cross-section of a cavity on the sample surface after 1 h of cavitation conducted under pure erosion conditions for a water-formed oxide filmed NAB sample. The cavity was found to be of 30- $\mu$ m diameter and about 10- $\mu$ m depth, with a large crack propagating into the sample microstructure, as seen at the right corner. Figure 5.25 (d) shows the magnified details of the crack (highlighted in (c)) revealing the crack growth and propagation into the microstructure along the  $\alpha$ - $\kappa_{III}$  phase boundaries [203].

For both E and T conditions, it was seen that the water-formed oxide filmed NAB surface suffered similar erosion trend. However, the wear scar images obtained after 1 h of cavitation erosion, with the combined effect of corrosion in 3.5% NaCl solution showed more aggressive wear pattern and surface roughness. The oxide film eroded under T conditions more rigorously, exposing the substrate microstructure more clearly than under E conditions.

The lamellar eutectoid phase boundaries are most susceptible to corrosion attack,

making them further vulnerable to wear via cavitation erosion. Which demonstrated the strong significance of the corrosion-enhanced erosion contribution to the overall damage. Hence, the roughness observed was the highest in these phase boundaries. In Figure 5.26 (a) the phases can be easily distinguished, especially after cavitation erosion-corrosion due to selective phase attack and wear at the  $\alpha$ - $\kappa_{III}$  as well as  $\alpha$ - $\kappa_{IV}$  phase boundaries, with the exposed  $\kappa_{IV}$  phases imbedded into the soft matrix (Figure 5.26 (b)) [203].

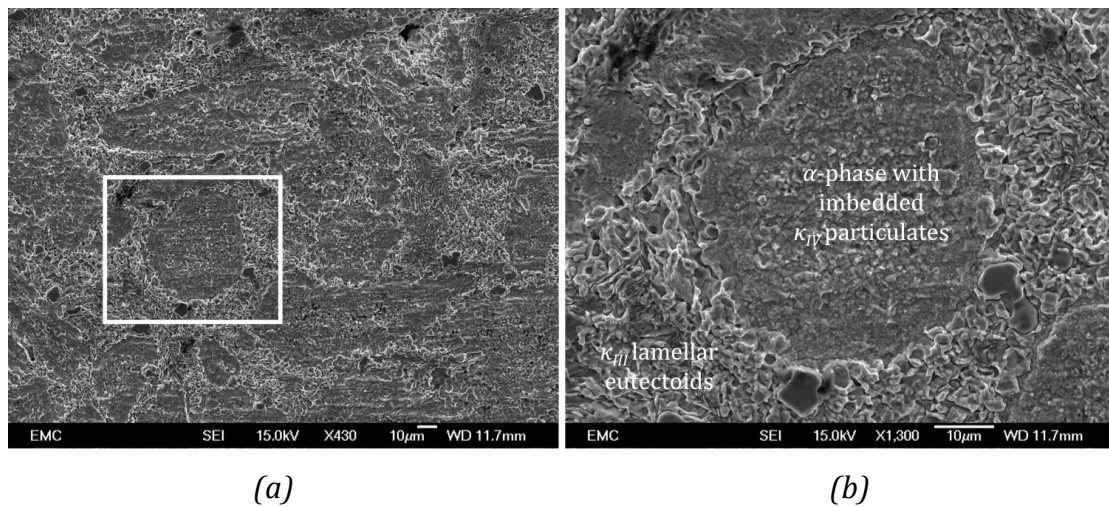


**Fig. 5.26:** SEM images of the distinguished phase erosion of the oxide filmed sample in 3.5% NaCl solution after 1 h of cavitation [203].

This was further proven on closer analysis of the eroded microstructure under SEM. Figure 5.27 illustrates the various different phases within the microstructure, obtained under SEM for the samples cavitated in 3.5% NaCl solution after 1 h of test [203].

It is evident from the figure that the softer matrix has been eroded and detached away, leaving behind small islands of harder iron-rich intermetallic phases exposed, especially at the highest concentration of grain boundaries. Islands of  $\kappa_I$  were seen at the erosion boundaries, whereas threads of  $\kappa_{III}$  were left exposed at regions with high  $\alpha$ - $\kappa_{III}$  eutectoid phases. Furthermore, particulates of  $\kappa_{IV}$  phase were also seen to become more prominent due to the  $\alpha$ -phase erosion at the phase boundaries [203].



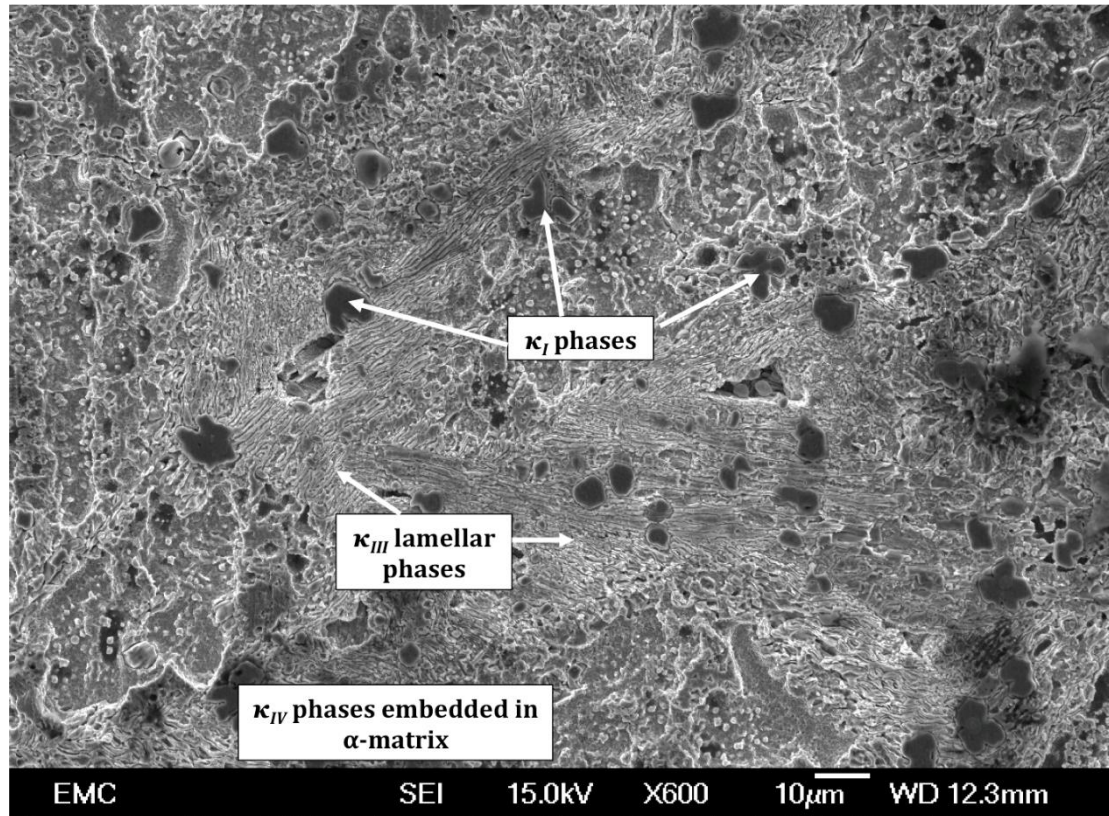


**Fig. 5.27:** SEM image of the eroded surface of NAB sample with water-formed oxide film after combined cavitation erosion-corrosion test conducted in 3.5% NaCl solution for 1 h [203].

To understand the impact of the cavitation erosion-corrosion on the subsurface microstructure, the samples were also transversely sectioned and analysed under SEM. Figures 5.28 shows the cross-sections of the sample surface after 1 h of cavitation erosion-corrosion test for the water-formed oxide filmed NAB sample. The cavities were found to be of about 50  $\mu\text{m}$  – 80  $\mu\text{m}$  in diameter and 10  $\mu\text{m}$  – 20  $\mu\text{m}$  in depth [203]. Comparing this to the depth of oxide film formed ( $\sim 1 \mu\text{m}$ ), and the reported selective phase and crevice corrosion (ranging 20  $\mu\text{m}$  – 40  $\mu\text{m}$ ), it was seen that not only did cavitation remove the oxide layer, but also propagated into the substrate as deep as the selective phase attacks and the crevice corrosion sites. Showing that the exposure to 3.5% NaCl solution rendered the substrate vulnerable to cavitation especially on the weakened sites. And hence, proving that corrosion indeed enhanced erosion.

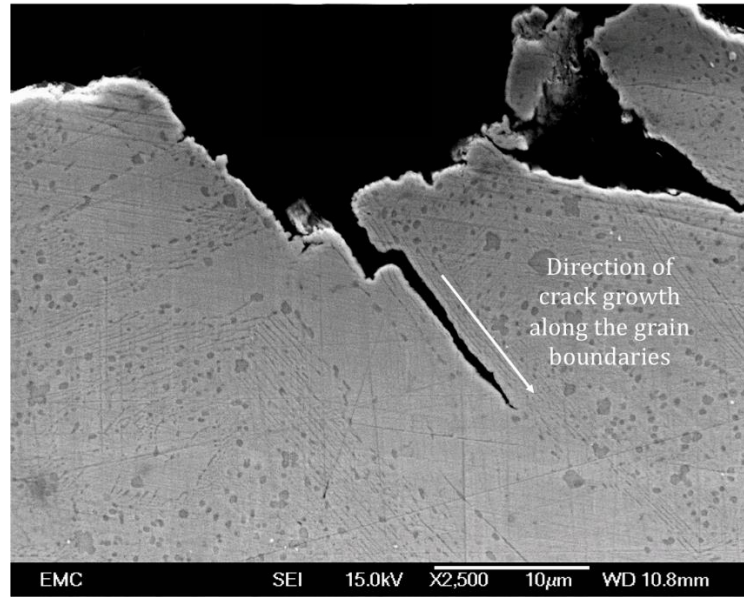


**Fig. 5.28:** SEM image of transverse section of NAB after 1 h of cavitation erosion-corrosion test in 3.5% NaCl solution with water-formed film showing crack propagating along the lamellar eutectoid grain boundaries [203].

Figure 5.28 exhibits a large crack with crack length of about 15  $\mu\text{m}$  propagating into the microstructure distinctly along the  $\alpha$ - $\kappa_{III}$  phase boundaries [203].

## 5.4 Discussion

From the intrinsic microstructural results obtained, it was evident that the microstructural properties of each material as well as the individual properties of each phase in the microstructure played very important roles in determining the cavitation behaviour of the materials. The microstructure size also played a significant role, as it was seen that more the grain boundaries (especially in case of NAB) more the material was vulnerable to boundary erosion and selective phase attacks. Also, softer phases surrounding the harder phases/intermetallic were seen to undergo erosion, due to the accumulation of subsurface strain caused by the repetitive hammering of imploding bubbles, and lower fracture toughness of the softer phase. This further caused subsurface crack initiation and propagation along the grain boundaries of phases with differing mechanical properties. This was true for both DSS and NAB samples. However, apart from

plastic deformation of the surface under the impact of cavitation, no microstructural changes were evident that could be observed via SEM, nor reported in the literature. Perhaps, further crystallographic analyses may add value to this, if any.

As seen for DSS, increased roughness during the first 30 minutes of cavitation erosion-corrosion proved the plastic nature of the cavitation mechanism. Striation patterns and ductile tearing were also seen within the cavities and cavity edges, which supported the fact that the cavities were indeed a result of plastic deformation. Furthermore, from the transverse sectioning of the sample, it was seen that the softer ferritic phase were the first site of attack, leaving behind the islands of harder austenitic phases. However, since the duplex structure of DSS is very strong, with large islands of austenite, DSS generally exhibited higher resistance to mechanical wear due to cavitation. Also, owing to its high chromium content within the composition, exhibited passivity and high corrosion properties. However, the cavity sizes observed under combined impact of erosion-corrosion was larger than that obtained under pure erosion conditions. This is mostly attributed to the enhancement of mass loss/cavity formation in the presence of corrosive 3.5% NaCl solution, showing enhancement of erosion especially due to corrosion. This is further proven in the following chapter that elucidates on the electrochemical properties of the materials. Also, from the erosion rates it was seen that DSS exhibited better erosion resistance until 2 h of cavitation, after which it exhibited higher mass loss rate as compared to the NAB sample, which showed a more gradual erosion rate trend.

For the air- as well as water-formed oxide films, due to their brittle and porous nature, combined with the low thickness, it was difficult to obtain the hardness of the films. However, it has been considered to be of the similar magnitude at the substrate [206]. As one of the main novelties of the research was to investigate the cavitation behaviour of NAB with water-formed oxide film, it was observed that after exposure to 3 months of 3.5% NaCl solution, the substrate underwent copper dissolution, and reaction with the chloride solution, forming protective oxide films of aluminium and copper. However, due to this dissolution and oxidation of the

substrate, the NAB samples underwent selective phase attack and crevice corrosion in the 3.5% NaCl solution that was observed to penetrate as deep as 50- $\mu\text{m}$ . This, in turn, caused the substrate to be more vulnerable to the severe impacts of cavitation erosion and erosion-corrosion, leading to higher erosion results, as obtained via mass loss and microstructural evaluation, compared to pure erosion results. Furthermore, water-formed oxide filmed NABs seemed to exhibit higher microstructural damage and roughness, evident from both images and average roughness values obtained using surface profilometry, than air-formed oxide filmed NABs.

Also seen from the periodic photographic evidence of the erosion evolution of NAB with water-formed oxide film over 5 h, the oxide film was seen to undergo pitting for the first 30 minutes, after which it started to undergo oxide removal, further roughening the surface until the oxide film was completely removed (between 2 h – 3 h of cavitation), after which, the substrate underwent selective phase attack along the  $\alpha$ - $\kappa$  phase boundaries and the sites of crevice corrosion. This assisted in proving the existence of synergy between cavitation erosion and corrosion, as well as demonstrating that corrosion did in fact enhance cavitation erosion for both air- and water-formed oxide filmed NAB samples. No significant  $\beta$  and retained martensitic  $\beta'$ -phases were seen within the cavitated microstructure of NAB. Moreover, neither of the two phases, if present, were observed to have any effect on the cavitation behaviour of NAB, both in distilled water or 3.5% NaCl solution.

From the discussion and results obtained, it can be concluded that in order to protect a propeller from severe cavitation erosion-corrosion, it is crucial to immune the materials from corrosion. For materials like NAB that are difficult to prevent from forming oxide layers on the surface in corrosive environment, reduction in corrosion may be promoted by either heat-treating the alloy to remove beta phases (such as NES 747 NAB), adding alloying element that help increase the passivity of the composition, coating it with a protective oxide or corrosion resistant material, providing cathodic protection, or coupling it with a sacrificial anode.



## 5.5. Summary

The investigations of tribo-corrosion relationship between wear and corrosion conducted for DSS and NAB samples with oxide films formed under the two different conditions, air and immersion in 3.5% NaCl solution were conducted. All test materials were observed to have roughening of the material surface indicating the existence of plastic deformation, extrusion, work hardening and high strain, as verified under the SEM.

It was concluded that for DSS as well as both the types of NAB samples, cavitation erosion and corrosion had synergistic roles in the combined effects of erosion-corrosion. The surface profilometry, surface roughness and microstructural morphology were analysed for the samples after the cavitation test. Both probe tip as well as the sample surfaces were seen to have eroded. Alicona and Talysurf were both employed to obtain the surface profiles as well as the surface roughness of the two materials. Alicona was also used to measure the volumetric mass loss observed for the samples after cavitation and compared with the gravimetric mass loss results.

DSS generally showed higher resistance to cavitation erosion and corrosion compared to NAB, especially until 3 h of cavitation test, after which it showed drastic erosion trend. For DSS, the microstructure underwent selective phase attack, with the soft ferritic matrix more vulnerable to cavitation than the austenitic phases. DSS was also seen to undergo ductile failure in the cavitated zone in the form of extrusion of the austenite at the cavitation pit along with microcracks and cleavage facets, and striation patterns on the wear scar. It exhibited higher erosion under the combined effect of corrosion to the cavitation test, displaying the significant influence of corrosion-enhanced erosion.

NAB was found to be more susceptible to erosion under both the conditions as compared to DSS with prominent selective cavitation erosion of alpha phase in the microstructure since DSS is harder than NAB. Both air-formed and water-formed oxide filmed NAB samples underwent higher mass loss than DSS. And the water-

formed filmed samples seemed more vulnerable than the air-formed oxide film. NAB samples with both types of oxide films underwent selective phase attack at mainly the  $\alpha$ - $\kappa_{III}$  eutectoid phase boundaries. The selective phase attack and corrosion of NAB immersed in 3.5% NaCl solution was more prominent due to the presence of chloride with the corroded depth reaching up to 20  $\mu\text{m}$  beneath the exposed surface, propagating deeper into the substrate.

SEM analyses revealed that the wear mechanisms of the cavitated sample surfaces with both air and water-formed oxide films were found to be similar in nature. The sample surfaces were seen to undergo selective cavitation erosion-corrosion attack at the  $\alpha$ -phase and the  $\alpha$ - $\kappa$  phase boundaries with ductile deformation around the cavity while the  $\kappa$  precipitates and precipitate-free  $\alpha$ -phase zones were found to suffer no visible cavitation after 1 h of cavitation test in both distilled water as well as 3.5% NaCl.

The first site of attack to take place was the  $\alpha$ - $\kappa_{III}$  eutectoid phase boundaries. The sites of most aggressive attacks exhibited large cracks propagating into the microstructure along the  $\alpha$ - $\kappa_{III}$  phase boundaries, hence the regions with high lamellar  $\kappa_{III}$  phases were most susceptible to wear, crack initiation and propagation. It was also found that softer  $\alpha$ -matrix surrounding the hard secondary phases being more vulnerable to cavitation attack as compared to the  $\kappa$  phases and the precipitate-free  $\alpha$  zones, leaving the islands of harder iron-rich  $\kappa$  phases to be exposed, especially at the highest concentration of grain boundaries.  $\kappa_I$  phases islands and threads of  $\kappa_{III}$  phases were seen at the erosion boundaries. Also particulates of  $\kappa_{IV}$  phase were also seen to become more prominent due to the  $\alpha$ -phase erosion at the phase boundaries. However, the wear features of the cavitation erosion-corrosion of water-formed oxide filmed sample surfaces were much more rougher than the wear scars observed for the samples with air-formed film.



# Chapter 6:

# Electrochemical

# analysis

---

Along with the microstructural analyses of the test materials, in order to understand the mechanical implications of cavitation, it is equally important to analyse the corrosion aspects of the cavitation phenomenon, as well as the electrochemical response of the materials to cavitation. Test materials were subjected to OCP and EIS (with and without cavitation) as well as potentiodynamic polarization tests. Their corresponding results have been used to characterize the

materials based on their corrosion behaviour and properties, especially when subjected to cavitation.

Also, for the quantification of synergy between cavitation erosion and corrosion, it was necessary to conduct tests under pure corrosion, as well as combined cavitation erosion-corrosion conditions, where the materials were subjected to 1 h of corrosion without cavitation, and 1 h of cavitation in 3.5% NaCl solution, kept at OCP. The main aim was to quantify individual contribution of corrosion and its influence on erosion. However, the underlying mechanisms occurring during cavitation erosion-corrosion in conjunction to one another is very complex, and one cannot be easily isolated from the other. Attempts were made to obtain quantitative values under each condition, assuming negligible influence from the other.

This chapter aims to explain the individual electrochemical behaviour of the sample materials to corrosion, the effect of cavitation on their corrosion properties and their electrochemical responses, and hence, the validation of synergistic relation between erosion and corrosion.

## **6.1. Open circuit potential analysis**

### ***6.1.1. Open circuit trends***

From the electrochemical tests conducted, OCP curves were obtained for DSS, air-formed oxide-filmed NAB, and water-formed oxide-filmed NAB tested under pure corrosion (C) and erosion-corrosion (T) conditions as shown in Figure 6.1. All the tests were conducted for 1 h in 3.5% NaCl solution. For the cavitation erosion-corrosion tests, cavitation was applied to the samples after 600 seconds to obtain the change in the electrochemical behaviour of the sample materials.

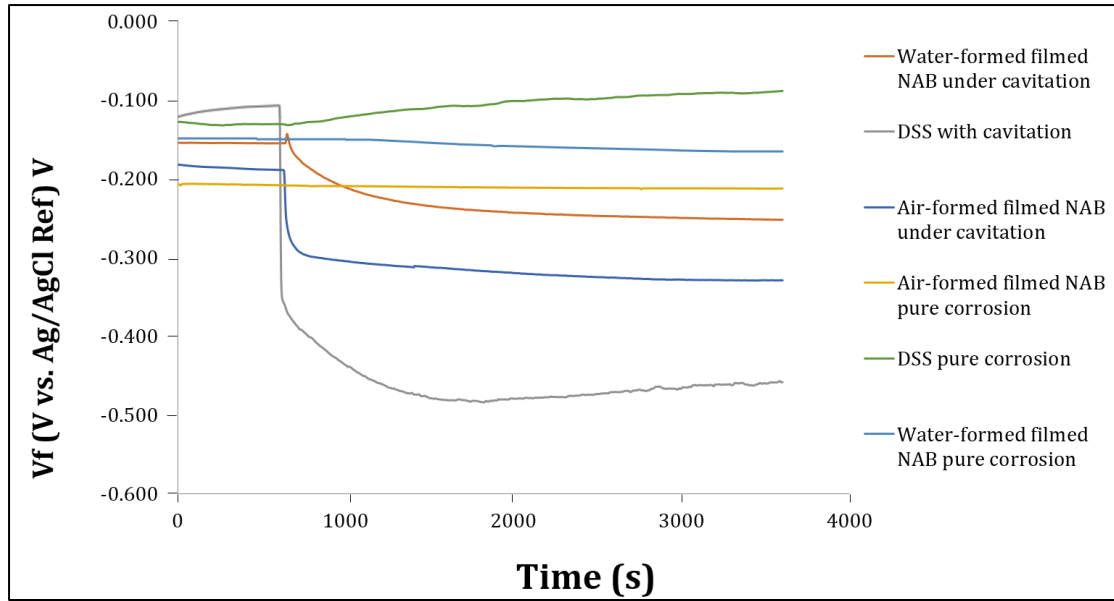


**Fig. 6.1:** OCP for DSS, air-formed filmed NAB and water-formed filmed NAB in 3.5% NaCl solution for 1 h with and without cavitation as adapted from references [18], [202], [203].

Where,  $V_f$  is the reference potentials in volts. It can be seen from Figure 6.1 that under pure corrosion, the measured OCPs slightly shift positively from -0.149 V to -0.088 V for DSS within 1 h of immersion in 3.5% NaCl solution, but negatively by 0.006 V from -0.207 V to -0.213 V for air-formed filmed NAB.

From the plot, it was also seen that the water-formed oxide filmed NAB had higher passivation for both pure corrosion and cavitation erosion-corrosion. Figure 6.1 shows that the water-formed filmed NAB gradually shifted negatively (from -0.149 V to -0.165 V) under pure corrosion tests. This may be due mass transfer through the porous oxide films during its immersion in the 3.5% NaCl solution. However, compared to this, there is a dramatic negative shift observed in OCP (from -0.15 V to -0.25 V) upon cavitation impact. The same trend was exhibited by air-formed filmed NAB sample as well, although the OCP of water-formed filmed surface was more anodic by 0.02 – 0.05 V than the air-formed filmed surface under both test conditions. The negative shift and stability was attained more gradually over time in about 600 s [203].

The OCP of DSS sharply dropped from -0.07 V to -0.375 V once the cavitation rig

activated, but attained stability within 600 s at a lower value (between -0.47 V to -0.49 V), which may be attributed to the disruption of the passive layer by cavitation erosion. Similarly, the OCP for the air-formed filmed NAB samples had a drastic negative drop from -0.17 V to about -0.3 V on application of cavitation. The cavitating NAB attained stability within 120 s at a lower potential of -0.31 V [18]. From these trends, it can be concluded that water-formed filmed NAB exhibited best stability among the three, and hence, better resistance under cavitation erosion-corrosion. Both air-formed and the water-formed filmed NAB attained stability faster than DSS after the application of cavitation.

It may also be noted that under cavitation impact, the OCPs of DSS shifted slightly to positive with time under both C and T conditions. This may demonstrate that re-passivation process of DSS under cavitation, thereby, reducing cavitation-caused erosion in long term. However, it was observed to be opposite for NAB with slight decrease of OCP while under cavitation over time. The cavitated samples were then observed under the microscope for their surface features. Figure 6.2 show the optical images for the samples before and after 1 h of cavitation erosion-corrosion for all three samples, taken from the central eroded region of the samples.

Figure 6.2 (a) shows the optical image of the air-formed oxide filmed NAB with the microstructure similar to that of a polished sample. After 1 h of OCP, air-formed oxide-filmed NAB was the only one to show a difference in its microstructure. As seen in Figure 6.2 (b), a slight colouration was seen to form on the microstructure, suggesting progressive corrosion/oxide formation on the sample material. On further application of cavitation, cavities of sizes ranging from 20  $\mu\text{m}$  to 50  $\mu\text{m}$  were visible especially at the  $\alpha$ - $\kappa$  phase boundaries, as seen in Figure 6.2 (c).



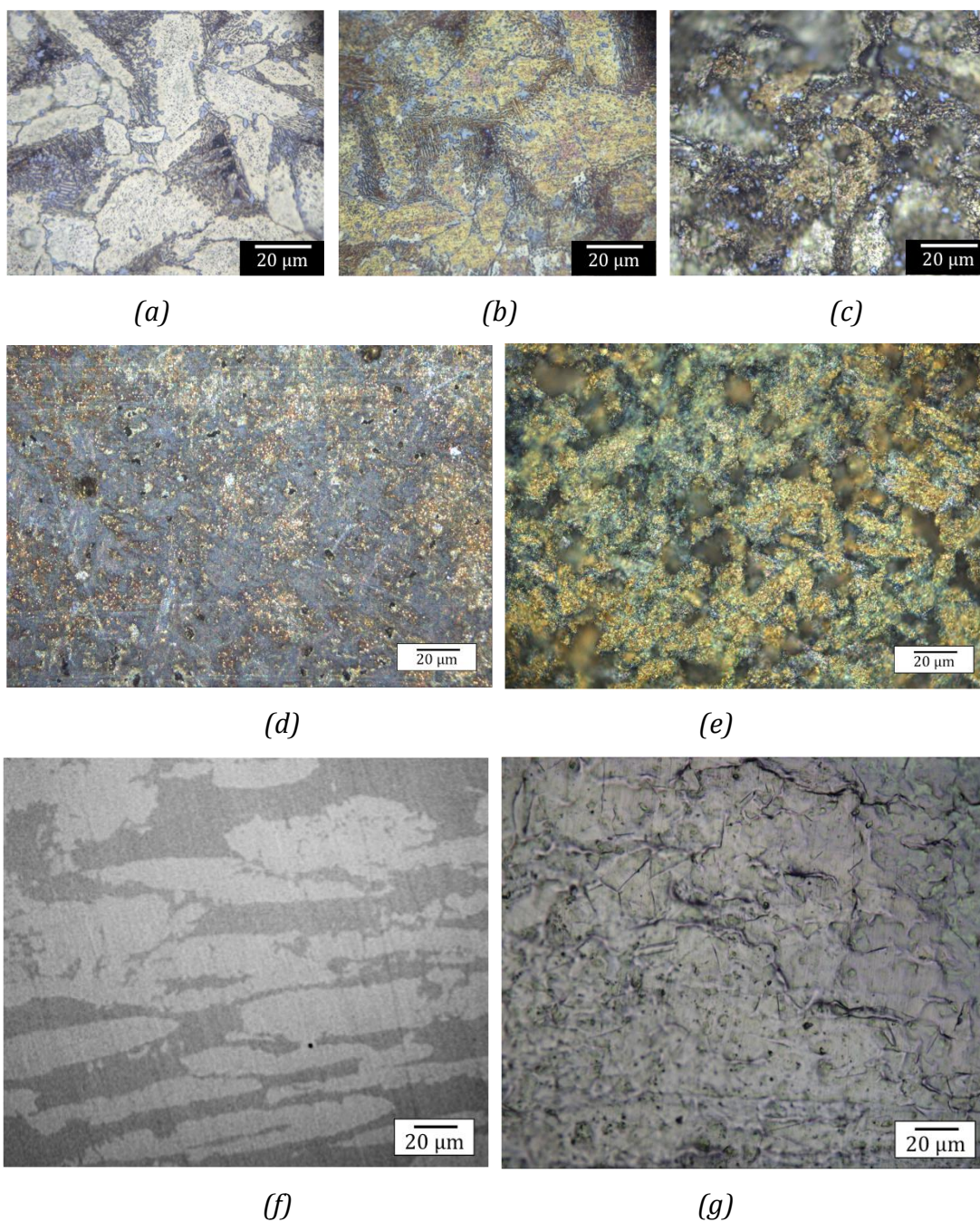


**Fig. 6.2:** Optical images of the cavitated region from the central region of the air-formed oxide filmed NAB samples (a) before OCP and cavitation; (b) after 1 h of OCP; and (c) after 1 h of cavitation while kept at OCP in 3.5% NaCl solution. Water-formed oxide filmed NAB (d) before OCP and cavitation, and (e) after 1 h of cavitation while kept at OCP in 3.5% NaCl solution. And DSS (f) before OCP and cavitation, and (g) after 1 h of cavitation while kept at OCP in 3.5% NaCl solution.

Comparatively, water-formed oxide filmed NAB and DSS showed no difference between pre-electrochemical test and after 1 h of OCP test. Hence, only the optical



images before and after 1 h of cavitation erosion kept under OCP were shown in Figures 6.2 (d) – (g). Figure 6.2 (d) and (f) are the optical images of water-formed oxide filmed NAB and DSS before C or T tests. As seen in the figure, both DSS and water-formed oxide filmed NAB underwent cavitation after 1 h of erosion-corrosion test. While DSS showed roughening of the surface topography (Figure 6.2 (g)), the oxide-film on NAB was partially removed, and there were also cavities of sizes ranging between 10  $\mu\text{m}$  – 30  $\mu\text{m}$  observed on the surface under the microscope, see Figure 6.2 (e).

This disruption of the protective layer as well as the material surface by the rapid and violent implosion of cavitation bubbles, observed both on the OCP trends and via microscope, was considered to be the cause of the drastic negative shifts of the corrosion potentials of the materials.

#### ***6.1.2. Water-formed oxide filmed NAB***

The OCP trend of the immersion filmed NAB was also further analysed in details. Figure 6.3 shows the OCP trends of air- and water-formed oxide filmed NABs tested under static corrosion conditions in 3.5% NaCl solution, as well as distilled water. Whilst, the trend shows that the samples tested under distilled water showed excellent corrosion properties, i.e. passivity and positive potentials, the corrosion potentials of both NAB samples fell in a similar range when tested in 3.5% NaCl solution. It must be noted that the potentials of air-formed filmed samples were marginally lower than that of water-formed filmed samples (between -200 to -220 mV).

Four samples of water-formed filmed NAB were tested 2 – 4 times for OCP each. The samples were also recorded for mass change, measured gravimetrically using precision mass balance. The OCP values were obtained under static corrosion conditions in 3.5% NaCl solutions. Wood [204] tabulated these OCP values and their corresponding mass changes in Table 6.1. For most of the samples, there was no visible change in the oxide films after the static corrosion test as observed under optical microscope.

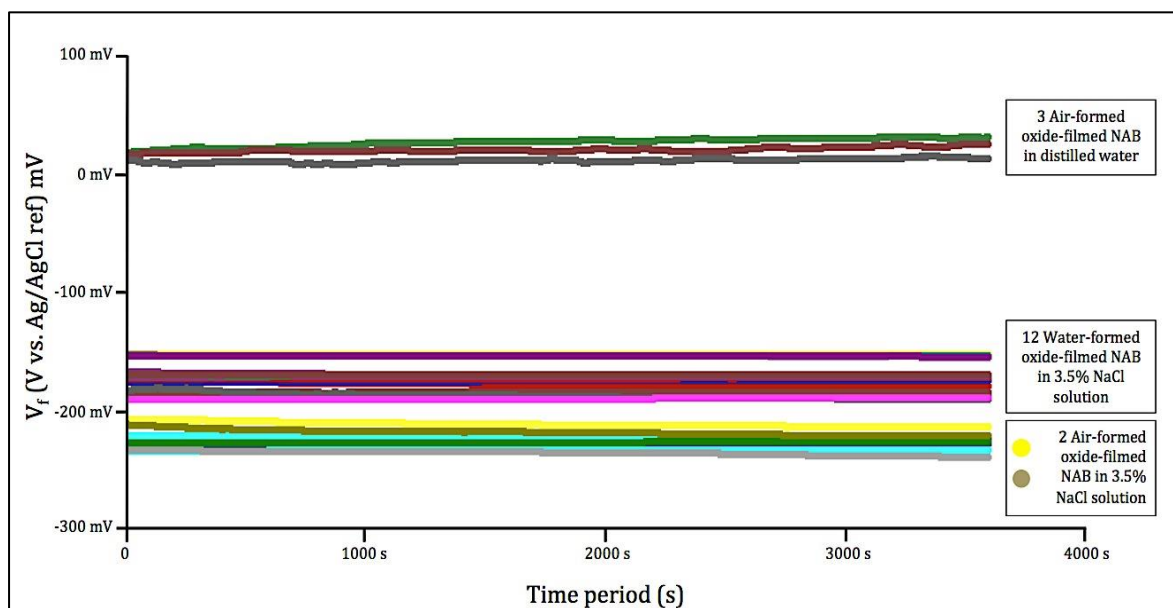


**Fig. 6.3:** OCP for NAB with air- and water-formed film in distilled water and 3.5% NaCl solution for 1 h each.

Samples 1 and 4, with  $\text{Al}_2\text{O}_3$  film and light-greenish  $\text{Cu}_2\text{O}$  film layer as established from section 4.2.2.2 and Equation 4.6, were seen to have partial film removal of the  $\text{Cu}_2\text{O}$  film after 1 h of corrosion test [204]. This change in the film is considered to be due to mass transfer, turbulence in the medium due to cavitation clouds, and other such disturbances of the oxide surface, that may cause the brittle and soft  $\text{Cu}_2\text{O}$  film layer to be inadvertently removed, although caution has been taken to not disturb the oxide layer.

Also seen in Table 6.1 is the mass gain in case of air-filmed NAB samples, which results in a negative value for C when quantifying synergy. The relationship between the OCPs and their corresponding mass loss/gain values were plotted in Figure 6.4 in order to correlate them. From the graph, it was noticed that a linear relationship existed between the OCP and the mass changes. However, samples with only partial film coverage (as stated in the comments in table 6.1) did not lie on the linear trend obtained [204].

Samples	OCP ranges	Mass changes	Comments on the films (as observed under optical microscope)	
			Before test	After test
Air-formed film 1	-206 to -212 mV	(-) 0.61 ± 0.04 mg	None to very light brown colouration	Light colouration to no visible change to the film
Air-formed film 2	-211 to -220 mV	(-) 0.89 ± 0.05 mg		
Oxide filmed sample 1	-158 to -189 mV	3.57 mg ± 0.07 mg	Fully formed dark Al <sub>2</sub> O <sub>3</sub> film (intact) with light greenish-blue brittle and soft CuO film	Partial removal of copper oxide layer without any visible effect on Al <sub>2</sub> O <sub>3</sub>
		3.19 ± 0.08 mg		
		3.08 ± 0.08 mg		
Oxide filmed sample 2	-168 to -222 mV	1.92 ± 0.04 mg	Fully formed film with brown Al <sub>2</sub> O <sub>3</sub> film and no copper oxide film	No visible change to the Al <sub>2</sub> O <sub>3</sub> film
		1.45 ± 0.05 mg		
		2.20 ± 0.06 mg		
		1.92 ± 0.04 mg		
Oxide filmed sample 3	-141 to -153 mV	0.92 ± 0.02 mg	Partially formed film with brown Al <sub>2</sub> O <sub>3</sub> film	No visible change to the Al <sub>2</sub> O <sub>3</sub> film
		0.98 ± 0.05 mg		
Oxide filmed sample 4	-153 to -173 mV	4.22 mg ± 0.05 mg	Fully formed dark Al <sub>2</sub> O <sub>3</sub> film (intact) with light greenish-blue brittle and soft CuO film	Partial removal of CuO layer without any visible affect on Al <sub>2</sub> O <sub>3</sub>
		5.32 ± 0.02 mg		
		6.39 ± 0.06 mg		

**Table 6.1:** OCP and mass changes for the water-formed oxide-filmed NAB samples as tested in 3.5% NaCl solution for 1 h each [204].

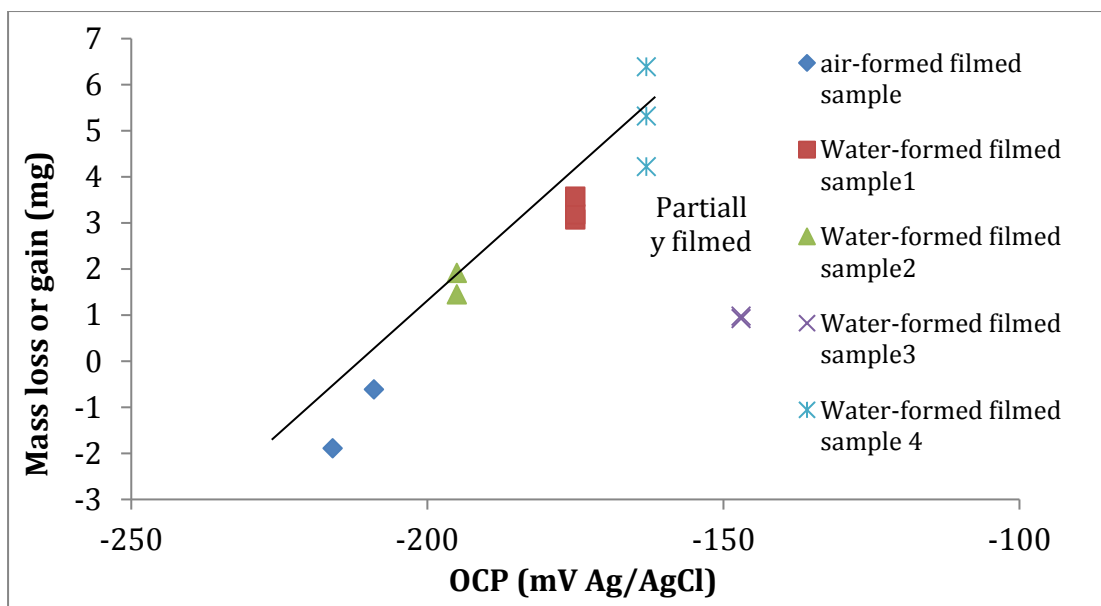
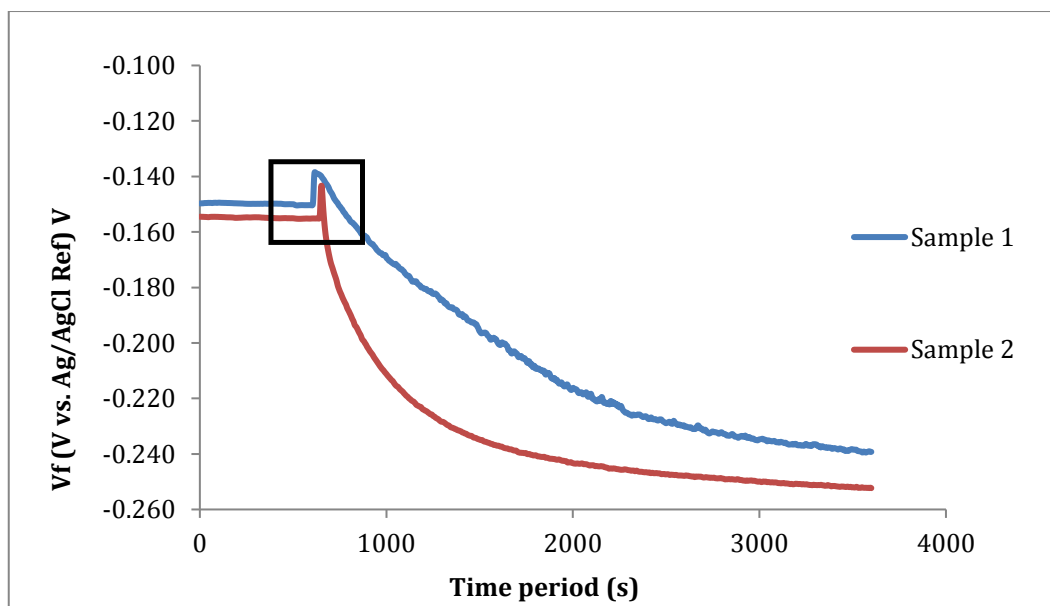


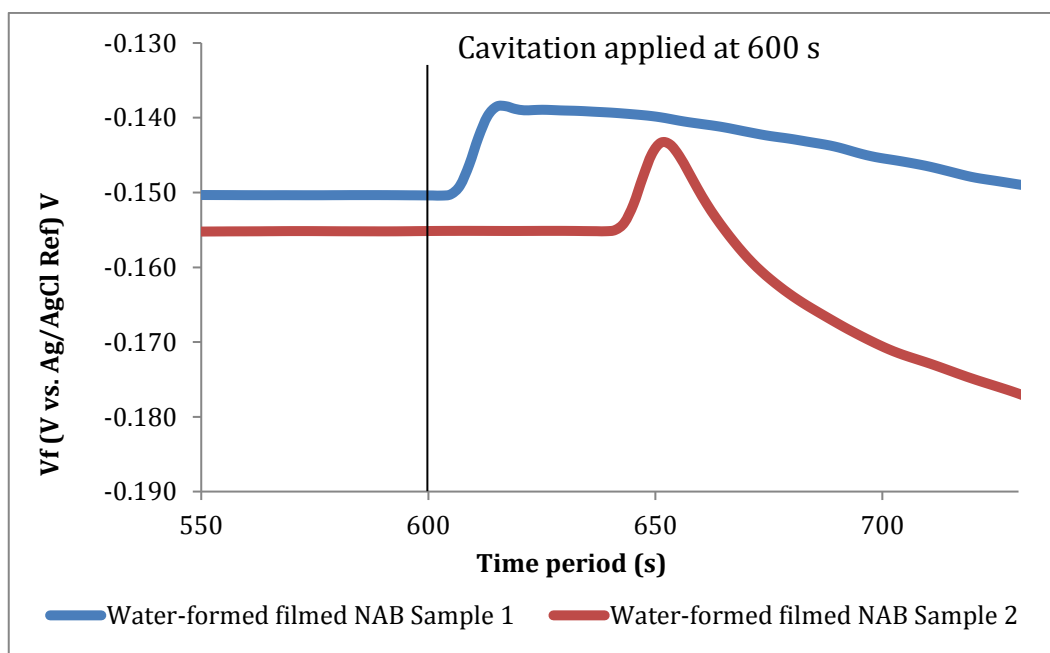
**Fig. 6.4:** Mass change data plotted against the OCP for air- and water-formed oxides on NAB after pure static corrosion tests in 3.5% NaCl solution tested for 1 h each [204].

As seen from Figure 6.4, it was concluded that for the water-formed oxide filmed NAB samples, the more electropositive the OCP, the higher the mass loss incurred on the samples. This suggested that the higher the passivation or protection (due to oxide formation) of the sample, the higher the mass loss incurred due to corrosion. From the linear slope plotted for the points, an increment of 8 mg per 100 mV in OCP was derived. The mass loss values varied from 1 to over 6 mg of loss, which may influence the quantification of the synergy (S) term [204].

The OCP trend of the water-formed oxide filmed NAB subjected to cavitation in 3.5% NaCl solution for 1 h was also analysed in details. Figure 6.5 (a) and (b) give the OCP trend-lines for two water-formed filmed NAB samples. It can be seen from the magnified image of the trend in Figure 6.5 (b) that as soon as cavitation was applied there was a sharp rise in the potentials before following the similar trend as the air-formed filmed samples of undergoing a dramatic negative shift in the OCPs upon cavitation impact. This suggested that there was an impact of cavitation and the incubation period on the corrosion trend of the samples.



(a)



(b)

**Fig. 6.5:** (a) OCP trends for water-formed oxide-filmed NAB samples in 3.5% NaCl solution for 1 h; (b) magnified section of the OCP during incubation period when under cavitation.

From the erosion rate obtained in chapter 5, section 5.1.1., for NAB, the incubation period was established to be between 30 – 60 s. There was a visible peak of the potentials at the said incubation period, seen in Figure 6.5 (b). Also, when compared to the OCP trend of the air-formed filmed NAB sample the peak of

potentials towards more positive value during the incubation period was very distinct, as seen in Figure 6.6. This may be due to the properties of the oxide film. During the incubation period, as soon as the oxide film was damaged, the trend rose to electropositive potentials for about 20 s for both sample 1 and sample 2. Due to the stochastic nature and porous integrity of the oxide films present, the impact of rigorously collapsing cavities may cause the oxide film to disrupt and compact, or accelerate the passivation process, thus reducing pores formation/blocking transport of chemicals, until the incubation period. The non-steady-state conditions of cavitation may lead to varying thickness of the film, double layer affect, as well as the modified distribution of reactants. Beyond which the water-formed oxide film starts to erode, with cavitation inducing more pores and pits onto the surface, albeit more gradually and slowly than the air-formed oxide film.

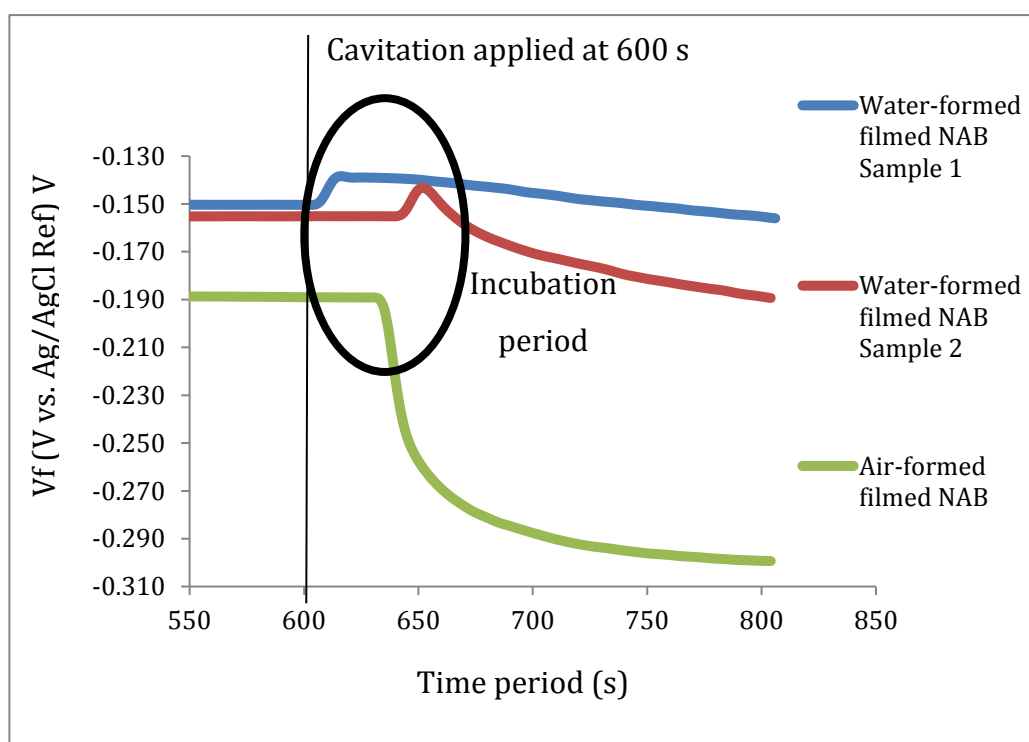


**Fig. 6.6:** The OCP trend for NAB with air and water-formed oxide film in 3.5% NaCl solution at the incubation period.

## 6.2. Electrochemical impedance spectroscopy analysis

Typically, data gathered through EIS are graphically represented in Nyquist plots and Bode plots. A Bode plot represent the impedance magnitude ( $|Z|$ ) and phase angle ( $\phi$ ) as a function of frequency, which are generally plotted on a logarithmic scale due to the impedance and the frequency often spanning over orders of magnitude. However, while the frequency-dependence of the impedance of the device under test is explicit in case of the Bode plots, it is specifically implicit for the Nyquist plots, and hence, the AC frequency of the selected data points requires indication.

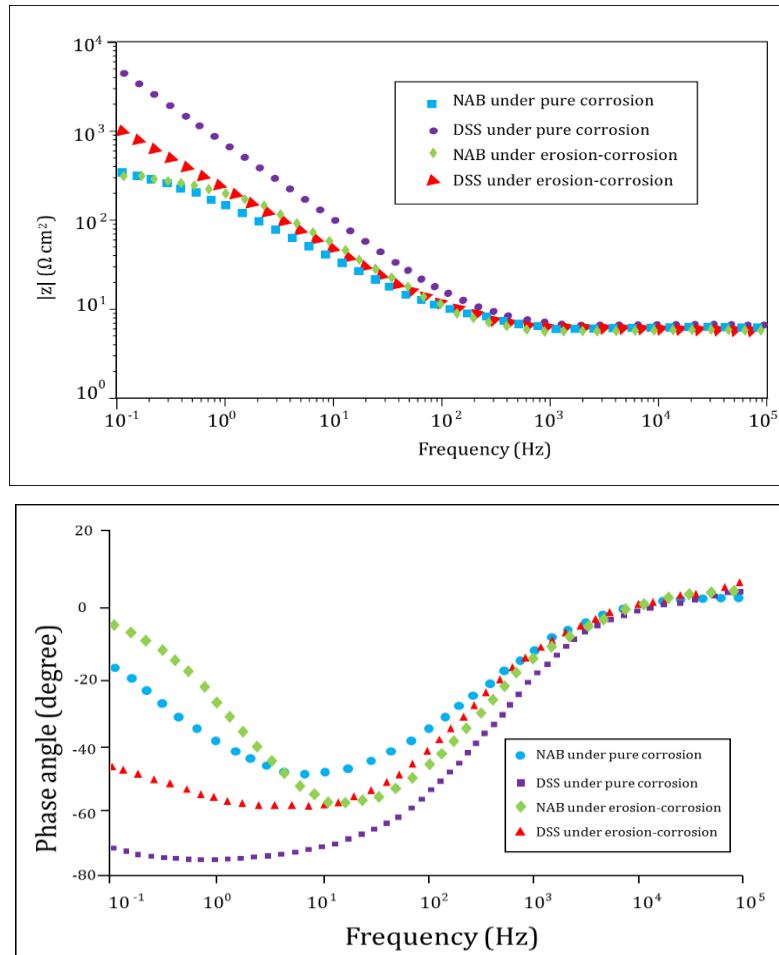


**Fig. 6.7:** Bode plot for DSS and air-formed oxide filmed NAB in 3.5% NaCl solution under pure corrosion and during cavitation [18], [202].

Figure 6.7 shows the EIS Bode plots for the DSS and air-formed oxide filmed NAB

samples during and without cavitation. It can be seen that for both materials EIS spectra exhibit single time-constant behaviour in the investigated frequency range. Although it is clear that the impedance was higher for DSS in saltwater alone without cavitation as compared to DSS undergoing cavitation erosion-corrosion, it was seen that the impedance of NAB under corrosion was slightly lower than that under cavitation erosion-corrosion [18].

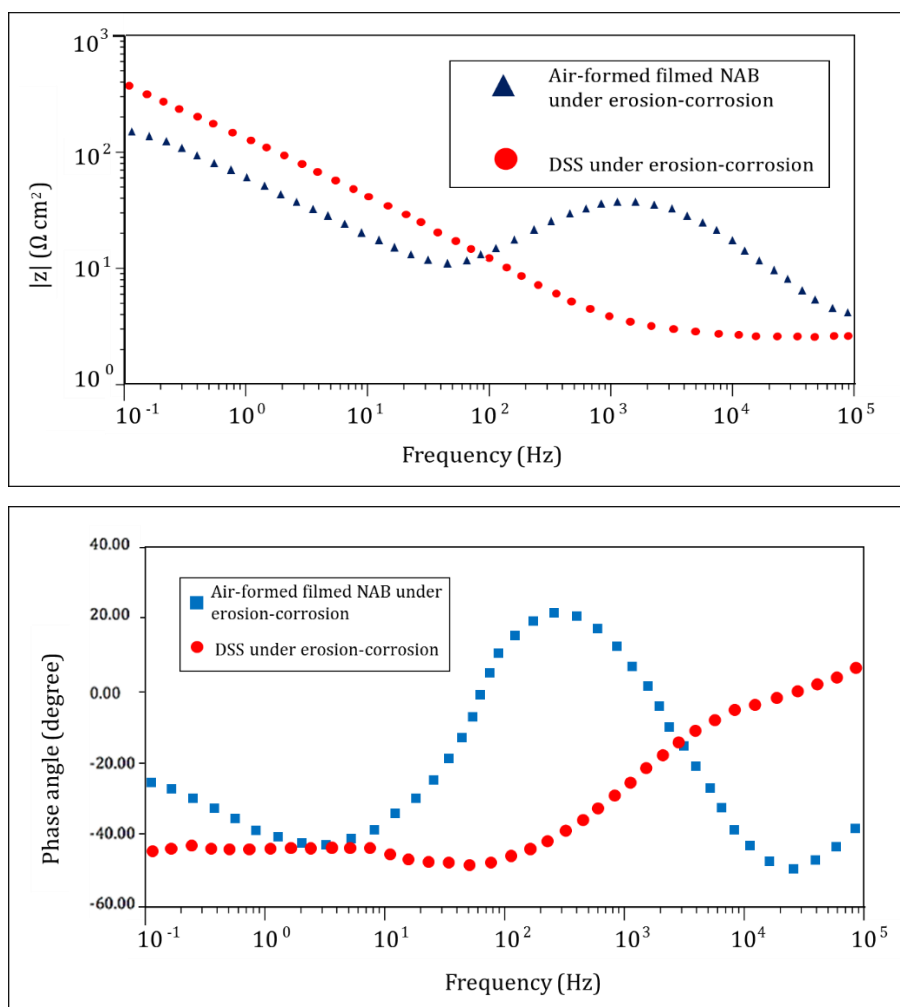
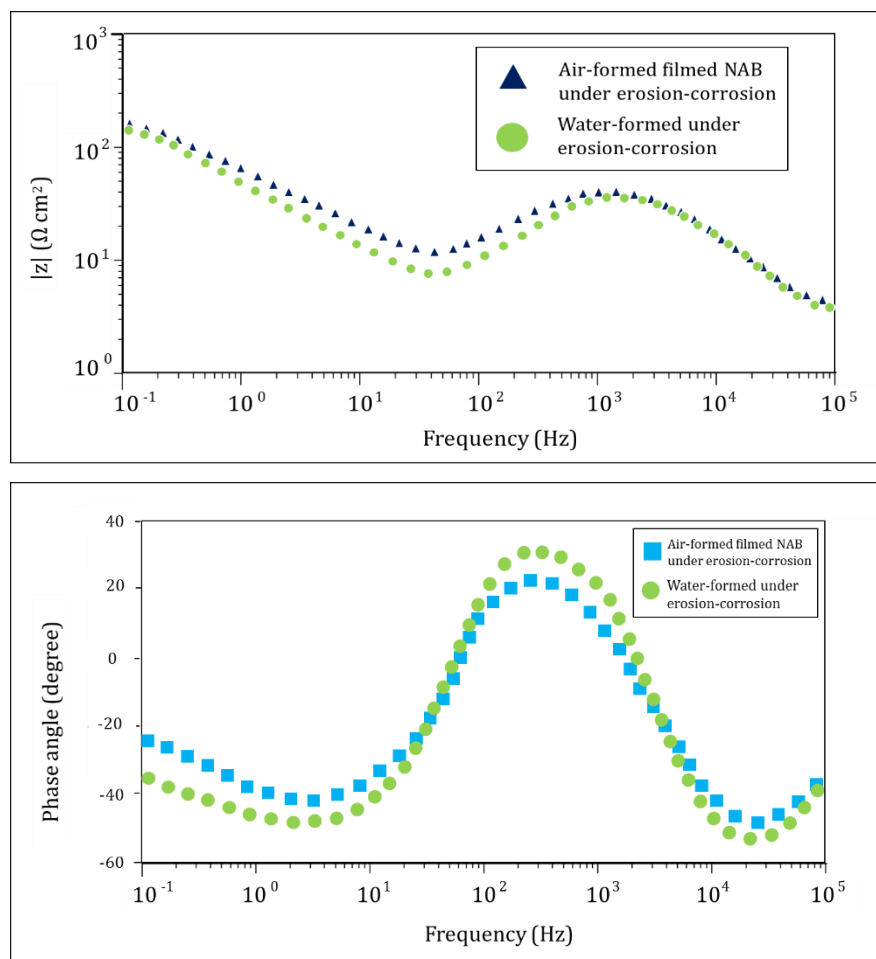


**Fig. 6.8:** Bode plot of DSS and air-formed filmed NAB obtained after 1-h cavitation in 3.5% NaCl solution.

Also, comparisons were made for the EIS obtained for DSS and NAB with air-formed film after 1 h of cavitation in 3.5% NaCl solution. Figure 6.8 shows the EIS bode plot for DSS and air-formed filmed NAB, taken after 1 h of cavitation in 3.5% NaCl solution. One of the most interesting observations was the similar EIS trend exhibited by NAB with air-formed film after 1 h of cavitation and that obtained for



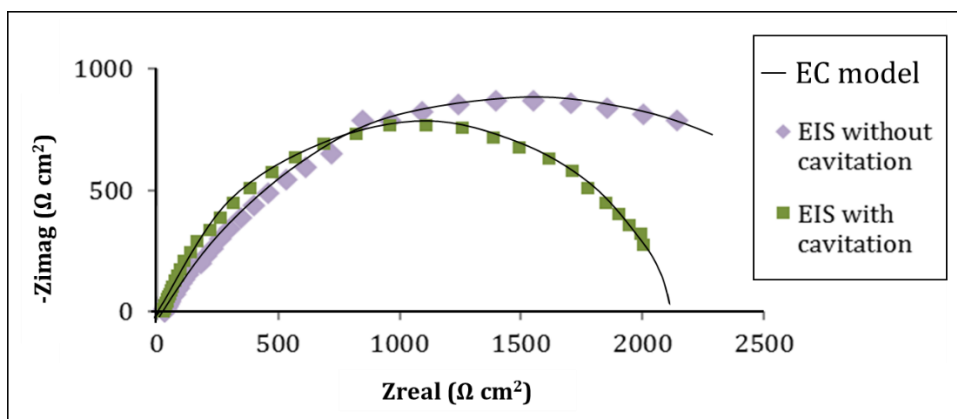
NAB with water-formed film while under the cavitation erosion-corrosion conditions. Whereas, DSS shows very slight variation from the EIS bode curves obtained under C and T conditions when compared to the trend obtained after undergoing 1 h of cavitation erosion-corrosion.



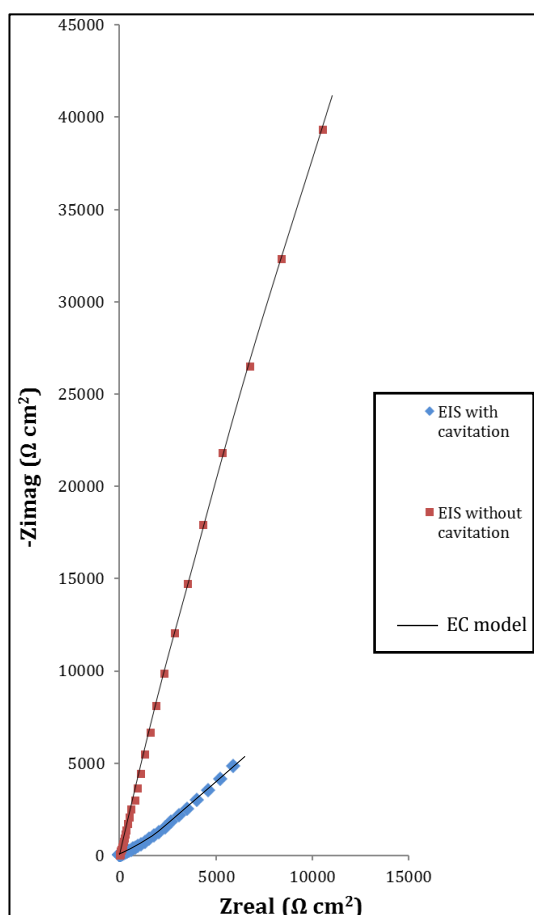
**Fig. 6.9:** Bode plot for air-formed filmed NAB after 1 h of cavitation, and NAB with water-formed film while under the cavitation erosion-corrosion conditions.

Figure 6.9 compares the EIS obtained for the NAB with air-formed film after 1 h of cavitation and water-formed filmed NAB under T. From the figure, it is understood that after undergoing cavitation and removal of the protective oxide film, the samples exhibit very similar properties. Furthermore, as observed from the microstructural analyses in chapter 5, three months immersion of NAB in 3.5% NaCl solution induces crevice corrosion and selective phase attack, making the surface microstructure more vulnerable to erosion. Thus, giving very similar trend to the EIS trend of already cavitated surface of air-formed filmed NAB subjected

to corrosion. This also further supports the speculation on the strong contribution of corrosion-enhanced erosion especially for immersion-filmed NAB. Figure 6.10 (a) and (b) show the Nyquist plots for both DSS, air-formed and water-formed oxide filmed NAB samples under C and T conditions.



(a)



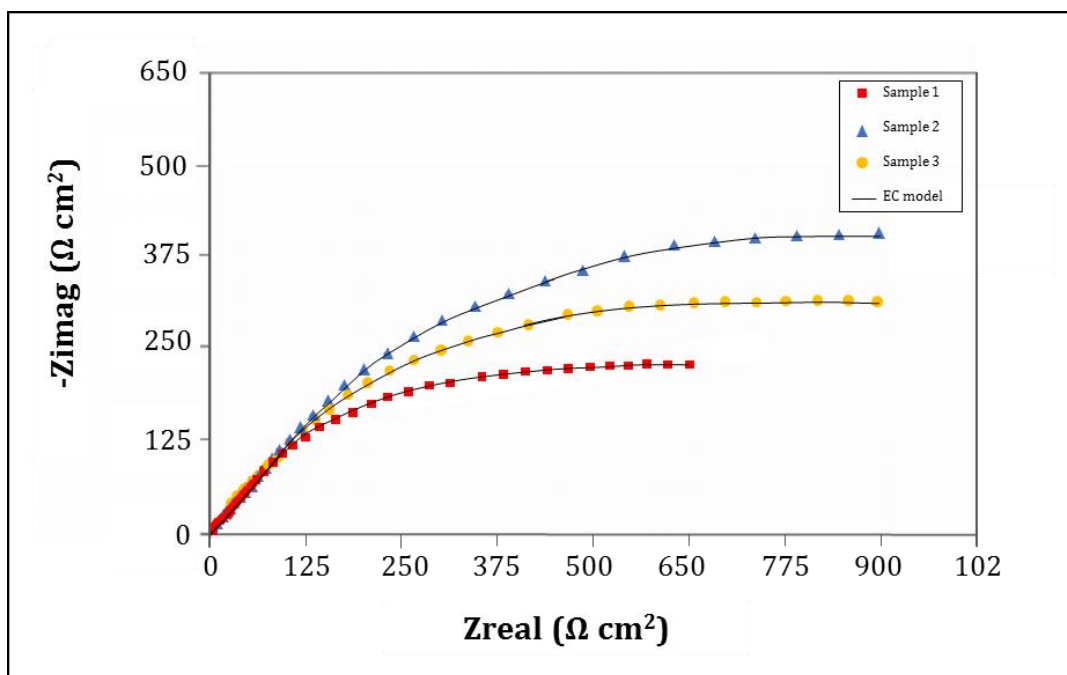
(b)

**Fig. 6.10:** Nyquist plots for (a) air-formed filmed NAB, and (b) DSS samples in 3.5% NaCl solution with and without cavitation.

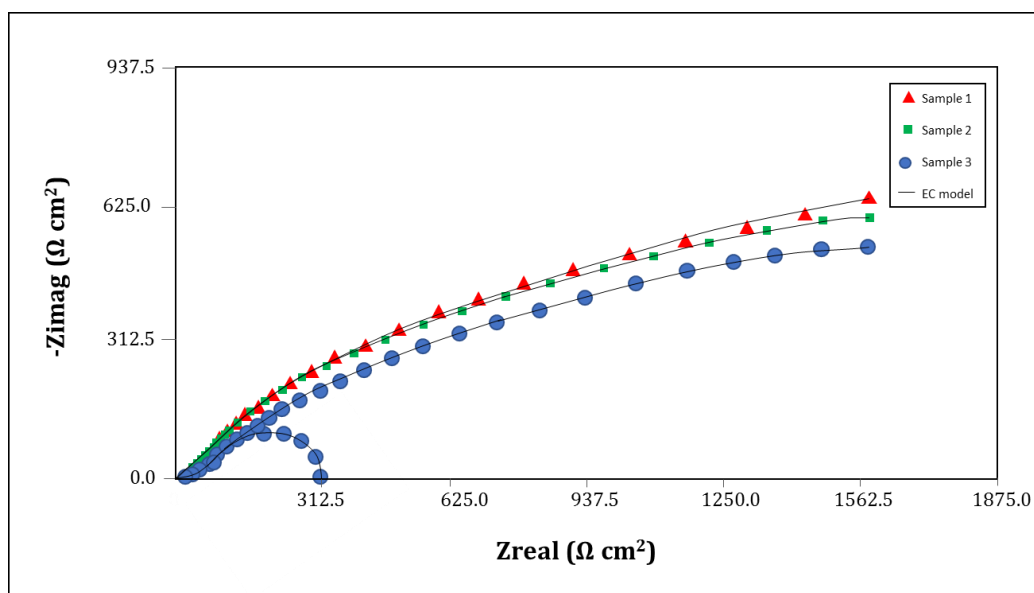
Nyquist plots are generally represented by semicircles or arcs, as seen in Figure 6.10 (a), where the shape of the curve provides insight into the possible mechanisms taking place in the cell, such as single time-constant, diffusion, etc. It can be clearly seen that both materials exhibited single time-constant plots with one distorted semi-circle neither of them underwent diffusion whether under pure corrosion or cavitation erosion-corrosion tests. The radius of semi-circle is relevant to polarization resistance, where the larger the semicircle is, the higher the polarization resistance. From the Nyquist curves it can be seen that for both materials, the polarization resistance is significantly decreased with cavitation with much smaller semicircles. DSS typically exhibits the single time-constant plot as shown in Figure 6.10 (b). Whereas, a typical Nyquist plot for NAB would exhibit diffusion along with a single time-constant semi-circle due to the initial copper dissolution [205]. However, it was not found in the Nyquist plot in Figure 6.10 (a) due to the forced mass transfer by the violent cavitation clouds and also due to the close proximity of the sonotrode probe to the sample surface.

Figure 6.11 (a) and (b) show the Nyquist plots for water-formed oxide filmed NAB under C and T conditions, respectively. Compared to the Nyquist plots obtained for DSS and the air-formed filmed NAB, the Nyquist plots for the water-formed filmed NAB samples gave varying results. The plots obtained under pure corrosion conditions were similar to that obtained for air-formed filmed NAB sample (Figure 6.11 (a)). Large single time-constants were observed that corresponded to that of the air-formed filmed NAB samples but at much higher resistance values.

However, under cavitation, the Nyquist trend changed into a spiral time-constant (Figure 6.11 (b)), exhibiting an impedance loop at the low-frequency region, with the resistance dropping to 1000 times lower to that seen for pure corrosion. This is believed to be from the incubation period. It is considered to be due to the change in the oxide surface properties with the sudden collapsing of bubbles, causing the change in the Nyquist plots, before rupturing the protective oxide films, forming pits and pores. These pits and pores then promote mass transfer.



(a)



(b)

**Fig. 6.11:** Nyquist plots for three water-formed filmed NAB samples in 3.5% NaCl solution under (a) pure corrosion, and (b) the combined erosion-corrosion conditions.

The EIS results obtained were also verified using fit models. Fit models or equivalent circuit models are used to model and analyse EIS spectra results that can be built in the GAMRY Instrument Echem Analyst software. The electrochemical cells are simulated in the software by incorporating various

factors such as electrode double layer capacitance, electrode kinetics, diffusion layer and solution resistance. Each element in the model has a known impedance behaviour, which is described in terms of electrical components such as resistors, capacitors, inductors, etc. along with a few specialized electrochemical elements like Warburg for diffusion. The impedance of the element depends on the element type and the values of the parameters that characterize that element. For the sample materials used, both DSS and the two types of NAB samples were considered to have passive layer and a protective oxide layers respectively. These layers, especially when eroded by the action of cavitation, may become porous. These pores could be considered as non-coated portions of the substrate. However, due to their small size, the exchange of the electrolyte between the pore and the bulk material may be hampered, therefore, the ion concentration inside the pores could differ from the bulk concentration. This results in an electrolyte resistance,  $R_{\text{pore}}$ , which may be different from the bulk electrolyte (solution) resistance  $R_s$ .

Figure 6.12 gives the respective equivalent circuit that incorporated the pores in the passive layer on the material surface where,  $R_s$  is the bulk solution resistance,  $R_{\text{pore}}$  is the resistance of the pores,  $C_{\text{pl}}$  is the capacitance of the passive layer, and  $R_{\text{inner}}$  and  $C_{\text{inner}}$  are the resistance and constant phase element of the metallic substrate under the passive layer.

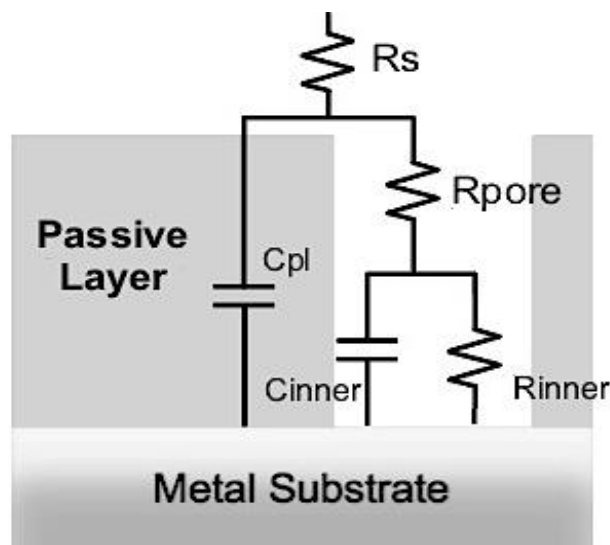


**Fig. 6.12:** A porous passive layer with the resulting equivalent circuit [202].

For NAB, the protective oxide layer is considered to be a mixed Cu/Al oxide, mostly assumed to be  $\text{Al}_2\text{O}_3$ , which is a non-conductive ceramics, hence, considering there is no electron passing through this layer, it is modelled using only one capacitance,  $C_{\text{pl}}$ . Similarly, for DSS, the high chromium content acts as the anodic element that forms chromium oxide under electrochemical reaction, protecting DSS from corrosion. The passive layer formed is again considered as a non-conductive layer and hence, only one capacitance is modelled for it too. Then the interface between the solution and the material substrate through the pore needs to be considered, hence the model incorporates the resistance of the inner substrate layer,  $R_{\text{inner}}$ , and the constant phase element (in  $\Omega^{-1} \text{cm}^{-2} \text{s}^n$ ),  $C_{\text{inner}}$ , parallel with  $R_{\text{inner}}$ . Constant phase element is an equivalent electrical circuit component that models the electrochemical behaviour of an imperfect capacitor and is often used to explain the system heterogeneity. Table 6.2 gives the model parameters used to plot the EIS data in Figure 6.13 for DSS, air-formed filmed NAB, and water-formed filmed NAB samples.

Model parameters	DSS		NAB with Air-formed oxide layer		NAB with Water-formed oxide layer	
	With Cav.	Pure Corrosion	With Cav.	Pure Corrosion	With Cav.	Pure Corrosion
$R_s (\Omega)$	5.222 $\pm 0.029$	5.721 $\pm 0.035$	4.570 $\pm 0.027$	5.336 $\pm 0.031$	2.781 $\pm 0.03$	171.40 $\pm 3.00$
$R_{\text{inner}} (\Omega)$	1296 $\pm 22$	17130 $\pm 63$	238.9 $\pm 2.85$	265.9 $\pm 3.37$	97.03 $\pm 1.19$	84260 $\pm 70$
$R_{\text{pore}} (\Omega)$	107 $\pm 2.2$	193.5 $\pm 6.3$	43.83 $\pm 0.80$	51.02 $\pm 1.56$	4.96 $\pm 0.06$	3602 $\pm 35$
$C_{\text{pl}} (\text{F})$	$198 \times 10^{-6}$ $\pm 1.95 \times 10^{-6}$	$87.40 \times 10^{-6}$ $\pm 0.82 \times 10^{-6}$	$141.30 \times 10^{-6}$ $\pm 1.72 \times 10^{-6}$	$192.70 \times 10^{-6}$ $\pm 2.37 \times 10^{-6}$	$4.86 \times 10^{-6}$ $\pm 0.14 \times 10^{-6}$	$22.33 \times 10^{-9}$ $\pm 0.20 \times 10^{-9}$
$C_{\text{inner}} (\text{F})$	$526 \times 10^{-6}$ $\pm 7.57 \times 10^{-6}$	$104 \times 10^{-6}$ $\pm 1.54 \times 10^{-6}$	$250.60 \times 10^{-6}$ $\pm 5.86 \times 10^{-6}$	$785.60 \times 10^{-6}$ $\pm 13.02 \times 10^{-6}$	$3.48 \times 10^{-3}$ $\pm 36.24 \times 10^{-6}$	$454.9 \times 10^{-9}$ $\pm 4.34 \times 10^{-9}$

**Table 6.2:** Parameters for the fit models used for air-formed filmed NAB, water-formed filmed NAB and DSS under C and T conditions.

From the fit model illustrated in Figure 6.13, the resistance elements at the pores and the inner layer were compared for all the results obtained from EIS test for both NABs and DSS, and plotted in Figures 6.7 and 6.8.

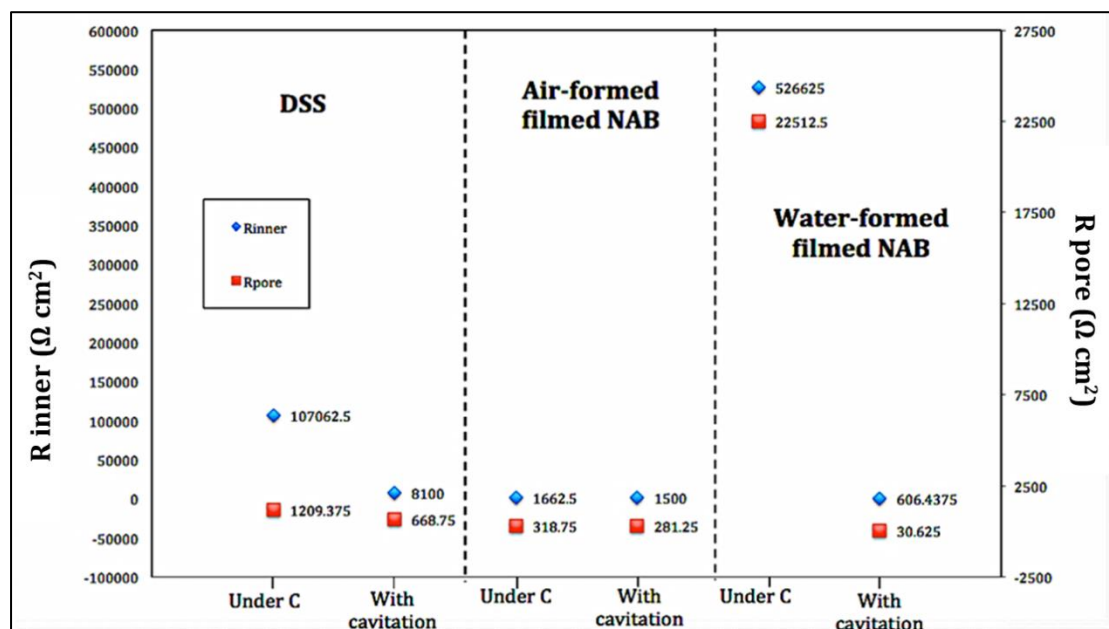


**Fig. 6.13:** EIS plots for DSS and air-formed as well as water-formed oxide filmed NABs under C and T test conditions, obtained using fit models.

From Figure 6.13 it can be seen that in all cases,  $R_{inner}$  was higher than  $R_{pore}$ , showing higher corrosion resistance of the substrate due to the protective films, which reduce mass transfer. DSS exhibited higher substrate layer resistance for both pure corrosion and combined cavitation erosion-corrosion measurements as compared to the air-formed filmed NAB. The pore resistance for DSS under cavitation is almost 5 times the pore resistance for air-formed filmed NAB under C conditions. This high resistance for DSS may be explained from the chemical composition and microstructural analysis of the sample in chapter 4 and 5, where it was seen that a high percentage of chromium was present in the chemical composition of DSS, giving it high passivity to corrosion.

The pore resistance for the air-formed oxide filmed NAB under both C and T conditions were seen to be comparatively lower than the substrate resistance. The  $R_{inner}$  and  $R_{pore}$  for air-formed filmed NAB are seen to be lower than that of DSS.

Also, it can be seen that for the air-formed filmed NAB the substrate resistance ( $R_{\text{inner}}$ ) is higher than the pore resistance ( $R_{\text{pore}}$ ) in both cases. The substrate and pore resistance of NAB subjected to C was slightly higher than that obtained under T. This could be due to an increase in pore sizes or numbers induced under cavitation, enhancing mass transport, causing the decrease in the  $R_{\text{inner}}$  and the  $R_{\text{pore}}$  value. However, the values did not differ by a large margin, which could be due to the surface undergoing rapid passivation process even though under the cavitation impact, causing the corrosion process to slow down.

The  $R_{\text{inner}}$  and  $R_{\text{pore}}$  for water-formed oxide filmed NAB samples under pure corrosion were seen to have the highest magnitude. This is attributed to the high resistance of the thick  $\text{Al}_2\text{O}_3$  film formed on the surface after 3 months of immersion. This resulted in low mass transfer, and hence high  $R_{\text{inner}}$  and  $R_{\text{pore}}$  values. However, under cavitation, the water-formed filmed NAB seemed to give the lowest  $R_{\text{inner}}$  and  $R_{\text{pore}}$  among the three sample materials. This goes to show that since the substrate of a water-formed filmed NAB had been weakened by selective phase attack and crevice corrosion, along with Cu dissolution while immersed in 3.5% NaCl solution, once the oxide layer was removed by the action of imploding bubbles, the substrate was most vulnerable to corrosion, exhibiting low resistance.

### 6.3. Potentiodynamic polarization

For the pure corrosion test, DSS and NAB samples with oxide layers formed under the two different conditions were also subjected to potentiodynamic polarization scanning at  $0.167 \text{ mV s}^{-1}$  scan rate under static conditions using GAMRY potentiostat in 100 ml of 3.5% NaCl solution.

The polarization curve measured was the log current (in Ampere) against the potential vs. the reference electrode of Ag/AgCl, measured at room temperature in 3.5% NaCl solution. The samples had an exposed surface area of  $6.25 \text{ cm}^2$ . Figure 6.14 plots the two polarization curves of DSS after scanning under static



conditions in 100 ml of 3.5% NaCl solution at  $0.167 \text{ mV s}^{-1}$  scan rate; showing Tafel extrapolation derived from the anodic and cathodic reaction plots. These assisted in locating the corrosion current densities, and calculate the subsequent corrosion rates.

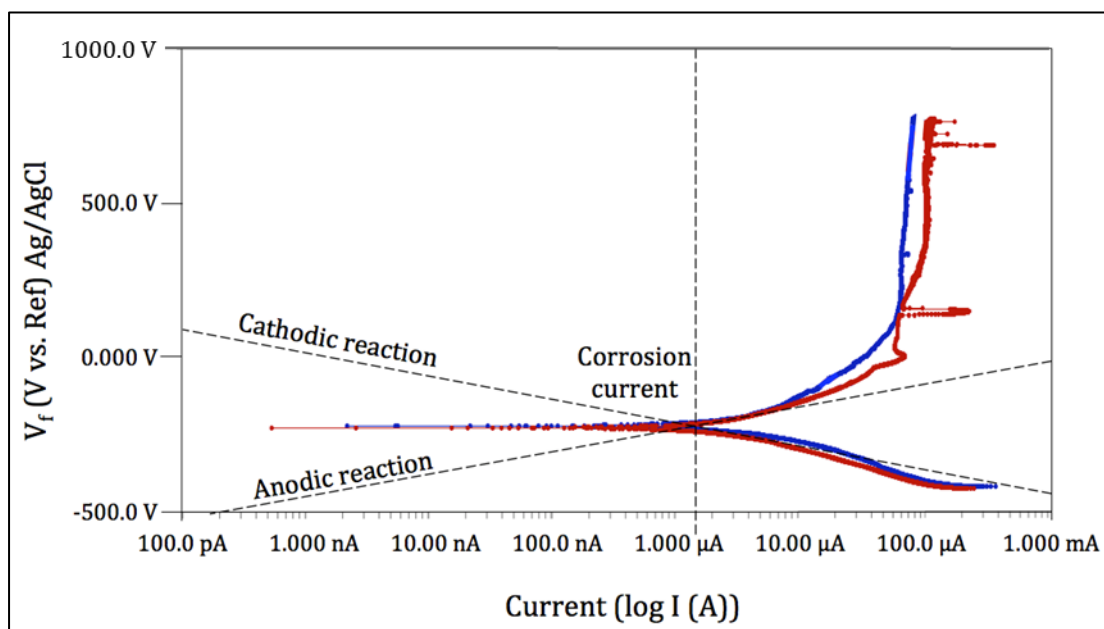


**Fig. 6.14:** Polarization curves for DSS in 3.5% NaCl solution, showing the location of the current density derived from Tafel extrapolation.

From Figure 6.14, it can be seen that the corrosion current for DSS is about  $0.5 - 1 \mu\text{A}$ , obtained using Tafel extrapolation. This gives a current density of  $0.16 \mu\text{A cm}^{-2}$  for DSS.

Figure 6.15 plots the two polarization curves for NAB samples with air and water-formed films, comparing the current rates and active regions for the two samples [203].

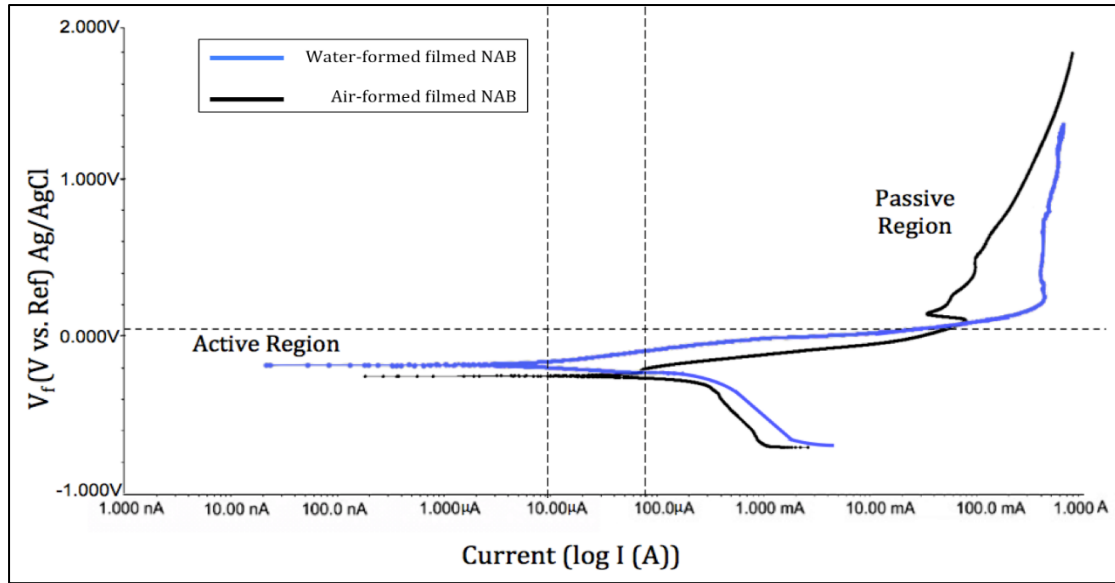


**Fig. 6.15:** Polarization curves for NAB samples with air-formed and water-formed oxide films in 3.5% NaCl solution [203].

From Figure 6.15, the corrosion currents can again be obtained using Tafel extrapolation. The corrosion currents for NAB with air and water-formed films are 100  $\mu\text{A}$  and 10  $\mu\text{A}$ , respectively. From which, the corrosion current densities ( $i_{\text{corr}}$ ) are calculated as 16  $\mu\text{A cm}^{-2}$  for the air-formed oxide filmed NAB, and 1.6  $\mu\text{A cm}^{-2}$ , for the water-formed oxide filmed NAB.

From these  $i_{\text{corr}}$  values the mass loss rates of the samples can be calculated using Faraday's laws of electrolysis or Faradaic conversion, as given in Equation 6.1 [227].

$$\text{Current density, } i_{\text{corr}} = \frac{\text{Mass loss rate} \times \text{number of electrons freed} \times \text{Faraday's constant}}{\text{Atomic mass of corroding element} \times \text{exposed area}} \dots (6.1)$$

Where, Faraday's constant = 96485 C mol<sup>-1</sup>

The method of measuring mass loss via current density is further elaborated in chapter 7. From Figures 6.14 and 6.15, the free corrosion potentials for the cathodic protection tests obtained are tabulated in Table 6.3.

Samples	Cathodic protection potentials
Air-formed filmed NAB	-400 mV
Water-formed filmed NAB	-400 mV
DSS	-250 mV

**Table 6.3:** *free corrosion potentials for the cathodic protection tests for the test samples.*

## 6.4. Discussion

From the results obtained, it was seen that both DSS and NAB (with air- and water-formed oxide films) exhibited high corrosion properties under pure corrosion. DSS was most anodic under pure corrosion conditions, however, when subjected to cavitation, water-formed oxide filmed NAB appeared to be most anodic, compared to the NAB with air-formed oxide film and DSS. The passivity of DSS was attributed to the high chromium content in its composition, however, for NAB, its varying corrosion properties for the different oxide films were attributed to the corrosion properties of the individual oxide films. As mentioned in section 5.1.1.2, since the water-formed oxide layer took about 2 h for full removal before the substrate is fully exposed, the corrosion property was considered to be kept intact longer than the air-formed filmed NAB samples, giving it the high corrosion resistance even under cavitation.

However, under cavitation, it was also seen that the water-formed filmed NAB gave the lowest  $R_{inner}$  and  $R_{pore}$  values among the three sample materials (Figure 6.13). This was considered due to the already weakened microstructure of the substrate, caused by selective phase attack and crevice corrosion, as found under microstructural analyses. There was also additional potential Cu dissolution expected in 3.5% NaCl solution. Also, the oxide film formed is generally very porous and brittle. Due to this, although the free potentials were the most anodic for water-formed filmed NAB under cavitation, the action of implosion created more pores and pittings for higher mass transfer, resulting in lower resistance of the substrate and pore for NAB.

Also, as mentioned in section 4.2.3.2, while the protective layer of aluminium oxide formed of NAB has a film thickness that can go up to 1  $\mu\text{m}$  that provide sufficient corrosion resistance, to achieve back the substantial oxide layer thickness may take days. And hence, during the continuous hammering under cavitation test over a period of 1 h, it makes it difficult for a thick oxide layer to form back quickly [193], [221].

It was also seen that for water-formed oxide filmed NAB samples, the more electropositive the OCP the higher the mass loss incurred on the samples (Figure 6.4). This suggested that the higher the passivation or protection of the sample, the higher the mass loss incurred due to corrosion [204]. Furthermore, the EIS bode and Nyquist plots also exhibited that under the influence of cavitation, the corrosion properties of all the materials changed, exhibiting lower resistance than under pure corrosion.

As also observed from the microstructural analyses in chapter 5, three months immersion of NAB in 3.5% NaCl solution induced crevice corrosion and selective phase attack, making the surface microstructure more vulnerable to erosion. Thus, giving very similar trend to the EIS trend of already cavitated surface of air-formed filmed NAB subjected to corrosion. This also further supports the speculation on the strong contribution of corrosion-enhanced erosion especially for immersion-filmed NAB.

## 6.5. Summary

OCP data were obtained for all the three test samples and compared. The data obtained from the electrochemical measurements for the pure corrosion showed that DSS trend was stable at -145 mV. Whereas, air-formed NAB trend was stable at -210 mV, exhibiting that DSS is nobler than NAB under pure corrosion conditions. The OCP for water-formed film was also found to be higher than for the air-formed film, owing to its thick protective oxide layer.

For cavitation erosion-corrosion test, the cavitation was applied at the 600<sup>th</sup> second; the OCP results obtained showed de-passivation of the materials with a negative shift in their potentials. This potential shift could be attributed to the disruption of the protective layer on the material surface by the rapid and violent implosion of cavitation bubbles. It was observed that the DSS attained stability within 600s at -490 mV, whereas NAB attained stability in 100 s at -300 mV. For DSS, there was a positive shift in the OCP trend with time under both pure corrosion and the combined erosion-corrosion conditions, implying strong re-passivation characteristics of DSS.

The OCP of water-formed filmed surface was more anodic by 20-50 mV than the air-formed filmed surface. Both samples sifted negatively the application of cavitation, while conducting OCP before reaching stability again. The water-formed film reached stability much more gradually in 600 sec than the air-formed film that reached stability within 100 sec. OCP of water-formed filmed NABs were also investigated during the cavitation incubation period, where it was seen that the potentials drastically shifted to positive during the incubation period, before following the same trend as its air-formed counterpart.

To further analyse the corrosion behaviours of the test samples, EIS curves, both bode and nyquist, were also presented. The EIS measurement suggested re-passivation of the material surface for DSS, and the protective nature of the oxide layer of NAB samples even under cavitation, indicating high corrosion resistance properties for both the sample materials.

The EIS results were further analysed under fit models where it was seen that the pore and the substrate resistances of DSS were higher for both pure corrosion and combined cavitation erosion-corrosion measurements as compared to the air-formed filmed NAB. The pore resistance for DSS under cavitation is almost 5 times the pore resistance for air-formed filmed NAB under C conditions. This was attributed to the high percentage of chromium present in the chemical composition of DSS. The pore and the substrate resistances for water-formed

oxide filmed NAB samples under pure corrosion were seen to have the highest magnitude. However, under cavitation, they were in fact the lowest among the three sample materials. This was explained by the microstructural analysis that the substrate of a water-formed filmed NAB had been weakened by selective phase attack and crevice corrosion, along with Cu dissolution while immersed in 3.5% NaCl solution, causing low resistance.

The three material samples were also subjected to potentiodynamic polarization, to obtain mass loss rate under pure corrosion, and also to determine the potentials for performing cathodic protection of the materials. From the polarization curves, it was concluded that the current density for DSS was the lowest ( $0.16 \mu\text{A cm}^{-2}$ ), followed by water-formed oxide filmed NAB ( $1.6 \mu\text{A cm}^{-2}$ ), and lastly, the air-formed oxide filmed NAB ( $16 \mu\text{A cm}^{-2}$ ).



# Chapter 7:

# Synergy

# quantification

---

## 7.1. Introduction

Synergy can be measured in terms of two common factors, mass loss incurred by combined contribution of erosion and corrosion, or the mean depth of penetration rate. The equation for synergy according to ASTM G-119 standards is commonly written as:



$$T = S + E + C \quad \dots(7.1)$$

Where,  $T$  is the total mass loss or overall cavitation erosion-corrosion rate,  $C$  is the pure corrosion contribution,  $E$  is the pure erosion contribution, and  $S$  represents the combined contribution due to synergistic effect [228].  $S$  can also be represented using Equation 7.2:

$$S = T - (E+C) = \Delta E + \Delta C \quad \dots(7.2)$$

Where,  $\Delta E$  = corrosion-enhanced erosion, and  
 $\Delta C$  = erosion-enhanced corrosion.

The underlying mechanisms for corrosion-enhanced erosion,  $\Delta E$ , may generally include removal of work-hardened surfaces due to corrosion, exposing the softer substrate to the erosion mechanisms; selective phase attack of grain boundaries; as well as increase in the number of stress-concentrating defects caused by corrosion micro-pitting [229].

Whereas, the mechanisms involved in erosion-enhanced corrosion,  $\Delta C$ , can occur due to factors such as local acidification occurring within the erosion pits, which results in acceleration of corrosion rates, prohibiting further film formation; surface roughening due to erosion, causing an increase in ion transportation by high turbulence levels; or change in mechanical properties of the sample material, such as lowering of the fatigue strength, due to corrosion [229]. Evidence for erosion-enhanced corrosion has also been given by various studies undertaken, discussed later in the chapter [17], [164], [230]–[232].

For DSS and air-formed filmed NAB, the tests were carried in five different methods, used to calculate the synergy for the test samples. For water-formed filmed NAB, only three different methods were used.

As mentioned in chapter 4, section 4.3, synergy tests were conducted under three different test conditions, namely, pure erosion, pure corrosion, and combined

erosion-corrosion as per ASTM G-119 standards [233]. For E tests, three samples were subjected to cavitation erosion in 5 L of triple distilled water for 1 h. And three samples were subjected to cavitation erosion in 3.5% NaCl solution with cathodic protection for 1 h. The potentials for the cathodic protections were obtained via potentiodynamic polarization of each sample.

The C were also obtained in two different ways, gravimetrically by using mass balance, and from the potentiodynamic polarization curves. The samples were subjected to in-situ electrochemical measurements kept at OCP in 3.5% NaCl solution for 1 h. EIS analysis was also conducted in order to understand the corrosion trend of each test sample. Two samples of each material were also subjected to potentiodynamic polarization, at a potential range between -1 to 2 V. From the corrosion rates given by the polarization graphs, C was obtained by applying Faradaic conversion. Free corrosion potentials of specimens in 3.5% NaCl solution was measured under both quiescent and cavitation conditions. Which, in turn, provided with the combined cavitation erosion-corrosion results (T). All six samples were cavitated in 5 L of 3.5% NaCl solution for 1 h while subjected to OCP.

The synergy measurement was obtained using three main approaches, namely the gravimetric mass loss method, the volumetric mass loss method, and mean depth of penetration rate method. Under the gravimetric method, the erosion rates (E) were obtained in two different ways: by erosion in 5 L of distilled water for 1 h, and by subjecting the samples to cavitation erosion in 3.5% NaCl solution with cathodic protection for 1 h. Alicona InfiniteFocus 3D non-contact optical profilometer was used to obtain the synergy value using the MDPR method, and the volumetric mass loss method.

The initial aim mainly employed gravimetric method as the means of quantifying synergy, however, several variables and factors rendered quantification of T, E and C accurately difficult. And hence, other test methods were adopted and tried in order to find the most reliable combination to obtain S. Figure 7.1 describes the various methods used.

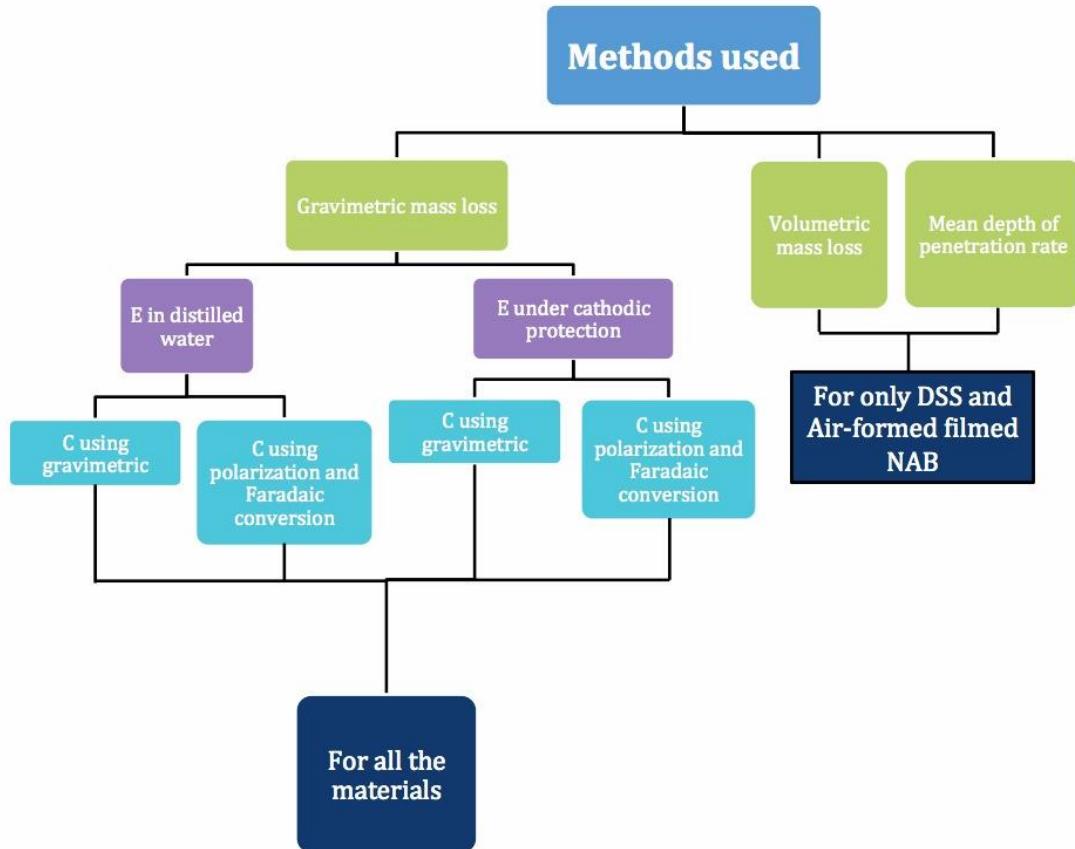


**Fig. 7.1:** Flow chart for different methods used for synergy evaluation.

Hence, from the results obtained, and using Equation 7.1, synergy rates were calculated for each sample material. The aim of the present chapter was to attempt to quantify and understand the existence of synergism between erosion and corrosion in the overall cavitation erosion–corrosion damage of the marine propeller materials in 3.5% NaCl solution at room temperature using five different methods. However, given the variables in the synergy results under each test conditions, and also the high error accumulation, the exact value of  $S$  was difficult to evaluate. Furthermore, it was difficult to resolve  $S$  into the separate  $\Delta E$  and  $\Delta C$  components. Also, the  $\Delta C$  component of  $S$  was further difficult to measure directly using electrochemical techniques due to the rapid and aggressive nature of the cavitation clouds produced in the experimental set up, affecting the ohmic drop [202].

## 7.2. Synergy evaluation

### 7.2.1. Gravimetric method

For the gravimetric analysis, the samples were prepared before and after each test. Samples were cleaned with alcohol (methanol), then with distilled water, before drying with pressurized air. They were then left to completely dry on a clean surface for 12 h – 24 h before being weighed in the precision mass balance at least five times, calibrated before every measurement. The resultant weight used was the average of the five weights measured. The samples were then subjected to the corresponding tests under E, C and T conditions, before repeating the whole cleaning and weighing process again.

Using Equations 7.1 and 7.2, and considering gravimetric values from Table 7.1, the synergy can be calculated as:

Material used	$T$ (mg)	$E$ (mg)	$C$ (mg)	$S$ $= T - (E + C)$ (mg) Using Equation 7.1	$(S/T) \times 100$ (%)
Air-formed oxide-filmed NAB	1.48 $\pm$ 0.02	1.00 $\pm$ 0.05	-0.61 $\pm$ 0.04	1.09 $\pm$ 0.11	73 % $\pm$ 8%
Water-formed oxide-filmed NAB	24.39 $\pm$ 2.00	7.34 $\pm$ 0.30	2.93 $\pm$ 1.00	14.12 $\pm$ 3.30	58 % $\pm$ 13%
Duplex Stainless Steel	0.96 $\pm$ 0.02	0.71 $\pm$ 0.02	-0.10 $\pm$ 0.02	0.35 $\pm$ 0.06	36 % $\pm$ 6%

**Table 7.1:** Synergism summary for the samples using mass loss measurements. DSS and air-formed filmed NAB results taken from [18].

It can be seen from Table 7.1 that for air- and water-formed filmed NABs and DSS samples, synergy had measurable impact on their cavitation erosion-corrosion.

While the synergy between cavitation wear and corrosion for air-formed oxide filmed NAB was found to be 73%, it was comparatively lower at 58% and 36% for the water-formed filmed NAB and DSS, respectively. There was also uplift in the mass loss values for NAB with water-formed film than that with air-formed film.

The lower synergy for DSS could be attributed to DSS having low stacking fault energy and higher mechanical strength than NAB [18]. It is also observed that there was a gain in mass by about 0.6 mg for NAB after the OCP test for pure corrosion, and about 0.1 mg mass gain in case of DSS. Whereas, for water-formed filmed NAB, there was mass loss reported under C. Due to this varying magnitude of C values, polarization technique was employed to obtain C.

### **7.1.2. Polarization method**

It was seen that when using gravimetric method for C, it was giving negative values, i.e. mass gain. Also, as seen from chapter 6, there were issues with varying C values obtained using gravimetric method, depending upon the type oxide/passive film present. Additionally, C exhibited sensitivity to pre-exposure conditions particularly for NAB. Hence, polarization technique was adapted to replace the gravimetric results for C.

As mentioned in chapter 6, section 6.3, the corrosion current density ( $i_{\text{corr}}$ ) of water-formed and air-formed oxide filmed NABs are found to be  $1.6 \mu\text{A cm}^{-2}$  and  $16.0 \mu\text{A cm}^{-2}$ , respectively, and  $0.16 \mu\text{A cm}^{-2}$  for DSS, using Tafel extrapolation of the anodic and cathodic lines on the polarization curves. From these values of  $i_{\text{corr}}$  the corrosion rates of the samples were calculated, which further aided in measuring the subsequent mass loss using Faradaic conversion, given by Equation 7.3 – 7.6 [227].

For mass loss using corrosion rate under static polarization conditions:

$$\text{Corrosion rate (mm y}^{-1}\text{)} = \frac{5.12 \times i_{\text{corr}} \times \text{Equivalent weight}}{\text{Density}} \quad \dots (7.3)$$

Where,

$$\text{Equivalent wt. (g)} = \sum \left( \frac{\text{mass fraction of alloy} \times \text{atomic weight of each element}}{\text{Valency}} \right) \quad \dots(7.4)$$

The mass fraction of the corroding for NAB was considered for copper (80%), and for DSS, it was considered for iron (63%) and chromium (22%). The atomic weight of copper is  $63.5 \text{ g mol}^{-1}$ , and that of iron and chromium are  $56 \text{ g mol}^{-1}$  and  $52 \text{ g mol}^{-1}$ , respectively.

Also, corrosion rate can also be written in terms of mass loss as [227]:

$$\text{Corrosion rate (mm y}^{-1}\text{)} = \frac{\text{mass loss} \times k}{\text{density} \times \text{exposed area} \times \text{time}} \quad \dots (7.5)$$

Where  $k$  is a constant that defines the units for the corrosion rate, here it is  $8.76 \times 10^4$  [227]. From there, the mass loss rate can be calculated using Equation 7.6:

$$\text{Mass loss rate} = \frac{i_{\text{corr}} \times \text{Atomic mass of corroding element} \times \text{exposed area}}{\text{number of electrons freed} \times \text{Faraday's constant}} \quad \dots(7.6)$$

Where, the rate of mass loss is in  $\text{mg cm}^{-2} \text{ h}^{-1}$ , and

Faraday's constant =  $96485 \text{ C mol}^{-1}$

For NAB, considering the redox reactions 4.8 and 4.9 from chapter 4, the corroding element was considered to be copper, forming cuprous oxide and then cupric. The number of free electrons was considered as 2.

And as for DSS, the corroding element was considered to be iron,



And hence, the number of free electrons was 2. Thus, the mass loss values obtained

for pure corrosion using polarization at 0.167 mV s<sup>-1</sup> scan rate are given in Table 7.2:

Sample surface	$i_{\text{corr}}$ ( $\mu\text{A cm}^{-2}$ )	Mass loss (in mg)
DSS	0.16	$0.0017 \pm 0.0002$
Air-formed filmed	16.0	$0.197 \pm 0.002$
Water-formed filmed	1.6	$0.0197 \pm 0.0002$

**Table 7.2:** Current density and mass loss obtained for NAB with air-formed oxide film and water-formed oxide film from polarization scanning in 3.5% NaCl solution.

From Table 7.2, the mass loss incurred for DSS was found to be the lowest, at 0.0017 mg ( $\pm 0.0002$ ) mg. NAB with air-formed film gave the highest amount of mass loss value, of 0.19 mg ( $\pm 0.01$ ) mg, and for water-formed filmed samples, it was the lowest, at 0.019 mg ( $\pm 0.001$ ) mg. These  $i_{\text{corr}}$  values are found consistent with the literature [179], [180], [234][235]. From the mass losses in Table 7.2, synergy values were evaluated and tabulated in Table 7.3.

In addition, the cavitation erosion resistance in distilled water ( $R_E$ ), corrosion resistance in 3.5% NaCl solution ( $R_C$ ), and the cavitation erosion–corrosion resistance in 3.5% NaCl solution ( $R_T$ ) was also calculate, which is defined as the reciprocal of the mass loss rate over a time period, given by Equations 7.8 –7.10:

$$R_T = t/T \text{ (h mg}^{-1}\text{)} \quad \dots(7.8)$$

$$R_E = t/E \text{ (h mg}^{-1}\text{)} \quad \dots(7.9)$$

$$R_C = t/C \text{ (h mg}^{-1}\text{)} \quad \dots(7.10)$$

Where, t is the test time period.

<b>Material used</b>	<b>T (mg)</b>	<b>R<sub>T</sub></b> Using Equation 7.8 <b>(h mg<sup>-1</sup>)</b>	<b>E (mg)</b>	<b>R<sub>E</sub></b> Using Equation 7.9 <b>(h mg<sup>-1</sup>)</b>	<b>C (mg)</b>	<b>R<sub>C</sub></b> Using Equation 7.10 <b>(h mg<sup>-1</sup>)</b>	<b>S = T - (E + C)</b> Using Equation 7.1 <b>(mg)</b>	<b>(S/T) x 100 (%)</b>
Air-formed oxide-filmed NAB	1.48 ± 0.02	0.67	1.00 ± 0.05	1.00	0.19 ± 0.002	5.27	0.28 ± 0.072	19% ± 5%
Water-formed oxide-filmed NAB	24.39 ± 2.00	0.04	7.34 ± 0.30	0.14	0.019 ± 0.002	52.76	17.05 ± 2.302	70% ± 9%
Duplex Stainless Steel	0.96 ± 0.05	1.04	0.71 ± 0.02	1.41	0.002 ± 0.001	500.00	0.25 ± 0.071	26% ± 7%

**Table 7.3:** Synergism summary obtained for DSS, NAB with air- and water-formed oxide films obtained from gravimetric analysis for T and E, and polarization scanning for C in 3.5% NaCl solution.

As seen in Table 7.3, the total mass loss incurred under the combined effect of cavitation erosion and corrosion for NAB samples with water-formed film was much higher than the total mass loss observed for air-formed oxide filmed samples and DSS. Also, the mass loss incurred in distilled water was significantly lower than that found under T for all the materials.

The resultant synergy calculated for samples with water-formed film (70%) was found to be about 3.7 times higher than the synergy calculated for samples with air-formed film (19%), and 2.7 times higher than that for DSS (26%). For DSS, the polarization and Faradaic conversion yielded very small C value, and hence, did not contribute much to the S calculation in Equation 7.1, implying that erosion was the predominant contributor towards S.



Also, from the resistance values obtained in Table 7.3, the materials were ranked according to their  $R_T$  and  $R_E$  values as:

$$\text{DSS} > \text{Air-formed filmed NAB} > \text{Water-formed filmed NAB}$$

And under the C conditions, the materials were ranked according to their corrosion resistance as:

$$\text{DSS} > \text{Water-formed filmed NAB} > \text{Air-formed filmed NAB}$$

This shows that DSS, having higher mechanical and corrosion properties (as stated in section 4.2) exhibited better resistance to pure erosion, pure corrosion as well as cavitation erosion-corrosion than all the other samples. And air-formed filmed NAB samples performed better than the water-formed filmed NAB samples under E and T conditions. This may be attributed to the weakening of the substrate microstructure, sans the removal of the protective oxide layer during cavitation, due to the pre-existing selective phase attack and crevice corrosion induced by 3 months of immersion in 3.5% NaCl solution. However, the water-formed filmed NAB showed much higher resistance to corrosion than air-formed filmed NAB, owing to its thick protective oxide layer.

### **7.2.2. Volumetric method**

The material mass loss was also obtained from the volumetric analysis conducted using the Alicona. The value of volumetric mass loss for each sample was calculated using the density of the samples.

Where,

Density of NAB =  $7.65 \text{ g cm}^{-3}$ , and

Density of DSS =  $7.80 \text{ g cm}^{-3}$ .

The volume loss data used were the ones as tabulated in chapter 5, Table 5.2. This method was used for DSS and air-formed filmed NAB samples only, since

volumetric analysis of water-formed filmed NAB samples was not very accurate, such as loss of data, especially due to the thick layer of porous and fragile oxide film. The resultant synergy calculated is presented in Table 7.4. The  $R_T$  and  $R_E$  values plotted in Figure 7.2.

Samples	T (mg)	$R_T$ Using Equation 7.9 (h mg <sup>-1</sup> )	E (mg)	$R_E$ Using Equation 7.10 (h mg <sup>-1</sup> )	C (mg)	S = T - (E+C) Using Equation 7.1 (mg)	S/T x 100%
Air-formed filmed NAB	1.29 ± 0.05	0.77	0.88 ± 0.04	1.13	0.00 ± 0.02	0.41 ± 0.11	31% ± 7%
DSS	0.82 ± 0.03	1.20	0.63 ± 0.03	1.60	0.00 ± 0.02	0.19 ± 0.08	23% ± 10%

**Table 7.4:** Synergism summary for the samples using volumetric mass loss method.

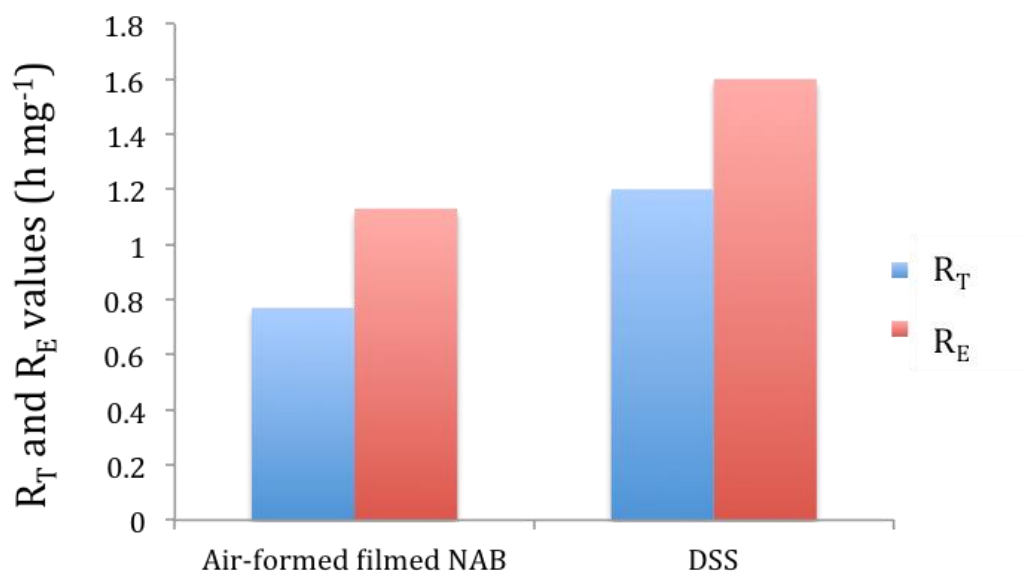


**Fig 7.2:**  $R_T$  and  $R_E$  graph for DSS, and NAB with air-formed oxide films obtained from the volumetric mass loss analysis for T and E.

Figure 7.2 shows, the resistance of both air-formed filmed NAB and DSS to pure erosion was higher than the resistance to cavitation erosion-corrosion when analysed under Alicona for MDPR. And again, DSS showed better resistance to cavitation under both E and T conditions than that of NAB sample.

### ***7.2.3. Cathodic protection method for pure erosion test***

Two samples of each material were tested for pure erosion by applying cathodic protection to the samples. It was seen that air-formed oxide-filmed NAB gave a negative synergy i.e. antagonism, at -16%. However, the synergy for both DSS and water-formed filmed NAB was found to be positive at 28% and 69%, respectively. The negative synergy implies that corrosion in fact reduced the mass loss under the combined effect of erosion and corrosion for air-formed filmed NAB, as compared to mass loss obtained under E. One of the reasons for this is that there are competitions between corrosion and passivation as is always the case, and the cavitation impact has different effects on corrosion and passivation. This reflects to the repassivation kinetics as well as the composition of the protective oxide film on the NAB samples, reducing the mass loss incurred under the combined influence of erosion and corrosion.

On comparing Table 7.3 and 7.5, it was seen that distilled water exhibited lower mass loss under E, when compared to cathodic protection test for air- and water-formed filmed NAB, although, the difference was more significant in case of the air-formed filmed sample. Whereas, for DSS, cathodic protection seemed to reduce the amount of mass loss compared to that obtained under distilled water. Analysing the NAB samples under the SEM, it was observed that under cathodic protection the number of cavities had actually increased, which has also been reported in the literature [181], [180]; although, the grain-boundary attack was reported to be lower than that under distilled water.

<b>Material used</b>	<b>T (mg)</b>	<b>E (Under Cathodic protection) (mg)</b>	<b>R<sub>E</sub> Using Equation 7.9 (h mg<sup>-1</sup>)</b>	<b>C Using Equation 7.6 (mg)</b>	<b>S = T - (E+C) Using Equation 7.1 (mg)</b>	<b>(S/T) x 100 (%)</b>
Air-formed oxide-filmed NAB	1.48 ± 0.02	1.52 ± 0.05	0.65	0.19 ± 0.002	- 0.24 ± 0.072	-16 ± 5%
Water-formed oxide-filmed NAB	24.39 ± 2.00	7.55 ± 0.20	0.13	0.019 ± 0.002	16.84 ± 2.202	69 ± 10%
DSS	0.96 ± 0.02	0.69 ± 0.03	1.45	0.002 ± 0.001	0.27 ± 0.051	28 ± 5%

**Table 7.5:** Mass loss measurements and synergy quantification for the test samples using cathodic protection for the pure erosion test after 1 h in 3.5% NaCl solution.

Figure 7.3 plots the  $R_T$  and  $R_E$  graph for DSS, NAB with air-formed oxide film and NAB with water-formed oxide film from Table 7.3 and 7.5. The values were obtained using gravimetric mass loss analysis for T in 3.5% NaCl solution, and E in distilled water as well as under cathodic protection in 3.5% NaCl solution.  $R_c$  was not plotted in the same graph since the values were of much higher range compared to the  $R_T$  and  $R_E$  values for the sample materials.

From the  $R_T$  and  $R_E$  values, the test materials were again ranked according to their degradation resistance as:

DSS > Air-formed filmed NAB > Water-formed filmed NAB

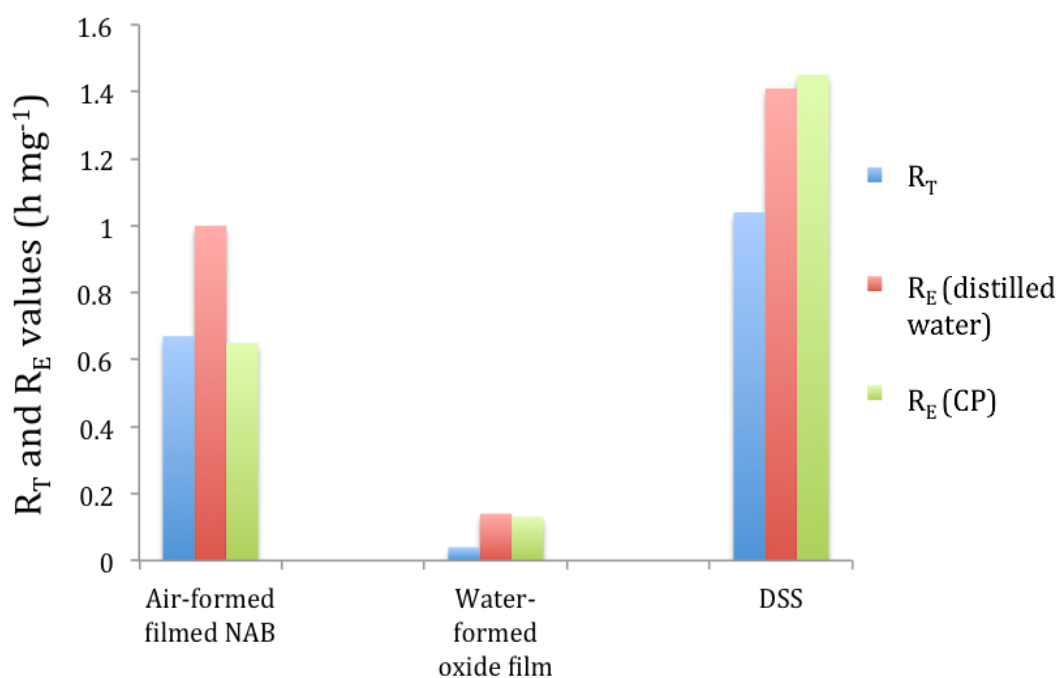


**Fig. 7.3:**  $R_T$  and  $R_E$  graph for DSS, and NAB with air- and water-formed oxide films obtained from Table 7.3 and 7.5.

From Figure 7.2, it can be seen that for all the sample materials the resistance to pure erosion was higher than the resistance to the combined effect of erosion and corrosion. However, for air-formed filmed NAB, the erosion under cathodic protection yielded higher mass loss than T (as seen in Table 7.5) and hence, the resistance was also lower. One explanation of this can be the cushioning effect provided by the corrosion reactions and radicals forming under T conditions that result in the lower mass loss when compared to the cathodically protected cavitation erosion. Decreasing the cathodic potentials to about -1 V may provide higher protection.

Again, for water-formed oxide filmed NAB sample, the resistance to pure erosion under both distilled water as well as cathodic protection was higher than under the combined influence of erosion-corrosion. However, the resistance to erosion in distilled water was higher than resistance to erosion under cathodic protection, meaning higher mass loss under cathodic protection than under distilled water. DSS on the other hand showed increased mass loss under distilled water than under cathodic protection, showing that cathodic protection in fact retarded

erosion rate better than distilled water. Overall, DSS had much higher resistance to T and E under both the E conditions compared to NAB with air- and water-formed oxide films, owing to its higher mechanical properties and strong passivity to corrosion.

#### 7.2.4. Mean depth of penetration method

Another common way of quantifying synergy is by measuring the mean depth of penetration rate, using either contact or non-contact profilometry. From the values obtained during the experiments done using Alicona (as tabulated in chapter 5), the synergy can be calculated using the values tabulated in Table 7.6.

Material used	Mean depth of penetration rate (in $\mu\text{m h}^{-1}$ )			$S = T - (E+C)$ ( $\mu\text{m h}^{-1}$ )	$(S/T) \times 100$ (%)
	E (Distilled water)	T	C	Using Equation 7.1	
Air-formed filmed NAB	$0.645 \pm 0.003$	$0.955 \pm 0.005$	$0.000 \pm 0.001$	$0.310 \pm 0.009$	32% $\pm 1\%$
DSS	$0.460 \pm 0.003$	$0.598 \pm 0.005$	$0.000 \pm 0.001$	$0.138 \pm 0.009$	23% $\pm 2\%$

**Table 7.6:** Synergy quantification for the samples using the MDPR method.

Since, the mean depth of penetration rate in case of pure corrosion under 3.5% NaCl was negligible for both samples due to their high corrosion resistance, the C value were negligible, giving the synergy value only based on the MDPR for pure erosion and the combined cavitation erosion and corrosion tests. This proved that the materials tested exhibited very good resistance to corrosion, showing negligible MDRP under pure corrosion, whereas under the combined effect of erosion and corrosion, it underwent corrosion, showing the existence of synergy. Again, the synergy for NAB (32%) was found to be higher than DSS (23%),

although the values were lower than the ones obtained using the gravimetric methods. These values were closer to the results obtained by other studies in the literature [162], [229], [236].

Materials	$R_T$	$R_E$	$R_C$
Air-formed filmed NAB	1.05	1.55	$\infty$
DSS	1.67	2.17	

**Table 7.7:**  $R_T$  and  $R_E$  values for air-formed filmed NAB and DSS from the MDPR values.

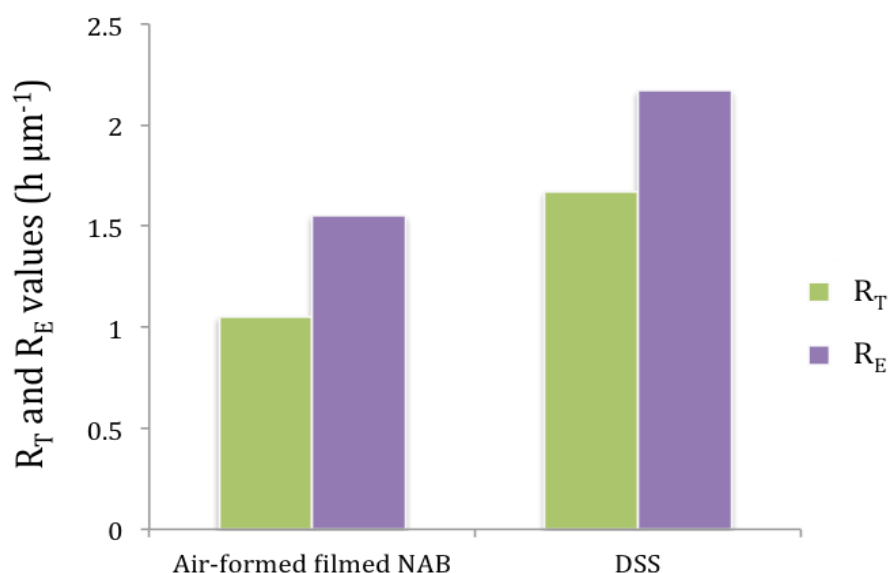


**Fig. 7.4:**  $R_T$  and  $R_E$  plots for air-formed filmed NAB and DSS from the MDPR values.

From Figure 7.4, it was seen that, similar to the trend in Figures 7.1 and 7.2, the resistance of both air-formed filmed NAB and DSS to pure erosion was higher than their resistance to cavitation erosion-corrosion, when analysed under Alicona for MDPR. And again, DSS showed better resistance to cavitation under both E and T conditions than the air-formed filmed NAB.

### 7.3. Comparison of the synergy values and discussion

The synergy results obtained using the five different methods mentioned are summarised in Table 7.7 to compare the values with one another.

Materials used	Methods Used to give S%					
	MDPR ( $\mu\text{m h}^{-1}$ ) (Measured by Alicona) E in distilled water	Volumetric Mass Loss (mg) (Measured by Alicona) E in distilled water	Gravimetric mass loss (mg)			
			E in distilled water (E and T Measured via mass balance)		E using Cathodic protection (E and T Measured via mass balance)	
			Gravimetric Mass loss for C	Faradaic conversion for C	Gravimetric Mass loss for C	Faradaic conversion for C
Air-formed filmed NAB	32% $\pm 1\%$	31% $\pm 7\%$	73% $\pm 8\%$	19% $\pm 5\%$	38% $\pm 8\%$	-16% $\pm 5\%$
Water-formed filmed NAB	-	-	58% $\pm 13\%$	70% $\pm 9\%$	57% $\pm 10\%$	69% $\pm 10\%$
DSS	23% $\pm 2\%$	23% $\pm 10\%$	36% $\pm 6\%$	26% $\pm 7\%$	38% $\pm 8\%$	28% $\pm 5\%$

**Table 7.7:** Synergism summary for NAB and DSS using distilled water, cathodic protection, mean depth of penetration rate, volumetric mass loss, and Faradaic conversion methods.

Table 7.7 tabulates the measured synergy for DSS and air-formed oxide filmed NAB using the five different methods of synergy measurement. It can be seen from the table that synergy had measurable impact on the cavitation erosion-corrosion of DSS and all the NAB samples.

For air-formed oxide filmed NAB, the synergy tests using the 5 different methods



gave varying results, ranging from -16 to 73%. The synergy was found to be 31% using the volumetric mass loss method, and 32% using MDP method. Under the gravimetric mass loss technique, the synergy values obtained were 73% for E (in 5 L of distilled water for 1 h), and 19% by employing polarization and Faradaic conversion for C. Whereas, the synergy values obtained using cathodic protection gave a negative synergy of -16% for C obtained via Faradaic conversion, and 38% for C obtained using gravimetric method.

In case of water-formed oxide film NAB, only three different methods (gravimetric, cathodic protection and Faradaic conversion) were employed to estimate the synergy between cavitation erosion and corrosion. The synergy obtained using polarization and the Faradaic conversions were in the range of 69 – 70% for both E conditions. Whereas, using gravimetric mass loss method for C, the synergies were seen to drop to 57 – 58% for both the E conditions.

For DSS, the synergy values were comparatively lower, ranging between 23 – 38%. The higher values of 36% and 38% were obtained only for those where the C was measured via gravimetric method. For all the other methods employed, the synergy values for DSS were found to lie below 30%.

As seen from the microstructural analyses in chapter 5 and the electrochemical responses in chapter 6, the main synergistic mechanism at play for the three materials was the enhancing of corrosion rate by removal of the passive or protective film by erosion, although it was most prominent for NAB with water-formed oxide film. As mentioned in section 5.3.1.3, three months immersion of NAB in 3.5% NaCl solution could cause up to 50- $\mu$ m deep crevice corrosion and selective phase attacks in the  $\alpha$ - $\kappa$ III eutectoid phase boundaries (as seen in chapter 5, Figure 5.25), resulting in sponge like porous surface layer. This, in turn, resulted in the water-formed oxide film NAB samples to be more susceptible to erosion as well as cavitation erosion-corrosion than NAB with air-formed oxide film, giving higher mass loss under E and T. Also, from the results obtained, it can be concluded that the porous and brittle oxide films erode away much faster than the substrate. Thus, causing higher material loss under E for substrate with water-

formed oxide film, when compared to substrate with air-formed oxide film. And under the synergistic effect of cavitation erosion and corrosion in a chloride solution, it undergoes higher copper dissolution. And hence, this further increases the material loss due to the combined impact of erosion and corrosion. The synergy was hence higher for the water-formed filmed NAB, putting the sample at higher risk of damage induced by combined impact of cavitation erosion and corrosion. This shows that the environmental exposure of NAB to seawater is very important, and that the implications of this exposure without surface treatment may cause higher cavitation than for NAB with surface treatment.

Additionally, an interesting observation made from Tables 7.1, 7.4, and 7.6 was the influence of  $\Delta E$ , corrosion-enhanced erosion, for all three samples. This can be seen numerically from the increase in mass loss or the MDPR data under T when compared to the individual E and C values, giving a higher  $\Delta E$  contribution towards synergy. Thus, further validating the results that were acquired from the microstructural analyses of the three test materials. Whereas, the E and T results obtained from Table 7.5, especially for air-formed filmed NAB, showed that the influence of corrosion on cavitation in fact reduced the mass loss, when compared to the mass loss obtained under E. In theory, as marine propellers dock and function in the marine environment throughout their service life, this would deem a propeller made from NAB unfit for functioning within months. However, in reality, the propellers are not generally subjected to cavitation at such high intensities as under the ultrasonic transducer. And the severity and location of cavitation always differs depending on the conditions. Also, in practical usage, the oxide films formed on the propellers get enough intervals for the damaged oxide films to heal, re-instating their good corrosion properties.

### **7.3.1. Discussion**

Synergy and the interaction between corrosion and erosion have often raised curiosity in the recent years for its ability to correlate wear and corrosion. At the same time it has also become a subject of debate whether the technique is suitable as well as reproducible [237]–[239]. Synergy has generally been measured in

terms of mass loss incurred or mean depth of penetration rate by combined contribution of erosion and corrosion. Some authors have suggested that corrosion leads to increased abrasion resistance in some materials [239], while others may hold a differing opinion.

The synergy values obtained under the various methods employed in the current research are in general comparable with the synergy results obtained by several other studies [162], [229], [236]. The study by Neville, Hodgkiess and Dallas [236] found the synergy for 2205 DSS eroded under liquid-solid jet impingement under saline solution to be about 20%, whereas the vibratory cavitation as well as hydrodynamic cavitation erosion-corrosion synergy tests conducted by Wood and Hutton [229] showed  $S/T$  % values between the range of 30% to >60% for various materials tested under 3% NaCl solution such as grey cast iron, 1020 mild steel, 304 SS and copper alloys. Several engineering alloys tested in 3.5% NaCl solution by Kwok, Cheng and Man showed very low (negligible)  $S/T$  % of damage for corrosion resistant materials such as 316 SS, 304 SS and Zeron 100 super DSS [162]. However, it must be noted that these studies were carried out with varying conditions, and considering the mean depth of penetration rate (MDPR) as their means of calculating synergy over a long period of test time.

In a study conducted by Wood and Fry [17], they investigated the fundamental synergistic mechanisms of cavitation erosion and corrosion for copper and cupro-nickel alloys in seawater. The tests were conducted in an all-plastic cavitation tunnel comprising of a 60° symmetrical wedge cavitation source. The specimens of 10 × 20 mm working section were held under potentiostatic control in a flowing seawater system at an upstream flow velocity of 14.7 m s<sup>-1</sup>. The synergy measured using the depth of penetration method for copper in seawater after 4.5 h was found to range between 10 – 29% at different over-potentials of 5 – 100 mV. Whereas, for Cu – Ni alloys it ranged between 30 – 50%. It was found that the synergistic effect was most marked when the cavitation erosion occurred in presence of mild corrosion with 50 – 70% of the damage caused due to pure erosion only.

In another study, Wood and Hutton [229] plotted the ratio of the synergistic wear to corrosive wear (S/C) against the ratio of erosive wear to corrosive wear (E/C). These tests were conducted using hydrodynamic cavitation, slurry impingement with aqueous slurries containing 2% silica sand particles, and vibratory cavitation for various steels and cast iron in a slurry pot, copper and curpo-nickel alloys, in various corrosive and non-corrosive solutions. The numbers designated to the points are used to identify the type of materials and the experimental conditions they were subjected to. These were obtained from the results published in literature [229], as summarized in Table 7.8.

Point no.	Material	Ref.	Point no.	Material	Ref.	Point no.	Material	Ref.
1	A514	[240]	15	MS1020	[93]	29	Cu	[17]
2	SS-316	[240]	16	MS1020	[93]	30	Cu	[17]
3	SS-316	[240]	17	MS1020	[93]	31	Cu	[17]
4	REM 500	[240]	18	SS-304	[93]	32	Cu	[17]
5	REM 500	[240]	19	SS-304	[93]	33	Cu	[241]
6	A514	[240]	20	SS-304	[93]	34	MS1020	[242]
7	SS-316	[240]	21	Cu	[17]	35	Fe	[243]
8	SS-316	[240]	22	Cu	[17]	36	Fe	[244]
9	REM 500	[240]	23	Cu	[17]	37	Fe	[244]
10	REM 500	[240]	24	Cu	[17]	38	Fe	[244]
11	Cu	[241]	25	Cu	[17]	39	Fe	[244]
12	Cu	[241]	26	Cu	[17]	40	Fe	[244]
13	Cu	[241]	27	Cu	[17]			
14	G cast Fe	[16]	28	Cu	[17]			

**Table 7.8:** Data used for S/C vs. E/C map (as plotted in Figure 7.4) and their corresponding references [204], [229].

The S/C and E/C values for the materials from the current research were also calculated and plotted in the graph using Table 7.3, as shown in Table 7.9.

<b>Materials</b>	<b>S/C</b>	<b>E/C</b>
NAB with air-formed film	1.42	5.07
NAB with water-formed film	865	373
Duplex Stainless Steel	144	408

**Table 7.9:** *S/C and E/C values calculated for DSS and the two types of oxide-filmed NAB samples using gravimetric method for E measurement, and polarization and Faradaic conversion for C measurement.*

Figure 7.5 illustrates the linear relationships between S/C vs. E/C plot along with the current results from the NAB and DSS samples [204], [229]. The solid line represents the materials having medium S/C values (i.e. up to 30% of total wear affected by synergy); whereas, materials having high S/C values (i.e. more than 60% of total wear affected by synergy) are represented by the broken line. Points below the solid line were considered as low S/C values, with less than 10% of total wear affected by synergy. And for E/C values above 50, the points could not be distinguished between high and low S/C values [229].

It can be seen in Figure 7.5, that NAB with air-formed oxide film lies on the low-medium S/C value, whereas, NAB with water-formed oxide film lies out of the trend at a higher risk zone of cavitation erosion-corrosion [204], [229]. From this it can be concluded that NAB with air-formed oxide film exhibit low risk as propeller materials to cavitation erosion-corrosion. However, on prolonged exposure to salt solution, seawater, chloride solution, or any such corrosive environment, the material suffers from selective phase attack and crevice corrosion as seen from the microstructural analyses in chapter 5, and becomes vulnerable to the combined effect of cavitation erosion-corrosion.

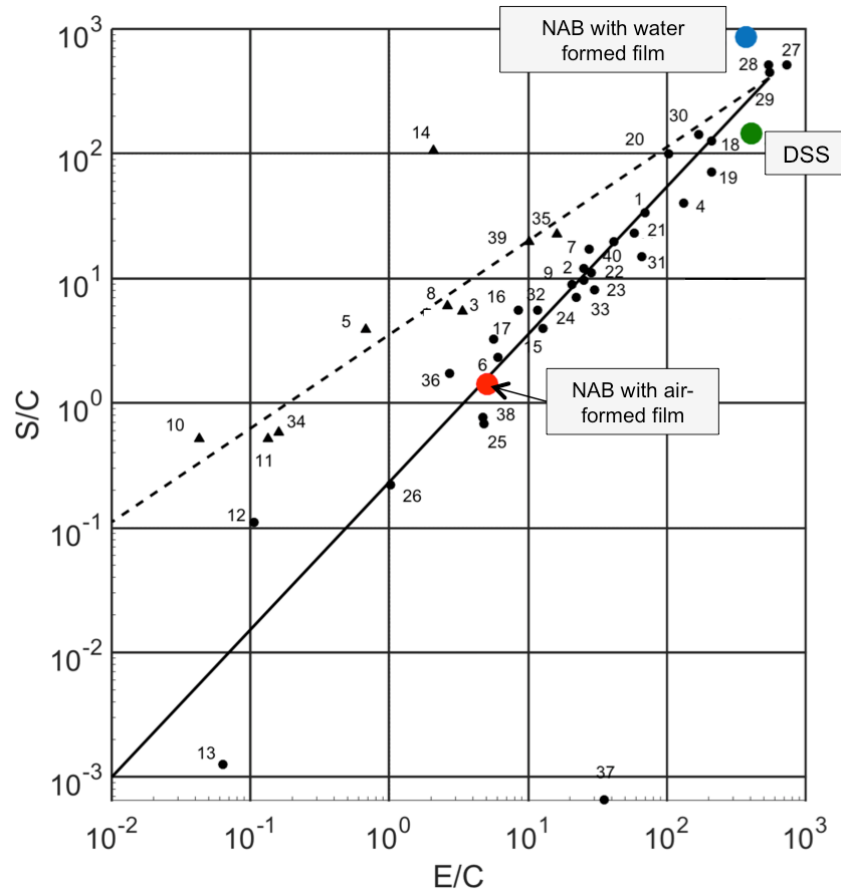


**Fig. 7.5:** Extended  $S/C$  vs.  $E/C$  plot showing the locations of DSS, air-formed filmed and water-formed filmed NAB on the graph plotted using data from Table 7.8, adapted from Ref. [203], [204].

DSS, as seen from Figure 7.5, also lies below the solid trend, exhibiting low synergy. However, although DSS is at lower risk to cavitation erosion-corrosion in general compared to the NAB samples, it lies above the air-formed filmed NAB point. This is due to the low corrosion rates (as obtained from its polarization curve) that resulted in a high  $E/C$  value of about 400. Due to which, the  $S/C$  values could not be clearly distinguished as high or low as stated in [229].

For a heat-treated NAB such as NES 747 part 2 NAB, the synergy between erosion and corrosion has been reported to be negative by Barik, et al. [207]. This is attributed to the lack or low percentage of  $\beta$ -phase, removed during the heat-treatment. Thus, changing the microstructure of the material. This, in turn, results in higher corrosion resistance as the ordered  $\beta$ -phase has been established to be

one of the phases vulnerable to corrosion attack [205]. Which in turn, would affect the T and S values, giving different results compared to non-heat-treated NAB.

In the study reported by Barik, Wharton, Wood, et. al. [207], [235] the authors performed sand slurry jet impingement solid particle erosion-corrosion of NES 747 part 2 NAB. The tests conditions were conducted on a rig with a horizontal jet of salt solution impinging the NAB sample at 90° with silica sand particles of 135 µm or 235 µm mean sizes at 3% w/w concentration. E values were obtained by subjecting the samples to CP at 200 mV below the corrosion potential under erosion-corrosion conditions. Flow corrosion and total combined loss rates were determined without the addition of solids and CP respectively. Sectioning the erosion scars, and looking in to the subsurface microstructure and its depth profile revealed a strain-hardened layer under eroded surfaces. This was also considered responsible for the negative S value. This increase in strain hardening also reduced the erosion rate under T conditions. This suggested that corrosion in fact enhanced plastic flow, thereby increasing strain in the near surface as compared to the pure erosion case [207].

In another study, Kwok, Cheng and Man [162] investigated the synergistic effect of cavitation erosion and corrosion of copper-based alloys and bronze, among many other engineering alloys with the help of a 20 kHz ultrasonic vibrator at an amplitude of 30 µm in distilled water and in 3.5% NaCl solution at a temperature of 23°C. They calculated the synergy via mean depth of penetration rate method and concluded that the cu-based alloys had a synergy percentage of 2.7 - 4.5% with 95 – 97% of the total damage attributed to pure erosion only. It was also found that corrosion only played a minor role of about 0.1 – 1.8% in the overall cavitation erosion–corrosion for copper-based alloys.

Bello, Wood and Wharton [237] attempted to evaluate synergy for 304, 316 and 327 grade stainless steels via three different approaches, two-body, three-body and a mixed abrasion wear mode. They observed that the values of mechanical abrasion losses were 10 times higher than those of electrochemical losses. Two-body method was seen to give large degree of scatter in results, with negative

synergy obtained for 316 and 327 SS; whereas, positive synergies were obtained for the two sample materials under both mixed- and three-body abrasions. Repassivation kinetics and/or composition of the passive films on 316 and 327 SS were considered responsible for reducing the overall synergy level of two-body abrasion, producing negative synergies. For 304 SS, only positive synergies were seen, owing to 304 SS having weaker repassivation/passive oxide film structure. For 316 SS, synergy was observed to be almost independent of the level of pure abrasion, indicating stronger repassivation rates (and hence negative synergy). While, for 327 SS, the passive film was seen to remain intact at pure abrasion condition below  $1 \times 10^{-12} \text{ N m}^2$ , giving negative synergies, beyond which the film was ruptured or removed, increasing the S values.

These results, although informative, were measured via different means under varying conditions, and hence cannot be readily compared to the results obtained in the current study. However, a relative comparison can be drawn based on the results obtained, such as in all the cases, erosion had higher contribution upon synergy. The results obtained by the different studies is considered to be due to the fact that synergy, as it has been evaluated, is a three-dimensional entity that cannot be calculated or quantified easily. Quantification of  $\Delta E$  and  $\Delta C$  is the hardest part of the synergy method. It is not easy to isolate one from the other. There will always be certain percentage, no matter how small, of corrosion even in pure erosion method for both distilled water conditions and cathodic protection due to the exposure to the elements. Also, it may inadvertently promote other degradation mechanisms such as hydrogen embrittlement, especially in steel samples. There will also be a small percentage of corrosion-induced erosion under C conditions. Additionally, surface effects such as passive films, transformations, strain hardening, grain refinement/orientation etc. may significantly influence the electrochemical measurements of C as well as  $\Delta C$ , since, E (with  $\Delta E$ ) and T are bulk material measurements [204].

Many attempts have been made in the past to understand and quantify the S into the separate corrosion-enhanced erosion and the erosion-enhanced corrosion components. Researchers have been able to correlate them with microstructural



analyses [230], or measure them using experimental (such as electrochemical) tests [164], [231], [232]. However, it has still proven difficult to be able to accurately quantify or separate the components from the S term.

A study by Malka et. al. was conducted on AISI 1018 carbon steel using 1% NaCl solution, purged with CO<sub>2</sub> for inducing corrosion and silica sand as the erodent, in order to investigate the interaction between corrosion and erosion processes. They also attempted to quantify the synergism in realistic flow environments, such as sudden pipe constrictions, expansions, and protrusions. The experiments were especially designed to understand the contribution of erosion and corrosion as individual processes, and over the net synergism. They observed that in fact erosion seemed to enhance corrosion as well as vice versa, with each contributing significantly to the overall synergism. However, the dominant process was the effect of corrosion on erosion, with corrosion almost doubling in the presence of erosion, as observed from the experimental results. This was supported by their previous speculation of erosion assisting corrosion rate by increasing local turbulence, and therefore, mass transfer, and surface roughening [164].

Others tried to determine the  $\Delta E$  component from the anodic polarisation measurement. The erosion-enhanced corrosion of UNS S32304 stainless steel and carbon steel under impingement by NaCl solution was investigated by Zheng et. al., [231] using results from electrochemical analysis. The contribution of  $\Delta E$  on the material was quantified using potentiostatic polarization. Similarly, Aribu, et. al. [232] attempted to understand the synergy between erosion and corrosion of lean duplex stainless steels, UNS S32101 and UNS S32304, in aerated 3.5% NaCl solution. The results were compared to that of UNS30403 austenitic stainless steel and UNS S32205 DSS. They measured the corrosion rates of the alloys under impingement using 3.5% NaCl solution with 500-ppm sand at 15 m s<sup>-1</sup>. The corrosion current density, obtained from the anodic polarisation plots using Tafel plots, was used to calculate the erosion-enhanced corrosion using Faradaic conversion.

### ***7.3.2. Limitations of the techniques used***

As presented in Ref [18], the gravimetric mass loss results were considered more reliable. This is because, although both gravimetric as well as volumetric mass loss measurements are useful and efficient in their own account, they both have major shortcomings.

On one hand, while the data obtained by precision mass balance are generally considered accurate up to 0.01 mg, several factors may affect these results. Sediments of eroded titanium probe tip may get deposited on to the sample surface, un-dissolved solute sediments in the water may accumulate on the surface, water-retention due to absorption via porous layers/coats, if any, may occur, as well as other impurities that cannot be detected and fully prevented may affect the data. Also, as the samples are introduced to a corrosive environment, if they have low corrosion resistance, it is difficult to differentiate the amount of mass actually lost by the material after the erosion test due to the aforementioned potential accumulation of sediments and formation of corrosion products. The mass balance does not take into account these factors and this could cause deviation in the final result.

On the other hand, volumetric analyses can be equally crude since the highest magnification achievable using Alicona is 1000x, which could cause loss of data especially for very smooth and reflective surfaces. In case of sedimentation, corrosion products, micro-scratches, and burrs existing on the sample surface, Alicona would not differentiate and perform selective volume loss. This again could cause deviation from the desirable results. At lower magnifications or while analysing highly reflective surfaces, it may also manifest its own roughness and waviness of the surface, as was the case with the polished surfaces of the sample materials used for the experiments undertaken. Hence, S/T % obtained using gravimetric method for E and T, and polarization technique for C was considered more preferable.

Furthermore, the errors for E, C and T all sum up (as seen from the synergy

summary tables for each method) while quantifying S, which can lead to significant errors. Additionally, an important factor often overlooked, and needs to be realized, is the percentage error for the S/T % values obtained under each individual method. Often, the S values and the corresponding S/T % are quoted in literature without the error bar. However, as seen from Table 7.7, these error % values are not negligible, making the S and S/T values less reliable than assumed. This, in turn, further makes quantification of S even harder.

Buffered pH solutions have been considered to move the surface from being corrosion active to immune. Also, corrosion being time dependent, long exposures to corrosive/marine environment pre-test may add other complication such as bio-fouling associated with seawater immersion [204].

## 7.4 Summary

Synergy tests were conducted according to ASTM G-119 standards of employing three distinct tests: pure erosion (E), pure corrosion (C), and the combination of erosion-corrosion (T). Equation (7.1) was employed to quantify synergy from the results obtained for E, C and T.

Synergy values for DSS and air-formed filmed NAB were measured using five different approaches, and that for the water-formed filmed NAB was measured using three different approaches. This included the gravimetric mass loss method where the mass loss incurred under E, C and T were measured using a mass balance; under the gravimetric method, the pure erosion rates were obtained under two different conditions, 1 h cavitation in distilled water, and in 3.5% NaCl solution while subjected to cathodic protection.

Due to the inconsistencies in the C values measured via mass balance, polarization technique, along with Faradaic conversions of corrosion rates to mass loss were adapted instead as the third approach. The fourth and the fifth approaches were the volumetric mass loss and the MDPR methods, conducted using Alicona only

for the air-formed filmed NAB and DSS, with E obtained in distilled water. Tables 7.1, 7.3, 7.4, 7.5 and 7.6 summarised the E, C and T values obtained that help quantify S value for each approaches. The gravimetric approach for T and E, with E tested in distilled water, and polarization technique for C was considered most reliable and hence, preferable among all the other methods used.

Table 7.7 further summarised the S/T % found under each test method of all the test materials and compared the results. From the tests conducted and the resultant S values, it was seen that 1 h of exposure to cavitation and corrosion had measurably high synergistic effect on the cavitation erosion-corrosion of NAB (air- and water-formed filmed) and DSS. The extensive study conducted shows that synergy is three-dimensional.

The synergy quantification, the most reliable methods, the critical analyses of the found results, the literature review on the past results obtained, and the limitations of all the methods were discussed.



# **Chapter 8:**

# **Conclusion and**

# **Future Work**

---

The aim of the research, as mentioned in the introduction chapter, was to understand the microstructural as well as electrochemical behaviour of DSS and NAB, and their responses to cavitation erosion-corrosion using ultrasonic vibratory transducer under ASTM G-32 standards. The goal was to investigate the relation between cavitation erosion and corrosion, and the synergistic interaction between them.

## 8.1. Conclusion

A critical review of the literature focusing on the ultrasonic vibratory type of cavitation testing showed that ultrasonic vibration was the most accelerated and repeatable approach to obtain cavitation results for a wide range of engineering materials. Several researches observed the tribocorrosion effects of the mechanical damage of cavitation erosion, the effect of combined cavitation erosion-corrosion damage, and the synergistic interaction between cavitation erosion and corrosion. Several different methods of quantifying synergy included gravimetric analysis, mean depth of penetration techniques, and electrochemical analysis. In addition to that, microstructural analyses were also made on the test materials using SEM for material characterization, and understanding their microstructural behaviour under cavitation.

Studies have also tried to characterize the influence of corrosion on cavitation erosion using potentiodynamic polarization, EIS, and linear polarization resistance with and without cavitation. However, the conclusions drawn were only based on the corrosion potentials, mass loss changes and mean depth of penetration rate during the cavitation measurements. This leaves the subject of the dynamics of cavitation erosion process combined with the corrosion of material not well understood, especially at the micro level.

In the current research conducted, it was concluded that DSS as well as both the types of NAB samples underwent cavitation erosion and corrosion, and exhibited significant amount of synergy. For DSS, the microstructure underwent selective phase attack, with the soft ferritic matrix more vulnerable to cavitation than the austenitic phases. DSS was also seen to undergo ductile failure in the cavitated zone in the form of extrusion of the austenite at the cavitation pit along with microcracks and cleavage facets, and striation patterns on the wear scar.

As for NAB, both the air-formed as well as the water-formed oxide filmed samples were seen to undergo higher mass loss compared to DSS. SEM analyses revealed that the wear mechanisms of the cavitated sample surfaces with both air and

water-formed oxide films both underwent selective cavitation erosion-corrosion attack at the  $\alpha$ - $\kappa_{III}$  eutectoid phase boundaries as the first site of attack, with ductile deformation around the cavity. The  $\kappa$  precipitates and precipitate-free  $\alpha$ -phase zones were found to suffer no visible cavitation after 1 h of cavitation test in both distilled water as well as 3.5% NaCl. The sites of most aggressive attacks exhibited large cracks, propagating into the microstructure along the  $\alpha$ - $\kappa_{III}$  phase boundaries.

Samples were also tested under potentiodynamic polarization in order to obtain the corresponding mass loss rate, obtained via Faradaic conversion of their corrosion densities, and potentials for cathodic protection. From the polarization curves and the subsequent mass loss rate, it was seen that DSS showed the lowest mass loss, followed by water-formed oxide filmed NAB, and finally, the highest mass loss measured was that for air-formed oxide film.

These results also helped reinforce and explain the results obtained from mathematical evaluation of S. As discussed in chapter 7, the synergies were evaluated using 5 different methods for DSS and air-formed filmed NAB, 3 different methods for water-formed filmed NAB. For the air-formed oxide filmed NAB, the synergy tests using the 5 different methods gave varying results, ranging from -16 to +73%. Under the gravimetric mass loss technique, the synergy values obtained were 73% for E in 5 L of distilled water for 1 h, and 19% by employing polarization and Faradaic conversion for C. Whereas, the synergy values obtained using cathodic protection gave a negative synergy of -16% for C obtained via Faradaic conversion, and 38% for C obtained using gravimetric method. For water-formed oxide filmed NAB, only gravimetric, cathodic protection, and Faradaic conversion methods were employed. The synergy obtained using polarization and the Faradaic conversions were in the range of 69 – 70% for both E conditions. Whereas, using gravimetric mass loss method for C, the synergies were seen to drop to 57 – 58% for both the E conditions. DSS exhibited the lowest values for synergy, ranging between 23 – 38%, with 36% and 38% obtained only for those where the C was measured via gravimetric method. For all the other methods employed, the synergy values for DSS were below 30%. Each method had



their own individual advantages and disadvantages. On comparing each test methods of obtaining synergy, the S/T % obtained using gravimetric method for E and T, and polarization technique for C was considered most preferable.

Correlating the synergy results with the microstructural and electrochemical analyses, it was concluded that since DSS exhibited high corrosion resistance, and hence, low subsequent mass loss under C, the contribution of E was the most predominant on the erosion-corrosion of DSS. For the air- and water-formed filmed NABs, the microstructures were seen to undergo more severe erosion, with larger cavities under T conditions as compared to E conditions. This was also reflected in the synergy results, showing higher synergy for water-formed filmed NAB than the air-formed filmed NAB. Hence, in conclusion, it can said that DSS and NAB (with both types of film) exhibit substantial synergy between erosion-corrosion, evident from their microstructural as well as electrochemical results. However, prolonged exposure of non-heat-treated NAB in seawater will result in enhanced synergy, and hence, intermittent use of propellers made from as-cast NAB will result in faster degradation of the propellers.

## 8.2. Future Work

However, although the synergy measurement between cavitation erosion and corrosion is insightful in the behaviour of the propeller materials tested, it does not clearly explain the interaction between cavitation erosion and corrosion in full details. For example, the data obtained from electrochemical measurement for the cavitation erosion-corrosion test showed that both duplex stainless steel and nickel aluminium bronze exhibited high resistance to corrosion when subjected under cavitation. The cause of corrosion during cavitation is attributed to the removal of oxide layers in the case of NAB, but the mechanism of corrosion and passivity still needs to be clarified.

In the light of all the results obtained, there is still much left to be answered in the realms of electrochemistry, and the individual contributions of  $\Delta E$  and  $\Delta C$ . As

already established and stated numerous times in the literature, there exists very complex interplays between wear and corrosion. These complexities do not allow easy analysis of the localized corrosion occurring within the individual cavities as well as the entire cavitating region. Even though there are standard guidelines, such as ASTM 119 [233], to measure synergy using various techniques, such as electrochemical, gravimetric and profilometry, its quantification is still a matter of debate.

The synergy results obtained in the literature have all been very dispersive, due to the wide ranges of methods employed, and not easily comparable to one another. And although they present valuable information, accelerated test methods such as ultrasonic vibration may not allow real service conditions to be simulated. Neither do they represent real-time service relevant damage mechanisms, since corrosion mechanisms are often time dependent over different orders of magnitude to erosion mechanisms. These accelerated testing methods along with the variations in the measurement techniques, often sensitive to several varying aspects, used to quantify synergy can lead to uncertainties in results [204].

Also, few anomalies may exist due to certain assumptions made during the experiment such as, the erosion test without any external electrochemical application was considered as pure erosion test, however there was still a small level of corrosion taking place in the form of passivity of the individual materials itself. Instead of using distilled water cathodic protection can also be employed however, while cathodic protection can prevent corrosion it is difficult to suppress corrosion and hydrogen evolution simultaneously as also explained by Kwok, Cheng and Man [162]. Hydrogen could cause hydrogen embrittlement in stainless steels, but it may also exert a cushioning effect, reducing mechanical erosion, and this may potentially increase the relative contribution of synergism [18].

The future research work may delve deeper into the realm of the cavitation erosion-corrosion interaction, and try to understand their individual contributions and the combined underlying mechanisms.

### ***8.2.1 Modern composite propeller materials***

The other potential future approach to the research may include looking into new prospect propeller materials made of composites. It is well established that copper alloys such as NAB, various stainless steel grades and DSS are some of the most common propeller materials used. However, more recently, usage of composites to manufacture marine propellers has been extensively investigated and attempted in practice. This is mainly due to few favourable qualities of composites over metal alloys such as light weight, immunity towards corrosion, reduced noise generation, no magnetic signature and shape adaptability [245]–[247]. Hence, the next novel approach in this research would be towards the investigation of Ni-coated composite materials.

The common composite materials used comprise fibre reinforced plastic (FRP) such as E-glass (electrical) fibres with polyester resin, and carbon fibres with epoxy resins. Figure 6.2 shows a 12 inch FRP propeller made from glass and polyester resin painted in preparation for open water testing [248].



**Fig 8.1:** FRP propeller of diameter 305 mm painted in preparation for open water testing [248].

Several experimental and analytical studies have been made regarding the credibility of composites as propeller materials. Trials at sea on university run vessels have enabled to test the fitness of the composites for purpose of propellers made from glass reinforced, epoxy composite. Hydroelastic tests have been conducted in experimental tanks to help understand and improve the efficiency of the propeller under variety of operating conditions [248]. In 1990, a study was carried out at the University of Southampton Department of Mechanical Engineering to investigate the feasibility of producing propeller brackets (for supporting the propeller shaft emerging from the hull) with a composite material [249]. The work presented by Herath et. al, on the shape-adaptable composite marine propellers attempted to compare the results obtained numerically using Fluid-Structure Interaction of Finite Element Analysis and experimental results. Shape adaptability refers to the ability of a composite to adapt to their working conditions and deform with load changes, without the involvement of external mechanisms such as pitch based on the flow conditions and rotational speed in

order to achieve a higher efficiency [250]. A shape-adaptive propeller is flexible and designed so that the blades deform in such a way that the propeller performance is enhanced in comparison to that of a conventional metal propeller. The shape-adaptability can be achieved through the choice of the appropriate blade geometry and the optimum arrangement of composite materials [251].

However, composite propeller materials do not come without their own flaws. Designing a shape-adaptable composite propeller is significantly more complicated than designing an alloy marine propeller [250]. Composites can have high fracture toughness, but this must be specified and is not always easily or cost effectively achieved [248]. Also, several other factors may need to be well reviewed before considering composite propellers such as the porosity of the material and its potential water up take, the delamination of the composite layers, among several others. Another major disadvantage of using a composite propeller is that the damages incurred are often non-reparable.

A comprehensive study was undertaken by Orchard [252] to understand the cavitation behaviour of various marine composite samples. He conducted cavitation erosion test using the ultrasonic vibratory facility at the University of Southampton, for Carbon Fibre/polyurethane (CF) composites and E-glass with resin (G-10 standard) composites, among others, in tap water. From his studies, he measured the cumulative mass loss and erosion rates for the sample materials to rank them accordingly, based on their resistance against cavitation. Figure 8.2 shows the trends in mass loss as a function of cumulative exposure time for E-glass and CF composites.

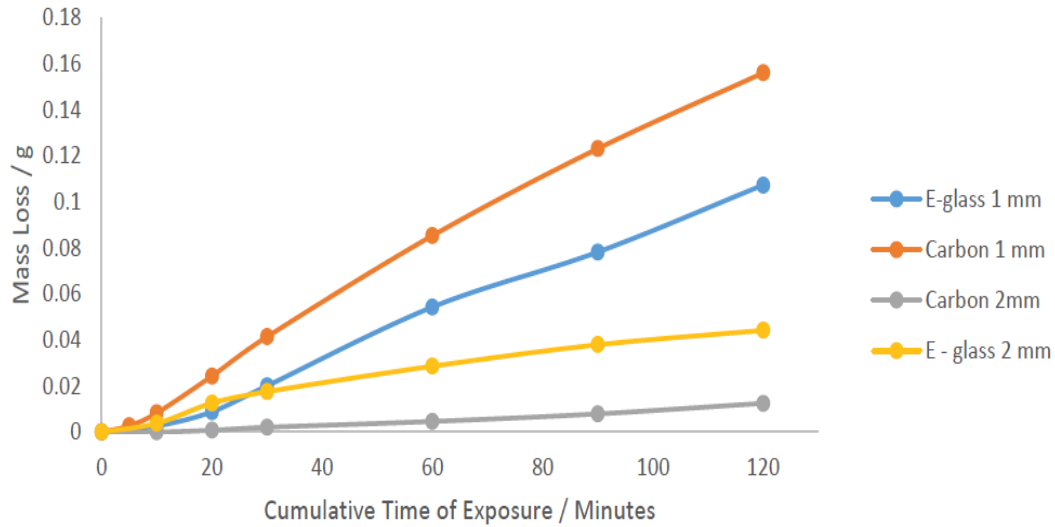


**Fig. 8.2:** Mass loss vs. cumulative exposure time plots for E-glass and carbon fibre composites for two different standoff distances [204], [252].

As seen from Figure 8.2, E-glass samples showed greater cavitation erosion resistance than the CF composites at a standoff distance of 1 mm. However, at a higher standoff distance of 2 mm, the CF composite samples were seen to have greater cavitation resistance. This was found to be due to the varying levels of resin layers on the surface of the two samples, and the properties of the fibres when exposed to cavitation. On optical analysis under a microscope, it was seen that the CF samples, having less resin top layer, had more exposed fibres that showed higher resistance at the lower intensities. The E glass sample, on the other hand, had thicker resin layer but more erosion resistant fibres and layout [252].

As soon as the top resin layer was penetrated, there was a rapid mass loss observed (shown by the accelerated mass loss over time in Figure 8.2). Figure 8.3 (a) shows the optical image of an E-glass sample, and Figure 8.3 (b) shows the eroded surface of CF composite sample with top resin layer removed, revealing the weaves closest to the surface obtained after 10 minutes of cavitation [252].

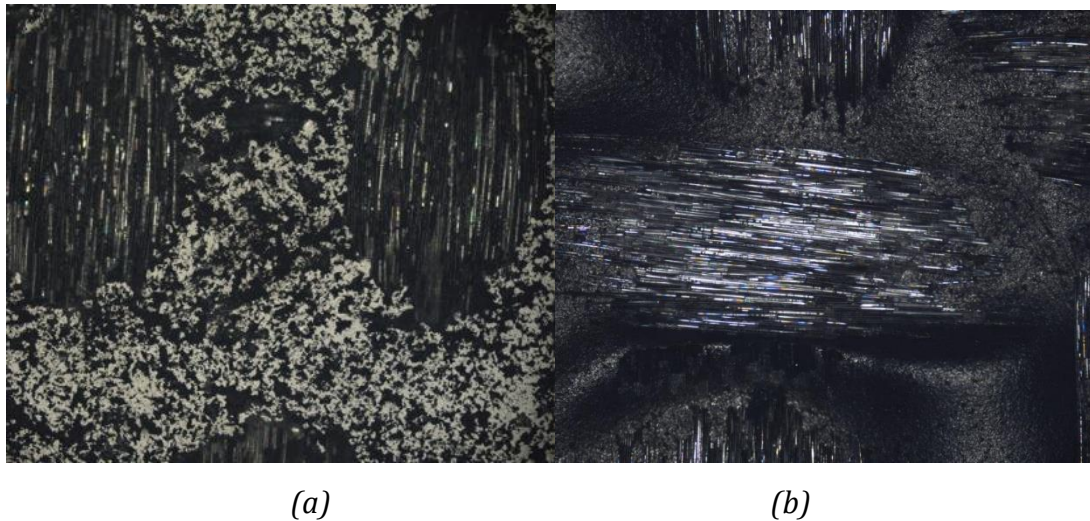


**Fig. 8.3:** Optical images of (a) E-glass sample [204], [252]; and (b) carbon fibre composite, cavitated for 10 minutes at 1 mm. The resin layers are clearly removed from the top of the weaves [252].

As seen from the figures, both samples underwent removal of resin. The polyurethane resin, being softer than the carbon fibres, was the first to be removed. Once the top layer of resin was penetrated the resin around the fibres were eroded by microjets formed by cavitation bubble impingements (as seen in Figure 8.3 (a)). The fibres were seen to fail due to brittle shear. Compared to NAB NES 747, the composite samples failed much faster, with 6-9 times the mass loss as obtained under the same test parameters [252].

In another study by Searle [248], the feasibility of manufacturing small marine propellers from continuous fibre reinforced polymer composite materials was examined. It has been shown that manufacturing propellers in composite materials is theoretically more cost effective than traditional materials. The manufacturing routes play a very important role when it comes to composite materials. It can throw light on the critical processing parameters necessary for successful production of laminates suitable for propellers and other high performance marine structures. Searle performed cavitation test on his FRP composite samples using a cavitation tunnel running at maximum velocity of over  $4 \text{ m s}^{-1}$  or 3000 rpm. The experiment investigated how the different elastic moduli of the composite as well as aluminium propellers affected the onset of cavitation.

It was found that the lower stiffness of the composite propeller delayed cavitation onset. The efficiency curves showed a shift that was caused by the higher flexibility of the composite propeller. However, he did conclude that more time was required for the experiments in the cavitation tunnel to substantiate the drop in efficiency of the composite propeller at  $4 \text{ m s}^{-1}$  water speed.

### ***8.2.2. Computational modelling simulation***

Several studies have also been conducted in the field of multiphase flow, and computational modelling of cavitation. Cavitation erosion prediction has been one of the most important yet difficult tasks in the designing of marine and boat propellers. Several qualitative methods, such as acoustic signals, paint tests or high-speed video image analyses, are employed to quantify such risks, especially in the field of computational fluid dynamics (CFD). Industrial institutes like Lloyds Register have, for years, invested on the computational simulations of a model/prototype as well as full-scale propeller cavitation. Acoustic emission (AE) technique, among many others, has been employed by Lloyds Register to complement their borescopic cavitation observation at the ship scale. However, the challenges of predicting the cavitation intensities, the type and the location of cavitation persist. Additionally, the parameters used to conduct the required simulations are greatly simplified.

Computational modelling of the flow between the vibrating sonotrode and the specimen has been performed using CFD techniques by Reddy, et. al. in order to aid the understanding of the cavitation dynamics generated [33]. Tests were conducted for the very same ultrasonic vibratory equipment used for the current research at different conditions considered for the vibration amplitude (or power setting) and the probe-specimen standoff distance. They attempted to replicate the experimental mechanisms of cavitation into the simulations. However, many limitations and simplifications were made, such as limiting the size of the bath in the simulation compared to that in the experiment, and the surface of the sample was assumed to remain intact throughout the simulation, whereas, the sample surface underwent erosion over time in the experiment. From their simulations,



it was concluded that a good correlation was obtained between the experiments and CFD simulations for the large-scale cavitation collapse frequencies. From their simulation, and the large-scale acoustic signatures measured during erosion tests, they were able to model a large-scale cavity volume collapse at the centre of the probe within the gap, as shown in Figure 8.4 for 1 ms.

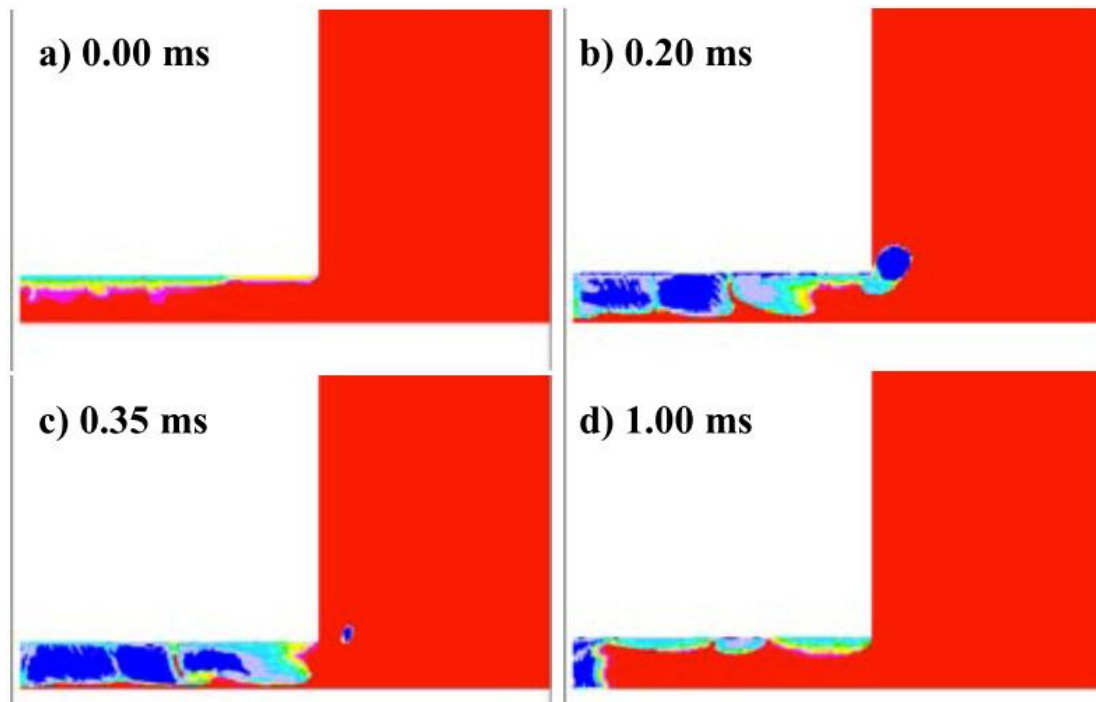


**Fig. 8.4:** Contour plots showing cavitation phenomena beneath the probe occurring within 1ms (where, blue signifies vapour, and red signifies liquid).

However, these studies have all been conducted for large-scale measurements and cavitation processes. To understand the phenomenon at micro-level, for individual bubble dynamics, more sophisticated techniques need to be employed.

Currently, a research is undertaken by Kim, from Fluid Structure Interactions, at University of Southampton, in collaboration with Lloyds Register, to investigate to model the cavitation process and understand the links between acoustic signal and type/location of cavitation, with the aid of an open source Computational Fluid Dynamics programme, openFOAM (version. 3.0.1), to simulate ultrasonic cavitation on a sonotrode. Attempts are being made to predict cavitation phenomena and pressure impact loads on a test specimen under the ultrasonic

probe.

The investigation of propeller cavitation is an ongoing challenge, both experimentally at real scale in the sea, model scale in the form of prototypes as well as lab based (such as in this research), and computationally. As already mentioned, the individual roles of each microstructural phase, and their combined responses to cavitation have been studied extensively in the literature. The mechanical aspects of cavitation have been observed under both SEM and optical microscopes. The electrochemical responses have also been observed and recorded via several means. However, the individual roles of both erosion and corrosion, as seen experimentally, have been difficult to quantify qualitatively and accurately, and, even more so, their individual contributions to the combined action of erosion and corrosion. Which has also been reflected in the difficulty observed in simulating cavitation erosion with corrosion in the past. It would be a long procedure before most aspects of the mechanism can be fully understood. Progresses have been made extensively in the experimental field. However, the simplification of techniques and parameters used currently limit the extent CFD and such programs can promote the understanding of cavitation to the micro-scale. Hence, as a final note, the next step for the subject, as a continuation of the presented research, will be to address these factors, whilst delving into the computational aspects of the marine propeller cavitation.



# Reference:

- [1] J. Carlton, "Cavitation," in *Marine Propellers and Propulsion*, 2nd ed., J. Carlton, Ed. Oxford: Butterworth-Heinemann, 2012, pp. 209–250.
- [2] Lloyd's Register, "Propeller root cavitation erosion," *Tech. Matters*, no. 1, pp. 4–5, 2006.
- [3] R. W. Whitesides, "Interesting Facts ( and Myths ) about Cavitation," vol. 225. PDHonline, Fairfax, 2012.
- [4] J. P. Ghose and R. P. Gokarn, "Propeller Materials," in *Basic Ship Propulsion*, Kharagpur: Allied Publishers, 2004, pp. 166–173.
- [5] E. C. Fitch, "Cavitation Wear In Hydraulic Systems," *Machinery Lubrication*, 2011. [Online]. Available: <http://www.machinerylubrication.com/Articles/Print/380>. [Accessed: 15-Aug-2013].
- [6] P. Shinde and A. Satam, "Cavitation Effect in Centrifugal Pump," vol. 2, no. 2, pp. 20–23, 2014.
- [7] Y. Kurosawa, K. Kato, S. Saito, M. Kubo, T. Uzuka, Y. Fujii, and H. Takahashi, "Basic study of brain injury mechanism caused by cavitation," *Engineering in Medicine and Biology Society, 2009. EMBC 2009. Annual International Conference of the IEEE*. pp. 7224–7227, 2009.
- [8] C. E. Brennen, "Bubble dynamics, damage and noise," *NREC*, 1994.
- [9] J. S. Carlton, "Cavitation," in *Marine Propellers and Propulsion*, Elsevier, 2012, pp. 431–458.
- [10] "Cavitation in Control Valves," *Samson*. Samson, Frankfurt, pp. 1–62, 2003.
- [11] E. A. Brujan, *Cavitation in Non-Newtonian Fluids - With Biomedical and Bioengineering Applications*. 2011.
- [12] P. A. Fitzsimmons, "Lloyd's Register Technology Days," Belfast, 2011.
- [13] R. J. K. Wood, J. Basumatary, and M.-H. Evans, "Energy-Related Tribocorrosion Research At The National Centre For Advanced Tribology at Southampton (nCATS)," *Second International conference on tribology*, 2011.

- [14] B. Vyas and I. L. H. Hansson, "The cavitation erosion-corrosion of stainless steel," *Corros. Sci.*, vol. 30, no. 8, pp. 761–770, 1990.
- [15] G. Engelberg, J. Yahalom, and E. Kalir, "Observations on the cavitation of steels," *Corros. Sci.*, vol. 25, no. 10, pp. 871–882, 1985.
- [16] W. J. Tomlinson and M. G. Talks, "Erosion and corrosion of cast iron under cavitation conditions," *Tribol. Int.*, vol. 24, p. 67, 1991.
- [17] R. J. K. Wood and S. A. Fry, "The Synergistic Effect of Cavitation Erosion and Corrosion for Copper and Cupro-Nickel in Seawater," *J. Fluids Eng.*, vol. 111, no. 3, pp. 271–277, 1990.
- [18] J. Basumatary, M. Nie, and R. J. K. Wood, "The Synergistic Effects of Cavitation Erosion–Corrosion in Ship Propeller Materials," *J. Bio- Tribo- Corrosion*, vol. 1, no. 2, p. 12, Mar. 2015.
- [19] H. Durrer, "Cavitation Erosion and Fluid Mechanics," *Sulzer Tech. Rev. [English ed.]*, vol. 68, no. 3, p. 7, 1986.
- [20] V. Ahuja, A. Hosangadi, and S. Arunajatesan, "Simulations of Cavitating Flows Using Hybrid Unstructured Meshes," *J. Fluids Eng.*, vol. 123, no. 2, p. 331, 2001.
- [21] R. T. Knapp, J. W. Daily, and F. G. Hammitt, "Cavitation," McGraw-Hill, New York, 1970.
- [22] "Marine Propeller | How Things Fly." [Online]. Available: <http://howthingsfly.si.edu/media/marine-propeller>. [Accessed: 20-Aug-2013].
- [23] "Basic Principles of Ship Propulsion," *Man Diesel & Turbo*. Man diesel & turbo, Copenhagen, pp. 1–42, 2011.
- [24] A. Wankhede, "Propeller, Types of Propellers and Construction of Propellers," *marineinsight*, 2010. [Online]. Available: <http://www.marineinsight.com/sports-luxury/equipment/propeller-types-of-propellers-and-construction-of-propellers/>. [Accessed: 20-Aug-2013].
- [25] "Propeller Advances," *McGraw-Hill Companies, Inc.*, 2012. [Online]. Available: <http://www.answers.com/topic/propeller-advances>. [Accessed: 20-Aug-2013].
- [26] S. P. Parker, "Propeller," in *McGraw-Hill Encyclopedia of Science and*

- Technology*, 11th ed., S. P. Parker, Ed. New York: The McGraw-Hill Companies, Inc., 2012.
- [27] J. E. Kerwin, "Marine Propellers," *Annu. Rev. Fluid Mech.*, vol. 18, no. 1, pp. 367–403, Jan. 1986.
  - [28] "Materials for Propeller Fabrication," in *Rules for Classification and Construction Materials and Welding*, 2nd ed., Hamburg: Germanischer Lloyd Aktiengesellschaft, 2009, pp. 1–11.
  - [29] moneycitymaniacs, "A Comparison of Commonly Used Propeller Materials | Eris Propellers on WordPress.com," *Eris propellers*, 2010. [Online]. Available: <http://erispropellersus.wordpress.com/2010/11/19/a-comparison-of-commonly-used-propeller-materials/>. [Accessed: 28-Aug-2013].
  - [30] "Boat propeller Problems - vibration, cavitation, tip erosion, excessive fuel consumption, general marine propeller problems," *Prop scan*. [Online]. Available: [http://www.propscanusa.com/propeller\\_problems.htm](http://www.propscanusa.com/propeller_problems.htm). [Accessed: 20-Aug-2013].
  - [31] S. D'Antonio, "Cavitation Erosion," *PassageMaker*, 2011. [Online]. Available: <http://www.passagemaker.com/channels/cavitation-erosion/>. [Accessed: 20-Aug-2013].
  - [32] "Cavitation," *McGraw-Hill Companies, Inc.*
  - [33] D. Reddy, D. Vlasic, C. Waylen, and C. Zegos, "Response Of The Propeller Materials To Cavitation Erosion Simulated Under Laboratory Conditions," *PRAD2010*, pp. 1–8, 2010.
  - [34] G. Kuiper, "Physics of cavitation: Gas Content," in *Cavitation in ship propulsion*, 2010, pp. 29–35.
  - [35] G. L. Chahine, "Nuclei Effects on Cavitation Inception and Noise," *25th Synopsium on Naval Hydrodynamics*, no. August. 25th Symposium on Naval Hydrodynamics, Newfoundland and Labrador, pp. 8–13, 2004.
  - [36] E. A. Brujan, "Nucleation," in *Cavitation in Non-Newtonian Fluids*, Berlin, Heidelberg: Springer Berlin Heidelberg, 2011, pp. 49–62.
  - [37] V. K. Shen and P. G. Debenedetti, "A kinetic theory of homogeneous bubble nucleation," *J. Chem. Phys.*, vol. 118, no. 2, p. 768, 2003.
  - [38] C. C. Church, "Spontaneous homogeneous nucleation, inertial cavitation and

- the safety of diagnostic ultrasound," *Ultrasound Med. Biol.*, vol. 28, no. 10, pp. 1349–1364, 2002.
- [39] R. Fürth and M. Born, "On the theory of the liquid state," *Math. Proc. Cambridge Philos. Soc.*, vol. 37, no. 3, p. 276, Oct. 2008.
  - [40] M. Strasberg, "Onset of Ultrasonic Cavitation in Tap Water," *J. Acoust. Soc. Am.*, vol. 31, no. 2, pp. 163–176, 1959.
  - [41] R. E. Apfel, "The Role of Impurities in Cavitation-Threshold Determination," *J. Acoust. Soc. Am.*, vol. 48, no. 58, pp. 1179–1186, 1970.
  - [42] A. A. Atchley and A. Prosperetti, "The crevice model of bubble nucleation," *J. Acoust. Soc. Am.*, vol. 86, no. 3, pp. 1065–1084, 1989.
  - [43] B. M. Borkent, "Interfacial phenomena in micro- and nanofluidics: nanobubbles, cavitation, and wetting," University of Twente [Host], 2009.
  - [44] B. M. Borkent, M. Arora, and C.-D. Ohl, "Reproducible cavitation activity in water-particle suspensions," *J. Acoust. Soc. Am.*, vol. 121, no. 3, p. 1406, 2007.
  - [45] C. E. Brennen, *Cavitation and Bubble Dynamics*. 1995.
  - [46] R. E. Dickerson, H. B. Gray, and G. P. Haight, "Equilibria involving liquids and solids," in *Chemical Principles*, 3rd ed., California: The Benjamin/Cummings Publishing Company, Inc., 1979, pp. 662–694.
  - [47] P. Eisenberg, "Cavitation," *Hydfionauthds Incorporated*. [Online]. Available: <http://web.mit.edu/hml/ncfmf/16CAV.pdf>.
  - [48] V. H. Arakeri, "Cavitation Inception," *Proc. Indian Acad. Sci.*, vol. 2, pp. 149–177, 1978.
  - [49] B. Schiavello and F. C. Visser, "Pump Cavitation — Various NPSHR Criteria, NPSHA Margins, and Impeller Life Expectency," 2009.
  - [50] G. P. Rao, K. Likith, and M. N. Akram, "Numerical Analysis of Cavitating Flow over A2d Symmetrical Hydrofoil," 2012.
  - [51] A. Bergant, A. R. Simpson, and A. S. Tijsseling, "Water Hammer with Column Separation: A Review of Research in the Twentieth Century," 2002.
  - [52] I. Akhatov, O. Lindau, a. Topolnikov, R. Mettin, N. Vakhitova, and W. Lauterborn, "Collapse and rebound of a laser-induced cavitation bubble," *Phys. Fluids*, vol. 13, no. 10, p. 2805, 2001.
  - [53] M. Tinguely, D. Obreschkow, P. Kobel, N. Dorsaz, A. De Bosset, and M. Farhat, "Energy partition at the collapse of spherical cavitation bubbles," vol. 2, p.

- 6009, 2012.
- [54] T. Sato, M. Tinguely, M. Oizumi, and M. Farhat, "Evidence for hydrogen generation in laser- or spark-induced cavitation bubbles," *Appl. Phys. Lett.*, vol. 102, no. 7, p. 74105, Feb. 2013.
  - [55] M. Tinguely, "The effect of pressure gradient on the collapse of cavitation bubbles in normal and reduced gravity PAR," vol. 5674, 2013.
  - [56] C. E. Brennen, "Fission of collapsing cavitation bubbles," *J. Fluid Mech.*, vol. 472, no. 1, pp. 1–8, Nov. 2002.
  - [57] M. Movassat, "Bubble Dynamics , Oscillations and Breakup under Forced Vibration," 2012.
  - [58] R. Bonhomme, J. Magnaudet, F. Duval, and B. Piar, "Inertial dynamics of air bubbles crossing a horizontal fluid–fluid interface," *J. Fluid Mech.*, vol. 707, pp. 405–443, Jul. 2012.
  - [59] J. P. Best, "The effect of non-spherical collapse on determination of explosion bubble parameters," Edinburg, South Australia, 2002.
  - [60] W. Lauterborn and H. Bolle, "Experimental investigations of cavitation-bubble collapse in the neighbourhood of a solid boundary," *J. Fluid Mech.*, vol. 72, no. 2, pp. 391–399, Mar. 2006.
  - [61] M. S. Plesset and R. B. Chapman, "Collapse of an initially spherical vapour cavity in the neighbourhood of a solid boundary," *J. Fluid Mech.*, vol. 47, no. 2, pp. 283–290, 1971.
  - [62] C.-D. Ohl, T. Kurz, R. Geisler, O. Lindau, and W. Lauterborn, "Bubble dynamics, shock waves and sonoluminescence," *Philos. Trans. R. Soc. A Math. Phys. Eng. Sci.*, vol. 357, no. 1751, pp. 269–294, Feb. 1999.
  - [63] C. F. Naude and A. T. Ellis, "On the mechanism of cavitation damage by non-hemispherical cavities collapsing in contact with a solid boundary," *ASME J. Basic Eng.*, vol. 83, pp. 648–656, 1961.
  - [64] T. B. Benjamin and A. T. Ellis, "The Collapse of Cavitation Bubbles and the Pressures thereby Produced against Solid Boundaries," *Philos. Trans. R. Soc. London. Ser. A, Math. Phys. Sci.*, vol. 260, no. 1110, pp. 221–240, Jul. 1966.
  - [65] G. L. Chahine, "Bubble Interaction an Between and a Free Surface," *J. Fluids Eng.*, pp. 708–716, 1977.
  - [66] D. C. Gibson and J. R. Blake, "The growth and collapse of bubbles near



- deformable surfaces," *Appl. Sci. Res.*, vol. 38, no. 1, pp. 215–224, 1982.
- [67] G. L. Chahine and R. Duraiswami, "Dynamical Interactions in a Multi-Bubble Cloud," *J. Fluids Eng.*, vol. 114, no. 4, pp. 680–686, Dec. 1992.
- [68] C. F. Delale and M. Tunç, "A bubble fission model for collapsing cavitation bubbles," *Phys. Fluids*, vol. 16, no. 11, p. 4200, Nov. 2004.
- [69] Y. Tomita and A. Shima, "High-Speed Photographic Observations of Laser-Induced Cavitation Bubbles in Water," *Acta Acust. united with Acust.*, vol. 71, no. 3, p. 11, 1990.
- [70] W. Lauterborn and C. Ohl, "Cavitation bubble dynamics," *Ultrason. Sonochem.*, vol. 4, pp. 65–75, 1997.
- [71] E. a. Brujan, T. Ikeda, and Y. Matsumoto, "On the pressure of cavitation bubbles," *Exp. Therm. Fluid Sci.*, vol. 32, no. 5, pp. 1188–1191, Apr. 2008.
- [72] G. W. Stachowiak and A. W. Batchelor, *Engineering Tribology*. Butterworth-Heinemann, 2001.
- [73] Y. Zhou and F. G. Hammitt, "Cavitation erosion incubation period," *Wear*, vol. 86, no. 86, pp. 299–313, 1983.
- [74] F. G. Hammitt, *Cavitation and multiphase flow phenomena*. McGraw-Hill Book Co., 1980.
- [75] F. Report, "The Specialist Committee on Cavitation Erosion on Propellers and Appendages on High Powered / High Speed Ships Final Report and Recommendations to the 24th ITTC," 2011.
- [76] G. E. Totten, D. K. Wills, and D. G. Feldmann, Eds., *Hydraulic Failure Analysis: Fluids, Components, and System Effects, Issue 1339*, 1st ed., vol. 3. Philadelphia: ASTM International, 2001.
- [77] F. Jean-Pierre and M. Jean-marie, *Fundamentals of cavitation*. Gernoble Sciences, 2003.
- [78] T. J. C. Van Terwisga and P. A. Fitzsimmons, "Cavitation Erosion – A review of physical mechanisms and erosion risk models," in *International Symposium on Cavitation*, 2009, no. 41, pp. 1–13.
- [79] Y. Tomita and A. Shima, "On the Behavior of a Spherical Bubble and the Impulse Pressure in a Viscous Compressible Liquid," *JSME*, vol. 20, pp. 1027–1035, 1977.
- [80] R. Hickling, "Effects of Thermal Conduction in sonoluminescence," *J. Acoust.*

- Soc. Am.*, vol. 35, no. 7, 1963.
- [81] C. E. Brennen, "Cavitation and Bubble Dynamics," *Oxford University Press*, 1995. [Online]. Available: <http://authors.library.caltech.edu/25017/4/chap3.htm>. [Accessed: 21-Aug-2013].
  - [82] A. Phillip and W. Lauterborn, "Cavitation erosion by single laser-produced bubbles," *J. Fluid Mech.*, vol. 361, no. 361, pp. 75–116, 1998.
  - [83] "Cavitation." pp. 1–22.
  - [84] M. M. Skinner and T. L. Wahl, "Evaluation of techniques for detection of cavitation on the runner of a model hydraulic turbine," Denver, 1991.
  - [85] "High power ultrasound and acoustic cavitation – Detection," *NPL*, 2007. [Online]. Available: <http://www.npl.co.uk/acoustics/ultrasonics/research/high-power-ultrasound-and-acoustic-cavitation-detection>. [Accessed: 07-Sep-2014].
  - [86] L. Alfayez, D. Mba, and G. Dyson, "The application of Acoustic Emission for detecting incipient cavitation and the best efficiency point of a 60KW centrifugal pump," *NDT E Int.*, vol. 38, no. 5, pp. 354–358, 2005.
  - [87] V. Bull, J. Civale, I. Rivens, and G. ter Haar, "A Comparison of Acoustic Cavitation Detection Thresholds Measured with Piezo-electric and Fiber-optic Hydrophone Sensors," *Ultrasound Med. Biol.*, vol. 39, no. 12, pp. 2406–2421, Dec. 2013.
  - [88] G. J. Price, "Detection and measurement of cavitation in sonochemistry and medical ultrasound," *39th Int. Congr. Noise Control Eng.*, vol. 8, pp. 6574–6582, 2010.
  - [89] G. Kuiper, "Types of Cavitation : Bubble Cavitation," *Cavitation in ship propulsion*, 2010.
  - [90] G. Kuiper, "Types of cavitation : Sheet Cavitation," in *Cavitation in ship propulsion*, 2011, pp. 36–46.
  - [91] G. Kuiper, "Vortex cavitation," in *Cavitation in ship propulsion*, 2012, pp. 65–83.
  - [92] P. Eisenberg, "Cavitation Damage," 1963.
  - [93] T. Okada, "Corrosive Liquid Effects on Cavitation Erosion," *J. Ship. Res.*, vol. 25, no. 4, pp. 271–284, 1981.

- [94] S. L. Kerr, "Determination of the relative resistance to cavitation erosion by the vibratory method," *ASME TRANS*, vol. 59, no. 5, pp. 373–408, 1937.
- [95] J. M. Mousson, "Pitting Resistance of Metals Under Cavitation Conditions," *ASME TRANS*, vol. 59, no. 5, pp. 399–408, 1937.
- [96] W. J. Rheingans, "Prevention and reduction of cavitation and pitting in hydraulic turbines," 2011. [Online]. Available: [http://www.frenchriverland.com/cavitation-prevention\\_&\\_reduction.htm](http://www.frenchriverland.com/cavitation-prevention_&_reduction.htm).
- [97] H. Nowotny, *Werkstoffzerstörung durch Kavitation: Untersuchungen am Schwinggerät*. VDI-Verlag, 1942.
- [98] W. J. Rheingans, "Accelerated cavitation research," *ASME TRANS*, vol. 72, no. 5, pp. 705–719, 1950.
- [99] S. W. Barnaby and C. W. Parsons, ".,," *Trans. Inst. Nav. Arch.*, no. 38, p. 232, 1897.
- [100] "Cavitation," *Asian Scientist Magazine*, 2013. [Online]. Available: [http://www.asianscientist.com/books/wp-content/uploads/2013/05/p172\\_chap01.pdf](http://www.asianscientist.com/books/wp-content/uploads/2013/05/p172_chap01.pdf).
- [101] J. I. Thornycroft and S. W. Barnaby, "Torpedo Boat Destroyers," *J. Am. Soc. Nav. Eng.*, vol. 7, no. 4, pp. 711–736, Mar. 1895.
- [102] E.-A. Weitendorf, "On the history of Propeller Cavitation and Cavitation Tunnels," *CAV2001*, no. 189 5, pp. 1–13, 1951.
- [103] R. Garcia and F. G. Hammitt, "Cavitation Damage and Correlations With Material and Fluid Properties," *J. Basic Eng.*, vol. 89, no. 4, p. 753, Dec. 1967.
- [104] B. G. Singer and J. Harvey, "Gas content and temperature effects in vibratory cavitation tests," *Wear*, vol. 52, pp. 147–160, 1979.
- [105] J. He and F. G. Hammitt, "Comparison of cavitation erosion test results from venturi and vibratory facilities," *Wear*, vol. 76, no. 3, pp. 269–292, 1982.
- [106] Y. Zhou, X. Wang, and F. G. Hammitt, "Vibratory cavitation tests at elevated temperature," vol. 85, pp. 319–329, 1983.
- [107] Y.-K. Zhou and F. G. Hammitt, "Vibratory cavitation erosion in aqueous solutions," *Wear*, vol. 87, no. 2, pp. 163–171, May 1983.
- [108] D. Li, G. Zou, G. Zheng, and X. Yong, "Effects of the Microstructures on Surface Layer Mechanical Properties of Stainless Steels Under Cavitation," *Chinese J.*

- Mater. Res.*, vol. 26, no. 3, pp. 274–278, 2012.
- [109] V. Riddei and G. Roch, “Cavitation erosion—a survey of the literature 1940–1970,” *Wear*, vol. 23, pp. 133–136, 1973.
- [110] “ASTM G32 - 16 Standard Test Method for Cavitation Erosion Using Vibratory Apparatus,” *ASTM international*, 2011. [Online]. Available: <http://www.astm.org/cgi-bin/resolver.cgi?G32-16>. [Accessed: 13-Feb-2013].
- [111] “ASTM G134 - 95(2010)e1 Standard Test Method for Erosion of Solid Materials by a Cavitating Liquid Jet.” [Online]. Available: <http://www.astm.org/Standards/G134.htm>. [Accessed: 23-Aug-2013].
- [112] “ASTM D2809 - 04e1 Standard Test Method for Cavitation Corrosion and Erosion Corrosion Characteristics of Aluminum Pumps With Engine Coolants,” 2011. [Online]. Available: <http://www.astm.org/DATABASE.CART/HISTORICAL/D2809-04E1.htm>. [Accessed: 13-Feb-2013].
- [113] BSI, “BS EN 60609-2:1999 - Cavitation pitting evaluation in hydraulic turbines, storage pumps and pump turbinesEvaluation in Pelton turbines,” *BSI*, 1998. [Online]. Available: <http://shop.bsigroup.com/ProductDetail/?pid=000000000030149195>.
- [114] BSI, “BS ISO 7146-2:2008 - Plain bearings. Appearance and characterization of damage to metallic hydrodynamic bearingsCavitation erosion and its countermeasures,” *BSI*, p. 30, 2008.
- [115] Mitterbauer, “BS ISO 7146-2:2008 -- Plain bearings. Appearance and characterization of damage to metallic hydrodynamic bearings -- Cavitation erosion and its countermeasures,” *International Standard*, vol. 2008. ISO, Switzerland, p. 20, 2008.
- [116] “DYNAFLOW - Research and Development in Applied Sciences.” [Online]. Available: <http://www.dynafloow-inc.com/>.
- [117] R. E. A. Arndt, “Vortex cavitation,” in *Fluid vortices*, vol. 30, S. I. Green, Ed. Dordrecht: Springer Netherlands, 1995, pp. 731–782.
- [118] R. W. Johnson, *The Handbook of Fluid Dynamics*. Boca Raton: Springer, 1998.
- [119] C. M. Preece, “Cavitation Erosion,” 1979, pp. 249–305.
- [120] A. Jayaprakash, J.-K. Choi, G. L. Chahine, F. Martin, M. Donnelly, J.-P. Franc,

- and A. Karimi, "Scaling study of cavitation pitting from cavitating jets and ultrasonic horns," *Wear*, vol. 296, no. 1–2, pp. 619–629, Aug. 2012.
- [121] J.-K. Choi, A. Jayaprakash, and G. L. Chahine, "Scaling of cavitation erosion progression with cavitation intensity and cavitation source," *Wear*, vol. 278–279, pp. 53–61, Mar. 2012.
- [122] I. Hansson and K. A. Morch, "Comparison of the initial stage of vibratory and flow cavitation erosion," in *International Conference on Erosion by Liquid and Solid Impact, 5 th, Cambridge, England, 1979*, pp. 60–61.
- [123] A. Karimi and F. Avellan, "Comparison of erosion mechanisms in different types of cavitation," *Wear*, vol. 113, pp. 305–322, 1986.
- [124] G. L. Chahine, J. Franc, and A. Karimi, "Laboratory Testing Methods of Cavitation Erosion," in *Advanced Experimental and Numerical Techniques for Cavitation Erosion Prediction*, vol. 106, K.-H. Kim, G. Chahine, J.-P. Franc, and A. Karimi, Eds. Dordrecht: Springer Netherlands, 2014, pp. 21–35.
- [125] B. Bachet, M. Dular, S. Baumgarten, G. Ludwig, and B. Stoffel, "Experimental investigations concerning erosive aggressiveness of cavitation at different test configurations," in *ASME Heat Transfer/Fluid Engineering Summer Conference, 2004*, pp. 1–12.
- [126] Z. Xiaojun, "Effect of surface modification processes on cavitation erosion resistance," Universidade Federal do Parane, 2002.
- [127] S. A. Barber, "An Examination of Cavitation Erosion Efficiency," University of Michigan, 1976.
- [128] Y. Iwai, T. Okada, and F. G. Hammitt, "Effect of temperature on the cavitation erosion of cast iron," *Wear*, vol. 85, no. 2, pp. 181–191, 1983.
- [129] H. G. Feller and Y. Kharrazi, "Cavitation erosion of metals and alloys," *Wear*, vol. 93, no. 3, pp. 249–260, Feb. 1984.
- [130] T. Okada, Y. Iwai, S. Hattori, and N. Tanimura, "Relation between impact load and the damage produced by cavitation bubble collapse," *Wear*, vol. 184, no. 2, pp. 231–239, 1995.
- [131] J.-P. Franc, M. Riondet, A. Karimi, and G. L. Chahine, "Impact Load Measurements in an Erosive Cavitating Flow," *J. Fluids Eng.*, vol. 133, no. 12, p. 121301, 2011.
- [132] J. R. Laguna-Camacho, R. Lewis, M. Vite-Torres, and J. V. Méndez-Méndez, "A

- study of cavitation erosion on engineering materials," *Wear*, vol. 301, no. 1–2, pp. 467–476, Apr. 2013.
- [133] K. S. F. Lew, E. Klaseboer, and B. C. Khoo, "A collapsing bubble-induced micropump: An experimental study," *Sensors Actuators A Phys.*, vol. 133, no. 1, pp. 161–172, Jan. 2007.
- [134] A. Moussatov, C. Granger, and B. Dubus, "Cone-like bubble formation in ultrasonic cavitation field," *Ultrason. Sonochem.*, vol. 10, no. 4–5, pp. 191–5, Jul. 2003.
- [135] J. R. Laguna-Camacho, R. Lewis, M. Vite-Torres, and J. V. Méndez-Méndez, "A study of cavitation erosion on engineering materials," *Wear*, vol. 301, no. 1–2, pp. 467–476, 2013.
- [136] S. Hattori and T. Itoh, "Cavitation erosion resistance of plastics," *Wear*, vol. 271, no. 7–8, pp. 1103–1108, Jul. 2011.
- [137] S. M. Ahmed, K. Hokkirigawa, Y. Ito, and R. Oba, "Scanning electron microscopy observation on the incubation period of vibratory cavitation erosion," *Wear*, vol. 142, pp. 303–314, 1991.
- [138] S. M. Ahmed, K. Hokkirigawab, and R. Oba, "Fatigue failure of SUS 304 caused by vibratory cavitation erosion," *Wear*, vol. 177, pp. 129–137, 1994.
- [139] M. Osman and S. M. Ahmed, "Investigation of cavitation damage progress in the incubation period using stepwise erosion and image process techniques," *J. Eng. Sci.*, vol. 42, pp. 683–702, 2014.
- [140] P. Ponthiaux, F. Wenger, D. Drees, and J. P. Celis, "Electrochemical techniques for studying tribocorrosion processes," *Wear*, Mar-2011. [Online]. Available: <http://linkinghub.elsevier.com/retrieve/pii/S0043164803005568>. [Accessed: 15-Nov-2012].
- [141] S. A. Perusich and R. C. Alkire, "Ultrasonically Induced Cavitation Studies of Electrochemical Passivity and Transport Mechanisms," *J. Electrochem. Soc.*, vol. 138, no. 3, p. 700, Mar. 1991.
- [142] N. V. Dezhkunov, A. I. Kulak, and A. Francescutto, "The effect of ultrasonic cavitation on model electrochemical processes," *Ultrasonics*, vol. 34, pp. 551–553, 1996.
- [143] P. R. Birkin, T. G. Leighton, D. G. Offen, and C. J. B. Vian, "Towards the

- understanding of a complex cavitation environment - electrochemistry, acoustics and imaging observations." International Institute of Noise Control Engineering, 01-Jun-2010.
- [144] B. Pollet, *Power Ultrasound in Electrochemistry. From Versatile Laboratory Tool to Engineering Solution*. Wiley, 2012.
- [145] H. S. Preiser and B. H. Tytell, "The Electrochemical Approach To Cavitation Damage and Its Prevention," *Corrosion*, vol. 17, no. 11, pp. 535–549, Jan. 1961.
- [146] A. Neville and B. a. B. McDougall, "Erosion– and cavitation–corrosion of titanium and its alloys," *Wear*, vol. 250, no. 1–12, pp. 726–735, Oct. 2001.
- [147] K. T. Gillen, R. W. Staehle, S. Matsuda, D. Kuron, S. Hofmann, J. H. Peavey, O. Rincon, M. Afzal, A. Press, T. Shibata, R. P. Frankenthal, J. Kroger, E. Society, M. Series, A. W. Aldag, R. C. Jermer, J. B. Lumsden, H. Okuda, K. Asami, and K. Hashimoto, "Ultrasonically Induced Cavitation Studies of Electrochemical Passivity and Transport Mechanisms," vol. 138, no. 3, pp. 700–707, 1991.
- [148] J. H. Neilson and A. Gilchrist, "Erosion by a stream of solid particles," *Wear*, pp. 111–122, 1967.
- [149] Y. Zheng, S. Luo, and W. Ke, "Effect of passivity on electrochemical corrosion behavior of alloys during cavitation in aqueous solutions," *Wear*, vol. 262, no. 11–12, pp. 1308–1314, May 2007.
- [150] P. Riesz, D. Berdahi, and C. L. Christman, "Free Radical Generation by Ultrasound in Aqueous and Nonaqueous Solutions," *Environ. Health Perspect.*, vol. 64, pp. 233–252, 1985.
- [151] Y. T. Didenko and K. S. Suslick, "The energy efficiency of formation of photons , radicals and ions during single-bubble cavitation," vol. 418, no. 2, pp. 394–397, 2002.
- [152] E. Stride and N. Sa, "Microbubble ultrasound contrast agents : a review," *Proc. Instn Mech. Engrs.*, vol. 217, pp. 429–447, 2003.
- [153] M. Takahashi, K. Chiba, and P. Li, "Free-radical generation from collapsing microbubbles in the absence of a dynamic stimulus," *J. Phys. Chem. B*, vol. 111, no. 6, pp. 1343–7, Feb. 2007.
- [154] T. P. Hoar, "Review Lecture - corrosion of metals: its cost and control," *Proc. R. Soc. L.*, vol. 348, pp. 1–18, 1976.

- [155] K. Ogino, A. Hida, and S. Kishima, "Susceptibility of type 431 stainless steel to erosion-corrosion by vibratory cavitation in corrosive media," *Wear*, vol. 116, pp. 299–307, 1987.
- [156] W. FU, "Microstructure changes during cavitation erosion for a steel with metastable austenite," vol. 16, no. 5, pp. 546–548, Oct. 2009.
- [157] Z. Li, J. Han, J. Lu, and J. Chen, "Cavitation erosion behavior of Hastelloy C-276 nickel-based alloy," *J. Alloys Compd.*, vol. 619, pp. 754–759, Jan. 2015.
- [158] M. Ahmad, J. I. Akhter, M. Akhtar, M. Iqbal, E. Ahmed, and M. A. Choudhry, "Microstructure and hardness studies of the electron beam welded zone of Hastelloy C-276," *J. Alloys Compd.*, vol. 390, no. 1, pp. 88–93, 2005.
- [159] Q. Zhang, R. Tang, K. Yin, X. Luo, and L. Zhang, "Corrosion behavior of Hastelloy C-276 in supercritical water," *Corros. Sci.*, vol. 51, no. 9, pp. 2092–2097, Sep. 2009.
- [160] Y. Ma, D. Lu, X. Mao, L. Zhang, and J. Cai, "Microstructure analysis of stress rupture performance of Hastelloy C-276 alloy at 650°C," *Xiyou Jinshu Cailiao Yu Gongcheng/Rare Met. Mater. Eng.*, vol. 39, no. 9, pp. 1571–1574, 2010.
- [161] M. Andrea, "Marcus Theory for Electron Transfer a short introduction," p. 13, 2008.
- [162] C. T. Kwok, F. T. Cheng, and H. C. Man, "Synergistic effect of cavitation erosion and corrosion of various engineering alloys in 3.5% NaCl solution," *Mater. Sci. Eng. A*, vol. 290, no. 1–2, pp. 145–154, Oct. 2000.
- [163] S. Z. Luo, Y. G. Zheng, M. C. Li, Z. M. Yao, and W. Ke, "Effect of Cavitation on Corrosion Behavior of 20SiMn Low-Alloy Steel in 3% Sodium Chloride Solution," *Corrosion*, vol. 59, no. 7, pp. 597–605, Jul. 2003.
- [164] R. Malka, D. A. Gulino, and M. Technology, "Erosion corrosion and synergistic effects in disturbed liquid-particle flow," *Corros. Nacexpo*, no. 6594, 2006.
- [165] Q.-Y. Wang, S.-L. Bai, and Z.-D. Liu, "Study on Cavitation Erosion–Corrosion Behavior of Mild Steel under Synergistic Vibration Generated by Ultrasonic Excitation," *Tribol. Trans.*, vol. 57, no. 4, pp. 603–612, Jun. 2014.
- [166] Y. Zheng, Z. Yao, X. Wei, and W. Ke, "The synergistic effect between erosion and corrosion in acidic slurry medium," *Wear*, vol. 186–187, pp. 555–561, Aug. 1995.



- [167] R. J. K. Wood, "Erosion–corrosion interactions and their effect on marine and offshore materials," *Wear*, vol. 261, no. 9, pp. 1012–1023, Nov. 2006.
- [168] C. T. Kwok, H. C. Man, and F. T. Cheng, "Cavitation erosion–corrosion behaviour of laser surface alloyed AISI 1050 mild steel using NiCrSiB," *Mater. Sci. Eng. A*, vol. 303, no. 1–2, pp. 250–261, May 2001.
- [169] K. Darowicki and J. Ryl, "Cavitation erosion , influence of electrochemical corrosion on cavitation – a review," 2011.
- [170] A. Thiruvengadam and S. J. Waring, "Mechanical properties of metals and their cavitation damage resistance," *J. Ship. Res.*, no. 10, pp. 1–9, 1966.
- [171] C. T. Kwok, F. T. Cheng, and H. C. Man, "Cavitation erosion and corrosion behaviors of laser-aluminized mild steel," *Surf. Coatings Technol.*, vol. 200, no. 11, pp. 3544–3552, Mar. 2006.
- [172] H. C. Man, C. T. Kwok, and T. M. Yue, "Cavitation erosion and corrosion behaviour of laser surface alloyed MMC of SiC and Si<sub>3</sub>N<sub>4</sub> on Al alloy AA6061," *Surf. Coatings Technol.*, vol. 132, no. 1, pp. 11–20, Oct. 2000.
- [173] C. T. Kwok, H. C. Man, and F. T. Cheng, "Cavitation erosion and pitting corrosion behaviour of laser surface-melted martensitic stainless steel UNS S42000," *Surf. Coatings Technol.*, vol. 126, no. 2–3, pp. 238–255, Apr. 2000.
- [174] C. T. Kwok, H. C. Man, and F. T. Cheng, "Cavitation erosion and pitting corrosion of laser surface melted stainless steels," *Surf. Coatings Technol.*, vol. 99, no. 3, pp. 295–304, Feb. 1998.
- [175] D. a. Shifler, "Understanding material interactions in marine environments to promote extended structural life," *Corros. Sci.*, vol. 47, no. 10, pp. 2335–2352, Oct. 2005.
- [176] M. M. Stack and B. D. Jana, "Modelling particulate erosion–corrosion in aqueous slurries: some views on the construction of erosion–corrosion maps for a range of pure metals," *Wear*, vol. 256, no. 9–10, pp. 986–1004, May 2004.
- [177] M. M. Stack, N. Corlett, and S. Zhou, "A methodology for the construction of the erosion-corrosion map in aqueous environments," *WEAR*, vol. 203, pp. 474–488, 1997.
- [178] R. H. Richman and W. P. Mcnaughton, "Correlation of cavitation properties of metals erosion behavior with mechanical," *Wear*, vol. 140, pp. 63–82,

- 1990.
- [179] A. Al-Hashem, P. G. Caceres, A. Abdullah, and H. M. Shalaby, "Cavitation Corrosion of Duplex Stainless Steel in Seawater," *Corros.*, vol. 53, no. 2, pp. 103–113, 1997.
  - [180] A. Al-Hashem, P. G. Caceres, W. T. Riad, and H. M. Shalaby, "Cavitation Corrosion Behavior of Cast Nickel-Aluminum Bronze in Seawater," *Corrosion*, vol. 51, no. 5, pp. 331–342, May 1995.
  - [181] A. Al-Hashem and W. Riad, "The role of microstructure of nickel-aluminium-bronze alloy on its cavitation corrosion behavior in natural seawater," *Mater. Charact.*, vol. 48, no. 1, pp. 37–41, Feb. 2002.
  - [182] S. P. Gadag and M. N. Srinivasan, "Cavitation erosion of laser-melted ductile iron," *J. Mater. Process. Technol.*, vol. 51, no. 1–4, pp. 150–163, Apr. 1995.
  - [183] "Cavitation Erosion Testing ( ASTM G32-92 )," *Sonics & Materials, Inc.*, 2011.
  - [184] M. Nad, "Ultrasonic horn design for ultrasonic machining technologies," *Appl. Comput. Mech.*, vol. 4, pp. 79–88, 2010.
  - [185] International Molybdenum Association and Stainless, Ed., *Practical Guidelines for the Fabrication of Duplex Stainless Steels*. International Molybdenum Association, 2009.
  - [186] "Duplex Stainless Steel," *IMO.A*. [Online]. Available: [http://www.imoa.info/moly\\_uses/moly\\_grade\\_stainless\\_steels/duplex\\_stainless\\_steel.php](http://www.imoa.info/moly_uses/moly_grade_stainless_steels/duplex_stainless_steel.php). [Accessed: 28-Aug-2013].
  - [187] C. M. Abreu, M. J. Cristóbal, R. Losada, X. R. Nóvoa, G. Pena, and M. C. Pérez, "Comparative study of passive films of different stainless steels developed on alkaline medium," *Electrochim. Acta*, vol. 49, no. 17, pp. 3049–3056, 2004.
  - [188] B. Wallén, "Corrosion of Duplex Stainless Steels in Seawater," 1998.
  - [189] R. Francis, "Bimetallic Corrosion," 1982.
  - [190] S. Aribo, "Corrosion and Erosion-Corrosion Behaviour of Lean Duplex Stainless Steels in Marine and Oilfield Environments," University of Leeds, 2014.
  - [191] "Stainless Steel - Duplex 2205," *aalco*. [Online]. Available: [http://www.aalco.co.uk/datasheets/Stainless-Steel\\_1.4462-2205\\_102.ashx](http://www.aalco.co.uk/datasheets/Stainless-Steel_1.4462-2205_102.ashx). [Accessed: 28-Aug-2013].

- [192] C. Formula, T. Covered, K. Properties, and M. Properties, "Stainless Steel - Grade 2205 Duplex ( UNS S32205 )," 2011.
- [193] W. Fredriksson, "Depth Profiling of the Passive Layer on Stainless Steel using Photoelectron Spectroscopy," Uppsala Universitet, 2012.
- [194] A. Kocijan and M. Jenko, "The corrosion behaviour of Duplex Stainless Steel in Chloride solutions studied by XPS," *Mater. Technol.*, vol. 43, no. 4, pp. 195–199, 2009.
- [195] C. Örnek, A. H. Ahmed, and D. L. Engelberg, "Effect of Microstructure on Atmospheric-Induced Corrosion of Heat-treated Grade 2205 and 2507 Duplex Stainless Steels," in *Eurocorr*, 2012, pp. 1–10.
- [196] M. F. Nobell, "Corrosion Behavior of Duplex Stainless Steels in Acidic-Chloride Solutions Studied with Micrometer Resolution," Royal Institute of Technology, 2003.
- [197] E. A. Culpan and G. Rose, "Microstructural characterization of cast nickel aluminium bronze," *J. Mater. Sci.*, vol. 13, no. 8, pp. 1647–1657, Aug. 1978.
- [198] A. Jahanafrooz, E. Hasan, G. W. Lorimer, and N. Ridley, "Microstructural Development in Complex Nickel-Aluminum Bronzes," *Metall. Trans.*, vol. 14, no. October, pp. 1951–1956, 1983.
- [199] N. E. Christensen, J. Kudrnovský, and C. O. Rodriguez, "Metamagnetic behavior in Fe<sub>3</sub>Si and Fe<sub>3</sub>Al," *Int. J. Mater. Sci.*, vol. 1, pp. 1–15, 2007.
- [200] F. Hasan, J. Iqbal, and N. Ridley, "Microstructure of as-cast aluminium bronze containing iron," *Mater. Sci. Technol.*, vol. 1, no. 4, pp. 312–315, 1985.
- [201] K. B. Faires, "Characterization Of Microstructure And Microtexture In Longitudinal Sections From Friction Stir Processed Nickel-Aluminum Bronze," North Carolina State University, 2003.
- [202] J. Basumatary and R. J. K. Wood, "Different methods of measuring synergy between cavitation erosion and corrosion for nickel aluminium bronze in 3.5 % NaCl solution," *Submitt. to Tribol. Int.*, pp. 1–26, 2017.
- [203] J. Basumatary and R. J. K. Wood, "Synergistic effects of cavitation erosion and corrosion for nickel aluminium bronze with oxide film in 3.5 % NaCl solution," *Submitt. to Wear Mater.*, 2017.
- [204] R. J. K. Wood, "Marine wear and tribocorrosion," *Submitt. to Wear Mater.*, 2017.

- [205] H. Meigh, "Cast and Wrought Aluminium Bronzes: Properties, Processes and Structure," *Inst. Mater. 1 Carlt. House Terrace, London, SW 1 Y 5 DB, UK, 2000. 404*, 2000.
- [206] A. Schüssler and H. E. Exner, "The corrosion of nickel-aluminium bronzes in seawater—I. Protective layer formation and the passivation mechanism," *Corros. Sci.*, vol. 34, no. 11, pp. 1793–1802, 1993.
- [207] J. A. Wharton, R. C. Barik, G. Kear, R. J. K. Wood, K. R. Stokes, and F. C. Walsh, "The corrosion of nickel-aluminium bronze in seawater," *Corros. Sci.*, vol. 47, no. 12, pp. 3336–3367, 2005.
- [208] J. A. Wharton and K. R. Stokes, "The influence of nickel–aluminium bronze microstructure and crevice solution on the initiation of crevice corrosion," *Electrochim. Acta*, vol. 53, no. 5, pp. 2463–2473, 2008.
- [209] B. G. Ateya, E. A. Ashour, and S. M. Sayed, "Corrosion of  $\alpha$ -Al Bronze in Saline Water," *J. Electrochem. Soc.*, vol. 141, no. 1, pp. 71–78, Jan. 1994.
- [210] P. Süry and H. R. Oswald, "On the corrosion behaviour of individual phases present in aluminium bronzes," *Corros. Sci.*, vol. 12, no. 1, pp. 77–90, 1972.
- [211] F. King, C. D. Litke, M. J. Quinn, and D. M. Leneveu, "Corrosion potential of copper in chloride solutions as a function of oxygen concentration and mass-transfer coefficient," *Corros. Sci.*, vol. 37, no. 5, pp. 833–851, 1995.
- [212] S. Hattori and E. Nakao, "Evaluation of Cavitation Erosion based on Erosion Particles," *CAV2001*, 2001.
- [213] H. S. Cambell, "Aluminium bronze alloys - corrosion resistance guide," no. 80. Copper Development Association, p. 30, 1981.
- [214] D. Zhang, R. Chen, W. Zhang, Z. Luo, and Y. Li, "Effect of microstructure on the mechanical and corrosion behaviors of a hot-extruded nickel aluminum bronze," vol. 23, no. 2, pp. 113–120, 2010.
- [215] R. C. Barik, J. A. Wharton, R. J. K. Wood, K. S. Tan, K. R. Stokes, and M. Planck, "Erosion and Erosion-Corrosion Performance of Cast and Thermally Sprayed Nickel-Aluminium Bronze," 2011.
- [216] E. A. Culpan and G. Rose, "Corrosion Behaviour of Cast Nickel Aluminium Bronze in Sea Water," *Br. Corros. J.*, vol. 14, no. 3, pp. 160–166, Jan. 1979.
- [217] A. V. Takaloo, M. R. Daroonparvar, M. M. Atabaki, and K. Mokhtar, "Corrosion Behavior of Heat Treated Nickel-Aluminum Bronze Alloy in Artificial

- Seawater," *Mater. Sci. Appl.*, vol. 2, no. 11, pp. 1542–1555, 2011.
- [218] "Corrosion: Galvanic Corrosion," *Specialty Steel Industry of North America*. [Online]. Available: <http://www.ssina.com/corrosion/galvanic.html>. [Accessed: 12-Sep-2013].
- [219] F. King, "Corrosion Resistance of Austenitic and Duplex Stainless Steels in Environments Related to UK Geological Disposal A Report to NDA RWMD," Cumbria, 2009.
- [220] J. H. Horwath, "Why Nickel Aluminum bronze for sea water pumps," *Ampco Pumps Company*, 2002. [Online]. Available: [http://www.amcopumps.com/media/1881/Why\\_NiAlBz\\_For\\_Saltwater.pdf](http://www.amcopumps.com/media/1881/Why_NiAlBz_For_Saltwater.pdf).
- [221] A. Daroonparvar, M. R. Atabaki, Mazar, M. Vakilipour, "Effect of pre-heat treatment on corrosion behaviour of nickel-aluminium bronze alloy," *Assoc. Metall. Eng. Serbia*, vol. 17, no. 4, pp. 183–198, 2011.
- [222] I. Gurrappa, "Cathodic protection of cooling water systems and selection of appropriate materials," *J. Mater. Process. Technol.*, vol. 166, no. 2, pp. 256–267, 2005.
- [223] R. J. D. Tilley, *Understanding Solids: The Science of Materials (Google eBook)*, 2nd ed. John Wiley & Sons, 2013.
- [224] G. C. Gould, "Some observations on erosion by cavitation and impingement," in *Characterization and Determination of Erosion Resistance*, American Society for Testing and Materials, 1970, pp. 182–211.
- [225] C. T. Kwok, H. C. Man, and F. T. Cheng, "Cavitation erosion and damage mechanisms of alloys with duplex structures," *Mater. Sci. Eng. A*, vol. 242, no. 1–2, pp. 108–120, Feb. 1998.
- [226] C. T. Kwok, H. C. Man, and F. T. Cheng, "Cavitation erosion of duplex and super duplex stainless steels," *Scr. Mater.*, vol. 39, no. 9, pp. 1229–1236, Oct. 1998.
- [227] ASTM G102 - 89, "Standard Practice for Calculation of Corrosion Rates and Related Information," vol. 89, no. Reapproved. 1999.
- [228] "ASTM G119 - 16 Standard Guide for Determining Synergism Between Wear and Corrosion," *ASTM Handbook*, 2016. [Online]. Available: <https://www.astm.org/Standards/G119.htm>. [Accessed: 23-Nov-2016].

- [229] R. J. K. Wood and S. P. Hutton, "The synergistic effect of erosion and corrosion: published results," *Wear*, vol. 140, pp. 387–394, 1990.
- [230] J. Malik, I. H. Toor, W. H. Ahmed, Z. M. Gasem, M. A. Habib, R. Ben-Mansour, and H. M. Badr, "Investigations on the corrosion-enhanced erosion behavior of carbon steel AISI 1020," *Int. J. Electrochem. Sci.*, vol. 9, no. 12, pp. 6765–6780, 2014.
- [231] Z. B. Zheng and Y. G. Zheng, "Erosion-enhanced corrosion of stainless steel and carbon steel measured electrochemically under liquid and slurry impingement," *Corros. Sci.*, vol. 102, pp. 259–268, Jan. 2016.
- [232] S. Aribio, R. Barker, X. Hu, and A. Neville, "Erosion-corrosion behaviour of lean duplex stainless steels in 3.5% NaCl solution," *Wear*, vol. 302, no. 1–2, pp. 1602–1608, 2013.
- [233] "ASTM G119 - 16 Standard Guide for Determining Synergism Between Wear and Corrosion," *ASTM international*, 2016. [Online]. Available: [http://www.astm.org/cgi-bin/resolver.cgi?G119-09\(2016\)](http://www.astm.org/cgi-bin/resolver.cgi?G119-09(2016)). [Accessed: 07-Jun-2014].
- [234] C. ka Wing, "Corrosion Behaviour of Duplex Stainless Steel," City University of Hong Kong, 2011.
- [235] R. C. Barik, J. A. Wharton, R. J. K. Wood, and K. R. Stokes, "Electro-mechanical interactions during erosion – corrosion," *Wear*, vol. 267, pp. 1900–1908, 2009.
- [236] A. Neville, T. Hodgkiess, and J. T. Dallas, "A study of the erosion-corrosion behaviour of engineering steels for marine pumping applications," *Wear*, vol. 186–187, pp. 497–507, Aug. 1995.
- [237] J. O. Bello, R. J. K. Wood, and J. a. Wharton, "Synergistic effects of micro-abrasion–corrosion of UNS S30403, S31603 and S32760 stainless steels," *Wear*, vol. 263, no. 1–6, pp. 149–159, Sep. 2007.
- [238] F. Assi and H. Böhni, "Study of wear-corrosion synergy with a new microelectrochemical technique," in *Wear*, 1999.
- [239] F. Ferrer, H. Idrissi, H. Mazille, P. Fleischmann, and P. Labeeuw, "A study of abrasion–corrosion of AISI 304L austenitic stainless steel in saline solution using acoustic emission technique," *NDT E Int.*, vol. 33, no. 6, pp. 363–371, 2000.

- [240] B. W. Madsen, "Measurement of erosion-corrosion synergism with a slurry wear test apparatus," *Wear*, vol. 123, no. 2, pp. 127–142, 1988.
- [241] S. A. Fry and R. J. K. Wood, "The synergistic effect of cavitation erosion and corrosion." Southampton, 1985.
- [242] R. Simoneau, J. Fihey, and R. Roberge, "The effect of corrosion in low-intensity cavitation erosion," in *Cavitation Erosion in Fluid Systems*, 1981, pp. 71–81.
- [243] Y. Oka and M. Matsumura, "Cavitation erosion-corrosion," in *6th Int. Conference on Erosion by Liquid and Solid Impact*, 1983, p. 11.
- [244] Y. Oka, M. Matsumura, and M. Yamawaki, "Slurry erosion-corrosion on commercially pure iron in a vibratory testing facility-mechanism of erosion-corrosion under predominantly erosion conditions," in *7th Int. Coqf on Erosion by Liquid and Solid Impact*, 1987, p. 39.
- [245] N. L. Mulcahy, B. G. Prusty, and C. P. Gardiner, "Hydroelastic tailoring of flexible composite propellers," *Ships Offshore Struct.*, vol. 5, no. 4, pp. 359–370, Aug. 2010.
- [246] N. L. Mulcahy, B. G. Prusty, and C. P. Gardiner, "Flexible Composite Hydrofoils and Propeller Blades," in *International Maritime Conference 2010: Maritime Industry - Challenges, Opportunities and Imperatives*, 2010, pp. 438–448.
- [247] Y. L. Young and Y. L. Young, "Hydroelastic Behavior Of Flexible Composite Propellers In Wake Inflow," in *16th International Conference On Composite Materials*, 2007, pp. 1–6.
- [248] T. J. Searle, "The Manufacture of Marine Propellers in Moulded Anisotropic Polymer Composites," University of Plymouth, 1998.
- [249] A. Shenoï and A. Gordon, "Ships 'P' brackets in composite materials : a feasibility study." 1991.
- [250] M. T. Herath, B. G. Prusty, G. H. Yeoh, M. Chowdhury, and N. St, "Development of a shape-adaptive composite propeller using bend-twist coupling characteristics of composites," in *3rd International Symposium on Marine Propulsion*, 2013, no. May, pp. 128–135.
- [251] N. L. Mulcahy, P. Croaker, D. G. McGuckin, P. A. Brandner, and N. Kessissoglou, "Optimisation applied to composite marine propeller noise,"

pp. 1–8, 2014.

[252] W. Orchard, “Cavitation Erosion Damage on Marine Composites,”  
Southampton, 2016.



# Appendix A

---

Journal published in Wear of Materials (2017): “Synergistic effects of cavitation erosion and corrosion for nickel aluminium bronze with oxide film in 3.5% NaCl solution.”



# Synergistic effects of cavitation erosion and corrosion for nickel aluminium bronze with oxide film in 3.5% NaCl solution

J. Basumatary\*, R.J.K. Wood

National Centre of Advanced Tribology at Southampton, University of Southampton, Highfield SO17 1BJ, United Kingdom

## ARTICLE INFO

### Article history:

Received 3 September 2016

Received in revised form

10 January 2017

Accepted 12 January 2017

### Keywords:

Cavitation erosion-corrosion

Tribo-corrosion

Synergy

Nickel aluminium bronze

## ABSTRACT

Cavitation erosion-corrosion of nickel aluminium bronze with oxide films formed under two different conditions, oxide formed in air for 1 week and oxide formed after 3 months immersion in 3.5% NaCl solution, was conducted using a 19.5 kHz indirect ultrasonic vibratory system at a peak-to-peak amplitude of  $80 (\pm 0.2) \mu\text{m}$  in 3.5% NaCl solution. The synergistic interactions between the cavitation erosion and corrosion were determined via experiment comprising of three different tests: pure cavitation erosion test in distilled water, pure in-situ electrochemical corrosion tests using open circuit potentials (OCP) and polarization scanning, and a combination of cavitation erosion-corrosion kept at OCP in 3.5% NaCl solution to understand the overall synergism existing between cavitation wear and corrosion. The results were then analysed and compared using mass loss analysis. Scanning electron microscopy was used to analyse microstructural characteristics of the cavitated sample surfaces, as well as the transverse-sections of the surface features. It was seen that samples with water formed film exhibited high synergy and was more susceptible to selective phase attack and phase boundary erosion in comparison to air-formed film.

© 2017 Elsevier B.V. All rights reserved.

## 1. Introduction

Cavitation is a tribo-corrosion phenomenon known to occur within marine environment that may cause destruction of ships, boats and submarine propellers as well as rudders, greatly affecting their efficiency and reducing their life. Generally known to be a very complex process, it depends on the type and unsteadiness of the process along with the physical response of the propeller and rudder materials to the cavitation impact itself [1]. There have been many counter-measures to prevent or reduce further damage by cavitation. But due to ever increasing usage and sizes of bulk carriers and ocean liners, cavitation has become more prominent an issue. In a marine system, the marine propulsion system in general seems to be at a high risk of exposure to cavitation and its detrimental effects. Hence, a propeller material has certain properties that it must meet before it can be considered fit for boat and ship propeller fabrication. The properties required in a propeller material vary depending on the duty and service conditions of its vessel, however, certain factors are more commonly desirable for a propeller material to possess, such as high mechanical strength including ductility, fracture toughness and

tensile strength, strength to weight ratio, high resistance to general corrosion, crevice corrosion and corrosion fatigue in seawater, high cavitation erosion resistance, high resistance to impingement attack, and ability to be repaired easily including weldability [2].

Understanding the material behaviour in different wear conditions as well as environments, and the synergistic interaction between the cavitation erosion and corrosion adds valuable insight into understanding the cavitation behaviour of the propeller materials.

As-cast nickel aluminium bronze (NAB), UNS C98500 (CuAl10Fe5Ni5), is a conventional marine propeller material alloy that has been studied in the literature to understand the role of its microstructure and material behaviour against cavitation erosion-corrosion. With the ability to retain its original smooth machined surface over a long period of time, and high notch resistance, as well as resistance to failure under impact when notched, it has become greatly valued as a marine propeller material [3]. As classed by Lloyd's Register, in the early 1960s the use of high-tensile brass accounted for about 64% of all of the propellers produced whereas, NAB accounted for only 19%. However, by the mid 1980s NAB had acquired almost complete dominance over the other materials, accounting for about 82% of the propellers. This is attributed to a combination of high mechanical properties and superior corrosion resistance in seawater demonstrated by NAB over other engineering materials [2].

\* Corresponding author.

E-mail addresses: [jan.basumatary@gmail.com](mailto:jan.basumatary@gmail.com), [jb10g11@soton.ac.uk](mailto:jb10g11@soton.ac.uk) (J. Basumatary).

### 1.1. Synergy

Cavitation erosion-corrosion of NAB has since been studied most extensively to understand the behavioural response of NAB to cavitation, its microstructural characteristics, and more importantly the relation between cavitation erosion and corrosion of NAB. The tribo-corrosion process which involves mechanical as well as electro-chemical interactions is known as synergism of wear and corrosion [4]. One way to determine this relationship is via performing a synergy experiment that involves three different types of test [5,6]: (1) pure erosion tests to determine the erosive wear rate; (2) pure corrosion tests to determine the corrosive wear rate; (3) combined erosion and corrosion tests to determine the total wear rate. These experiments allow evaluation of the synergistic effect, by using Eq. (1) conforming to ASTM G119 standards [7]:

$$S = T - (E + C) \quad (1)$$

Where,

S is the synergistic wear rate,

E the erosive wear rate (test (1))

C the corrosive wear rate (test (2)), and

T the total wear rate (test (3)).

S, T, E and C can be either mass loss or depth-of-penetration rates.

$$S = T - (E + C) = \Delta E + \Delta C \quad (2)$$

Where,  $\Delta E$  = corrosion enhanced erosion, and  $\Delta C$  = erosion enhanced corrosion. The underlying mechanisms for  $\Delta E$  may generally include removal of work-hardened surfaces due to corrosion, exposing the softer substrate to the erosion mechanisms; selective phase attack of grain boundaries; and an increase in the number of stress-concentrating defects (such as caused by corrosion micro-pitting). Whereas,  $\Delta C$  can occur due to local acidification occurring within the erosion pits, which may accelerate corrosion rates and prohibit further film formation; surface roughening due to erosion; or change in mechanical properties of the sample material, such as lowering of the fatigue strength, due to corrosion [8]. However, many attempts have been made in the past to understand and quantify the S into the separate  $\Delta E$  and  $\Delta C$  components. Attempts have been made to correlate them with microstructural analyses [9], or measure them using experimental (such as electrochemical) tests [10]–[12]. However, it has still proven difficult to be able to accurately quantify or separate the components from the S term.

A previous study was conducted to understand the synergy between cavitation erosion and corrosion of air-formed oxide filmed NAB in 3.5% NaCl solution and distilled water [5]. Microstructural analysis was conducted for the eroded samples to understand the mechanisms involved. However, not much has been understood about the cavitation of NAB in the presence of a thick protective oxide layer that is known to form in the marine environment after only a few months of exposure. Furthermore, the impact it has on the synergistic interactions between the cavitation erosion and corrosion is also unknown. Hence, the aim and objective of the present study was to understand the impact of a water-formed oxide layer on the material behaviour during cavitation erosion-corrosion, and compare it with that of an air-formed filmed sample, along with the corrosion aspects of cavitation, the existence of synergism between erosion and corrosion, and the overall cavitation erosion-corrosion damage at room temperature in 3.5% NaCl solution.

For this, the synergy experiment was conducted by means of an indirect ultrasonic vibratory system as presented in Ref. [5]. The experiment conducted comprised of three different tests: pure

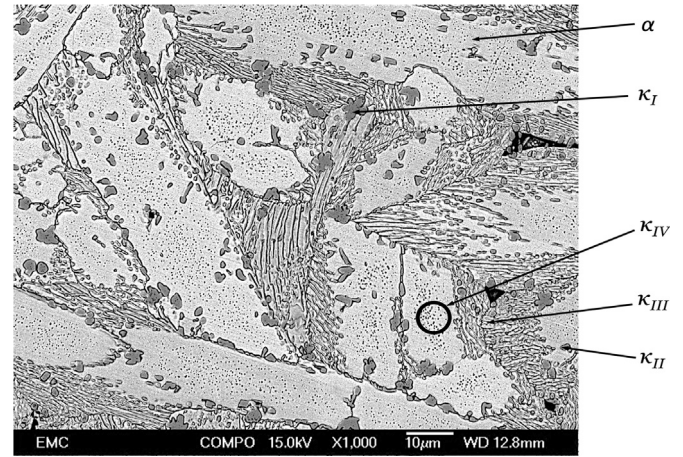


Fig. 1. SEM backscattered electron image of the microstructural morphology of cast NAB at a magnification of 1000x [34].

cavitation erosion test in distilled water, pure corrosion tests using open circuit potentials (OCP) and polarization scanning in 3.5% NaCl solution, and a combination of cavitation erosion-corrosion kept at OCP in 3.5% NaCl solution. The results for T and E were then analysed and compared using gravimetric mass loss analysis.

### 1.2. NAB microstructure and material behaviour

NAB is a copper-based alloy (80 wt%) with aluminium as its main alloying element (10 wt%). In addition to that, it also constitutes 5 wt% of Fe and Ni each among other traces of elements. Together, these elements help NAB form its complex microstructure, which generally comprises of columnar grains of copper-rich solid solution known as  $\alpha$ -phase and a small volume fraction of  $\beta$ -phase or retained martensitic  $\beta'$ -phase, surrounded by four different types of Fe-rich intermetallic kappa ( $\kappa$ ) phases. Among these intermetallic phases,  $\kappa_I$  phase is rosette shaped precipitate ranging from 5–10  $\mu\text{m}$  in diameter.  $\kappa_{II}$  phase is smaller (ranging from 1–2  $\mu\text{m}$  in diameter) dendritic rosette shaped phase distributed mostly at the  $\alpha/\beta$  boundaries.  $\kappa_{III}$  phase is a fine lamellar “finger-like” eutectoid structure. And  $\kappa_{IV}$  phase is a fine precipitation with highest Fe-content among the intermetallics that is of varying sizes ( $< 0.5 \mu\text{m}$  in diameter) with plate-like morphology and is distributed throughout the  $\alpha$ -matrix [3,5, 8–11].

Fig. 1 shows the general microstructural morphology of as-cast NAB tested in this paper under Scanning electron microscope (SEM) at 1000x magnification where,  $\kappa_I$  and  $\kappa_{II}$  are the globular dendritic structures,  $\kappa_{III}$  is the lamellar structure, and  $\kappa_{IV}$  is the very fine particulate imbedded within the  $\alpha$ -matrix.

The  $\kappa_I$ ,  $\kappa_{II}$  and  $\kappa_{IV}$  phases are all distributed in the nickel-aluminium structure of  $\text{DO}_3 \text{Fe}_3\text{Al}$  crystal structure.  $\text{DO}_3$  crystal structure is an ordered face centred cuboid (FCC) crystal unit cell with four body centred cubes (BCC) and four  $\text{Fe}_3\text{Al}$  cubes arranged alternatively.  $\kappa_{III}$  phase, on the other hand, is a Ni-rich  $\text{B}_2$  structure, which is a BCC unit with Ni elements at the eight corners but with Al element at the centre of the cube. Fig. 2 illustrates the crystal structures of  $\kappa_I$ ,  $\kappa_{II}$  and  $\kappa_{IV}$  phases as  $\text{DO}_3 \text{Fe}_3\text{Al}$ ,  $\kappa_{III}$  phase as  $\text{B}_2 \text{NiAl}$  [11,12].

The chemical compositions, in weight %, for the alloy as well as the individual phases obtained under energy-dispersive X-ray spectroscopy (EDS) are tabulated in Table 1.

As-cast NAB used for the research had high mechanical properties with a density of  $7.65 \text{ g cm}^{-3}$ , an ultimate tensile strength of 650 MPa, a yield strength of 270 MPa, and a hardness of 160 Hv. [13].

The general corrosion rate of NAB in seawater is considered to be  $0.06 \text{ mm year}^{-1}$  [14,15]. For the longevity of propellers functioning in a harsh environment like seawater, it is very important

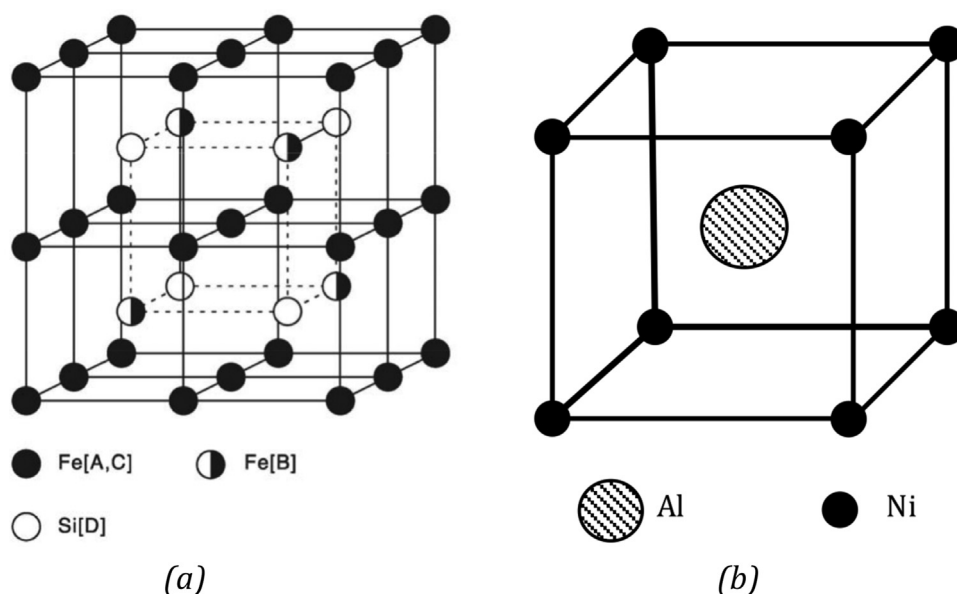


Fig. 2. (a)  $\text{Fe}_3\text{Al DO}_3$  structure, and (b)  $\text{NiAl B}_2$  structure [11,12].

Table 1

Chemical composition of the individual phases in the NAB samples as tested under EDS.

Micro-structural Phases	Chemical composition in weight %						Morphology	Structure
	Cu	Si	Al	Mn	Fe	Ni		
Alloy	80.25	0.03	8.79	3.56	4.63	5.10	–	–
$\alpha$	85.39	–	7.19	0.87	3.35	3.20	FCC solid solution	–
$\kappa_I$	15.08	1.66	13.29	1.72	57.53	10.72	Rosetta globular	$\text{Fe}_3\text{Al (DO}_3\text{)}$
$\kappa_{II}$	17.61	1.52	14.02	1.50	51.90	13.44	Dendritic	$\text{Fe}_3\text{Al (DO}_3\text{)}$
$\kappa_{III}$	45.15	–	18.76	1.19	10.90	24.00	Lamellar	$\text{NiAl (B}_2\text{)}$
$\kappa_{IV}$	13.00	7.00	19.00	2.00	64.00	6.00	Cuboidal	$\text{Fe}_3\text{Al (DO}_3\text{)}$

that the materials used for the propellers are highly corrosion resistant. One of the ways to determine the corrosion properties of a metal or alloy is by locating its position in the galvanic series to understand how it would fair in the seawater environment. The galvanic potentials of NAB in flowing salt water at a velocity of  $2.5$  to  $4 \text{ m s}^{-1}$  at a temperature range of  $10$ – $27^\circ\text{C}$  is between  $-0.15$  to  $-0.22 \text{ V}$  [16–18]. This good corrosion resistance of NAB has been attributed to the formation of a protective oxide layer predominantly comprising of aluminium oxide near the substrate and copper oxide formed on the outer layer, when exposed to a corrosive environment. These films generally take several weeks to reach a thickness of  $900$ – $1000 \text{ nm}$ , which are not susceptible to localised breakdown and consequent pitting in the presence of chlorides and therefore, making NAB very resistant to corrosion by seawater, but may exhibit a different corrosion behaviour from the NAB substrate when disrupted via external means, such as cavitation [14,19].

### 1.3. Corrosion behaviour and selective phase attack

In an alloy with multi-phase composition, the various phases tend to have different electrochemical potentials due to which, there exists a tendency for the most anodic phase to be corroded preferentially. This is called selective phase attack. The extent of corrosion depends on how great the potential difference is between the anodic phase and the surrounding phases, and upon the distribution and intrinsic corrosion resistance of the anodic phases [14].

In case of NAB, the copper-rich  $\alpha$ -phase and aluminium-rich phases tend to undergo localised galvanic corrosion when coupled

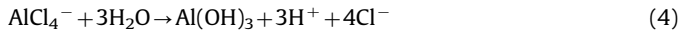
with the cathodic  $\kappa$  phases, which tend to have higher electro-negativity as compared to  $\alpha$ -phase. This selective phase attack affects especially the narrow bands of  $\alpha$ -phase adjacent to the lamellar  $\kappa_{III}$  phases, from where it may spread further into the  $\kappa_{III}$  phase itself [3,5,10,20–25]. This vulnerability of  $\alpha$ - $\kappa_{III}$  phase boundary is considered to be due to its continuous nature. This selective phase attack of the  $\alpha$ - $\kappa_{III}$  phase boundaries may reach up to a depth of  $100 \mu\text{m}$  in just a month of submersion in seawater [25]. A form of selective phase attack that arises in aluminium bronzes is commonly known as “dealuminification,” where the aluminium in the alloy undergoes selective dissolution, resulting in a residue of spongy porous copper, which retains the original shape and dimensions of the component but has little mechanical strength. NAB has been known to suffer from dealuminification in acidic media both in service and in laboratory tests, and also, infrequently in marine environment [14,26]. Generally the existence of the retained  $\beta$ -phase, especially in non-heat-treated NAB, has a negative effect on dealuminification corrosion of aluminium bronzes, since it occurs first at the interface of the  $\alpha$ -matrix and the  $\beta$ -phase and then further develops within the  $\beta$ -phase [27,28]. It has been found that controlling of the factors such as the composition of the alloy, and cooling rate from the working temperature of the cast, may ensure reduction in dealuminification of the alloy [14,26].

### 1.4. Oxide film formation processes

There have been several studies on the corrosion behaviour of NAB alloy and its protective oxide film formation. Schüssler and



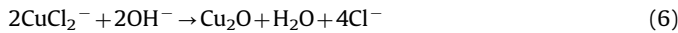
Exner [34] established that when the oxide-free substrate surface is introduced to a corrosive environment, the aluminium in the alloy would preferentially oxidize first in the presence of oxygen. However, after a certain thickness is achieved, the formed alumina film, prevents further diffusion of aluminium, leaving copper to oxidize on the surface of the corrosion product [19,29]. The formation of the  $\text{Al}_2\text{O}_3$  oxide layer is done by “complexation” of aluminium by chloride as demonstrated in Eq. (3), which is then followed by hydrolysis of the chloride product to form  $\text{Al}(\text{OH})_3$  layer (Eq. (4))



The chloride ions released play an important role in the formation and properties of protective oxide films especially on copper-based alloys. Hence, it has been observed and established by Wharton and Stokes that the most prominent oxide forming in aerated chloride media on a NAB surface is  $\text{Cu}_2\text{O}$  [25]. This is because the main corrosion process in such environment mainly constitutes of the dissolution of copper to form a dichlorocuprous anion complex [25,30,31], given by Eq. (5):



The  $\text{Cu}_2\text{O}$  may form via a number of processes in  $\text{Cl}^-$  containing environments, the extent of which depends on the relative chloride ion concentration and pH. The oxide layers are considered are formed by a dissolution process shown in Eq. (6) [32] [37].



The predominant cathodic reaction in aerated solutions given by Eq. (7):



## 2. Methodology

### 2.1. Sample preparation

12 samples were prepared for the tests. Each sample had a dimension of  $25 \times 25$  mm with a thickness of 5 mm with a tolerance of  $\pm 2$  mm. The samples were all wired with the help of M3 screws at one side for facilitating electrochemical analyses. The

sample surfaces were all coated with lacquer on 5 of the 6 sides of the sample, except one, the surface being monitored for oxide formation. 6 samples of NAB were wet polished with 120-, 800, 1200- and 4000- silicon carbide ( $\text{SiC}$ ) abrasive papers and kept aside in 6 individual clean and uncontaminated plastic bags to form air-formed films for a maximum of 1 week.

The other 6 samples were wet polished with 120-, 800, 1200- and 4000-  $\text{SiC}$  grit paper and then submerged in 3.5%  $\text{NaCl}$  solution for 3 months to form a thick layer of water-formed oxide film on the samples. Fig. 3 shows the differences in the optical images of the oxide-films formed after 1 week of air exposure and 3 months of submersion in 3.5%  $\text{NaCl}$  solution.

From Fig. 3(a), it can be seen that considering the protective oxide film formation is a slow process, especially in the absence of corrosive environment like seawater, there is not a significance difference in the microstructure of the substrate after 1 week of exposure to air, although the  $\kappa_{III}$  phases seemed to appear more prominent, meaning localised etching or selective phase attack at the phase boundaries. Whereas, in Fig. 3(b) the sample immersed for 3 months in 3.5%  $\text{NaCl}$  solution had a completely different morphology where the microstructural details of the base material were no longer clearly visible.

### 2.2. Protective oxide film

The corrosion resistance of NAB is attributed to the formation of protective oxide film on NAB. This formation may occur either in air or submerged in corrosive environment like chloride solution. The rate of oxide film growth is much more rapid when fully immersed in corrosive solution than in air. The oxide layer mainly comprises of cuprous oxide ( $\text{Cu}_2\text{O}$ ) and aluminium oxide or alumina ( $\text{Al}_2\text{O}_3$ ) films, with traces of copper salts and hydrochlorides ( $\text{Cu}_2(\text{OH})_3\text{Cl}$  and  $\text{Cu}(\text{OH})\text{Cl}$ ) that form after long exposures to chloride solutions like 3.5%  $\text{NaCl}$  solutions or seawater. These oxides tend to adhere firmly to the substrate, giving very little permeability to liquid corrodant once formed. The oxide layer formed on the substrate/base metal is mostly aluminium-rich, whereas, the oxide formed in the outer regions is generally richer in copper. The oxide films rich in copper, according to Poggie et al., have mechanical properties similar to those of the parent aluminium bronze and are resistant to mechanical disruption during sliding. They greatly reduce the corrosion rate by decreasing the anodic dissolution reactions of aluminium and copper, hampering not only the ionic transport across the oxide layers, but also decreasing the rate of the cathodic reaction on these oxide layers.

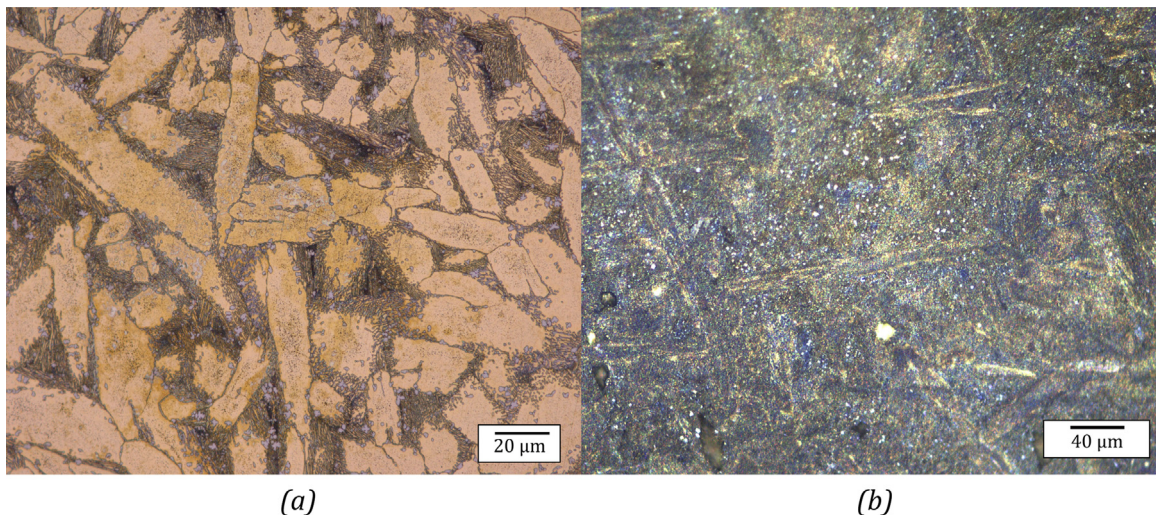
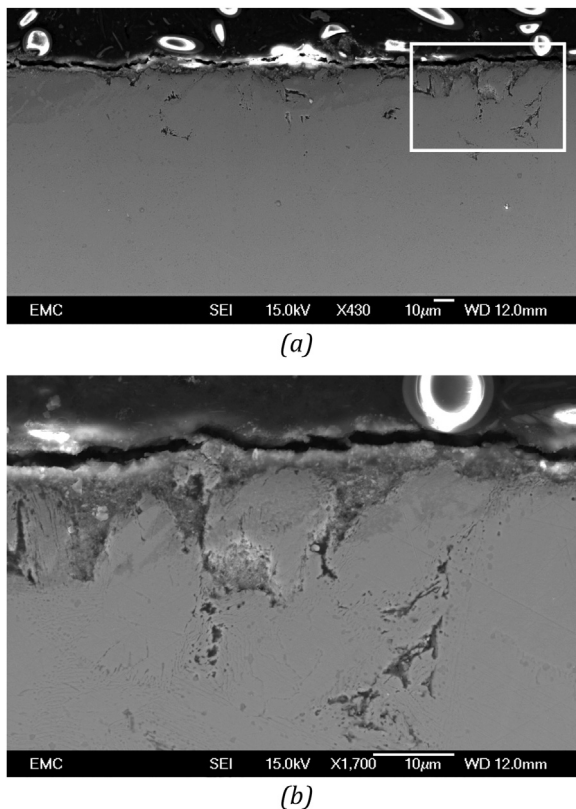


Fig. 3. 600x optical image of general oxide film (a) after 1 week in air; (b) after 3 months of immersion in 3.5%  $\text{NaCl}$  solution.



**Fig. 4.** SEM images the oxide film cross-section on the NAB substrate after 3 months of immersion in 3.5% NaCl solution: (a) selective phase corrosion attack reaching up to 40  $\mu\text{m}$  in depth; (b) the area selected in (a) showing selective corrosion of the  $\kappa_{III}$  phase under the surface.

The oxide films are also considered resistant to most chemical attack, provide good resistance to flow velocity (up to  $22.9 \text{ m s}^{-1}$ ), and heal rapidly when damaged especially in a corrosive environment like seawater in the presence of oxygen [19,20,25,29].

These oxide films, especially alumina, are relatively hard and abrasive but brittle and notch sensitive like other ceramics. If the oxide film is breached, the substrate becomes vulnerable to galvanic corrosion [19]. The oxide film formed in air was barely

visible to the naked eye, but after conducting microstructural analysis under SEM, it was found to be less than 20 nm. Whereas, the oxide film formed in 3.5% NaCl solution was found to have a thickness of 1000–1200 nm (Fig. 4(b)). It should be noted that the thick oxide layer formed after 3 months of submersion in 3.5% NaCl solution have rough porous surface topography and the thickness of the layer does not form homogeneously throughout the surface. This is considered to be due to the inhomogeneous distribution of aluminium and copper, the oxide forming elements in the alloy itself. As reported by Wharton and Stokes, the thickness of the protective oxide films vary with different aluminium content on the phases in aluminium bronzes due to the increased electrical insulation of the region with thicker aluminium oxide [25].

As found by Wharton and Stokes [30], the selective corrosion of the  $\kappa_{III}$ -phase can extend up to a depth of 200–300  $\mu\text{m}$  after 6.5 months of immersion. They also found that under crevice corrosion, the crevice inlet sustained attack at the  $\alpha$ -phase of the eutectoid up to a depth of 20–40  $\mu\text{m}$ , while the  $\kappa_{III}$ -phase was increasingly more susceptible further below 40  $\mu\text{m}$ . This was verified on cross-sectioning of the NAB sample with a thick layer of water-formed oxide layer above the substrate formed after 3 months of immersion in 3.5% NaCl solution showing crevice and selective phase corrosion attack 40  $\mu\text{m}$  deep below the surface (Fig. 4(a) and (b)). The composition of the layer, obtained in EDS, mostly comprised of Cu, Al and O. Corrosion mainly took place at the  $\alpha$ - $\kappa_{III}$  lamella eutectoid phase boundaries, and its corroded depth could be as deep as 20  $\mu\text{m}$  beneath the exposed surface, propagating deeper into the substrate (as shown in Fig. 4(b)).

### 2.3. Experimental procedure

For the cavitation evaluation, the test samples used were cavitated in the same manner as in Ref. [5] under an ultrasonic vibratory cavitation transducer, UIP1000hd, at the tribology laboratory, University of Southampton. The samples were held in a perspex bath using perspex fixture for the indirect cavitation process conforming to the ASTM standard G32-10 [33] [38]. The samples were kept at a constant gap of 2 mm from the sonotrode tip surface. Fig. 5 gives the schematics of the test arrangement [5]. The sonotrode was operated at a frequency of 19.5 kHz and peak-to-peak amplitude of  $80 (\pm 0.2) \mu\text{m}$ .

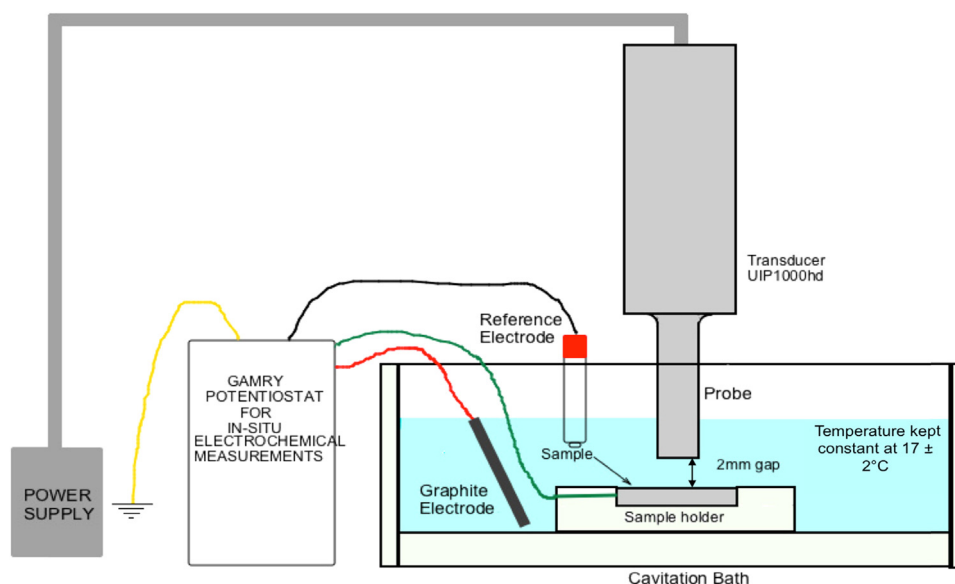


**Fig. 5.** Schematics of the cavitation rig with specimen connected to the electrochemical potentiostat, GAMRY Ref600, for cavitation erosion and corrosion measurements [5].

The tests were conducted for 1 hour each, and the tip surface of the sonotrode was ground to fine surface finish of up to  $0.6\ \mu\text{m}$  after each cavitation test using lathe at the engineering and design manufacturing centre (EDMC) at University of Southampton. The liquid mediums used for the experiments were 5 L of distilled water and 5 L of 3.5% NaCl solution prepared in the lab for the tests. The temperature and the pH of the water were monitored to remain constant at a room temperature of  $17 \pm 0.5\ ^\circ\text{C}$  and pH of 7.5–8.5 throughout the experiment.

The electrochemical tests were conducted using the GAMRY Reference 600 potentiostat to monitor and obtain the OCP and polarization curves for the samples. The parameters for conducting the OCP and polarization tests were set and performed in the GAMRY Framework software, whereas the data obtained were analysed in the GAMRY Echem Analyst software.

The gravimetric weights of the samples were recorded before and after each experiment with suite 500 precision weighing machine for gravimetric analyses ( $\pm 0.01\ \text{mg}$ ). The samples were analysed for microstructural characterization using JOEL (JSM6500F) scanning electron microscope (SEM) employed for microstructural morphology analysis before and after cavitation.

To investigate the synergy for the two sample types, three different tests were conducted in order to obtain the synergistic results between cavitation wear and corrosion. For the pure corrosion (C) tests, all the samples were subjected to OCP and polarization test in 3.5% NaCl solution. For pure erosion (E) test the samples were cavitated in 5 L of distilled water for 1 hour. Finally, for the combined cavitation erosion-corrosion (T), the samples were cavitated in 5 L of 3.5% NaCl solution for 1 hour while subjected to electrochemical tests kept under OCP.

### 3. Results and discussions

#### 3.1. Electrochemical comparison

Fig. 6 is the OCP curve obtained for NAB with air-formed and water-formed oxide films in pure corrosion and erosion-corrosion in 3.5% NaCl solution, where  $V_f$  is the reference potentials in volt. From the electrochemical tests, it was seen that the water-formed oxide film had higher passivation for both pure corrosion and cavitation erosion-corrosion. The figure shows that the air-formed film NAB reached stability at  $-210\ \text{mV}$  under pure corrosion, whereas the water formed film NAB reached stability at  $-150\ \text{mV}$ .

It was observed that the measured OCP shifted slightly negatively by about 6 mV from  $-207\ \text{mV}$  to  $-213\ \text{mV}$  for air-formed film, and by almost 20 mV for water-formed film from  $-149\ \text{mV}$  to  $-165\ \text{mV}$  under pure corrosion tests. This indicated that the protective oxide films on both NAB samples were slowly broken down due to localized corrosion, causing selective phase attack, during

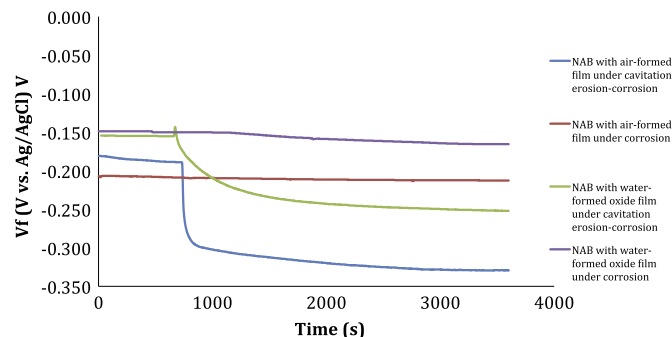


Fig. 6. OCP for NAB with air-formed oxide film and water-formed oxide film in 3.5% NaCl solution for 1 h with and without cavitation.

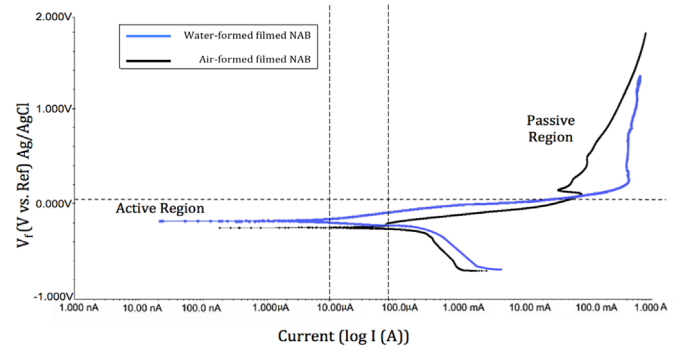


Fig. 7. Polarization curves for NAB with air-formed oxide film and water-formed oxide film in 3.5% NaCl solution for 6 hours.

its immersion in the 3.5% NaCl solution. However, there is a dramatic negative shift in OCP upon cavitation impact. The OCP of water formed film surface was more anodic by 20–50 mV than the air-formed film surface.

For the cavitation erosion-corrosion tests, the cavitation was applied to samples held under OCP after 600 seconds. As can be seen from Fig. 6, for the air-formed film samples there was a drastic negative drop observed in the OCP from  $-170\ \text{mV}$  to about  $-300\ \text{mV}$  on applying cavitation, while the cavitating NAB reached stability within 120 seconds at a lower potential of  $-310\ \text{mV}$  [5]. Whereas, for the water-formed oxide film NAB the OCP shifted from  $-151\ \text{mV}$  to about  $-250\ \text{mV}$  before attaining stability, although the negative shift and stability was attained more gradually over time in about 600 seconds. Therefore, it can be concluded that NAB with water-formed film exhibited better corrosion resistance under static as well as cavitation erosion-corrosion over time. It is also noteworthy that under cavitation impact, the OCP very gradually shifted towards more negative value with time.

Therefore, it can be concluded that NAB with water-formed film exhibited better corrosion resistance under static as well as cavitation erosion-corrosion over time. It is also noteworthy that under cavitation impact, the OCP very gradually shifted towards more negative value with time. Both mass transfer and the disruption of the protective layer as well as the material surface by the rapid and violent implosion of cavitation bubbles, observed both on the OCP trends and via microscope, was considered to be the cause of the drastic negative shifts of the corrosion potentials of the materials. For the pure corrosion test, samples with oxide layers formed under the two different conditions and having an exposed surface area of  $6.25\ \text{cm}^2$  were subjected to potentiodynamic polarization at a scan rate of  $0.167\ \text{mV s}^{-1}$  under static conditions using GAMRY potentiostat in 100 ml of 3.5% NaCl solution. Fig. 7 plots the two polarization curves comparing the current rate and active regions of the two samples.

For NAB comprising of 80% copper, the main corrosion reaction is generally considered to be for copper [30]. Hence, the sample materials were considered to undergo rapid copper dissolution as shown in Equations (8)–(9) taking place in the electrochemical cell:



From the polarization results obtained, it can be seen that the corrosion current density ( $I_{\text{corr}}$ ) of water-formed oxide film NAB is lower at  $1.6\ \mu\text{A cm}^{-2}$  than  $I_{\text{corr}}$  of air-formed oxide film NAB at  $16.0\ \mu\text{A cm}^{-2}$ .



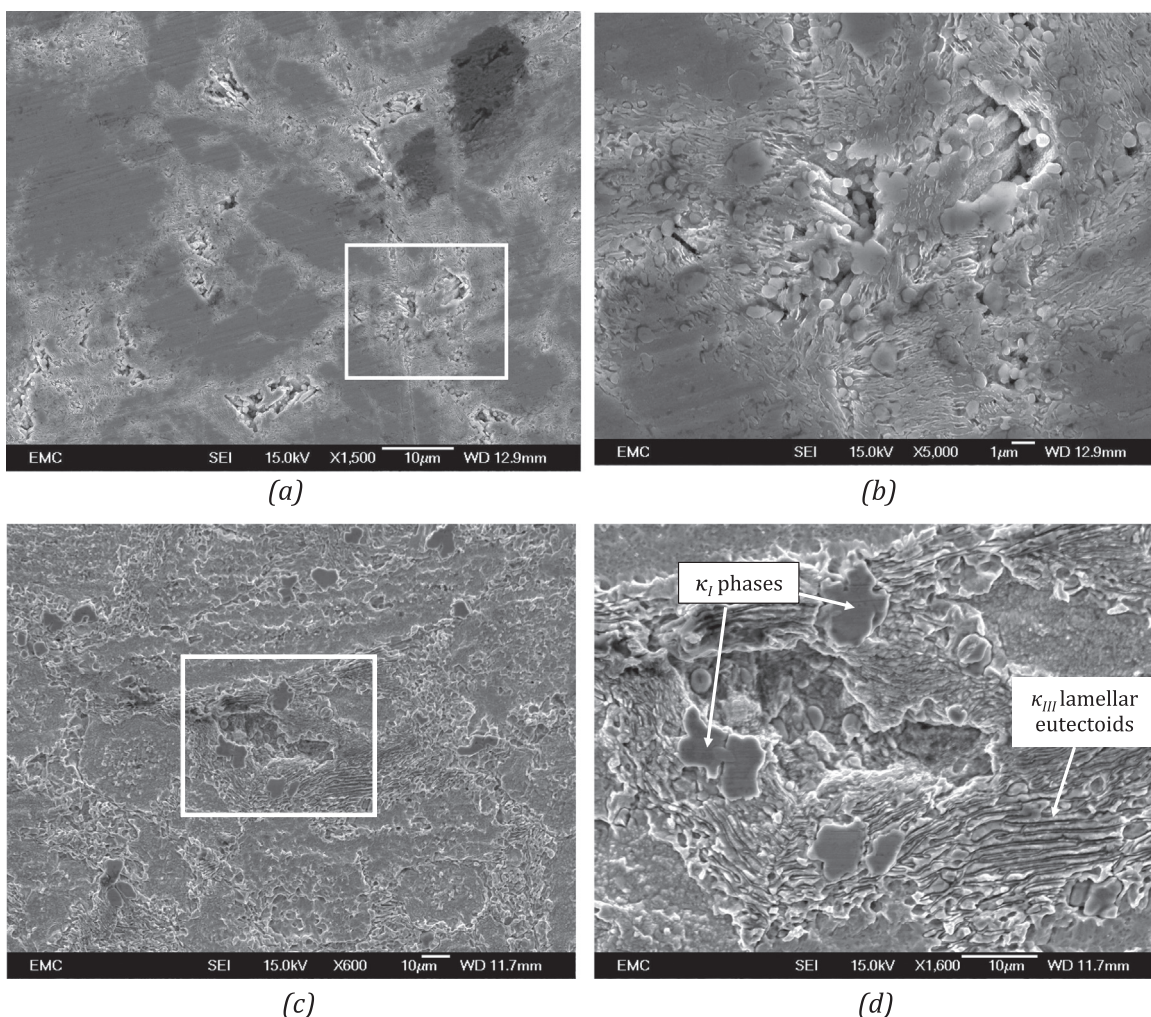


**Fig. 8.** SEM images of (a) small selective phase attack on air-formed film at a magnification of x1500 in distilled water; and (b) magnification of the selected area at x5000; (c) SEM image of a 50 μm large cavity on the sample surface undergone cavitation erosion-corrosion in 3.5% NaCl solution; (d) the magnified image of a cavity in (c) showing selective phase attack at the α-κ phase boundaries leaving κ<sub>I</sub> globules and κ<sub>III</sub> lamellar phases exposed [34].

**Table 2**

Current density and mass loss obtained for NAB with air-formed oxide film and water-formed oxide film from polarization scanning in 3.5% NaCl solution for 6 h.

NAB sample surface	Current density (in μA cm <sup>-2</sup> )	Mass loss (in mg)
Air formed filmed	16.0	0.2 ± 0.01
Water formed filmed	1.6	0.02 ± 0.01

The corrosion rates of the samples were calculated, which further aided in measuring the subsequent mass loss found using Eq. (10).

$$\text{Mass loss rate} = \frac{3.729 \times 10^{-5} \times I_{\text{corr}} \times \text{Atomic mass of corroding element}}{\text{number of electrons freed}} \quad (10)$$

Where, the rate of mass loss is in mg cm<sup>-2</sup> h<sup>-1</sup>. the corroding element was considered to be copper, and the number of freed electrons was taken as 2 (from Equations (8) and (9)).

Hence, the mass loss values obtained for pure corrosion after polarization are as given in Table 2.

### 3.2. Microstructural morphology

For the microstructural analysis of the cavitated surface for air-formed film under SEM, it was found that the soft α-matrix, especially surrounding the hard iron-rich κ phases, seemed to be most vulnerable to cavitation attack as compared to the κ phases and the precipitate-free α zones. The cavity sizes ranged between 10–30 μm in distilled water (see Fig. 8(a) and (b)) as also reported in ref [5], especially at the α-κ<sub>III</sub> grain boundaries. Whereas, the cavities were recorded to be much larger, 50–80 μm, for the cavitation erosion-corrosion test in 3.5% NaCl solution. It was also found that the materials underwent selective cavitation erosion-corrosion attack in 3.5% NaCl solution at the α-κ<sub>III</sub> phase boundaries as seen in Fig. 8(c) and (d); hence the regions with high lamellar κ<sub>III</sub> phases were most susceptible. Also seen in Fig. 8(d) are κ-phases exposed due to the surrounding soft α phase being eroded away.

The transverse section of the cavitation erosion pattern in an air-formed oxide filmed NAB sample is shown in Fig. 9. The cross-sectional imaging confirmed that the adverse site of attack was mostly at the α-κ phase boundaries. Once the cavitation erosion took place, several micro-cracks initiated at these erosion sites, and from there on propagated into the microstructure, especially along the α-κ grain boundaries. Also, several subsurface cracks were observed, however the origin and mechanism of these cracks



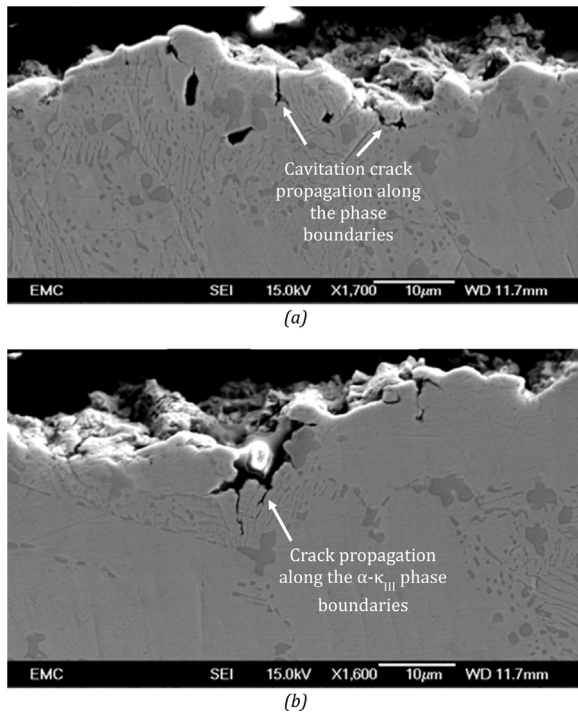


**Fig. 9.** SEM images of transverse sections of NAB after 1 hour of cavitation erosion-corrosion test in 3.5% NaCl solution with air-formed film showing crack propagation along the  $\alpha$ - $\kappa_{III}$  phase boundaries and plastic deformation.

are not fully determined.

Fig. 10(a) and (b) show optical images of the transverse section of an air-formed filmed surface cavitated in 3.5% NaCl solution for 5 h. Fig. 10(a) shows a series of cracks formed under the surface up to a depth of 150  $\mu\text{m}$  and interesting crack formation along the  $\alpha$ - $\kappa$  phase boundaries especially beneath the largest cavity, about 50  $\mu\text{m}$  in size. Fig. 10(b) shows the magnified image of the crack feature. There are a number of stresses acting upon the surface, such as the tensile/compressive shear stress, repetitive loading of the cavitation cloud, subsurface shear stress build-up, as well as the material property itself that may mitigate cracks along the weakest grain boundaries, and several subsurface cracks, as seen in Fig. 10(a). The formations of the subsurface cracks are speculated to be due to the interaction between the slip lines of the  $\alpha$ -rich matrix and the hard secondary phases. The  $\alpha$ -matrix, having

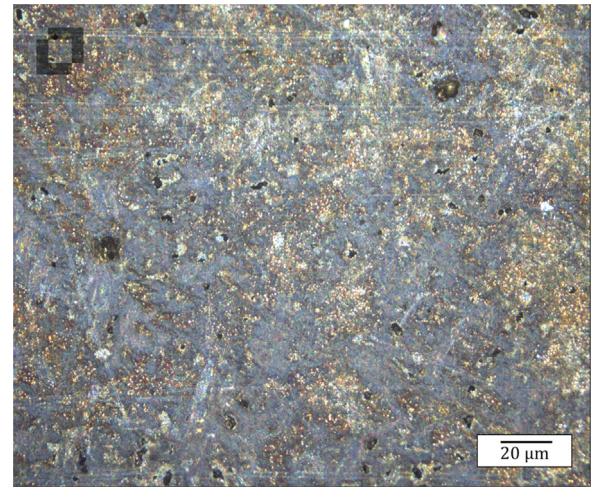


**Fig. 11.** Image of water-formed oxide filmed NAB surface before cavitation erosion-corrosion.

an FCC structure follows the preferential  $\langle 111 \rangle$  slip plane. The subsurface layer generally procures more dislocation than the surface itself. With repetitive or cyclic loading there tends to be pile-ups of dislocations along the subsurface layer that leads to the formation of voids. This is further enhanced within the material with multi-phases with differences in the hardness. The dislocation is then said to pile against the hard secondary phases, forming voids primarily due to plastic flow of softer matrix around hard secondary phase particles within the microstructure [35] [39]. This, combined with the accumulate subsurface strain, lower fracture toughness of the softer phase against the hard phases with higher mechanical property gives way to stress concentration at the grain boundaries, which then eventually results in the failure under cyclic impact stress generated by the cavitation clouds. And hence, causing the subsurface cracks.

However, it should not be disregarded that these cracks may in fact be initiating somewhere on the surface and propagating along the weak grain boundaries with low fracture toughness and into the surrounding microstructure. Further detailed sectioning and characterization of these cracks would be required to explain these cracks, their mechanisms and the crack initiation processes.

For the water-formed film, the wear mechanism was found to be same as the air-formed film. However, the oxide film formation, the film thickness, and the impact of corrosion in chloride solution

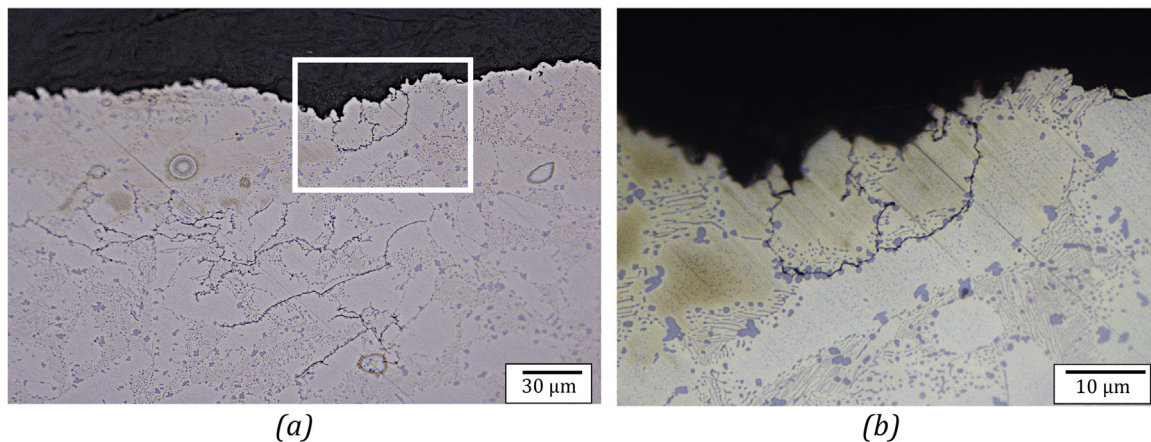


**Fig. 10.** Optical images of: (a) dendritic surface and potential subsurface cracks at 200x; and (b) detail of the selected area in (a) of surface cracks forming along the grain boundaries at 1200x after 1 h of cavitation erosion-corrosion test in 3.5% NaCl solution.



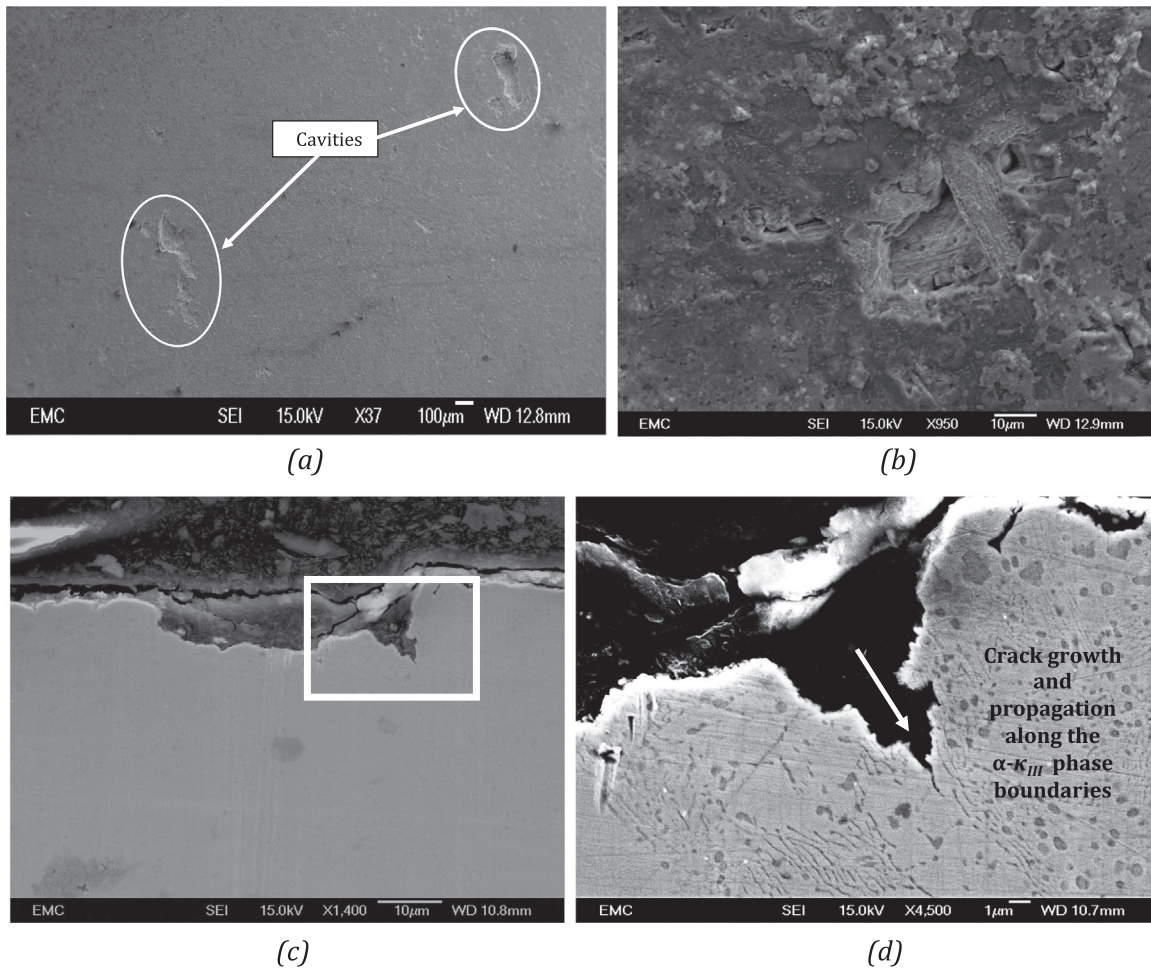


**Fig. 12.** SEM images of water-formed oxide film on NAB sample under pure E conditions: (a) cavities formed on the sample surface after 1 h of cavitation erosion-corrosion; (b) magnified image of the cavities on the surface; (c) transverse-sections of a cavity at x1400; (d) detailed magnified image of a cavity in (d) exhibiting crack growth and propagation along the  $\alpha$ - $\kappa_{III}$  phase boundaries.

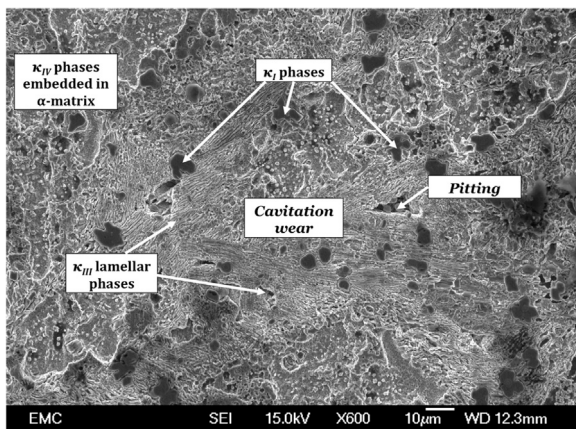


**Fig. 13.** SEM image of the eroded surface of NAB sample with water-formed oxide film after combined cavitation erosion-corrosion test conducted in 3.5% NaCl solution for 1 h.

played a significant role in the cavitation erosion-corrosion behaviour of NAB immersed in 3.5% NaCl solution for 3 months. Fig. 11 shows the water-formed un-cavitated oxide film on NAB, where the microstructure of the substrate is not clearly distinguishable.

From the cavitation erosion-corrosion results obtained, it was observed that the phase boundaries, as already weakened by crevice corrosion and selective phase attack, were the first site of

attack for cavitation erosion-corrosion. Fig. 12(a) shows the cavitation erosion pattern on the roughened oxide surface, detailing a cavity formed due to the erosion for 1 h in distilled water. On closer analysis under the SEM, the erosion was seen to expose the  $\alpha$ - $\kappa_{III}$  phase boundaries under the oxide film, shown in Fig. 12(b).

Fig. 12(c) shows the transverse sections of a cavity on the sample surface after 1 hour of cavitation conducted under pure E conditions for a water-formed oxide film on NAB sample. The cavity was found to be of 30-μm diameter with a large crack propagating into the microstructure. Fig. 12(d) shows the magnified details of the crack (highlighted in (c)) revealing the crack growth and propagation into the microstructure along the  $\alpha$ - $\kappa_{III}$  phase boundaries. Fig. 12(c) and (d) show the cavitation erosion pattern on the surface, detailing a cavity formed due to the erosion of the  $\alpha$  phase at the  $\alpha$ - $\kappa_{III}$  phase boundary, leaving globules and lamellar structures of  $\kappa_I$  and  $\kappa_{III}$  phases exposed.

The wear scar images obtained after 1 hour of cavitation erosion, with the combined effect of corrosion (T) in 3.5% NaCl solution showed more aggressive wear scar and surface roughness, as seen in Fig. 13, illustrating the various different phases within the microstructure. It is evident from the figure that the softer matrix has been eroded and detached, leaving behind small islands of harder iron-rich  $\kappa$  phases exposed, especially at the highest concentration of grain boundaries. Islands of  $\kappa_I$  were seen at the erosion boundaries, whereas threads of  $\kappa_{III}$  were left exposed at regions with high  $\alpha$ - $\kappa_{III}$  eutectoid phases. Furthermore,



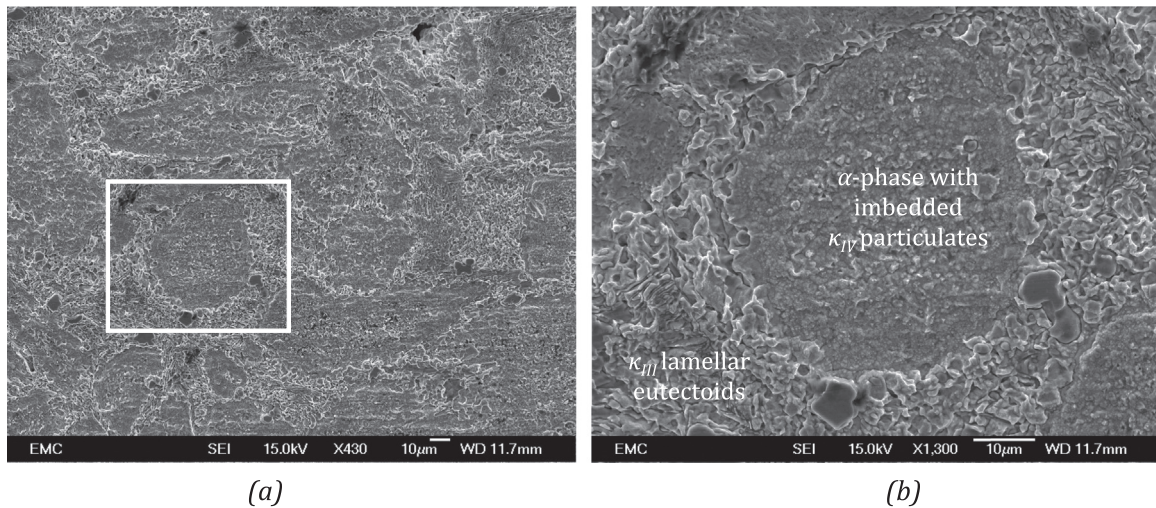


Fig. 14. SEM images of the distinguished phase erosion of the oxide filmed sample in 3.5% NaCl solution after 1 h of cavitation.

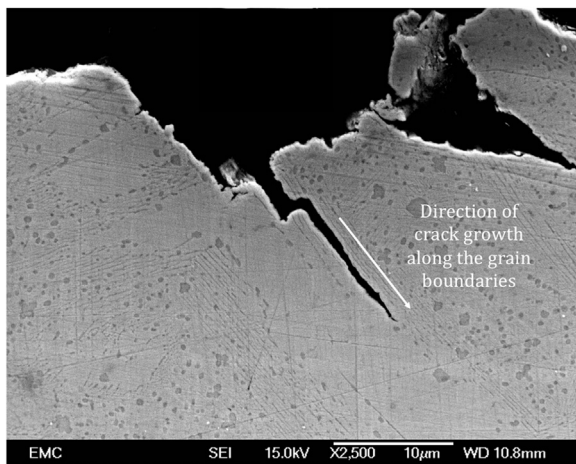


Fig. 15. SEM images of transverse sections of NAB after 1 h of cavitation erosion-corrosion test in 3.5% NaCl solution with water-formed film showing cracks propagating along the lamellar eutectoid grain boundaries.

**Table 3**  
Synergism summary for NAB samples with oxide films formed under air and water.

NAB sample with	T (mg)	E (mg)	C (mg)	S=T-(E+C) (mg)	(S/T) x 100
Air-formed oxide film	1.48 ± 0.02	1.00 ± 0.05 (in Distilled water)	0.2 ± 0.01	0.28 ± 0.08	19%
Water-formed oxide film	24.39 ± 2.00	7.34 ± 0.30 (in Distilled water)	0.02 ± 0.01	17.03 ± 2.30	70%

particulates of  $\kappa_{IV}$  phase were also seen to become more prominent due to the  $\alpha$ -phase erosion at the phase boundaries.

For both E and T conditions, it was seen that the water-formed oxide filmed NAB surface suffered similar erosion trend. The lamellar eutectoid phase boundaries were seen to be most susceptible to corrosion attack, making them further vulnerable to wear via cavitation erosion. Hence, the roughness observed was the highest in these phase boundaries. In Fig. 14(a) the phases can be easily distinguished, especially after cavitation erosion-corrosion due to selective phase attack and wear at the  $\alpha$ - $\kappa_{III}$  as well as  $\alpha$ - $\kappa_{IV}$  phase boundaries, with the exposed  $\kappa_{IV}$  phases imbedded into the soft matrix (Fig. 14(b)).

Fig. 15(a) and (b) show the transverse sections of the sample surface after 1 h of cavitation erosion-corrosion test for the water-formed oxide filmed NAB sample. The cavities were found to be of about 50–80  $\mu\text{m}$  in diameter. Fig. 15 exhibits a large crack propagating into the microstructure along the  $\alpha$ - $\kappa_{III}$  phase boundaries.

"As seen from the microstructural analyses obtained, it was concluded that the main synergistic mechanism at play for the test materials was the  $\Delta E$  mechanism, where the erosion rate of the substrate was enhanced due to selective corrosion attack at the grain boundaries under T. This was more prominent for NAB with water-formed film due to the pre-exposure to corrosion environment, subjecting to corrosion prior to cavitation."

### 3.3. Synergy measurement

Using Eq. (1), the synergy was calculated for the two types of oxide filmed NAB samples. The results comparing synergism for samples with air-formed as well as water-formed oxide films are tabulated in Table 3.

As seen in Table 3, the total mass loss incurred under the combined effect of cavitation erosion and corrosion for NAB samples with water-formed film was much higher (almost 20 times) than the mass loss observed for air-formed oxide filmed sample. Also, the mass loss incurred in distilled water for the water-formed film was significantly lower than that found under T by about 5.6 times for water-formed film. The resultant synergy calculated for samples with water-formed film was found to be about 2.2 times higher at 70% than the synergy calculated for samples with air-formed film (19%).

"Air-formed filmed NAB samples performed better than the water-formed filmed NAB samples under E and T conditions. This may be attributed to the weakening of the substrate microstructure, sans the removal of the protective oxide layer during cavitation, due to the pre-existing selective phase attack and crevice corrosion induced by 3 months of immersion in 3.5% NaCl solution. However, the water-formed filmed NAB showed much higher resistance to corrosion than air-formed filmed NAB, owing to its thick protective oxide layer."

Comparing the synergy results with the studies conducted before, in the studies conducted by Wood and Fry [6] the synergy was found to range between 10–29% for copper, and 30–50% for Cu-Ni alloys. They investigated the fundamental mechanisms of the synergistic effect of cavitation erosion and corrosion for copper and cupro-nickel alloys in seawater. These results were measured using the depth of penetration method in seawater after 4.5 hours

at different overpotentials of 5 – 100 mV. The tests were conducted in an all-plastic cavitation tunnel comprising of a 60° symmetrical wedge cavitation source. The specimens of 10 × 20 mm working section were held under potentiostatic control in a flowing seawater system at an upstream flow velocity of 14.7 m s<sup>-1</sup>. It was hence concluded that the synergistic effect was most marked when the cavitation erosion occurred in presence of mild corrosion with 50–70% of the damage caused due to pure erosion only [6].

In another study, Kwok, Cheng and Man [40] investigated the synergistic effect of cavitation erosion and corrosion of copper-based alloys and bronze, among many other engineering alloys with the help of a 20 kHz ultrasonic vibrator at an amplitude of 30 μm in distilled water and in 3.5% NaCl solution at a temperature of 23 °C. They calculated the synergy via mean depth of penetration rate method and concluded that the Cu-based alloys had a synergy percentage of 2.7–4.5% with 95–97% of the total damage attributed to pure erosion only. It was also found that corrosion only played a minor role of about 0.1–1.8% in the overall cavitation erosion–corrosion for copper-based alloys [36].

Whereas, in the study reported by Barik, Wharton, Wood, et. al. [25], [41] the authors reported negative synergy for NES 747 part 2 NAB. They performed sand slurry jet impingement solid particle erosion–corrosion of NES 747 part 2 NAB samples, conducted on a rig with a horizontal jet of salt solution impinging the NAB sample at 90° with silica sand particles of 135 μm or 235 μm mean sizes at 3% w/w concentration. E values were obtained by subjecting the samples to CP at 200 mV below the corrosion potential under erosion–corrosion conditions. Flow corrosion and total combined loss rates were determined without the addition of solids and CP respectively. They observed strain hardening as the cause of the negative S value layer, sectioning the erosion scars and looking in to the subsurface microstructure and its depth profile. The increase in strain hardening also reduced the erosion rate under T conditions. They concluded that corrosion in fact enhanced plastic flow, thereby increasing strain in the near surface as compared to the pure erosion conditions [25].

These results, although informative, were measured via different means under varying conditions, and hence cannot be readily compared to the results obtained in the current study, however, a relative comparison can be drawn based on the results obtained, such as in all the cases, erosion had higher contribution upon synergy.

It can be concluded that the oxide film, being porous and brittle, erode away much faster than the substrate, causing higher material loss under pure erosion for substrate with water-formed oxide film when compared to substrate with air-formed oxide film. And under the combined effect of cavitation erosion and corrosion in a chloride solution, it undergoes higher copper dissolution and hence, further increases material loss due to the combined impact of E and C. Additionally, an interesting observation made from Table 3 was the influence of ΔE, corrosion[HYPER]enhanced erosion, for both the samples. This can be seen numerically from the increase in mass loss value under T when compared to the individual E and C values, giving a higher ΔE contribution towards synergy. Thus, further validating the results that were acquired from the microstructural analyses of the test materials. Whereas, the E and T results obtained showed that the influence of corrosion on cavitation in fact reduced the mass loss, when compared to the mass loss obtained under E. This suggests that 3 months immersion of NAB in 3.5% NaCl solution caused up to 50-μm deep selective phase attacks in the α-κ<sub>III</sub> eutectoid phase boundaries, resulting in sponge like porous surface layer. This in turn resulted in the water-formed oxide filmed NAB samples to be more susceptible to cavitation erosion–corrosion than NAB with air-formed oxide film, giving higher mass loss under E and T. The synergy was

hence higher for the water-formed filmed NAB, putting the sample at higher risk of damage induced by combined impact of cavitation erosion and corrosion. In theory, this would deem NAB unfit as marine propeller materials as the marine propellers dock and function in the marine environment throughout their service lives. However, in reality, the propellers may not be subjected to cavitation at such high intensities as under the ultrasonic transducer. Also, in practical usage, the oxide films formed on the propellers get enough intervals for the damaged oxide films to heal, re-instituting their good corrosion properties.

#### 4. Conclusion

The investigation of synergy conducted for NAB samples with oxide films formed under the two different conditions, air and immersion in 3.5% NaCl solution concluded that:

- Both the types of NAB samples had measurable synergy under cavitation erosion and corrosion. The synergy was calculated to be at 70% for water-formed filmed NAB, whereas, it was about 19% for the air-formed filmed samples.
- Thick layer of 1–1.2 μm oxide film comprising mainly of Al<sub>2</sub>O<sub>3</sub> and Cu<sub>2</sub>O were found on the NAB sample with oxide film formed after 3 months of immersion in 3.5% NaCl solution.
- The water-formed filmed sample underwent higher mass loss than the sample with air formed oxide film. NAB samples with both types of oxide films underwent selective phase attack at mainly the κ<sub>III</sub> phases and the α-κ<sub>III</sub> eutectoid phase boundaries.
- SEM analyses revealed that the wear mechanisms of the cavitated sample surfaces with both air and water formed oxide films were found to be similar in nature with the first site of attack to take place at the α-κ<sub>III</sub> eutectoid phase boundaries.
- The selective phase attack and corrosion of NAB immersed in 3.5% NaCl solution was more prominent due to the presence of chloride with the corroded depth reaching up to 20–50 μm beneath the exposed surface, propagating deeper into the substrate.
- The sites of most aggressive attacks exhibited large cracks propagating into the microstructure along the α-κ<sub>III</sub> phase boundaries, hence the regions with high lamellar κ<sub>III</sub> phases were most susceptible to wear, crack initiation and propagation.
- Electrochemical results indicated that the OCP of water formed filmed surface was more anodic by 20–50 mV than the air-formed filmed surface.
- Both samples sifted negatively on the application of cavitation while conducting OCP, before reaching stability again. The water-formed film reached stability much more gradually in 600s than the air-formed film that reached stability within 100s.

#### References

- [1] G.E. Totten, D.K. Wills, D.G. Feldmann (Eds.), *Hydraulic Failure Analysis: Fluids Components, and System Effects*, 3, ASTM International, Philadelphia, 2001 (Issue 1339, 1st ed.).
- [2] J.S. Carlton, *Marine propellers and propulsion*, in: *Bay Propeller*, Second, 2007, pp. 382–393.
- [3] A. Al-Hashem, W. Riad, *The role of microstructure of nickel–aluminium–bronze alloy on its cavitation corrosion behavior in natural seawater*, *Mater. Charact.* 48 (1) (2002) 37–41.
- [4] R.J.K. Wood, J. Basumatary, M.-H. Evans, *Energy-related tribocorrosion research at the National Centre for Advanced Tribology at Southampton (nCATS)*, in: *Proceedings of the Second International Conference on Tribology*, 2011.
- [5] J. Basumatary, M. Nie, R.J.K. Wood, *The synergistic effects of cavitation erosion–corrosion in ship propeller materials*, *J. Bio-Tribo-Corros.* 1 (2) (2015) 12.
- [6] R.J.K. Wood, S.A. Fry, *The synergistic effect of cavitation erosion and corrosion for copper and cupro-nickel in seawater*, *J. Fluids Eng.* 111 (3) (1990) 271–277.
- [7] ASTM G119 - 16 standard guide for determining synergism between wear and

- corrosion, ASTM International, 2016. Available: <http://www.astm.org/cgi-bin/resolver.cgi?G11-09> (accessed 07.06.14), 2016.
- [8] R.J.K. Wood, S.P. Hutton, The synergistic effect of erosion and corrosion: published results, *Wear* 140 (1990) 387–394.
  - [9] J. Malik, I.H. Toor, W.H. Ahmed, Z.M. Gaseem, M.A. Habib, R. Ben-Mansour, H. M. Badr, Investigations on the corrosion-enhanced erosion behavior of carbon steel AISI 1020, *Int. J. Electrochem. Sci.* 9 (12) (2014) 6765–6780.
  - [10] R. Malka, D.A. Gulino, M. Technology, Erosion corrosion and synergistic effects in disturbed liquid-particle flow, *Corros. Nacexpo* (2006) (no. 6594).
  - [11] Z.B. Zheng, Y.G. Zheng, Erosion-enhanced corrosion of stainless steel and carbon steel measured electrochemically under liquid and slurry impingement, *Corros. Sci.* 102 (2016) 259–268.
  - [12] S. Aribio, R. Barker, X. Hu, A. Neville, Erosion–corrosion behaviour of lean duplex stainless steels in 3.5% NaCl solution, *Wear* 302 (1–2) (2013) 1602–1608.
  - [13] E.A. Culpan, G. Rose, Microstructural characterization of cast nickel aluminium bronze, *J. Mater. Sci.* 13 (8) (1978) 1647–1657.
  - [14] F. Hasan, J. Iqbal, N. Ridley, Microstructure of as-cast aluminium bronze containing iron, *Mater. Sci. Technol.* 1 (4) (1985) 312–315.
  - [15] K.B. Faires, Characterization of Microstructure and Microtexture in Longitudinal Sections from Friction Stir Processed Nickel–Aluminum Bronze, North Carolina State University, 2003.
  - [16] A. Jahanafrooz, E. Hasan, G.W. Lorimer, N. Ridley, Microstructural development in complex nickel–aluminum bronzes, *Metall. Trans.* 14 (1983) 1951–1956.
  - [17] J. Basumatary, R.J.K. Wood, Different methods of measuring synergy between cavitation erosion and corrosion for nickel aluminium bronze in 3.5% NaCl solution, *Tribol. Int.* (2017) 1–26.
  - [18] N.E. Christensen, J. Kudrnovsky, C.O. Rodriguez, Metamagnetic behavior in Fe<sub>3</sub>Si and Fe<sub>3</sub>Al, *Int. J. Mater. Sci.* 1 (2007) 1–15.
  - [19] H.S. Cambell, Aluminium bronze alloys - corrosion resistance guide, no. 80. Copper Development Association, 1981, pp. 30.
  - [20] B. Wallén, Corrosion of Duplex Stainless Steels in Seawater, 1998.
  - [21] Corrosion: galvanic corrosion, Specialty Steel Industry of North America. Available: <http://www.ssina.com/corrosion/galvanic.html> (accessed 12.09.13).
  - [22] F. King, Corrosion Resistance of Austenitic and Duplex Stainless Steels in Environments Related to UK Geological Disposal, a Report to NDA RWMD, Cumbria, 2009.
  - [23] J.H. Horwath, Why nickel aluminum bronze for sea water pumps, Ampco Pumps Company, 2002. Available: [http://www.ampcopumps.com/media/1881/Why\\_NiAlBz\\_For\\_Saltwater.pdf](http://www.ampcopumps.com/media/1881/Why_NiAlBz_For_Saltwater.pdf).
  - [24] H. Meigh, Cast and Wrought Aluminium Bronzes: Properties, Processes and Structure, Institute of Materials, 1 Carlton House Terrace, London SW1Y 5DB, UK, 2000 (404 pp.).
  - [25] J.A. Wharton, R.C. Barik, G. Kear, R.J.K. Wood, K.R. Stokes, F.C. Walsh, The corrosion of nickel–aluminium bronze in seawater, *Corros. Sci.* 47 (12) (2005) 3336–3367.
  - [26] D. Zhang, R. Chen, W. Zhang, Z. Luo, Y. Li, Effect of microstructure on the mechanical and corrosion behaviors of a hot-extruded nickel aluminum bronze, *Acta Metall. Sin.* 23 (2) (2010) 113–120.
  - [27] R.C. Barik, J.A. Wharton, R.J.K. Wood, K.S. Tan, K.R. Stokes, M. Planck, Erosion and Erosion–Corrosion Performance of Cast and Thermally Sprayed Nickel–Aluminium Bronze, 2011.
  - [28] E.A. Culpan, G. Rose, Corrosion behaviour of cast nickel aluminium bronze in sea water, *Br. Corros. J.* 14 (3) (1979) 160–166.
  - [29] A.V. Takaloo, M.R. Daroonparvar, M.M. Atabaki, K. Mokhtar, Corrosion behavior of heat treated nickel–aluminum bronze alloy in artificial seawater, *Mater. Sci. Appl.* 2 (11) (2011) 1542–1555.
  - [30] J.A. Wharton, K.R. Stokes, The influence of nickel–aluminium bronze microstructure and crevice solution on the initiation of crevice corrosion, *Electrochim. Acta* 53 (5) (2008) 2463–2473.
  - [31] Z. Han, H. Zhao, Effect of  $\beta$  martensite transformation on dealuminification behavior of Cu–9Al–2Mn alloy in a marine environment, vol. 345, 2003, pp. 8–13.
  - [32] Z. Han, Y.F. He, H.C. Lin, Dealloying characterizations of Cu–Al alloy in marine environment, *J. Mater. Sci.* 9 (2000) 393–395.
  - [33] S. Fonlupt, B. Bayle, D. Delafosse, J.–L. Heuze, Role of second phases in the stress corrosion cracking of a nickel–aluminium bronze in saline water, *Corros. Sci.* 47 (2005) 2792–2806.
  - [34] A. Schüssler, H.E. Exner, The corrosion of nickel–aluminium bronzes in seawater—I. Protective layer formation and the passivation mechanism, *Corros. Sci.* 34 (11) (1993) 1793–1802.
  - [35] B.G. Ateya, E.A. Ashour, S.M. Sayed, Corrosion of  $\alpha$ -Al bronze in saline water, *J. Electrochem. Soc.* 141 (1) (1994) 71–78.
  - [36] P. Süry, H.R. Oswald, On the corrosion behaviour of individual phases present in aluminium bronzes, *Corros. Sci.* 12 (1) (1972) 77–90.
  - [37] F. King, C.D. Litke, M.J. Quinn, D.M. Leneveu, Corrosion potential of copper in chloride solutions as a function of oxygen concentration and mass-transfer coefficient, *Corros. Sci.* 37 (5) (1995) 833–851.
  - [38] ASTM G32 - 16 standard test method for cavitation erosion using vibratory apparatus, ASTM International, 2011. Available: <http://www.astm.org/cgi-bin/resolver.cgi?G32-16> (accessed 13.02.13).
  - [39] N.P. Suh, The delamination theory of wear, *Wear* 25 (1) (1973) 111–124.
  - [40] C.T. Kwok, F.T. Cheng, H.C. Man, Synergistic effect of cavitation erosion and corrosion of various engineering alloys in 3.5% NaCl solution, *Mater. Sci. Eng. A* 290 (1–2) (2000) 145–154.
  - [41] R.C. Barik, J.A. Wharton, R.J.K. Wood, K.R. Stokes, Electro-mechanical interactions during erosion–corrosion, *Wear* 267 (2009) 1900–1908.

# Appendix B

---

Journal paper submitted to Tribology Internationals (2017): “Different methods of measuring synergy between cavitation erosion and corrosion for nickel aluminium bronze in 3.5% NaCl solution.



# Different methods of measuring synergy between cavitation erosion and corrosion for nickel aluminium bronze in 3.5% NaCl solution

J. Basumatary<sup>1</sup>, R. J. K. Wood<sup>1</sup>

<sup>1</sup>University of Southampton, SO17 1BJ, United Kingdom

## Abstract

In order to understand the combined detrimental effects of cavitation erosion and corrosion in seawater on a conventional marine alloy, nickel aluminium bronze, five different methods were employed to obtain synergism. The experiments were conducted using an ultrasonic vibratory horn functioning at 19.5 kHz frequency and  $80\text{ }\mu\text{m} \pm 0.2\text{ }\mu\text{m}$  peak-to-peak amplitude. The test methods used to obtain the synergy included gravimetric mass loss technique, volumetric mass loss and mean depth of penetration rate methods, and polarization technique. The cavitated surfaces were microstructurally characterized via scanning electron microscopy. Synergism was found to have measurable impact on the cavitation erosion-corrosion of NAB, with its microstructure undergoing selective phase attack, resulting in increased material removal especially in the presence of corrosive environment.

**Keywords:** cavitation; erosion; tribo-corrosion; synergism;

## 1. Introduction

Cavitation occurs when a liquid reaches its boiling point, even at ambient temperatures, when its absolute pressure drops below its vapour pressure, causing the liquid to vaporize and produce cavities. These cavities grow rapidly and collapse asymmetrically, forming small diameter ( $\sim 10\text{ }\mu\text{m}$ ) microjets impinging at a speed up to  $200\text{ m s}^{-1}$  [1]. This in turn creates spots of very high water hammer and stagnation pressure. Bubble collapse can create instantaneous temperature at the bubble centre reaching as high as  $8500\text{ }^{\circ}\text{C}$  [2], emitting destructive shock waves [3], [4]. It has various detrimental consequences such as pitting, surface wear, micro-cracking, noise, sonoluminescence, and corrosion if at a close vicinity to a solid surface [5], [6].

Cavitation erosion is a fluid-to-surface type of erosion that occurs when a portion of the fluid is first exposed to tensile stresses that cause the fluid to boil, then exposed to compressive stresses that cause the vapour bubbles to implode. It requires a high relative motion between the surface and the fluid. The implosion

produces shock waves and causes microjets to impinge against the surfaces. It is a tribo-corrosion phenomenon, which is a result of the combination of mechanical as well as electrochemical actions. Its complexity depends on the type and unsteadiness of cavitation, the response of the material to the cavitation energy imparted, and the surrounding corrosive environment [7], [8].

Bubble collapse causes surface/sub surface stresses. These stresses are generally enhanced at stress risers (notches, tears, welding defects, etc.) or at heterogeneous areas of the material such as at the directionality of metal flow, and can generate microcracks. These micro-cracks propagate to the point where the material can no longer withstand the impulse load that the imploding bubbles foist. Therefore, a rough surface is prone to cavitation erosion. And since pits and a rough profile characterize the cavitation damage, the damage increases as the surface becomes rougher [4].

Cavitation wear is mechanical in nature and cannot occur without the application of the tensile and compressive stresses. Cavitation wear damage undergoes several periods of activity. Depending on the surface structure, the material surface is deformed, loosened and eventually eroded in various ways due to the frequent strain from the shock waves. The rate of erosion is a function of the exposure period and it increases from negligible values, reaching a maximum before decreasing again and finally levelling off to a steady value[4], [9]–[11].

Marine propulsion systems are at an optimum risk of exposure to cavitation that essentially results in very expensive dry-docking, maintenance, repair, etc. Currently, nickel aluminium bronze (NAB), UNS C98500, is a conventional marine alloy used for the fabrication of marine propellers, due to its mechanical properties, and resistance towards corrosion in seawater [12], [13]. NAB gets its corrosion properties from a thick layer of protective oxide film predominantly composed of aluminium oxide ( $\text{Al}_2\text{O}_3$ ) near the substrate with copper oxide ( $\text{Cu}_2\text{O}$ ) formed mostly on the outer layer [52]. These films generally take several weeks immersed in seawater, depending on the environmental conditions, to reach a substantial thickness of up to 1  $\mu\text{m}$  that will have a visible black/brown colouration over the alloy surface. They provide sufficient corrosion resistance, but may exhibit different corrosion behaviour for the NAB substrate when disrupted. However, the protective layer is not susceptible to localised breakdown and consequent pitting in the presence of chlorides, which makes NAB very resistant to corrosion by seawater [13], [53].

To understand the behaviour of NAB in different cavitation erosion and corrosion conditions, substantial studies have been done to understand its microstructural characteristics, and the relationship between cavitation erosion



and corrosion occurring in NAB [14]–[17]. This combined interaction between erosional aspects of cavitation and corrosion is termed as synergy. Several studies have been conducted and proven the existence of synergy between cavitation erosion and corrosion on marine materials such as stainless steel (SS), copper alloys, manganese bronze, and NAB among others [7], [18]–[30].

Synergy can be measured in terms of two common measurements, mass loss incurred by combined contribution of erosion and corrosion or the mean depth of penetration rate (MDPR). According to the ASTM G119 [31] guidelines for determining synergy during erosion–corrosion test, the equation for synergy is commonly written as Equation (1):

$$T = S + E + C \quad \dots(1)$$

Where, T is the overall cavitation erosion-corrosion rate, C is pure corrosion contribution; E is the pure erosion contribution, and S the combined contribution due to synergistic effect. From Equation (1), S can be also represented as in Equation (2):

$$S = T - (E+C) = \Delta E + \Delta C \quad \dots(2)$$

Where,  $\Delta E$  = corrosion enhanced erosion, and  $\Delta C$  = erosion enhanced corrosion.

It has raised curiosity in the recent years for its ability to correlate erosion and corrosion. At the same time it has also become a subject of debate whether the technique is suitable, as well as reproducible. Some authors have suggested that corrosion leads to increased abrasion resistance in some materials [32]–[35]. While, several authors mentioned the effect of corrosion on the rate of abrasion, generally leading to an increased weight loss [33], [36]–[38]. Most authors reported that abrasion increased the kinetics of corrosion [37]–[39]. Reports have also been made where the synergy results seemed to be dependent more on techniques and test conditions adopted during the tests as well as the impact of corrosive solution, the material property, and also the type of materials itself. For most alloys and metal samples the most significant impact was found at a mild corrosive environment [25], [26], [34], [40]–[44].

Tomlinson and Talks [35] studied the cavitation erosion–corrosion of various types of cast iron in 3% sodium chloride solution. The samples were eroded using a 20 kHz ultrasonic cavitation device at peak-to-peak amplitude of 15  $\mu\text{m}$  in distilled water, increasing the salinity by 0.02% and 3%, at 50 °C. The standoff distance was kept constant at 1 mm. They found that the fractional weight loss due to pure corrosion ranged from 1% to 10% while that due to corrosion-induced erosion ranged from 16% to 90%.

Neville, Hodgkiess, et. al. [43], conducted an experiment on the synergy between the solid particle erosion-corrosion behaviour of engineering steels for marine pumping applications. They conducted a series of electromechanically based erosion tests under high-velocity ( $100 \text{ m s}^{-1}$ ) liquid impingement of 3.5% NaCl solution, and liquid-solid slurry impingement comprising of 3.5% NaCl and 1000 ppm cast silica sand flowing at  $25 \text{ m s}^{-1}$ . The materials used were C-Mn steel, UNS S31603 stainless steel and 2205 duplex stainless steel. The angle of impingement was  $90^\circ$ , whereas the temperature was kept constant at  $50^\circ\text{C}$  in both cases. They concluded that corrosion had a significant effect on the material under the combined synergistic erosion-corrosion process. It was also found that increasing hardness yielded a lower total mass loss. However, these hardness correlations were not apparent when corrosion was under consideration.

In a study conducted by Bello, Wood and Wharton [34] on UNS S30403, S31603 and S32760 stainless steel, they attempted to evaluate the synergistic effects of micro-abrasion-corrosion using three approaches. They used two-body, mixed and three-body abrasion methods. They used SiC abrasives (with a mean particle size of  $4.5 \mu\text{m}$ ) in slurry. The slurries used were distilled water based for pure abrasion, and 3.5% NaCl solution based for abrasion-corrosion tests. The erosion test was conducted with a 22 mm diameter alumina ball in the micro-abrasion apparatus. The synergy resulting from a two-body wear mode was highly variable with a large degree of scatter. UNS S31603 and S32760 stainless steel gave negative synergy for two-body abrasion, while a positive synergy was seen for mixed and three-body abrasion. For S32760 stainless steel this result was attributed to its repassivation kinetics and/or the presence of a passive film. However, when the higher wear rate were reached, the film was ruptured or removed, leading to increase in the synergy. For S30403, only positive synergies were reported, attributing it to weak repassivation/passive oxide film structure.

The initial aim mainly was to study the quantification and sensitivity of synergism and antagonism between mechanical and electrochemical processes for air-filmed as-cast NAB.

Several variables and factors rendered accurate quantification of T, E and C difficult. And hence, the aim of the study was to perform different test methods in order to find the most reliable combination to obtain synergism found between erosion and corrosion for the test material. Furthermore, synergy is also highly dependent on the microstructure of the material, the environment, and the duration exposure, hence spatial and temporal aspects of Tribocorrosion testing must be considered. The cavitation experiments were conducted by means of an indirect ultrasonic vibratory system as presented in Ref [44] at room temperature.

## 2. Material and methodology

### 2.1 Test material

The test material used for the research was cast NAB C95800 (without heat treatment). The empirical composition of the cast NAB used is Cu-Al-Fe-Ni, with a nominal composition of 10% aluminium, 5% nickel and 5% iron. The alloy's property comes from a very complex network of microstructures. It generally consists of columnar grains of face centred cubic (FCC) copper-rich solid solution known as  $\alpha$ -phase and a small volume fraction of  $\beta$ -phase or retained martensitic  $\beta'$ -phase, surrounded by a series of intermetallic Fe-rich kappa phases [14], [16], [44]–[46].

Among the intermetallic compounds,  $\kappa_I$  phase is rosette shaped precipitate formed at high temperatures in high Fe-content alloys and hence, is the coarsest among them ranging from 5  $\mu\text{m}$  – 10  $\mu\text{m}$  in diameter,  $\kappa_{II}$  phase is smaller than  $\kappa_I$  phase and form a dendritic rosette shape which is distributed mostly at the  $\alpha/\beta$  boundaries, ranging from 1  $\mu\text{m}$  – 2  $\mu\text{m}$  in diameter, and  $\kappa_{IV}$  phase is a fine Fe rich precipitation of varying sizes (<0.5  $\mu\text{m}$  in diameter) with plate-like morphology that are distributed throughout the  $\alpha$  grains along certain crystallographic directions forming within the  $\alpha$ -matrix at 850°C.  $\kappa_{III}$  phase is a fine lamellar “finger-like” eutectoid structure and forms at the boundary of  $\kappa_I$  phase [14], [44], [45], [47], [48].

The mechanical properties of the test samples used for the study are summarised in table 1.

Ultimate tensile strength	Yield strength	Density	Hardness
650 MPa	270 MPa	7.65 g cm <sup>-3</sup>	160 HB

**Table 1:** Mechanical properties of C95800 NAB

The general corrosion rate of NAB in seawater is considered to be 0.06 mm year<sup>-1</sup> [13]. The galvanic potentials of NAB in flowing salt water is between -0.1 V to -0.25 V at a velocity of 2.5 to 4 m s<sup>-1</sup> at a temperature range of 10 °C – 27 °C with reference to saturated calomel half-cell -0.15 V to -0.22 V [49]–[51].

### 2.2 Experimental procedure

Six samples of as-cast NAB were prepared for the experiments. Each sample had a dimension of 25 mm x 25 mm ( $\pm 2$  mm) with a thickness of 5 mm ( $\pm 0.5$  mm). The test sample surfaces facing the cavitation rig were wet polished using 120-

800-, 1200- and 4000-grit silicon carbide (SiC) abrasive papers, and 6  $\mu\text{m}$  diamond paste. They were then cleaned with distilled water and methanol before blow-drying them. The surfaces away from the sonotrode tip were coated with lacquer for protection against exposure to corrosion. The samples were left inside six individual, clean and uncontaminated plastic bags for a week to ensure the formation of air-formed oxide films. The preparation procedure was repeated for each sample after each test in order to reuse the samples.

The test samples were tested using the experimental conditions and procedure as given in previous work conducted, found in Ref [44] using indirect ultrasonic vibratory transducer operating at a frequency of 19.5 kHz and an amplitude of  $80\ \mu\text{m} \pm 0.2\ \mu\text{m}$  (peak-to-peak). The ultrasonic vibratory apparatus was used for the research as it is the most commonly used device that produces a periodic pressure field, inducing the periodic growth and collapse of a cloud of cavitation bubbles [54]. The ultrasonic vibration mechanism also provides the fastest approach to obtaining cavitation results for a wide range of engineering materials amongst all the various cavitation test methods [55]. The indirect cavitation method was chosen in order to conduct in-situ electrochemical analysis. The time period for each test was 1 h, except the polarization test, in fresh batch of mediums. The standoff distance between the sample and the ultrasonic transducer was kept constant at 2 mm. The temperature and the pH of the water were monitored to remain constant for each test at room temperature of  $17\ ^\circ\text{C} \pm 0.5\ ^\circ\text{C}$  and a pH range of 7.5 - 8.5. Figure 1 gives the schematics of the test arrangement.

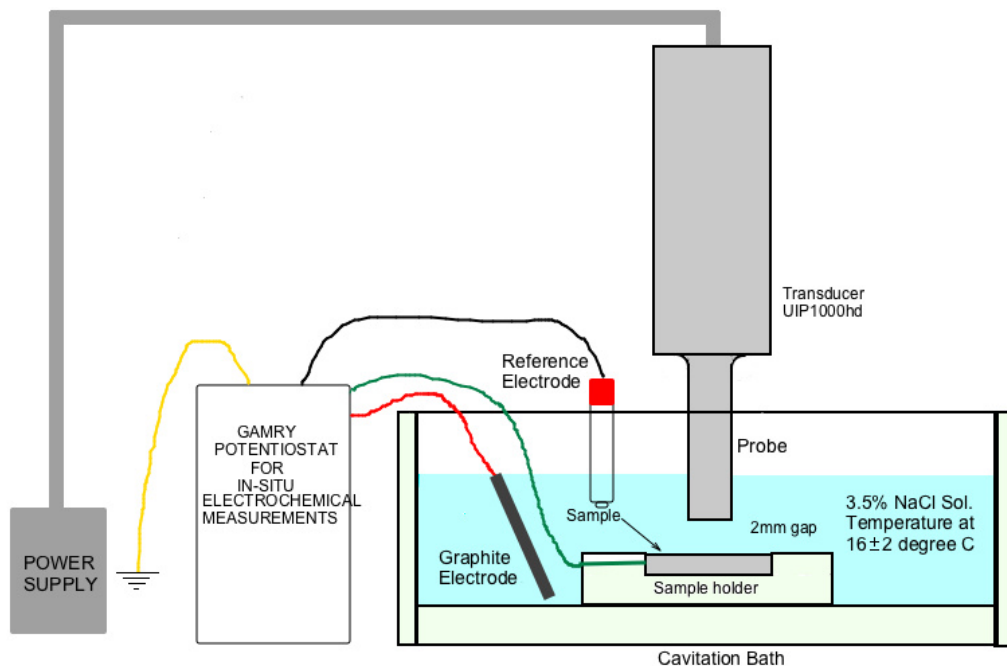


**Fig. 1:** Schematics of the cavitation rig with specimen connected to the potentiostat for cavitation erosion-corrosion measurements [44].

The synergy measurement was obtained using three main approaches, namely the gravimetric mass loss method, the volumetric mass loss method, and mean depth of penetration rate (MDPR) method. Under the gravimetric method, the erosion rates (E) were obtained in two different ways: by erosion in 5 L of distilled water for 1 h, and by subjecting the samples to cavitation erosion in 3.5% NaCl solution with cathodic protection for 1 h. The corrosion rates (C) were also obtained in two different ways, gravimetrically by using mass balance, and from the potentiodynamic polarization curves. Alicona InfiniteFocus 3D non-contact optical profilometer was used to obtain the synergy value using the MDPR method, and the volumetric mass loss method. Alicona was also employed to obtain surface topography and roughness measurements at a vertical resolution of 10 nm – 50 nm.

For the electrochemical tests the samples were kept at OCP using the GAMRY Ref600 potentiostat while their EIS values were monitored. The EIS frequencies used were between 100000 (initial) Hz - 0.1 (final) Hz. The samples were used as the working electrodes, with Ag/AgCl as the reference electrode and graphite rod as the counter electrode. The parameters for conducting the OCP and EIS tests were set and performed in the GAMRY Framework software. The samples were tested under C and T conditions 3 times each. The data obtained were analysed in the GAMRY Echem Analyst software. For the polarization test, two samples were subjected to potentiodynamic polarization scan at a scan rate  $0.167 \text{ mV s}^{-1}$  under static conditions in 3.5% NaCl solution in order to obtain pure corrosion rate in terms of mass loss by applying Faraday's laws of electrolysis. The potential of -400 mV against silver chloride electrode (Ag/AgCl) was also obtained from the polarization curve for the pure erosion test in 3.5% NaCl solution subjected to cathodic protection.

For the synergy evaluation, five different synergy values were calculated for the samples. Using Equation (1), three tests were conducted for each sample in order to obtain the synergy rates.

- Pure erosion (E): Two different methods were employed for the pure erosion test. Three samples were subjected to erosion performed in 5 L of triple distilled water for 1 h. And three samples were subjected to cavitation erosion in 3.5% NaCl solution with cathodic protection for 1 h.
- Pure corrosion (C): Four samples were subjected to in-situ electrochemical measurements kept at open circuit potential (OCP), and electrochemical impedances spectroscopy (EIS) analysis were conducted in 3.5% NaCl solution for 1 h. Two sample materials were also subjected to potentiodynamic polarization, at a potential range between -1 V to 2 V, to obtain C by applying Faradaic conversion.

- Combined cavitation erosion-corrosion (T): all six samples were cavitated in 5 L of 3.5% NaCl solution for 1 h while subjected to OCP.

The masses of the samples were recorded before and after each experiment with a precision mass balance for gravimetric analyses ( $\pm 0.01$  mg). Each sample was weighed 5 times, each after recalibration of the balance after every measurement, and an average was considered per test. The samples were analysed for microstructural characterization using JOEL (JSM6500F) scanning electron microscope (SEM) employed for microstructural morphology analysis before and after cavitation at an acceleration voltage of 15.0 kV, a probe current at medium (6 nA – 13 nA), and a working distance of 10 mm and above. For clearer microstructural evaluation backscattered electron imaging was also employed. Samples were also transverse sectioned to observe the subsurface impacts of cavitation on the microstructure. For SEM analysis of the transverse sections, the samples were cut laterally with diamond saw, and then hot-mounted in Bakelite resin mould. The interested surface was then polished using 1200- and 4000- grit SiC abrasive paper before mirror finishing it with 1 and 6  $\mu\text{m}$  diamond paste.

### 3. Results and discussion

Table 2 gives the chemical composition in weight %, for the alloy as well as the individual phases obtained under EDS.

Micro-structural Phases	Chemical composition in weight %					
	Cu	Si	Al	Mn	Fe	Ni
Alloy	80.25	0.03	8.79	3.56	4.63	5.10
Alpha	85.39	-	7.19	0.87	3.35	3.20
Kappa 1	15.08	1.66	13.29	1.72	57.53	10.72
Kappa 2	17.61	1.52	14.02	1.50	51.90	13.44
Kappa 3	45.15	-	18.76	1.19	10.91	23.99
Kappa 4	3.10	4.01	10.99	2.05	72.80	7.05

**Table 2:** Chemical composition of the individual phases in the as-cast NAB (C95800) samples, confirmed under EDS.

#### 3.1 Surface analysis

Cavitation erosion damage undergoes several periods of activity. To understand the gradual mass loss rate and the erosion behaviour of each materials, the

material erosion wear rate is typically analysed by conducting cavitation on the samples over a period of time, with periodic mass loss measurements at each interval. Hence, the erosion wear rate curve for as-cast NAB sample, represented in Figure 2 shows the cumulative erosion rate, plotted as a function of erosion time, obtained after each exposure by dividing cumulative weight loss by total exposure time.

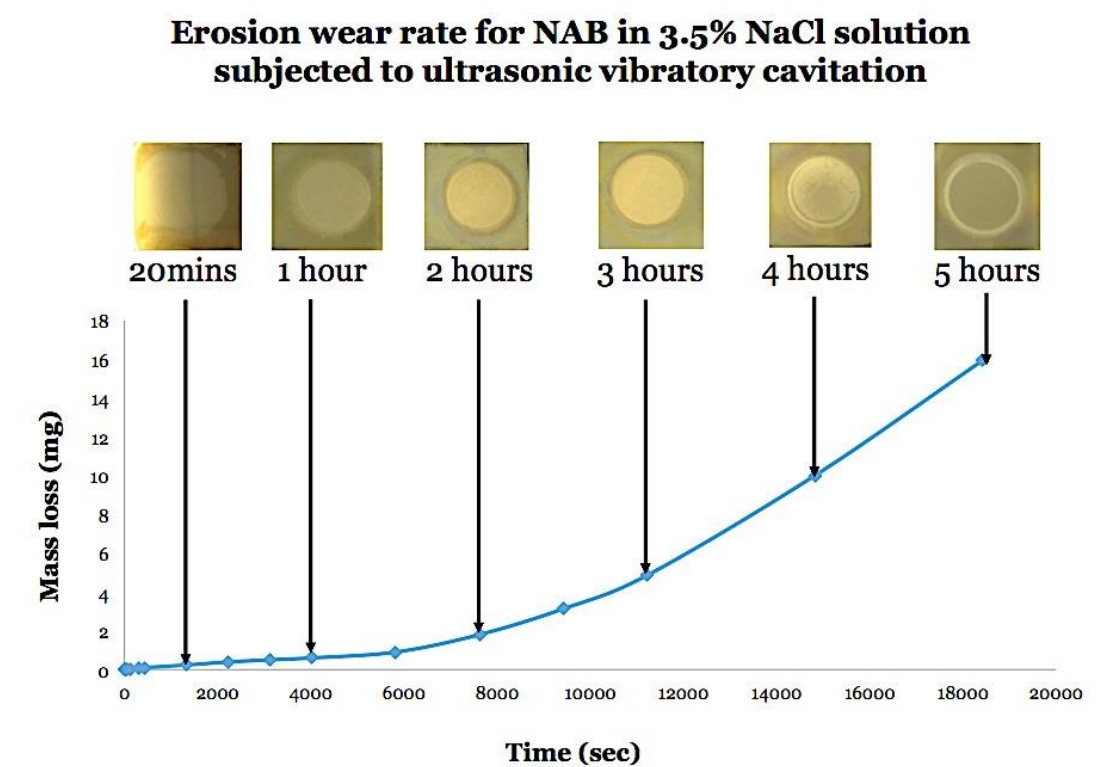


**Fig. 2:** Cumulative cavitation erosion rate curve for NAB tested in 3.5% NaCl solution for a time period of 5 h and 14 min.

Figure 3 shows the optical image of a NAB sample after 1 week of air-formed oxide film formation, with distinct microstructures, before subjecting to cavitation in 3.5% NaCl solution.



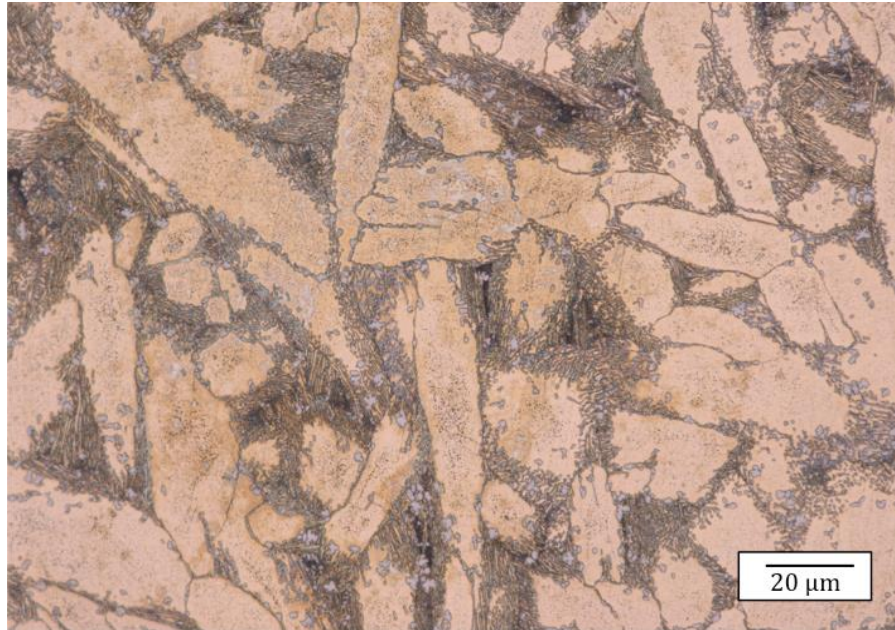


**Fig. 3:** Microstructure of air-formed oxide filmed NAB before cavitation as seen under the optical microscope.

Figures 4 (a)-(f) show the optical images of air-formed oxide filmed NAB surface under cavitation in 3.5% NaCl solution over time, taken from the centre of the erosion scar. First, the removal of oxide layer from around the phase boundaries was observed (Figure 4 (a)) in the form of light brown oxide layer islands found in the alpha region, after 30 min of cavitation in 3.5% NaCl solution. After 1 h of cavitation, (Figure 4 (b)), the microstructure seemed to undergo cavitation erosion as well as selective phase attack at the phase boundaries.

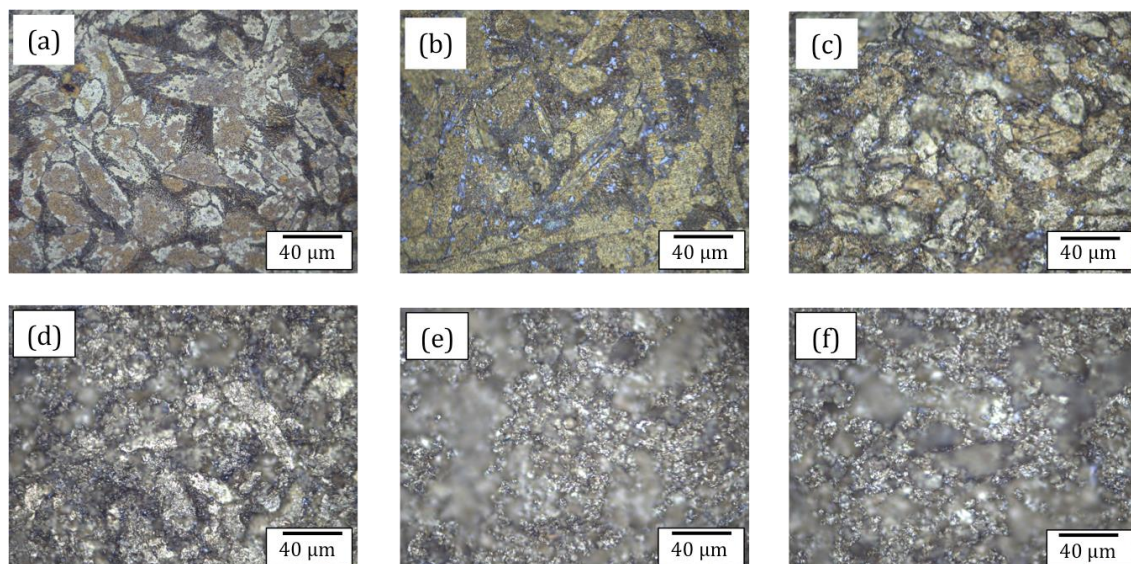


**Fig 5:** Optical images of the progression of cavities on air-formed oxide filmed NAB after cavitation erosion for (a) 30-min, (b) 1 h, (c) 2 h, (d) 3 h, (e) 4 h, and (f) 5 h in 3.5% NaCl solution, showing the increasing roughness of the surface, and growth in cavity sizes with time.



On further cavitation, the cavities seemed to gradually grow in size from 10- $\mu\text{m}$  (Figure 4 (c)) to up to 80- $\mu\text{m}$  (Figure 4 (f)), while the overall surface roughness also seemed to increase over time after 2, 3, 4 and 5 h of cavitation (Figure 4 (c)-(f)). The number of cavities also increased after 5 h of cavitation, as seen in Figure 4 (f).

The cavitated surface of the test sample appeared to comprise of three easily distinguishable damage regions, formed in concentric rings of cavitated and non-cavitated regions around a centrally damaged area as seen in Figure 5. The surface topography was then obtained by scanning the sample surface laterally across the diameter.

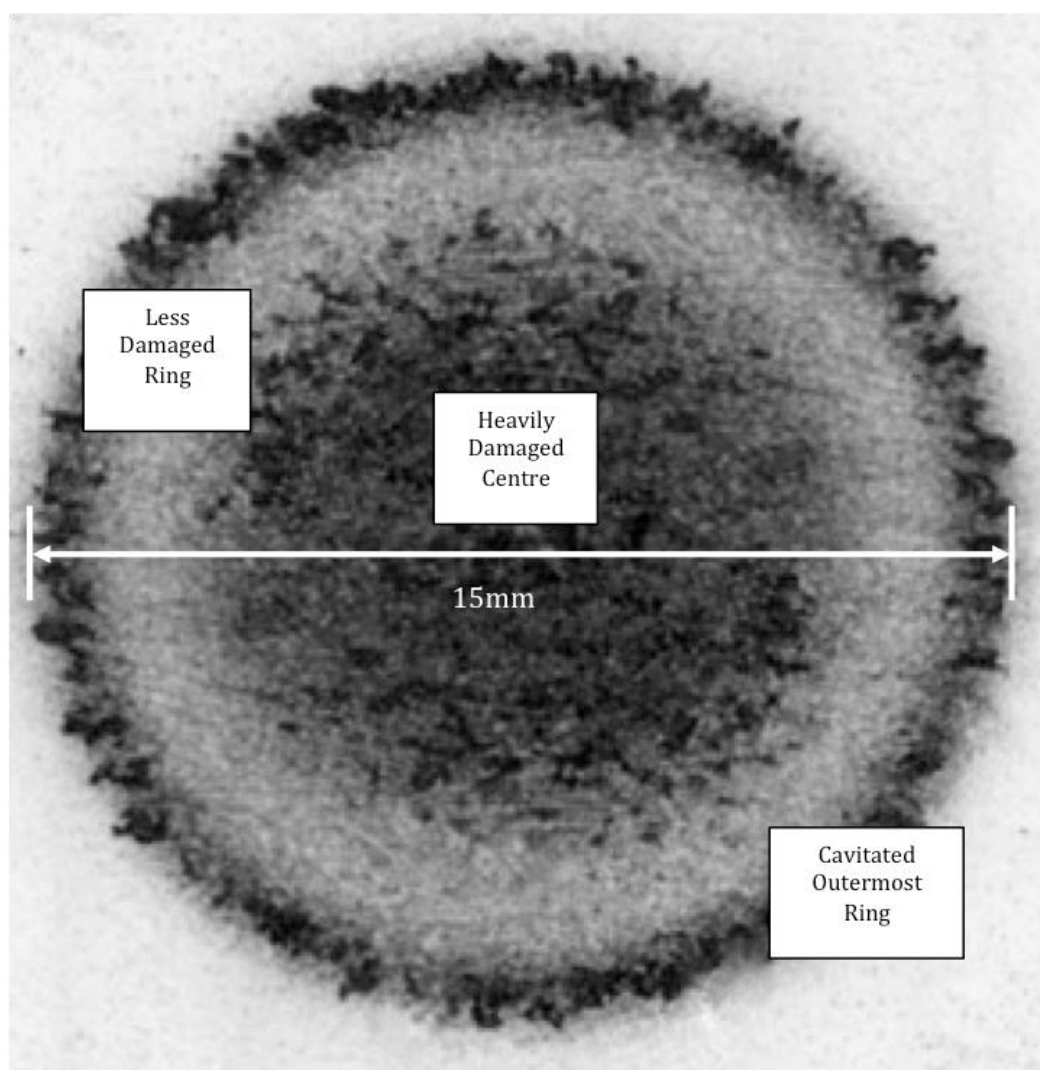


**Fig. 5:** Surface profile at the centre of the cavitated surface of NAB after 1 h of test measured in Alicona.

From the scanned topography profile it was clearly seen that the outer ring undergoes more material loss than the centre with higher surface roughness at the edge of the eroded region. Figures 6 (a) and (b) show the wear profile of air-

formed oxide filmed NAB sample cavitated for 1 h in distilled water, and in 3.5% NaCl solution, respectively.

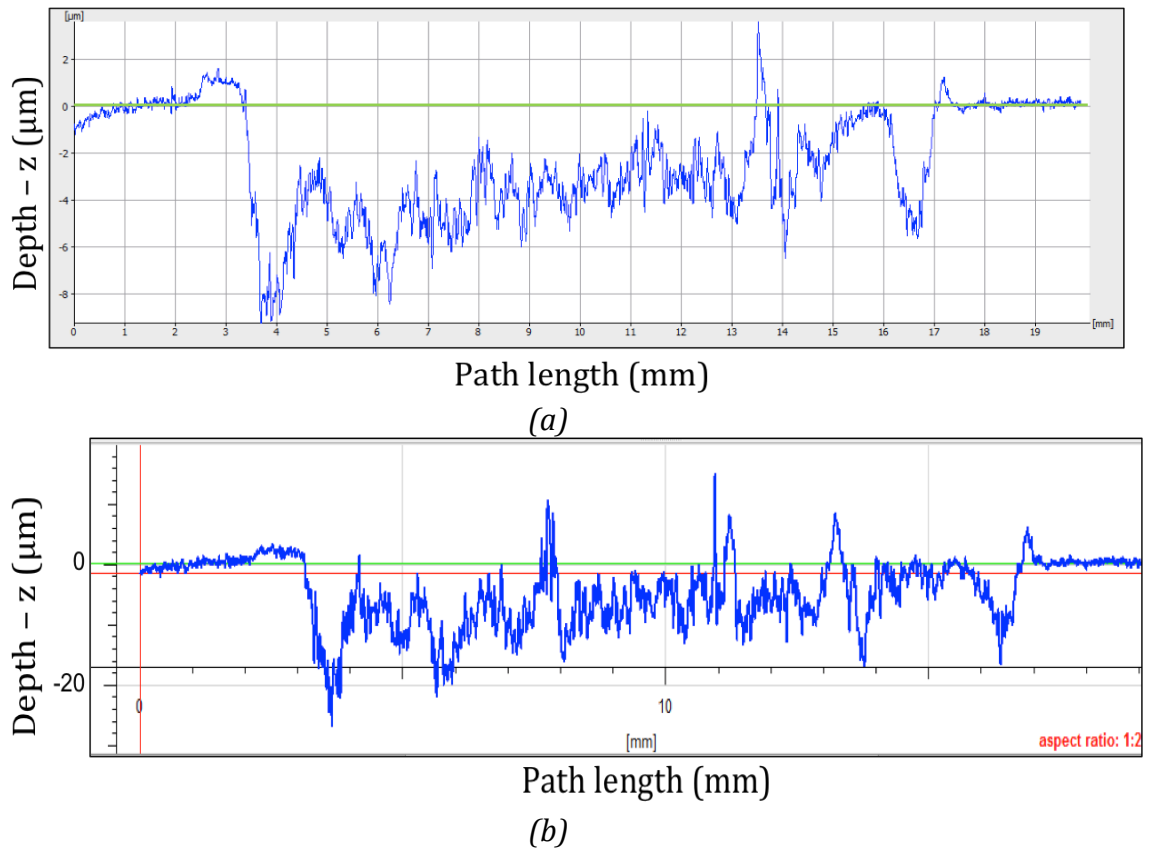


**Fig. 6:** Wear scar profile of air-formed oxide filmed NAB after cavitation in (a) distilled water, and (b) in 3.5% NaCl solution for 1 h, obtained using Alicona 3D profilometer.

The wear profile of the air-formed oxide filmed NAB cavitated in 3.5% NaCl solution (Figure 5 (b)) exhibited much higher erosion profile (almost double), compared to the profile obtained in distilled water (Figure 5 (a)).

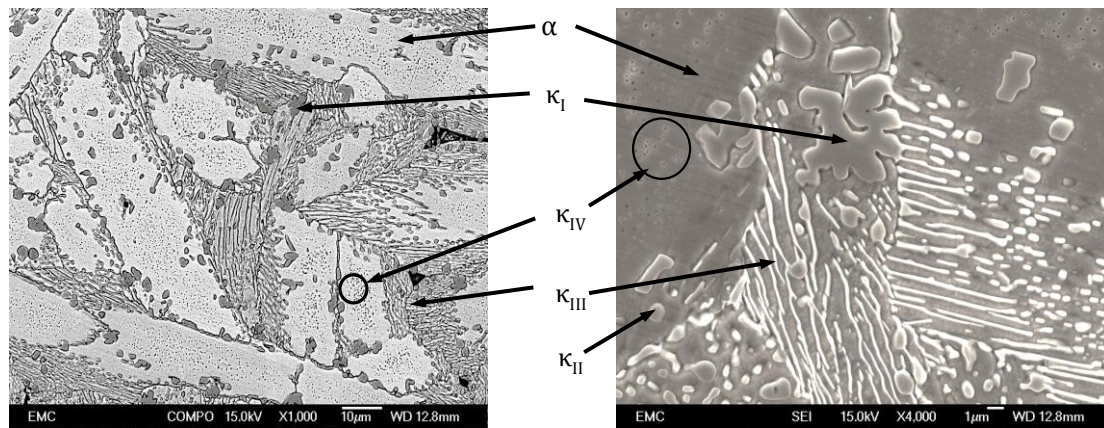
After conducting the cavitation tests on the samples, the surface profilometry and  $R_a$ , mean depth of penetration (MDP) and the volume loss were measured using both Alicona. Table 2 tabulates the measured values of  $R_a$  before cavitation, in distilled water and in 3.5% NaCl solution with and without cathodic protection. Whereas, the MDP and the volume loss were measured for the samples cavitated in distilled water for pure erosion, and the combined erosion-corrosion test in 3.5% NaCl solution.

Average surface roughness, $R_a$ (in $\mu\text{m}$ )				Mean depth of penetration, MDP (in $\mu\text{m}$ )		Measured volume loss (in $\text{mm}^3$ )	
Before cavitation	Distilled water	3.5% NaCl sol. With CP	3.5% NaCl sol.	Distilled water	3.5% NaCl sol.	Distilled water	3.5% NaCl sol.
0.063 $\pm 0.003$	0.153 $\pm 0.003$	0.160 $\pm 0.003$	0.165 $\pm 0.003$	0.645 $\pm 0.003$	0.955 $\pm 0.003$	0.115 $\pm 0.003$	0.169 $\pm 0.003$

**Table 3:** Average roughness, mean depth of penetration and volume loss measured under pure erosion and combined erosion-corrosion test conditions using Alicona.

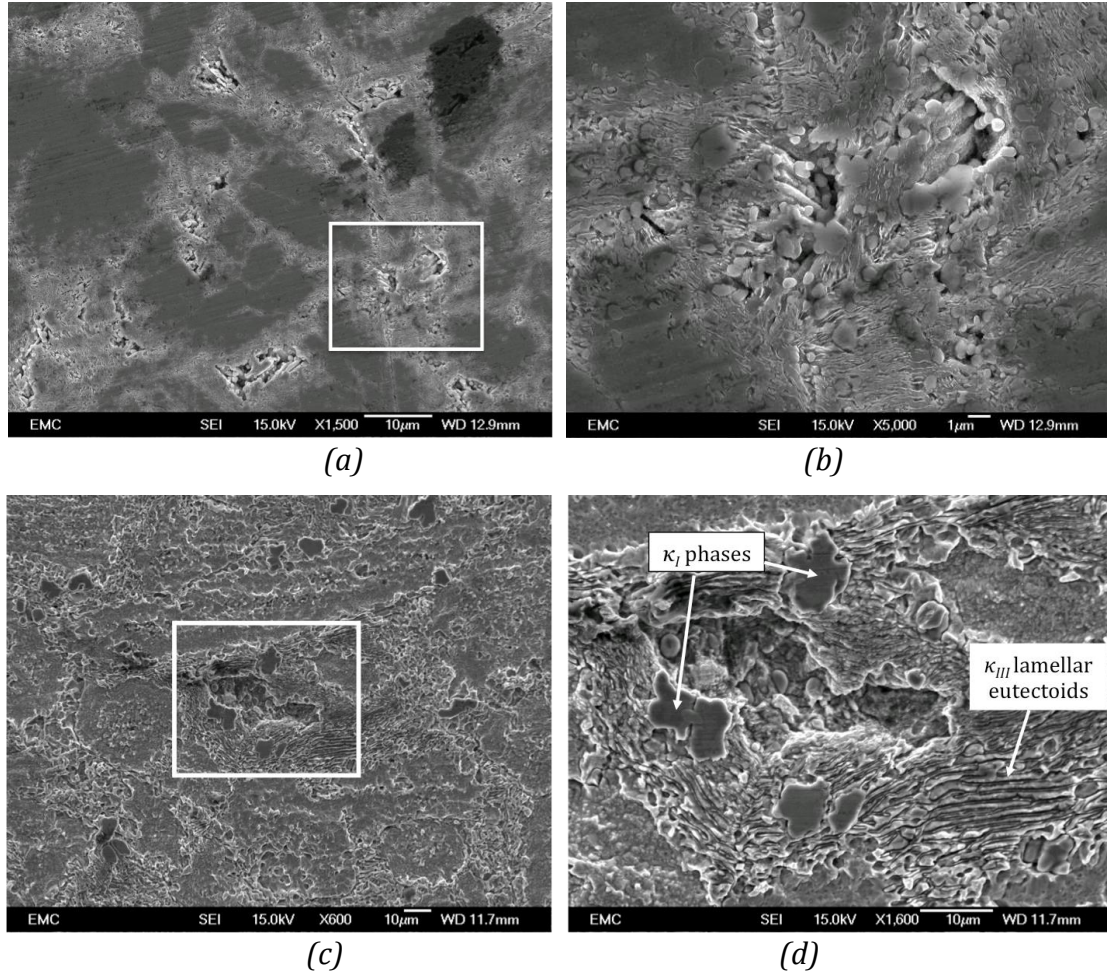
### 3.2 Microstructural analysis

Figure 7 shows the general microstructural morphology of the as-cast NAB C95800 used for the experimental study, taken under SEM.



**Fig. 7:** Microstructural morphology of as-cast NAB.  $\kappa_I$  is the globular dendritic structure,  $\kappa_{III}$  is the lamellar “finger-like” structure, and  $\kappa_{IV}$  is the very fine particulate imbedded within the  $\alpha$  matrix.

The samples were observed under the SEM for microstructural analysis before and after each test. Figure 8 (a) and (b) show the magnified images of the microstructures of a cavitation-eroded region for NAB tested in distilled water for 1 h. And Figure 8 (c) and (d) depict the microstructures of a cavitation-eroded region for NAB cavitated for 1 h in 3.5% NaCl solution.



**Fig. 8:** SEM compo/backscattered images of (a) small boundary erosion on air-formed filmed NAB in distilled water; (b) shows the magnified image of the cavities of size 10-μm at the selected area in (a); (c) SEM image of a 50-μm large cavity on the sample surface undergone cavitation erosion-corrosion in 3.5% NaCl solution; and (d) the magnified image of a cavity in (c) showing selective phase attack at the  $\alpha$ - $\kappa$  phase boundaries leaving  $\kappa_I$  globules and  $\kappa_{III}$  lamellar phases exposed.

For the cavitation erosion-corrosion test in distilled water, small cavities of sizes 10 μm – 30 μm were found in the grain boundaries as shown in Figure 8(b). This was considered to be due to the soft  $\alpha$ -matrix surrounding the hard iron-rich  $\kappa$  phases being most vulnerable to cavitation attack. The  $\kappa$ -precipitates and precipitate-free  $\alpha$ -zones did not suffer any visible cavitation after 1 h of cavitation test in distilled water, as also reported in ref [44].

Comparatively, the cavitation erosion-corrosion test in 3.5% NaCl solution exhibited much larger cavities ranging between 50 μm – 80 μm. This again proved that NAB underwent selective phase attack at the  $\alpha$ - $\kappa$  phase boundaries, although more aggressively than under distilled water, leaving  $\kappa_I$  globules and  $\kappa_{III}$  lamellar phases exposed, Figure 8 (c).



Figure 9 (a) and (b) show the transverse cavitation erosion pattern on the surface after 1 h of testing in distilled water, detailing a cavity formed due to the erosion of the  $\alpha$ -phase at the  $\alpha$ - $\kappa$  phase boundary. Enlarged image of the transverse sections of the cavities show cavity growth and crack propagation along the  $\alpha$ - $\kappa_{III}$  phase boundaries (Figure 9 (b)).

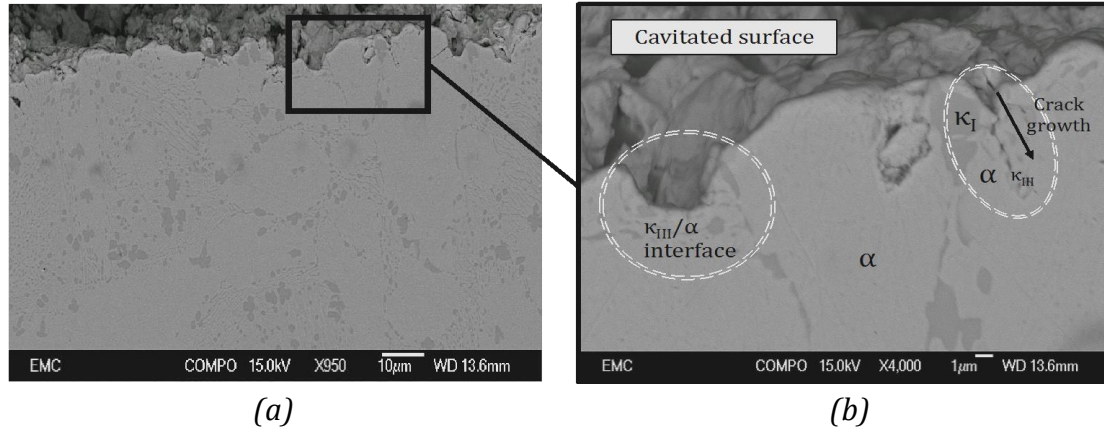


**Fig. 9:** SEM images of NAB sample under pure E (distilled water) conditions: (a) transverse-sections of a cavity; (b) detailed magnified image of cavities in (a), exhibiting crack propagation along the  $\alpha$ - $\kappa_{III}$  phase boundaries.

SEM imaging of the transverse sections of the cavitated NAB surface under 3.5% NaCl solution revealed the selective phase erosion leading to micro-crack propagation into the material across the  $\alpha$ - $\kappa$  interface. From the SEM results, it can be concluded that the material undergoes enhanced erosion in the presence of corrosion, i.e.  $\Delta E$  has a higher contribution to the synergistic relation between wear and corrosion.

From the intrinsic microstructural results obtained, it was evident that the microstructural properties of the material, as well as the individual properties of each phase within the microstructure, played very important role in determining the cavitation behaviour of the materials. The sizes on these microstructural phases also played significant role, as it was seen that more the grain boundaries, more the material was vulnerable to boundary erosion and selective phase attacks. Softer phases surrounding the harder intermetallics were seen to undergo erosion more, due to the accumulation of subsurface strain caused by the repetitive hammering of imploding bubbles, and lower fracture toughness of the softer phase.

### 3.3 Electrochemical analysis

Four samples were subjected to pure corrosion test under OCP, and three samples were subjected to combined erosion-corrosion test kept at OCP. Figure 10 is the OCP curve obtained for NAB in pure corrosion and erosion-corrosion in

3.5% NaCl solution, where  $V_f$  is the reference potentials in millivolt. It can be seen NAB reached stability at -210 mV under pure corrosion. For the combined erosion-corrosion tests, the cavitation was applied to the sample kept under OCP after a delay of about 600 s [44].

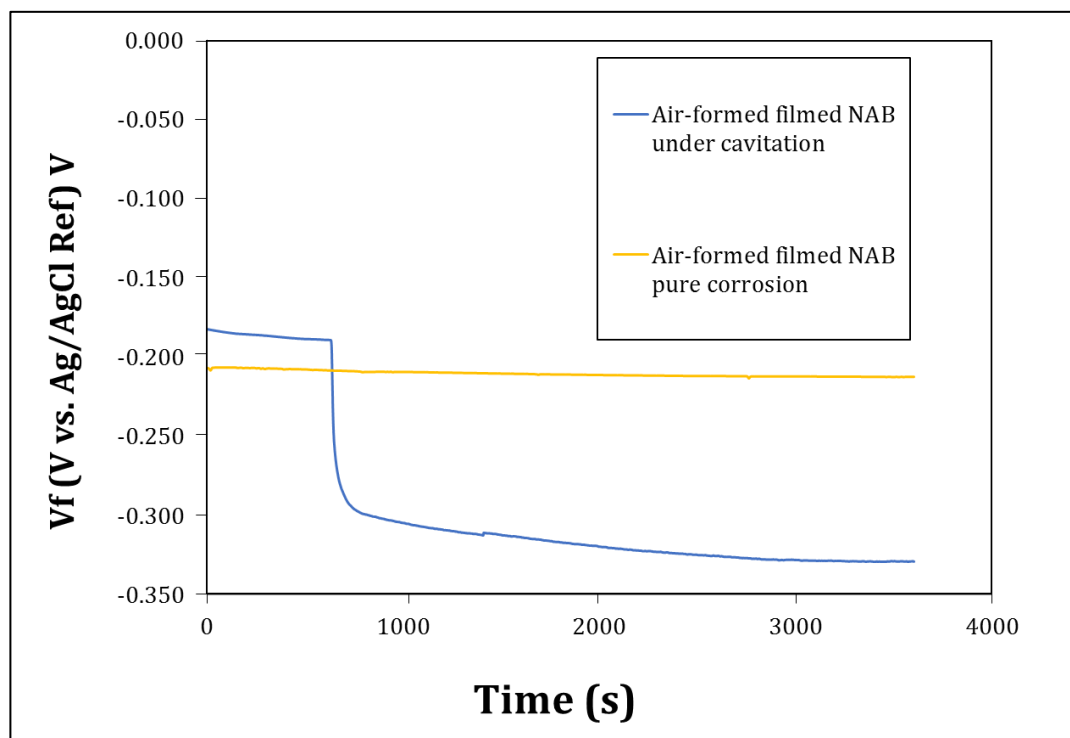


**Fig. 10:** OCP for NAB in 3.5% NaCl solution for 1 h with and without cavitation [44].

It can be seen that under pure corrosion, the measured OCP shift slightly negatively at around -210 mV. This indicates that the thin layer of air-formed protective oxide film on NAB can be slowly broken down due to localized corrosion, causing selective phase attack, during its immersion in the 3.5% NaCl solution. However, there is a dramatic negative shift in OCP upon cavitation impact. As seen from Figure 8, the OCP shifted from -170 mV to about -300 mV upon the application of cavitation, but attained stability within 150 s at a lower potential (of -310 mV). It is noteworthy that under cavitation impact the OCP very gradually shifted towards more negative value with time, meaning gradual depassivation of the surface over time.

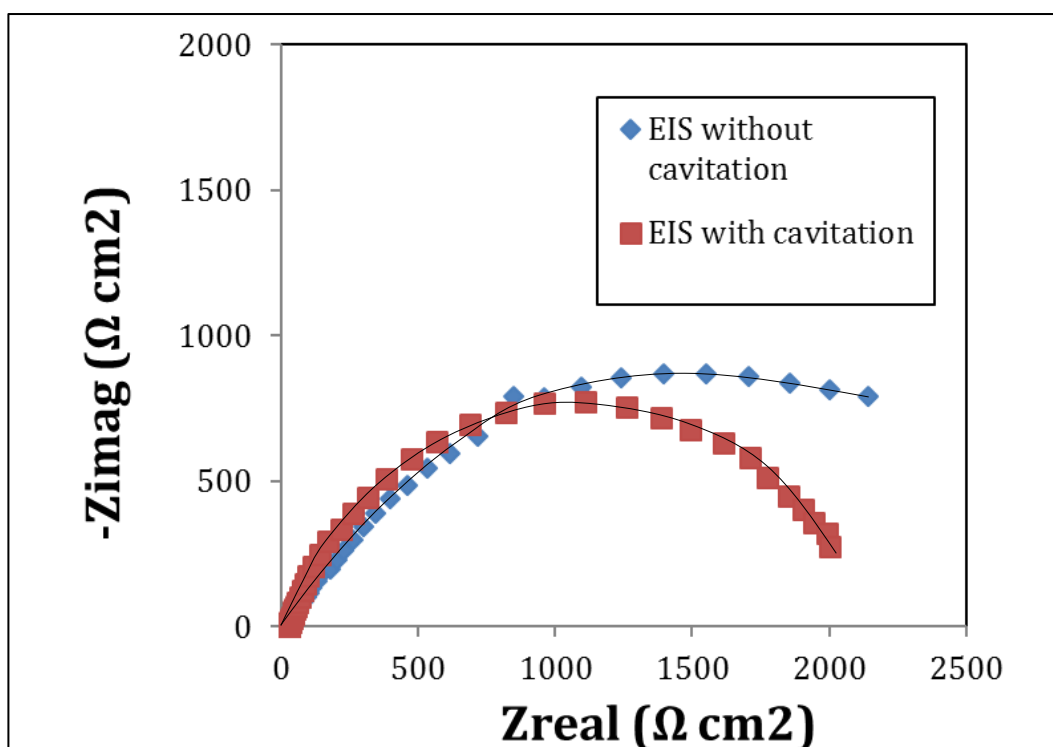


**Fig. 11:** Nyquist plots for NAB samples in 3.5% NaCl solution with and without cavitation.

Figure 11 is the Nyquist curves for the NAB samples undergoing pure corrosion and combined erosion-corrosion test. It can be clearly seen that the material exhibited single time-constant plots with single semi-circles and did not undergo diffusion, either under pure corrosion or cavitation erosion-corrosion tests. The radius of semi-circle is relevant to polarization resistance, where the larger the semicircle is, the higher the polarization resistance. From Figure 12 it can be seen that the polarization resistance is significantly decreased with cavitation with much smaller semicircles, which indicate the polarization resistance.

Figure 12 shows the EIS Bode plots for the NAB samples under pure corrosion and during cavitation. It can be seen that the EIS spectra in both cases exhibit single time-constant behaviour in the investigated frequency range. It was seen that the impedance of NAB under corrosion was slightly lower than that under cavitation erosion-corrosion.

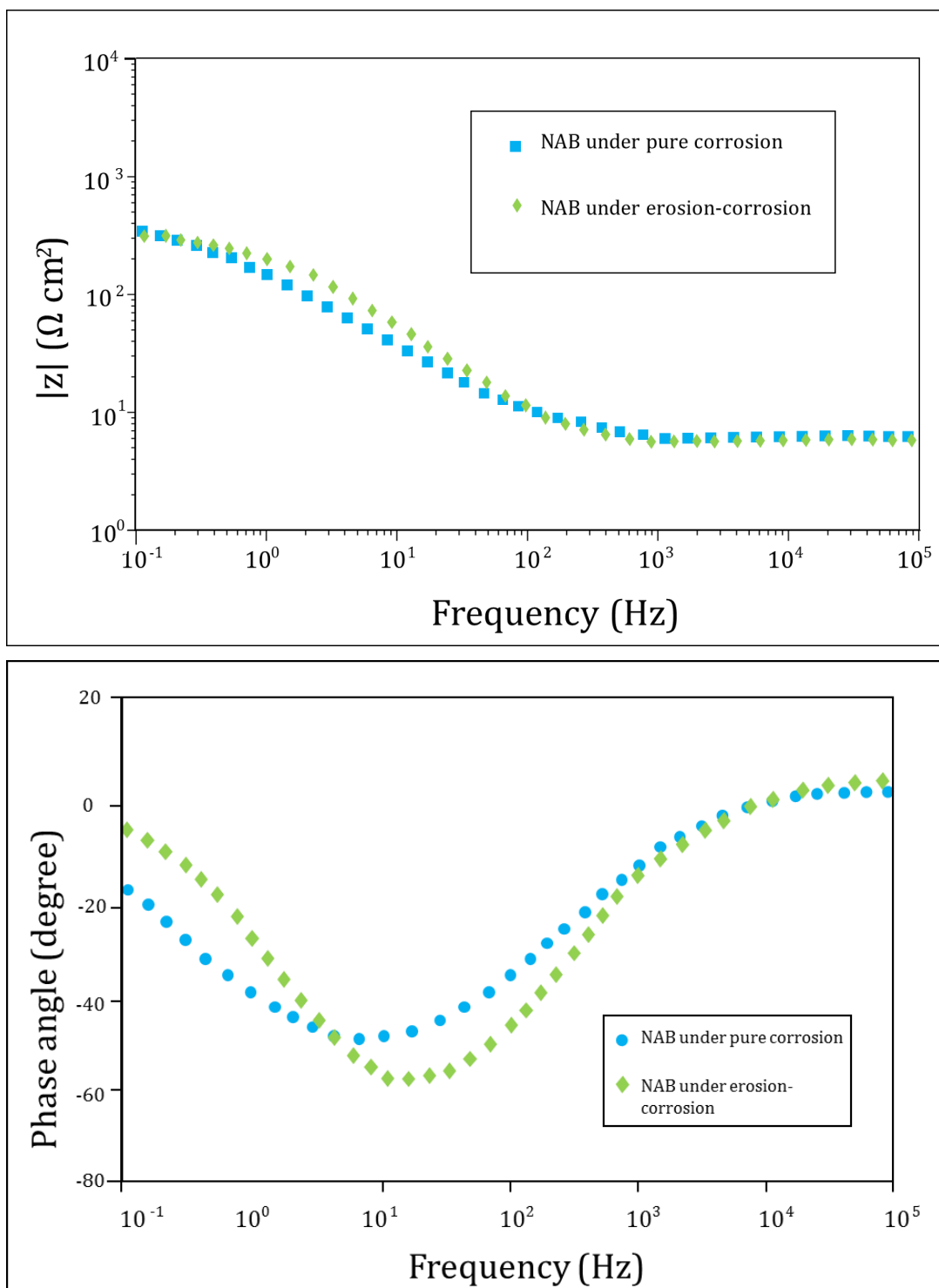


**Fig. 12:** EIS Bode curve for NAB in 3.5% NaCl solution under pure corrosion and during 1 h of cavitation.

The EIS results obtained were also verified using fit models. Fit models or equivalent circuit models are used to model and analyse EIS spectra results that can be built in the GAMRY Instrument Echem Analyst software. The electrochemical cells are simulated in the software by incorporating various factors such as electrode double layer capacitance, electrode kinetics, diffusion



layer and solution resistance. The impedance of the element depends on the element type and the values of the parameters that characterize that element. The protective oxide layer on NAB subjected to cavitation may become porous. These pores could be considered as non-coated portions of substrate. However, due to their small size, the exchange of the electrolyte between the pore and the bulk material may be hampered, therefore, the ion concentration inside the pores could differ from the bulk concentration. This results in an electrolyte resistance  $R_{\text{pore}}$  different from the bulk electrolyte (solution) resistance,  $R_s$ . For NAB, the protective oxide layer is considered to be a mixed Cu/Al oxide, mostly assumed to be  $\text{Al}_2\text{O}_3$ , which is a non-conductive ceramics, hence, considering there is no electron passing through this layer, it is modelled using only one capacitance,  $C_{\text{pl}}$ . Then the interface between the solution and the material substrate through the pore needs to be considered, hence the model incorporates the resistance of the inner substrate layer,  $R_{\text{inner}}$ , and the constant phase element,  $C_{\text{inner}}$ , parallel with  $R_{\text{inner}}$ .

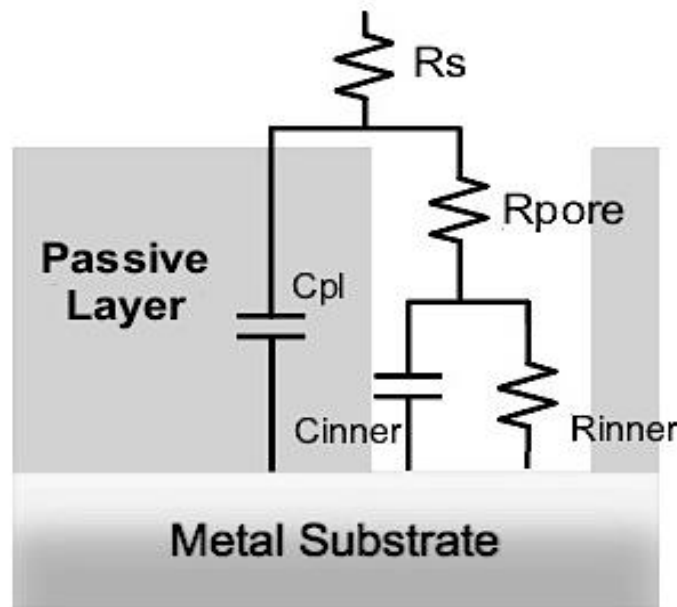


**Fig. 13:** A porous non-conductive coating layer with the resulting equivalent circuit.

Figure 13 gives the respective equivalent circuit that incorporated the pores in the passive layer on the material surface where,  $R_s$  is the bulk solution resistance,  $R_{\text{pore}}$  is the resistance of the pores,  $C_{\text{pl}}$  is the capacitance of the passive layer, and  $R_{\text{inner}}$  and  $C_{\text{inner}}$  are the resistance and constant phase element of the metallic substrate under the passive layer. From the fit model illustrated in Figure 14, the resistance elements at the pores and the inner layer were compared for the results obtained from EIS test for NAB plotted in Figure 12.

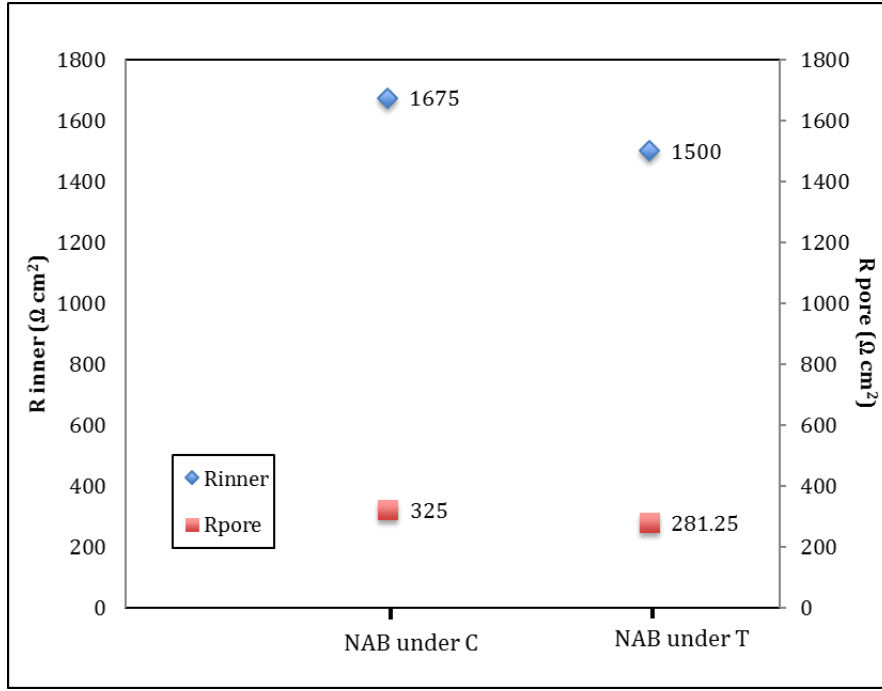


**Fig. 14:** EIS fit plot for NAB under C and T conditions.

From Figure 14 it can be seen that for NAB the substrate resistance ( $R_{\text{inner}}$ ) is higher than the pore resistance ( $R_{\text{pore}}$ ) in both cases. The substrate and pore resistance of NAB subjected to C was higher than that obtained under T. This can be due to an increase in pore sizes or numbers induced under cavitation, enhancing mass transport, causing the decrease in the  $R_{\text{inner}}$  and the  $R_{\text{pore}}$  value. However, the values do not differ by a large margin, which could be due to the surface undergoing rapid passivation process even though under the cavitation impact, causing the corrosion process to slow down.

Figure 15 plots the polarization curves for NAB. The potential of -400 mV against silver chloride electrode (Ag/AgCl) was also obtained from the polarization curve for the pure erosion test in 3.5% NaCl solution subjected to cathodic protection.

The sample materials were expected to undergo rapid redox reactions as shown from Equations (3) - (6) taking place in the electrochemical cell [16].

Anodic reaction:



And cathodic reaction:



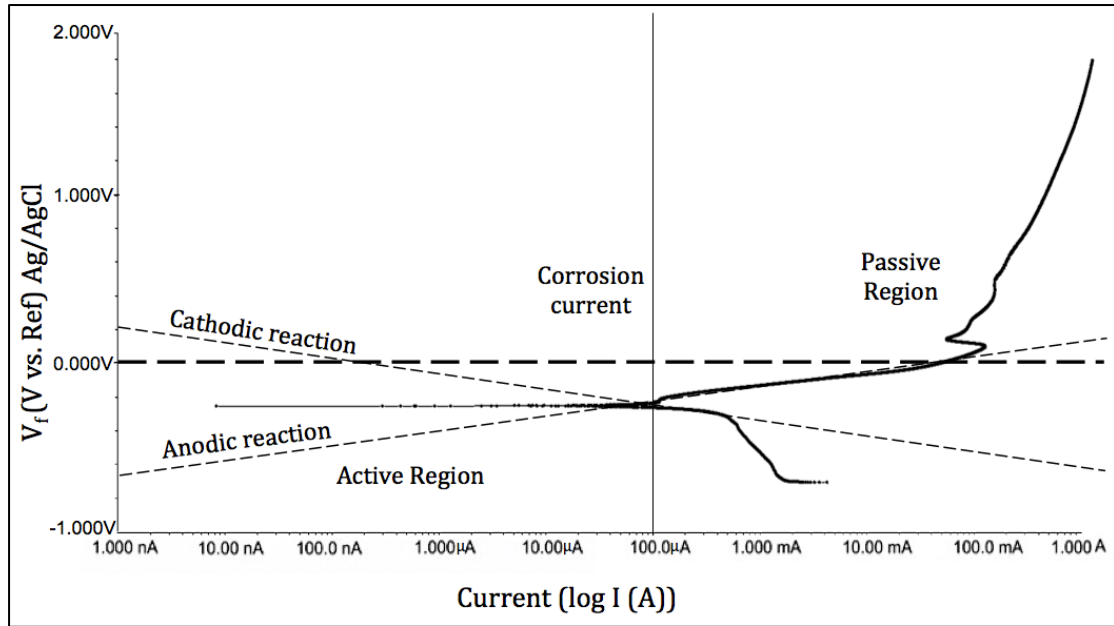


**Fig. 15:** Polarization curve for the NAB in 3.5% NaCl solution showing Tafel extrapolation of corrosion current.

From the polarization results the corrosion current density ( $I_{\text{corr}}$ ) was found to be at  $16.0 \mu\text{A cm}^{-2}$  using Tafel extrapolation. From the  $I_{\text{corr}}$  value the mass loss rate of the sample was calculated using Faradaic conversion, given by Equation (7).

$$\text{Mass loss rate} = \frac{I_{\text{corr}} \times \text{Atomic mass of corroding element} \times \text{exposed area}}{\text{number of electrons freed} \times \text{Faraday's constant}} \quad \dots(7)$$

Where, the rate of mass loss is in  $\text{mg cm}^{-2} \text{h}^{-1}$ , and Faraday's constant =  $96485 \text{ C mol}^{-1}$

From Equations (3) and (4), the corroding element was considered to be copper, and the number of free electrons ( $n$ ) was considered 1 and 2. Hence, the mass loss values obtained for pure corrosion using the potentiodynamic polarization technique were found to be  $0.382 \text{ mg} \pm 0.002 \text{ mg}$  for  $n = 1$ , and  $0.197 \text{ mg} \pm 0.002 \text{ mg}$  for  $n = 2$ .

### 3.4 Synergy evaluation

Using Equation (1), the synergy was calculated using five different methods. The first method used mass loss as the parameter for synergy. The second and third methods employed Alicona to obtain the volumetric mass loss and the mean depth of penetration rate from Table 2 as the parameters for measuring synergy, all obtained in distilled water as the medium for pure erosion.

The pure erosion test was also conducted in 5 L of 3.5% NaCl solution while subjecting the samples to cathodic protection as the fourth method. It must be noted that the pure corrosion test provided a negative value for the synergy calculation due to a gain in mass observed gravimetrically after each test. Due to this the results were rather dispersive and hence, the fifth method employed polarization technique to obtain C. Table 4 tabulates the measured synergy values for NAB for each test, obtained using the five different methods to estimate the synergy between cavitation erosion and corrosion.

Method Used	T (mg)	E (mg)	C (mg)	S=T-(E+C) (mg) Using Equation (1)	(S/T) x100
MDPR ( $\mu\text{m h}^{-1}$ ) (Measured by Alicona)	0.955 $\pm$ 0.003	0.645 $\pm$ 0.005 (in distilled water)	0.000 $\pm$ 0.002	0.310 $\pm$ 0.010	32%
Volumetric Mass Loss (mg) (Measured by Alicona)	1.29 $\pm$ 0.05	0.88 $\pm$ 0.04 (in distilled water)	0.00 $\pm$ 0.02	0.41 $\pm$ 0.11	31%
Gravimetric mass loss (mg) (Measured by mass balance)	1.48 $\pm$ 0.02	1.00 $\pm$ 0.05 (in distilled water)	-0.61 $\pm$ 0.04	1.09 $\pm$ 0.11	73%
Gravimetric mass loss (mg) (Measured by mass balance)	1.48 $\pm$ 0.02	1.52 $\pm$ 0.05 (with cathodic protection)	-0.61 $\pm$ 0.04	0.57 $\pm$ 0.11	38%
Gravimetric mass loss (mg) (T and E measured by mass balance, C calculated by Equation 7)	1.48 $\pm$ 0.02	1.00 $\pm$ 0.05 (in distilled water)	0.197 $\pm$ 0.002 For n = 2;	0.28 $\pm$ 0.072	19%
			0.394 $\pm$ 0.002 For n = 1 (Polarization and Faradaic conversion)	0.098 $\pm$ 0.072	6%

**Table 4:** Synergism summary for NAB obtained using five different test methods.

The highest synergy measured from the 5 different methods (tabulated in Table 4) was found to be 73% under gravimetric method (method 3) while the lowest resulted from method 5 with E conducted for 1 h in 5 L of distilled water. This yielded 6 - 19% synergy when a polarization method was used for C. The gravimetric results measured using the cathodic protection method for E was found to give a synergy of 38%. As for the results obtained via Alicona, the synergy was found to be 31% using the volumetric mass loss method, and 32% using MDPR method. The value of E was higher than C in every method. The values of T were higher than E, except for the cathodic protection method. From the results, it can be inferred that corrosion tends to enhance mass loss, except in the case where cathodic protection was used to determine E, where corrosion appeared to have a negative effect on total mass loss.

From Table 4 it can be seen that distilled water exhibited lower mass loss when compared to cathodic protection test. On analysing under the SEM, it was observed that under cathodic protection the number of cavities had actually increased, which has also been reported in the literature [14], [15]. Hence, there was an increase in the mass loss observed when applying cathodic protection, although the grain-boundary attack was lower than that found in distilled water. This gives an interesting result showing that using distilled water reduces mass loss by about 0.5 mg relative to the CP technique, giving almost double the synergy obtained under other two conditions.

The best method for S quantification is probably method 5 where gravimetric measurements are used for E and T (E from distilled water experiments) and C is from polarization and Faraday conversion techniques. However, it is uncertainty on the value of n for Faradaic conversion and thus only a range of S% can be given.

In a study by Kwok, Cheng and Man [22], the synergistic effect of cavitation erosion and corrosion of copper-based alloys and bronze, among many other engineering alloys using an 20 kHz ultrasonic vibrating cavitation at a peak-to-peak amplitude of 30  $\mu\text{m}$  in distilled water and in 3.5% NaCl solution at 23 °C was investigated. It was found that synergism had a significant effect on the mass loss with it contributing up to 85% total damage. They calculated the synergy via mean depth of penetration rate method and concluded that the Cu-based alloys had a synergy percentage of 2.7 - 4.5% with 95 – 97% of the total damage attributed to pure erosion only. It was also found that corrosion only played a minor role of about 0.1–1.8% in the overall cavitation erosion–corrosion for copper-based alloys. They also performed several experiments on laser treated metals such as austenitic steel alloy and NiCrSiB-1050-2 alloy in 3.5% NaCl solution [56].

In the studies conducted by Wood and Fry [25], they investigated the fundamental mechanisms of the synergistic effect of cavitation erosion and corrosion for copper and cupro-nickel alloys in seawater. The test was conducted in an all-plastic cavitation tunnel comprising of a 60° symmetrical wedge cavitation source. The specimens of 10 mm × 20 mm working section were held under potentiostatic control in a flowing seawater system at an upstream flow velocity of 14.7 m s<sup>-1</sup>. The synergy was measured using the depth of penetration method, tested for 4.5 h. They found that that the synergistic effect was most marked when the cavitation erosion occurred in the presence of mild corrosion with 50 - 70% of the damage caused due to pure erosion only. However, corrosion was responsible for 50% of the overall penetration depth. The synergy was found to range between 10 – 29% at different over-potentials of 5 mV – 100 mV for copper, and between 30 – 50% for Cu-Ni alloys. Their preliminary results also suggested that depth of penetration measurements gave clearer indication of the level of synergistic effect compared to mass loss measurements with the majority of the depth of penetration being caused by synergistic mechanisms.

Wood and Hutton [57] plotted the ratio of the synergistic wear to corrosive wear (S/C) against the ratio of erosive wear to corrosive wear (E/C). These tests were conducted using hydrodynamic cavitation, slurry impingement with aqueous slurries containing 2% silica sand particles, and vibratory cavitation for various steels and cast iron in a slurry pot, copper and cupro-nickel alloys, in various corrosive and non-corrosive solutions. These were obtained from the results published in literature [57], as summarized in Table 5.

Point no.	Material	Ref.	Point no.	Material	Ref.	Point no.	Material	Ref.
1	A514	[36]	15	MS1020	[58]	29	Cu	[25]
2	SS-316	[36]	16	MS1020	[58]	30	Cu	[25]
3	SS-316	[36]	17	MS1020	[58]	31	Cu	[25]
4	REM 500	[36]	18	SS-304	[58]	32	Cu	[25]
5	REM 500	[36]	19	SS-304	[58]	33	Cu	[59]
6	A514	[36]	20	SS-304	[58]	34	MS1020	[60]
7	SS-316	[36]	21	Cu	[25]	35	Fe	[61]
8	SS-316	[36]	22	Cu	[25]	36	Fe	[62]
9	REM 500	[36]	23	Cu	[25]	37	Fe	[62]
10	REM 500	[36]	24	Cu	[25]	38	Fe	[62]
11	Cu	[59]	25	Cu	[25]	39	Fe	[62]
12	Cu	[59]	26	Cu	[25]	40	Fe	[62]
13	Cu	[59]	27	Cu	[25]			
14	G cast Fe	[35]	28	Cu	[25]			

**Table 5:** Data used for S/C vs. E/C map (as plotted in Figure 16) and their corresponding references [57], [63] .

The S/C and E/C values for air-formed NAB from the current study were also calculated and tabulated in Table 6, and plotted in the graph using the synergy calculation in Table 4.

Material	S/C	E/C
NAB with air-formed film (n=1)	0.20	2.54
NAB with air-formed film (n =2)	1.42	5.07

**Table 6:** S/C and E/C values calculated for air-formed oxide-filmed NAB samples using gravimetric method for E measurement, and polarization and Faradaic conversion for C measurement.

Figure 16 illustrates the linear relationships between S/C vs. E/C plot along with the current results from the NAB. The numbers designated to the points are used to identify the type of materials and the experimental conditions they were subjected to. The solid line represents the materials having medium S/C values (i.e. up to 30% of total wear is affected by synergy); whereas, materials having high S/C values (i.e. more than 60% of total wear is affected by synergy) are represented by the broken line. Points below the solid line were considered as low S/C values, with less than 10% of total wear affected by synergy. And for E/C values above 50, the points could not be distinguished between high and low S/C values. Also, it can be seen that data from this paper for NAB (with air-formed oxide film) lies on the medium S/C value [57], [63].

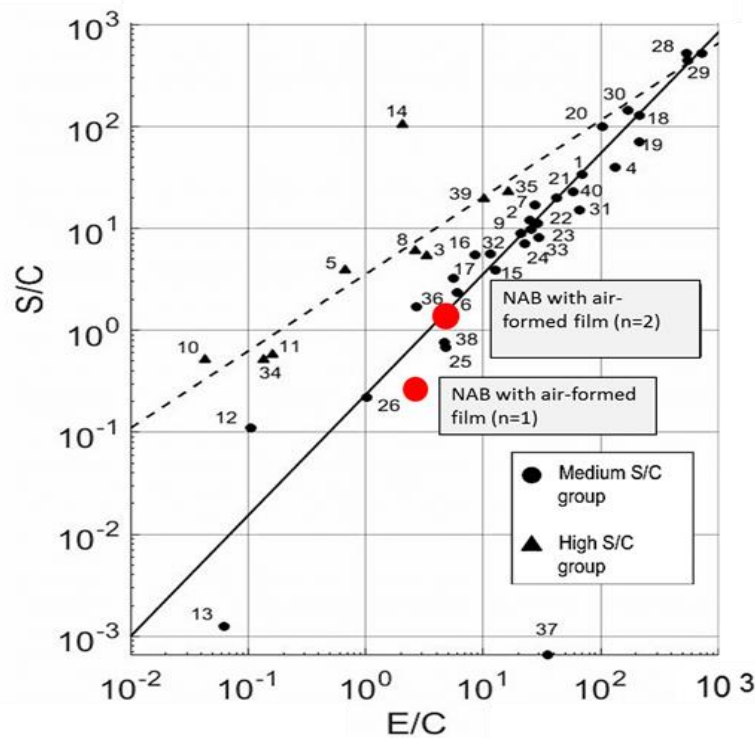


**Fig 16:** S/C vs E/C curve [57], [63].

### 3.5 Limitations of the methods used

As presented by the author [44], the gravimetric mass loss results were considered more reliable. This is because, although both gravimetric as well as volumetric mass loss measurements are useful and efficient in their own account, they both have major shortcomings.

On one hand, while the data obtained by precision mass balance are generally considered accurate up to 0.01 mg, several factors may affect these results. Water-retention due to absorption via porous layers/coats or selective phase attack may occur that make accurate mass loss measurements difficult. On the other hand, the volumetric analyses can be equally crude since the highest magnification achievable using Alicona is 1000x. It can suffer from loss of data for very smooth and reflective surfaces, or due to re-entrant topography of the surface. Also, in the case where there are sediments, corrosion products, micro-scratches, and burrs existing on the sample surface, it may not clearly differentiate these to allow selective volume loss measurement. This again causes deviation from the true result. Hence, S/T % obtained using gravimetric method for E and T, and polarization technique for C was considered more preferable.

From the study, it must be noted that the errors for E, C and T all sum up while quantifying S, which can lead to significant errors. Given the variables in the synergy results under each test conditions, and also the high error accumulation, the exact value of S is difficult to evaluate. Additionally, an important factor often overlooked, and needs to be realized, is the percentage error for the S/T % values obtained under each individual method. Often, the S values and the corresponding S/T % are quoted in literature without the error bars. However, as seen from the results, these error % values are not negligible, making the S and S/T values less reliable than assumed. Furthermore, it is difficult to resolve S into the separate  $\Delta E$  and  $\Delta C$  components. Also, the  $\Delta C$  component of S is further difficult to measure directly using electrochemical techniques due to the rapid and aggressive nature of the cavitation clouds produced in the experimental set up, affecting the IR drop. In the light of all the results obtained, there is still much left to be answered in the realms of electrochemistry, and the individual contributions of  $\Delta E$  and  $\Delta C$ .

## 4. Conclusion

From the experiments conducted it was concluded that:

- The synergy was calculated using five different methods, involving gravimetric mass loss, measured using a precision mass balance for the samples eroded under both distilled water, and 3.5% NaCl solution while under cathodic protection using GAMRY Potentiostat. Volumetric mass loss and MDPR both employed Alicona non-contact profilometry measurements. The C measurements were obtained using polarization and Faraday conversion methods.



- Synergy was found to be 31% using the volumetric mass loss method, 32% using MDPH method, 74% using gravimetric mass loss in distilled water, 38% using the cathodic protection method, and 31% using the Faraday conversion technique.
- Due to a mass gain observed for C under the OCP method, the result obtained via the polarization technique was considered more realistic and reliable, which gives 6-19% synergism. This range was due to the uncertainty of the exact electrochemical reactions occurring and the number of electrons being transferred. Further studies are needed to elucidate the exact reactions occurring over extended immersion periods.
- Under cathodic protection the number of cavities increased, giving higher mass loss through pitting than that under distilled water, however the grain-boundary attack was lower than that in distilled water.
- The soft  $\alpha$ -matrix surrounding the hard  $\kappa$ -phases seemed most vulnerable to cavitation attack, under both E and T conditions.
- NAB was found to be susceptible to prominent selective phase attack of the  $\alpha$ - $\kappa$  phase interfaces in the microstructure in the presence of corrosive environment.

## Acknowledgments

The author would like to thank Lloyd's Register for funding the work.

## References

- [1] N. K. Bourne and J. E. Field, "A high-speed photographic study of cavitation damage," *J. Appl. Phys.*, vol. 78, no. 7, pp. 4423–4427, 1995.
- [2] Y. Tomita and A. Shima, "On the Behavior of a Spherical Bubble and the Impulse Pressure in a Viscous Compressible Liquid," *JSME*, vol. 20, pp. 1027–1035, 1977.
- [3] J. P. Ghose and R. P. Gokarn, "Propeller Materials," in *Basic Ship Propulsion*, Kharagpur: Allied Publishers, 2004, pp. 166–173.
- [4] E. C. Fitch, "Cavitation Wear In Hydraulic Systems," *Machinery Lubrication*, 2011. [Online]. Available: <http://www.machinerylubrication.com/Articles/Print/380>. [Accessed: 15-Aug-2013].
- [5] W. Lauterborn and C. Ohl, "Cavitation bubble dynamics," *Ultrason. Sonochem.*, vol. 4, pp. 65–75, 1997.
- [6] C.-D. Ohl, T. Kurz, R. Geisler, O. Lindau, and W. Lauterborn, "Bubble dynamics, shock waves and sonoluminescence," *Philos. Trans. R. Soc. A Math. Phys. Eng. Sci.*, vol. 357, no. 1751, pp. 269–294, Feb. 1999.
- [7] Y. Zheng, S. Luo, and W. Ke, "Effect of passivity on electrochemical

- corrosion behavior of alloys during cavitation in aqueous solutions," *Wear*, vol. 262, no. 11–12, pp. 1308–1314, May 2007.
- [8] G. E. Totten, D. K. Wills, and D. G. Feldmann, Eds., *Hydraulic Failure Analysis: Fluids, Components, and System Effects, Issue 1339*, 1st ed., vol. 3. Philadelphia: ASTM International, 2001.
  - [9] Y. Zhou and F. G. Hammitt, "Cavitation erosion incubation period," *Wear*, vol. 86, no. 86, pp. 299–313, 1983.
  - [10] F. G. Hammitt, *Cavitation and multiphase flow phenomena*. McGraw-Hill Book Co., 1980.
  - [11] "Cavitation in Control Valves," *Samson*. Samson, Frankfurt, pp. 1–62, 2003.
  - [12] R. Francis, "Bimetallic Corrosion," 1982.
  - [13] H. S. Cambell, "Aluminium bronze alloys - corrosion resistance guide," no. 80. Copper Development Association, p. 30, 1981.
  - [14] A. Al-Hashem and W. Riad, "The role of microstructure of nickel–aluminium–bronze alloy on its cavitation corrosion behavior in natural seawater," *Mater. Charact.*, vol. 48, no. 1, pp. 37–41, Feb. 2002.
  - [15] A. Al-Hashem, P. G. Caceres, W. T. Riad, and H. M. Shalaby, "Cavitation Corrosion Behavior of Cast Nickel-Aluminum Bronze in Seawater," *Corrosion*, vol. 51, no. 5, pp. 331–342, May 1995.
  - [16] J. A. Wharton and K. R. Stokes, "The influence of nickel–aluminium bronze microstructure and crevice solution on the initiation of crevice corrosion," *Electrochim. Acta*, vol. 53, no. 5, pp. 2463–2473, 2008.
  - [17] H. M. Shalaby, A. Al-Hashem, H. Al-Mazeedi, and A. Abdullah, "Field and laboratory study of cavitation corrosion of nickel aluminium bronze in sea water," *Br. Corros. J.*, vol. 30, no. 1, pp. 63–70, 1995.
  - [18] C. T. Kwok, H. C. Man, and F. T. Cheng, "Cavitation erosion and damage mechanisms of alloys with duplex structures," *Mater. Sci. Eng. A*, vol. 242, no. 1–2, pp. 108–120, Feb. 1998.
  - [19] C. T. Kwok, H. C. Man, and F. T. Cheng, "Cavitation erosion of duplex and super duplex stainless steels," *Scr. Mater.*, vol. 39, no. 9, pp. 1229–1236, Oct. 1998.
  - [20] C. T. Kwok, H. C. Man, and L. K. Leung, "Effect of temperature, pH and sulphide on the cavitation erosion behaviour of super duplex stainless steel," *Wear*, vol. 211, no. 1, pp. 84–93, Oct. 1997.
  - [21] S. Z. Luo, Y. G. Zheng, M. C. Li, Z. M. Yao, and W. Ke, "Effect of Cavitation on Corrosion Behavior of 20SiMn Low-Alloy Steel in 3% Sodium Chloride Solution," *Corrosion*, vol. 59, no. 7, pp. 597–605, Jul. 2003.
  - [22] C. T. Kwok, F. T. Cheng, and H. C. Man, "Synergistic effect of cavitation erosion and corrosion of various engineering alloys in 3.5% NaCl solution," *Mater. Sci. Eng. A*, vol. 290, no. 1–2, pp. 145–154, Oct. 2000.
  - [23] H. Yu, Y. G. Zheng, and Z. M. Yao, "The cavitation erosion and erosion-

- corrosion behavior of carbon steel in simulating solutions of three rivers of China," *Mater. Corros.*, vol. 57, no. 9, pp. 705–714, Sep. 2006.
- [24] A. Sakamoto, H. Funaki, and M. Matsumura, "Seminar influence of galvanic macro-cell corrosion on the cavitation erosion durability," *Int. cavitation Eros. test Semin.*, 2000.
  - [25] R. J. K. Wood and S. A. Fry, "The Synergistic Effect of Cavitation Erosion and Corrosion for Copper and Cupro-Nickel in Seawater," *J. Fluids Eng.*, vol. 111, no. 3, pp. 271–277, 1990.
  - [26] R. J. K. Wood, "Erosion–corrosion interactions and their effect on marine and offshore materials," *Wear*, vol. 261, no. 9, pp. 1012–1023, Nov. 2006.
  - [27] K. Darowicki and J. Ryl, "Cavitation erosion , influence of electrochemical corrosion on cavitation – a review," 2011.
  - [28] Y. Zheng, Z. Yao, X. Wei, and W. Ke, "The synergistic effect between erosion and corrosion in acidic slurry medium," *Wear*, vol. 186–187, pp. 555–561, Aug. 1995.
  - [29] Q.-Y. Wang, S.-L. Bai, and Z.-D. Liu, "Study on Cavitation Erosion–Corrosion Behavior of Mild Steel under Synergistic Vibration Generated by Ultrasonic Excitation," *Tribol. Trans.*, vol. 57, no. 4, pp. 603–612, Jun. 2014.
  - [30] R. Malka, D. A. Gulino, and M. Technology, "Erosion corrosion and synergistic effects in disturbed liquid-particle flow," *Corros. Nacexpo*, no. 6594, 2006.
  - [31] "ASTM G119 - 16 Standard Guide for Determining Synergism Between Wear and Corrosion," *ASTM international*, 2016. [Online]. Available: [http://www.astm.org/cgi-bin/resolver.cgi?G119-09\(2016\)](http://www.astm.org/cgi-bin/resolver.cgi?G119-09(2016)). [Accessed: 07-Jun-2014].
  - [32] B. Vyas and I. L. H. Hansson, "The cavitation erosion-corrosion of stainless steel," *Corros. Sci.*, vol. 30, no. 8, pp. 761–770, 1990.
  - [33] M. Matsumura, "Erosion-Corrosion of Metallic Materials in Slurries," *Corros. Rev.*, vol. 12, no. 3–4, p. 321, 1994.
  - [34] J. O. Bello, R. J. K. Wood, and J. a. Wharton, "Synergistic effects of micro-abrasion–corrosion of UNS S30403, S31603 and S32760 stainless steels," *Wear*, vol. 263, no. 1–6, pp. 149–159, Sep. 2007.
  - [35] W. J. Tomlinson and M. G. Talks, "Erosion and corrosion of cast iron under cavitation conditions," *Tribol. Int.*, vol. 24, p. 67, 1991.
  - [36] B. W. Madsen, "Measurement of erosion-corrosion synergism with a slurry wear test apparatus," *Wear*, vol. 123, no. 2, pp. 127–142, 1988.
  - [37] FanAiming, LongJiming, and TaoZiyun, "An investigation of the corrosive wear of stainless steels in aqueous slurries," *Wear*, vol. 193, no. 1, pp. 73–77, 1996.
  - [38] Y. Li, G. T. Burstein, and I. M. Hutchings, "Influence of environmental composition and electrochemical potential on the slurry erosion-corrosion of aluminium," *Wear*, vol. 181–183, no. Part 1, pp. 70–79, 1995.

- [39] S. Zhou, M. M. Stack, and R. C. Newman, "Characterization of Synergistic Effects Between Erosion and Corrosion in an Aqueous Environment Using Electrochemical Techniques," *CORROSION*, vol. 52, no. 12, pp. 934–946, 1996.
- [40] M. M. Stack and B. D. Jana, "Modelling particulate erosion–corrosion in aqueous slurries: some views on the construction of erosion–corrosion maps for a range of pure metals," *Wear*, vol. 256, no. 9–10, pp. 986–1004, May 2004.
- [41] M. M. Stack, N. Corlett, and S. Zhou, "A methodology for the construction of the erosion-corrosion map in aqueous environments," *WEAR*, vol. 203, pp. 474–488, 1997.
- [42] D. a. Shifler, "Understanding material interactions in marine environments to promote extended structural life," *Corros. Sci.*, vol. 47, no. 10, pp. 2335–2352, Oct. 2005.
- [43] A. Neville, T. Hodgkiess, and J. T. Dallas, "A study of the erosion-corrosion behaviour of engineering steels for marine pumping applications," *Wear*, vol. 186–187, pp. 497–507, Aug. 1995.
- [44] J. Basumatary, M. Nie, and R. J. K. Wood, "The Synergistic Effects of Cavitation Erosion–Corrosion in Ship Propeller Materials," *J. Bio- Tribo- Corrosion*, vol. 1, no. 2, p. 12, Mar. 2015.
- [45] E. A. Culpan and G. Rose, "Microstructural characterization of cast nickel aluminium bronze," *J. Mater. Sci.*, vol. 13, no. 8, pp. 1647–1657, Aug. 1978.
- [46] A. Jahanafrooz, E. Hasan, G. W. Lorimer, and N. Ridley, "Microstructural Development in Complex Nickel-Aluminum Bronzes," *Metall. Trans.*, vol. 14, no. October, pp. 1951–1956, 1983.
- [47] F. Hasan, J. Iqbal, and N. Ridley, "Microstructure of as-cast aluminium bronze containing iron," *Mater. Sci. Technol.*, vol. 1, no. 4, pp. 312–315, 1985.
- [48] K. B. Faïres, "Characterization Of Microstructure And Microtexture In Longitudinal Sections From Friction Stir Processed Nickel-Aluminum Bronze," North Carolina State University, 2003.
- [49] "Corrosion: Galvanic Corrosion," *Specialty Steel Industry of North America*. [Online]. Available: <http://www.ssina.com/corrosion/galvanic.html>. [Accessed: 12-Sep-2013].
- [50] F. King, "Corrosion Resistance of Austenitic and Duplex Stainless Steels in Environments Related to UK Geological Disposal A Report to NDA RWMD," Cumbria, 2009.
- [51] J. H. Horwath, "Why Nickel Aluminum bronze for sea water pumps," *Ampco Pumps Company*, 2002. [Online]. Available: [http://www.ampcopumps.com/media/1881/Why\\_NiAlBz\\_For\\_Saltwater.pdf](http://www.ampcopumps.com/media/1881/Why_NiAlBz_For_Saltwater.pdf).
- [52] H. Meigh, "Cast and Wrought Aluminium Bronzes: Properties, Processes and Structure," *Inst. Mater. 1 Carlt. House Terrace, London, SW 1 Y 5 DB, UK*,

2000. 404, 2000.

- [53] A. Daroonparvar, M. R. Atabaki, Mazar, M. Vakilipour, "Effect of pre-heat treatment on corrosion behaviour of nickel-aluminium bronze alloy," *Assoc. Metall. Eng. Serbia*, vol. 17, no. 4, pp. 183–198, 2011.
- [54] R. W. Johnson, *The Handbook of Fluid Dynamics*. Boca Raton: Springer, 1998.
- [55] G. L. Chahine, J. Franc, and A. Karimi, "Laboratory Testing Methods of Cavitation Erosion," in *Advanced Experimental and Numerical Techniques for Cavitation Erosion Prediction*, vol. 106, K.-H. Kim, G. Chahine, J.-P. Franc, and A. Karimi, Eds. Dordrecht: Springer Netherlands, 2014, pp. 21–35.
- [56] C. T. Kwok, H. C. Man, and F. T. Cheng, "Cavitation erosion–corrosion behaviour of laser surface alloyed AISI 1050 mild steel using NiCrSiB," *Mater. Sci. Eng. A*, vol. 303, no. 1–2, pp. 250–261, May 2001.
- [57] R. J. K. Wood, "Marine wear and tribocorrosion," *Submitt. to Wear Mater.*, 2017.
- [58] T. Okada, "Corrosive Liquid Effects on Cavitation Erosion," *J. Ship. Res.*, vol. 25, no. 4, pp. 271–284, 1981.
- [59] S. A. Fry and R. J. K. Wood, "The synergistic effect of cavitation erosion and corrosion." Southampton, 1985.
- [60] R. Simoneau, J. Fihey, and R. Roberge, "The effect of corrosion in low-intensity cavitation erosion," in *Cavitation Erosion in Fluid Systems*, 1981, pp. 71–81.
- [61] Y. Oka and M. Matsumura, "Cavitation erosion-corrosion," in *6th Int. Conference on Erosion by Liquid and Solid Impact*, 1983, p. 11.
- [62] Y. Oka, M. Matsumura, and M. Yamawaki, "Slurry erosion-corrosion on commercially pure iron in a vibratory testing facility-mechanism of erosion-corrosion under predominantly erosion conditions," in *7th Int. Conf on Erosion by Liquid and Solid Impact*, 1987, p. 39.
- [63] R. J. K. Wood and S. P. Hutton, "The synergistic effect of erosion and corrosion: published results," *Wear*, vol. 140, pp. 387–394, 1990.

# Appendix D

---

Journal paper published under ASTM (2013): “Energy-Related Tribo-Corrosion Research At The National Centre For Advanced Tribology.”

# Energy-Related Tribo-Corrosion Research At The National Centre For Advanced Tribology at Southampton (nCATS)

R.J.K. Wood<sup>1</sup>, J. Basumatary<sup>1</sup> and M.-H. Evans<sup>1</sup>

<sup>1</sup>National Centre for Advanced Tribology at Southampton,  
Engineering Sciences, University of Southampton, Highfield, Southampton, SO17 1BJ, UK

---

## Abstract

This paper is based on a keynote lecture given at the Third International Conference on Tribo-Corrosion, sponsored by ASTM International and held at the Georgia Institute of Technology, Atlanta, GA, April 19–20, 2012. It summarises the tribo-corrosion-related research relevant to the energy sector that has taken place over the past 30 years at the National Centre for Advanced Tribology at Southampton at the University of Southampton in the United Kingdom. Research is presented that relates to multiple components in energy generation/conversion systems and involves a wide range of tribo-corrosion mechanisms. These include cavitation erosion-corrosion of turbomachinery, abrasion-corrosion of downhole drilling equipment, erosion-corrosion of nuclear slurry handling components, bearing degradation of renewable energy systems (wind turbines), erosion-corrosion in nuclear power plants, erosion-corrosion in non-renewable energy systems (oil and gas), and tribochemical processes in internal combustion engines. Work from other research groups is also used to show the importance of understanding tribo-corrosion in energy generation/conversion systems.

**KEYWORDS:** tribo-corrosion issues, energy, nCATS

## 1. Introduction

Tribocorrosion is defined as the material deterioration or transformation resulting from simultaneous action of wear and corrosion [1]. The detrimental effect of tribocorrosion results from a combined mechanical attack and an aggressive environment and can be disastrous [2]. It is known to be a highly complicated phenomenon involving mechanical factors, electrochemical factors, formation and removal of the passive film and tribofilm, and either synergy or antagonism of these factors [3]. Tribocorrosion occurs in many engineering applications with researchers tackling related problems with experimental and analytical approaches; however, the actual mechanisms involved require further research [4–5]. It is clear that the investigation of tribocorrosion requires the control of the chemical conditions during a wear test [1].

One of the important tribocorrosion types is that of erosion-corrosion. This is known to occur wherever energized solids, liquid droplets or cavitation bubbles entrain in a flowing fluid. In industrial activities including fluid flow handling at increasing velocities, such as the food industry [6], automotive components [7], hydroelectric power plants [8–10], marine pumping [11–12], nuclear power plants [13], petroleum industry (energy extraction), hydroelectric schemes and nuclear energy, the sand particles or liquid droplets may enter or cavitation bubbles may form that may lead to

component deterioration [14-16].

The combined action of wear and corrosion processes can result in significant mutual interaction beyond the individual contributions of mechanical wear and corrosion that may significantly increase total material losses in aqueous environments, thus producing a synergistic effect [5]. Quantification of wear/corrosion synergism can help in lowering of the overall material loss. ASTM G119-09 is the standard guide for determining synergism between wear and corrosion. The procedures outlined, however, cannot be used for systems in which any corrosion products such as oxides are left on the surface after a test, resulting in a possible weight gain. [17]. A few other relevant latest versions of ASTM standards and their respective applications are listed below:

- ASTM G3, *Standard Practice for Conventions Applicable to Electrochemical Measurements in Corrosion Testing*, 89(2010), Vol. 03.02. [18]
- ASTM G5, *Standard Reference Test Method for Making Potentiostatic and Potentiodynamic Anodic Polarization Measurements*, 94(2011)e1, Vol. 03.02. [19]
- ASTM G15, *Standard Terminology Relating to corrosion and corrosion testing*, Vol. 03.02. [20]
- ASTM G40-12, *Standard Terminology Relating to Wear and Erosion*, Vol. 03.02. [21]
- ASTM G59-97, *Standard Test Method for Conducting Potentiodynamic Polarization Resistance Measurements*, 97(2009), Vol. 03.02. [22]
- ASTM G102-89, *Standard Practice for Calculation of Corrosion Rates and Related Information from Electrochemical Measurements*, 89(2010), Vol. 03.02. [23]

The tribological contacts that suffer from tribocorrosion are various such as sliding, fretting, rolling or impingement, resulting in reduced performance and lifetime of installations, machines and devices with moving components, and controlling of certain manufacturing processes such as chemical-mechanical polishing [1-2].

### **1.1. Background of Tribocorrosion**

The history of tribocorrosion dates back to 1875 when Edison first observed a variation in friction coefficient at various applied potentials [1]. Recently, Tribocorrosion research funding has led to activity in biomedical and nuclear sectors but the energy sector, which is greatly affected, has yet to consistently invest in this area with the exception perhaps of Oil and Gas.

The effects of tribocorrosion are found to be most pronounced on passive metals, as their corrosion resistance is due to a thin protecting oxide film [5]. Most corrosion-resistant engineering alloys belong to this category. This paper provides an introduction to the developing field of tribocorrosion especially in energy sector and an overview of the latest research within nCATS.

### **1.2. Tribocorrosion in nCATS**

Research in tribocorrosion at Southampton started in the early 1980's with Prof. Wood's PhD studies into cavitation erosion-corrosion sponsored by the Admiralty Research Establishment (MOD) and supervised by Prof S. P. Hutton, [24-29].

Research in the 1990's looked at solid particle erosion-corrosion related to oilfield components such as valve, pumps and pipelines fittings. Consultancy in the area of tribocorrosion has been offered since 1995 initially through the Mechanical Engineering



Consultancy Service which is now part of the Research Institute for Industry of the University of Southampton since 1999, the tribocorrosion of components handling nuclear waste slurries has been studied funded by BNFL/ Sellafield Ltd. Tribochemical research has focused on wear corrosion within lubricated contacts. The main advancements in tribocorrosion understanding have been made by the PhD students who have worked in this area, namely Puget (1999); Speyer (2002), Tan (2002) and Rajahram (2010) in erosion corrosion; Bello (2003) and Symonds (2003) in oilfield coatings; Barik (2006); Panchalialah (2007); Booth (2008) in tribochemistry; Thakare (2008) in abrasion-corrosion drilling; Ismail (2010) in downhole drilling; and the current students Evans in wind energy, Basumatary in cavitation erosion-corrosion, Love and Sutton in DLC coating. The research has been sponsored by Chevron, GE Aviation, DSTL (MOD), BP, Schlumberger, EPRC, BNFL/Sellafield Ltd., Rolls Royce, and Lloyd's Register. We have also four visiting professors working in tribocorrosion Higgs, Mischler, Sun and Uchida from USA, Europe, China and Japan respectively.

## 2. Energy related tribocorrosion issues

There are wide ranges of tribo-corrosion issues in the energy sector. The phenomenon of tribocorrosion is very essential to understand in order to obtain efficient and reliable generation of energy. It affects multiple components in energy generation/conversion systems. In the energy systems tribocorrosion may include temperature oxidation of turbine engine components, abrasion-corrosion of downhole drilling equipment [29], erosion-corrosion of slurry handling [30], renewable energy systems (offshore wind, tidal and wave turbines)[31], erosion-corrosion and/or fretting in nuclear power plant [32], non-renewable energy systems (oil and gas) [14], automotive (tribochemistry) [7], and soon.

It involves a wide spread of wear-corrosion interactions induced by fretting, erosion, abrasion, oxidation, sliding, rolling, bending (fatigue) and impact wear processes in parallel with a wide range of chemical and electrochemical processes [14]. Only a small subset of these can be presented in this paper with Table 1 giving a summary of the sector and tribocorrosion studies included in the paper:

Table 1: Summary of the energy – tribocorrosion research within nCATS.

Energy sector	Tribocorrosion study in nCATS
<b>Turbomachinery</b>	Cavitation Solid particle erosion
<b>Nuclear</b>	Liquid droplet impingement erosion Slurry erosion-corrosion
<b>Flow Corrosion</b>	Cooling system Heat Exchanger Biofilms
<b>Renewable</b>	Tidal Wind Biofouling
<b>Oil/gas</b>	Abrasion-corrosion Erosion-corrosion Downhole drilling
<b>IC engines</b>	Tribochemistry

Relatively few of the papers published in the field of tribocorrosion relate to issues in energy conversion systems; however, several studies that do address this important technology area will be discussed under the headings given in Table 1.

### 3. Turbomachinery

Turbomachines are devices that exchange energy with a fluid using continuously flowing fluid and rotating blades, e.g. aircraft engines and wind turbines [33]. Turbomachinery is essential as the majority of the power generation and transportation rely on turbo-machines. They have to function in extreme environments such as high pressures, high temperature, high altitude, etc., and thus, result in a number of tribocorrosion induced by erosion under the influence of various factors such as cavitation, solid particles, etc [15, 33-40].

#### 3.1. Cavitation

Excessively low pressures in liquid medium lead to a phenomenon called cavitation, which is the change in the phase of the liquid to vapour and occurrence of bubbles (cavities). It has significant importance in a wide range of applications from engineering (turbomachinery) to medicine (lithotripsy) [41]. It occurs when the absolute pressure falls below the saturated vapour pressure for the liquid, which causes the liquid to boil even at ambient temperature encountered by hydraulic turbomachines. Vapour bubbles form that then collapse near component surfaces as the fluid pressure rises again. The bubble collapse creates a very high instantaneous pressure, which can significantly 'erode' the material surface, lowering the machine performance and life [41]. Hence, cavitation erosion results from the repeated impulsive loading of the material by high intensity short duration pressures loads, due to shock waves and bubble re-entrant jet impacts (water hammer pressure). Figure 1 shows the leading edge cavitation effect and the cavitating vortices over a two-dimensional NACA0009 hydrofoil [34-36, 39].

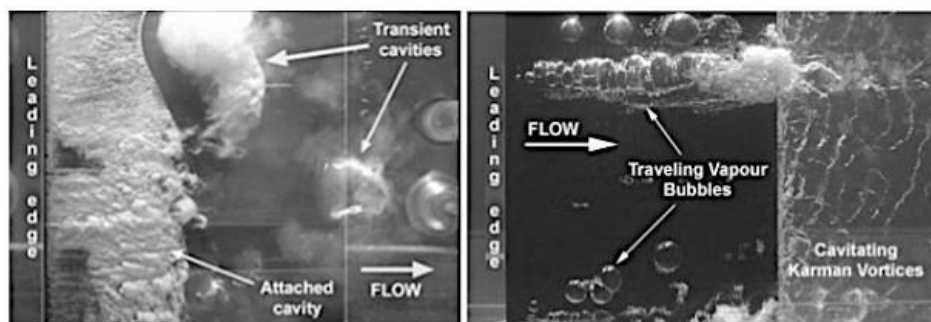


Figure 1 – Leading edge cavitation (left) and cavitating Karman vortices (right) in a water flow over a 2-D NACA0009 hydrofoil [34]

Prediction of the occurrence of cavitation as well as the material performance is very important since it leads to a loss of mechanical efficiency. However, this is a very difficult endeavour as it involves good knowledge of both the material and the cavitation environment to which it will be subjected. This prediction is, however, commonly expected or required by new turbomachinery blade or propeller designers. At present the industry has to rely on several factors such as laboratory testing, use of accelerated erosion testing methods and comparative tests between the new material and previously used materials [37,38]. For example, the EROCAV project on ship propeller designs has looked at seven different types of cavitation where erosion tend to occur:

(1) fluctuating/travelling sheet cavitation, (2) cloudy tip vortex, (3) severe/unstable mid-chord cavitation developing into clouds, (4) vortices originating from the leading edge on the tip, ending cloudy, (5) foaming root cavitation, root vortex cavitation, ending cloudy, (6) foaming sheet close to trailing edge, and (7) sheet cavitation along the leading edge of the face side, breaking up into clouds. Hence, the relative severity of cavitation damage depends on the details of the local flow, which has important consequences for tidal turbine blade designs[31].

On a weight-loss versus time curve (Figure 2) the initial period where little material loss is observed, called the incubation period, is very difficult to observe in some accelerated tests, but its duration is actually very important to the determination of the life of the cavitating device [35]. Figure 2 show micrographs (in the graph) of the incubation period and during the acceleration period.

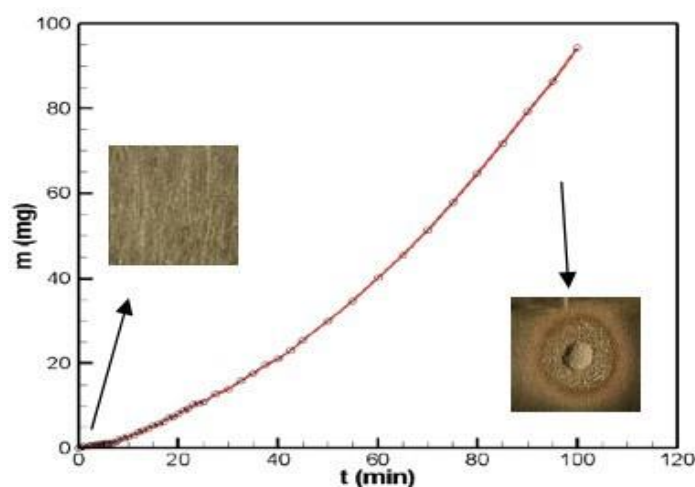


Figure 2 – Erosion progression curve for Al 1100-0 obtained in a cavitation jet erosion test [35].

The cavitation erosion-corrosion in turbomachinery, ship propellers and naval structures leads to material loss (i.e. blade and pipe wall thinning) and pitting of metal surface and unwanted cavitation noise [40].

### 3.2. Solid particle erosion-corrosion

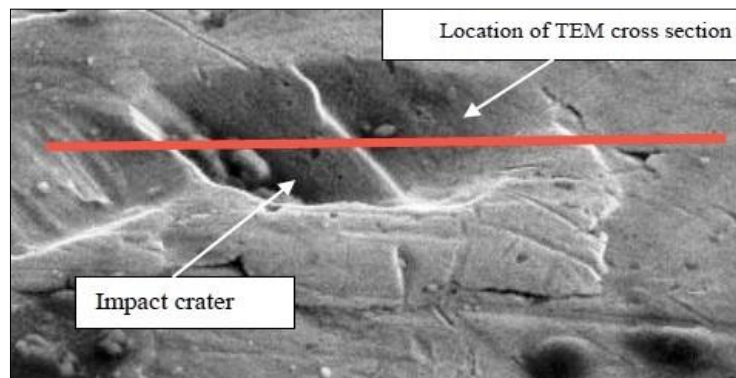
Solid particle erosion-corrosion is the wear phenomenon caused by the combined process of solid particle erosion and the electrochemical process of corrosion, which leads to a synergistic interaction, enhancing wear rate of the material. This causes severe problems to engineering components exposed to these conditions [42,43].

In an experiment conducted by an nCATS PhD student, Shiva Rajahram, gravimetric experiments were performed using a sand slurry pot erosion tester. The slurry pot erosion tester was modified to perform in-situ electrochemical investigations. Results obtained showed a rise in the erosion-corrosion rates and synergy levels with rise in velocity, temperature and sand concentration. This was partly due to the continuous rupture of the oxide film leading to an erosion-enhanced corrosion synergistic effect. The erosion-corrosion rates were found to be a function of the kinetic energy of the particles, the number and the size of the particles impacting the surface.

The largest interaction was found to occur between velocity and sand concentration [42,43]. A comprehensive investigation performed on the evolution of wear on the

surface and subsurface of UNS S31603 using Scanning Electron Microscopy (SEM), Focused Ion Beam (FIB), Scanning Transmission Electron Microscopy (STEM) and Transmission Electron Microscopy (TEM) revealed that a three-layer grain structure consisting of nano-grains, micro-grains and deformed bulk grains was seen to evolve with time [44]. Figure 3(a) illustrates the SEM image of the single particle impact crater, and figure 3(b) shows the dark-field STEM image of the lamella that has been removed to elucidate the micro-structural characteristics surrounding of the impact crater. It can be seen that the impacted region is slightly indented measuring at a depth of  $1\mu\text{m}$  and a width of approximately  $5\mu\text{m}$ .

TEM investigations revealed the formation of numerous cracks and folding of crater lips on the surface due to strain imposed by repeated particle impact. Figure 4 shows the delamination of the surface, forming an extruded lip, and shearing of the microstructure along the lip direction, enhancing crack propagation. A thin composite structure consisting of a layer of chromium oxide was formed along with some erodent fragments embedment, as well as strain induced phase transformation at the surface that were enhanced by the formation of crater lips over this structure. The crater lips formed by impacting sand particles appeared to crack on the surface, believed to be caused by corrosive action accelerating material removal (figure 4). Figure 5 shows the TEM image of the sample under pure erosion undergoing phase transformation at the surface, showing presence of cracks and deformed grains [42–44].



(a): SEM image of the single particle impact crater

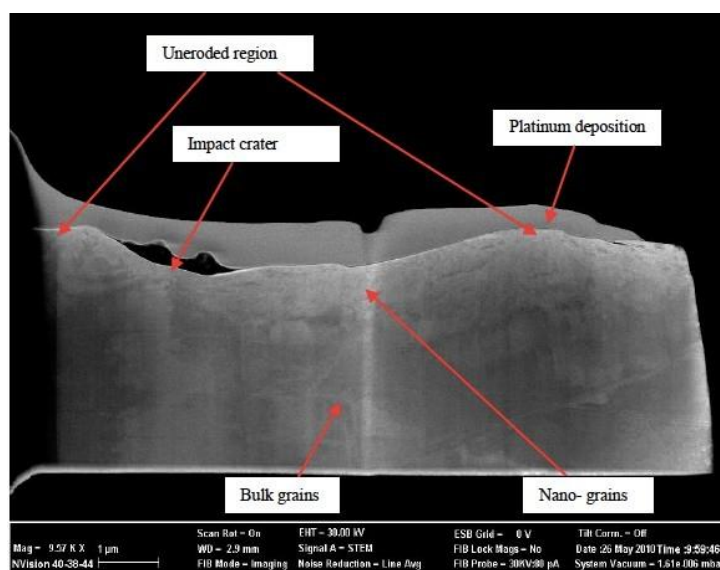


Figure 3 – (a) SEM image of the single particle impact crater [42]. (b): STEM dark-field image of the lamella of a single impact crater [42].

The nano-scale phase transformations, which were observed as a result of the solid particle impact, were thought to cause local galvanic cells, thus enhancing the corrosion rate [42]. This is because, as we know, iron metal, when exposed to oxygen, undergoes redox reaction where the electrons generated during the anodic reaction on the metal is consumed by the oxygen reduction process. Figure 6 shows the schematic electrochemical reaction process during galvanic corrosion.

The redox reaction taking place is given by:

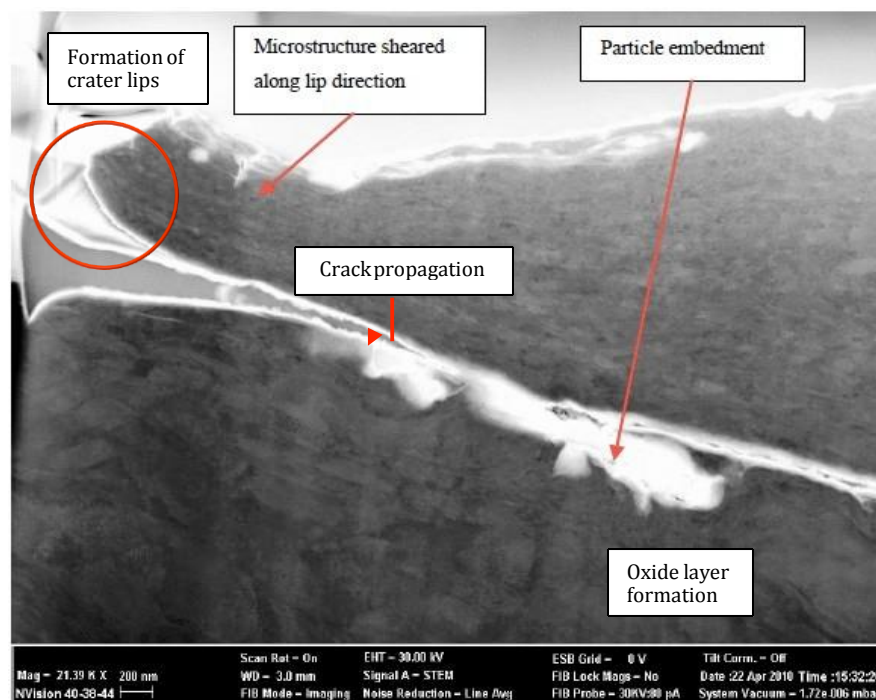
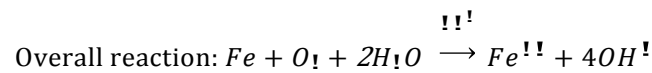
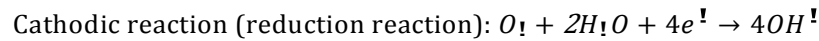
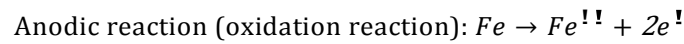


Figure 4 – TEM (dark-field) image showing extruded lip region, and the crack extending underneath it [42]

However, the solid particles impact the material non-uniformly across the surface since, the anodic reaction occurs predominantly on the impacted area, while the cathodic reaction occurs on the uneroded surface. This forms a corrosion cell between the two eroded and uneroded surfaces, leading to a lower local corrosion potential in the eroded area, causing galvanic current flow between the two surfaces. These formations of the microgalvanic cells in the various impacted regions, and passive film rupture contribute to the erosion enhanced corrosion synergistic effect.

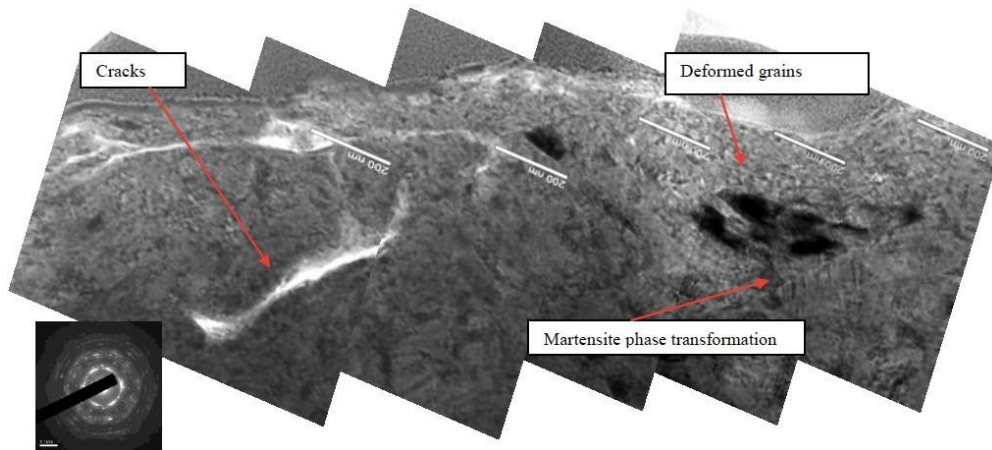


Figure 5 – TEM (bright-field) image of the sample subjected to pure erosion showing cracks, martensite phase transformation and deformed grains [42]

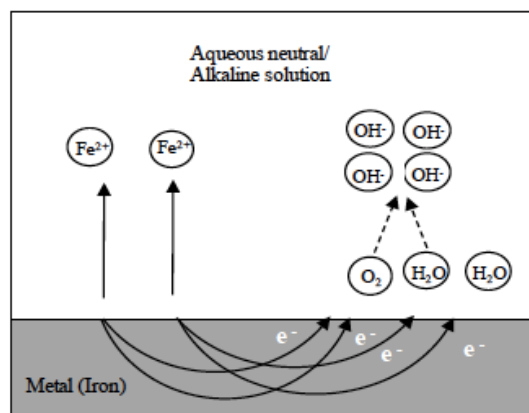


Figure 6 – Schematic diagram showing the galvanic corrosion process [42]

## 4. Nuclear

### 4.1. Nuclear reactors

The main prerequisites for the efficient production of energy from nuclear power reactors are the high degree of reliability, as well as predictability of performance in engineering components and plant. New nuclear power plants are expected to operate for longer durations and to higher safety standards. Consequently, the reliability of components is critical, and in the context of coatings increased efforts are needed to understand the long-term tribology in a reactor environment. Of interest are Diamond-Like Carbon (DLC) coatings, which are known for their high hardness, low coefficient of friction, and wear resistant properties. This work concerns the tribology of DLC coatings in a distilled water environment, as a foundation for future work in a Pressurised Water Reactor (PWR) environment [45].

Work by Sutton at nCATS is currently looking at three commercially available DLC coatings, investigated to help understand the dynamics of transfer layer formation and decay, when sliding against 52100 steel ball bearings in distilled water. Optimum tribological behaviour was observed during interfacial sliding between the transfer layer and DLC coating. Alternatively, shear of the carbonaceous transfer layer from the contact region resulted in growth of an iron oxide layer comprised of maghemite and hematite, as identified by Raman spectra. Three-body abrasive wear involving iron oxide wear particles explained the high wear rate of the DLC coatings in the case of shear [45].

It is known that tribochemical reactions between a DLC coating and a steel ball bearing can lead to high friction by the mechanisms of Li et al [46]. Initially high friction is observed for a non-hydrogenated DLC coating – which decreases as a transfer layer forms. Two hydrogenated DLC coatings show a similarly low coefficient of friction throughout the initial stage of the test. As wear debris is sheared in the contact, tribochemical reactions occur, which increase the shear strength of the transfer layer (the average bond energy of C–O and C=O is 0.21 eV compared to 0.08 eV for a C–H bond [47]). This leads to a gradual increase in the coefficient of friction. A subsequent decrease in friction was observed as the transfer layer thinned.

Martin's work regarding OH-terminated DLC coatings sliding against each other in alcohol suggested that lower friction is observed than compared to H-terminated DLC coatings, but only at very high contact pressures (7GPa). This is because OH- termination prevents bonding between the carbon atoms of each surface, reducing the frictional force, whereas H-termination leads to C–C bonding at this contact pressure. Although, it is generally acknowledged in the literature that the introduction of water vapour will cause the coefficient of friction of hydrogenated DLC coatings to increase [48]; On the contrary, non-hydrogenated DLC coatings show high adhesion in inert environments, and lower friction with increasing water vapour pressure [49]. This is due to the preferential adsorption of polar species onto the DLC coating, such that the frictional properties of the DLC coatings are controlled by the environmental species as opposed to the hydrogen content of the DLCcoating.

The formation of a transfer layer is important to sustain low friction, and prevent high adhesion between a DLC coating and steel ball bearing. In the work done by Sutton, as a transfer layer formed (evidenced by contact potential measurements and optical microscopy), a small increase in the coefficient of friction was observed. This is suggested to be due to tribochemical reactions between the wear debris and water, which act to increase the shear strength of the transfer layer, leading in increased friction. As the transfer layer is lost from the contact, the coefficient of friction decreases again [45].

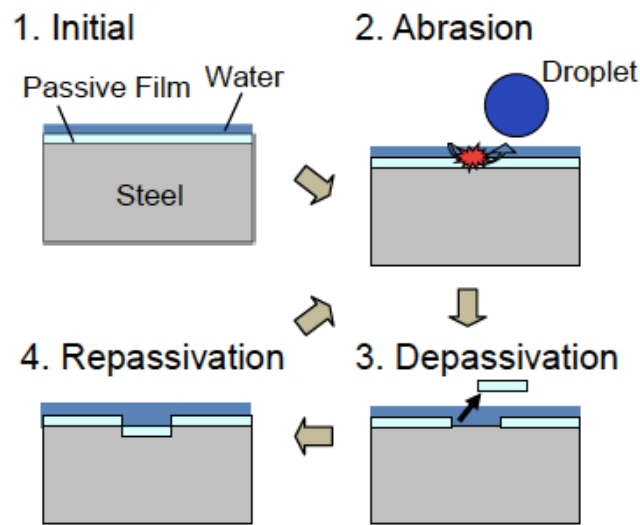
## **4.2. Liquid dropletimpingement erosion**

In recent times, pipe wall thinning due to liquid droplet impingement (LDI) at bends in pipes and orifices is known to be one of the major concerns of nuclear as well as fossil fuel plants [14,50]. The major parameters influencing the LDI erosion are impact velocity and droplet size [51]. However, the effect of impact velocity has not been clearly understood especially for the threshold velocity, below which erosion rate is zero or negligible small, due to which, although most of the empirical formulae related to LDI have focused on the mechanical process involved, it has been shown that corrosion processes may also be involved especially at low flow rates using a numerical simulation [51-54]. The authors also suppose that the synergism of mechanical and chemical factors due to depassivation and repassivation, shown in Figures 7(a) and (b), can have significant effects on material loss by LDI[14,55].

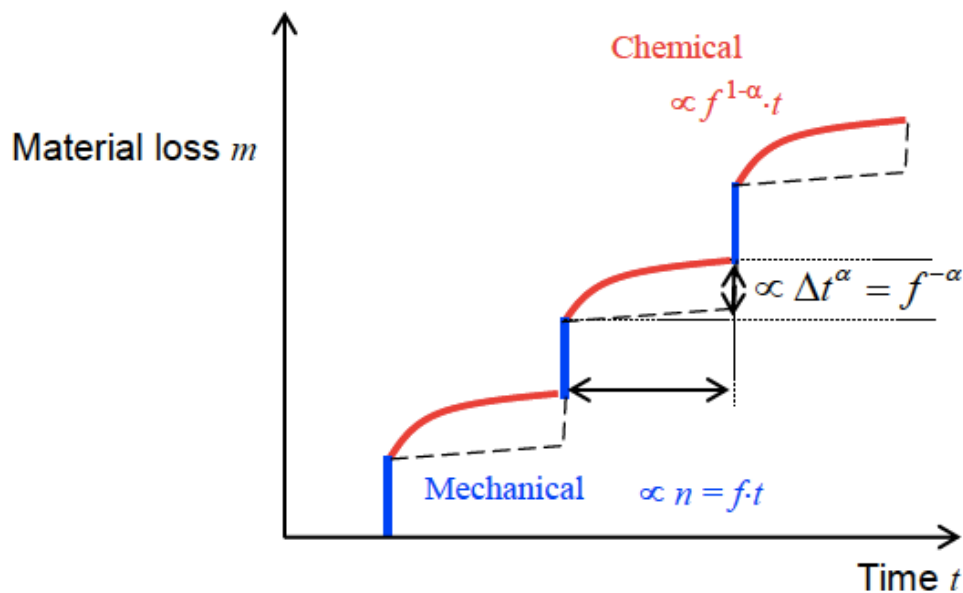
To verify the effects of the chemical factor, an impact-fretting experiment of a type 304stainless steel at low frequency was conducted in pure water environment The impact-fretting condition was chosen to allow a balanced corrosion-mechanical stimulus rather than current LDI experiments which are extremely energetic and mechanical process dominant and are not appropriate for tribocorrosion studies of LDI in low velocity streams [14].



This kind of tribocorrosion may need to be considered at various contacts in power plants such as the nuclear fuel rod, steam generator tubes, heat exchanger tubes etc. and their supports, which involves impact-fretting motion in pure water [56].



(a) Schematic of depassivation and repassivation of a metal surface due to LDI (Liquid Droplet Impingement).



(b) Schematic of synergistic material loss

Figure 7 – (a) Schematic of depassivation and repassivation of a metal surface due to LDI (Liquid Droplet Impingement), (b) Schematic of synergistic material loss [14].

In a pressurized water reactor, typically, components and associated supports are excited by a range of configurations such as sliding, fretting and impact. Most of the materials are passivating alloys working in a relatively aggressive environment such as high temperatures, pressure, boric acid, and lithium hydroxide [57]. This peculiar environment and the motions highlighted previously are favourable to tribocorrosion mechanisms [14].



## **4.2. Nuclear sludge**

Reprocessing plant needs to transfer radioactive slurry from holding ponds to a processing plant and needed to be sure that erosion and erosion-corrosion levels caused by impingement of the transported solids on internal slurry handling components e.g. pipes, pumps, valves, nozzles, and any surfaces likely to be impinged with it were going to be at minimal levels. Significant expertise in erosion and a commercial scale erosion testing facilities had been developed at the University of Southampton and in collaboration with the University of Nottingham in the UK. A full-scale version of an actual pumping system was set up and the research highlighted the mechanism and areas of critical erosion wear and engineering and materials solutions resulting in several journal and conference papers [58-63].

## **5. Flow corrosion**

### **5.1. Cooling systems**

Erosion-corrosion in the cooling systems has been observed to occur in pipe bends (elbows), tube constrictions, and other structures that alter flow direction or velocity. The mechanism for this type of corrosion is that the energetic flow of fluid induces the wall shear stress and flow field instabilities, which removes any protective film or metal oxide from the metal surface occurring either in the presence, or in the absence of suspended matter in the flow stream [64]. Deposits disturb the surface flow and increase turbulence causing protective surface layers to be locally removed. The simultaneous action of erosion and corrosion produces intense localized wastage [65]. Stronger films can be removed at a relatively low fluid velocities in presence of the suspended particle than in absence of the suspended matter, where, once the metal surface is exposed, it is attacked by the corrosive media and eroded away by the fluid friction, which if does not repassivate quickly enough by forming a layer of metal oxide, significant damage may occur [64]. Formation of tubercles, i.e. the formation of a corrosion product and deposit mound above a corroded area, usually on a steel or cast iron surface, form a friable outer crust of brown ferric oxide and other deposited materials. Figure 8 shows a heavily tuberculated supply line from a steel mill [65].

Some materials are more resistant than others to erosion-corrosion under the same fluid conditions, and found to be most prevalent in soft alloys, such as copper and aluminium. Increasing the flow rate of the fluid in the cooling application may increase its performance, however, this may lead to increase erosion-corrosion. Hence, it is important to determine how great an impact increasing of the flow rate will have on the thermal performance, since, even the slightest of the improvement in the performance of the heat exchanger or cold plate may cost its longevity significantly [64].

Improving the flow lines within the pipe by deburring (i.e. smoothing out irregularities) may help minimizing erosion-corrosion; also, bends with larger angles, and gradually changing pipe diameters, rather than abrupt variations, reduce the erosion-corrosion significantly. Keeping the same diameter tubing, doubling of the flow rate in the turbulent region of flow does not result in doubling of the thermal performance. However, doubling the flow rate in the laminar and transitional regions may more than double the heat exchanger's performance. Other methods include slowing the flow rate (minimizing turbulence), reducing the amount of dissolved oxygen, changing the pH, and changing the pipe material to a different metal or alloy [64].

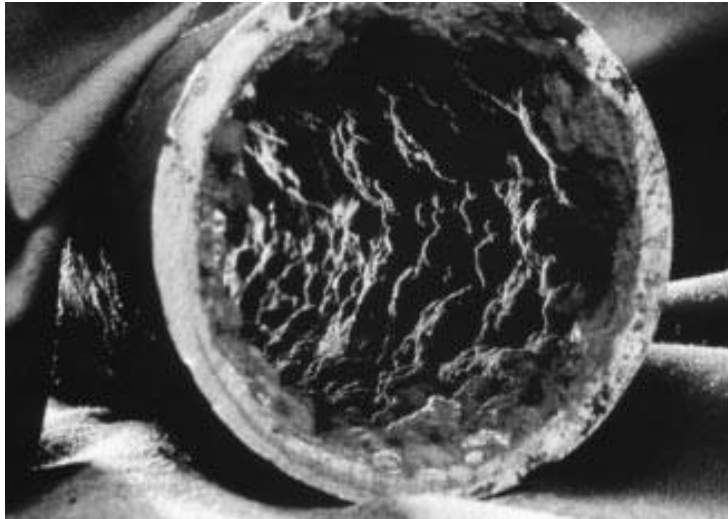


Figure 8 – Severe tuberculation in a 4-inch diameter mill water supply line [65]

## 5.2. Heat exchangers

Corrosion in heat exchanger applications must be considered whether it may or may not be a concern for some applications. The cost of corrosion is always more significant than the replacement of the heat exchanger or element. Process down time, change out cost, accessing the equipment and pressure testing are all incur additional costs to the corrosion process [66].

Due to the varied designs and application of heat exchangers and the fact that they can contain many different fluids under various flow and temperature ranges. In general, heat exchanger companies will not make material recommendations to guard against corrosion because the source of corrosion can vary and change. Also the fluid chemistry and environment can change over the operating life of the exchanger, even just for short periods of time (such as a spike in water chemistry)[66].

Factors affecting flow corrosion include fluid chemistry, fluid (or metal) temperature, flow rate, the composition of material, material forming history, welding, maintenance or cleaning frequency, fouling, and biofilm formation [66].

## 5.3. Biofilms

Microbiologically Influenced Corrosion (MIC), also known as microbial corrosion or biological corrosion, is the deterioration of metals as a result of the metabolic activity of microorganisms on the metal [66]. About dozens of bacteria known cause the microbiologically influenced corrosion of metals, such as carbon steels, stainless steels, aluminium alloys and copper alloys, in water and soil, especially with pH of 4-9, and at a low temperature range of 10-50°C. For example, the Sulphate reducing bacteria (SRB) is often responsible for the accelerated corrosion damages to ships and offshore steel structures, figure 9 shows a microbial layer causing corrosion damage to a ship [66,67].



Figure 9 – Microbial surface interaction on marine vessels, propeller fans, etc. [67]

Biofilms formation on metals is the result of an accumulation process not necessarily uniform in time or space that starts immediately after metal immersion in the aqueous environment. A thin film of approximately 20–80 nm thickness may form due to the deposition of inorganic ions and organic compounds of high relative molecular mass in the first stage that can alter the electrostatic charge and wettability of the metal surface, facilitating its further colonization by bacteria [68]. In a short time, ranging from minutes to hours depending on the aqueous environment in which the metal is immersed, microbial growth and extracellular polymeric substance (EPS) production may result in the development of a biofilm. This biofilm is a dynamic system where the different transport processes and chemical reactions occur at the biofouled interface through the biofilm thickness [68-71].

Positive identification of MIC requires chemical, biological and metallurgical analysis of the waters, soils and the metal samples [71]. By demonstrating the microbial reactions interference with the corrosion processes and, thus, identifying the products obtained from these reactions on the surfaces of corroding metals by using appropriate analytical techniques may help quantify mechanisms of MIC. Thus, together with these products and the increasing corrosion rate, it can be proven that the specific mechanism of MIC is active [71,72].

## 6. Renewable energy

### 6.1. Wind

Wind turbine gearboxes tend to fail predominately at several critical bearing locations, by the modes of micro-pitting, smearing and white structure flaking (WSF) [73,74]. Premature wind turbine gearbox bearing failures in the form of WSF account for a large proportion of gearbox bearing failures and can occur in as little as 6 – 24 months of operation [75].

The formation of white etching cracks (WECs), and also perhaps butterflies, under rolling contact fatigue in the 1 mm zone beneath the contact surface are associated with WSF (see Figure 10). WECs and butterflies both have microstructural changes associated with their cracks. The microstructural change ‘white structure’ or ‘white etching area (WEA)’ refers to the appearance of the altered microstructure when cross sections are polished, etched with nital (~2% Nitric acid in ethanol) and examined

under reflected light. WECs tend to be shaped in irregular shaped networks with geometries depending on the sectioning direction, and butterflies are cracks initiating at stress raising microstructural defects and non-metallic inclusions forming due to cyclic shear stresses from rolling contact [74].

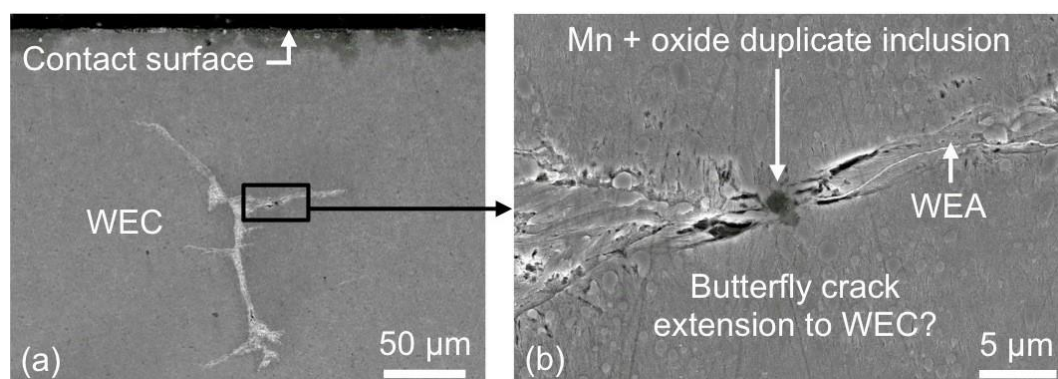


Figure 10 – Example of an inclusion-WEC interaction in a 100Cr6 bearing steel two-roller test specimen that was pre-charged with hydrogen. Images are circumferential cross-sections (in direction of travel), where over-rolling direction is left to right. (a) Shows a low magnification SEM image of a WEC in the etched condition. (b) SEM image of an inclusion or butterfly associated with a WEC. White etching area (WEA) is the microstructural change associated with the failure mode.

Hydrogen release and diffusion into bearing steel (sourced from water contamination or the lubricating oil) [74,76] and transient operating conditions not well understood [73,74] are thought to drive WSF. Hydrogen has been shown to diffuse into the steel during rolling element bearing tests [76-80] to contents between about 0.1 – 4.2 ppm [76,79,80], however to what level is likely in actual wind turbine gearbox bearings is currently unknown. This is due to practicality of removing bearings quickly and freezing them for thermal desorption analysis. Two mechanisms for hydrogen entry into bearings during operation are cited; (1) bulk diffusion continuously during operation from tribochemical reactions at nascent surfaces created by severe events [74] (see Figure 11), and (2) surface cracking begins and subsequently the lubricant or water contamination inside the cracks release hydrogen locally due to intense crack rubbing, the hydrogen diffusing into the surrounding crack tip vicinity [81,82]. If hydrogen enters the steel it will be detrimental to the steel's properties. The presence of diffusible hydrogen in bearing steel is thought to enhance fatigue crack initiation and propagation by localisation of plasticity at the fatigue crack tip [83,84] resulting in lowering of mode I and II stress limits for crack growth [83,85].

Tribochemical factors have been shown to heavily influence WSF formation. Lubrication additives such as anti-corrosion sulfonates have been shown to rapidly accelerate the formation of WSF (sulphur can act to inhibit the recombination of molecular hydrogen to  $H_2$  gas), whereas other surface protecting additives or base oils containing no hydrogen radicals have been shown to offer degrees of prevention to WSF [74]. Water, seawater and salt contamination from offshore environments are prevalent in some wind turbine gearboxes. Wind turbine gearbox can also often experience long standstills prior to grid connection and idling operation. Thus corrosion, fretting corrosion and removal of passivation films on raceways exposing nascent steel surfaces can occur.

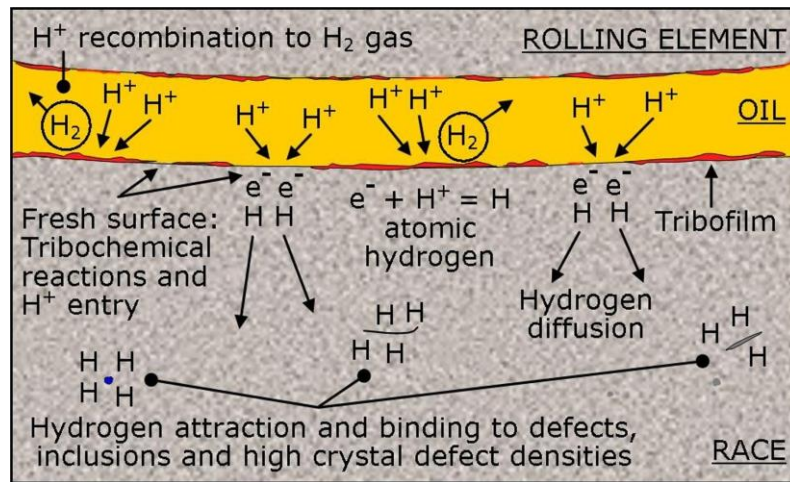


Figure 11 – Schematic of rolling element and race lubricated with oil, or similarly grease, containing hydrogen radicals. Hydrogen ions ( $H^+$ ) combine with electrons ( $e^-$ ) at nascent steel surfaces to form atomic hydrogen ( $H$ ). Atomic hydrogen attracts and strongly binds to crystal defects [74].

The initiation mechanisms of WECs are contested. Several mechanisms are cited, however there has so far been few studies confirming these. Subsurface initiation at non-metallic inclusions (perhaps associated with extension of butterfly cracks [85]), surface initiation (from surface flaws/cracks) and initiation from events such as high impacts/vibrations in the contact are cited [74]. Understanding the initiation process is important for designing solutions since subsurface initiation links to steel cleanliness, and surface crack/impact/vibration initiation links to surface engineering and tribological operating conditions. In the aim of verifying initiation and formation mechanisms of WECs, extensive work has been recently conducted [86-88]. Tomographic serial sectioning (small removals of material between 3 – 5  $\mu m$  per slice by polishing and imaging over 100's of slices) has been performed on a range of specimens/bearings subject to rolling contact fatigue; these including hydrogen charged two-roller test specimens at different diffusible hydrogen levels [86,88] industrial scale gearbox test bearings and actual wind turbine gearboxes from service [87]. Hydrogen pre-charging two-roller test specimens with diffusible hydrogen [86,88] has been conducted in nCATS in the aim of replicating the continuous bulk hydrogen diffusion entry mechanism during operation from tribochemical reactions at nascent surfaces created by severe events. Pre-charging the steel with diffusible hydrogen to differing levels has shown that the formation of butterflies and WECs can be quite sensitive to the bulk hydrogen content [88] where perhaps a threshold exists. The novel application of tomographic serial sectioning has enabled mapping and modelling of WECs for the first time, and revealed critical information about initiators (see Fig. 10). The combined evidence suggests that one mechanism of WEC formation in wind turbine gearbox bearings is due to subsurface WEC initiation from inclusions, either in a butterfly manner or non-butterfly manner; where small WECs link together to form larger WEC networks. In terms of steel cleanliness standards for wind turbine gearbox bearings in understand butterfly and WEC formation, it is suggested that more emphasis is required on the density of inclusions that are small/short [86-88].

## 6.2. Tidal

The current issues restricting the development of tidal current turbines include material selection, loading conditions and environmental impacts. As mentioned in a paper by Prof. R. Wood of University of Southampton, "the areas of concern for tribological components in tidal and offshore wind turbines include solid particle



erosion, cavitation erosion, foreign object damage of blades, tribocorrosion of blades and bearings, biofouling and ice build-up on blades causing increased drag, unknown and unusual loadings on bearings and seals, extremely high torques through the drive train of gearboxes as well as lubricant degradation particularly from salt water contamination and atmospheric corrosion. All of these add uncertainty to the lifetime of tidal and wind turbines” [31].

A rotating blade of the tidal turbine is bound to experience cavitation if the local blade surface speed of the turbine blade reaches a critical value for a given depth of immersion, which may be under the influence of tidal current, rotational speed and flow acceleration due to the blade hydrofoil shape. The relative severity of cavitation damage will depend on the details of the local flow. Typically, keeping the speed of rotation of the turbine as high as possible improves the hydrodynamic efficiency. Also, reducing the size of the step-up of rotation speed needed in the gearbox may contribute in improving of the hydrodynamic efficiency. Thus, it is likely that modification in turbine design may attribute in limiting of the amount of cavitation on turbine blades. Use of materials such as stainless steel may be necessary near the blade tip as composite surfaces often have a low threshold for erosion [31].

### **6.3. Biofouling**

Biofouling growth will affect wave machines perhaps more than submerged tidal systems. Surface and sub-marine structures have to withstand the aggressive marine environment with its corrosive salt water, fouling growth and abrasive suspended particles. Even at a depth of 5m, the tidal systems and the rotor hubs (low velocity parts) get covered with fouling [89]. Penetration of coatings/paints on tidal systems could lead to an accelerated coating paint loss due to substrate corrosion and interfacial de-bonding [90]. Figure 12 illustrates the biofouling of a nickle aluminium bronze [NAB] coupled titanium alloy disc immersed in seawater, for 12 months from January '03 till January '04, at National Oceanography Center, Southampton [NOCS]. [67].

Several methods may be employed to prevent biofouling and corrosion, particularly around seals, welds, bearing surfaces and electrical insulation materials, keeping the blades rotating in a particular speed, which reduces the risk of biofilm growth but, in turn, increases wear. Biofilm growth can also be constrained by applying antifouling paints, and using sonic and ultra-sonic systems [31].



Figure 12 – Biofouling of a NAB coupled Ti disc sample immersed in seawater for 12 months at National Oceanography Center at Southampton [67].

## 7. Oil and Gas

### 7.1. Abrasion-corrosion

Abrasion-corrosion in the power industry is a major concern for equipment such as apron conveyors, bucket elevators, screw conveyors and drag conveyors that are built to increase efficiency while withstanding abrasion-corrosion, and harsh temperatures. Increasing pressure to use multi-fuel options for power generation has enhanced the need for equipment to handle a variety of fuels and products such as coals, limestone, dust, wood, etc. Modern fossil-fuel power plants, including coal-fired systems, increasingly require components that can withstand higher temperatures and pressures to improve efficiency, lower maintenance costs and decrease emissions levels [14].

Many of the damage mechanisms that affect power plant performance are a combination of abrasion, corrosion and oxidation, in such that the abrasives damage the surface of the substrates causing oxidation (passivation), which on further damage (depassivation) induces faster corrosion, and hence, result in considerable operating costs [91]. The oil and gas extraction sectors also deal with extensive abrasion-corrosion issues associated with tar-sand handling to drilling operations, subjecting carbon steels and passive metals to tribocorrosion mechanisms [14]. Figure 13 describes the method of depassivation of the passivating coated surface on the substrate by the rolling action of a three-body abrasion induced by relative motion between the coated surface and a counter face.

For abrasion-corrosion a variation in synergy levels has been linked to the abrasion mechanism present in the contact. Figure 14 shows results from micro-abrasion-corrosion tests on types 304 and 316 stainless steel (UNSS30403 and S31603) and super duplex stainless steel (UNS 32760) in 3.5% NaCl solutions [91]. If the total abrasion-corrosion rate (AC) is given as:

$$\text{Total wear (AC)} = \text{pure abrasion (PA)} + \text{pure corrosion (PC)} + \text{synergy (S)}$$

The levels of synergy are represented as a percentage calculated by equation (1) where, PC (passive corrosion rates) are assumed negligible. Hence,

$$S/AC \times 100 = (AC - PA)/AC \times 100 \quad (1)$$

The synergy levels ( $S/AC \times 100$ ) are plotted against volume fraction of abrasive. The abrasive used was 4.5  $\mu\text{m}$  SiC particles. The abrasive mode is dependent of abrasive concentration. For low concentrations of abrasives a 2-body grooving abrasion process dominates, whereas 3-body rolling abrasion processes dominate in case of higher concentrations.

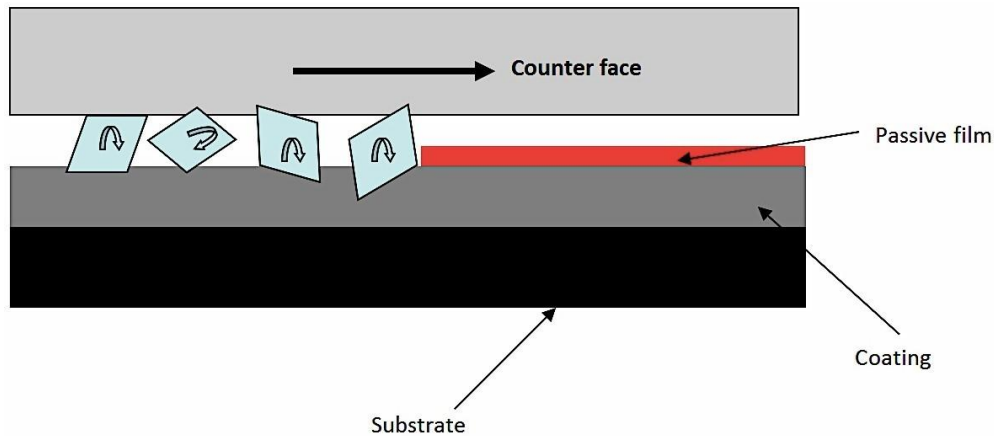


Figure 13 – Schematic showing depassivation of a passivating coated surface by three body rolling abrasion induced by relative motion between the coated surface and a counter face [91].

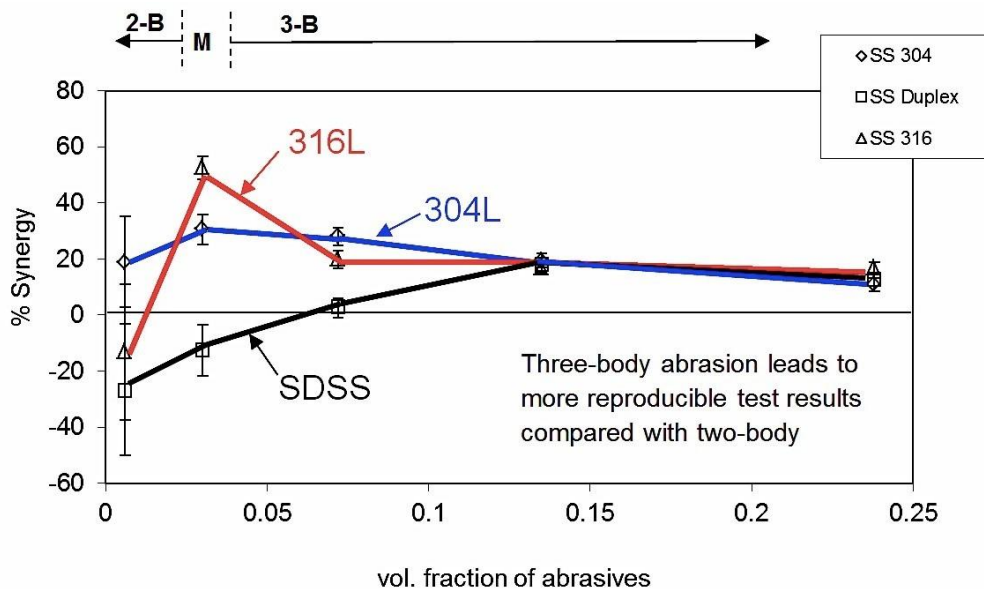


Figure 14 – Synergy % (S) vs. volume fraction of the abrasives for UNS S30403, S31603 and S32760. Low volume fraction of abrasive gives 2 body grooving abrasion while higher concentration generate 3-body rolling abrasion. Intermediate concentrations caused a mixed 2 and 3-body mode (M on figure) [91].

It can be seen from fig. 14 that the synergy resulting from a two-body wear mode was highly variable as evident by the large degree of scatter. Both S31603 and S32760



stainless steels produced negative values of  $S$  under this wear condition while  $S$  was positive for S30403. The large negative synergies produced by the two-body wear mechanism may be a reflection of the differences in repassivation kinetics and/or composition of the passive films reducing the overall level of two-body abrasion [91]. However, the mixed-mode region shows a significant reduction in scatter for each stainless steel. Likewise, all three stainless steel types within the three-body region showed improved reproducibility with increasing volume fraction of abrasive.

## 7.2. Erosion-corrosion

As mentioned in section 1, systems associated with energy extraction and generation suffer from multiple types of tribocorrosion and pipe flow systems in particular can suffer from solid particle erosion-corrosion (section 5.1). Due to the poor understanding of the physical erosion-corrosion mechanisms and their interaction, engineers face problems in predicting the erosion-corrosion rates, since no robust model is currently available that can aid component life modelling, material loss rates and locate vulnerable spots to localized high loss rates by erosion-corrosion [14]. Within nCATS, stainless steel type 316 was investigated as a model system for passive metals used in pumps, pipelines, valves etc. used in oil and gas sector and hydroelectric schemes (section 3.2) [42]. It is recognised that in the oil and gas sector there is an overwhelming use of carbon steel [92-95] and the atmosphere is mostly sweet ( $\text{CO}_2$ ) with no oxygen and specific filming behaviour is seen which impacts on erosion-corrosion rates. In passive materials this can affect recovery. For research into this area see references [92-95].

Focus has been on the evaluation of the synergistic or interactive terms to allow the total loss rate to be estimated based on separate erosion and corrosion data. As for abrasion-corrosion, synergy can be defined as the difference between erosion-corrosion and the summation of its two parts, and can be expressed by equations (2):

$$S = T - (C + E) \quad (2)$$

Where:

- T = gravimetric term relating to erosion-corrosion,
- C = gravimetric term relating to pure (flow) corrosion,
- E = gravimetric term relating to pure erosion, and
- S = gravimetric term relating to synergy.

Typically the evaluation of  $S$  will include an accumulation of errors associated with  $T$ ,  $E$  and  $C$  measurements and as such values for  $S$  should always be accompanied by quantified errors [14]. In addition, great care should be taken when obtaining pure mechanical loss rates as, for example, applying a cathodic potential to materials can alter their microstructure and mark the surface, thereby, influencing the loss rates. Synergy can be broken down into two components,  $\Delta E$  and  $\Delta C$ , where  $\Delta E$  is the corrosion-enhanced erosion and  $\Delta C$  is the erosion-enhanced corrosion, see equation (3).

$$S = \Delta E + \Delta C \quad (3)$$

There have been various attempts to attribute mechanisms to explain  $S$  values, which can be positive (synergistic) or negative (antagonistic) [14].

## 7.3. Downhole drilling

The downhole drilling companies encounter a major problem concerning high torque and drag that are exacerbated when directional drilling techniques are used. Hence,

reducing friction is key to reducing the requirements of drilling equipment as well as one of the most researched areas by the oil and gas companies [29].

An investigation by Ismail within nCATS used an electrochemical method to control friction and tribocorrosion for AISI 4340-steel/AISI 4340-steel, and AISI 4340 steel/sandstone sliding contacts lubricated by baseline solutions and the downhole drilling muds. The tribometer used was a pin-on-disc, modified to incorporate a three-electrode electrochemical cell allowing potential control of the rotating disc. The overpotential used was in the range of  $\pm 1$  V, the load and speed were kept constant at 50 N and  $0.03\text{ms}^{-1}$  respectively (to replicate downhole conditions to aqueous drilling muds). Lubrication involved the addition of electroactive friction modifier additives to allow electrochemical friction control [29].

No dependence of friction on over-potential was seen for the steel/sandstone contact when using the bentonite mud only. However, the octanoate additive resulted in lower friction at anodic over-potentials. The two contact arrangements employed, (i) steel pin/sandstone disc, and (ii) sandstone disc/steel pin, both yielded similar friction behaviour [29]. X-ray Photoelectron Spectroscopy (XPS) of worn surfaces of steel suggested the formation of a weak octanoate tribofilm at cathodic overpotentials, most likely caused by loosely packed adsorption. However, a robust tribofilm was observed at the anodic overpotentials due to the development of a relatively close-packed adsorption layer, which correlates with low values of current density that supports passivating the surface by forming a tribofilm, [29].

## **8. Automotive engines: tribochemistry**

Newly developed advanced materials offer lighter and stronger vehicles, but along come the challenges of appropriate lubrication of these new materials. In addition, with the growing concern for the environment, lubricant suppliers are put under extreme pressure to limit sulphur and phosphorous contents in engine oils, which are known to majorly contribute in the reduction of friction and wear in IC engines by forming a surface tribofilm. Obtaining optimum durability and fuel economy of tribological systems, especially where new materials and coatings or surface treatments are used relies on compatibility between the surface and the lubricant [96].

The use of DLC coatings in automotive engines is increasingly adopted by companies to the growing demand of improved fuel economy, emission reduction and component durability of passenger cars and the challenges associated with it [97,98].

A comprehensive study conducted by Neville et al. [96-99], showed that interactions of Zinc Dialkyldithiophosphate (ZDDP) and/or friction modifiers significantly influence the durability of DLC coating in the cam/follower tests, which was mainly controlled by the antiwear performance of additives, which in turn strongly influenced the mechanism of DLC wear. However, poor wear protection caused structural graphitisation of DLC coating making it darker than normal. This also caused reduction of hardness and increase in modulus leading to a gradual polishing wear of DLC coating [98,99].

Further studies conducted by Booth et al. [100,101], Penchaliah et al. [102,103], Harvey and Colleagues [104-108] reviewed mostly the electrostatic monitoring technique used for monitoring lubricated sliding contacts. The electrostatic charge

depends on material wear and charge species present in the lubricant (additives and contaminants).

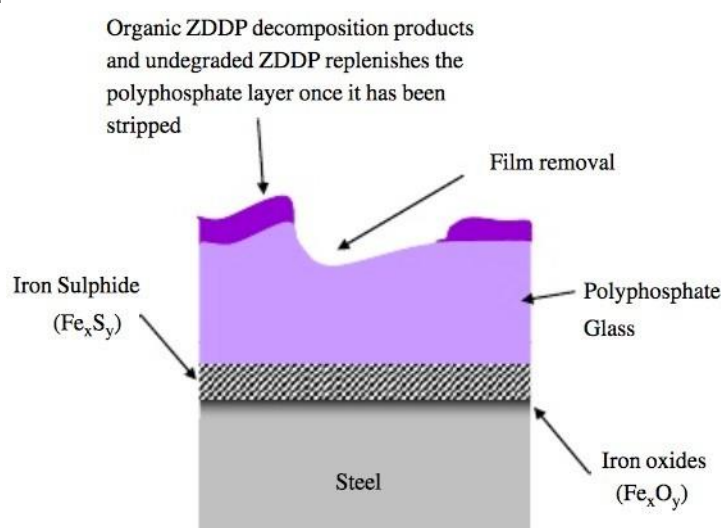


Figure 15 – three layers of a fully developed ZDDP antiwear film [100].

Booth et al. [100,101] presented investigation of additive-additive and additive-carbon black interaction, carried out on a pin-on-disc (PoD) tribometer. Results of online electrostatic charge and coefficient of friction measurements were recorded, along with post-test Electro-kinetic Sonic Amplitude (ESA) measurements, and pin and disc material loss was measured using three-dimension profilometry. Analysis of Variance (ANOVA) was used in order to statistically examine the obtained results to reveal interactions [100].

From the result obtained from Booth's work, primary ZDDP was found to form immature antiwear film that increased pin wear (see figure 15). It was verified from the electrostatic charge data, EAS and pin material loss measurement that interactions between carbon black and detergent, as well as carbon black and dispersant did occur, showing a complex formation between ZDDP and the dispersant [100,101]. Harvey and Morris concentrated mainly on monitoring of wear debris using electrostatic sensing, effects of oil-lubricants and lubricant chemistry effects on the electrostatic charge generation and transports, and investigation of the electrostatic charging mechanisms in oil-lubricated tribo-contacts including ceramics, composites and steel [104-109], whereas, Penchaliah's work involved the effects of diesel contaminants and carbon black on tribological performance of sliding contacts [102-103].

## 9. Conclusions

- Tribocorrosion is a growing research area for energy related applications and some examples of the breadth of the types of wear and corrosion interactions have been presented based on the research conducted within the national Centre for Advanced Tribology at Southampton(nCATS).
- The research into tribocorrosion at nCATS covers various energy sectors including: oil & gas production and exploration, nuclear, power generation, diesel engines, renewable energy (marine etc). It also covers interactions of multiple wear mechanisms such as fretting, sliding, erosion and abrasion with a corrosive environment or a complex biofilm induced corrosion environment.
- The approach taken within nCATS is to link the mechanical stimuli to the chemical/electrochemical processes and material science to allow a full

understanding of the surface degradation processes and to allow accurate modelling to start to be developed.

- a. The renewal of Nuclear energy plant in the UK is a potential growth area for UK tribocorrosion researchers to tap into.
- b. Consistent research funding is required by the energy sector in order to make progress towards predictive tools for applications suffering from tribocorrosion.

## Acknowledgement

ASTM for funding for the travel to the 3<sup>rd</sup> International Tribocorrosion conference at Georgia Institute of Technology, Atlanta in 2012.

## References

- [1]. Mathew, M. T., Pai, P. S., Pourzal, R., Fischer, A., and Wimmer, M. A., "Significance of Tribocorrosion in Biomedical Applications: Overview and Current Status," *Advances in Tribology*, Vol. 2009, 2009, 250986.
- [2]. Landolt, D. and Mischler, S., *Tribocorrosion of Passive Metals and Coatings*, EPFL Woodhead, Lausanne, Switzerland, 2011.
- [3]. Wood, R. J. K., "Tribocorrosion," *Shreir's Corrosion*, Vol. 2, R. A. Cottis, M. J. Graham, R. Lindsay, S. B. Lyon, and J. A. Richardson, Eds., Elsevier Science, New York, 2010, pp. 1005–1051.
- [4]. Iwabuchi, A., Lee, J. W., and Uchida, M., "Synergistic Effect of Fretting Wear and Sliding Wear of Co-Alloy and Ti-Alloy in Hank's Solution," *Wear*, Vol. 263, 2007, pp. 492–500.
- [5]. Mischler, S. and Ponthiaux, P., "A Round Robin on Combined Electro-chemical and Friction Tests on Alumina/Stainless Steel Contacts in Sulphuric Acid," *Wear*, Vol. 248, 2001, pp. 211–225.
- [6]. Proverbio, E. and Bonaccorsi, L. M., "Erosion-Corrosion of a Stainless Steel Distillation Column in Food Industry," *Eng. Failure Anal.*, Vol. 9, 2002, pp. 613–620.
- [7]. Park, M., "Engine Failure Caused by Erosion-Corrosion of Fuel Manifold," *Eng. Failure Anal.*, Vol. 9, 2002, pp. 673–681.
- [8]. Bjordal, M., Bardal, E., Rogne, T., and Eggen, T. G., "Combined Erosion and Corrosion of Thermal Sprayed WC and CrC Coatings," *Surf. Coat. Technol.*, Vol. 70(2–3), 1995, pp. 215–220.
- [9]. Bjordal, M., Bardal, E., Rogne, T., and Eggen, T. G., "Erosion and Corrosion Properties of WC Coatings and Duplex Stainless Steel in Sand-Containing Synthetic Sea Water," *Wear*, Vol. 186–187, 1995, pp. 508–514.
- [10]. Tu, J. P., "The Effect of TiN Coating on Erosion-Corrosion Resistance of a-Ti Alloy in Saline Slurry," *Corros. Sci.*, Vol. 42, 2000, pp. 147–163.
- [11]. Wood, R. J. K., Wharton, J. A., Speyer, A. J., and Tan, K. S., "Investigation of Erosion-Corrosion Processes Using Electrochemical Noise Measurements," *Tribol. Int.*, Vol. 35, 2002, pp. 631–641.
- [12]. Speyer, A. J., Wood, R. J. K., and Stokes, K. R., "Erosion of Aluminium-based Claddings on Steel by Sand in Water," *Wear*, Vol. 250, 2001, pp. 802–808.
- [13]. Keck, R.G., "Prediction and mitigation of erosive-corrosive wear in steam extraction piping," PhD thesis, Dept. of Mechanical Engineering, Massachusetts Institute of Technology, Massachusetts, USA (1987).
- [14]. Wood, R. J. K., Uchida, M., Thakare, M. R., and Sato, Y., "Tribocorrosion Issues in the Energy Sector," *Tribol. Int.* (submitted).
- [15]. Neville, A., Hodekeiss, T., and Dallas, J. T., "A Study of the Erosion-Corrosion Behaviour of Engineering Steel for Marine Pumping Applications," *Wear*, Vol. 186–187, 1995, pp. 497–507.

- [16]. Hamzah, R., Stephenson, D. J., and Strutt, J. E., "Erosion of Material Used in Petroleum Production," *Wear*, Vol. 186–187, 1995, pp. 493–496.
- [17]. ASTM G119-93, 1993, "Standard Guide for Determining Synergism between Wear and Corrosion," *Annual Book of ASTM Standards*, ASTM International, West Conshohocken, PA, Vol. 03.02.
- [18]. ASTM G3, 2010, "Standard Practice for Conventions Applicable to Electrochemical Measurements in Corrosion Testing," *Annual Book of ASTM Standards*, Vol. 3.02, ASTM International, West Conshohocken, PA.
- [19]. ASTM G5, 2011, "Standard Reference Test Method for Making Potentiostatic and Potentiodynamic Anodic Polarization Measurements," *Annual Book of ASTM Standards*, Vol. 3.02, ASTM International, West Conshohocken, PA.
- [20]. ASTM G15, 2004, "Standard Terminology Relating to Corrosion and Corrosion Testing," *Annual Book of ASTM Standards*, Vol. 3.02, ASTM International, West Conshohocken, PA.
- [21]. ASTM G40-12, 2012, "Standard Terminology Relating to Wear and Erosion," *Annual Book of ASTM Standards*, Vol. 3.02, ASTM International, West Conshohocken, PA.
- [22]. ASTM G59-97, 2009, "Standard Test Method for Conducting Potentiodynamic Polarization Resistance Measurements," *Annual Book of ASTM Standards*, Vol. 3.02, ASTM International, West Conshohocken, PA.
- [23]. ASTM G102-89, 2010, "Standard Practice for Calculation of Corrosion Rates and Related Information from Electrochemical Measurements," *Annual Book of ASTM Standards*, Vol. 3.02, ASTM International, West Conshohocken, PA.
- [24]. Wood, R. J. K. and Fry, S. A., "The Synergistic Effect of Cavitation Erosion and Corrosion for Copper and Cupro-nickel in Seawater," *J. Fluids Eng.*, Vol. 111, 1989, pp. 271–277.
- [25]. Wood, R. J. K. and Fry, S. A., "Corrosion of Pure Copper in Flowing Seawater under Cavitating and Non-cavitating Flow Conditions," *J. Fluids Eng.*, Vol. 112, 1990, pp. 218–224.
- [26]. Wood, R. J. K., Hutton, S. P., and Schiffrin, D. J., "Mass Transfer Effects of Non-cavitating Seawater on the Corrosion of Cu and 70-30 Cu-Ni," *Corros. Sci. J.*, Vol. 30(12), 1990, pp. 1177–1181, 1183–1201.
- [27]. Wood, R. J. K., "Use of Profilometric Measurements in Cavitation Erosion and Corrosion Studies," *Proc. Inst. Mech. Eng., Part C: J. Mech. Eng. Sci.*, Vol. 204, 1990, pp. 63–65.
- [28]. Wood, R. J. K. and Hutton, S. P., "The Synergistic Effect of Erosion and Corrosion: Trends in Published Results," *Wear*, Vol. 140(2), 1990, pp. 387–394.
- [29]. Ismail, M. N. F., 2010, "Reduction of Downhole Friction by Electrochemical Methods," Ph.D. thesis, University of Southampton, Southampton, UK.
- [30]. Stack, M., Abdelrahman, S., and Jana, B., "A New Methodology for Modelling Erosion-Corrosion Regimes on Real Surfaces: Gliding Down the Galvanic Series for a Range of Metal Corrosion Systems," *Wear*, Vol. 268(3–4), 2010, pp. 533–542.
- [31]. Wood, R. J. K., Bahaj, A.-B. S., Turnock, S. R., Wang, L., and Evans, M.-H., "Tribological Design Constraints of Marine Renewable Energy Systems," *Philos. Trans. R. Soc. London, Ser. A*, Vol. 368(1929), 2010, pp. 4807–4827.
- [32]. Berg, H.-P., "Corrosion Mechanisms and Their Consequences for Nuclear Power Plants With Light Water Reactors," *Reliability and Risk Analysis: Theory and Applications*, Vol. 2, 2009, pp. 57–68.
- [33]. Dixon, S. L., *Fluid Mechanics and Thermodynamics of Turbomachinery*, 5th ed., Elsevier Butterworth-Heinemann, Burlington, MA01803, USA, 2010.
- [34]. Farhat, M. and Avellan, F., "On the Detachment of a Leading Edge Cavitation," *CAV2001*, Swiss Federal Institute of Technology, Lausanne, Switzerland, 2001.
- [35]. Choi, J.-K., Jayaprakash, A., and Chahine, G. L., "Scaling of Cavitation Erosion

- Progression With Cavitation Intensity and Cavitation,” *Wear*, Vol. 278–279, 2012, pp. 53–61.
- [36]. Hammitt, F. G., “Damage to Solids Caused by Cavitation,” *Philos. Trans. R. Soc. London, Ser. A*, Vol. 260(1110), 1966, pp. 245–255.
- [37]. Morch, K. A., “Dynamics of Cavitation Bubbles and Cavitating Liquids,” *Treatise on Materials Science and Technology*, Vol. 16, 1979, pp. 309–355.
- [38]. Blake, J. R., Taib, B. B., and Doherty, G., “Transient Cavities Near Boundaries. Part I. Rigid Boundary,” *J. Fluid Mech.*, Vol. 170, 1986, pp. 479–497.
- [39]. Chen, D., Wang, J., and Chen, H., “Key Factors to Induce Cavitation-Erosion,” *Advanced Tribology: Proceedings of CIST2008 & ITSIFTtoMM2008*, Held in Beijing, on 24th–27th September 2008 Jointly published by Springer and Tsinghua University Press in Beijing, China, 2010, p. 31.
- [40]. DM&ME, 2012, “Cavitation and Its Control.” <http://www.dmme-engineering.com/blog/> (Last accessed 31 Oct 2012).
- [41]. Knapp, R. T., Daily, J. W., and Hammit, F. G., *Cavitation*, McGraw-Hill, New York, 1970.
- [42]. Rajahram, S. S., 2010, “Erosion-Corrosion Mechanism in Stainless Steel UNS S31603,” Ph.D. thesis, University of Southampton, Southampton, UK.
- [43]. Rajahram, S. S., Harvey, T. J., Walker, J. C., Wang, S. C., Wood, R. J. K., and Lalev, G., “A Study on the Evolution of Surface and Subsurface Wear of UNS S31603 during Erosion-Corrosion,” *Wear*, Vol. 271(9–10), 2011, pp. 1302–1313.
- [44]. Rajahram, S. S., Harvey, T. J., Walker, J. C., Wang, S. C., and Wood, R. J. K., “Investigation of Erosion-Corrosion Mechanisms of UNS S31603 Using FIB and TEM,” *Tribol. Int.*, Vol. 46, 2012, pp. 161–173.
- [45]. Sutton, D., 2010–2014, “The Effects of Interfacial Chemistry on the Tribology of Diamond-like Carbon Coatings against 52100 Steel in Distilled Water,” Ph.D. thesis, University of Southampton, Southampton, UK.
- [46]. Chen, J. M., “Friction-induced Physical and Chemical Interactions among Diamond-like Carbon Film, Steel Ball and Water and/or Oxygen Molecules,” *Diamond Relat. Mater.*, Vol. 15(9), 2006, pp. 1228–1234.
- [47]. Ronkainen, H. and Holmberg, K., “Environmental and Thermal Effects on the Tribological Performance of DLC Coatings,” *Tribology of Diamond-Like Carbon Films*, Volume editors: Christophe Donnet, Ali Erdemir, Springer, New York, 2008, pp. 155–200.
- [48]. Park, S. J., Lee, K. R., and Ko, D. H., “Tribochemical Reaction of Hydrogenated Diamond-Like Carbon Films: A Clue to Understand the Environmental Dependence,” *Tribol. Int.*, Vol. 37(11–12), 2004, pp. 913–921.
- [49]. Andersson, J., Erck, R. A., and Erdemir, A., “Frictional Behavior of Diamondlike Carbon Films in Vacuum and under Varying Water Vapor Pressure,” *Surf. Coat. Technol.*, Vol. 163, 2003, pp. 535–540. 863
- [50]. Li, R., Pellegrini, M., Ninokata, H., and Mori, M., “A Numerical Study on Turbulence Attenuation Model for Liquid Droplet Impingement Erosion,” *Ann. Nucl. Energy*, Vol. 38(6), 2011, pp. 1279–1287.
- [51]. Hattori, S., “Effects of Impact Velocity and Droplet Size on Liquid Impingement Erosion,” *International Symposium on the Ageing Management and Maintenance of Nuclear Power Plants*, The university of Tokyo, Fukuishi, Japan, 27<sup>th</sup> – 28<sup>th</sup> May, 2010, pp. 58–71.
- [52]. Sanchez-Caldera, L. E., 1984, “The Mechanisms of Corrosion-Erosion in Steam Extraction Lines of Power Stations,” Ph.D. thesis, Massachusetts Institute of Technology, Cambridge, MA.
- [53]. Xiong, J., Koshizuka, S., Sakai, M., and Ohshima, H., “Investigation on Droplet Impingement Erosion During Steam Generator Tube Failure Accident,” *Nucl. Eng. Des.*, Vol. 249, 2012, pp. 132–139.
- [54]. Koshizuka, S., Naitoh, M., Uchida, S., and Okada, H., “Evaluation Procedures for

- Wall Thinning Due to Flow Accelerated Corrosion and Liquid Droplet Impingement,” International Symposium on the Aging Management and Maintenance of Nuclear Power Plants, The University of Tokyo, 27<sup>th</sup> – 28<sup>th</sup> May, 2010, pp. 18–28.
- [55]. Ikohagi, T., Ebara, S., Fujisawa, N., Hashizume, H., Iwabuchi, A., Satou, M., Uchidate, M., Yamagata, T., and Yashiro, H., “Advanced Wall Thinning Prediction of Liquid Droplet Impingement Erosion,” International Symposium on the Aging Management and Maintenance of Nuclear Power Plants, The University of Tokyo, 27<sup>th</sup>– 28<sup>th</sup> May, 2010, pp. 47–57.
- [56]. Chitty, W. J. and Vernot, J.P., Tribocorrosion of passive metals and coatings: Tribocorrosion Issues in Nuclear Power Generation, pp. 424–440, volume editors: D. Landolt, S. Mischler, published by Woodland Publishing limited, Cambridge, UK, 2011.
- [57]. Park, J.-H., Chopra, O. K., Natesan, K., and Shack, W. J., Boric Acid Corrosion of Light Water Reactor Pressure Vessel Materials, Argonne National Laboratory, Washington, D.C., 2005.
- [58]. Wood, R. J. K., “Tribocorrosion of Coatings: A Review,” J. Phys. D: Appl. Phys., Vol. 40(18), 2007, pp. 5502–5521.
- [59]. Wood, R. J. K., “Erosion-Corrosion Interactions and Their Effect on Marine and Offshore Materials,” Wear, Vol. 261(9), 2006, pp. 1012–1023.
- [60]. Wood, R. J. K., Jones, T. F., Ganeshalingam, J., and Miles, N. J., “Comparison of Predicted and Experimental Erosion Estimates in Slurry Ducts,” Wear, Vol. 256(9–10), 2004, pp. 937–947.
- [61]. Wood, R. J. K. and Jones, T. F., “Investigations of Sand-Water Induced Erosive Wear of AISI 304L Stainless Steel Pipes by Pilot-Scale and Laboratory-Scale Testing,” Wear, Vol. 255(1–6), 2003, pp. 206–218.
- [62]. Wharton, J. A. and Wood, R. J. K., “Electrochemical Noise Measurements to Monitor Flow Corrosion of AISI 304L Stainless Steel,” UK Corrosion, Vol. 1–15, 2002, p. 1589.
- [63]. Wharton, J. A. and Wood, R. J. K., “Flow Corrosion Behaviour of Austenitic Stainless Steels UNS S30403 and UNS S31603,” Corrosion, Vol. 61, 2005, pp. 792–806.
- [64]. Lytron, 2012, “Erosion-Corrosion in Cooling Systems,” <http://www.lytron.com/Tools-and-Technical-Reference/Application-Notes/Erosion-Corrosion-in-Cooling-Systems> (Last accessed 26 Oct 2012).
- [65]. Herro, H. M., “Deposit-related Corrosion in Industrial Cooling Water Systems,” Corrosion, National Association of Corrosion Engineers, New Orleans, Louisiana, 17th–21st April, 1989, pp. 1–9.
- [66]. Deltathx, 2012, “Industrial Heat Exchangers: Corrosion,” [www.deltathx.com/uploadsdocs/corrosion.pdf](http://www.deltathx.com/uploadsdocs/corrosion.pdf) (Last accessed 26 Oct 2012)
- [67]. University of Southampton, 2012, “nCATS,” <http://www.southampton.ac.uk/ncats/Downloads/nCATS%20Launch%20Presentations/nCATS%20Launch%20-%20Dr%20Jeremy%20Webb%20-%20School%20of%20Biological%20Sciences.pdf> (Last accessed 4 Nov 2012).
- [68]. Videla, H. A., “Corrosion Inhibition in the Presence of Microbial Corrosion,” NACE International: Corrosion 96, NACE International, Denver, 24<sup>th</sup>– 29<sup>th</sup> March, 1996.
- [69]. Corrosionclinic, 2012, “Different Types of Corrosion: Microbiologically Influenced Corrosion (MIC),” [http://www.corrosionclinic.com/types\\_of\\_corrosion/microbiologically\\_influenced\\_biologically\\_microbial\\_corrosion.htm](http://www.corrosionclinic.com/types_of_corrosion/microbiologically_influenced_biologically_microbial_corrosion.htm) (Last accessed 26 Oct 2012).
- [70]. Videla, H. A. and Herrera, L. K., “Microbiologically Influenced Corrosion: Looking to the Future,” International Microbiology, Vol. 8(3), 2005, pp. 169–180.
- [71]. Characklis, W. C., “Fouling Biofilm Development: A Process Development,” Biotechnol. Bioeng., Vol. 23, 1981, pp. 1923–1960.

- [72]. Lewandowski, Z. and Beyenal, H., "Mechanisms of Microbially Influenced Corrosion," Marine and Industrial Biofouling, H.-C. Flemming, P. S. Murthy, R. Venkatesan, and K. E. Cooksey, Eds., Springer, New York, 2009, pp. 35–65.
- [73]. Kotzalas, M. N. and Doll, G. L., "Tribological Advancements for Reliable Wind Turbine Performance," Philos. Trans. R. Soc. London, Ser. A, Vol. 368, 2010, pp. 4829–4850.
- [74]. Evans, M.-H., "White Structure Flaking (WSF) in Wind Turbine Gearbox Bearings: Effects of 'Butterflies' and White Etching Cracks (WEC)," Mater. Sci. Technol., Vol. 28, 2012, pp. 3–22.
- [75]. Luycx, J., "Hammering Wear Impact Fatigue Hypothesis WEC/irWEA Failure Mode on Roller Bearings," Wind Turbine Tribology Seminar, Hansen Transmission, Kontich, Belgium, 16<sup>th</sup> Nov 2011.
- [76]. Tamada, K. and Tanaka, H., "Occurrence of Brittle Flaking on Bearings Used for Automotive Electrical Instruments and Auxiliary Devices," Wear, Vol. 199(2), 1996, pp. 245–252.
- [77]. Iso, K., Yokouchi, A., and Takemura, H., "Research Work for Clarifying the Mechanism of White Structure Flaking and Extending the Life of Bearings," SAE World Congress, Detroit, MI, 2005, SAE International, Warrendale, PA., 11<sup>th</sup> April, 2005.
- [78]. NSK, Long Life Bearings for Engine Accessories, Motion & Control NSK, Japan, 2004, pp. 1–10.
- [79]. Kohara, M., Kawamura, T., and Egami, M., "Study on Mechanism of Hydrogen Generation from Lubricants," Tribol. Trans., Vol. 49(1), 2006, pp. 53–60.
- [80]. Kino, N. and Otani, K., "The Influence of Hydrogen on Rolling Contact Fatigue Life and Its Improvement," JSAE Rev., Vol. 24(3), 2003, pp. 289–294.
- [81]. Gegner, J., "Tribological Aspects of Rolling Bearing Failures," Tribology— Lubricants and Lubrication, C.-H. Kuo, Ed., InTech, 2011, pp. 33–94.
- [82]. Schatzberg, P., "Inhibition of Water-accelerated Rolling-contact Fatigue," J. Lubr. Technol., Vol. 93, 1971, pp. 231–233.
- [83]. Fujita, S., Matsuoka, S., Murakami, Y., and Marquis, G., "Effect of Hydrogen on Mode II Fatigue Crack Behavior of Tempered Bearing Steel and Microstructural Changes," Int. J. Fatigue, Vol. 32, 2010, pp. 943–951.
- [84]. Murakami, Y., Kanezaki, T., Mine, Y., and Matsuoka, S., "Hydrogen Embrittlement Mechanism in Fatigue of Austenitic Stainless Steels," Metall. Mater. Trans. A, Vol. 39, 2008, pp. 1327–1339.
- [85]. Lewis, M. N. and Tomkins, B., "A Fracture Mechanics Interpretation of Rolling Bearing Fatigue," Proc. Inst. Mech. Eng., Part J: J. Eng. Tribol., Vol. 226, 2012, pp. 389–485.
- [86]. Evans, M.-H., Richardson, A. D., Wang, L., and Wood, R. J. K., "Investigation of Butterflies and White Etching Cracks (WECs) under Rolling Contact Fatigue in 100Cr6 Bearing Steel Using Serial Sectioning and Focused Ion Beam Tomography," Tribol. Int.
- [87]. Evans, M.-H., Richardson, A. D., Wang, L., and Wood, R. J. K., "Serial Sectioning Investigation of Butterfly and White Etching Crack (WEC) Formation in Wind Turbine Gearbox Bearings," Wear, 2013.
- [88]. Evans, M.-H., Richardson, A. D., Wang, L., and Wood, R. J. K., "Effect of Diffusible Hydrogen on Butterfly and White Etching Crack (WEC) Formation," Wear.
- [89]. Apolinario M, Couthino R. Understanding the biofouling of offshore and deep-sea structures. In: Hellio C, Yebra DMY, editors. Advances in Marine Antifouling Coatings and Technologies. Woodshead Publishing; Cambridge, UK: 2009. pp. 133–147
- [90]. Chambers, L. D., Stokes, K. R., Walsh, F. C., and Wood, R. J. K., "Modern Approaches to Marine Antifouling Coatings," Surf. Coat. Technol., Vol. 201, 2006, pp. 3642–3652.



- [91]. Bello, J. O., Wood, R. J. K., Wharton, J. A., "Synergistic Effects of Micro-Abrasion-Corrosion of UNS S30403, S31603 and S32760 Stainless Steels," *Wear*, Vol. 263, 2007, pp. 149–159.
- [92]. Neville, A., Hodekeiss, T., and Dallas, J. T., "A Study of the Erosion-Corrosion Behaviour of Engineering Steel for Marine Pumping Applications," *Wear*, Vol. 186–187, 1995, pp. 497–507.
- [93]. Neville, A. and Hodekeiss, T., "Characterisation of High-grade Alloy Behaviour in Severe Erosion-Corrosion Conditions," *Wear*, Vol. 233–235, 1999, pp. 596–607.
- [94]. Hamzah, R., Stephenson, D. J., and Strutt, J. E., "Erosion of Material Used in Petroleum Production," *Wear*, Vol. 186–187, 1995, pp. 493–496.
- [95]. Stack, M. M. and Pungwiwat, N., "Particulate Erosion-Corrosion of Al in Aqueous Conditions: Some Perspectives on pH Effects on the Erosion-Corrosion Map," *Tribol. Int.*, Vol. 35, 2002, pp. 651–660.
- [96]. Morina, A., Haque, T., and Neville, A., "Comparing Tribochemical Film Formation and Durability at Steel and CrN Coating Interface in Boundary Lubrication," *Tribology Online*, Vol. 5(4), 2010, pp. 187–194.
- [97]. Haque, T., Morina, A., and Neville, A., "Tribological Performance Evaluation of a Hydrogenated DLC Coating in Sliding/Rolling Contact—Effect of Lubricant Additives," *Proc. Inst. Mech. Eng., Part J: J. Eng. Tribol.*, Vol. 225(6), 2011, pp. 393–405.
- [98]. Haque, T., Morina, A., and Neville, A., "Effect of Friction Modifiers and Antiwear Additives on the Tribological Performance of a Hydrogenated DLC Coating," *J. Tribol.*, Vol. 132(3), 2010, pp. 1–13.
- [99]. Haque, T., Morina, A., and Neville, A., "Influence of Friction Modifier and Antiwear Additives on the Tribological Performance of a Non-hydrogenated DLC Coating," *Surf. Coat. Technol.*, Vol. 204(4), 2010, pp. 4001–4011.
- [100]. Booth, J. E., Nelson, K. D., Harvey, T. J., Wood, R. J. K., Wang, L., Powrie, H. E. G., and Martinez, J. G. "The Feasibility of Using Electrostatic Monitoring to Identify Diesel Lubricant Additives and Soot Contamination Interaction by Factorial Analysis," *Tribol. Int.*, Vol. 39, 2006, pp. 1564–1575.
- [101]. Booth, J. E., 2008, "The Feasibility of Using Electrostatic Charge Condition Monitoring for Lubricant Additive Screening," Ph.D. thesis, University of Southampton, Southampton, UK.
- [102]. Penchaliah, R., Harvey, T. J., Wood, R. J. K., Nelson, K., and Powrie, H. E. G., "The Effects of Diesel Contaminants on Tribological Performance on Sliding Steel on Steel Contacts," *Proc. Inst. Mech. Eng., Part J: J. Eng. Tribol.*, Vol. 225(8), 2011, pp. 779–797.
- [103]. Penchaliah, R., Harvey, T. J., Wood, R. J. K., Nelson, K., Powrie, H. E. G., Wang, L., and Yamaguchi, E. S., "Electrostatic Monitoring of the Effects of Carbon Black on Lubricated Steel/Steel Sliding Contacts," *Tribology and Interface Engineering Series*, Vol. 48, 2005, pp. 109–121.
- [104]. Harvey, T. J., Wood, R. J. K., Wang, L., Powrie, H. E. G., and Morris, S., "Real-time Monitoring of Wear Debris Using Electrostatic Sensing Techniques," *Proc. Inst. Mech. Eng., Part J: J. Eng. Tribol.*, Vol. 221(1), 2007, pp. 27–40.
- [105]. Harvey, T. J., Wood, R. J. K., Powrie, H. E. G., and Denuault, G., "Effect of Oil Quality on Electrostatic Charge Generation and Transport," *J. Electrostat.*, Vol. 55(1), 2002, pp. 1–23.
- [106]. Harvey, T. J., Wood, R. J. K., Powrie, H. E. G., and Denuault, G., "Investigation of Electrostatic Charging Mechanisms in Oil Lubricated Tribo-contacts," *Tribol. Int.*, Vol. 35(9), 2002, pp. 605–614.
- [107]. Wang, L., Wood, R. J. K., Harvey, T. J., Morris, S., Powrie, H. E. G., and Care, I., "Wear Performance of Oil Lubricated Silicon Nitride Sliding against Various Bearing Steels," *Wear*, Vol. 255(1–6), 2003, pp. 657–668.
- [108]. Wang, L., Wood, R. J. K., Harvey, T. J., Morris, S., Powrie, H. E. G., and Care, I.,

- "Feasibility of Using Electrostatic Monitoring for Oil Lubricated Ceramic to Steel Sliding Contacts," Tribological Research and Design for Engineering Systems, Proceedings of the 29th Leeds-Lyon Symposium on Tribology, Tribology Series, Elsevier, The Netherlands, Vol. 41, 2002, pp. 625–635.
- [109]. Wang, L., Wood, R. J. K., Powrie, H. E. G., and Care, I., "Electrostatic Wear Sensing of Ceramics–Steel Lubricated Contacts," Transient Processes In Tribology, Vol. 43: Proceedings of the 30th Leeds-Lyon Symposium on Tribology (Tribology and Interface Engineering), Elsevier, Leeds-Lyon, 2004, pp. 711–720.

# Appendix C

---

Journal paper published under Journal of Bio- and Tribo-corrosion (2015): “The synergistic effects of cavitation erosion-corrosion in ship propeller materials.”

# The Synergistic Effects of Cavitation Erosion–Corrosion in Ship Propeller Materials

J. Basumatary<sup>1</sup> · M. Nie<sup>1</sup> · R. J. K. Wood<sup>1</sup>

Received: 15 December 2014 / Revised: 3 March 2015 / Accepted: 5 March 2015 / Published online: 25 March 2015  
© Springer International Publishing AG 2015

**Abstract** Synergy tests were performed for two most common propeller materials, duplex stainless steel (DSS) and nickel aluminium bronze (NAB), by means of an indirect ultrasonic vibratory system. Tests were conducted for pure cavitation erosion in distilled water, pure corrosion using in situ electrochemistry under 3.5 % NaCl solution and a combination of cavitation erosion–corrosion to understand the overall synergism existing between the two. The results were analysed using gravimetric as well as volumetric analysis. Alicona and Talysurf were employed for the surface topography, and scanning electron microscope was used to see the microstructural morphologies of the samples under different conditions. As a result, the electrochemical tests held at open circuit potential showed that, although DSS exhibited higher resistance to corrosion under seawater alone, NAB exhibited much higher resistance to corrosion when subjected to cavitation. From the experiments conducted, it was concluded that synergy had measurable impact on the cavitation erosion–corrosion of both NAB and DSS. NAB was found to be more susceptible to erosion under both the conditions as compared to DSS with prominent selective cavitation erosion of alpha phase in the microstructure. The overall synergism of NAB was found to be higher than that of DSS.

**Keywords** Cavitation · Cavitation erosion · Cavitation erosion–corrosion · Propeller materials · Nickel aluminium bronze · Duplex stainless steel

## 1 Introduction

The simultaneous existence of mechanical erosion and electrochemical corrosion is a common scenario for engineering alloys used in marine environments, such as pump impellers and valves. The situation is further complicated by the fact that the effects of erosion and corrosion are in general not additive owing to the interaction between them. The overall damage arising from erosion and corrosion including the interaction between them is termed cavitation erosion–corrosion. The relative significance of corrosion, erosion and the interaction between them depends on the material and the environment system [1]. The nature of the interaction is determined by a number of factors, the more important ones being the passivity of the metal surface, the adherence of the corrosion product, the metallurgical state of the metal, the significance of the diffusion of dissolved oxygen, the presence of aggressive ions and the intensity of cavitation. These factors would determine the mode of corrosion and the rate of erosion–corrosion loss [2–4].

Several studies have been conducted and proven the existence of synergy between cavitation erosion and corrosion, and that this synergy can have a significant effect on the cavitation behaviour of the test materials [5–12]. Vyas and Hansson [1] conducted the ultrasonic vibrating cavitation on stainless steel (SS) in 3.5 % NaCl solution, and they found that the degree of intergranular corrosion of the sensitized SS increased with increasing cavitation density. They confirmed that for stainless steels due to the existence of the passive film, cavitation could accelerate or decelerate corrosion, depending on the intensity of cavitation and the metallurgical state of the SS specimens. Tomlinson and Talks [3] studied the cavitation erosion–corrosion of various types of cast iron in 3 % sodium chloride solution and found that the fractional weight loss due to pure corrosion ranged

---

✉ J. Basumatary  
jan.basumatary@gmail.com

<sup>1</sup> National Centre of Advanced Tribology in Southampton (nCATS), University of Southampton, Southampton, UK

from 1 to 10 %, while that due to corrosion-induced erosion ranged from 16 to 90 %. Between 1998 and 2006, Kwok C.T. performed several experiments on laser-treated metals such as austenitic steel alloy and NiCrSiB alloy in 3.5 % NaCl solution. It was found that the synergism was responsible for 50–70 % of total loss for laser-alloyed 1050 steel specimen and 20 % for laser surface-alloyed 316 SS specimen, and the cavitation erosion–corrosion resistance was noticed improved for 1050 and 316 SS, respectively [13–18]. In 2000, Kwok, Chen and Man conducted another ultrasonic vibrating cavitation at 20 kHz on nine different kinds of metals including cast irons and SS under 3.5 % NaCl solution [19]. From the experimental results, it was found that synergism had a significant effect on mass loss with up to 85 % total damage. This synergy effect was found to be due to several factors such as impact of corrosive solution, the material property and also the type of materials itself. The most significant impact was found at a mild corrosive environment [4, 20–22].

Few studies have also been conducted on ship propeller materials such as SS, copper alloys, manganese bronze and nickel aluminium bronze (NAB) among others. A synergy experiment conducted by Kwok, Cheng and Man ranked austenitic (304) stainless steels to have very high cavitation erosion resistance than austenitic 316 SS owing to its higher martensitic transformability and work hardenability and lower stacking fault energy of  $25 \text{ mJ m}^{-2}$  [23]. They also concluded that materials with high corrosion resistance such as copper alloys also displayed higher resistance to the erosion–corrosion synergy. They established that the effect of cavitation on corrosion behaviour particularly depended on two main effects of cavitation, corrosion film detachment and increase of mass transport [10]. Several cavitation corrosion tests were conducted by Al-Hashem, Caseres, Riad and Shalaby on propeller materials like cast-nickel aluminium bronze (NAB) and duplex stainless steel (DSS) in seawater using 20-kHZ ultrasonic vibrator under free corrosion and cathodic protection conditions, and they found that for DSS, the rate of mass loss was reduced by 19 % under cathodic protection, slightly reducing the subsequent number of cavities as a result. The attack was seen to be concentrated in the austenite phase but was eventually seen to spread to the ferrite phase. This was associated with ductile tearing, cleavage-like facets, river patterns and crystallographic steps at later stages. Specimen cross-sections revealed microcracks at the bottom of the cavities initiating from the ferrite matrix with crack propagation impeded by the austenite islands, branching along the parallel slip systems. They also observed an active shift in the free corrosion potential by about 140 mV when cavitation was applied, with a slight increase in the cathodic and anodic currents, shifting the corrosion potential in the noble direction by 75 mV [24].

However, their cavitation corrosion test of NAB showed a decrease of rate of mass loss by 47 % under cathodic protection and a shift in corrosion potential in the active direction by 70 mV. This could be attributed to the cushioning of bubble collapse by cathodic gas and elimination of electrochemical dissolution. They also observed under the optical and scanning electron microscopy that NAB seemed to suffer from selective corrosion of the copper-rich  $\alpha$  phase at its boundaries with intermetallic  $\kappa$  precipitates, while the  $\kappa$  precipitates and precipitate-free areas did not suffer corrosion. Also, it was found that selective corrosion was enhanced by cavitation erosion. Under only cavitation, large cavities were found with  $\alpha$ – $\kappa$  grain-boundary corrosion around the pit edge, whereas, in the presence of cathodic protection, the number of cavities was found to increase but the grain-boundary attack was seen to be absent. They also found microcracks of  $5 \mu$  to  $10 \mu\text{m}$  length were observed in the  $\alpha$  phase adjacent to  $\kappa$  precipitates along the cross section of the material. Selective phase corrosion and cavitation stresses were implicated as the causes of cracking [25, 26].

However, despite all the studies done so far, the study on synergistic effects existing between erosion and corrosion were usually carried out under different conditions by different authors, making results difficult to compare. Synergy can be measured in terms of two most common factors, mass loss incurred by combined contribution of erosion and corrosion or the mean depth of penetration (MDP) rate. The equation for synergy is commonly written as

$$T = S + E + C. \quad (1)$$

Here,  $T$  is the total mass loss or overall cavitation erosion–corrosion rate,  $C$  is the pure corrosion contribution;  $E$  is the pure erosion contribution, and  $S$  is the combined contribution due to synergistic effect.  $S$  can be also represented as in Eq. 2:

$$S = T - (E + C) = \Delta E + \Delta C, \quad (2)$$

where  $\Delta E$  = corrosion-enhanced erosion and  $\Delta C$  = erosion-enhanced corrosion. The present study was carried out in order to understand the existence of synergism between erosion and corrosion in the overall cavitation erosion–corrosion damage of the two most commonly used ship propeller materials, 2205 DSS and CuAl10Ni cast-NAB in 3.5 % NaCl solution at room temperature [10].

## 2 Experimental Method

The experiment for synergy between cavitation erosion–corrosion was conducted using indirect ultrasonic cavitation rig. Although several tests have been conducted in the

past using an ASTM G-32 direct cavitation system where a round sample disc is threaded into the probe tip; however, the contact between the sample material and the probe material could render electrochemical analysis difficult and could cause possible galvanic corrosion between the two resulting in either over- or under-evaluation of the corrosion-induced loss, and hence an indirect ultrasonic vibratory cavitation system was used instead of the direct system. Ultrasonic vibratory transducer UIP1000hd with a sonotrode horn made from titanium of diameter 15.9 mm was used for the cavitation experiment at a frequency of 20 kHz and a peak-to-peak amplitude of 80 micron at room temperature of  $17 \pm 0.5$  °C. The test samples were placed under an ultrasonic transducer with a vibrating probe of diameter 15.9 mm kept at a distance of 2 mm above the specimen surface for 1 h. The samples were tested for cavitation erosion in 5 L of distilled water, for cavitation corrosion in 5 L of 3.5 % NaCl aqueous solution using in situ electrochemistry kept at open circuit potential (OCP) and finally for cavitation erosion–corrosion in 3.5 % NaCl solution with in situ electrochemistry kept at OCP.

Precision weighing machine ( $\pm 0.01$  mg) was used to measure the gravimetric mass loss of each sample. Alicona measurements were taken using Alicona 3D optical profilometer to measure the volumetric mass loss of the samples along with surface roughness of cavitated regions and compared with each other, as well as surface topography. Form Talysurf 120 L was also employed to capture the overall surface roughness. Scanning electron microscopy was used to analyse the different microstructures obtained under different conditions and cavitation environment to compare the samples.

## 2.1 Propeller Materials Used

The materials used were 25 × 25-mm specimen samples of 2205 DSS and NAB with a thickness of 5 mm held under the horn with Perspex fixture for the indirect cavitation process. The surfaces of all the test samples were wet-polished using 1200 and 4000 grit silicon carbide (SiC) abrasive papers. Table 1 gives the mechanical properties of the ship propeller materials used for the experiment, and Table 2 gives the chemical compositions of the test materials used.

Ship propellers work in a very harsh environment under the sea, i.e. in a corrosive environment, for the majority of

their lifetime. Hence, it is only reasonable for the chosen test materials to be based not only on their high tensile strength but also on their resistance to corrosion. DSS has been well known for its high resistance to intergranular corrosion, hence they serve as great raw material for building the propellers. DSS used for the experiment was type 2205. Mechanical properties were 774 MPa ultimate tensile strength, 542 MPa yield strength with 34 % elongation and 233 Hv Vickers hardness. The microstructure consisted of a ferritic matrix with islands of austenite grains as shown in Fig. 1. DSS displays properties characteristic of both austenitic and ferritic stainless steels due to their composite microstructure and are found to be, in most cases, tougher than ferritic SS and have higher strength as well as corrosion resistance as compared to the generally used engineering austenitic SS [27].

Similarly, NAB is another lightweight conventional ship propeller alloy used for the experiment for its high-strength mechanical properties with an ultimate tensile strength of 650 MPa, yield strength of 270 MPa and 170 Hv Vickers hardness. It is also considered to exhibit excellent cavitation resistance against the seawater [26]. NAB has high ability to retain its original smooth machined surface over a long period of time, thereby retaining its high efficiency factor, and it also has the ability to resist failure under impact when notched, contributing greatly to its value as a

**Table 2** Chemical compositions of the materials used for the research

Material alloys composition (wt.%)	Nickel aluminium bronze	Duplex stainless steel (2205)
C (%)	–	0.024
Mn (%)	1.07	1.83
Ni (%)	4.73	5.66
Cr (%)	–	22.7
Mo (%)	–	3.01
Cu (%)	–	0.22
Sn (%)	<0.01	–
Al (%)	9.39	–
Pb (%)	0.01	–
Zn (%)	0.11	–
Fe (%)	4.53	–
W (%)	–	0.02
N (%)	–	0.02

**Table 1** Mechanical properties of the materials used for the research

Propeller material alloys	Ultimate tensile strength (MPa)	Yield strength (MPa)	Elongation (%)	Density (g/cm <sup>3</sup> )	Hardness (Hv)
2205 (duplex stainless steel)	774	542	34	7.8	233
Nickel aluminium bronze (NAB)	650	270	18	7.65	170



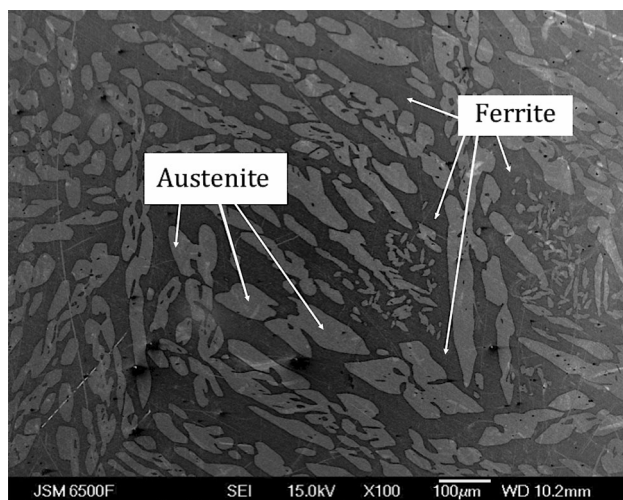
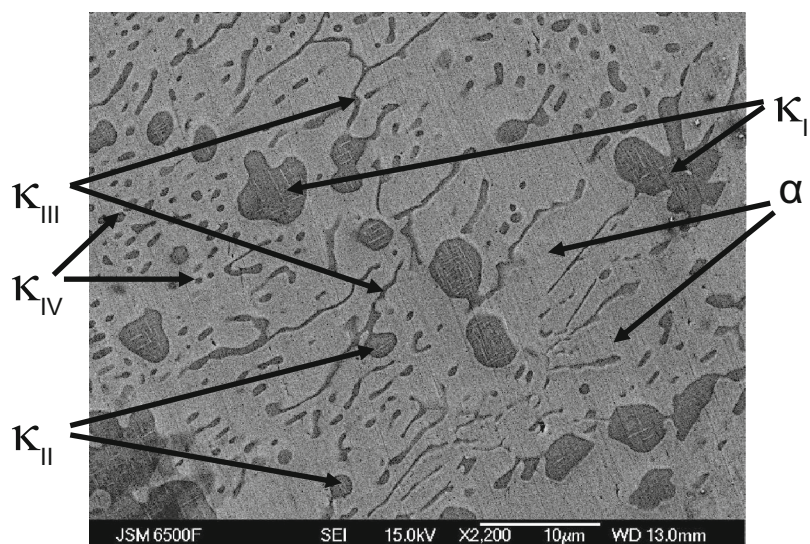


**Fig. 1** SEM morphology of a two-phase microstructure of austenite and ferrite grains of 2205 duplex stainless steel

propeller material [26]. The microstructure of NAB is more complex than DSS with three distinct phases namely  $\alpha$ ,  $\beta$  and four forms of kappa ( $\kappa_I$ ,  $\kappa_{II}$ ,  $\kappa_{III}$  and  $\kappa_{IV}$ ) in the as-cast microstructure. The microstructure generally consists of columnar grains of fcc copper-rich solid solution known as  $\alpha$  phase and a small volume fraction of lamellar eutectoid phases  $\beta'$  phase or martensitic  $\beta$  phase, surrounded by a series of intermetallic  $k$  phases. The  $\kappa_I$ ,  $\kappa_{II}$  and  $\kappa_{IV}$  phases are all iron-rich precipitates distributed in the nickel aluminium structure. Among these intermetallic compounds,  $\kappa_I$  phase is rosette-shaped precipitate formed at high temperatures in high-Fe content alloys and hence is coarser than the rest,  $\kappa_{II}$  phase is smaller than  $\kappa_I$  phase and form a dendritic rosette shape which is distributed mostly at the  $\alpha/\beta$  boundaries;  $\kappa_{III}$  phase is a fine lamellar “finger-like” eutectoid structure, forms at the boundary of  $\kappa_I$  phase and is rich in Ni, and  $\kappa_{IV}$  phase is a fine Fe-rich cruciform-

**Fig. 2** Microstructural morphology of Cu3 cast-NAB at a magnification of 100x.  $\kappa_{II}$  is the globular dendritic structure,  $\kappa_{III}$  is the lamellar “finger-like” structure and  $\kappa_{IV}$  is the very fine particulate imbedded within the alpha matrix (surrounding phase)



shaped precipitation of varying sizes with plate-like morphology that are distributed throughout the  $\alpha$  grains along certain crystallographic directions forming within the  $\alpha$  matrix beginning at 850 C[26, 28–30]. The  $\kappa_I$  and  $\kappa_{II}$  precipitates in the samples used for the experiment were found to be between 5 and 10  $\mu\text{m}$  and around 2  $\mu\text{m}$  in size, respectively. Figure 2 shows the SEM morphology of the NAB microstructure used in the experiment.

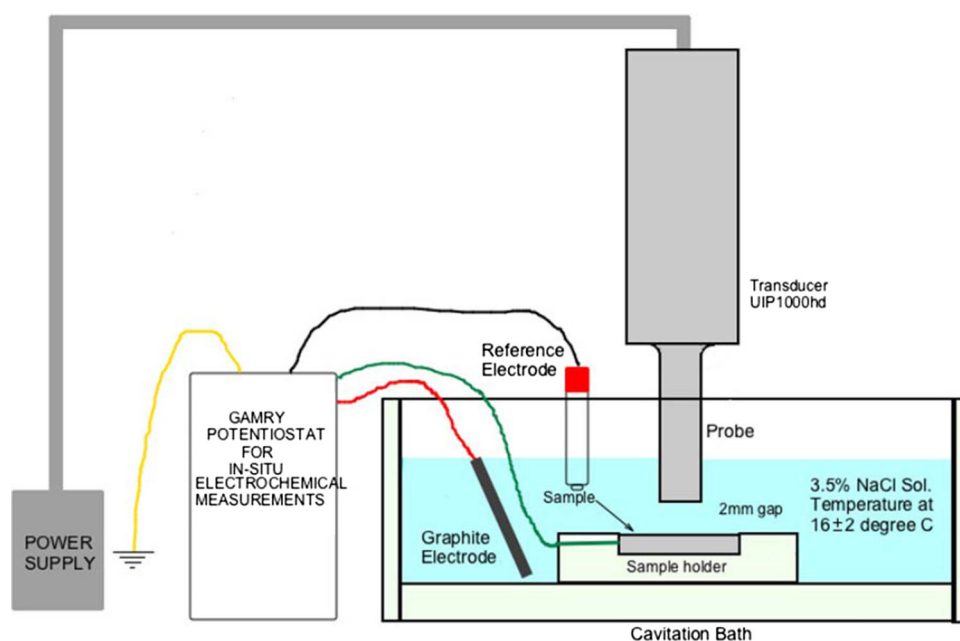
## 2.2 Cavitation Erosion Measurements

The first test conducted was the pure erosion test. The samples were cavitated in 5 L of stagnant distilled water for 1 h at a frequency of 20 kHz and a peak-to-peak amplitude of 80 micron. The samples were kept at a constant distance of 2 mm away from the sonotrode tip. The temperature and pH of the water were monitored before and after the experiment, starting from room temperature and a pH of 8.9. Weight of the sample was recorded both before and after each experiment with a precision weighing machine. The samples were then analysed under Alicona and Talysurf to obtain the surface roughness, maximum depth of penetration, volume loss and the subsequent volumetric mass loss incurred.

## 2.3 Electrochemical Measurements

For the erosion-corrosion test the samples were cavitated in 5 litres of 3.5 % NaCl salt water while kept under OCP for 1 hour with exactly the same electrochemical arrangements as for pure corrosion (as shown in Fig. 3). The samples were kept at OCP for 1 h in 5 L of 3.5 % NaCl solution where Ag/AgCl was used as the reference electrode, sample as the working electrode and graphite rod as the counter electrode.

**Fig. 3** Schematics of the cavitation rig with specimen under cavitation erosion–corrosion



For the erosion–corrosion test, the samples were cavitated in 5 L of 3.5 % NaCl salt water while kept under OCP for 1 h with exactly the same electrochemical arrangements as for pure corrosion (as shown in Fig. 3). The corrosion test preceded cavitation test by 10 min, and after 10 min the cavitation rig was switched on. The nature and properties of the sample materials as well as the corrosion products, formed in a corrosive environment, and the effects of cavitation determine the behaviour of the sample alloys as well as help characterize them.

### 3 Results and Discussions

For the erosion and erosion-corrosion test the concentric rings of cavitated and non-cavitated regions were formed around a centrally damaged area. This phenomenon could be attributed to the natural resonant frequency of the probe and probe tip itself. The total cavitated diameter was measured to be 15 mm across for both the materials as can be seen in Fig. 4. There was a gradual increase in the temperature of the liquid medium from 16–17 °C to 22 °C after cavitation; however, pH remained almost the same throughout the entirety of the experiments, i.e. between 8.5 and 9. This temperature rise could help enhance electrochemical reaction on the samples.

#### 3.1 Surface Profilometry and Morphology

The surface profilometry and average roughness ( $R_a$ ) and MDP of each sample after each test were measured using Alicona and Talysurf. Figure 5 shows the surface

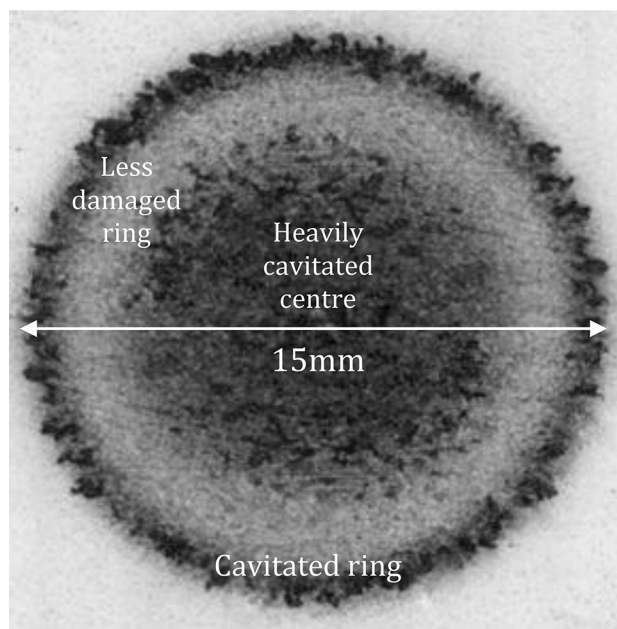


**Fig. 4** The cavitated surface of DSS

roughness and individually labelled damage regions of DSS sample after undergoing cavitation in distilled water obtained using Talysurf, which was employed to obtain the surface roughness across the diameter of the samples.

Alicona was also employed to measure the volume loss for each sample post cavitation. Table 3 tabulates the measured values of  $R_a$ , MDP and volume loss for NAB and DSS under each condition.

The SEM morphologies of NAB and DSS under distilled water as well as 3.5 % NaCl solution are shown in Fig. 6.



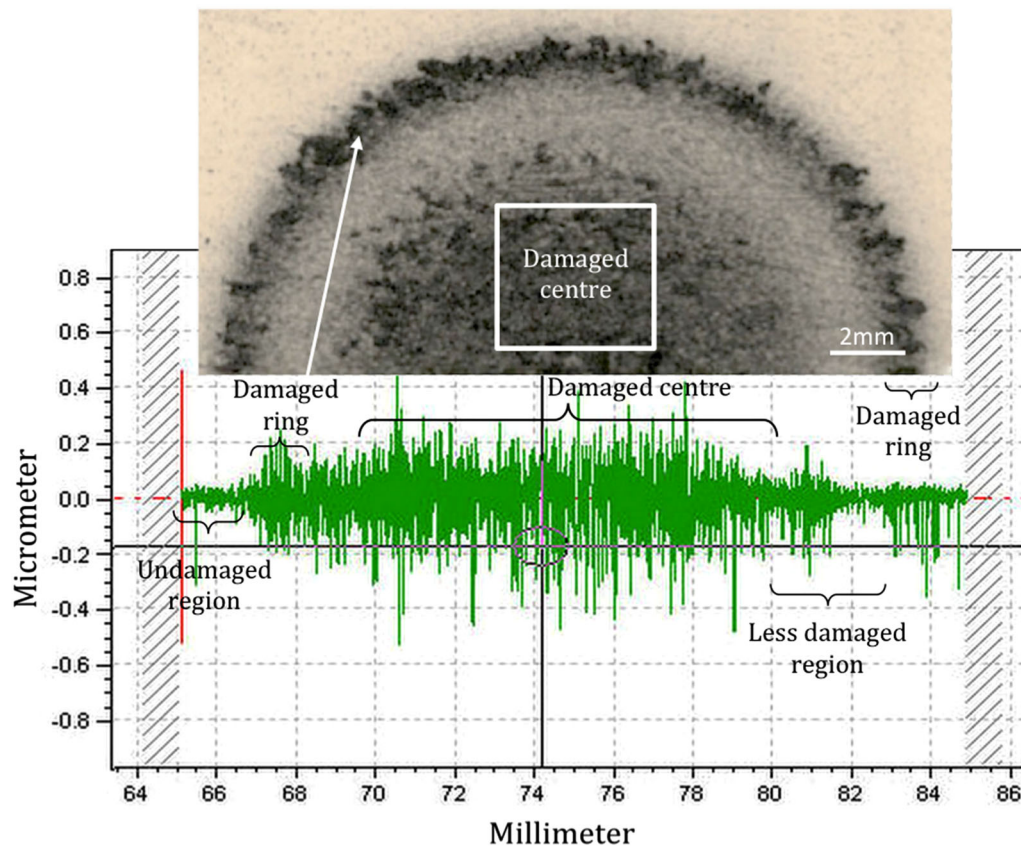


**Fig. 5** Talysurf surface roughness profilometry at the centre of the cavitated surface of DSS in distilled water

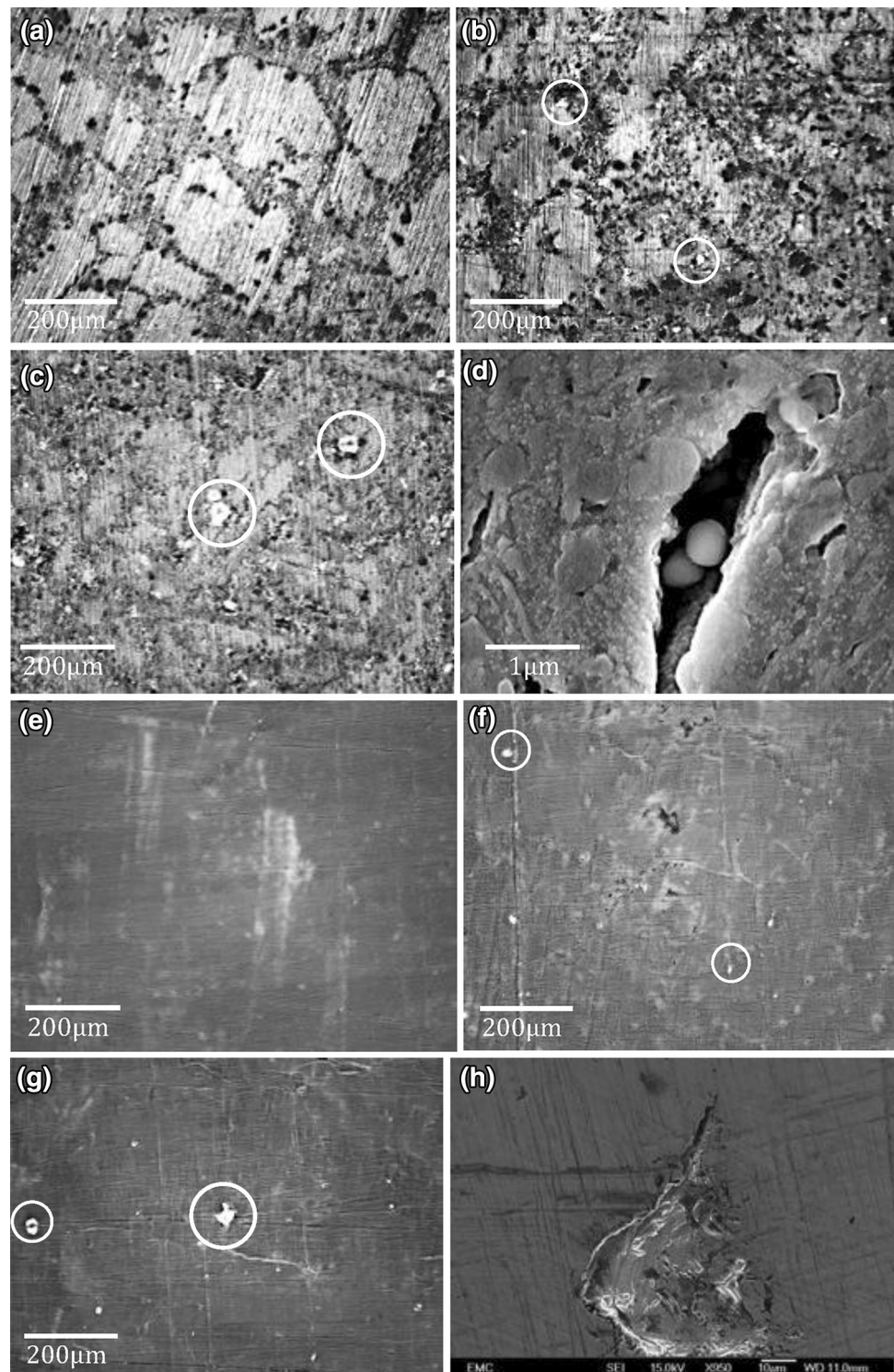
**Table 3** Average roughness, mean depth of penetration and volume loss measured using Alicona

Material used	Average surface roughness (nm)			Mean depth of penetration (nm)		Measured volume loss (mm <sup>3</sup> )	
	Uncavitated surface	Distilled water	3.5 % NaCl sol.	Distilled water	3.5 % NaCl sol.	Distilled water	3.5 % NaCl sol.
Nickel aluminium Bronze	49	153	165	645	955	0.115	0.169
Duplex stainless Steel	52	113	163	460	598	0.081	0.106

Figure 6a, e shows the general microstructures of NAB and DSS, respectively, where Fig. 6a exhibits the lighter  $\alpha$  phase with dark dendritic intermetallic kappa phases distributed in the copper-rich  $\alpha$  matrix and many visible Fe-rich  $\kappa_I$  and  $\kappa_{II}$  precipitates around the boundaries. Interfaces between the matrix, intermetallic and grain boundaries are generally the weak points in the microstructure of metallic materials that are more likely to be attacked by the cavitation. Figure 6b shows the morphology of NAB under cavitation in distilled water. Small cavities of sizes 10–30  $\mu\text{m}$  were found especially in grain boundaries as it was established that the material surface underwent selective cavitation at the  $\alpha$ - $\kappa$  phase boundaries. The  $\kappa$  precipitates and precipitate-free  $\alpha$  zones did not suffer any visible cavitation after 1 h of cavitation test in distilled water. For the cavitation erosion–corrosion test, the

cavities were recorded to be much larger, 50–80  $\mu\text{m}$ , and the sample surface had visible corrosion products. Figure 6d is the magnified (20,000 $\times$ ) image of one of the cavities on NAB tested under 3.5 % NaCl salt solution with spheres of silicon and aluminium oxides visible in the cavity. Large cavity was observed with globules of oxides formed in these cavities along with ductile tearing and corrosion of the boundaries of the  $\alpha$  columnar grains as seen in Figure 6d. Many factors could cause the results obtained such as the softer composition of the cu-rich  $\alpha$  phase as compared to much harder iron-rich intermetallic precipitates; it could be expected for the  $\alpha$  phase to be more susceptible to cavitation erosion. There were also grain-boundary attacks observed which could indicate that electrochemical dissolution within the structure may contribute in the cavitation damage. Another reason for the selective

**Fig. 6** **a** General microstructure of NAB at  $\times 100$  magnification, **b** cavitated region of NAB under distilled water after 1 h of exposure, **c** cavitated region of NAB under 3.5 % NaCl solution, **d**  $\times 20,000$  magnified cavitated region of NAB; **e** general microstructure of DSS, **f** cavitated region of DSS under distilled water after 1 h of exposure, **g** cavitated region of DSS under 3.5 % NaCl solution, **h**  $\times 960$  magnified cavitated region of DSS in 3.5 % NaCl solution



attack may be due to the cathodic behaviour of Fe-rich phase when compared with the  $\alpha$  phase which may induce galvanic corrosion. This conclusion is found consistent with the findings of previous works [26, 31–33].

As for DSS, the morphologies of DSS under both distilled water and salt solution were almost same with no

visible corrosion product. However, on comparing the cavity sizes, the cavities under 3.5 % salt solution were almost five times the size of that under distilled water, see Fig. 6f, g. On taking a closer look under SEM, it was seen that the cavitation attack was rather selective, with cavities attacking the ferritic matrix and the ferrite–austenite

boundaries. Figure 6h shows a  $40 \times 70\text{-}\mu\text{m}$ -large cavity formed in DSS under the salt solution where ductile failure can be seen in the form of extrusion of the austenite at the cavity boundary visible in Fig. 7. Also visible are tiny microcracks and cleavage-like facets that may have been caused by the austenite-to-martensite transformation either due to high strain or due to the high temperature accredited to cavitation. This result holds consistent with the findings of the study by Al-Hashem and Riad [34].

### 3.2 Electrochemical Results

Figure 8 is the OCP curve obtained for DSS and NAB in pure corrosion and erosion–corrosion in 3.5 % NaCl solution. All the tests were conducted for 1 h. For the cavitation erosion–corrosion tests, the cavitation rig was switched on after 600 s to obtain the change in the

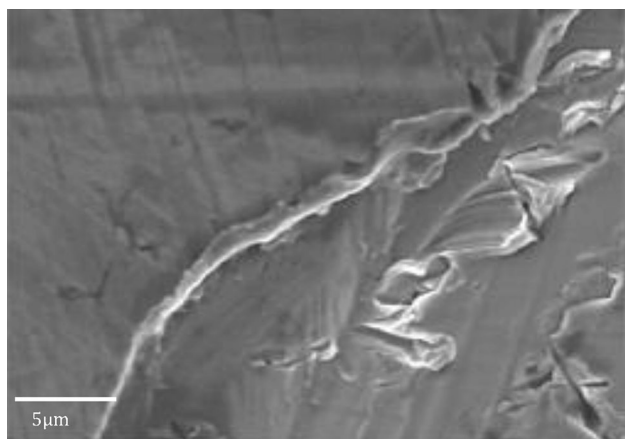


**Fig. 7** SEM images of plastic deformation at cavitation-damaged edge for DSS in distilled water

electrochemical behaviour of the sample materials. As can be seen from the trend, there was a negative shift of OCP from  $-70$  to  $-500$  mV. However, DSS was seen to attain stability within 10 min at a lower voltage, and this OCP shift can be attributed to the result of protective oxide layer destroyed by cavitation erosion. Similarly, the trend for NAB shifted to negative when the rig was turned on, but it attained stability much quicker than DSS (within 100 s) at a lower potential than that under pure corrosion. On comparing the OCP trend of the two materials when undergoing cavitation, it can be seen that while NAB reaches stability at  $-210$  mV at a lower voltage as compared to DSS, the stability of DSS attained after the rig is switched on is much lower than that of NAB showing that NAB has higher corrosion resistance than DSS. Similar to the results observed by Al-Hashem et al. [24], there was a shift in corrosion potential for DSS under cavitation in the active direction by 75 mV; however, there was not a very substantial shift in case of NAB. This may be due to the experimental reproducibility since several tests were conducted giving similar results.

Figure 9 shows the electrochemical impedance spectra (EIS) graph for the DSS and NAB samples with and without cavitation. From the figure, it can be seen that both the samples show very good resistance to corrosion both with and without cavitation. Although it is clear that the impedance was higher for DSS in saltwater alone without cavitation as compared to DSS undergoing cavitation erosion–corrosion, it was seen that the impedance of NAB under corrosion was slightly lower than that under cavitation erosion–corrosion. The reason for the high resistance to corrosion may be explained from Fig. 10a, b, where it can be seen that a high percentage of chromium was present in the chemical composition of DSS, and also a high

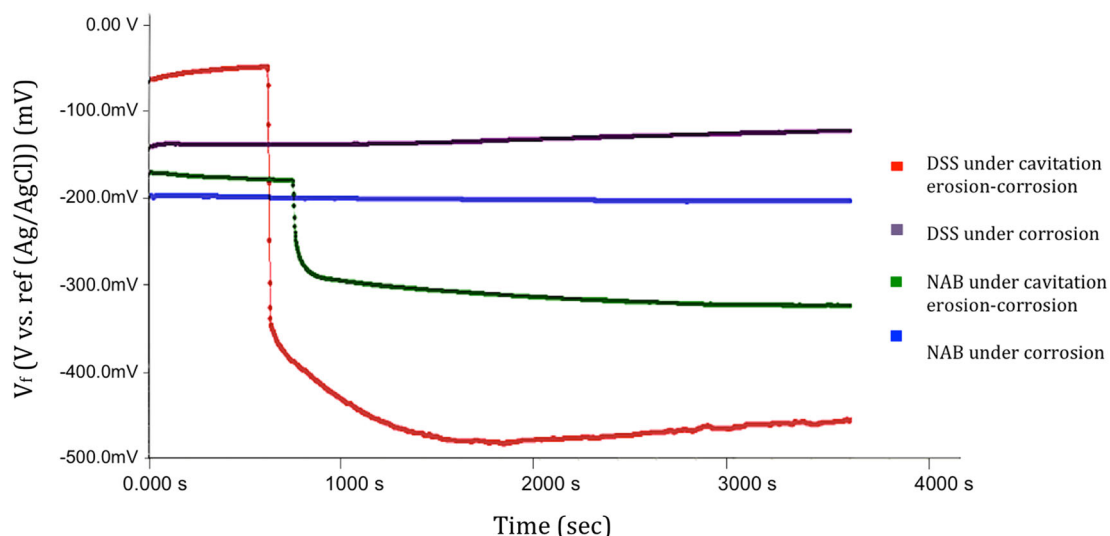


**Fig. 8** OCP for DSS and NAB in 3.5 % NaCl solution for 1 h with and without cavitation



percentage of silicon and aluminium oxides were formed on the surface of NAB. However, while DSS is highly corrosion resistant with a passive layer of iron oxide as well as chromium oxide forming to protect the surface from corrosion, the film thickness is in the range of 2 nm

[35]; whereas a passive layer of oxides forms in case of NAB that has a film thickness of 900–1000 nm [36]; this was further verified on taking EDX spectrum of cavitated NAB surface under distilled as well as 3.5 % NaCl solution, which indicated the presence of silicon ( $\text{SiO}_2$ ) and

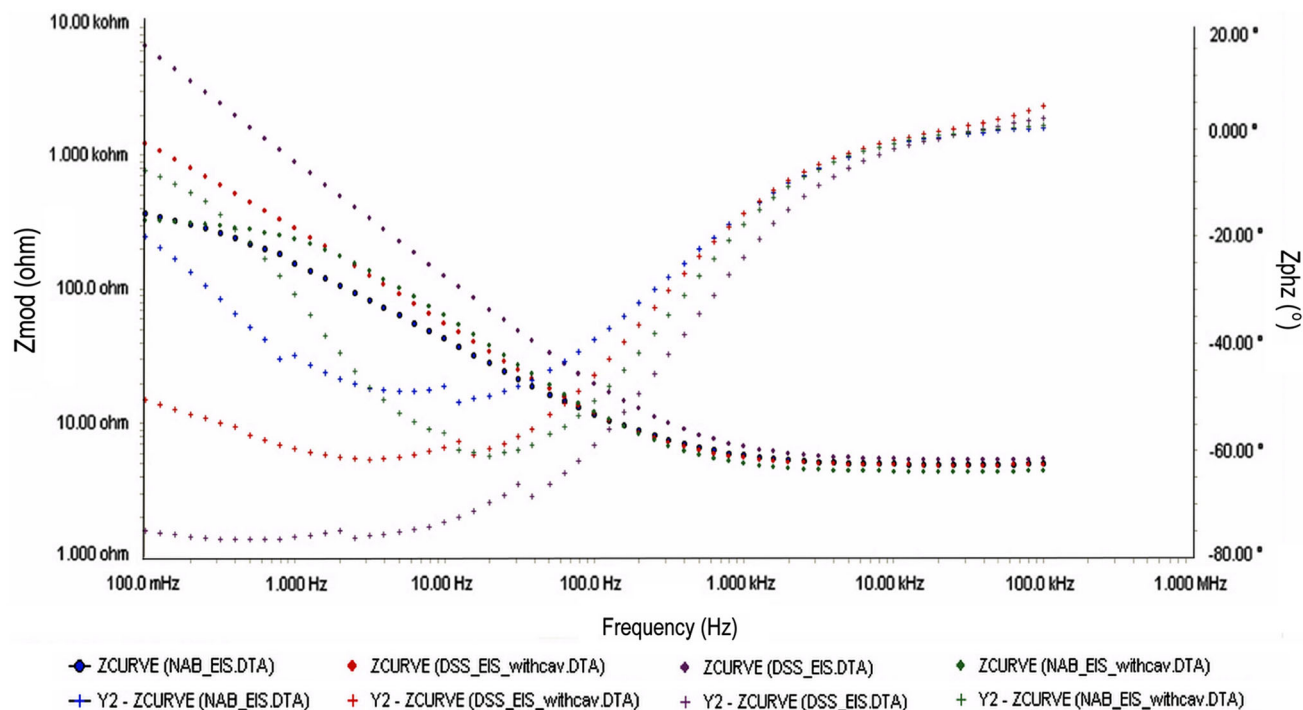


**Fig. 9** EIS for DSS and NAB in 3.5 % NaCl solution with and without cavitation

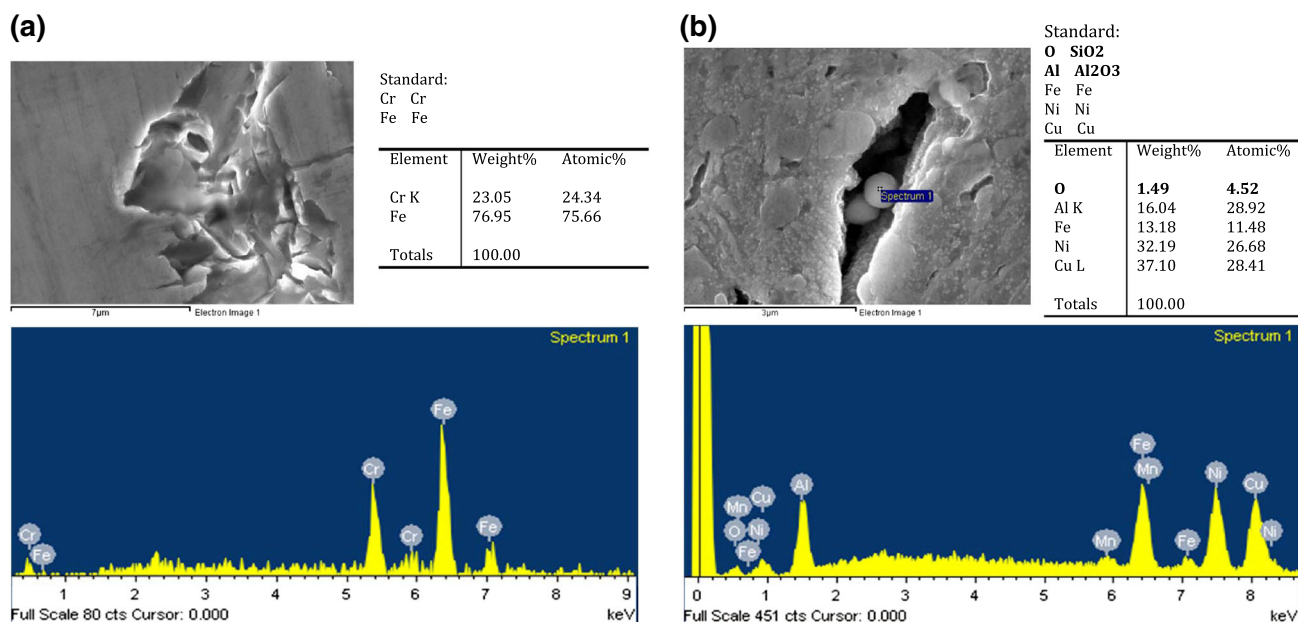


**Fig. 10** EDS spectrum of **a** DSS cavitated under 3.5 % NaCl solution and **b** NAB cavitated under 3.5 % NaCl solution

aluminium oxides ( $\text{Al}_2\text{O}_3$ ), see Fig. 10b. These may account for the high corrosion resistance of both the material samples used.

### 3.3 Synergy Calculation

From Table 3, the value of volumetric mass loss for each sample was extracted using the simple mass, volume and density formula:

$$\text{Density} = \text{mass/volume}, \quad (3)$$

where density of NAB =  $7.65 \text{ g/cm}^3$  and density of DSS =  $7.8 \text{ g/cm}^3$ . Hence, the following values are tabulated in Table 4 in order to compare the mass loss obtained using precision weighing machine and Alicona. The mass change observed during pure corrosion was mass gain rather than mass loss, hence it is considered negative since mass loss is considered positive.

From the pure corrosion measurements shown in Table 4 and Eq. 3, the thickness of the passive layer formed on the sample surface was calculated. The oxide layers consisting predominant of  $\text{Al}_2\text{O}_3$  in case of NAB and  $\text{Cr}_2\text{O}_3$  in case of DSS were found to be of thickness  $0.24 \mu\text{m}$  and  $0.03 \mu\text{m}$ , respectively.

Using Eqs. 1 and 2, and considering the values of gravimetric mass loss from Table 4, the synergy can be calculated and the values are tabulated in Table 5.

### 3.4 Discussion

It can be seen from Table 5 that for both NAB and DSS synergy has measurable impact on their cavitation erosion–corrosion. While the synergy between cavitation erosion and corrosion for NAB was found to be 73.6 %, it is almost half in case of DSS at 36.5 %, with  $\Delta C$  (erosion-enhanced corrosion) dominating the synergy result for both cases. These values are in general much higher when compared

with the synergy results obtained by other studies. The study by Neville, Hodgkiess and Dallas [37] found the synergy for 2205 DSS eroded under liquid–solid jet impingement under saline solution to be about 20 %, whereas the vibratory cavitation as well as hydrodynamic cavitation erosion–corrosion synergy tests conducted by Wood and Hutton [38] showed  $S/T$  % values to be in the range of 30% to >60 % for various materials tested under 3 % NaCl solution such as grey cast iron, 1020 mild steel, 304 SS and copper alloys. Several engineering alloys tested in 3.5 % NaCl solution by Kwok et al. [39] showed very low (negligible)  $S/T$  % of damage for corrosion-resistant materials such as 316 SS, 304 SS and Zeron 100 super DSS. However, it must be noted that these studies were carried out with varying conditions, and also most of these studies considered rate of depth of penetration as their means of calculating synergy.

One reason for the existence of synergy could be due to the difference in the quantity of dissolved gases present in each medium. While 3.5 % NaCl solution may have higher amount of dissolved oxygen, it also has dissolved minerals and radicals among other such factors that can affect the bubble nucleation, growth and impact. Distilled water is considered to have negligible amount of dissolved minerals, and hence cavitation impact and results obtained in distilled water can vary significantly from that in 3.5 % NaCl solution. Also, few anomalies may exist due to certain assumptions made during the experiment such as, the erosion test without any external electrochemical application was considered as pure erosion test; however, there was still a small level of corrosion taking place in the form of passivity of the individual materials itself. This alone may explain the difference in the mass change between the two materials for pure erosion test when comparing gravimetric with volumetric analyses. One way of immunizing the material from any corrosion could be by using the pH of the solution to move the material to immune section of pourbaix diagram in order to protect it from

**Table 4** Comparison between gravimetric mass loss and volumetric mass loss

Material used	In distilled water cavitation erosion loss (E)		In 3.5 % NaCl solution cavitation erosion–corrosion loss (T)		Pure corrosion mass gain (C) (mg)
	Gravimetric mass loss (in mg)	Volumetric mass loss (in mg)	Gravimetric mass loss (in mg)	Volumetric mass loss (in mg)	
Nickel aluminium bronze	1.00	0.88	1.48	1.29	−0.61
Duplex stainless steel	0.71	0.63	0.96	0.82	−0.10

**Table 5** Synergism summary for the samples

Material used	T (mg)	E (mg)	C (mg)	$S = T - (E + C)$ (mg)	$(S/T) \times 100$ (%)
Nickel aluminium bronze	1.48	1.00	−0.61	1.09	73.6
Duplex stainless steel	0.96	0.71	−0.10	0.35	36.5

corrosion. Also, instead of using distilled water, cathodic protection can also be employed to prevent the samples from corrosion; however, while cathodic protection can prevent corrosion, it is difficult to suppress corrosion and hydrogen evolution simultaneously as also explained by Kwok et al. [39]. Hydrogen could cause embrittlement in stainless steels, but it may also exert a cushioning effect, reducing mechanical erosion, and this may potentially increase the relative contribution of synergism.

For the synergy result, gravimetric mass loss values were considered due to the reason that, although both gravimetric as well as volumetric mass loss measurements are useful and efficient in their own account, they both have major shortcomings. While the data obtained using precision weighing machine can be considered accurate, several factors may affect the results, such as sediments of eroded titanium probe tip deposited on the sample, dissolved NaCl salt deposits and absorption of water by porous layers/coats if any, as well as other impurities that cannot be detected and fully prevented. Also, as the samples are introduced to a corrosive environment, if they are highly corrosive and form corrosion product immediately after erosion, it is hard to tell how much mass is actually lost accurately. The mass balance does not take into account these factors, and this could cause deviation in the final result. On the other hand, volumetric analyses using Alicona can be equally crude since the highest magnification achievable using Alicona is 100 $\times$ , which may sometimes cause loss of data while looking at very smooth and reflective surface, or due to re-entrant topography of the surface. Also, in case that there are sediments, corrosion products, micro scratches and burrs existing on the sample surface, Alicona cannot differentiate and do selective volume loss, which again causes deviation from the result. It may also manifest its own roughness and waviness of the surface when using lower magnification or highly reflective surface, which was applicable for the experiments undertaken. Due to this, gravimetric analyses were slightly more preferable.

#### 4 Conclusion

From the experiments conducted, it can be concluded that after a short period of exposure to cavitation both NAB and DSS have measurably high synergistic effect under cavitation erosion–corrosion. In the case of NAB, the synergy between cavitation wear and corrosion was found to be 73.6 % and for DSS it was found to be 36.5 %. The data obtained from electrochemical measurement for the cavitation erosion–corrosion test showed that, although duplex SS exhibited higher resistance to corrosion under seawater alone, NAB exhibited much higher resistance to corrosion when subjected to cavitation. Also, NAB attained

stability much faster and at higher potential than DSS, proving that it is more corrosion resistant.

The NAB surface was seen to undergo selective cavitation erosion–corrosion attack at the  $\alpha$  phase and the  $\alpha$ - $\kappa$  phase boundaries with ductile deformation around the cavity, while the  $\kappa$  precipitates and precipitate-free  $\alpha$  zones were found to suffer no visible cavitation after 1 h of cavitation test in both distilled water as well as 3.5 % NaCl. The DSS was seen to undergo ductile failure in the cavitated zone in the form of extrusion of the austenite at the cavitation pit along with microcracks and cleavage facets that could be attributed to the austenite-to-martensite transformation by either the high strain rate or high temperatures generated during cavitation. And because of that the erosion process was found to be predominantly of plastic nature with little of no fatigue failure noticed at this stage, due to this NAB was found to be more susceptible to erosion under both the conditions as compared to duplex SS with prominent selective cavitation erosion of alpha phase in the microstructure since DSS is harder than NAB. From the experiments conducted, it was concluded that synergy had measurable impact on the cavitation erosion–corrosion of both NAB and duplex SS, and the overall synergy for NAB was found to be higher than that for DSS.

**Conflict of interest** None.

#### References

1. Vyas B, Hansson ILH (1990) The cavitation erosion-corrosion of stainless steel. *Corros Sci* 30(8): 761–770
2. Engelberg G, Yahalom J, Kalir E (1985) Observations on the cavitation of steels. *Corros Sci* 25(10) 871–882
3. Tomlinson WJ, Talks MG (1991) Erosion and corrosion of cast iron under cavitation conditions. *Tribol Int* 24:67
4. Wood RJK, Fry SA (1989) The synergistic effect of cavitation erosion and corrosion for copper and Cupro-Nickel in seawater. *J Fluids Eng* 111(3):271
5. Kwok C, Man H, Cheng F (1998) Cavitation erosion and damage mechanisms of alloys with duplex structures. *Mater Sci Eng A* 242(1–2):108–120
6. Kwok CT, Man HC, Cheng FT (1998) Cavitation erosion of duplex and super duplex stainless steels. *Scr Mater* 39(9): 1229–1236
7. Zheng Y, Luo S, Ke W (2007) Effect of passivity on electrochemical corrosion behavior of alloys during cavitation in aqueous solutions. *Wear* 262(11–12):1308–1314
8. Kwok CT, Man HC, Leung LK (1997) Effect of temperature, pH and sulphide on the cavitation erosion behaviour of super duplex stainless steel. *Wear* 211(1):84–93
9. Luo SZ, Zheng YG, Li MC, Yao ZM, Ke W (2003) Effect of cavitation on corrosion behavior of 20SiMn low-alloy steel in 3% sodium chloride solution. *Corrosion* 59(7):597–605
10. Kwok C, Cheng F, Man H (2000) Synergistic effect of cavitation erosion and corrosion of various engineering alloys in 3.5% NaCl solution. *Mater Sci Eng A* <http://linkinghub.elsevier.com/retrieve/pii/S0921509300008996>

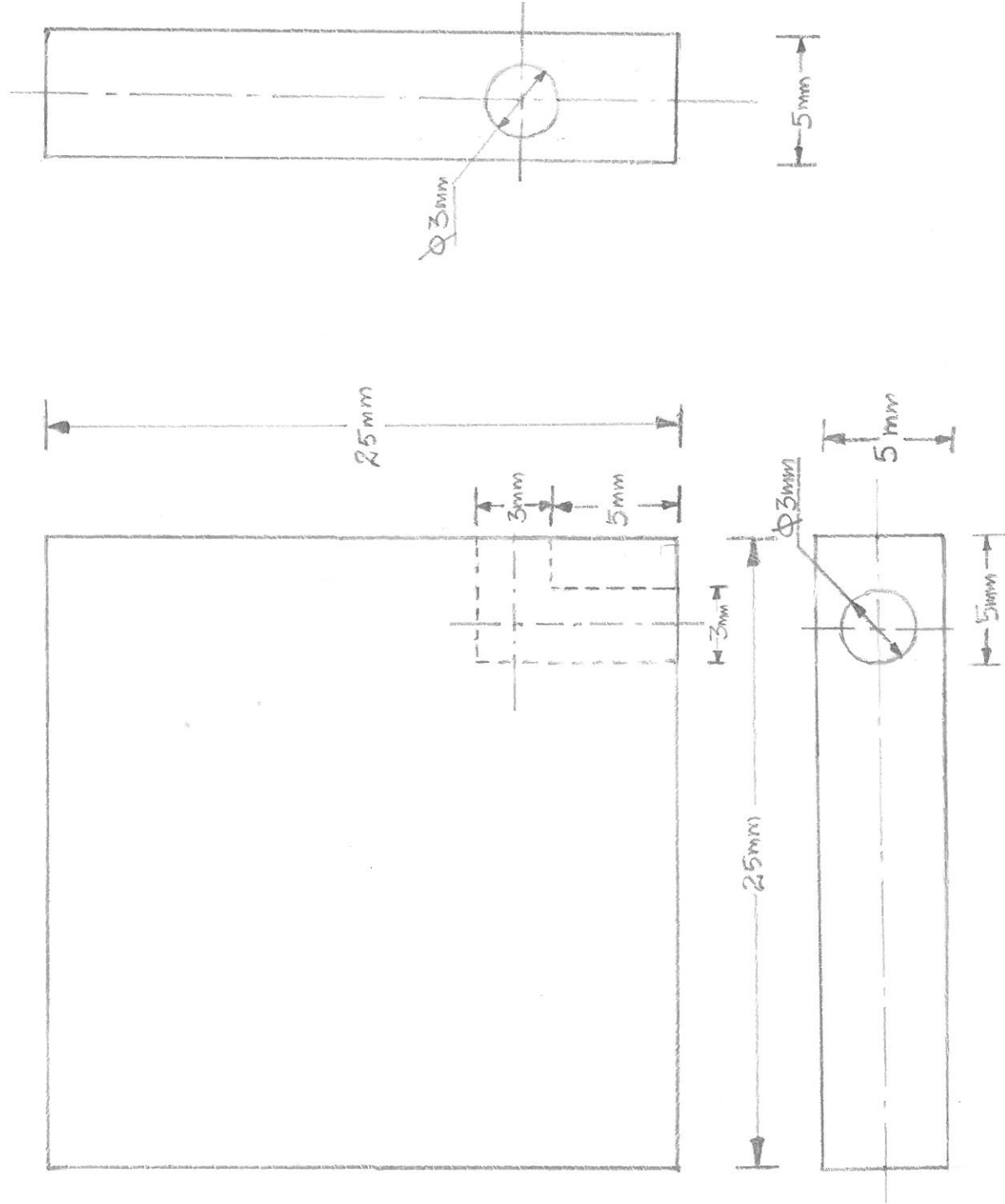
11. Yu H, Zheng YG, Yao ZM (2006) The cavitation erosion and erosion-corrosion behavior of carbon steel in simulating solutions of three rivers of China. *Mater Corros* 57(9):705–714
12. Sakamoto A, Funaki H, Matsumura M (2000) Seminar influence of galvanic macro-cell corrosion on the cavitation erosion durability. *Int cavitation Eros test Semin*
13. Thiruvengadam A, Waring SJ (1966) Mechanical properties of metals and their cavitation damage resistance. *J Ship Res* 10:1–9
14. Kwok C, Man H, Cheng F (2001) Cavitation erosion–corrosion behaviour of laser surface alloyed AISI 1050 mild steel using NiCrSiB. *Mater Sci Eng A* 303(1–2):250–261
15. Kwok CT, Cheng FT, Man HC Cavitation erosion and corrosion behaviors of laser-aluminized mild steel. *Surf Coat Technol* 200(11):3544–3552
16. Man HC, Kwok CT, Yue TM (2000) Cavitation erosion and corrosion behaviour of laser surface alloyed MMC of SiC and Si3N4 on Al alloy AA6061. *Surf Coat Technol* 132(1):11–20
17. Kwok C, Man H, Cheng F (2000) Cavitation erosion and pitting corrosion behaviour of laser surface-melted martensitic stainless steel UNS S42000. *Surf Coat Technol* 126(2–3):238–255
18. Kwok CT, Man HC, Cheng FT (1998) Cavitation erosion and pitting corrosion of laser surface melted stainless steels. *Surf Coat Technol* 99(3):295–304
19. Shifler DA (2005) Understanding material interactions in marine environments to promote extended structural life. *Corros Sci* 47(10):2335–2352
20. Stack MM, Jana BD (2004) Modelling particulate erosion–corrosion in aqueous slurries: some views on the construction of erosion–corrosion maps for a range of pure metals. *Wear* 256(9–10):986–1004
21. Stack MM, Corlett N, Zhou S (1997) A methodology for the construction of the erosion–corrosion map in aqueous environments. *Wear* 203:474–488
22. Wood RJK (2006) Erosion–corrosion interactions and their effect on marine and offshore materials. *Wear* 261(9):1012–1023
23. Richman RH, McNaughton WP (1990) Correlation of cavitation properties of metals erosion behavior with mechanical. *Wear* 140:63–82
24. Al-Hashem A, Caceres PG, Abdullah A, Shalaby HM (1997) Cavitation corrosion of duplex stainless steel in Seawater. *Corrosion* 53(2):103–113
25. Al-Hashem A, Caceres PG, Riad WT, Shalaby HM (1995) Cavitation corrosion behavior of cast nickel-aluminum bronze in seawater. *Corrosion* 51(5):331–342
26. Al-Hashem A, Riad W (2002) The role of microstructure of nickel–aluminium–bronze alloy on its cavitation corrosion behavior in natural seawater. *Mater Charact* 48(1):37–41
27. Duplex stainless steel *IMOA* (2013). [http://www.imoa.info/moly\\_uses/moly\\_grade\\_stainless\\_steels/duplex\\_stainless\\_steel.php](http://www.imoa.info/moly_uses/moly_grade_stainless_steels/duplex_stainless_steel.php). Accessed 28 Aug 2013
28. Culpan EA, Rose G (1978) Microstructural characterization of cast nickel aluminium bronze. *J Mater Sci* 13(8):1647–1657
29. Hasan F, Iqbal J, Ridley N (1985) Microstructure of as-cast aluminium bronze containing iron. *Mater Sci Technol* 1(4):312–315
30. Faires KB (2003) Characterization of microstructure and microtexture in longitudinal sections from friction stir processed nickel-aluminum bronze. North Carolina State University
31. Takaloo AV, Daroonparvar MR, Atabaki MM, Mokhtar K (2011) Corrosion behavior of heat treated nickel-aluminum bronze alloy in artificial seawater. *Mater Sci Appl* 02(11):1542–1555
32. Lorimer GW, Hasan F, Iqbal J, Ridley N (1986) Observation of microstructure and corrosion behaviour of some aluminium bronzes. *Br Corros J* 21(4):244–248
33. Culpan EA, Rose G (1979) Corrosion behaviour of cast nickel aluminium bronze in sea water. *Br Corros J* 14(3):160–166
34. Al-Hashem A, Riad W (2002) The effect of duplex stainless steel microstructure on its cavitation morphology in seawater. *Mater Charact* 47(2001):389–395
35. Fredriksson W (2012) Depth Profiling of the Passive Layer on Stainless Steel using Photoelectron Spectroscopy. Uppsala Universitet
36. Daroonparvar A, Atabaki MR, Mazar, Vakilipour M (2011) Effect of pre-heat treatment on corrosion behaviour of nickel-aluminium bronze alloy. *Assoc Metall Eng Serbia* 17(4):183–198
37. Neville A, Hodgkiess T, Dallas JT (1995) A study of the erosion–corrosion behaviour of engineering steels for marine pumping applications. *Wear* 186:497–507
38. Wood RJK, Hutton SP (1990) The synergistic effect of erosion and corrosion: published results
39. Kwok C, Cheng F, Man H (2000) Synergistic effect of cavitation erosion and corrosion of various engineering alloys in 3.5% NaCl solution. *Mater Sci Eng A* 290(1):145–154

# Appendix E

---

Drawing 1





- 1) Drill holes of diameter 3mm each.
- 2) The drill holes must open at a certain depth.
- 3) The longer drill hole must be threaded to be able to insert a socket set screw of diameter M3.